Cold Dwell Fatigue of Titanium Alloys: History, Current State, and Aviation Industry Perspective

September 2024

Final report

U.S. Department of Transportation
Federal Aviation Administration

NOTICE

Form DOT F 1700.7 (8-72)   Reproduction of completed page authorized

1. Report No. DOT/FAA/TC-23/40	2. Government Accession No.	3. Recipient's Catalog No.
4. Title and Subtitle Cold Dwell Fatigue of Titanium Alloys: History, Current State, and Aviation Industry Perspective		5. Report Date September 2024
		6. Performing Organization Code
7. Author(s) Adam Pilchak[1,2], Kate Fox[3], Eric Payton[4], Mirjam Wiedemann[5], Tom Broderick[6,7], Pierre Delaleau[8], Michael Glavicic[9], Nigel Jenkins[10], Jean-Manuel Ruppert[11], Brian Streich[12], Masayuki Tsukada[13], Vasisht Venkatesh[1], Andy Woodfield[14]		8. Performing Organization Report No.
9. Performing Organization Name and Address [1]Pratt & Whitney, East Hartford, CT; [2]Materials Resources LLC, Xenia, OHM; [3]Rolls Royce, plc, Derby UK, [4]University of Cincinnati, Cincinnati, OH; [5]MTU Aero Engines, Munich, Germany; [6]Air Force Research Laboratory, Wright Patterson AFB, OH; [7]Federal Aviation Administration, ; [8]Safran Aircraft Engines, Colombes, France; [9]Rolls-Royce Corp., Indianapolis IN, [10]Pratt & Whitney Canada, Ontario, CA; [11]Safran Helicopter Engines, Bordes, France; [12]Honeywell Aerospace, Phoenix, AZ; [13]IHI Corp. Tokyo, Japan; [14]GE Aerospace, Cincinnati, OH	10. Work Unit No. (TRAIS)	
	11. Contract or Grant No. 692M15-22-P-00018	
12. Sponsoring Agency Name and Address Federal Aviation Administration, William J. Hughes Technical Center Aviation Research Division, Atlantic City International Airport New Jersey, 08405	13. Type of Report and Period Covered Final Report, March 2022-April 2023	
	14. Sponsoring Agency Code	
15. Supplementary Notes		

16. Abstract

This report summarizes the current state of understanding related to cold dwell fatigue (CDF) of titanium alloys, which is a failure mechanism that can lead to uncontained failure of rotating components. Jet engine manufacturers have brought forward their collective field and spin rig experience related to CDF and coupled it with a thorough literature review to offer an aviation industry perspective on this critical safety issue. Numerous factors are known to influence susceptibility to CDF including intrinsic factors like alloy composition, microstructure, and residual stress as well as extrinsic factors like applied stress, dwell time, and temperature. Of particular importance is the presence of microtextured regions (MTRs) present in the material. Definitions and best practices for characterizing this microstructural feature are proposed. The mechanisms of damage accumulation, early crack nucleation, and rapid crack propagation through MTRs during CDF are reviewed along with additional effects of microtexture on material properties including conventional fatigue, sustained load cracking, and stress corrosion cracking. The microstructural condition of finished components depends on the details of billet processing, component forging, and heat treatment practice. The mechanisms of microstructure evolution at each step of the process are summarized and directional guidance is given relative to important factors controlling MTR and alpha colony formation. Laboratory coupon testing, accelerated tests for dwell sensitivity, and aspects of specimen versus component behavior are discussed. Multiple pathways that lead to CDF failure are summarized and strategies to mitigate the risk of CDF are highlighted including aspects of alloy composition, processing/microstructure relationships, design, and nondestructive inspection. This report concludes with identification of directions for further research. Several appendices are provided which summarize major research programs related to CDF and additional methods to characterize MTRs using destructive and nondestructive evaluations methods.

17. Key Words Titanium, Cold Dwell Fatigue, Fatigue, Thermomechanical Processing, Microtextured Regions, Macrozones, Dwell Debit, Mechanical Properties, Spin Rig Testing, Electron Backscatter Diffraction	18. Distribution Statement This document is available to the U.S. public through the National Technical Information Service (NTIS), Springfield, Virginia 22161. This document is also available from the Federal Aviation Administration William J. Hughes Technical Center at actlibrary.tc.faa.gov.		
19. Security Classif. (of this report) Unclassified	20. Security Classif. (of this page) Unclassified	21. No. of Pages 357	19. Security Classif. (of this report) Unclassified

Acknowledgements

Contents

Figures

Tables

Acronyms

Acronym	Definition
AIPT	Activity Integrated Project Team
AFRL	Air Force Research Laboratory
ASTM	American Society for Testing and Materials
BCC	Body centered cubic
BOR	Burgers orientation relationship
CDF	Cold dwell fatigue
CPCI	Crystallographic polarization classification imaging
CPFEM	Crystal plasticity finite element method
CRSS	Critical resolved shear stress
DIC	Digital image correlation
DREAM.3D	Digital Representation Environment for the Analysis of Microstructure in 3D
EBSD	Electron backscatter diffraction
ECI	Eddy current inspection
FAA	Federal Aviation Administration
FBH	Flat bottom hole
FEA	Finite element analysis
FPI	Fluorescent penetrant inspection
GE	General Electric
GFM	General forging machine or gyrational forging machine
GPD	Generalized Pareto distribution
HCF	High cycle fatigue
HCP	Hexagonal close packed
IPF	Inverse pole figure
JETQC	Jet Engine Titanium Quality Committee
LCF	Low cycle fatigue
LEFM	Linear elastic fracture mechanics
MAI	Metals Affordability Initiative
MTR	Microtextured region
NDE	Nondestructive evaluation
NTSB	National Transportation Safety Board
ODF	Orientation distribution function
OEM	Original equipment manufacturer

POD	Probability of detection
PW	Pratt & Whitney
SAW	Surface acoustic wave
SAE	Safran Aircraft Engines
SEM	Scanning electron microscopy
SLC	Sustained load cracking
SCC	Stress corrosion cracking
SRAS	Spatially resolved acoustic spectroscopy
SRO	Short range order
SWUT	Surface-wave ultrasonic test
TEM	Transmission electron microscope or transmission electron microscopy
Ti	Titanium
UFG	Ultra fine grain
UT	Ultrasonic testing
UTS	Ultimate tensile strength
UQ-PHCM	Uncertainty-quantified, parametrically homogenized constitutive model

Executive summary

Cold dwell fatigue (CDF) is a rare, but highly consequential failure mechanism that has resulted in multiple uncontained failures of fracture-critical rotating titanium alloy aero-engine components. At the request of the Federal Aviation Administration (FAA), members of the international Jet Engine Titanium Quality Committee (JETQC) have worked together to summarize the current state of understanding of CDF and identify key variables in the design, manufacture, and operation of rotating components that can mitigate the risk associated with CDF failures. To this end, the JETQC team has summarized the knowledge gained from a thorough review of decades worth of literature and collective industry experience from full scale component testing and field events. Together, the information offers a detailed, multi-scale view of this problem that stems from atomic scale deformation process and micromechanical phenomena to full scale component behavior. The intended audience for this report is necessarily wide and includes those in the aerospace industry (design, structures/lifing, manufacturing, quality, metallurgy), regulatory agencies, government laboratories, and academia.

There have been relatively few failures in the past 50 years suggesting the root cause is hidden within permissible variations of present industrial practices (e.g., from variations in combinations of composition, processing, and microstructural features). These, and other important factors like applied stress, stress state, residual stress, stressed volume, operating temperature, and dwell time at peak stress, are thus reviewed. While all of these factors are important with respect to CDF behavior, the most important factors are alloy composition, applied stress, and the presence and degree of microtextured regions (MTRs) present in the finished product. MTRs, also called macrozones, are clusters of alpha phase titanium that have a similar crystallographic orientation despite appearing as relatively fine, equiaxed grains when observed with light microscopy. MTRs can behave as larger effective structural units enabling large slip bands to develop which may lead to early crack nucleation under CDF loading conditions. Subsequent crack propagation within the initiating MTR can be up to 100 times faster as compared to average material. Thus, there is a need to explicitly take MTRs into consideration in damage tolerance calculations.

This work was motivated in part by an event in 2017 (BEA, 2020), which was the first known commercial instance of CDF failure in the alpha+beta titanium alloy Ti-6Al-4V in service. The investigation identified MTRs as a key contributor to the event and highlighted that these features should be taken into consideration in the design and certification of titanium components. To this end, we report progress toward industry-wide consensus on standard terminology to describe and quantitatively characterize the important aspects of MTRs that affect material properties. Links are provided to open-source routines to perform these operations.

The recognition of CDF in the Ti-6Al-4V alloy, which has accumulated significantly more successful flight hours compared to CDF-susceptible near-alpha alloys, further highlights the rarity of these events, but also demonstrates the need for JETQC to proactively determine the combination of factors that produce CDF in titanium and bring them under industrial control. MTRs originate during billet processing and may persist through forging and heat treatment. Each step of the process is reviewed, and microstructure evolution mechanisms are discussed. The importance of each step was ranked through a survey of jet engine manufacturers based on internal experience and associated technical literature.

JETQC recommends pursuing the following items to reduce risk of future field failures due to dwell fatigue to ensure continued safe operations:

- Modify existing design and lifing practices to provide improved protection from CDF in titanium, including defining acceptable limits of MTRs or colony microstructures in rotating components.

- Develop improved billet, forging, and heat treat practices that limit the degree of microtexture and improve the consistency of materials used for rotating parts.

- Develop standard methods for characterizing microtexture from electron backscatter diffraction data (EBSD) and develop correlations between this and other more practical destructive techniques including polarized light.

- Develop and industrialize non-destructive methods to characterize components with large colony or MTRs that do not meet design life intent due to potential reductions from CDF.

- Develop and apply models able to simulate behaviors in full scale components that are difficult to examine using specimen testing, for example, residual stress and stressed volume effects, etc.

- Develop high fidelity, mechanism-based models that consider the role of composition, processing, and microstructure/defects on material performance. These models should be developed using highly characterized materials with well-known and intentionally varied processing pedigrees. The breadth of material conditions should be wide enough to cover currently understood variations in production quality materials, including in-specification variations in alloy composition.

- Develop new rotor-grade, premium quality titanium alloys that consider the decades worth of composition and processing considerations summarized in this report and other associated literature that result in low susceptibility to cold dwell fatigue.

1 Background and significance of cold dwell fatigue

1.1 Intent

The primary purpose of this report is to describe a metallurgical condition that may lead to early crack initiation in titanium alloy engine components. We will present the state of the art in understanding of how this metallurgical condition is formed and evolves through hot working and heat treatment and may persist in finished, fielded components. We will describe how an international coalition of design, manufacturing, and materials science engineers are working together under the auspices of the Federal Aviation Administration's Jet Engine Titanium Quality Committee (JETQC) to eliminate this cause of early crack initiation and potentially premature failure in engine components. While this has been a longstanding and persistent topic that has been difficult to resolve, the present group believes that it is achievable through a collaborative and cooperative international effort. The Rotor Integrity Steering Committee (RISC), working under the Propulsion Subgroup, which is part of the Aerospace Industry Association, is focused on advanced lifing strategies and is also aware of and monitoring this matter.

The metallurgical condition referred to above is one of a microstructural feature, known as a microtextured region (MTR) or, alternatively, macrozone or primary alpha colony, in titanium alloys. Interest in MTRs has been renewed by a recent uncontained engine failure involving the industry workhorse Ti-6Al-4V alloy (BEA, 2020). However, the reader will learn in this report that other titanium alloys have occasionally experienced early crack initiation and premature failure related to this microstructural feature for more than fifty years. The failure mechanism of concern is known as cold dwell fatigue (CDF), dwell time fatigue, or simply dwell fatigue. In reading this report, the reader will gain a clear understanding of the key technical metallurgical challenges that must be overcome to minimize the risk of early crack initiation due to CDF.

The authors have convened under the auspices of the Federal Aviation Administration's Jet Engine Titanium Quality Committee (JETQC) to prepare this review, with the purpose of documenting the history, phenomenology, and current state of understanding regarding CDF from the perspective of the aviation industry. JETQC was formed by the FAA following the Sioux City accident, which was the result of a melt-related inclusion known as hard alpha (NTSB, 1990). JETQC successfully navigated this important safety issue with the aid of the premium quality titanium alloy supply chain collectively reducing the occurrence of hard alpha and high-density inclusions in premium quality melted products by more than two orders of magnitude following the Sioux City accident (NTSB, 1990; Woodfield & Lemaitre, 2020). In a

similar manner, the FAA has asked the JETQC community to work together with other industry experts to address the next 'weakest link' for safety in titanium alloys for demanding aerospace engine applications. Following the Sioux City event, the FAA released advisory circular (AC) 33-15.1 that provides guidance for the manufacturing and inspection of premium quality titanium for rotating components to avoid hard alpha inclusions (Pardee, 1998). As a result of the recent Ti-6Al-4V event (BEA, 2020), the FAA has asked JETQC for recommendations for a potential update to AC 33-15.1 that addresses key aspects of the manufacturing process that impact MTRs. This report serves as a companion to the potential revised AC providing the technical details supporting the recommendations. The information contained here can be used by the materials, design, and manufacturing communities to make more informed decisions leading to the safer operation of gas turbine engine components and other components that experience sustained peak loads now and in the future. It can guide the development of new processing routes to reduce the rate of occurrence of MTRs, enhanced nondestructive evaluation methods to detect MTRs, and creating new fatigue life prediction tools. With current fiscal constraints, a concerted and coordinated international effort is needed to align government regulators, national and defense laboratories, industry, and academia to address the most important remaining issues, which are highlighted near the end of this document.

1.2 Introduction

Cold dwell fatigue in titanium is a phenomenon well known in the aerospace industry because it has been implicated in several uncontained, in-service failures of fracture-critical rotating components like fan and compressor disks and fan blades. Cold dwell fatigue is a type of loading where a hold at high stress is imposed between periods of alternating stress. This type of hold, or dwell, at high peak stress can occur at any time during the flight, but the highest magnitudes are typically encountered during the takeoff, climb, and landing phases. The additional damage sustained during the hold at high stress can result in early crack nucleation and fast crack propagation resulting in failure earlier than would be expected during cycling without the dwell period. The modifier 'cold' emphasizes that the issue occurs in a relatively cool part of the engine. As such, susceptible components include fan and compressor disks, and the fan blades which experience high mean stress, though to a lesser extent. It is also important to consider thermal transients in addition to steady-state temperature when assessing susceptibility to CDF. For example, CDF can occur in thick section high-pressure compressor disks if the duty cycle exposes them to a significant stress for long enough at a temperature in the 'cold dwell regime' as they take some time to get to the equilibrium temperature following take-off.

There has been a significant amount of research performed to understand the metallurgical factors that influence CDF susceptibility which are described in detail in this report. Appendix A summarizes some of the key programs focused on cold dwell fatigue. At the root of the issue is the complex interplay between alloy composition, processing path, resulting microstructure, residual stress state, and operational usage (i.e., stress, stress state, and temperature). By aggregating knowledge gained over the years and putting it in context with learning obtained from specimen testing, fielded components, and spin rig test experience, the authors hope this report will help drive a practical engineering solution to this longstanding problem. A recurring theme in this report is the key contributing role that MTRs have on dwell susceptibility. These MTR features impact the processes of damage accumulation, crack nucleation, and crack propagation. MTRs originate during the conversion of ingot to billet and persist through *multiple* thermomechanical processing steps. Current practice involves metal working to convert large ingots to intermediate mill products that are forged, heat treated, inspected, and machined into a finished component. Despite the significant amounts of strain imposed during these hot-working operations, some degree of microtexture remains in virtually every finished component. However, while MTRs are present in virtually every fielded component, they will only initiate cracks early in components in very rare circumstances making it extremely challenging to determine the exact microstructural conditions which lead to CDF failures.

The intended audience for this report is wide and includes those in the aerospace industry, regulatory agencies, government research labs, and academia with broad ranges of prior experience with titanium and CDF ranging from just beginning to seasoned practitioners. In order to serve as a comprehensive resource, Section 2 begins with a review of the physical metallurgy of titanium alloys and discusses key aspects of their deformation behavior followed by an introduction to crystallography and a high-level overview of thermomechanical processing. In Section 3, we will describe and define the important attributes of MTRs and discuss methods to obtain a quantitative description of these features. These discussions provide the background for Sections 4, 5, 6, and 7 which cover the mechanisms of CDF (damage accumulation, small crack growth, and long crack growth), MTR effects on other properties, aspects of materials processing (conversion, forging, and heat treatment), and methods for characterizing mechanical properties, respectively. The engine original equipment manufacturers (OEMs) present the experience with CDF from field events and spin rig testing in Section 8 followed by a discussion of the various pathways to pursue and understand the root causes of these failures. Section 9 then provides a holistic interpretation of dwell fatigue which links the perspectives of materials, manufacturing processes, design, and nondestructive evaluation. We conclude this report with a discussion of unknowns and open questions intended to provide direction for further research.

1.3   Industry field events

Over the past fifty years there have been a number of in-service failures of fan and compressor disk components, some of which have been summarized in the literature or various reports (e.g., (Carr, et al., 2010; Cuddihy, 2016; Pugh, 2001; Ruffles, 1995)). Each event provided new insights, resulting in important changes to design, materials processing, lifing, or sustainment strategies. One of the most well-known incidents involving a titanium alloy component is the 1989 event of a DC-10 in Sioux City, Iowa. The fan disk on the tail mounted engine fractured mid-flight and the ejected fragments severed hydraulic lines that controlled key flight surfaces. The key contributor to this event was a melt-related inclusion known as a hard alpha. The nitrogen-rich anomaly presented as a large, hard inclusion which caused a stress concentration under service loading leading to early fatigue crack nucleation. This event had a profound effect on the titanium industry and resulted in the introduction of new hearth melting technologies, established new ultrasonic billet and forging inspection protocols, and led to the formation of JETQC (Woodfield & Lemaitre, 2020). The improvements to the melt process decreased the occurrence rate of high-density inclusions (HDIs) and hard alpha from approximately 1.6 per million pounds of titanium in the early 1990's to about 0.1 per million pounds in the mid 2010's.

MTRs are the next most critical feature of the microstructure after melt-related defects. They have been implicated in uncontained engine failures in the past and thus represent a safety concern. Before delving into the limited number of events on record, we must note that Ti alloys have been used in turbine engines for more than six decades which equates to at least 10 to 100 billion titanium component flight cycles. Many components were produced before MTRs were recognized and nevertheless flew successfully and were retired without any issues related to dwell. Trends in engine technology to support increasingly efficient commercial aircraft without incurring significant additional cost have the potential to push existing alloys nearer their limits – thus representing a potential new risk to rotating components. Hence this review should serve as a timely reminder to pay careful attention to processing routes to ensure material *quality* over and above all else. In the following sections, we briefly review some of the major failure events associated with cold dwell fatigue. A more detailed discussion of the results of the metallurgical investigations for these events is included in 8.1.

1.3.1   Early 1970's Ti-685 RB211 fan disks

The failure of two RB211-22 fan disks in 1972 and 1973 (Ruffles, 1995) is often cited as the first instance of a cold dwell fatigue failure in the field. The disks were made of a near-alpha alloy, Ti-685, in the beta annealed condition. None of the burst disk hardware was ever found but other

similar hardware was examined in order to understand the failure mechanism. It was concluded that the early failures were a consequence of:

- a significant dwell time in the take-off and climb part of the flight cycle,

- relatively high bulk residual stress arising from the forging and beta heat treatment operation,

- a relatively coarse colony structure in the thicker sections of the disk due to lower cooling rates, and

- pre-existing material anomalies initiated from regions containing pores. The latter were understood to be most likely to have been caused at the ingot production stage in manufacture; the failure locations were suspected to be subsurface and were not believed to be related to hard-alpha anomalies.

Taken together, these factors produced significantly accelerated fatigue crack growth from pre-existing material anomalies.

1.3.2 1980's-1990's Ti-6242 CF6 compressor spools

GE's CF6 model experienced numerous cracks and separations due to CDF (called dwell time fatigue, or DTF, in some earlier reports), in the Ti-6242 high pressure compressor spool machined from a single forging in the 80's and 90's. The majority of crack origins were in the disk bores. Over the years, there were various manufacturing processes used to produce the 3-9 spool forging as outlined in (Garvey, 2000; Hall & Garvey, 1998). Originally, a 16" diameter billet was used to forge a one-piece spool. Later, a 13" billet was used to permit more strain into the billet to improve properties and inspectability. Eventually, the spools were produced by forging stages 3-5 and 6-9 from 12" and 13" billet and joining them via welding before being heat treated and machined to the final shape. In the 1980's through the mid 1990's, GE's suppliers began forging the front and rear sections from 9" and 10" billet, respectively. In all, a total of four CF6 separation events were related to cold dwell fatigue and all in-service events occurred in one-piece billet spools. An additional 21 cracks were found during a subsequent nondestructive evaluation campaign via eddy current inspection; some of these cracked components were two-piece spools (Hall & Garvey, 2000).

1.3.3 1998 Ti-6242 impeller

Another notable event occurred when there was an uncontained failure of a Ti-6242 high pressure centrifugal impeller disk in Palm Springs on May 10, 1998, during takeoff roll on a

small general aviation aircraft. The part, produced by Honeywell, had 9,741 hours and 9,080 cumulative cycles since new and had been reworked according to a service bulletin after about 3,000 hours and 3,250 cycles. The National Transportation Safety Board (NTSB) (Crispin, Jackson, Cummins, & Mecalo, 2000) initially did not classify the failure as cold dwell fatigue, instead declaring that "While the impeller showed evidence of a subsurface fatigue origin, the percipient cause of the separation was not definitively determined." Metallurgical evaluation revealed no anomalies in terms of chemistry, local hardness, or microstructure. In addition, the fractographic inspection ruled out the role of melt-related defects, but it was noted that the origin was not typical of previously observed field failures. Because of the subsurface origin and faceted appearance of the initiation site and absence of striations within this region, Honeywell suspected that cold dwell fatigue may have contributed to the event.

1.3.4 2017 GP7270 Ti-6Al-4V fan disk

In late September 2017, the Ti-6Al-4V fan disk from an Engine Alliance GP7270, one of four powering an Airbus A380 enroute from Paris, France to Los Angeles, USA, was liberated at cruising altitude over Greenland (BEA, 2020). The plane diverted to Goose Bay, Canada and landed without further incident or injury to any crew or passengers. Almost the entire fan disk exited the engine, and the remaining piece did not contain the primary origin site. The fan fragment was recovered after a nearly two-year long search campaign (BEA, 2019) which included aerial scans using synthetic aperture radar followed by a ground recovery effort (YouTube, n.d.2019). The subsequent investigation revealed that the crack initiated from a subsurface origin near the middle of one of the fan hub slots that holds the root of the fan blade. This investigation verified that melt-related anomalies played no role in the event, and chemistry and microstructure were within Pratt & Whitney's specifications. The fan disk had 30,757 hours and 3,532 cycles at the time of the event. The investigation concluded that the fracture was consistent with cold dwell fatigue.

The report cited the following factors as likely to have contributed to the event:

- engine designer's/manufacturer's lack of knowledge of the cold dwell fatigue phenomenon in the titanium alloy, Ti-6Al-4V,

- absence of instructions from the certification bodies about taking into account macro-zones (i.e., colony of similarly oriented alpha grains) and the cold dwell fatigue phenomenon in the critical parts of an engine, when demonstrating conformity,

- absence of non-destructive means to detect the presence of unusual macro-zones in titanium alloy parts, and

- an increase in the risk of having large macro-zones with increased intensity in large Ti-6Al-4V forgings due to bigger engines, and in particular, bigger fans.

1.3.5 2018 Ti-6Al-4V fan blade event

In February 2018, a PW4077 turbofan engine suffered an in-flight separation of one of the fan blades during a flight from San Francisco, California to Honolulu, Hawaii (Pratt & Whitney, 2018). The blades in this engine are made from Ti-6Al-4V and feature a hollow core, a wide chord, and are ~40.5" in length. The fracture occurred transverse to the airfoil about 6.7" from the root and, while the origin was smeared during the event, it appeared to have initiated ~1-2 grain diameters subsurface at an inner cavity of the hollow blade. There was evidence of coarse machining marks at the radius feature near the origin, which may have contributed to the event. The subsequent investigation did not find any evidence to support high cycle fatigue (HCF) failure. Dwell fatigue was not implicated in the initiation process, but rather the fracture was attributed to low cycle fatigue (LCF), with a suspected contribution from dwell during crack propagation.

1.3.6 2006 Ti-8Al-1Mo-1V fan blade event

In July 2006, a GE CF34-3 engine experienced a fan blade out event during a climb maneuver early in the flight as it departed from Barcelona (Rosenker, 2008). The pilots shut down the engine and successfully returned to the airport. At the time of the incident, the engine had accumulated 8,899 cycles. The blade was manufactured from the Ti-8Al-1Mo-1V alloy and was attached to the disk through a series of tangs with drilled holes that accommodated a pin to hold it in place.

The fatigue crack initiated subsurface with a CDF (or dwell time fatigue) appearance, with associated underlying MTRs. The affected population of fan blades originated from a particular supplier that used a larger input bar diameter (3.5") to produce the blades and consequently there was a lesser amount of forge work. The resulting fan blade microstructure in the region of the fatigue crack initiation consisted of larger, more intense MTRs. The aluminum content of the failed blade was also at the highest level of aluminum permitted in the specification (Ministerio Detransportes: Movilidad Y Agenda Urbana., 2006).

1.3.7 From field events to scientific understanding

It is clear that CDF loading conditions have been implicated in a wide array of material failure events in different engine components with different potential root causes, amplified by the presence of MTRs. The challenge in linking CDF field events to a microstructural origin stems

directly from the complexity of the microstructure evolution during processing of two-phase titanium alloys, the complexity in quantitatively characterizing the microstructure, and challenges in reproducing various aspects of the crack propagation mechanisms in CDF in a laboratory setting. In the subsequent sections, we will provide the reader with the necessary background to understand and appreciate the current understanding of the role of MTRs in CDF of titanium engine components, before returning in Section 8 to the results of the metallurgical failure analysis investigations from the field events highlighted above. Section 2 covers the physical metallurgy of two-phase titanium alloys; Section 3 presents the current 'gold standard' for characterization of the relevant microstructures; Section 4 discusses the micromechanisms of CDF damage accumulation, crack nucleation, and crack growth; Section 5 covers the role of microtexture with other load cycles that lead to a dwell-like effect; Section 6 covers the origins of MTRs during the processing of two phase Ti alloys; and Section 7 presents the key aspects of mechanical testing. Afterwards, field and spin rig events are revisited in Section 8 highlighting the details of the metallurgical evaluation of the events followed by a discussion of strategies to mitigate the risk due to CDF in Section 9. Finally, Section 10 discusses the gaps in the current understanding of the CDF and highlights areas that require future work.

2   Physical metallurgy of two-phase titanium alloys

2.1   Alloy classification

There are many excellent sources covering the physical metallurgy of titanium (for example, see (Froes, 2015; Lütjering & Williams, 2007)). Here, we briefly review the salient points that are relevant to the remaining content in this article. At room temperature, pure titanium has a hexagonal close packed (HCP) crystal structure known as the α phase. Upon heating, it undergoes an allotropic transformation from α → β at a temperature of 882 ℃. This temperature can be increased or decreased by the addition of alloying elements. Elements which raise the β transus are known as α stabilizers and these may be substitutional (Al) or interstitial (C, O, N) while those that depress the β transus are β stabilizers. Some β stabilizers form an isomorphous phase diagram with Ti (V, Mo, Nb, Ta) while others are eutectoid formers (Fe, Mn, Cr, Ni, Cu Si, and H). The elements Zr and Sn are relatively neutral resulting in no major change to the β transus. Titanium alloys are typically classified as α, α+ β, or β alloys depending on the composition of the alloy and according to their position in a pseudo-binary through a β isomorphous phase diagram (Figure 1).
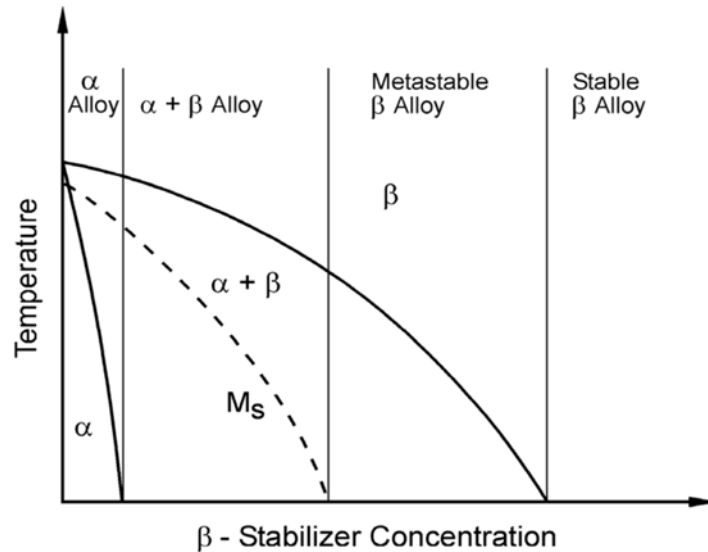
Figure 1. Schematic representation of the pseudo-binary β isomorphous phase diagram

Alpha alloys include the various grades of commercial purity titanium as well as alloys like Ti-5Al-2.5Sn and Ti-3Al-2.5V. In practice, these alloys will contain a small amount of beta phase at room temperature due to the presence of iron and/or small amounts of beta stabilizing elements. Since the alloys used for rotating applications contain both alpha and beta phase, the alpha class is not further discussed in this report. The class of alpha+beta alloys has a range in Figure 1 that extends from the alpha/alpha+beta phase boundary to the martensite start (M_s) temperature at room temperature. This class contains the majority of alloys used for turbine engine materials like Ti-6Al-4V, Ti-6Al-2Sn-4Zr-2Mo, and Ti-5.8Al-4Sn-3.5Zr-0.5Mo-0.7Nb-0.35Si-0.06C (i.e., TIMETAL® 834 or Ti-834), among others. Some alloys, like Ti-6Al-2Sn-4Zr-2Mo and Ti-834 are on the dilute side of the α+β region and are appropriately called near-α alloys. Despite falling within the alpha+beta phase field at room temperature, the metastable beta alloys have the unique property that they do not transform martensitically when quenched from above the beta transus due to a higher concentration of beta stabilizers. These alloys respond strongly to heat treatment in the two-phase field and can form very highly refined alpha phase leading to very high strength albeit often at the expense of ductility and damage tolerance, though this is not always the case. This class includes alloys like Ti-6Al-2Sn-4Zr-6Mo and Ti-5Al-2Sn-2Zr-4Mo-4Cr (Ti-17). The so-called aluminum and molybdenum equivalence (Figure 2, image courtesy of TIMET) represent a convenient way to express the influence of all alloying elements on a normalized basis. The aluminum equivalence is expressed as $Al_{EQ}= Al + 1/3Sn + 1/6Zr + 10(O + C + 2N)$ (Lütjering & Williams, 2007) in weight percent. There are multiple equations one can find in the literature for the molybdenum equivalence, but the one which includes the greatest number of beta stabilizing alloying elements is $Mo_{EQ} = 1.0Mo + 0.67V + 0.44W + 0.28Nb +$

0.22Ta + 1.6Cr + 1.25Ni + 1.7Co + 2.9Fe − 1.0Al (wt.%) (Weiss & Semiatin, 1998). With respect to CDF, as discussed in more detail in Section 9.2, the near-alpha class of alloys, i.e. those alloys with higher Al_{EQ}, are the most susceptible to dwell fatigue and the sensitivity diminishes as the level of beta stabilizing elements and hence Mo_{EQ} increases.

2.2 Microstructures and deformation behavior of two-phase titanium alloys

The microstructure and hence properties of titanium alloys can be manipulated through heat treatment and thermomechanical processing. The volume fraction, size, morphology, and composition of each phase has important implications on the deformation behavior of the material as well as the balance of strength, ductility, and fatigue properties. This section briefly introduces the typical microstructures encountered in two-phase titanium alloys which include lamellar, bimodal, equiaxed, and mill-annealed.

ALLOY			Al equiv. / Mo equiv.	T_β °F	T_β °C
Ti 834			5.8Al-4Sn-3.5Zr-0.7Nb-0.5Mo-0.3Si-0.06C	1913	1045
Ti 1100			6Al-2.75Sn-4Zr-0.4Mo-0.45Si	1859	1015
Ti 829		"Near α"	5.5Al-3.5Sn-3Zr-1Nb-0.25Mo-0.3Si	1859	1015
Ti 685			6Al-5Zr-0.5Mo-0.25Si	1877	1025
6-2-4-2			6Al-2Sn-4Zr-2Mo-0.1Si	1823	995
8-1-1			8Al-1Mo-1V	1922	1050
Ti 679			2.25Al-11Sn-4Zr-1Mo-0.25Si	1742	950
5-1-1-1			5Al-1Sn-1Zr-1V-0.8Mo	1795	979
Ti 6-4			6Al-4V	1832	1000
6-6-2			6Al-6V-2Sn	1751	955
Ti 550		"α + β"	4Al-2Sn-4Mo-0.5Si	1787	975
62S			6Al-2Fe-0.1Si	1850	1010
6-2-2-2-2			6Al-2Sn-2Zr-2Mo-2Cr-0.25Si	1805	985
6-2-4-6			6Al-2Sn-4Zr-6Mo	1724	940
SP 700			4.5Al-3V-2Mo-2Fe	1670	910
βCEZ			5Al-2Sn-4Zr-Mo-2Cr-1Fe	1652	900
Ti-17			5Al-2Sn-2Zr-4Mo-4Cr	1634	890
βIII		"Near β"	11.5Mo-6Zr-4.5Sn	1418	770
10-2-3			10V-2Fe-3Al	1472	800
555			5Al-5V-5Mo-3Cr-0.5Fe	1580	860
β21 S			15Mo-2.7Nb-3Al-0.2Si	1544	800
15-3-3-3			15V-3Cr-3Al-3Sn	1400	760
LCB			6.8Mo-4.5Fe-1.5Al	1463	795
βC			3Al-8V-6Cr-4Mo-4Zr	1247	675

Figure 2. Classification of titanium alloys and corresponding aluminum and molybdenum equivalencies

2.2.1 Lamellar microstructures

Lamellar microstructures are the microstructure which is naturally formed in two-phase titanium alloys upon cooling from above the beta transus. This includes materials simply heated into the single-phase field (i.e., beta-annealed, as well as those materials that are deformed in the beta phase field prior to cooling). For either operation, care must be taken to control the grain size because beta grain growth kinetics are rapid in the absence of any alpha phase (Ivasishin, Semiatin, Markovsky, Shevchenko, & Ulshin, 2002) (Semiatin, Soper, & Sukonnik, 1996; Semiatin, Fagin, Glavicic, Sukonnik, & Ivasishin, 2001). Upon cooling to room temperature

11

from above the beta transus, titanium undergoes an allotropic transformation where beta→alpha+beta. The alpha phase consumes most of the beta grain during this transformation and hence the term *prior* beta grain is used to describe what was the beta grain at elevated temperature. Upon slow cooling from the high temperature β phase, the α phase nucleates heterogeneously at prior β grain boundaries forming a layer of alpha phase on the beta grain boundaries known as grain boundary alpha. With further undercooling the α phase begins to nucleate heterogeneously at the prior beta grain boundaries and grow toward the interior of the β grains as a series of parallel platelets of alpha phase separated by retained beta phase. Packets of similarly oriented alpha/beta platelets are known as alpha colonies. With further undercooling, new alpha colonies may nucleate heterogeneously from existing alpha phase in a process known as sympathetic nucleation. The size of the alpha colonies and thickness of individual alpha platelets depends on the cooling rate with slower cooling rates favoring large colonies and thicker plates while faster cooling rates favor smaller colonies and thinner alpha platelets.

The alpha and beta phases have a crystallographic orientation relationship known as the Burgers orientation relationship (BOR) (Burgers, 1934) which aligns the following planes/directions: $(0001)_\alpha||\{110\}_\beta$, $\langle11\bar{2}0\rangle_\alpha||\langle1\bar{1}1\rangle_\beta$, and $\{10\bar{1}0\}_\alpha||\{112\}_\beta$.

Inspection of the symmetries of the parent (beta) and child (alpha) crystal structures show that there are six {110} planes, each containing two <111> directions. The relationships above can only be satisfied by one specific set of planes/directions within each family and hence there are twelve unique alpha phase orientations that can arise from a given parent beta grain orientation. With slow cooling rates, diffusional growth processes are favored over nucleation and the observed microstructure is dominated by a small fraction of the total number of variants (Sargent, Kinsel, Pilchak, Salem, & Semiatin, 2012). The crystallographic constraints of the BOR results in a set of six possible misorientations between two alpha variants inherited from the same prior beta grain (Table 1). Several authors have reported that the inherited variants tend to minimize both short (Wang, Aindow, & Starink, 2003) and long range (Sargent, Kinsel, Pilchak, Salem, & Semiatin, 2012) internal elastic strain energy through a self-accommodation mechanism that minimizes the overall transformation strains associated with the allotropic transformation. The transformation strains arise from the differences in volume of the HCP alpha phase and body centered cubic (BCC) beta phase as well as the lattice parameters and elastic properties. Shi (2014) analyzed this phenomenon using phase field simulation and also addressed the role of prior beta grain boundary misorientation on variant selection and grain boundary alpha as well as internal variants.

Table 1. Misorientations between two alpha colonies inherited from the same prior beta grain

Type	Angle/axis Representation of Misorientation
1	Identity
2	$60°/\langle 11\bar{2}0 \rangle$
3	$60.83°/\langle \overline{1.377}\ \bar{1}\ 2.377\ 0.359 \rangle$
4	$63.26°/\langle \overline{10}\ 5\ 5\ 3 \rangle$
5	$90°/\langle 1\ \overline{2.38}\ 1.38\ 0 \rangle$
6	$10.53°/[0\ 0\ 0\ 1]$

If the material is cooled quickly from above the β transus, via water quenching, for example, nucleation of new α variants is favored over the growth of existing ones due to the increased undercooling. This results in a microstructure consisting of interpenetrating lenticular α phase, often referred to as a basketweave or Widmanstätten microstructure. Colony formation is suppressed in this case and instead each lath adopts a different variant of the BOR. There are multiple factors that influence which specific variants are observed including the prior grain boundary misorientation and grain boundary plane orientation, elastic interactions, residual stress, and prior deformation. These are not discussed in detail here but see References (Sargent, Kinsel, Pilchak, Salem, & Semiatin, 2012) (Glavicic, et al., 2008; 2016; Pilchak, Banerjee, & Williams, 2016; Shi, 2014; Zeng & Bieler, 2005) for additional discussion.

With rapid quenching on thin sections (> ~20 K/s), it may be possible to suppress the diffusion-mediated nucleation and growth process to form acicular martensite called α' but this structure is generally not observed in industrial components due to the large size of the parts where the cooling rate becomes limited by the thermal conductivity of titanium. The beta → alpha' martensitic reaction is morphologically similar to the basketweave microstructure but is distinguishable by the chemical composition. The shear-induced transformation from beta to alpha' occurs rapidly and the product phase inherits the composition of the parent phase. This should be confirmed with energy dispersive spectroscopy in the transmission electron microscope prior to concluding that alpha' is present. The alpha phase is also supersaturated in beta stabilizing elements which slightly affects the lattice parameter leading to peak broadening in x-ray diffraction spectra (Zeng & Bieler, 2005).

Due to the alignment of important slip systems from the BOR, dislocations are able to traverse the interphase boundaries relatively easily. This results in relatively low strength and poor crack nucleation resistances for materials like castings or large, slow-cooled parts which have large colonies and hence large slip lengths. Wegmann et al. (1997) have developed a heat treatment to

overcome this shortcoming and strengthen the beta phase ribs by performing a second heat treatment high in the alpha beta phase field to reduce the alpha volume fraction and supersaturate the beta lamellae with alpha stabilizing elements. This allows a fine distribution of secondary alpha to form between the primary alpha laths which introduces additional barriers to slip.

Some alloys may be subjected to an additional heat treatment at a low temperature in the alpha+beta phase field (e.g., 500-550 $^{\circ}$C / 24h) to promote the formation of a fine distribution of coherent α_2 particles with the composition Ti_3Al which can increase strength but has the detrimental effect of promoting slip planarity and strain localization, which reduces ductility. In some cases, it is possible to promote short range order (SRO) which has a similar effect on slip behavior as α_2. As discussed by Brandes (Brandes, 2008) the heat treatment and cooling rate are both important factors with respect to SRO and α_2 formation. Samples rapidly quenched from solution heat treatment tend to suppress SRO and α_2 while slow cooling or aging tend to promote α_2 formation. Alloys with higher aluminum equivalence have higher $\alpha \rightarrow \alpha + \alpha_2$ transformation temperatures (Figure 3) while beta-stabilizing elements (e.g. Mo, Fe, V) tend to reduce it.
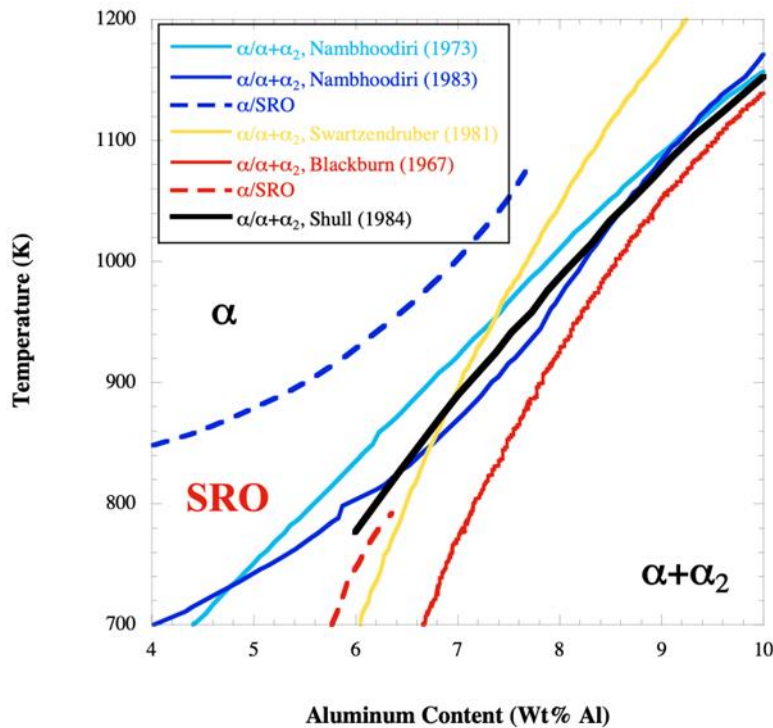
Figure 3. Compilation of Ti-rich side of Ti-Al phase diagram from several researchers

2.2.2 Alpha + beta processed microstructures

The lamellar or basketweave microstructures formed during cooling from above the beta transus can be converted to an equiaxed or bimodal condition via thermomechanical processing and

14

subsequent heat treatment. The equiaxed condition contains a high-volume fraction of spheroidized alpha. By solution heat treating high in the alpha+beta phase field, the volume fraction of equiaxed alpha can be reduced at temperature and subsequent fast cooling results in decomposition of the beta phase into a lamellar microstructure that is commonly referred to as secondary alpha or transformed beta. The composite structure of equiaxed alpha and transformed beta is known as the bi-modal microstructure. The morphology of the transformed beta can take on a lamellar or basketweave morphology depending on the cooling rate. Upon water quenching or air cooling from the solution temperature, the metastable beta phase decomposes into the secondary alpha phase via nucleation and growth. The morphology of this phase depends on the cooling rate. A fine, interpenetrating basketweave microstructure will form under rapid cooling rates like those induced by water quenching of thin section parts. Under more moderate cooling rates, like those encountered during air cooling or water quenching of parts with large section thickness, alpha lamellae thickness increases, and small alpha colonies form between the primary alpha particles. The most important features with respect to material properties are the primary alpha particle size and volume fraction as well as the secondary morphology (i.e., basketweave or colony) and lath thickness. In practice, the volume fraction of transformed beta phase is usually higher than that of the primary alpha. The kinetics of the transformation to secondary alpha depends on alloy composition with more heavily beta-stabilized alloys (e.g., Ti-6246) able to form basketweave microstructures at slower cooling rates compared to learner alpha+beta alloys (e.g., Ti-6-4) or near-alpha alloys (e.g., Ti-6242 or Ti-834) (Qiu, et al., 2014).

The mechanism responsible for the morphological change from lamellar to equiaxed alpha begins during deformation and completes during subsequent solution heat treatment. During deformation, low angle boundaries are created within the lamellae and the misorientation of these gradually increases with increasing levels of strain (Doherty, et al., 1998; Weiss, Welsch, Froes, & Eylon, 1985). During subsequent heat treatment, which includes the reheating between hot working operations, depending on temperature, the beta phase penetrates along these boundaries thereby completing the separation and additional diffusional processes like termination end migration help complete the spheroidization process. A more thorough discussion of the mechanism can be found in the literature (Semiatin & Furrer, 2009). We emphasize that the process of subgrain formation and beta phase penetration does not result in the formation new highly misoriented grains, which is typical of classical recrystallization, but instead results in morphologically spheroidized alpha grains that have a relatively similar orientation as the parent colony from which they formed. This is the fundamental mechanism behind the formation of MTRs. Historically, the development of spheroidized primary alpha was the focus of billet conversion and forging without any regard to the underlying MTRs since these

features were only recognized in the early 90's (see Appendix B) with the advent of automated EBSD (Woodfield, Gorman, Corderman, Sutliff, & Yamrom, 1996).

As evident in the pseudo-binary isomorphous phase diagram, different heat treatment temperatures will result not only in different volume fractions of primary alpha but also different compositions of the alpha and beta phases. This is known as the elemental partitioning effect. Higher heat treatment temperatures will increase the concentration of alpha stabilizers in the alpha phase which has important implications on slip character in these phases as well as the affect the kinetics of beta phase decomposition during cooling. Alloys containing a higher fraction of beta stabilizing elements, which are typically heavy, slow diffusing elements such as Mo, results in finer microstructural features due to the slower diffusion rates and lower temperature at which the phase transformations occur, thus favoring nucleation over growth. The alpha coarsening kinetics for these alloys are also reduced making it easier to retain a fine equiaxed alpha particle size. As in the beta-processed or beta-annealed condition, an aging treatment low in the alpha+beta phase field can promote α_2 formation or SRO.

2.3   Deformation mechanisms of titanium alloys

Titanium alloys do not contain hard second phases or particles like other structural materials based on aluminum, nickel, and iron which often act as stress concentrators and prime sites for crack nucleation. As a result, mechanical properties such as strength, ductility, and fatigue crack initiation resistance depend very strongly on microstructure and free slip distance (i.e. the distance that a dislocation can travel without significant resistance to further movement). Prime sites for fatigue crack nucleation are those where local perturbations in microstructural length scale and/or crystallographic orientation lead to an enhanced state of local stress that results in more rapid fatigue damage accumulation. Microstructures with larger slip lengths include slower cooled beta-heat-treated materials and alpha+beta processed materials with large MTRs with unrecrystallized beta phase with aligned secondary alpha colonies. Alloys with these microstructures will be subject to increased dislocation-pileup-induced internal stresses and therefore more likely to encounter early crack nucleation under dwell conditions.

The HCP alpha and BCC beta phases are both elastically anisotropic. The hexagonal crystal structure of the alpha phase results in a naturally anisotropic response and the modulus depends on the orientation of the c-axis relative to the imposed stress axis. In single crystals, the modulus is highest along the c-axis and decreases about 45% to a minimum orthogonal to the c-axis in pure titanium. The modulus is isotropic within the basal plane. Measurement of the single crystal elastic constants in Ti-6242 single colonies by Kim and Rokhlin (2002) have suggested the beta

phase is more elastically anisotropic than the alpha phase with a Zener anisotropy ratio $(2C_{44}/(C_{11}-C_{12}))$ approaching 5 compared to a value of ~1.4 for the alpha phase. It is worth noting that the beta phase was a deduced value after removing the influence of the alpha phase based on analysis of a single-phase alpha alloy with a similar composition. However, Hemery et al. (2020) have consolidated elastic constants for a range of more heavily beta stabilized alloys from the literature and show that the anisotropy is a strong function of composition. The authors report that the beta phase Zener anisotropy ratios generally exceed that of alpha phase titanium and may be as high as 8.2 for the Ti-10V-2Fe-3Al alloy. The elastic anisotropy has important implications on ultrasonic scattering as discussed in Appendix C, as well as on the deformation behavior.

With regard to plasticity, titanium alloys undergo deformation by slip and twinning, with the former being the more active deformation mechanism in industrially useful near-alpha and alpha+beta alloys. While not shut down completely, twinning is greatly reduced in alloyed titanium and, while small twins have been observed in dwell fatigue specimens (Lavogiez, Hémery, & Villechaise, 2020a), to date they have not been implicated with the dwell fatigue crack nucleation process. As it has not been widely implicated as an important deformation mechanism with respect to dwell fatigue, the interested reader is referred to Partridge's classic article (Partridge, 1967) for discussion of twinning in titanium. The close packed $<11\bar{2}0>$ or $<a>$ direction is the most important slip direction in the alpha phase. Dislocations with $1/3<11\bar{2}0>$ Burgers vectors can slip on the (0001) basal plane, the three prismatic $\{10\bar{1}0\}$ planes, and the first order pyramidal $\{10\bar{1}1\}$ plane. When loaded along the [0001] c-axis, however, the $<a>$ vector has zero resolved shear stress and hence dislocations with $<c+a>$ Burgers vectors are necessary to accommodate shape change along this direction. The $<c+a>$ dislocations are in the $<11\bar{2}3>$ direction and have been observed to glide on $\{10\bar{1}1\}$ and $\{11\bar{2}2\}$ planes.

The critical resolved shear stress (CRSS) for slip in alpha phase titanium varies with crystallographic orientation and temperature (Figure 4). Williams et al. (2002) have performed compression experiments on single crystals of various Ti-xAl alloys (x = 1.4, 2.9, 5, and 6.6 wt%) at various temperatures and analyzed the dislocation behavior using transmission electron microscopy (TEM). The single crystals were oriented for either $<a>$ for slip on basal or prism planes or loaded parallel to the [0001] axis to enforce non-basal deformation modes. The Ti-6.6Al alloy is the most relevant alloy investigated due to its close composition to the alpha phase of the most industrially important near-alpha and alpha+beta alloys. At room temperature, the CRSS for basal and prismatic slip were quite similar with basal slip reaching a critical value ~200 MPa and prismatic slip being only slightly weaker at ~190 MPa. By comparison, the CRSS for deformation along the c-axis, which requires $<c+a>$ dislocation motion, was nearly 4x

stronger at ~765 MPa. The authors also noted that slip character depended strongly on temperature. Crystals oriented for basal deformation exhibited planar slip character at all temperatures, but the slip band spacing varied with temperature. At the lowest temperature (-321 ºF), slip bands were finely distributed with small spacing while coarse, more widely spaced planar slip was observed with increasing temperature. Aging to promote Ti_3Al formation resulted in further localization of slip. The CRSS of all slip systems decreased with increasing deformation temperature, but the magnitude of change for <c+a> slip is greater than for basal and prism <a> slip, which both decrease monotonically but remain essentially equivalent to one another with increasing temperature.

The yield point and flow stress of titanium alloys depends on the applied strain rate at room and low temperatures before decreasing in the intermediate regime and increasing dramatically at hot-working temperatures. May complemented the early work on single crystal compression by performing microtension experiments on single crystals of Ti-6.7Al (May, 2010). Tests were performed at three different strain rates (1.7, 5.3, and 9.7 x 10^{-4} s^{-1}) from which the CRSS and rate sensitivities of prism, basal, and pyramidal <c+a> slip were obtained. The CRSS results from these and other literature are shown in Figure 5. This work revealed strong differences in the CRSS and rate-dependence of each family of slip systems under tensile loading. In particular, the basal slip system had a rate dependence of 0.155, which was about double that for the prismatic slip system (0.086). In contrast the pyramidal <c+a> slip system had significantly lower rate dependence (0.015). Figure 5 also demonstrates the presence of tension-compression asymmetry in the yield behavior of Ti alloys (data is for a strain rate of 1.7 x 10^{-4} s^{-1}). Rate-sensitivity is an important factor with respect to dwell fatigue as it controls the yield behavior and stress relaxation response, which collectively impact the propensity for the formation of intense dislocation pileups that can lead to early crack nucleation.
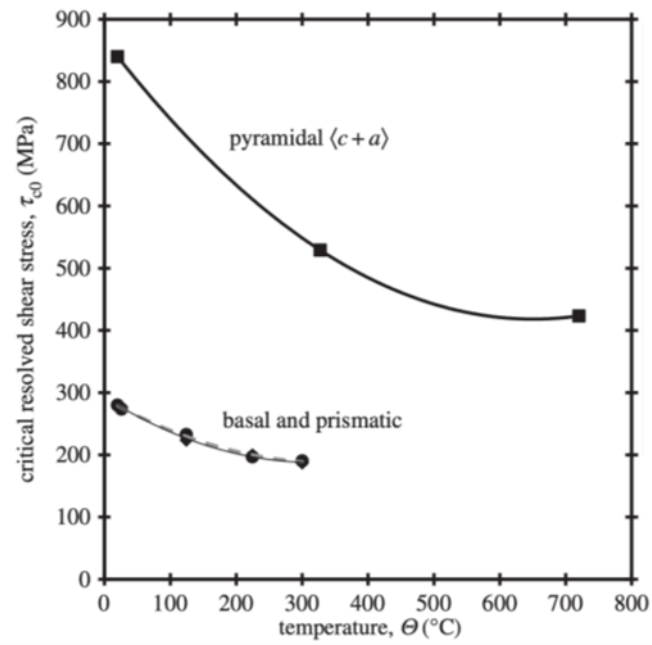
Figure 4. Temperature dependence of the CRSS of alpha phase Ti-6.6Al
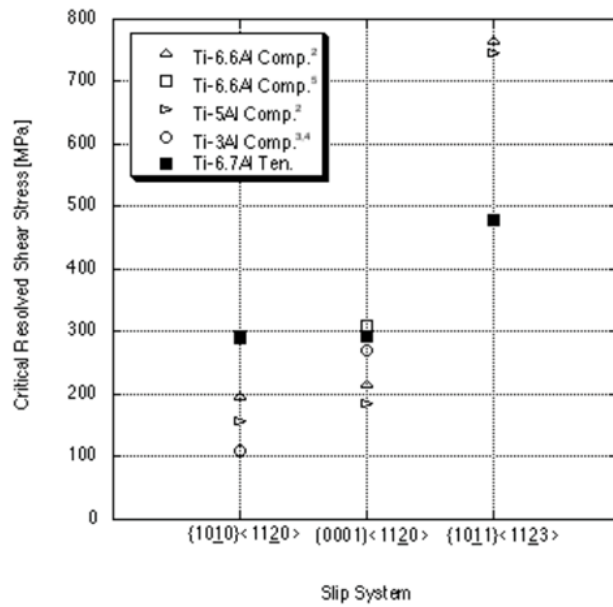
Figure 5. Summary of CRSS values for various binary Ti-xAl compositions

Suri et al. (1999) and Savage et al. (2004) have analyzed the case of slip in alpha/beta single colonies adhering to the BOR. The orientation relationship results in some unique relationships as it relates to slip behavior. The basal plane is parallel to one of the {110} planes and one of the $\langle 11\bar{2}0 \rangle$ in that plane is parallel to a $\langle 1\bar{1}1 \rangle$ direction in the beta phase (typically referred to as the a_1 direction), but as shown in Figure 6, there is a second $\langle 11\bar{2}0 \rangle$ direction that is ~10.5° from the other $\langle 1\bar{1}1 \rangle$ direction (known as a_2) and the third $\langle 11\bar{2}0 \rangle$ direction (a_3) has no closely aligned beta phase slip system. Figure 6 shows multiple depictions of the BOR including composite pole figures where the important planes and directions of the BOR are superimposed on the same pole figure. One of the 12 variants of the BOR viewed along the [0001]α ∥ (110)β direction. The lattice invariant line (macroscopic alpha/beta interface) is parallel to the <335>β that is nearest to the a_1 direction. The a_1, a_2, and a_3 directions are evident as well as the alignment of (0001) with one {110}. The schematic lath structure is from Suri et al. (1999). The consequence of basal plane alignment on slip transmission through alpha/beta interfaces and alpha colony boundaries with 10.5° misorientation is shown in the lower right of Figure 6.
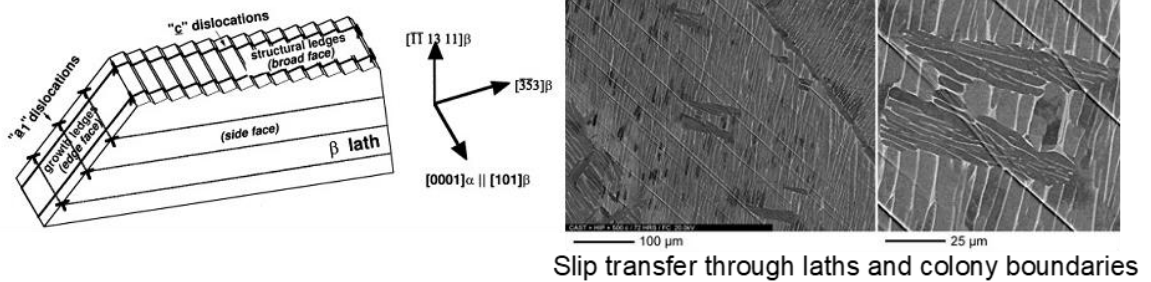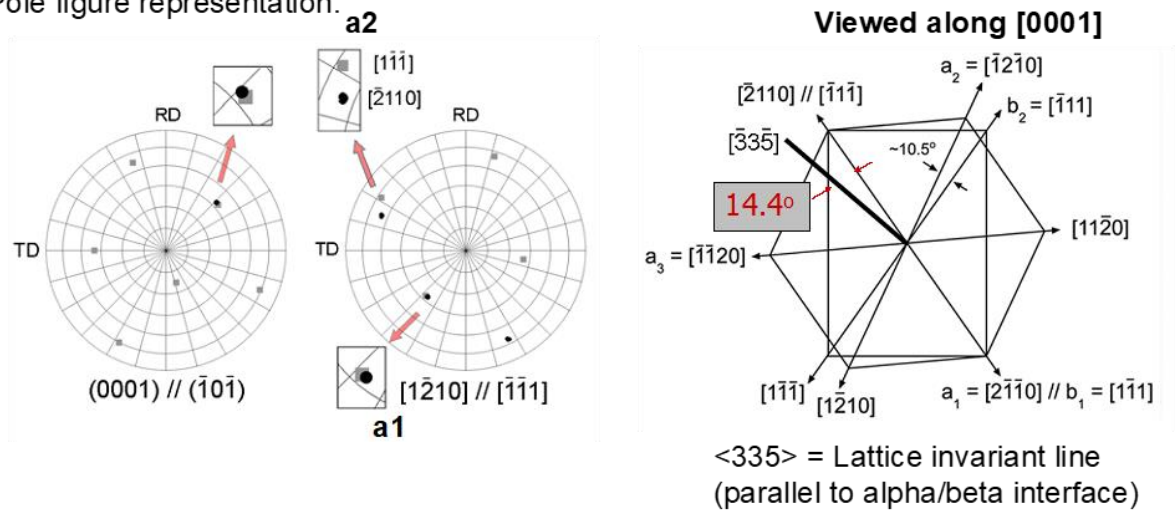
Figure 6. Multiple depictions of the BOR

In addition to these basal slip systems, the prismatic $\{1\bar{1}00\}\langle11\bar{2}0\rangle$ slip systems share similar relationships with the beta phase $\{112\}\langle111\rangle$ slip systems. One set is well aligned, another set is closely aligned, and a third set is not well aligned at all. Because of the preferential alignment of these slip systems, and by virtue of dislocation reactions at the alpha/beta interface it is possible for dislocations to pass through the interphase boundary (Suri, Viswanathan, Neeraj, Hou, & Mills, 1999; Savage, Tatalovich, & Mills, 2004). Nevertheless, residual dislocations are observed at these interphase boundaries, which inhibit subsequent dislocation motion and thus provide some degree of strengthening. These effects are evident in the anisotropy in the CRSS observed for the various slip systems as illustrated in Figure 7. In general, the prismatic <a> CRSS increases in the order $a_1 < a_2 < a_3$ for Ti-6242 deformed in tension and compression (May, 2010). It is worth noting that the data in Figure 7 for Ti-6Al-4V come from highly textured Ti-6Al-4V and not from single colonies. In contrast to the prismatic slip system, basal <a_2> slip has the highest CRSS followed by basal <a_1> and basal <a_3> has the lowest CRSS despite not having a closely aligned set of Burgers vectors in each phase. With respect to CDF, slip transmission

through aligned secondary alpha colonies is an important factor affecting the total slip length and hence strength of dislocation pileups.
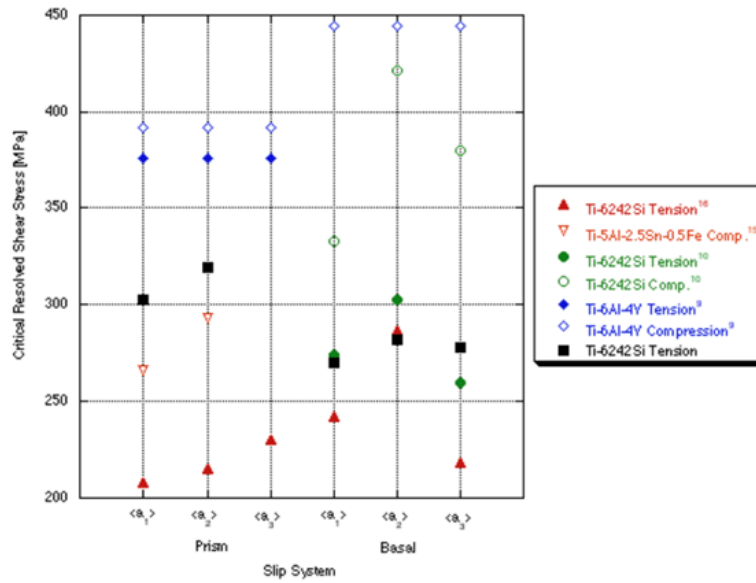
Figure 7. CRSS for slip in single colonies of various titanium alloys

2.4 Crystallographic texture

Crystallographic texture is, in essence, a statistical description of where a material lies in relation to two extremes of microstructure: (1) an isotropic polycrystalline material and (2) a single crystal. This is shown schematically in Figure 8 which shows a perfectly smooth, completely isotropic peanut butter on one end and an anisotropic perfect single crystal is on the right.
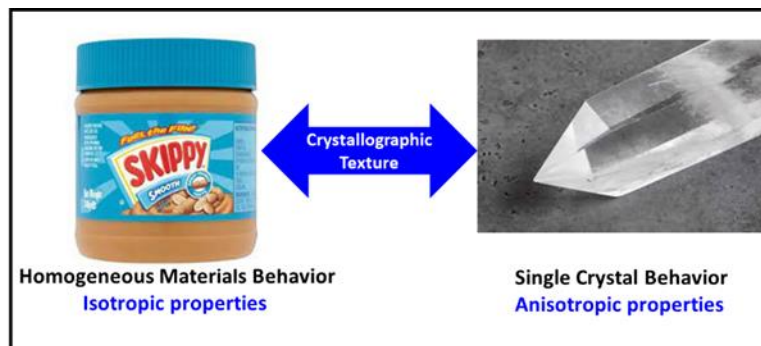
Figure 8. Continuum of material states of crystallographic texture

For single crystals physical and mechanical properties are known to vary as a function of crystal direction. For example, the modulus of elasticity can be tabulated as a function of specific crystallographic direction (Table 2) for single crystal forms of any metal (Hertzberg, Vinci, &

Hertberg, 2012). At the opposite end of the extreme is a polycrystalline metal that has been processed to be isotropic. To achieve isotropic properties, the individual grains (or crystals) that make up the macroscopic object must be randomly arranged such that the net behavior becomes an "average" of the behaviors of all the individual crystals in the volume. In between these two extremes, the properties of the metal become a weighted average of properties of the single crystal whose value then lies somewhere in the middle of the extremes of single crystal properties and isotropic properties. The methodology of how to calculate this weighted average is known as the study of crystallographic texture which is based upon an understanding of the crystal structure of the material, an understanding of the anisotropy in single crystal properties, and an understanding of statistics. For this reason, the degree of preferred orientation, or texture, is expressed in units of "times random" and it represents a statistical probability of finding grains oriented with a particular crystal direction aligned in a specific direction in the specimen coordinate system.

Table 2. Modulus of elasticity as a function of crystal direction for some cubic metals

Metal	Modulus of Elasticity as a function of crystal direction (GPa)		
	<100> Direction	<110> Direction	<111> Direction
Aluminum	63.7	72.6	76.1
Copper	66.7	130.3	191.1
Iron	125.0	210.5	272.7
Tungsten	384.6	384.6	384.6

The following analogy may be used to help the reader understand crystallographic texture. Imagine you are a child playing with square toy blocks. One of your parents asks you to stop playing and put your blocks away in a container that will be completely full of these toy blocks when all of these toy blocks are put away. Next, imagine the toy block (red block in Figure 9) is a single crystal and the toy container (yellow block in Figure 9) is a polycrystalline sample with its Cartesian coordinate system defined with axes RD, TD, and ND (Figure 9).
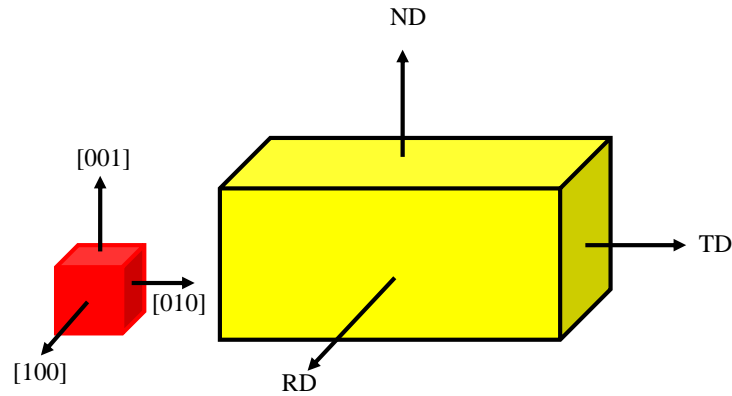
Figure 9. Red toy block (crystal) and yellow container (represents polycrystalline sample)

Now, imagine you are very lazy and decide to throw the blocks into the container. In this case the blocks will be randomly arranged within the toy container and the resulting polycrystalline specimen will have isotropic properties as all of the grains (i.e., the crystallographic orientations, within the volume are randomly oriented).

However, now imagine you are a meticulous person with incredible patience who will stack the blocks in the container so that the [100] crystal directions are aligned with the specimen coordinate system RD, TD, and ND (Figure 10). If you fill the entire container in this manner the yellow polycrystalline container (sample) will behave as a single crystal.
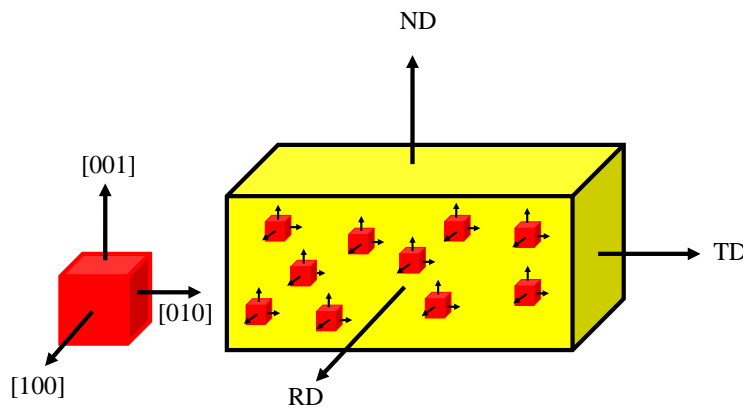
Figure 10. Red toy block (crystal) and yellow polycrystalline container partially filled with blocks in a specific manner

Next, imagine that a portion of the box is filled in the meticulous and prescriptive manner, but you get tired of doing this and finish the job by throwing the blocks in the container randomly to get the job done quickly. In this case, the sample will be somewhere in the middle between being a single crystal and being completely random. Thus, the overall degree of crystallographic texture in the yellow toy box depends upon how many blocks were put into the box in a

meticulous manner as opposed to those thrown randomly in. Hence in a simplistic sense, this amount of work laying the blocks down meticulously before you grew tired is in effect is what preferred orientation or texture measures, but with respect to how material properties (such as elastic modulus) are distributed within the specimen coordinate system.

This analogy is also applicable to the case of multiple texture components. Imagine instead that you are playing with two friends and all of you are meticulous and like to place the same toy blocks in the container, however each of you prefer to orient your blocks in a different specific fashion (Figure 11). Moreover, if the three of you fill the toy container at different rates such that the total number of blocks placed in the toy container by each individual are different (more or less work performed by each person) the various texture components contributed by each person will be different. Then the three of you grow tired and begin throwing the toy blocks into the container to finish cleaning up. In this case there are three unique texture components present in the toy box plus a random component. The three texture components arise from the number of toy blocks placed in the container by the three friends prior to growing tired, and a random texture component from when the friends began to throw the toy blocks in the container. In this case the relative magnitudes of the texture components, or weighted average is described by the number of blocks that each individual placed inside the container in a specific manner divided by the total number of blocks in the container.
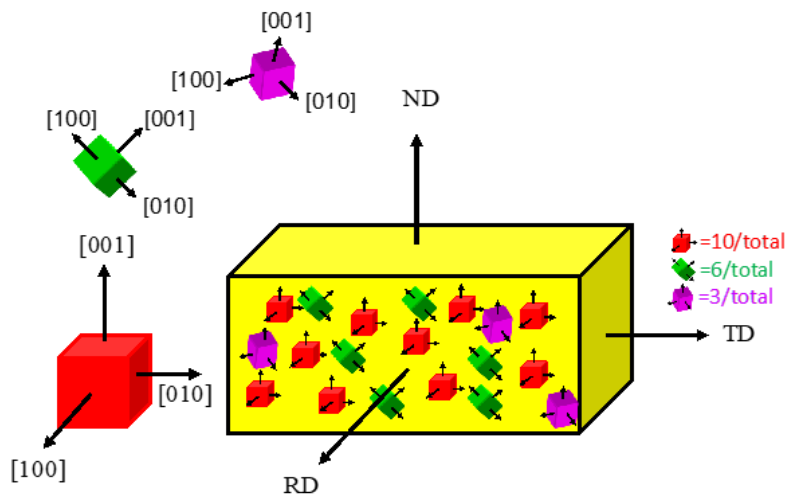
Figure 11. Multiple toy block orientations (crystal) inside yellow container (polycrystalline specimen)

Euler angles are commonly used to describe how the orientations present within a polycrystalline aggregate. The HCP crystal structure is aligned with a specimen reference frame through three successive rotations φ_1, Φ, and φ_2. The manner in which the polycrystalline aggregate as a

whole is visualized is done so with pole figures. Pole figures are two-dimensional projections of a three-dimensional sample coordinate system and identify the location of the crystallographic plane normals, or poles. For example, the (0001) pole figure indicates the distribution of (0001) plane normals in a specimen, relative to the fixed laboratory reference frame of that specimen. For the reader to understand what a pole figure is, and how a crystals Euler angles impact a pole on a pole figure, let us envision two sets of Cartesian coordinate systems that have been rotated in some fashion with respect to one another, Figure 12, (Rollett, 2020). The orange coordinate system represents the specimen reference frame and the green coordinate system represents the crystal reference frame.

Initial position, crystal frame (green, K_B in Bunge) aligned with reference (sample, K_A in Bunge) frame (orange)

New position, crystal frame (green) rotated with respect to the reference (sample) frame (orange)
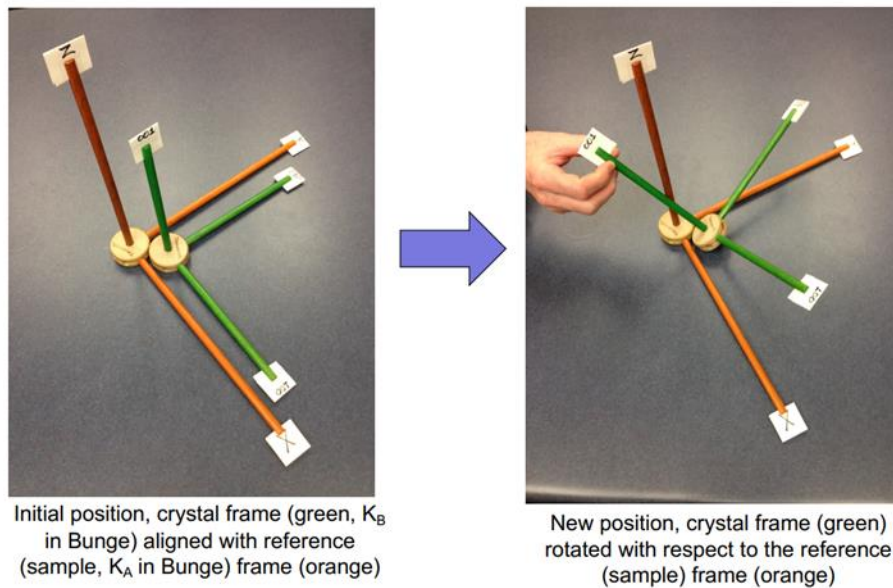
Figure 12. Rotation of crystal reference frame with respect to specimen reference frame

Any arbitrary rotation such as this can be reduced to three Euler rotations that are performed successively one after the next which bring the sample reference frame into coincidence with the crystal reference frame (active rotations) or vice versa (passive rotations). The first step in the methodology for these rotations to describe the orientation of any crystal is that the crystal and specimen reference frames are originally set to be coincident with one another for the orientation $\varphi_1 = 0$, $\Phi = 0$, and $\varphi_2 = 0$, see Figure 13 (Bunge, 1982).
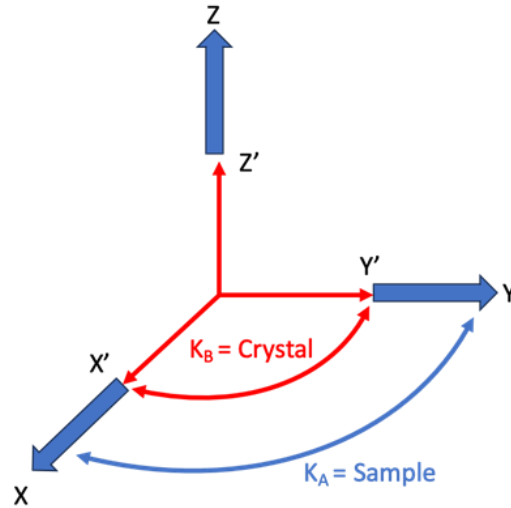
Figure 13. Placement of crystal and specimen reference directions coincident with one another

For the cubic system, since its crystal directions are orthogonal to one another, there is no ambiguity on how the crystal reference frame is placed in relation to the specimen reference frame. However, for the HCP crystal system one can choose to have the x-direction of the specimen coordinate system aligned with the a_1 direction in the HCP crystal system (green arrows in Figure 14) or have the y-direction aligned with the a_2 direction in the HCP crystal system (red arrow in Figure 14). This is a choice that has been made differently by EBSD manufactures: (1) EDAX/TSL chooses the green arrow configuration and (2) the other popular manufacturer Oxford/HKL chooses the red arrow configuration. For the purpose of the following discussion, we will choose to plot images using the EDAX or green arrow configuration. EDAX/TSL uses the Z-X-Z convention which involves (1) first a rotation about the sample and crystal Z axes which are initially parallel, (2) followed by a rotation about the new crystal X axis (called X'), and (3) followed by a rotation about the newest crystal Z axis (i.e., Z').
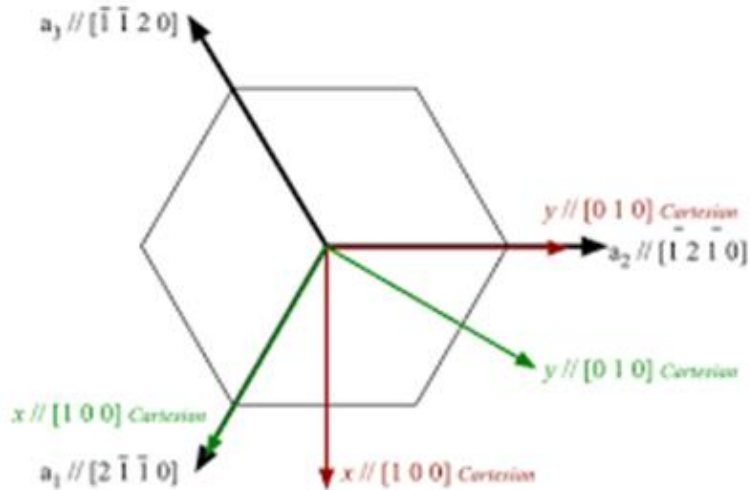
Figure 14. Alignment of the HCP crystal system in the cartesian specimen reference frame

Having selected the $\varphi_1 = 0$, $\Phi = 0$, and $\varphi_2 = 0$ crystal orientation, the next step is to define the series of rotations required to express an arbitrary orientation within the sample reference frame. This first step is to rotate the crystal clockwise by an angle of φ_1 about the Z-axis (Figure 15), modeled after Bunge (1982).
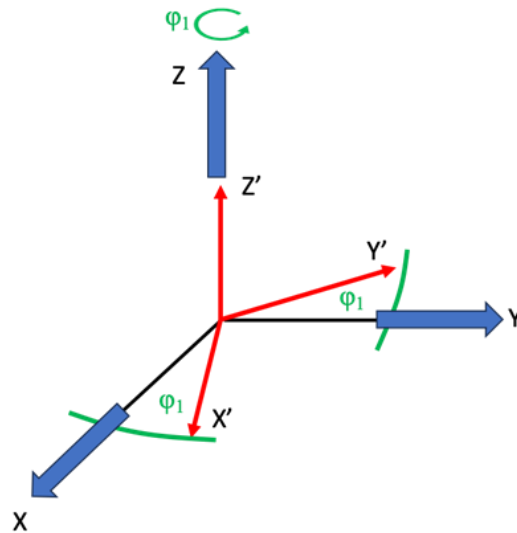
Figure 15. Placement of crystal and specimen reference directions after rotation of φ_1 about the Z-axis

For the chosen HCP basis (EDAX/TSL green arrows in Figure 14), a 43-degree rotation of φ_1 about the Z-axis (according to the right-hand rule, i.e., thumb along the rotation axis and a counter clockwise rotation) does not change the (0002) pole figure as shown in Figure 16.

28
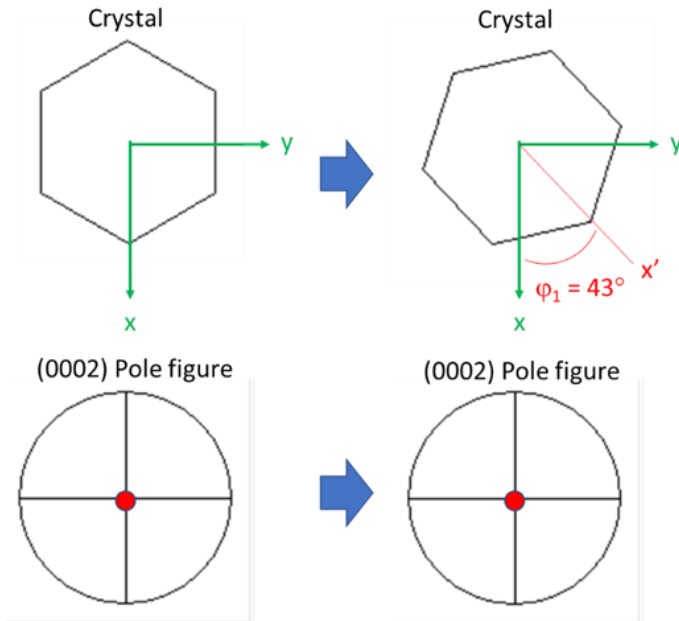
Figure 16. Visualization of a $\varphi_1 = 43°$ rotation about the sample Z-axis

The next step is to perform a rotation about the X' axis (i.e., the new crystal X axis) with a right-hand rule rotation of Φ (Figure 17), modeled after Bunge (1982).
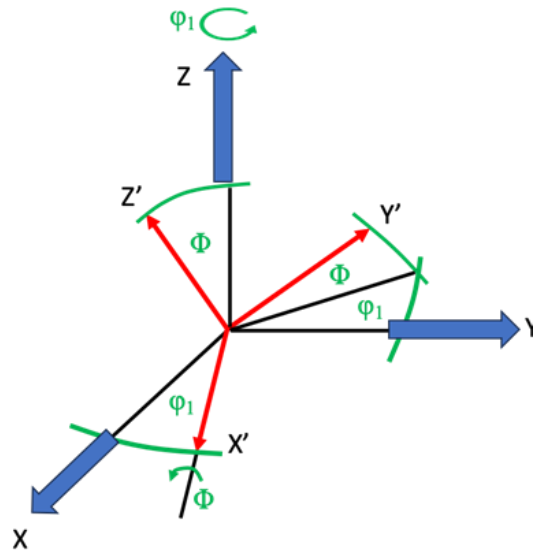
Figure 17. Crystal and specimen reference directions after additional rotation of Φ about the X'-axis

In order to demonstrate this on the hexagonal crystal shown in Figure 16, we choose to perform a fifty-degree rotation about the X' axis (i.e. the new crystal $\langle 2\bar{1}\bar{1}0 \rangle$) and denote this Euler angle as Φ (Figure 18).

29
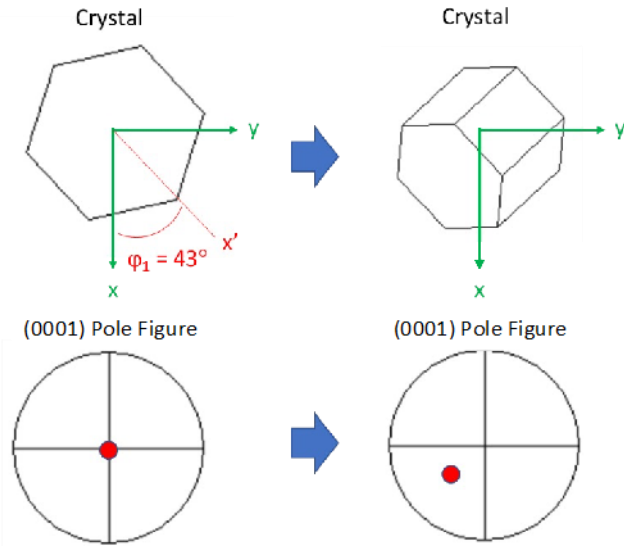
Figure 18. Visualization of a 50° rotation
In Φ about the X'-axis for the crystal and (0001) pole figure

At this point it is worth stopping for a moment to reflect on what these first two rotations have done. For the chosen reference frame (i.e., X axis pointing south and Y axis pointing east) the first rotation φ_1 about the Z-axis sets the quadrant of the (0001) pole in which:

- Values of φ_1 about the z-axis that are less than 90° places the (0001) pole in the third quadrant of the pole figure.

- Values of φ_1 about the z-axis that are more than 90° and less than 180° places the (0001) pole in the second quadrant of the pole figure.

- Values of φ_1 about the z-axis that are more than 180° and less than 270° places the (0001) pole in the first quadrant of the pole figure.

- Values of φ_1 about the z-axis that are more than 270° and less than 360° places the (0001) pole in the fourth quadrant of the pole figure.

Thus the first Euler angle φ_1 can be thought of as the angle that defines the quadrant where the crystal direction that is aligned with the Z-axis at $\varphi_1 = 0$, $\Phi = 0$, and $\varphi_2 = 0$ points (in our crystal example the c-axis of the HCP system), and the second rotation Φ about the X' axis sets the inclination angle of the (0001) pole. It is worth emphasizing that the sample reference frame can be defined by the user in most modern EBSD software and thus the quadrants mentioned above may change as a function of this choice. It is essential to understand the correlation between the microscope coordinate system and the sample coordinate system within which the Euler angles are defined. More generally, the first two Euler angles are related to the sample reference frame

30

as shown in Figure 19. The φ_1 rotation is measured as a rotation about the Z-axis from the -Y axis while Φ is the angle between the sample X direction and the (0001) pole.
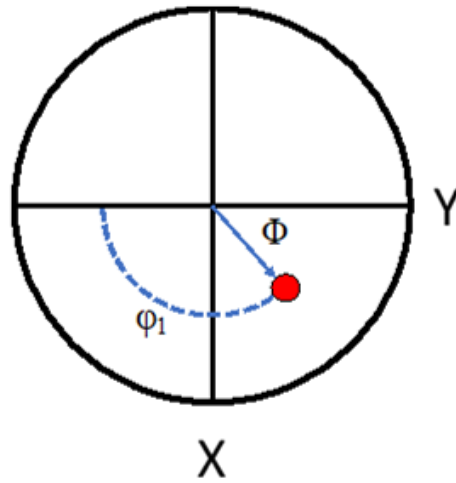
Figure 19. Correlation between angles φ_1 and Φ, the sample reference frame, and (0001) pole

Finally, the last step to define an arbitrary orientation is to rotate the crystal counterclockwise about the Z' axis (Figure 20), modeled after Bunge (1982).
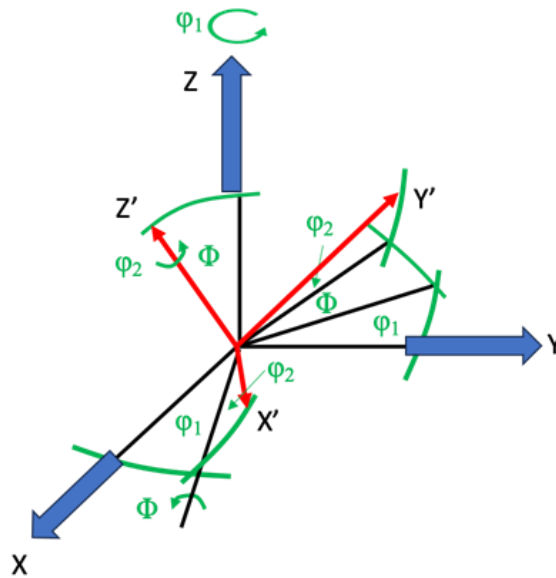
Figure 20. Placement of crystal and specimen reference directions after additional rotation of φ_2 about the Z'-axis

In order to demonstrate this rotation with a HCP crystal, we choose to perform a 20° rotation (φ_2) about the Z' axis (Figure 21).
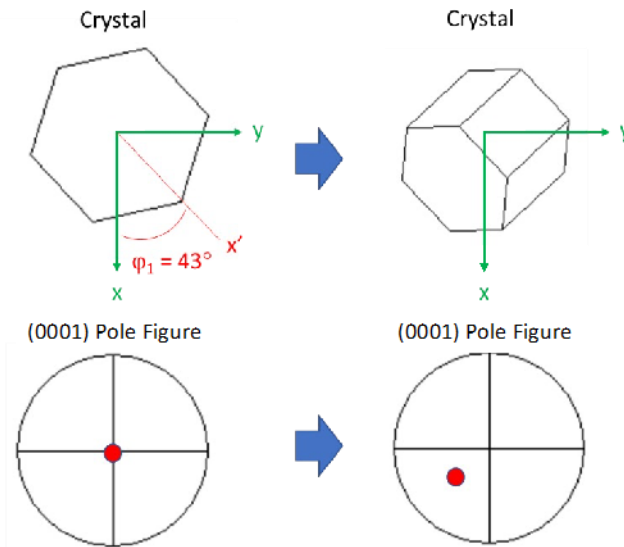
Figure 21. Visualization of a $\varphi_2 = 20°$ rotation about the Z'-axis

It is immediately evident that the (0001) or location of the c-axis does not move, but the location of the prism planes have been rotated. Hence, the third Euler angle φ_2 can be thought of as a rotation that aligns the crystal directions that were originally aligned with the X and Y reference directions at $\varphi_1 = 0$, $\Phi = 0$, and $\varphi_2 = 0$, and the application of the three Euler angles in the regimented manner described above can fully describe the orientation of a crystal with respect to the specimen reference frame.

Because the direction of the (0001) pole only gives us a partial picture of the crystallographic plane that is perpendicular to the normal direction in a (0001) pole figure, multiple pole figures are typically plotted when the texture of a material is examined. In particular, it is common to examine $\{11\bar{2}0\}$, $\{10\bar{1}0\}$ and $\{10\bar{1}1\}$ pole figures. Furthermore, while this discussion has focused on discrete orientations, there are many orientations present in a polycrystalline aggregate. In this case, pole figures are typically represented as a probability density depicted using colored contour maps. The probability density of orientations is normalized such that a uniformly random texture has a value of 1.0 over the entire surface of the pole figure.

While pole figures illustrate crystallographic orientations within the sample reference frame, inverse pole figures (IPFs) are used to identify crystallographic planes perpendicular to a particular direction in the sample reference frame (viz., Figure 22). Moreover, the colors of these IPFs are typically used in EBSD maps presented to show the size of MTRs in the microstructure that are measured with EBSD. Once again because IPF's describe the plane normal with respect to a specimen direction, multiple IPF's are required to completely specify the directions of a crystal in an EBSD map.
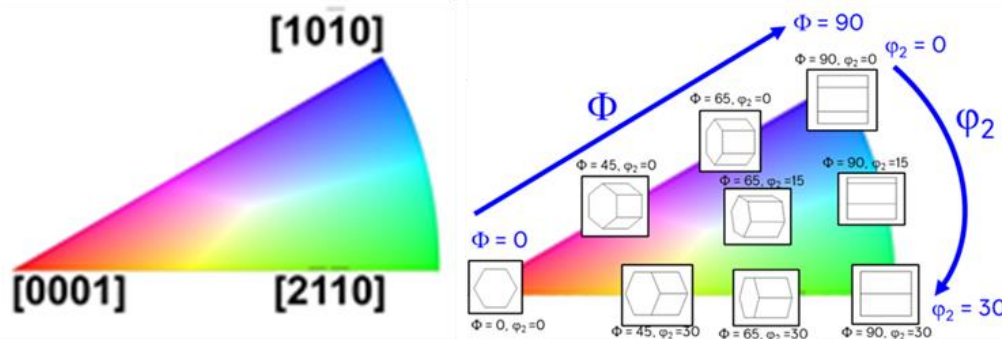
Figure 22. Inverse pole figure for HCP crystals

Inverse pole figures (IPFs) are useful because they identify the particular {hkl} or {hkil} plane(s) that are perpendicular to a given vector of interest in the sample coordinate system. For example, an IPF plotted perpendicular to a metallographic sample's normal direction will indicate the crystallographic plane parallel to the plane of polish. These diagrams have also found application in demonstrating the crystallographic plane exposed to the fracture surface after one accounts for the spatial orientation of the facet itself using quantitative tilt fractography (Pilchak & Williams, 2011; Sinha, Mills, & Williams, 2006). In contrast to pole figures, which show the location of all poles normal to a family of planes, IPFs are represented on a reduced order space often called the standard triangle which varies with crystal symmetry, and which collapses symmetrically equivalent orientations such that only one pole is shown per family. While a full description of the orientation of crystals requires 2-3 complimentary IPFs (depending on crystal symmetry and whether planes or directions are plotted), it is common to visualize the microstructure using a single IPF direction. The normal direction, Z, to the polished surface of the specimen is conventionally used, and denoted IPF-Z. Examples of discrete orientations represented as crystal glyphs, pole figures, and the corresponding IPF-Z colors, are shown in Figure 23. This figure was developed to help readers less familiar with EBSD to interpret such data when they encounter it in the literature or see it in presentations.

The color of each grain is represented by the stereographic triangle for the alpha phase of titanium, which is provided in the key at the top of the figure. The top image shows a series of

grains with the basal plane in the plane of polish and thus the c-axis is normal to this plane. These orientations vary through a systematic rotation about the c-axis, as indicated by the wireframe crystals drawn in the center of each grain. The corresponding (0001) pole figure for each grain is shown in the row beneath the image containing the series of grains. The pole figure is a unit sphere that represents a fixed sample reference frame, or, alternatively, a laboratory coordinate system. They denote where the pole (i.e., the direction normal to a crystallographic plane) intersect the unit sphere and hence can be used to determine the angles between crystallographic directions and directions of interest in the sample reference frame (e.g., a stress axis). Typically, only the poles which intersect the upper hemisphere of the unit sphere are plotted, as is the case in Figure 23. The $\{11\bar{2}0\}$ pole figures corresponding to each grain are shown below the (0001) pole figures. Note that rotations about the c-axis of the crystal do not produce a change in IPF-Z color because the surface normal remains coincident with (0001), while they do produce changes in the pole locations in the $\{11\bar{2}0\}$ pole figures. Six spots appear on the $\{11\bar{2}0\}$ pole figure when the basal pole is normal to the plane of polish due to the symmetry of the pole figure (i.e., points 180 degrees apart on the periphery of the pole figure are equivalent orientations).

The middle row of data in Figure 23 shows the effect of rotating the crystal about the Y-axis in the sample reference frame (vertical direction) which produces c-axis orientation relative to the surface normal of the specimen ranging from (0001) (red) to $(1\bar{1}00)$ (blue), tracing the upper left edge of the stereographic triangle. The orientation of the c-axis and a-axes sweep systematically across the pole figure with these rotations. The bottom portion of Figure 23 illustrates the range of colors and corresponding pole figures for the case of a c-axis in the crystal collinear with the Y-direction in the specimen. In this last case, the crystal plane normal coincident with the surface normal of the specimen ranges from $(1\bar{1}00)$ (blue) to $(\bar{1}2\bar{1}0)$ (green), following along the arc on the right edge of the stereographic triangle.
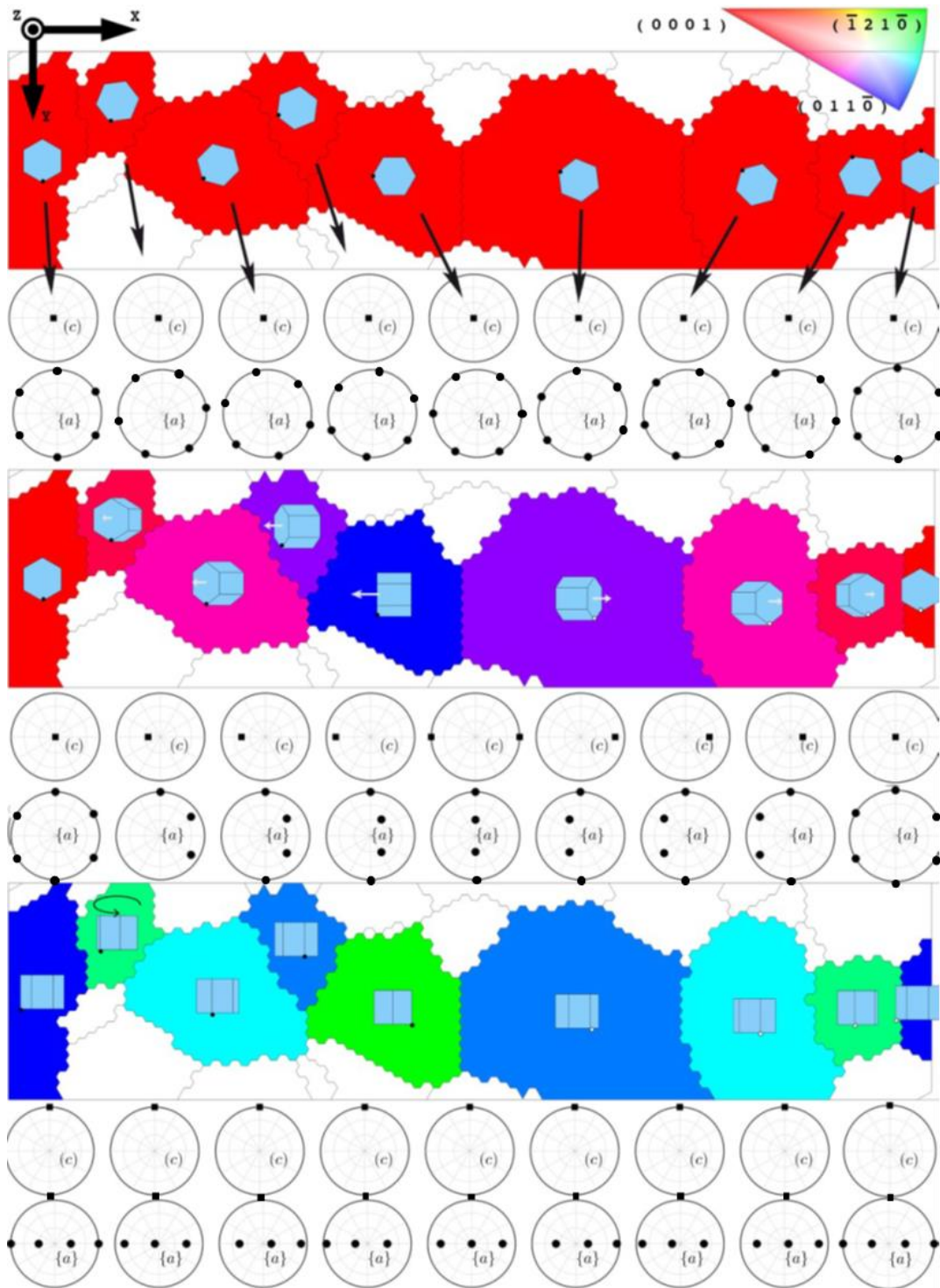
Figure 23. Representation of crystal orientations as crystal glyphs, IPF-Z coloring, and on (0001) and $\{11\bar{2}0\}$ pole figures

Crystallographic texture is the presence and degree of preferred crystallographic orientation in a material. Texture, often called macrotexture to distinguish it from *microtexture*, is represented on pole figures, inverse pole figures, and orientation distribution functions. The difference between randomly oriented crystals, a crystallographic texture, and microtexture is illustrated in Figure 24. Each of the three images show EBSD data as pixels colored by the location of the specimen surface normal in the alpha phase crystal reference frame (i.e., an IPF-Z coloring scheme for crystals with hexagonal symmetry). Figure 24(a) shows a random crystallographic texture, in the crystal orientation at each measurement point (pixel) in the grid is random. Figure 24(b) shows the same scan area with a crystallographic texture, resulting in a larger fraction of the pixels appearing in shades of red. Figure 24(c) contains exactly the same orientations as Figure 24(b), and thus exactly the same crystallographic texture; however, there is a spatial correlation in the orientations such that the orientations corresponding to a surface normal aligned with the c-axis of the crystal are clustered into a region running from the upper left to the lower right of the image. An MTR is broadly defined as such a cluster of spatially correlated grains with similar c-axis orientation, although specific definitions of these features are addressed in Section 3.1.
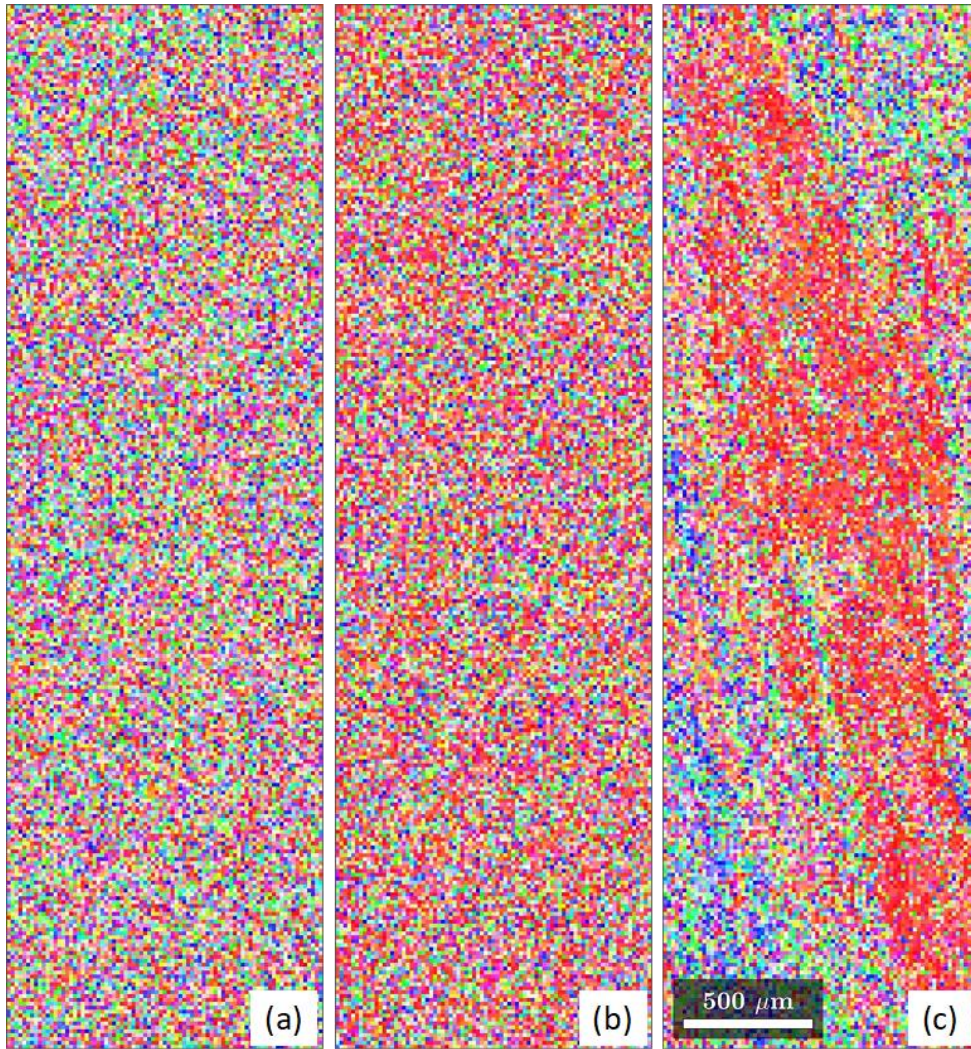
Figure 24. Difference between (a) random orientations (b) crystallographic texture and (c) microtexture

The orientation distribution function (ODF) is a complete and continuous representation of orientations in a given volume of material. It is used in quantitative texture analysis to determine the volume fraction of orientations relative to a fixed sample coordinate system. There are many ways to represent crystallographic orientations including Euler angles, quaternions, and Rodrigues vectors, for example. ODFs are classically represented as 2D sections through a three-dimensional cube with axes $(\varphi_1, \Phi, \varphi_2)$. As the triplet of Euler angles defines a specific orientation, so too does a point in the ODF. Because of crystallographic symmetries, it is possible that multiple points in the ODF represent the same crystallographic orientation. As a result, the ODF is usually restricted to the so-called fundamental region where each point represents a unique orientation. The fundamental region for the hexagonal alpha phase is $0° \leq \varphi_1 \leq 180°$, $0 \leq \phi \leq 90$, and $0 \leq \varphi_2 \leq 60$. ODFs can be calculated from a series of pole

37

figures measured by x-ray diffraction, for example, or from a series of discrete measurements, such as those obtained by electron backscatter diffraction (EBSD), the latter being far more common today due to the speed of EBSD and the additional learning that comes from understanding the spatial distribution of orientations. The density of poles in a given volume of material are determined by fitting the orientation data to spherical harmonics. The coefficients of the harmonic series expansion can be used to fully represent the texture of the material. The complete mathematical treatment of ODFs can be found in the work by Bunge (1982).

3 Characterization and quantification of microtextured regions

Titanium alloys have a broad range of microstructural features accessible by thermomechanical processing and heat treatment. The majority of titanium used for critical gas turbine engine applications are in the alpha+beta processed and heat-treated condition, though some components are manufactured in the beta-processed or beta-heat treated condition. As shown in Figure 25, these microstructural conditions each have a hierarchy of features that span about seven orders of magnitude. The entire range of microstructural features collectively influences mechanical properties of the material and hence must be considered and controlled during processing. Some of the features (colonies, MTRs, prior beta grains) are so large they approach the length scale of component-relevant features (web thickness, fillets/radii) resulting in one or a few of each feature across the section thickness. The small number of features across the section size coupled with the anisotropy induced by crystal orientation can lead to mechanical response that deviates significantly from the isotropic continuum solutions often used in design. Typical product feature length scales for disks and integrally bladed rotors (also known as bladed disks or blisks) for civil aircraft are as follows:

- bores tend to have length scales in the 10's of mm

- webs or diaphragms are of the order of a few mm to low 10's of mm

- Disk blade slots or airfoil blade root fillets on blisks tend to have small volumes of material under high stress and the high stressed regions would typically be < 10 mm for a single feature.

Furthermore, the vertical black line in Figure 25 is a reference point for ~0.75 mm (~1/32") which corresponds to the common definition of the surface length for an initiated "engineering" fatigue crack under low cycle fatigue conditions (Harrison & Winstone, 1996).

It is also evident that some MTRs or colonies may exceed this value. As discussed in Section 4.3, dwell fatigue crack growth rates remain high in MTRs and hence conventional damage tolerance analysis may be anticonservative in this case.

Microstructure characterization is an essential practice in the development of critical aerospace components and in the quality control process. Standard metallographic techniques like optical and scanning electron microscopy (SEM) are used to assess various features of the microstructure such as the size, morphology, and volume fraction of primary and secondary alpha. Backscattered electron imaging is the preferred method due to the higher spatial resolution compared to optical microscopy. Backscattered electron imaging is sensitive to chemical composition and the elemental partitioning effect of the alpha and beta stabilizing elements which occurs during processing provides good contrast among the constituents (Searles, et al., 2005). Today, these images can be easily segmented using open-source software (e.g., FIJI (Schindelin, et al., 2012)), commercial packages (e.g., MIPAR (Sosa, Huber, Welk, & Fraser, 2014)), or codes developed using image processing routines within Matlab or Python, for example. Features like alpha2 (Ti_3Al), short range order, and ultra-fine secondary alpha laths are too small to observe with SEM and hence the transmission electron microscope (TEM) may be necessary for some special analyses but is not generally needed for routine characterization or quality control. Image processing for scientific images and microstructural features has been described extensively by Russ and Neal (2018) and hence will not be covered further here, as our primary focus is on describing methods for characterizing and quantifying microtexture in titanium alloys.
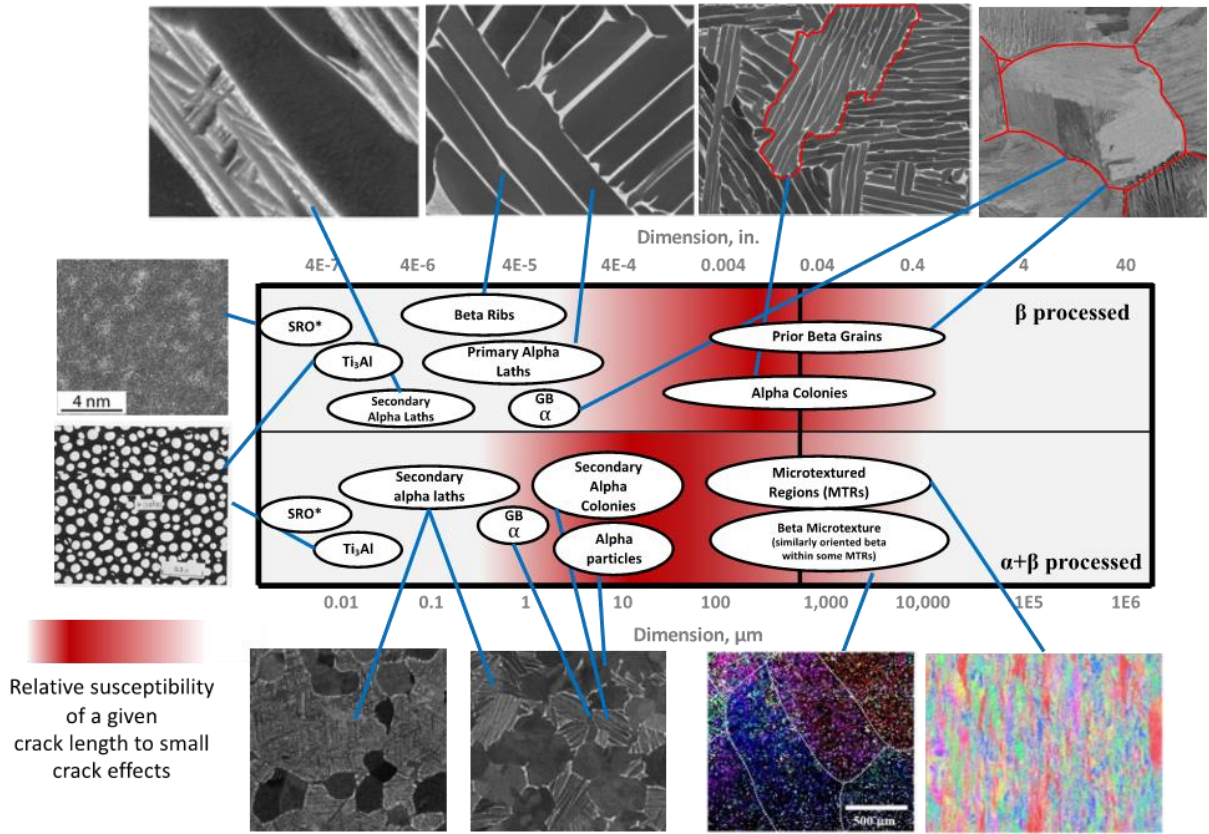
Figure 25. Hierarchy and length scale of microstructural features in alpha+beta processed and beta-processed material

3.1 Definition of microtextured regions/macrozones

Microtextured regions (MTRs), also called macrozones, are localized regions in alpha+beta converted billet, bar, plate, or an alpha+beta forged component where neighboring regions of alpha phase have a similar crystallographic orientation. The primary source of this crystallographic alignment is the equiaxed alpha grains established during spheroidization of a colony following quenching from the last time that the material is above the beta transus, however, the transformed beta phase in bimodal microstructures also plays an important role in the MTR characteristics. Ideally, the transformation from beta to alpha will result in secondary alpha that is highly misoriented with respect to the dominant primary alpha orientation. However, in some cases the orientation of the underlying beta phase may present a {110} plane that is closely aligned with (0001) in the primary alpha which may result in preferential selection of this variant of the BOR (Germain, et al., 2008; Gey, Bocher, Uta, Germain, & Humbert, 2012). MTRs were first identified by Woodfield et al. (1996) shortly after the development of automated electron backscatter diffraction (EBSD) which allowed the determination of local crystallographic orientations with high-spatial resolution. Since then, there have been significant

advances in scanning electron microscopes and EBSD systems that have enabled measurement and indexing of diffraction patterns at a rate of several thousands of points per second. This, coupled with multi-tile acquisition and stitching methods (Pilchak & Williams, 2011; Pilchak, Shiveley, Shade, Tiley, & Ballard, 2012), has enabled large areas of material to be characterized leading to a more thorough understanding of MTR characteristics. While EBSD methods provide great insight, it is noteworthy that optical microscopy has been routinely used for decades as the standard method for evaluating the metallographic structure of periodic cutups and qualifying products for release. Due to the lack of sensitivity to crystallographic orientation in bright field optical microscopy, the primary alpha volume fraction, aspect ratio, and alignment are key features of interest that may indicate a microtextured state. This is often referred to as "spaghetti alpha" in the literature (e.g., (Chesnutt, Thompson, & Williams, 1978)).

MTRs may behave as large effective structural units during deformation (Rugg, Dixon, & Dunne, 2007), although recent work by Harr et al. (2021) has demonstrated that not all MTRs behave this way under dwell fatigue loading at room and elevated (120 ºC and 200 ºC) temperature. The differences in response may be due to variations in the character of the MTRs resulting from unique thermomechanical processing routes. This necessitates a more thorough description of MTRs and thus the following terminology has been recommended to the FAA for inclusion to the updated advisory circular AC 33-15.1 (Pardee, 1998):

- **Microtextured Region (MTR):** A localized region in an alpha/beta converted billet or an alpha/beta processed component forging where neighboring alpha grains or secondary alpha platelets have similar crystal orientations such that the feature may act as a larger structural unit during deformation or crack growth. MTR size, shape, density, intensity, frequency, orientation, orientation spread, neighboring region characteristics, volume fraction, and primary alpha volume fraction, are important parameters when characterizing MTR features. These features are known to impact dwell-fatigue capabilities. MTRs are also sometimes referred to as "macrozones" or "primary alpha colonies". MTR regions were identified once electron backscatter diffraction methods were developed which allowed correlation of specific microstructural features with their underlying crystallographic orientation.

- **MTR density:** A measure of the area fraction of the alpha grains in an MTR that have a similar basal (0001) plane orientation. This factor includes contributions from both primary alpha and secondary alpha platelets.

- **MTR size frequency:** The number of MTR features of a given size within a volume of titanium.

- **MTR intensity:** A measure of the range of variation of crystallographic orientations of all of the alpha grains within an MTR that includes weighted contributions from the fraction of well-aligned alpha grains as well as the fraction of not well-aligned grains. The weighting of contributions is a function of alignment and area (or volume) fraction. Low MTR orientation spread with high MTR density would be referred to as an intense MTR. A material having intense MTRs does not imply anything regarding the material's macrotexture (i.e., the macrotexture could be weak or strong in a material having intense MTRs).

- **MTR neighboring regions:** The region surrounding MTR features. These could include MTR features of different character or regions of substantially randomly orientated alpha (average orientation regions). The neighborhood surrounding MTR features are critical to the potency of MTRs impact on dwell fatigue.

- **MTR orientation:** The dominant crystallographic orientation of the alpha grains and colonies within an MTR region. MTRs with the basal plane oriented nearly perpendicular to the principal stress direction are classified as "Hard MTRs". Combinations of other orientations that enable easy basal or prismatic slip relative to a stress axis are classified as "Soft MTRs". Both "hard" and "soft" MTRs influence dwell fatigue performance of titanium materials. The "soft" regions accumulate significant creep strain during dwell while the "hard" regions are potent crack nucleation sites and then offer very limited resistance to crack propagation. ESBD or similar methods are needed to assess crystallographic orientations.

- **MTR orientation spread:** A measure of the average crystallographic misorientations of the similarly aligned alpha phase grains within an MTR.

- **MTR quantification:** Methods to quantify MTR size, shape, density, intensity, frequency, orientation, orientation spread, neighboring region characteristics, volume fraction, and primary alpha volume fraction, are important parameters when characterizing MTR features. This characterization requires a means of discerning and measuring alpha grain orientations.

- **MTR shape:** The general geometric morphology of a contiguous area of similar alpha grain orientations, which may be expressed as the aspect ratio of longest and shortest dimensions, or the ratio of the axes of an ellipse fit to the MTR in 2D cross-section.

- **MTR size:** The size of a contiguous region of similar alpha phase orientations plus all other grains internal to this region often expressed as an area or equivalent diameter in 2D cross-section.

- **Non-contiguous MTR size:** The size of a region of similar alpha phase orientations that are not necessarily in direct contact with one another plus all other grains internal to this region.

- **MTR volume fraction:** The summed volume (or area) of all MTR features, including all grains internal to the MTRs, divided by the total volume (or area) of titanium investigated.

The density, intensity, orientation, size, and shape of MTRs in a volume are best represented by cumulative distribution functions, although histograms may also be used. The former has the advantage of more clearly representing the upper tail of the distribution, which contains the most important MTRs with respect to crack nucleation and faceted crack propagation and hence total dwell fatigue lifetime. The correlation between these variables and dwell fatigue lifetime as inferred from the literature (Ghosh, et al., 2007; Liu & Dunne, 2021; Mills, et al., 2018; Pilchak & Williams, 2011; Toubal, Bocher, & Moreau, 2009) (Woodfield A. , Gorman, Corderman, Sutliff, & Yamrom, 1996; Woodfield A. , Gorman, Sutliff, & Corderman, 1999) is summarized in Table 3. It must be noted that correlations exist between several variables. For a constant MTR volume fraction, as MTR size increases, MTR frequency decreases; with constant MTR frequency, as MTR volume fraction increases, MTR size must also increase. Low MTR orientation spread with high MTR density would be referred to as an intense MTR. A material having intense MTRs does not imply anything regarding the material's macrotexture (i.e., the macrotexture could be weak or strong in a material having intense MTRs). Thus, a volume of material could have a low volume fraction of intense MTRs.

Finally, it is worth emphasizing that the phrase *microtextured regions* is reserved for the regions of aligned primary and/or secondary alpha in alpha+beta forged and alpha+beta heat treated materials. The aligned features formed during cooling from beta-forging or beta heat treatment are most accurately referred to as alpha colonies. The two terms should not be used interchangeably.

Table 3. Correlations between MTR attributes and dwell fatigue lifetime

MTR Characteristic	Dwell Fatigue Life
Density	Decreases with increasing density
Frequency	Decreases with increasing frequency
Intensity	Decreases with increasing intensity
Orientation	Decreases with increasing fraction of intense hard and soft orientations
Orientation Spread	Increases with increasing orientation spread
Shape	Modeling suggests it decreases with increasing aspect ratio (Y. Liu & Dunne, 2021), but component experience shows conflicting results indicating more work is needed to understand the impact of MTR shape
Size	Decreases with increasing size
Volume Fraction	Decreases with increasing volume fraction

3.2 Best practices for characterization of microtexture

As requirements for components trend toward higher performance with reduced weight at reasonable cost, it will be necessary to control microtexture (and macrotexture) to fully optimize material properties and component performance. This is challenging, however, because of the relatively large areas (> 100 mm^2) which must be analyzed to obtain a reasonable statistical distribution of texture/microtexture for each sample as well as the high spatial resolution that must be used to properly characterize MTRs. This issue is compounded by heat-to-heat, billet-to-billet, and forging-to-forging variability as well as sample-to-sample variability based on differences in the character of MTRs in mill products as well as variation in thermomechanical history for each location in a part (Gey, Bocher, Uta, Germain, & Humbert, 2012).

The diagram in Figure 26 provides an overview of the methods that have been investigated for characterizing MTRs, separated by destructive and nondestructive methods, with color coding according to the relative level of maturity. In this context, destructive implies sectioning and metallographic preparation while nondestructive implies techniques that can be applied to machined billets or components (either in sonic shape or finish machined). The maturity scale is a qualitative assessment at the time of writing based on our collective experience with these methods. The categories are defined as follows:

- **Limited development** represents that a small number of papers have been published which demonstrate that the technique has some level of sensitivity to detecting MTRs.

- **Ongoing work** implies that the technique has moved beyond a few academic investigations and is being further matured by small business(es) or industry, which may include development of methods to quantify MTR metrics.

- **Developed** indicates that the technique has reached a higher level of maturity and clearly demonstrates high sensitivity to MTRs; protocols for data collection are established.

- **Industrialized** means that the technique has been widely adopted by industry and/or is being used in some capacity to understand and manage risk to components.

As evident from the maturity scale, and not surprisingly, more work has been performed on characterization techniques for metallographically prepared surfaces. EBSD is presently considered the "gold standard" as it provides the best spatial resolution and most accurate measurement of local orientation. Techniques based on polarized light microscopy, however, are being pursued due to the potential of capturing data over much larger areas at higher spatial resolution than is typically used for EBSD while having lower cost. Significant progress has been made and this approach is showing strong promise. Development has been bolstered by US Air Force and US Navy funding under the Small Business Innovative Research (SBIR) program. Two small businesses, Advanced Optical Technologies (AOT) and Materials Resources, LLC (MRL) have developed microscopes and are making measurements as a service and are also producing microscopes for sale.

Eventually, industry would like to move toward complete volumetric characterization of MTRs using nondestructive methods. Various nondestructive evaluation (NDE) techniques have been assessed for their sensitivity to detecting MTRs. While not as mature as the destructive techniques, there are many methods showing promise, including both bulk and surface acoustic waves (ultrasonics) as well as eddy current inspection. Polarized light methods have potential for providing details of surface-connected MTRs on machined components, however, more work needs to be done to verify the tolerance to surface roughness and the impact of shot peening. It is worth noting that while the EBSD technique itself is fully developed and moving toward industrialization, there are currently no industry-wide standards for MTR characterization. Under the auspices of the US Air Force Research Laboratory's Metals Affordability Initiative (MAI) (Bayha, Evans, & Furrer, 2002; Martin & Evans, 2000), however, there are OEMs working together to align on a methodology. Thus, in this section, we present the current best practices for MTR quantification for destructive sectioning via EBSD. For the reader interested in alternate characterization methods, we have included a comprehensive literature review summarizing destructive and nondestructive characterization techniques in Appendix B and Appendix C.
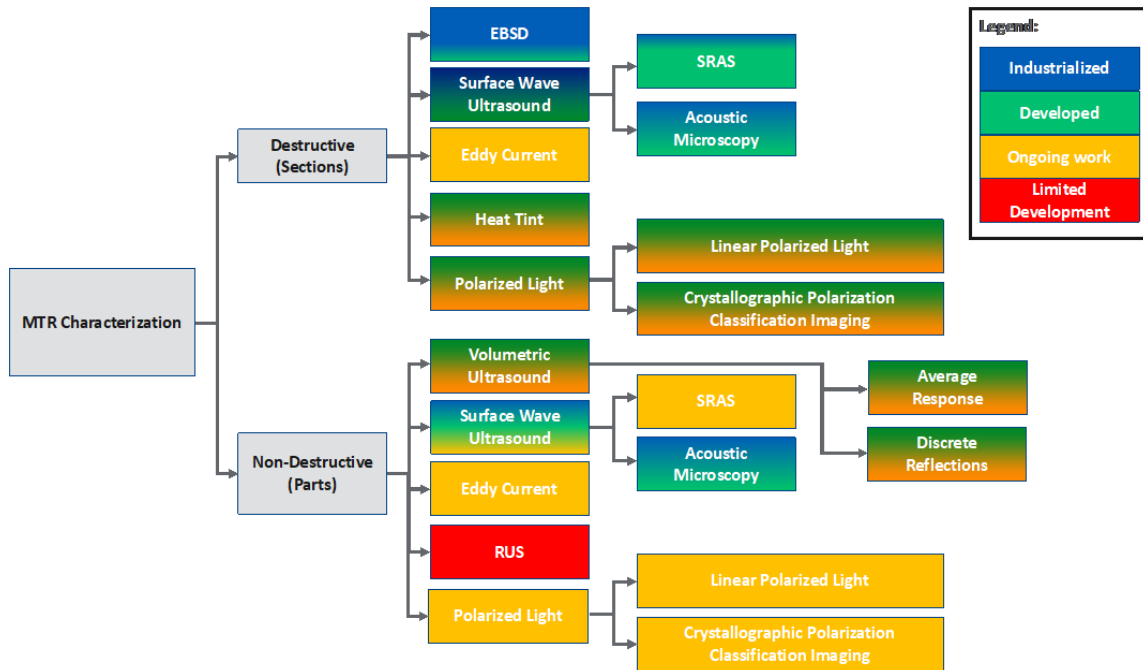
Figure 26. Summary of destructive and nondestructive methods for characterizing MTRs

A noteworthy development was presented at the 15th World Conference on Titanium held in Edinburgh, Scotland in 2023. GE Aerospace reported on the development of a surface-wave ultrasonic test (SWUT) MTR inspection methodology that has been used *on-wing* to identify parts with high degrees of microtexture in the machined and peened surface condition (Klaassen et al., 2023). This technique relies on the fact that Rayleigh surface acoustic waves travel at different velocities in MTRs, depending on the angle between the average MTR c-axis direction and the direction of acoustic wave propagation (Kim & Rokhlin, 2009). Sectioning of selected parts showed the measured level of MTRs determined via electron backscatter diffraction (EBSD) corresponded to the SWUT response. Additionally, a clear correlation was established between the SWUT response measured on parts and the detailed billet processing records for each of the parts.

In follow-on work, the SWUT technique was applied to billet sections and forging macroslices with qualitative correlations established between the SWUT and the underlying microtexture obtained by EBSD. Figure 27 shows SWUT images for two transverse billet slices of (i) smaller and (ii) larger diameter. These images show circumferential differences that have been related back to local macrotexture of MTRs using SWUT and EBSD on radial-axial slices cut from the transverse slices, as shown in Figure 27. The elongated MTRs are evident in the radial-axial SWUT scans and correlate with the corresponding mid-radius EBSD scans, with the larger diameter billet having more discrete MTRs with lower aspect ratio as compared to the smaller

diameter billet. Each transverse billet slice SWUT scan took approximately 1 hour, with the scans not optimized for speed; the billet slices were in the ground condition that is typically used for billet macroetch inspection.
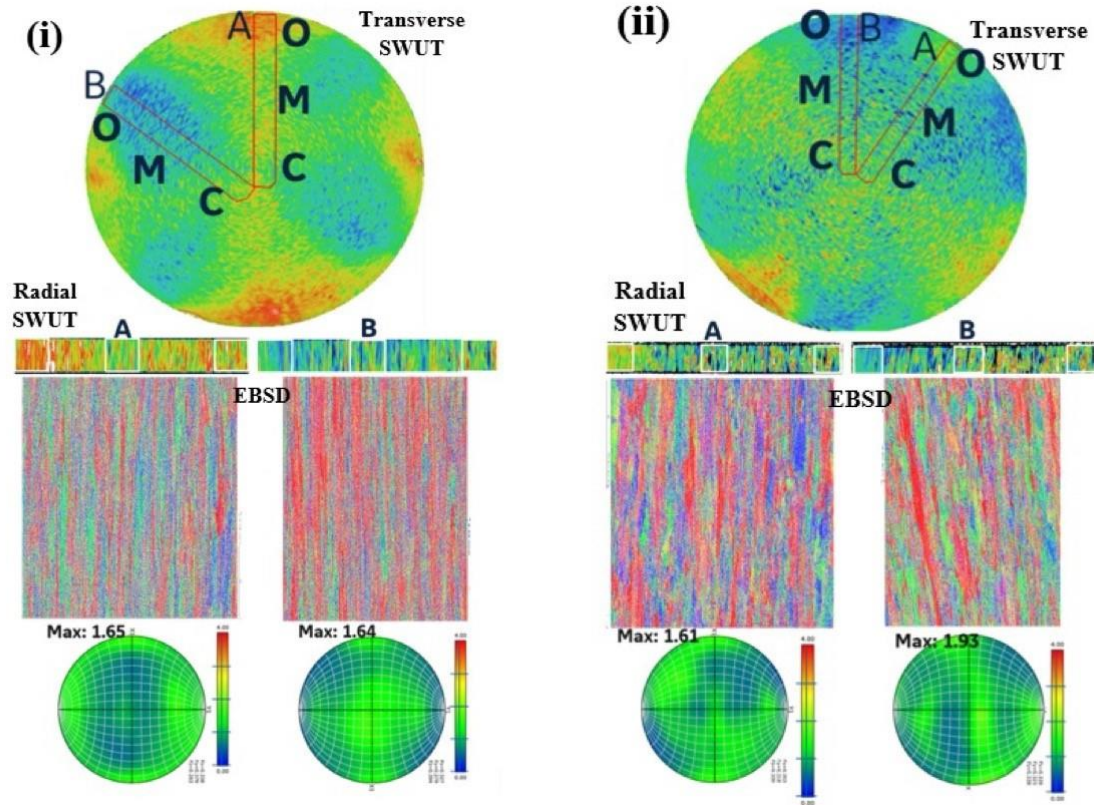
Figure 27. SWUT and EBSD data taken from (i) smaller (ii) larger diameter transverse billet slices

3.2.1 Introduction to electron backscatter diffraction

Electron Backscatter Diffraction is an SEM-based technique by which electrons incident on a crystalline material scatter elastically and incoherently within the material such that the Bragg condition is simultaneously satisfied for all atomic planes. A fraction of these electrons will be backscattered and exit the sample surface forming two 'cones' of radiation with a small Bragg angle (one on each side of the source) for every set of atomic planes with an appropriate structure factor. Because diffraction occurs simultaneously from multiple families of planes, the cones intersect at specific distances and angles depending on the local crystallographic orientation of the diffracting volume. In order to measure the orientation, a cerium oxide-coated glass screen is placed in close proximity to the sample. The screen coating exhibits the property of fluorescence, (i.e., it glows when struck by the electrons and a digital camera placed at some distance behind the lead glass is used to capture a digital image of the pattern). Named after their

47

discoverer, the Kikuchi bands appear as lines when they intersect the phosphor screen (Nishikawa & Kikuchi, 1928). The lines are identified via the Hough transform, and subsequently compared to a precalculated look-up table to determine the actual crystal orientation. Under the best performance conditions, the absolute orientation can be determined to better than ~0.5° while the point-to-point misorientation is of the order of 0.1°; however, in a typical investigation it appears realistic to expect that >90% of the indexed patterns are within ~1° of the correct absolute orientation (Bingham, Lograsso, & Laabs, 2010). EBSD is able to discern crystal orientation as well as phase distribution as shown in Figure 28.
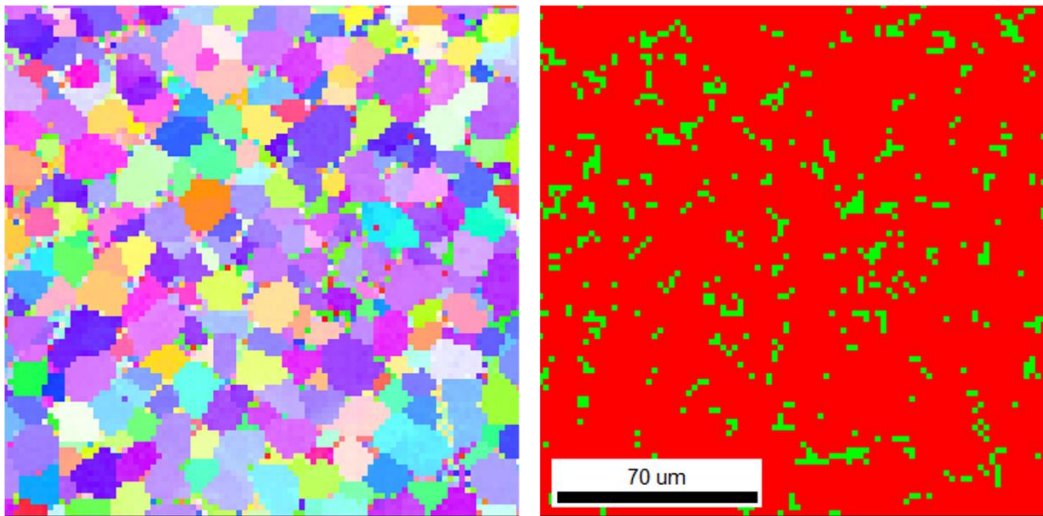
Figure 28. Normal direction inverse pole figure colored crystal orientation map (left) and phase map (right)

Single tile collected at 500x magnification and 2 μm resolution. Beta phase is colored green

EBSD is able to provide the detailed level of characterization required to characterize both the internal structure of MTRs and, when combined with multi-tile acquisition strategies (Pilchak, Shiveley, Tiley, & Ballard, 2011; Pilchak, Shiveley, Shade, Tiley, & Ballard, 2012), also the broad areas needed to capture reasonable statistics. It has the benefit of providing a complete description of the orientation, which is often represented as a series of three Euler angles. Most commercial EBSD systems use Bunge's ZXZ convention that describes an active coordinate transformation from the sample reference frame to the crystal reference frame. Note that an initial choice must be made to attach the hexagonal unit cell to the sample reference frame, which varies by EBSD vendor (Figure 14). The reader is thus urged to refer to the documentation and pay careful attention to the spatial and crystallographic reference frames for their instruments of choice.

There is a tradeoff between scan resolution, observation area, and data collection time. The optimum scan resolution (step size) depends on the length scale of the microstructural features of interest as well as the intent of the scan. For example, if one were interested in quantifying the primary alpha size and volume fraction, a very fine step size (~0.5 µm) would be necessary. In order to quantify the aspects of microtexture defined in Section 3.1 while balancing acquisition time and cost, larger step sizes in the range of 2~5 µm are often used to characterize MTRs. Furthermore, the large scan areas required to characterize MTRs necessitates the use of beam-control scans, automated stage movement, and finally stitching of the tiles into a single dataset. Since repositioning the stage takes a reasonable amount of time (~10 seconds), there is a motivation to use lower magnifications during imaging and hence reduce the total number of tiles in a scan. However, Nolze (2007) has discussed the impact of image distortions in the SEM and the impact on EBSD measurements. Low magnifications require large beam deflections to reach the perimeter of the scan and barrel or pincushion distortions in the SEM can lead to low pattern fidelity and a significant number of misindexed points. In extreme cases, the distortions can lead to small, but potentially meaningful changes in the measured crystallographic orientation. Due to the many potential variables in setting up a scan (working distance, accelerating voltage, current, etc.) and the variation in quality of SEM columns and beam deflectors, it is recommended that a series of scans are performed on a single crystal (e.g. silicon or nickel) at various magnifications to determine the magnitude of these scanning artifacts and choose a set of parameters with tolerable error/uncertainty. In our experience, using 500~800X magnification (or 160~200 µm scan width) offers a good balance between data quality and collection time.

3.2.2 Sample preparation

For the long measurement times required for MTR characterization, one must pay attention to drift issues caused by specimen charging under high accelerating voltages and beam currents. When mounting specimens, conductive bakelite (containing graphite) is a good option. It can also be helpful to ground the surface of the specimen to the specimen holder using silver or graphite paint. Silver paint is often found to provide a better conduction to the chamber than graphite. In either case, the paints include solvents and must be allowed to dry for at least one hour for polymerization. Depending on the paint used, drying can sometimes be accelerated using a hair dryer or a low temperature oven set to <100°C. Evaporation of a thin layer of carbon (<5 nm) has also been shown to provide good drift mitigation without significantly interfering with EBSD data collection.

Because of the complex, three-dimensional nature of the MTRs, it is recommended that the MTRs be viewed from three orthogonal planes. At least one of these planes should be perpendicular to principal stress axis, if known. EBSD requires a highly polished, damage-free surface to generate suitable diffraction patterns. There are multiple paths to this end state including various mechanical approaches as well as electropolishing. The sample may be mounted or unmounted, although mounting makes manual polishing easier. With electropolishing, unmounted specimens are preferred.

Near-alpha and alpha-beta Ti alloy specimens can be prepared using standard metallographic polishing techniques using SiC paper with water as a lubricant, starting from 120-240 grit and successively moving to finer grits (320, 400, 600, 800, 1000, 1200). Careful attention to the final polishing steps is critical for obtaining good quality EBSD patterns. After 1200 grit, some metallographers find success with a step at 2000 grit while others prefer to lap with 3-µm grit diamond with an oil-based lubricant. Some metallographers find success following this step with a 1-µm grit diamond polishing step or a 0.3-micron colloidal silica polishing step on a rubber pad. Others use progressively finer diamond pastes including 6-, 3-, and 1-µm. An alternative to diamond paste that has proven successful, if schedule allows, is performing vibratory polishing overnight with 1-µm media.

Most users characterizing MTRs achieve their final polish using chemomechanical polishing with a non-crystallizing 0.05 µm colloidal silica solution containing hydrogen peroxide (Jackson, 2023; Okawa & Watanabe, 2009) on a vibratory polisher for at least 4 hours, and often overnight in excess of 15 hours, but usually less than 24 hours. Vibratory polisher power should typically be set to 50-70% such that specimens continuously rotate. To extend colloidal silica solution life, up to ⅓ of the solution volume of deionized water may be added. It is usually beneficial to weigh down specimens in 1-1.5" metallographic mounts in the polisher with a mass of ~400g per cm^2, though similar quality polishing results can be achieved with longer polishing times and lower masses.

While most metallographers employ mechanical polishing for EBSD characterization of MTRs, it is also possible to electropolish specimens. Prior to electropolishing as a final step, the same procedure should be followed as for mechanical polishing up to 1200 grit SiC paper. After this step, electropolishing is performed using a 5% perchloric acid (70%) solution (remainder anhydrous/glacial acetic acid or 35% butyl cellulose and 60% methanol) at -35 to -50°C and 20-25 V for 1-4 minutes.

Other polishing recipes can be used to produce specimens faster than the procedures described; however, the above recommendations are known to be capable of producing suitable surface qualities for EBSD.

3.2.3 Sample alignment for large-area EBSD

Once a damage-free surface has been obtained, the next step is to clean the specimen with acetone, methanol, ethanol, or isopropanol. The latter three tend to leave streak-free surfaces so even if cleaned in acetone it is recommended to perform a final rinse with methanol, ethanol, or isopropanol. Ethanol may be preferred in both applications for chemical safety.

Next, it is essential to make sure that the plane of polish is parallel with the plane of the stage travel. If it is not, the focal point of the electron beam will not be constant with the specimen surface leading to defocused patterns and low confidence indexing, or even preclude the possibility of indexing the pattern at all. This is especially prevalent in the transformed beta regions of bimodal microstructures. Since many sample holders are inserted into the stage with a screw mechanism, it is important to note that the plane of the sample may not default to this position. While many users employ parallel polishing techniques, another way to circumvent this issue is to use an adjustable sample holder. The one shown in Figure 29(a) was custom fabricated at the Air Force Research Laboratory but is a simple design consisting of three screws to hold the sample and three screws with springs to provide tension inserted at an angle below the sample which adjusts the specimen plane. A small circular bubble level is used to align the stage with the specimen. First, the level is placed on the stage platen at 0° tilt (Figure 29(b)) and the SEM tilt axis is used to set the reference point. Next, the sample is inserted and lightly held using the upper three screws. A clean piece of filter paper is placed on the sample to protect the polished surface and the level is placed on top of this (Figure 29(c)). Finally, the lower three adjustment screws are used to level the sample plane with the original reference point (Figure 29(d)). Clean gloves should be worn throughout this entire procedure. Note: If you touch the table, a pen, a doorknob, etc., the gloves are no longer clean and need to be replaced.

Once successfully leveled, the SEM is pumped down to obtain a good vacuum and the electron beam is activated. While optimal imaging conditions vary somewhat depending on the model, calibration, and configuration of the SEM and EBSD detector, the typical accelerating voltage for collecting EBSD data for MTR analysis is 15-20 kV at a spot size that provides a current of around 5-8 nA, though larger beam currents may also be used. Using 15 kV gives a better spatial resolution but, with the very same probe current, increases the scan duration by a factor of ~2. In general, more current is better and produces sharper diffraction patterns. In our experience, even

fine transformed beta can be successfully indexed at currents as high as 50 nA. Achieving such large beam currents may require using a larger final aperture (e.g., 50 to 100 µm).

The best results are often obtained at the typical specimen tilt of ~70° and a working distance of 15-20 mm. Dynamic focus correction and tilt correction should be used when available on the microscope. The microscope and EBSD system need to be calibrated at least annually to ensure that all distance measurements are accurate, pixels are square, and distortions are minimized. It is recommended that the operator performs regular visual checks with a grid on a monocrystalline Si wafer to ensure the system appears to be reasonably calibrated. The user may refer to standards such as ASTM E2627 or ISO 13067 for additional information relevant to quantitative microstructure characterization using EBSD.

Since imaging over large areas in the SEM can be affected by pincushion and barrel distortions and collecting many small tiles can sometimes result in challenges in stitching EBSD scan data together, it is often beneficial to collect data in larger scan frames, when possible, as enabled by large depth-of-field imaging modes on some SEMs. When stitching must be used, a good balance between tile size and imaging distortions has been found with individual tile areas between 0.15 x 0.15 mm and 0.5 x 0.5 mm. Most EBSD data collection software includes an option for stage control which will allow automated multi-tiling.
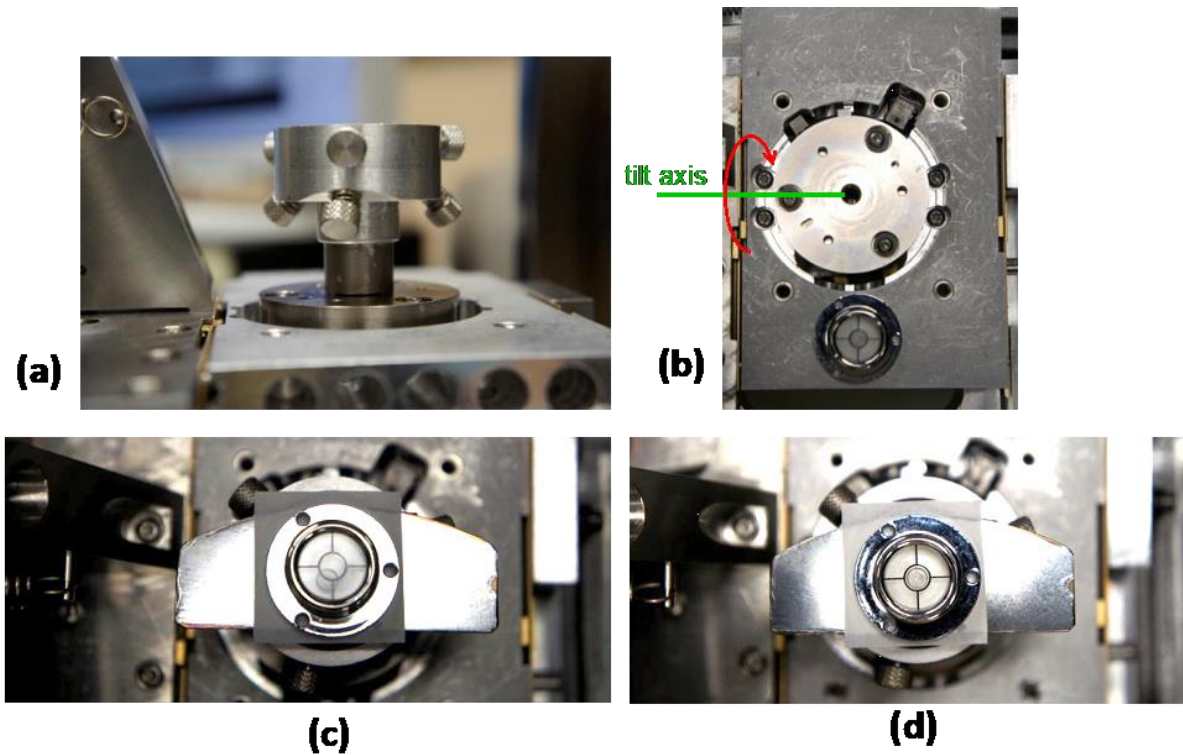
Figure 29. Method for ensuring sample surface and stage plane are parallel

3.2.4 Scan parameters for EBSD analysis

EBSD cameras are available with a range of pixel resolutions. The desired orientation accuracy of ~0.5-1.0° can be achieved with binning that results in an EBSD pattern of at least 120 px square. For example, 8 x 8 binning is acceptable on an EBSD camera with 1024 x 1344 px resolution, as it produces a pattern of 128 x 168 px, in excess of the 120 px square rule-of-thumb.

Appropriate exposure time on the EBSD camera varies with a number of experimental conditions and equipment parameters, including the sensitivity of camera, probe current, binning, accelerating voltage, specimen tilt, and location of the scan region relative to the detector. The maximum exposure time should be chosen that does not result in overexposure (i.e., "washing out") of the center of the pattern image.

Most newer systems allow dynamic flat fielding (background handling) of the Kikuchi pattern. While this can slow down collection times by ~20%, it is often preferred to static background subtraction during EBSD data collection for MTR characterization due to the change in the brightness center location on the EBSD camera over relatively large scan areas and due to differences in electron backscatter coefficient between phases. In EBSD data collection software that provides options for the flat fielding operation, good results can be obtained whether the

image processing operation uses subtraction or division, and a blurring operation that includes ~100 passes is often sufficient for the ~120 px binned pattern rule-of-thumb. When not using dynamic flat-fielding, the operator should be aware that large grains can affect the static background collection, and approximately 50-200 grains, depending on texture strength, must be in the observation area to obtain a good background. Some further improvements can be obtained using image equalization methods to improve the contrast of the diffraction patterns, such as intensity histogram normalization or histogram expansion. This image processing operation is done automatically in some EBSD data collection software.

It is found that accurate indexing of the hexagonal phase typically requires at least 8 bands to be identified. The region of interest (Oxford/Bruker) or rho fraction (TSL) should be >90%, and ideally approaching 100% in order to capture the maximum number of bands.

Some reductions in the fraction of unindexed points, such as for specimens with moderate levels of residual stress or for which surface polish is not optimal, can be obtained using frame integration. To avoid increasing data collection times, it is best to keep the number of frames small (generally two) and the rate relatively high (~20 ms). In some cases, residual strain due to processing or residual damage from prior loading may result in difficulty in obtaining EBSD patterns. In such instances, a low temperature anneal (e.g., 650 °C for 2 h) may alleviate some of the dislocation content.

The step size is also an important factor in data quality and generally depends on the type of information one is looking to obtain. Larger step sizes may overlook some critical elements such as the morphology of the transformed beta phase and the relative fraction of transformed beta phase that shares a similar crystallographic orientation to the primary alpha phase. Larger step sizes will also tend to under sample the statistics of the beta phase. An example of single tile dataset from Ti-6Al-4V in the equiaxed condition collected with a 2 µm step size is shown in Figure 28. At this resolution, the beta phase is also reasonably well captured for this microstructure, which does not contain any transformed beta phase. A single tile does not provide much indication to the degree of microtexture present in a material. A multi-tile scan from the same material (Figure 30) shows that there is, in fact, substantial microtexture present in the material. This is due largely to the slow cooling rates from solution heat treat which permitted coarsening of the primary alpha grains until they contacted one another.
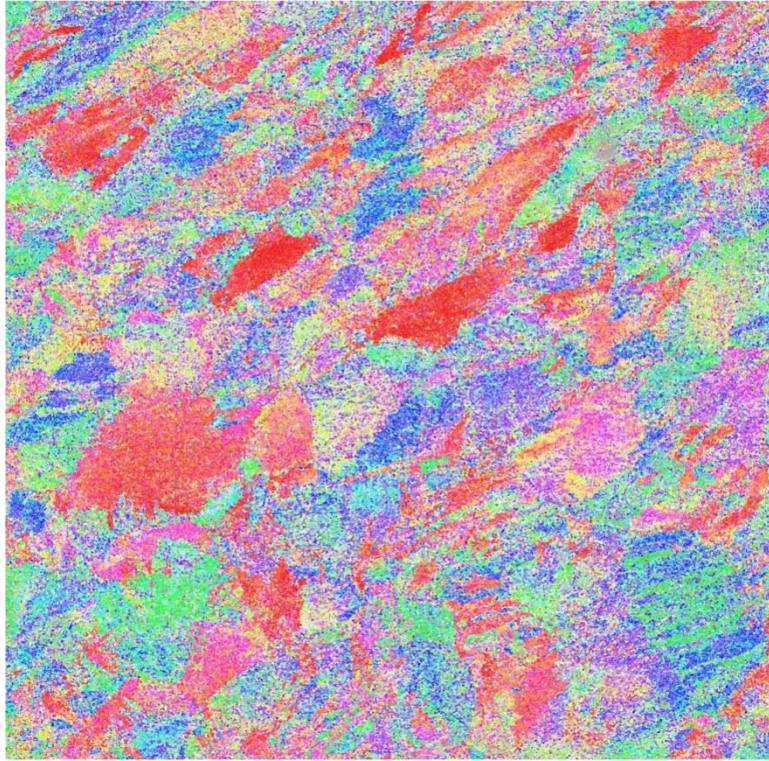
Figure 30. Multi-tile dataset of equiaxed Ti-6-4 material collected at 2 µm resolution
(image width = 6.35 mm)

The impact of scan resolution and fraction of primary alpha on the appearance of microtexture was investigated with the dataset in Figure 31. Various fractions of transformed beta were simulated in original dataset by randomly selecting primary alpha particles to convert to "transformed" beta phase with basketweave morphology. Particles were selected at random as candidates to convert to transformed beta until the volume fraction of remaining alpha was within 0.5% of the desired value. An algorithm was used to sample an orientation from the beta phase orientation distribution function for each selected primary alpha particle and then these regions were transformed to secondary alpha phase with the alpha phase orientations that adhered to the Burgers *or* for the selected beta phase orientation. The number of variants per transformed beta region was sampled from a probability density function that favored two to six alpha variants (peaking at four), though single and counts greater than six were also allowed at ~1/6 to 1/8 the probability of the others. The results suggest that the step size for characterizing MTRs should be a function of the primary alpha volume fraction with smaller sizes (e.g., 2~3 µm) being used for lower fractions (e.g. < ~30%) while larger step sizes (5~8 µm) may be tolerated for higher volume fractions (e.g. > ~50%).
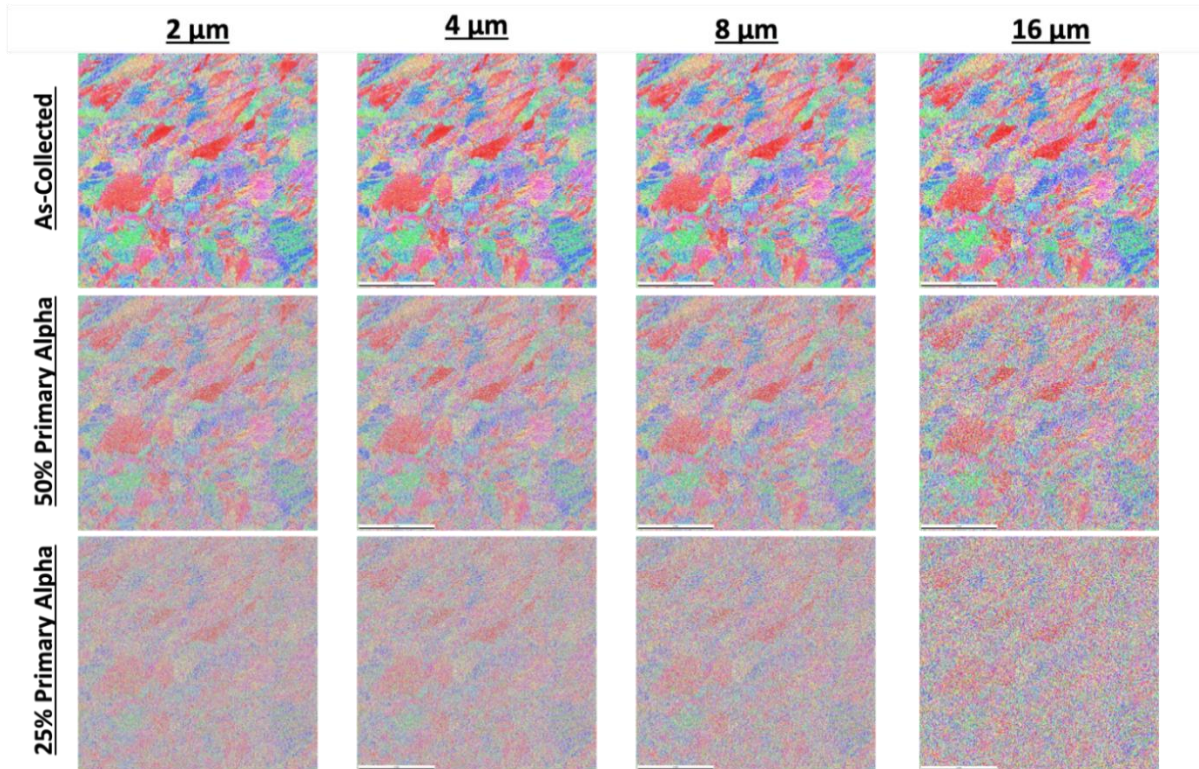
Figure 31. Effect of resolution and fraction of primary alpha on EBSD crystal orientation maps

3.2.5 Quantification of microtextured regions

As discussed in Section 3.1, there are multiple attributes of MTRs that are important with respect to how they behave during dwell fatigue loading. These attributes impact the deformation behavior, crack nucleation process, and crack propagation in different ways that are addressed further in Section 4. The following sections describe strategies to obtain quantitative metrics for the attributes in Section 3.1 from EBSD data. The approach is derived from work by many researchers over several decades and represents the current state of the art in MTR characterization (see Appendix B). Obtaining quantitative values for MTR metrics involves segmenting the EBSD data, performing feature extraction, and then analyzing the characteristics of individual MTRs.

3.2.5.1 Segmentation and feature extraction of MTR

Pilchak et al. (2016a) developed a series of filters and a workflow within the Digital Representation Environment for the Analysis of Microstructure in 3D (DREAM.3D) software suite (Groeber & Jackson, 2014) to segment and quantify MTRs from EBSD data. The filters are embedded in a DREAM.3D binary that is available online (Pilchak, et al., 2016b). The pipeline is also available at the same location. The pipeline was adapted for use by industry for several MAI programs (Venkatesh, et al., 2016; Venkatesh, et al., 2020) to develop correlations between

MTR attributes and dwell fatigue capability. The modified pipeline and additional post-processing filters developed by the MAI consortium are currently being reviewed by engine OEMs and the US Air Force for public release. These DREAM.3D filters have several features which are not currently available in commercial EBSD analysis packages that aid in MTR segmentation. As discussed by Harr et al. (2021), different characterization strategies may be needed based on whether the interest is related to slip continuity leading to crack nucleation versus quantifying the MTR size that would sustain faceted crack propagation and thus correlate to the size of the faceted initiation sites on dwell fatigue fracture surfaces. The DREAM.3D filters can accommodate both.

3.2.5.1.1 Segmentation of MTRs with contiguous alpha phase orientations

Commercial software packages use a burn algorithm to segment pixels of similar crystallographic orientations into grains. This involves selecting a seed pixel in the dataset and calculating the crystallographic *misorientation* between it and all first nearest neighbors. A misorientation can be fully defined by identifying the common crystallographic axis between two crystals and the rotation about that axis that will bring the two crystals into coincidence. If the neighboring pixels are misoriented less than a user-specified angle, usually selected to be between 2º and 5º, the seed pixel and the appropriate neighbors are grouped into a grain. The process is repeated iteratively for each added neighbor until the algorithm exhausts and can no longer find any neighbor pixels within the tolerance angle. A new seed pixel is selected, and the process continues until all pixels are assigned to a grain. Single pixels can be considered grains, although in practice, a minimum number of pixels comprising a grain is usually specified to help eliminate misindexed points near grain boundaries.

The standard burn algorithm, however, may not be capable of capturing MTR characteristics. Figure 32 shows a schematic example of two hexagonal crystals that share a common c-axis but are misoriented by 30º about this axis. Two pixels having these orientations would be identified as two separate grains in commercial software, however, they would behave identically under a load imposed normal to the plane of the page. Similarly, if loaded in a basal- or prism-soft orientation, they would have high resolved shear stress on two <a> type slip systems resulting in similar behavior. Further, due to the transverse isotropy of the hexagonal lattice, the grains would behave elastically identical. For this reason, the new DREAM.3D filters introduced an option to group pixels into features based on the c-axis misorientation. The pipelines utilized by the MAI programs employed the c-axis misorientation filter and enforced nearest-neighbor connectivity. The filter settings were reported by Venkatesh et al. (2020) and are shown in Table 4. As a result of imposing nearest neighbor connectivity, this type of analysis produces MTR sizes that are smaller than what appear visually to the trained metallurgist in inverse pole figure

maps, especially for microstructures containing a moderate-to-low volume fraction of primary alpha. It does, however, reveal clusters of features that represent effective slip lengths within the MTRs which are not discernible by eye. The MTR segmentation workflow developed under the MAI programs can be obtained from Venkatesh et al. (2020). For more information or to gain access to the software, please contact:

- Vasisht Venkatesh (Senior Fellow, Materials Modeling and Behavior)
  vasisht.venkatesh@prattwhitney.com
- Ryan Noraas (Senior Principal Engineer)
  ryan.noraas@prattwhitney.com
- Adam Pilchak (Senior Fellow, Alloys)
  adam.pilchak@prattwhitney.com

Although this code is a research tool for MTR quantification, there is consensus among the authors that it can be used to benchmark the effects of processing routes on MTR characteristics and also to develop useful correlations between these characteristics and material properties.
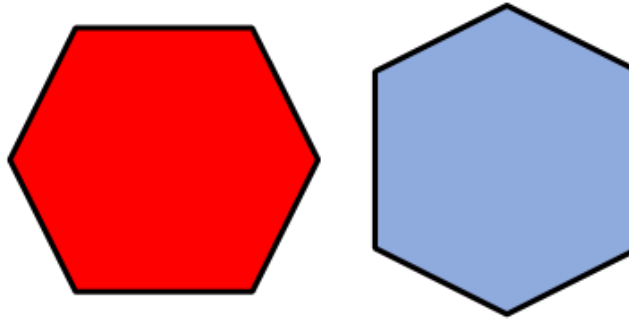
Figure 32. Example of two hexagonal crystals separated by 30° rotation about [0001]

Table 4. DREAM.3D-based MTR parameters and values utilized in MAI programs

DREAM.3D Parameter	Value
Confidence index	0.20
Segment Features (c-axis misorientation)	20 deg.
Minimum MTR Size	10,000 µm2
Hard MTR Classification	$\{10\bar{1}7\} < 25$ deg. from stress axis
Soft MTR Classification	[0001] 70-90 deg. from stress axis
Initiator MTR Classification	[0001] 40-50 deg. from stress axis

3.2.5.1.2   Segmentation of MTRs with non-contiguous alpha phase orientations

Depending on prior processing steps (solution heat treatment temperature and cooling rate) as well as the step size used for EBSD data collection, the similarly oriented primary alpha grains may be separated by highly misoriented transformed beta in bimodal titanium microstructures which would disrupt the classical burn algorithm resulting in artificially small MTR sizes that would not mirror the size of the faceted initiation sites. If one is interested in identifying MTR sizes for use in damage tolerance modeling methodologies or to relate to results obtained from ultrasonic investigations, for example, it is recommended to use the non-contiguous grouping method developed by Pilchak et al. (2016a). A hierarchy of descriptors are used to describe the MTRs and their constituents at different length scales. These descriptors appear in the header of the outputs from the DREAM.3D pipeline (i.e., comma separate value file) and include:

- Pixels: These are the raw data obtained from EBSD, which includes the orientation (expressed as Bunge Euler angles), the spatial coordinates (x,y), and various attributes that describe the pattern quality and goodness of fit. These vary by EBSD vendor, but include the image quality, confidence index, and fit for the EDAX/TSL systems.

- Features: These are groups of alpha-phase pixels that define alpha grains, which may include both primary alpha and transformed beta.

- Parents: A collection of alpha features that constitute an MTR; because some grains within an MTR may be highly misoriented, the MTR parents may have "holes" or gaps within them.

- Checked: Checked features comprise all the alpha features that were evaluated to join a particular MTR and thus checked MTRs are distinct from parents in that they contain no holes or gaps.

The pipeline also has an option to use a two-step segmentation process to relax the constraint of nearest-neighbor connectivity. This approach is useful for identifying the size of the MTRs that may present at faceted regions on the fracture surface. In the first step, a classic burn algorithm is used to group pixels into grains with a small misorientation tolerance angle, usually taken to be 2°. These grains may comprise primary alpha or transformed beta regions. The c-axis misorientation is then used in a second step to aggregate grains into MTRs. The c-axis misorientation tolerance angle is typically $\sim20^\circ$, which is considerably larger than threshold used to segment the alpha grains. This value is similar to the 20° misorientation tolerance used by Woodfield et al. (1996; 1999) to quantify MTRs in the early days of automated EBSD, but overcomes the issue identified in Figure 32. The user has an option to use either contiguous or

non-contiguous grouping. In the former, alpha grains must share at least the edge of a pixel to be grouped into the same MTR. This approach is best suited to study the interconnectivity of grains that can lead to long slip lengths. It fails, however, to capture the MTR sizes expected by serial polishing into dwell fatigue fracture surfaces. For this, the non-contiguous grouping method is used wherein the centroid of each alpha grain serves as a seed for a second burn algorithm. An inspection radius is defined around the centroid of each seed alpha grain identified in step one. The radius of the inspection area is equal to a user-defined multiple of the mean average diameter of the alpha grains from step one. This is typically taken to be about 1.3 to 1.5 and may need further adjustment based on the volume fraction of primary alpha and the scan resolution. The c-axis misorientation of each grain within the search radius is considered relative to that of the seed grain and the burn algorithm progresses until all alpha particles are grouped into an MTR or "parent" feature. The user must also select the criterion for comparing the c-axis orientation of a potential new grain to add to the MTR. Two options exist including (1) the local alpha-to-alpha c-axis misorientation and (2) the running average method whereby each newly considered alpha feature is compared to the mean MTR c-axis orientation (the mean orientation is recalculated when each new alpha feature is added to the MTR). Following this step, some MTRs may have only a single grain and hence a minimum MTR size threshold is applied to eliminate the small MTRs that are inconsequential to dwell performance. Due to the massive number of neighbors, the algorithm is computationally intensive but has been parallelized and benefits considerably from multi-core platforms. The result of this two-stage segmentation is shown in Figure 33. A comparison of the results of the contiguous and non-contiguous MTR segmentation pipelines is shown in Figure 34. Parts a through e of this figure show: (a) normal direction inverse pole figure map (b) unique MTR map from contiguous segmentation (c) unique MTR map from contiguous segmentation after applying a minimum size threshold for MTR areas less than 10,000 µm2 (d) unique MTR map from non-contiguous segmentation (e) unique MTR map from non-contiguous segmentation after applying a minimum size threshold for MTR areas less than 10,000 µm2. The .json file containing the non-contiguous MTR segmentation pipeline can be downloaded from (Pilchak, et al., 2016a; 2016b).
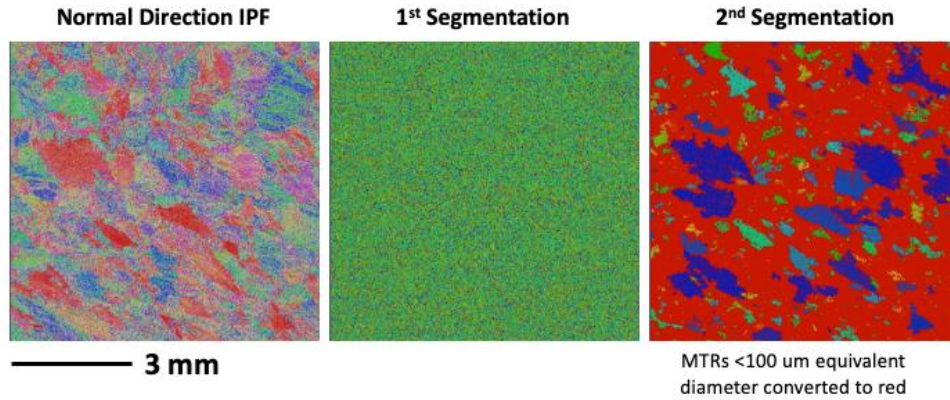
Figure 33. Two-stage MTR segmentation
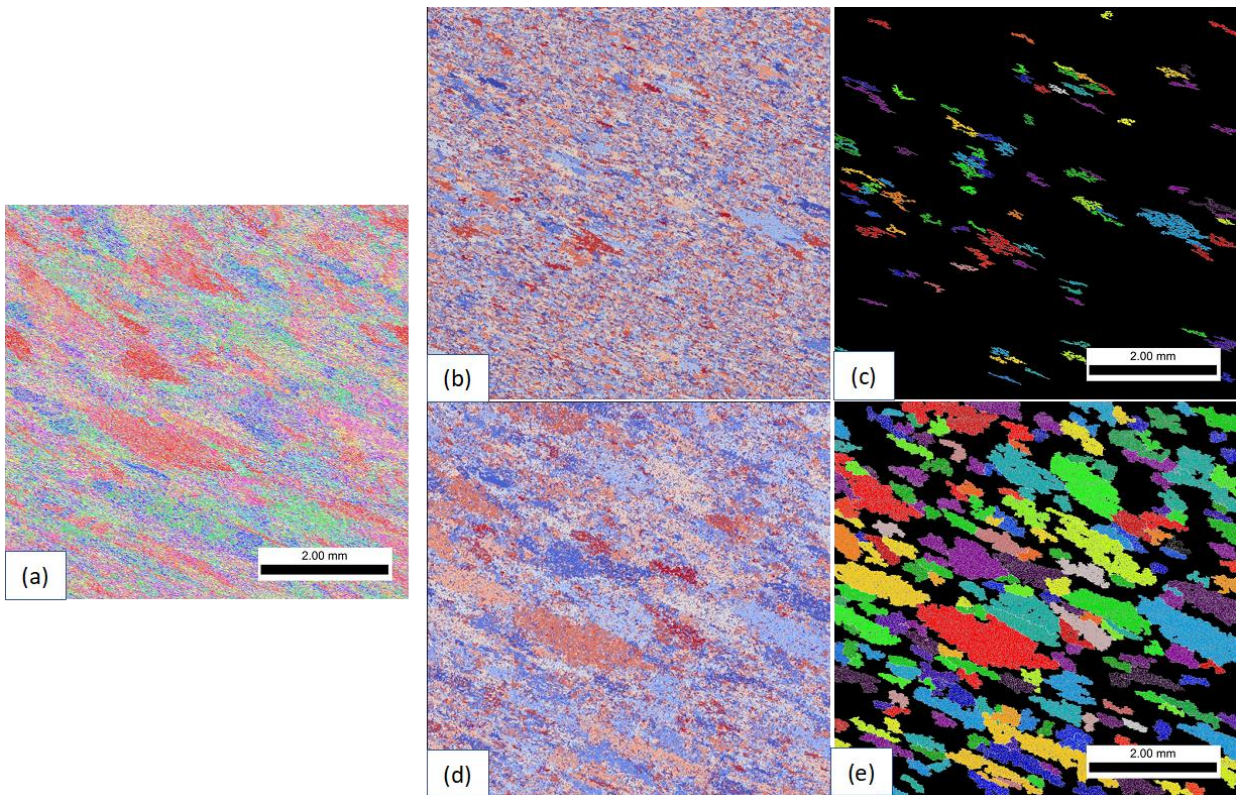
Figure 34. Comparison of contiguous and non-contiguous pipelines for characterizing MTRs
(a) normal direction inverse pole figure map (b) unique MTR map from contiguous segmentation (c) unique MTR map from contiguous segmentation after applying a minimum size threshold for MTR areas less than 10,000 μm² (d) unique MTR map from non-contiguous segmentation (c) unique MTR map from non-contiguous segmentation after applying a minimum size threshold for MTR areas less than 10,000 μm²

61

The various MTR metrics (introduced in Section 3.1) of interest are calculated once segmentation is accomplished. The bases for these calculations are described below:

- **MTR density**: the fraction of pixels within the entire area of each MTR that are similarly oriented. It is calculated as the ratio of the alpha pixels grouped into the MTR over the total number of pixels checked to join the MTR. An example of this calculation is shown in Figure 35.

- **MTR frequency**: the number of MTRs per unit volume of material. Since EBSD is generally collected on two-dimensional cross sections covering an area (S_o), a stereological correction must be used to convert the measurement area to an effective volume (V_o). Drawing on the pioneering work of Murakami (1994; 2019) on inclusions in steels, one approach to do this assumes that the 'thickness' of the inspected area would, on average, be of the order of the MTR size. Thus, the inspection volume can be calculated from the average MTR diameter (d_{MTR}) as $V_o = (S_o)(d_{MTR})$. The choice of minimum MTR size will affect the average MTR diameter so care must be taken in making this choice. Alternatively, because the MTRs are so much larger than the inclusions originally investigated by Murakami and they also have a much wider distribution of sizes, the maximum MTR size in the field of view ($d_{MTR,max}$) may be a sensible choice, i.e. $V_o = (S_o)(d_{MTR,max})$, or some intermediate value between these two. As discussed by Murkami (1994; 2019), these are approximations and hence the choice should be informed by computer simulation. Furthermore, it could be calibrated to model predictions of fatigue lifetime which include MTR size.

- **MTR volume fraction**: As noted by Woodfield et al. (1996; 1999), the MTR volume fraction is a key factor in the dwell susceptibility of near-alpha alloys. This attribute can be calculated simply by summing the total checked MTR area over the total scan area.

- **MTR intensity:** The intensity is a measure of the range of variation of crystallographic orientations in an MTR. As originally conceived by Pilchak et al. (2017), the intensity metric aggregated the MTR size, density, and average c-axis misorientation of each MTR into a single parameter. This was intended to quantify the relative severity of various MTRs in EBSD scans. The size and density were proportional to intensity as both factors would lead to a more damaging material state, while the c-axis misorientation was in the denominator as larger spreads in c-axes would tend to diminish the potency of a given MTR to developing long-range slip bands and sustaining rapid faceted crack propagation.

At present, we propose eliminating the size metric from the equation and defining the intensity as the ratio of MTR density (ρ_{MTR}) to MTR orientation spread (Δg_{MTR}).

- **MTR neighboring regions:** Each MTR constitutes an area (in 2D) and thus may have other MTRs or random material adjacent to it. The MTR neighboring regions will each have an associated orientation, density, and intensity. These can be obtained from the DREAM.3D pipeline for neighboring regions that share at least one pixel edge.

- **MTR orientation**: The MTR orientation is the arithmetic average of the c-axis orientation of all the similarly oriented alpha at the MTR parent level of grouping (i.e., excluding the highly misoriented alpha grain orientation). The dominant c-axis orientation can be obtained by the area-weighted average of unit vectors parallel to the c-axis orientation (c_n):

$$\langle g_{MTR} \rangle = \frac{1}{A}\sum_n A_n\, c_n \qquad\qquad 1$$

- The MTR average orientation is useful for classifying MTRs as hard or soft. Hard MTRs typically have c-axes less than ~15° from the stress axis while soft MTRs are more highly inclined and may deform by basal slip ($\langle g_{MTR} \rangle$ approximately $30^o - 50^o$ from the stress axis) or prism slip ($\langle g_{MTR} \rangle$ approximately $70^o - 90^o$ from the stress axis).

- **MTR orientation spread**: The orientation spread within an MTR, Δg_{MTR} (Figure 36. MTR orientation spread and corresponding map), is the average value of the kernel average misorientation of the similarly aligned alpha grains within an MTR (i.e., at the MTR parent level of grouping). In contrast to typical EBSD analysis where the kernel misorientation is calculated at the pixel level, the calculation is performed at the alpha grain level and thus provides an MTR-averaged measure of *local* misorientations. This metric may be useful in relation to propensity for easy slip transmission in an MTR as well as easy faceted crack propagation.

- **MTR shape**: The geometric morphology of an MTR is calculated from the second-order moments of the MTR at the 'checked' level of grouping (i.e., with all holes/gaps from highly misoriented alpha filled in). This calculation returns a best fit ellipsoid to the MTR including the major and minor axis lengths as well as the principal axis directions and aspect ratio. See the DREAM.3D documentation for the filter 'Find Feature Shapes' (Jackson, 2023) for further details.

- **MTR size**: The MTR size is a byproduct of the MTR shape calculation. The size can be described by the major and minor axis lengths or expressed as an equivalent area or circle equivalent diameter (Figure 37).

The procedures described above represent current best practices to segment and quantify MTRs, around which the industry is aligning. These approaches build on prior work that has been reviewed and discussed in detail in Appendix B.
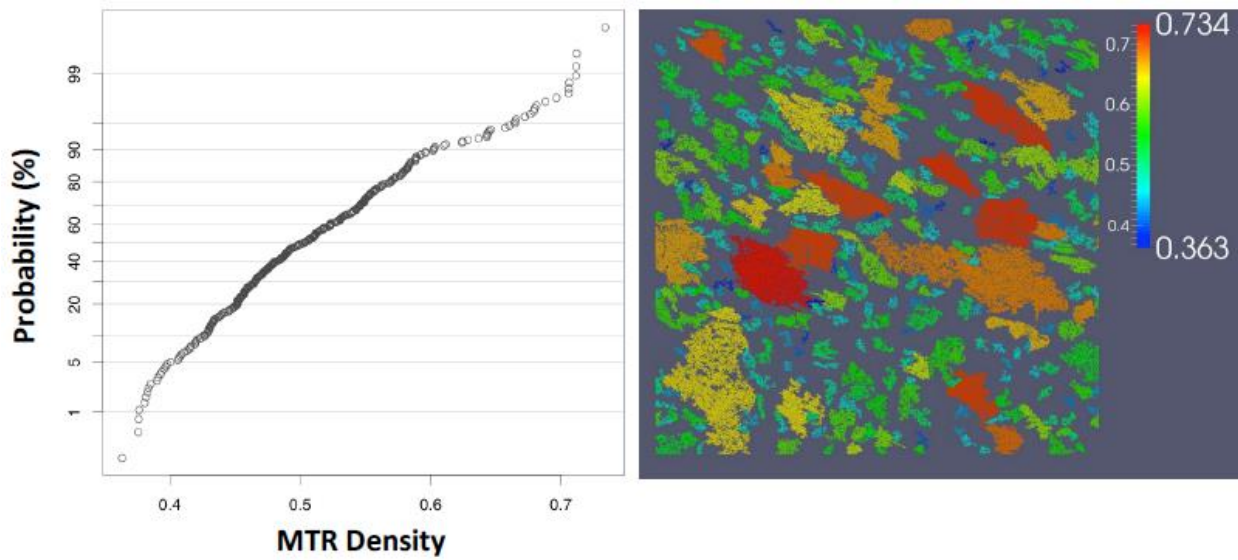
Figure 35. MTR density distribution and corresponding map for MTRs > 100 µm
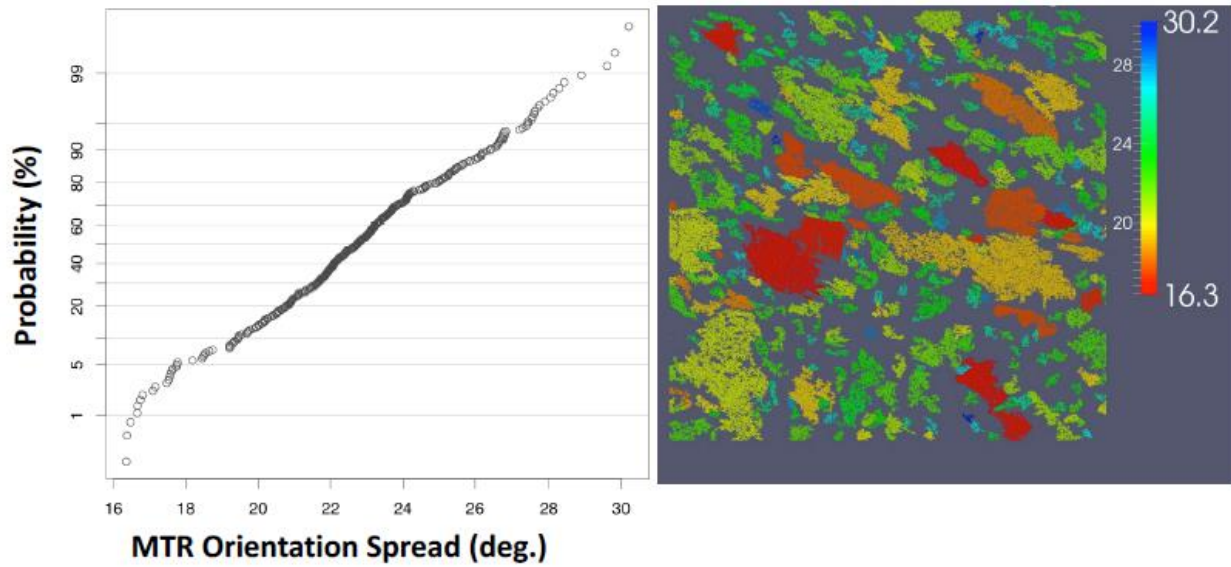
Figure 36. MTR orientation spread and corresponding map for MTRs > 100 µm
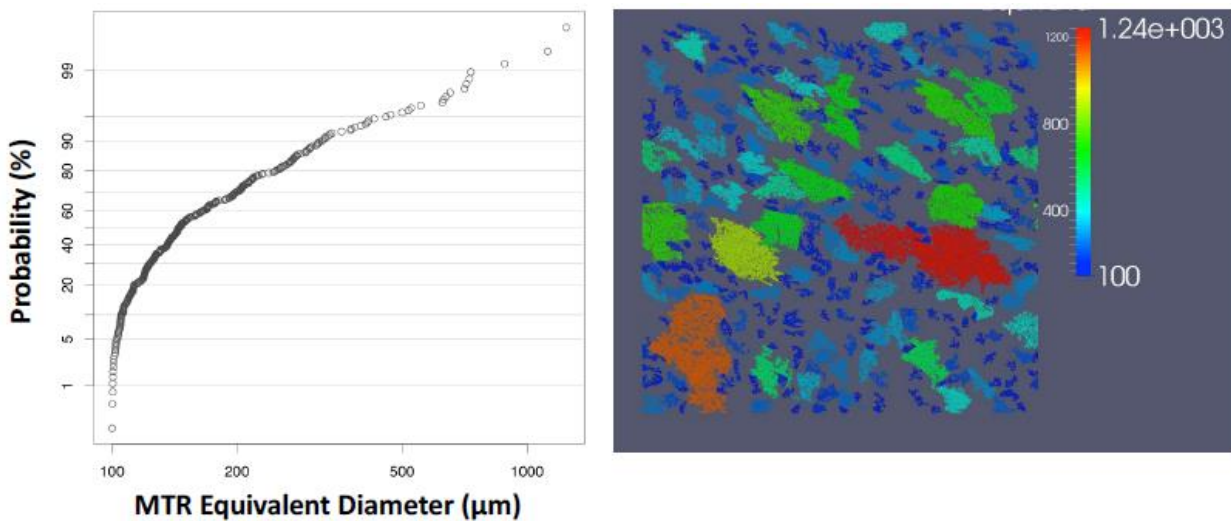
Figure 37. MTR equivalent diameters and associated map for MTRs > 100 µm

3.2.5.3 Microtexture genealogy

At the 15th World Conference on Titanium in Edinburgh, Pratt & Whitney presented a paper that described a pragmatic model for probabilistic life prediction of components subjected to cold dwell fatigue (Burlatsky, Furrer, Venkatesh, Noraas, & Barker, 2023). The physics-based model described a critical assemblage of MTRs as a hierarchy of features within the hard-oriented MTR

coupled with adjacent soft-oriented grains. Termed the MTR genealogy, the hard-oriented region consisted of a "child" with c-axis misorientations ranging between 0° and 10°, a "parent" with c-axis misorientations between 10° and 20°, and a "grandparent" with c-axes between 20° and 35°. Another feature critical to crack nucleation is the presence of soft-oriented material. Since crack nucleation occurs at the alpha particle length scale, the number of grains touching the child MTR are quantified. These features have c-axis orientations inclined to the stress axis, deform by basal slip, and give rise to the smooth, nearly featureless initiation facets observed on cold dwell fatigue fracture surfaces. The model can also consider stress- and strain-controlled loading scenarios as well as the impact of stressed volume on lifetime. The framework also considers macroscopic creep and associated stress redistribution. Location-specific MTR characteristics, which are directly related to local thermomechanical history, are used to calculate the probability of failure in multiple zones of the part to establish the component behavior.

4 Mechanisms of cold dwell fatigue failure

Failure due to dwell fatigue is a multi-stage and hierarchical process connecting atomic scale deformation mechanisms to specimen or component fracture. It involves the development of fatigue damage in the form of dislocation debris and pileups, which lead to load shedding and crack nucleation, short crack propagation, long crack propagation, and final fracture. In this section, we review the understanding for the operative mechanisms in each of these stages.

4.1 Damage accumulation

Titanium alloys are unique from other structural metals in that they creep at room temperature. From the macroscopic perspective, dwell fatigue results in considerably more macroscopic strain accumulation than conventional fatigue due to the increased time spent above the proportional limit. In contrast to high temperature creep deformation, where dislocation climb and vacancy concentration play a strong role, low-temperature creep in titanium is a result of core diffusion and dislocation glide (Tanaka, Yamada, Sato, & Jimbo, 2006) and thermally activated escape of dislocations from obstacles (e.g., solutes) on the slip plane (Zheng, Balint, & Dunne, 2017). This is one source for the strong rate-sensitivity of titanium alloys, which varies among the families of slip planes. The other source is related to microstructural configuration, texture, and total accumulated plastic strain (Waheed, S., Zheng, Balint, & Dunne, 2019).

Strain-time history for dwell fatigued specimens mirror those of conventional creep specimens with an initial transient (stage I) followed by steady-state strain accumulation (stage II) and finally showing increased strain rates just prior to rupture (stage III). Some authors have

compared strain accumulation during conventional fatigue, creep, and dwell fatigue. At the same peak stress level, it is observed that strain accumulation rates are lowest for conventional fatigue and highest for dwell fatigue with static creep being intermediate (Figure 38). Dwell fatigue samples accumulate more creep strain because recovery mechanisms that activate during the unloading cyclic result in enhanced strain accumulation rates during subsequent loading (Sinha, Mills, & Williams, 2004; White, Loretto, Smallman, & Winstone, 1984). It is worth noting that most literature observations involve a small number of specimens and thus some literature may show static creep accumulating more strain than dwell fatigue (e.g., (Lefranc, Doquet, Gerland, & Sarrazin-Baudoux, 2008)) in which the authors tested at stresses exceeding the 0.2% yield. In analyzing a large number of specimens, it is clear that the general trend is that dwell fatigue accumulates more strain than creep. When the opposite behavior is observed, it is believed to be the result of sample-to-sample variability in microstructure, texture, and microtexture. This leads to differences in yield strength such that samples are not actually tested at the same fraction of their specific yield strength.
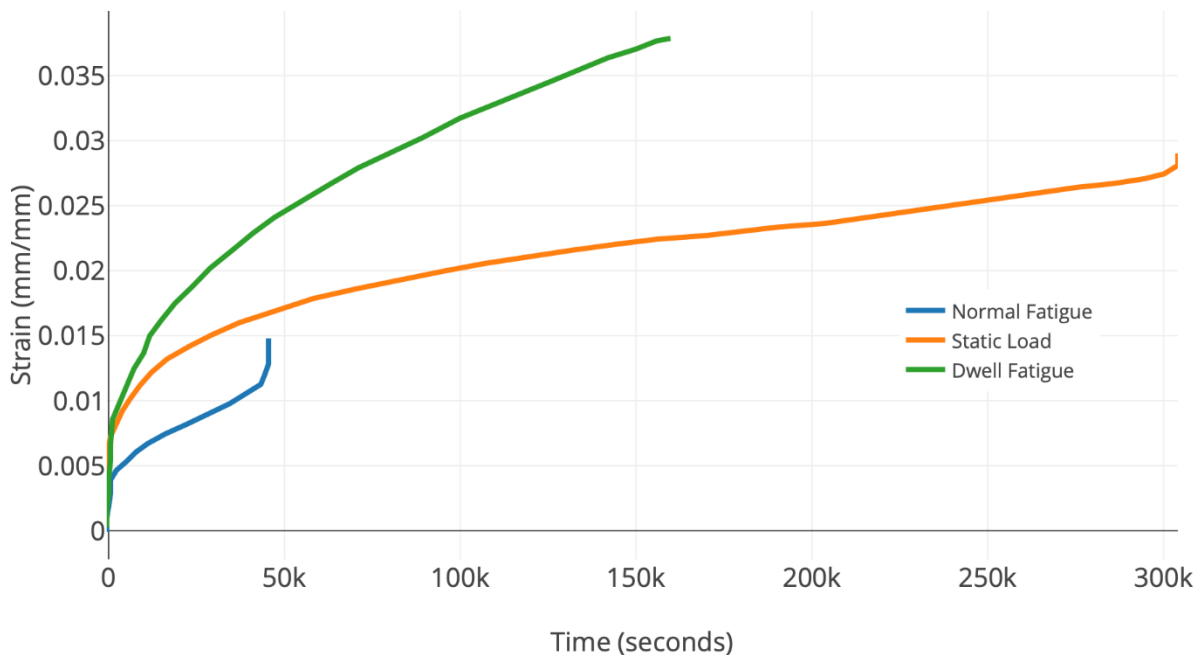
Figure 38. Comparison of strain accumulation rates in Ti-6242 under cyclic, dwell, and creep loading tested at 95% of the yield strength

In contrast to classical high temperature, diffusion-controlled mechanisms like Nabarro-Herring or Coble creep, the fundamental mechanism in Ti alloys is related to dislocation glide in grains well oriented for <a>-type slip on basal or prism planes due to the low CRSS and rate-sensitivity. Mills et al. observed highly planar slip on <a> type slip systems with prominent screw

67

alignment (Ghosh, et al., 2007). On pyramidal <c+a> slip systems they observed both straight edge dislocations and jogged screw dislocations. Castany et al. (2007) and Joseph et al. (2018) have observed that long segments of screw dislocations are emitted from alpha/beta interfaces and grain boundaries. Once initiated, slip occurs until a barrier like a grain or phase boundary is encountered. At this point, slip may be impeded forming a dislocation pileup or the boundary may be amenable to slip transfer if there are closely aligned slip systems with sufficient resolved shear stress in the neighboring grain. When dislocations pass through interfaces, residual dislocations are left at the interface due to imperfect alignment between slip systems. These represent a weak barrier for subsequent dislocations, however, after a sufficient number of dislocations enter the pileup, a complete dislocation is formed which becomes mobile thereby relieving the stress at the interface and the process repeats again.

For the case of blocked slip bands, a stress field of significant strength will be developed upon repeated loading with a hold at peak stress. This pileup has an associated stress field comprised of tensile and shear components, the magnitude of which depends on the total available slip length and the number of dislocations in the pileup. The stress concentration results in redistribution of internal stresses wherein soft oriented material loses its load carrying capacity which must be accommodated by the neighboring hard-oriented regions. Evans (1987b) was the first to describe this in the context of dwell fatigue. He developed a two-element stress redistribution model based on strong and weak grains (Figure 39). If such grains are subjected to the same remote stress, the differences in crystal orientation, slip system availability, and the associated CRSS values will drive different deformation rates in each. To ensure compatibility, the model assumed both regions would accumulate the same total creep strain, which drove a higher stress in the strong material as the weaker material underwent time-dependent creep deformation resulting in stress relaxation. While relatively simple, this model provided very useful insights into the active micromechanical processes and set the stage for more detailed models based on the crystal plasticity finite element method (CPFEM) (e.g., (Dunne, Rugg, & Walker, 2007; Hasija, Ghosh, Mills, & Joseph, 2003)). Indeed, these models have faithfully reproduced microscopic stress redistribution and have termed this "load shedding" to keep it distinct from the macroscopic stress redistribution that occurs at the component scale.
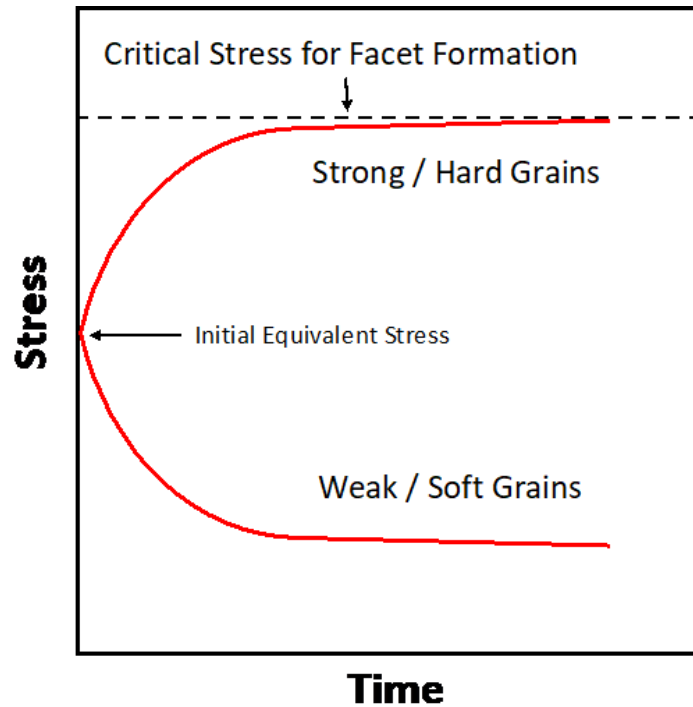
Figure 39. Two-element stress redistribution model for dwell fatigue

With this mechanism in mind, the effective slip length becomes an important factor. Rugg et al. (2007) have discussed the concept of the effective structural unit size in titanium alloys, which describes the length scale over which deformation processes of interest do not recognize boundaries or interfaces. Perhaps the clearest example of this is alpha colonies consisting of alternating alpha and beta lamellae which are in BOR with one another. Slip bands can traverse these interphase boundaries readily. MTRs represent another potential effective structural unit, and it was generally believed that slip could readily traverse these features. However, Harr et al. (2021) have recently investigated this using large-area EBSD analysis and mesoscale optical digital image correlation (DIC). The authors assessed the effect of temperature on the development of slip bands during dwell fatigue in heavily microtextured Ti-6242 at room temperature, 120 °C, and 200 °C. The authors found that long-range slip bands spanning many alpha particles were exclusively formed on basal planes at all temperatures and no long-range slip was observed on prism or pyramidal slip systems. Interestingly, the large basal slip bands were found to occur within nominally hard-oriented MTRs but did not span the entire diameter of the MTR as identified by DREAM.3D segmentation or by what most metallurgists would identify as the MTR boundary manually (Figure 40). In this Figure, Basal and pyramidal slip bands observed with digital image correlation are shown in light grey and black, respectively, in the IPF map while basal slip bands are shown in black in the Schmid factor map. Closer

inspection of the orientations showed that there was a subset of basal soft orientations with high basal <a> Schmid factor contained *within* the hard MTR and spatially arranged such that they were parallel to the basal slip trace. In Figure 41(a), the grains are co-located such that the basal slip band trace crosses all grains. In contrast, the same grains in Figure 41(b) are not co-located such that each slip band operates independently with no chance of slip transfer and the development of a strong pileup. In addition, it was noted that slip accumulated more rapidly and in greater amounts at known dwell-sensitive temperatures (room temperature and 120 °C) compared to the non-dwell sensitive temperature of 200 °C.
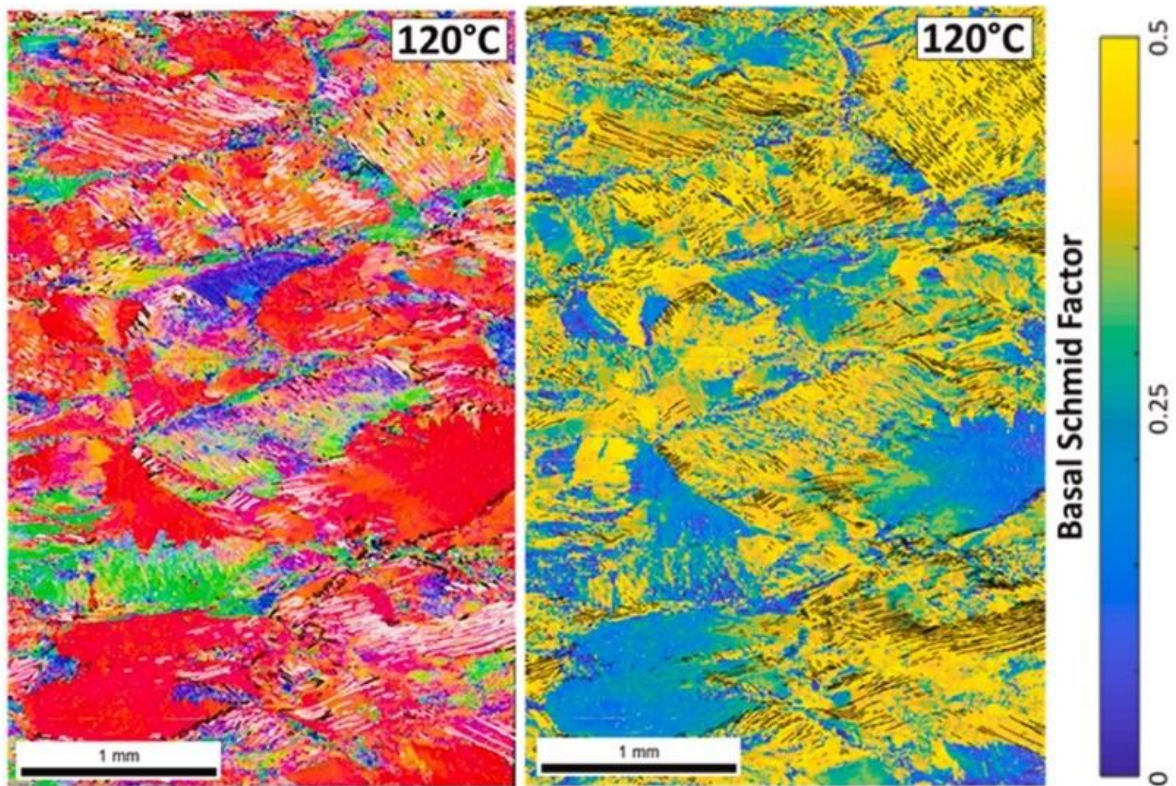
Figure 40. Stress axis (vertical) inverse pole figure and basal Schmid factor maps for Ti-6242
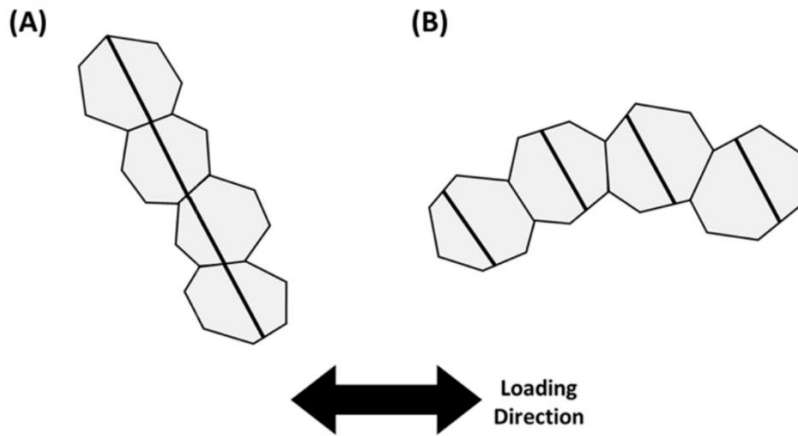
Figure 41. Spatial arrangement required for slip percolation across multiple alpha phase constituents

The single crystal anisotropy discussed in Section 2.3 gives rise to strongly heterogeneous deformation behavior during tensile and fatigue loading. For example, Lunt et al. (2017) used electron back scatter in conjunction with DIC to examine the deformation behavior of Ti-6Al-4V in material with various degrees of elongated MTRs by performing tensile tests at various orientations relative to the elongation direction. At 2.5% strain, material with low degrees of microtexture exhibited homogeneous elastic and plastic deformation. Deformation was also fairly homogeneous in strongly microtextured material when loaded along the elongation direction, which was attributed to the fact that the global texture resulted in virtually all grains being well oriented for easy prismatic and basal slip. In contrast, when the strongly microtextured material was loaded at 45° or 90° to the elongation direction there was highly heterogeneous strain accumulation with strong preference for prismatic and basal slip, respectively. Material with intermediate microtexture also exhibited heterogeneous plastic deformation when the majority of grains had their c-axes parallel to the loading direction. Based on Schmid factor analysis, this deformation could not be linked to any specific slip system, though there was some correlation with likely activation of <c+a> slip systems. The investigation also showed that for the material conditions investigated, those with higher yield strengths were more likely to exhibit heterogeneous deformation. The overall texture controls the yield stress, but microtexture controls the onset of micro-scale yielding, which can drive damage accumulation and lead to nucleation.

Mills et al. (2018) and Pilchak et al. (2012) have analyzed the dislocation structures beneath two crack nucleation sites in dwell fatigued Ti-8Al-1Mo-1V which provide insight into damage accumulation that precedes crack nucleation. The authors showed that the damage ultimately resulting in crack nucleation formed via extensive planar <a>-slip on the basal plane, leading to a

dislocation pileup against a thin beta phase rib which had a neighboring hard-oriented grain. Analysis of location orientations revealed that there were no closely aligned slip systems to permit easy slip transfer. The spacing between the basal <a> dislocations decreased with decreasing distance from the fracture plane. Moreover, pyramidal <c+a> dislocations were formed between the basal <a> slip bands to maintain compatibility with the adjacent hard grain. Residual contrast from the basal <a> slip bands were visible while imaging with conditions to observe the <c+a> dislocations indicating that the basal slip occurred first and the <c+a> dislocations formed second and became pinned on the former. The density of <c+a> dislocations increased with decreasing distance from the hard/soft boundary and increased further with decreasing distance from the fracture plane. The beta phase had extensive plastic deformation, but the dislocation density was too high to determine which slip planes were active. Along with the applied load, the stress concentration associated with the pileup in the "basal soft" grain led stimulated wavy <a> and <c+a> slip in the adjacent hard grain. Similar to the earlier observations of White et al. (1984), the traces of the wavy slip were on an irrational plane close to (0001). White et al. (1984) also observed that sessile [c] dislocations were associated with stacking faults on the basal plane of beta-annealed IMI-829 subjected to dwell fatigue. The authors hypothesized that these immobile [c] dislocations could contribute to crack nucleation.

Joseph et al. (2020) have also a detailed TEM analysis of dwell fatigued alpha+beta processed Ti-6242 that was aged to promote alpha2 (Ti$_3$Al) formation. The authors analyzed hard/soft grain pairs where the soft grain was well oriented for prismatic <a> slip. They found a high density of dislocations in both grains, which increased with the misorientation between the grains. The hard grains had a higher density of dislocations which was suggested to be a consequence of internal stresses developed by the pileups in the soft grain. The soft grains were found to deform by slip on two complementary prism planes and slip transfer was not observed. Both basal <a> and pyramidal <c+a> slip was observed in the hard grain. Basal <a> dislocations multiplied by junction formation while pyramidal dislocations multiplied by superjog formation (Joseph, Joseph, Lindley, & Dye, 2020).

4.2   Crack nucleation

4.2.1 Basic features of dwell fatigue fracture surfaces

At sufficiently high stresses, the damage accumulated during repeated dwell cycling inevitably leads to crack nucleation, which has a variety of meanings depending on one's background and discipline. To the materials scientist, a crack nucleates when atomic bonds are broken and there are two new surfaces created. To the practical engineer who is managing the life of a component

through inspection, a nucleated crack would imply one that is detectable using modern nondestructive evaluation tools, which is of the order of hundreds of micrometers. Between this and the following section on crack propagation, we will address both perspectives, which are a combination of grain-scale crack nucleation and the early stages of crack propagation.

Crack nucleation sites in Ti alloys subjected to dwell fatigue are generally subsurface and exhibit characteristic faceted initiation sites which reflect light readily under optical microscopy leading to a shiny, appearance near the origin. At higher magnification, crack origins are found to consist of many individual transgranular facets, and the size of each facet is commensurate with the size of the microstructural feature beneath it. This includes the primary alpha and transformed beta constituents in alpha+beta processed material and the alpha colony size in beta-forged and beta heat-treated materials. The size of the faceted region on dwell fatigue fracture surfaces of alpha+beta processed materials corresponds closely to the size of the underlying hard-oriented MTR in which the crack initiates (Pilchak & Williams, 2011; Sinha, Spowart, Mills, & Williams, 2006). Evans (1987b) noted that the spatial orientation of the facets varied with the magnitude of applied stress based on observations of dwell fatigue fracture surfaces in beta heat treated Ti-685. At high applied stresses exceeding the alloy yield strength, facets tended to be highly inclined (i.e., "shear dominated" facets) to the stress axis whereas lower applied stresses tended to form facets nearly orthogonal to the stress axis ("stress dominated" facets).

4.2.2 Mechanisms of crack nucleation

Based on the understanding of conventional fatigue crack nucleation, it was difficult to rationalize how such an event could occur on a plane with very little or zero resolved shear stress (Evans W. , 1987b; Evans & Gostelow, 1979) during the early days of investigation into dwell fatigue. The pioneering work of Evans and Bache (1994) and Bache et al. (1996) made significant progress in answering this question and essentially all of the current theories of crack nucleation can be traced back to their work. The authors invoked Stroh's early work on the stress fields around dislocation pileups (Stroh, 1954). They suggested (Figure 42, modeled after (Evans & Bache, 1994)) that a source slip band in a grain suitably oriented for slip (the "weak grain," which later became known as the "soft grain") resulted in a stress field that was sufficient to activate basal slip in an adjacent "strong grain" (later to be referred to as the "hard grain" in the literature). It was believed that the stress field due to the dislocation pileup promoted basal slip in the hard grain leading to crack nucleation and propagation along (0001).
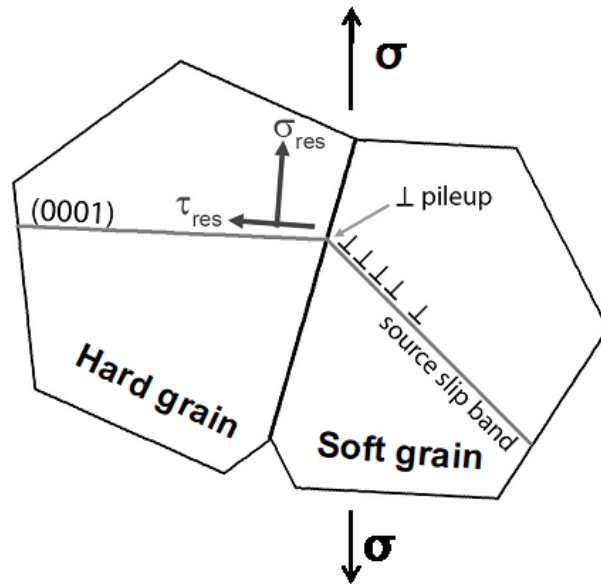
Figure 42. Stroh-based dwell fatigue crack nucleation mechanism under uniaxial stress

The work of Pilchak et al. (2012) provides additional insight into the mechanism and early stages of growth. The authors analyzed two dwell crack nucleation sites in Ti-8Al-1Mo-1V with TEM. In both cases, the nucleation process involved two primary alpha grains separated by a thin beta rib. The soft primary alpha grain was well oriented for basal slip and developed intense, planar slip bands which piled up against a thin beta rib. Numerous pyramidal <c+a> dislocations were observed to span the basal slip bands and these increased in density with decreasing distance from the hard/soft boundary and also with decreasing distance to the fracture surface. Due to the imaging conditions used in the TEM, it was determined that <c+a> dislocations were pinned by the basal slip bands. At one initiation site, prism and basal <a> slip was observed along with extensive <c+a> slip in the adjacent hard grain. At the second initiation site, predominantly <c+a> slip was observed with an isolated basal slip band well below the fracture surfaces. The authors suggested that this indicated the important role of <c+a> slip in the crack growth process. The authors observed significant dislocation activity within the first ~1 μm beneath the fracture surface indicating that the fracture process zone is highly localized and that crack tip opening displacement is predominantly accommodated by <c+a> slip.

Tympel et al. (2016) was the first to observe and briefly mention the presence of low angle (0001) twist boundaries in the vicinity of dwell crack nucleation sites. Hexagonal networks of screw dislocations were observed in the as-received material. Some of these networks were observed to disintegrate after dwell loading at high stresses, though it was also noted that these networks were cites for basal plane faceting. More recently, Lavogiez et al. (2020a; 2020b) have

analyzed a large number of crack nucleation sites on dwell fatigue specimens of Ti-6Al-4V and further elaborated on the details of the basal-soft initiation sites. The study revealed that pairs of primary alpha grains well oriented for basal slip and separated by (0001) twist boundaries were prime sites for crack nucleation. The twist angle was most commonly in the range of 10° – 20° and the grain boundary plane was parallel to the basal planes. Intense localized slip was observed to precede crack nucleation after which the nucleated crack grew along the basal plane twist boundary. The angle between the basal pole and the stress axis was observed to be most commonly between 20° and 50° for dwell fatigue cracks.

Hemery et al. (2021) have shown that this mechanism is broadly applicable to various Ti alloys (Ti-6-4, Ti-6242, and Ti-6246) in bimodal microstructures with various primary alpha volume fractions and sizes as well as different transformed beta morphology and varying degrees of microtexture. Various alloy compositions investigated also show that the volume fraction of transformed beta does alter the crack nucleation mechanism. Hemery et al. (2021) and Liu et al. (2023) have used high resolution digital image correlation (HR-DIC) to investigate strain localization near basal twist boundaries. These investigations revealed that intense slip localization occurred at basal twist boundaries where the grain boundary plane was also parallel to (0001), but not at other twist boundaries where the slip planes were not coincident with the grain boundary plane. Under loading, only a fraction of basal twist boundaries exhibited strain localization. This was a rather rare configuration of microstructure and constituted ~10^{-6} of the total grain boundary length or ~10^{-4} of the total twist boundary length. To date, no work has been performed identifying the stage of mechanism of basal twist formation nor the stage of processing during which it forms. Hemery et al. (2021) have also analyzed basal twist boundary interfaces with high resolution TEM and confirmed that there is no beta phase present.

4.2.3 Crystallography of dwell fatigue facets

Conventional cyclic fatigue cracks in titanium alloys form by the development of planar slip bands on basal planes with highly resolved shear stress followed by crack nucleation and growth along these slip bands (Pilchak & Williams, 2010). The near-orthogonal facets on dwell fatigue fracture surfaces, however, form by a different mechanism that results in non-basal fracture. This is true for colony and bimodal microstructures. Davidson and Eylon (1980) used selected area electron channeling to investigate the crystallographic plane of the facets in Ti-685 with a colony microstructure and found that the facet planes were generally inclined 10° to 15° from the basal plane. The authors also showed that a single facet may be comprised of two alpha colonies sharing a common (0001) and misoriented by 10.5^o about [0001]. Sinha et al. (2007) later used electron backscatter diffraction (EBSD) and quantitative tilt fractography to show that the

fracture plane in the hard grain of alpha+beta processed Ti-6242 was also inclined ~15º to the basal plane, which is an irrational plane close to $\{10\bar{1}7\}$ (Davidson & Eylon, 1980; Pilchak & Williams, 2011; Sinha, Mills, & Williams, 2007). Similar observations have been made on the Ti-8Al-1Mo-1V alloy (Pilchak & Williams, 2010; Pilchak & Williams, 2011). It is worth noting that this plane is close to hydride habit plane and indeed hydrogen has been observed to interact with crack tips in alpha phase titanium (Shih, Robertson, & Birnbaum, 1988). While a subtle detail, explaining this preference for fracture on an irrational $\{hkil\}$ plane will be essential to a comprehensive understanding of the fundamental mechanisms which lead to cold dwell fatigue.

4.2.4 Crack nucleation in the alpha+beta processed condition

Dwell crack nucleation in alpha+beta processed materials with equiaxed or bimodal microstructures occurs within the primary alpha phase. This is likely a consequence of the compositional effect on slip planarity and localization leading to stronger dislocation pileups as well as the fact that dislocations can propagate essentially unimpeded (aside from interaction with solutes) toward the final obstacle (i.e., grain boundary) whereas the alpha/beta interfaces in deforming alpha colonies represent a series of obstacles, albeit relatively weak ones (see Section 2.3). With respect to spatial orientation, the majority of facet normal directions are nearly aligned to the stress axis (Evans W. , 1987a; Pilchak & Williams, 2011; Sinha, Mills, & Williams, 2007) and the fracture plane is inclined ~15º to the basal plane (Davidson & Eylon, 1980; Pilchak & Williams, 2011; Sinha, Mills, & Williams, 2007).

Through detailed fractography in a high-resolution scanning electron microscope, Pilchak and Williams (2011) traced the fine microscopic markings on the facet surfaces back to the *specific* crack origin within this sea of facets. Here, the authors found a smooth, flat, and nearly featureless facet (the "initiating grain") surrounded by multiple so-called propagation facets with normal vectors also oriented nearly parallel with the stress axis (Figure 43). The surface topography of the propagation facets was distinctly different than that of the smooth facet and exhibited evidence of highly localized plastic flow resulting in non-complementary tear ridges on the facet surfaces. This is in stark contrast to the complementary features one finds on faceted features during cyclic fatigue crack growth. Quantitative analysis via EBSD and the tilt fractography method showed that the plane of the smooth facet (the "soft grain" in this case) was parallel to the basal plane (Pilchak, Brandes, Williams, & Williams, 2012; Pilchak & Williams, 2011) while the adjacent hard grain had its c-axis nearly parallel to the stress axis. This result has been confirmed multiple times on both failed laboratory specimens and components indicating it is operative at the high stresses typically used in the lab and the lower stresses used for

operational hardware. The sample in Figure 43 was Ti-8Al-1Mo-1V tested at 95% of the yield strength at a load ratio of 0.1 with a 1-sec ramp to and from peak stress.
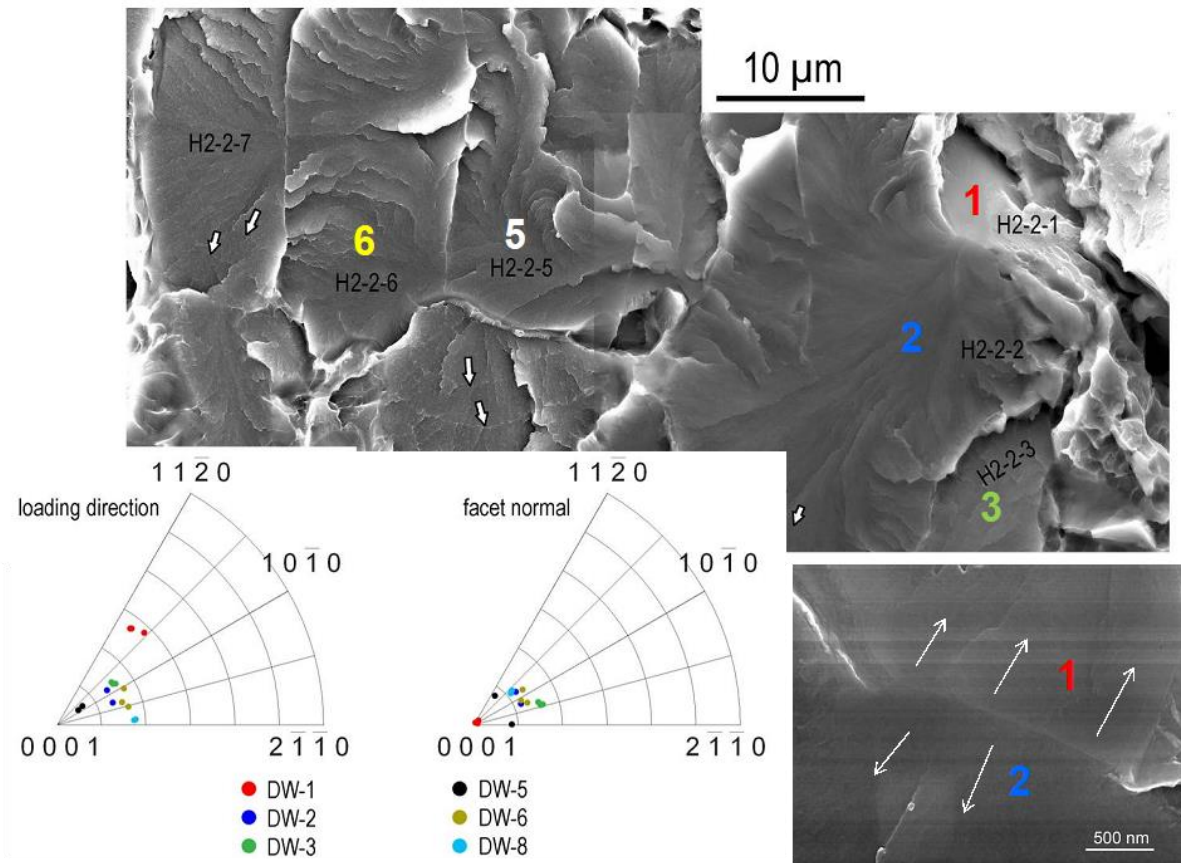
Figure 43. Observation of the crack nucleation site on a Ti-811 dwell sample

4.2.5 Crack nucleation in the beta-forged or beta-heat treated condition

Dwell crack nucleation occurs transgranularly in colony microstructures as a result of the development of intense planar slip bands in soft-oriented grains that result in significant load shedding onto the adjacent hard-oriented grains. Early work by Eylon and Hall (1977), Evans and Gostelow (1979) and Evans (1987b) revealed that colony microstructures formed by slow cooling above the beta transus are particularly susceptible to cold dwell. Large life debits were found for coarse colony microstructures and the debit could be reduced by reducing the colony size and, hence, the effective slip length and size of each facet. These works also demonstrated that the number of facets was greater at low stresses compared to high stresses, and the crack growth rate was found to be faster under dwell loading when compared to cyclic fatigue, especially at $\Delta K < 20$ MPa m$^{1/2}$. Eylon and Hall (1977) observed crack nucleation at a micropore less than 10 μm in maximum length in one dwell fatigue specimen, which caused a further debit

in crack nucleation lifetime compared to pore-free material. In general, the soft grain is one well oriented for basal slip, but it is worth noting that nucleation may occur from prism soft/hard grain combinations with very coarse grains that have limited availability of basal soft/hard grain orientations (Sackett, Germain, & Bache, 2007). Additional data may be needed to further confirm the soft grain orientation for materials with colony microstructures.

Metallographic observations in the vicinity of the faceted initiation sites showed intense shear band formation across the alpha colonies which caused distortion and offsets at the alpha/beta interfaces (Eylon & Hall, 1977). Germain et al. (2020) have captured high resolution images of these offsets (Figure 44) on prismatic systems. Lefranc et al. (2008) have observed cavity formation at these locations, which were commonly associated with pyramidal and basal slip systems.
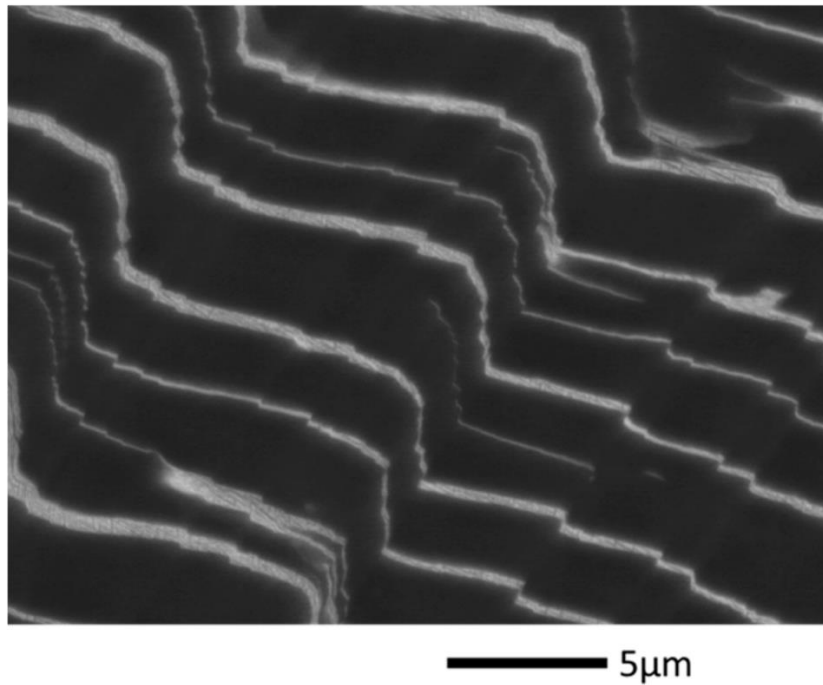
Figure 44. Slip-induced offsets alpha/beta interface

Germain et al. (2020) have analyzed the faceted initiation site on a specimen extracted from beta forged Ti-6242 disk material tested with a peak stress of 900 MPa. The authors lightly polished into the fracture surface and observed that the nucleation site spanned a prior beta grain boundary. The two beta grains shared a common {110} direction and the BOR-related alpha transformed preferentially onto this plane resulting in a similar alpha phase orientation across the grain boundary. The authors analyzed a large region of the forging and concluded that about 45% of the boundaries shared a common {110} direction and hence were amenable to forming beta-

grain-spanning alpha colonies. With respect to the stress axis, the c-axes of the colonies that comprised the nucleation facet were 18º~22º from the stress axis. This orientation is capable of deforming by basal slip under the high applied stresses. The fracture surface morphology suggests that the crack nucleated at the prior beta grain boundary and grew outward along both colonies. However, adjacent to the initiation site in the plane of polish was a comparatively smaller colony well oriented for prismatic slip, which likely provided the necessary creep damage and load shedding that cause nucleation. In contrast to the work of Lefranc et al. (2008), the authors did observe shear-induced offsets of alpha/beta interfaces in colonies well oriented for prismatic slip. Finally, it is noted that because of the misorientation relationships between two colonies inherited from the same prior beta grain enforced by the BOR, it is unlikely that basal twist boundaries are involved in the process as discussed previously for alpha+beta forged material.

4.2.6 Dwell fatigue cracks at the mesoscale

While the above discussion has focused largely on the earliest stages of crack nucleation, Rokhlin's group used microfocus x-rays under the FAA-sponsored program at The Ohio State University (Ghosh, et al., 2007) to monitor mesoscale crack nucleation in alpha+beta forged Ti-6242. The authors observed multiple cracks initiating in the test volume. Several cracks that initiated early during cycling were observed to arrest at small sizes, presumably due to the size of the hard-MTR and the lack of further hard-oriented grains to sustain faceted growth. The fatal crack was found to initiate later in life but grew quickly to a large size and ultimately fractured. Sinha et al. (2006) later analyzed the fracture surface and serial-sectioned into the critical faceted initiation site and confirmed the presence of a large, hard-oriented MTR that was similar in size to the faceted region.

4.2.7 Distinguishing dwell fatigue from cyclic fatigue

In situations where the cause of failure is not known, for example when a crack is found in a fielded component during routine inspection, the above discussion highlighted three unique characteristics that can be used to distinguish dwell fatigue facets from cyclic fatigue facets. First, the facets are oriented approximately normal to the stress axis whereas facets formed during conventional low and high cycle fatigue testing are inclined to the stress axis regardless of the applied load. Second, the crystallographic plane exposed to the fracture surface is parallel to (0001) in cyclic fatigue whereas it is inclined ~15º (+/- ~5º) for dwell fatigue facets. These first two aspects can be obtained using the quantitative tilt fractography method (Pilchak & Williams, 2011; Sinha, Mills, & Williams, 2007; Sinha, Spowart, Mills, & Williams, 2006). Finally, the two types of facets exhibit different topography when imaged at high magnifications. Dwell

fatigue facets contain small tear ridges parallel to the direction of crack growth which are non-complementary and mate peak-to-peak on adjacent halves of the fracture surface. Cyclic fatigue facets, on the other hand, show sharper, more angular features that are complementary on adjacent halves of the fracture surface.

4.3   Crack propagation

The development of an engineering crack occurs by the combination of grain-scale, hard/soft grain interactions plus subsequent crack propagation up to a nondestructively detectable crack size, which varies with inspection method (e.g., fluorescent penetrant inspection (FPI), eddy current inspection (ECI), ultrasonic testing (UT)). The mechanism of crack propagation in titanium alloys is strongly dependent on the underlying microstructure and crystallographic orientation. This is a result of the availability of slip systems to accommodate deformation around the crack tip which permits crack tip opening displacement and crack extension. Under dwell fatigue conditions, faceted crack propagation through hard-oriented grains is preferred at small crack lengths. In contrast to cyclic fatigue where faceted growth gradually diminishes as the cyclic plastic zone size increases giving rise to striation growth (Pilchak & Williams, 2010; 2011), this mechanism will occur in hard oriented grains until there are no more suitably oriented grains available. Furthermore, the rate of faceted crack propagation is much faster than striation growth at equivalent crack size (Pilchak A. , 2013) which enables the crack front to move readily through the microtextured region in which it initiated. Several authors have demonstrated that the size and shape of the faceted region at dwell fatigue crack nucleation sites in near-alpha alloys is directly related to the size and shape of the underlying microtextured region in which the crack initiated (Ghosh, et al., 2007; Pilchak & Williams, 2011; Sinha, Spowart, Mills, & Williams, 2006).

The alpha+beta alloys Ti-6Al-4V presents a slightly different fracture surface which often consists of multiple transgranular, flat, faceted nucleation sites on basal planes which coalesce via faceted growth through hard grains, mixed faceted and striation growth, or ductile microvoid coalescence, depending on the underlying microstructure and applied stress level. At high stresses or elevated temperatures multiple 'pockets' of nucleation sites may be present whereas lower stress levels, such as those found in components, more closely resemble the near-alpha nucleation sites with a single origin within a large, faceted region (BEA, 2020). Significantly more work is needed to understand the nuances of Ti-6Al-4V.

Returning to crack propagation rates, the work of Rohklin (Ghosh, et al., 2007), Pilchak (2013), Pilchak et al. (2016a), and Pilchak and Williams (2011) have shown that growth rates in the

faceted region following nucleation can be up to two orders of magnitude greater than long cracks under equivalent driving force. While the 'small crack effect' (Suresh, 1998) has been well known for quite some time, it is important to note that when growing through suitably oriented hard MTRs, dwell fatigue cracks can (1) grow an order of magnitude faster than conventional small cracks under continuous cycling, and (2) sustain these accelerated growth rates until there are no more suitably oriented grains and the underlying MTR is exhausted. This leads to an important conclusion that the design and lifing strategies must be intimately tied to the manufacturing process and that microstructure/microtexture-based requirements should be strongly considered in material definitions for engine OEMs.

Pilchak et al. (2016a) reported small crack growth rates applicable to the early stages of growth within hard-oriented MTRs (Figure 45). The authors performed large-area EBSD scans and used a focused ion beam to put 20 to 30 micrometer micro-notches within very large hard- and soft-oriented MTRs. They performed dwell fatigue tests with a two-minute hold and used acetate replicas to measure crack extension in a Ti-6Al-4V alloy. The authors further compared these data with conventional cyclic small crack tests and also long crack data measured from compact tension specimens for both loading types. The results (Figure 45) showed that there was overlap between small crack growth under continuous cycling and dwell FCG in soft-oriented MTRs and that there was essentially no effect of dwell on long crack growth. Small cracks growing through hard-oriented MTRs, on the other hand, were about an order of magnitude faster than the conventional small cracks and dwell fatigue cracks in soft MTRs. These are important data to consider for those with interest in managing dwell fatigue from a damage tolerance perspective. The data in Figure 45 were collected with a 120 sec hold time at R = 0.05 and a 1-sec ramp to and from peak stress.
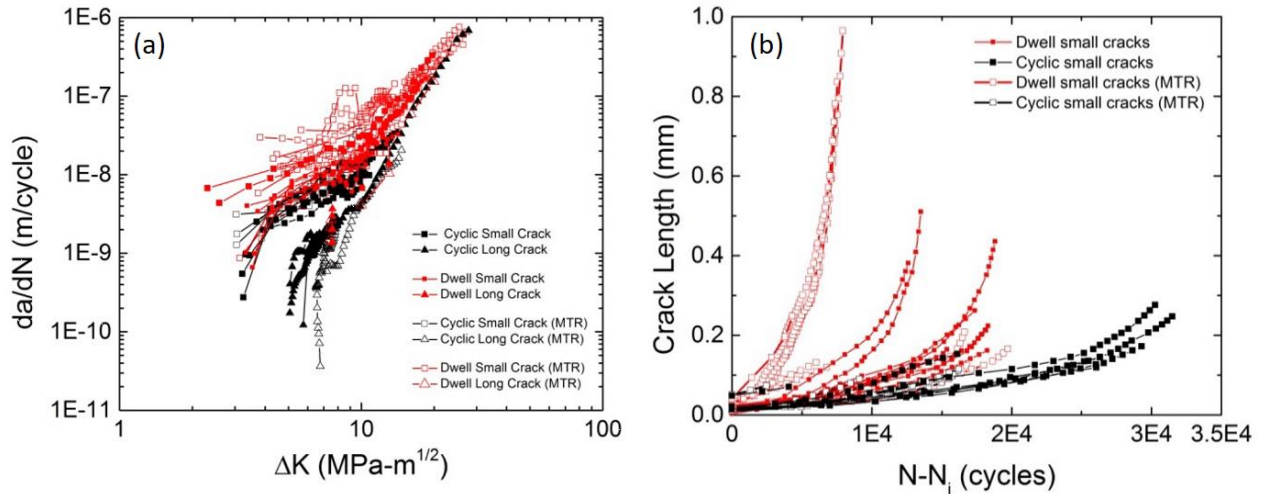
Figure 45. (a) Small and long fatigue crack growth rates in da/dN vs. ΔK space and (b) in crack depth vs cycle space after subtracting the nucleation lifetime

Brown and Hicks (1983) have reported similar accelerated crack growth in beta heat-treated IMI-685 under cyclic and dwell conditions. In this condition, the authors reported small crack growth rates were up to four orders of magnitude faster under dwell loading compared to cyclic long cracks growing at equivalent ΔK. Brown and Hicks further reported that such 'small crack effects' persisted to physically large crack sizes up to ~3.5 mm. In contrast to the data in Figure 45(a), Brown and Hicks showed faster growth rates at ΔK up to ~30 MPa m$^{1/2}$. They also observed variability in crack growth rates due to local microstructural arrangements, which resulted in temporary crack arrest at colony and prior beta grain boundaries.

Unpublished research by Pilchak et al. (2012) measured the growth rates of internal and surface-connected dwell fatigue cracks in beta-forged and alpha+beta heat treated Ti-6242. The material was cut from remnants of pancake 3 from the Ohio State Cold Dwell Fatigue program (Ghosh, et al., 2007) (Appendix A). Surface cracks were monitored with acetate replication while subsurface cracks were monitored by interrupting the test and using x-ray computed tomography with a voxel size of ~7 µm. The work was undertaken to determine if there were measurable differences in growth rate for surface vs. subsurface cracks due to potential environmental effects on the former. Cracking was observed on both inclined planes and planes nearly normal to the stress axis. The ΔK calculations utilized the projected crack length perpendicular to the stress axis. The results (Figure 46) showed no clear trend between surface cracks (SC) and subsurface cracks (C). Furthermore, there was a wide range of crack growth rates observed due to periodic and temporary arrest of the crack front. Nevertheless, the vast majority of data points lie well above the Paris regime of the long cracks with some rates exhibiting close to two orders of magnitude increase over the long crack at equivalent driving force.
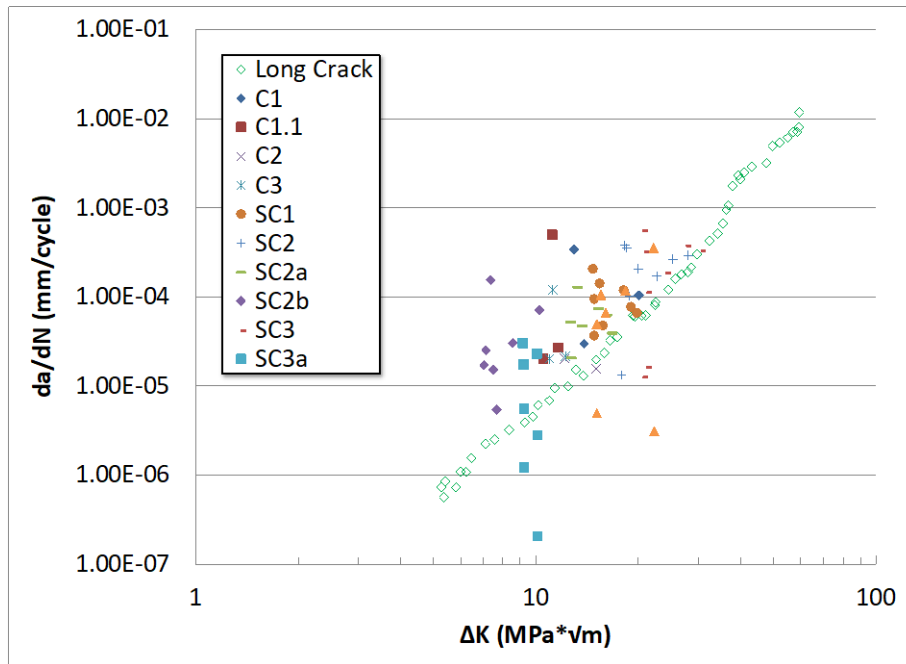
Figure 46. Comparison of long and small dwell crack growth rates in beta-forged Ti-6242

With respect to long crack growth, some authors have reported that dwell accelerates crack growth, others report dwell decreases crack growth rate, and some report no effect of dwell at all (Bache, 2003; Chesnutt, Thompson, & Williams, 1978; Chesnutt & Paton, 1980; Evans & Gostelow, 1979; McBagonluri, Akpan, Mercer, Shen, & Soboyejo, 2005) (Shaniavski & Losev, 2003; Shen, Soboyejo, & Soboyejo, 2004b; 2004a; Sommer & Eylon, 1983; Stubbington & Pearson, 1978).

Crack acceleration was generally observed at low values of ΔK where microstructural sensitivity and the propensity for faceted growth is known to be greatest (Suresh, 1998). Chesnutt and Paton (1980) observed acceleration of up to 30x and noted the effect was worse at colder temperatures. Many of these early experiments, however, were conducted on compact tension specimens where the crack front is large relative to the microstructural features and thus is sampling a wide range of microstructure and crystallographic orientations. This factor, along with variations in microstructure and, perhaps, more importantly, texture can explain these conflicting results. This view is supported by observations on beta heat treated microstructures, which tend to have much larger microstructural features and hence have a greater chance for a significant portion of the crack front to have orientations suitably aligned for faceted growth. With respect to microstructure, Postans and Jeal (1978) have shown a dwell sensitivity in Ti-685 with a coarse lamellar microstructure when subjected to 5 min dwell periods compared to 15 cycle/min tests.

The basketweave variant of the same alloy exhibited the same crack growth rate under both test conditions.

Stubbington and Pearson (1978) investigated the effect of dwell periods on fatigue crack growth in Ti-6-4 rolled bar. This work, largely under referenced in the open literature, was funded by the United Kingdom Ministry of Defense after the RB211 engine failures (see Section 1.3.1) when Ti-6-4 was being considered as an alloy replacement for Ti-685. A 57-mm diameter bar was forged, rolled, and heat treated to obtain a range of microstructures with varying primary alpha volume fraction, as seen in Figure 47 (modeled after Stubbing and Pearson (1978)). The texture of these materials was characterized with x-ray diffraction and it was found that all materials exhibited a transverse texture (i.e., basal poles oriented predominantly perpendicular to the sheet normal and rolling direction). It is noted that the texture measurements were made on the transverse plane and thus while the (0001) pole figures in Figure 47 seem to show a basal texture, they in fact represent a transverse texture. While this work predated the development of EBSD and the concept of microtexture, given today's state of knowledge one could be confident that if EBSD were performed on these same specimens they would exhibit MTRs highly elongated in the rolling direction (e.g., similar to those shown in Figure 48). This is an important realization in the interpretation of Stubbington and Pearson's results as they relate to CDF. In their work, notched test coupons were cut from five different orientations of the plate (TS, TL, SL, LT, and LS; defined in Figure 49(a)) at various temperatures (ranging from 20 ºC to 125 ºC) and loading conditions, which included conventional cyclic fatigue at 0.3 Hz and dwell low cycle fatigue with a 5, 15, or 45 min hold at maximum stress.

Testing of LT specimens revealed a fracture surface topography consisting of a zig-zag pattern in relation to the rolling direction (RD). During periods of 45-minute dwell crack growth was coplanar with the principal (0001) texture component and perpendicular to the applied load. During cyclic crack growth at 0.3 Hz, the fracture surface was perpendicular to the 45-minute dwell surface (Figure 49(b)) and exhibited the typical faceted morphology associated with dwell (Figure 49(c)). With our current understanding of the orientations that produce facets under dwell loading, and an understanding that the underlying microtexture likely resembled Figure 48, it is reasonable to conclude that the 45-minute dwell fracture surfaces were basal-oriented.

Moreover, if one examines the crack growth rate, it is observed that imposing a dwell time at peak stress increases the crack growth rate about an order of magnitude compared to specimens cycled at 0.3 Hz (Figure 50(a) and (b)). Finally, temperature, test direction and primary alpha content were varied, and these parameters all affected the rates at which the crack lengths changed (Figure 50(c) and (d)). Again, these results were all in line with the knowledge of today

regarding Ti-6Al-4V and its susceptibility to cold dwell. In this work, there were approximately 7x and 45x increases in da/dN for a five- and 45-minute dwell periods, respectively. Stubbington and Pearson (1978) further noted a microstructural dependence whereby crack growth rates were greatest for material annealed at low temperature with a high-volume fraction of alpha and decreased with increased annealing temperature corresponding to lower volume fractions of primary alpha. Thus, it can be reasonably concluded that dwell time, texture, and microstructural variations may be a key factor in explaining there have been conflicting reports of the role of dwell on long crack growth rates.
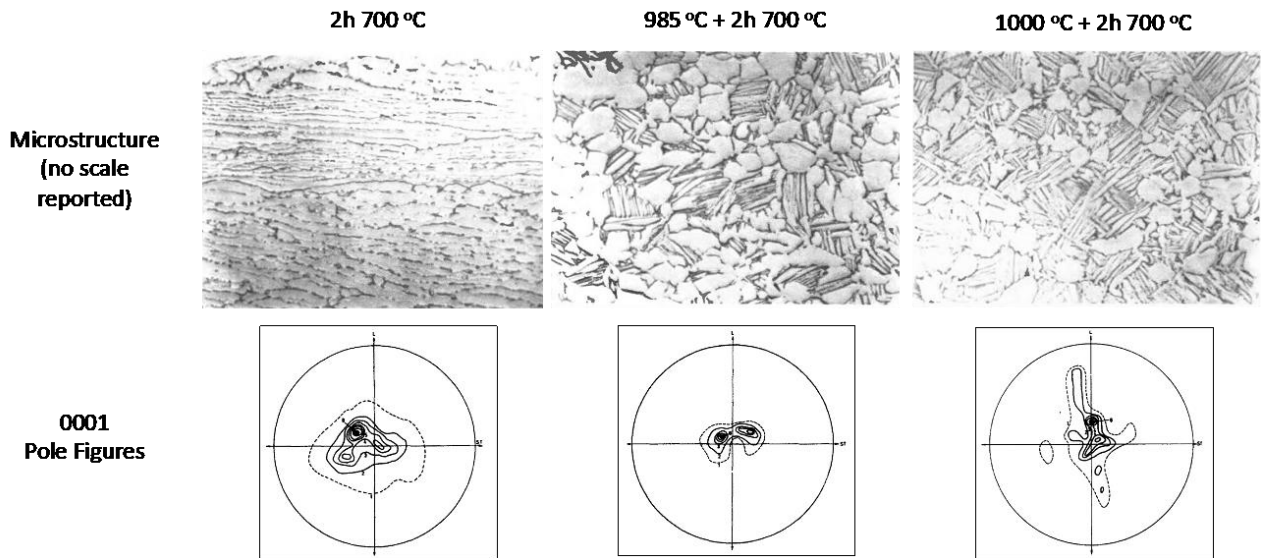
Figure 47. Microstructure and pole figures produced for designated heat treatments of Ti-6-4
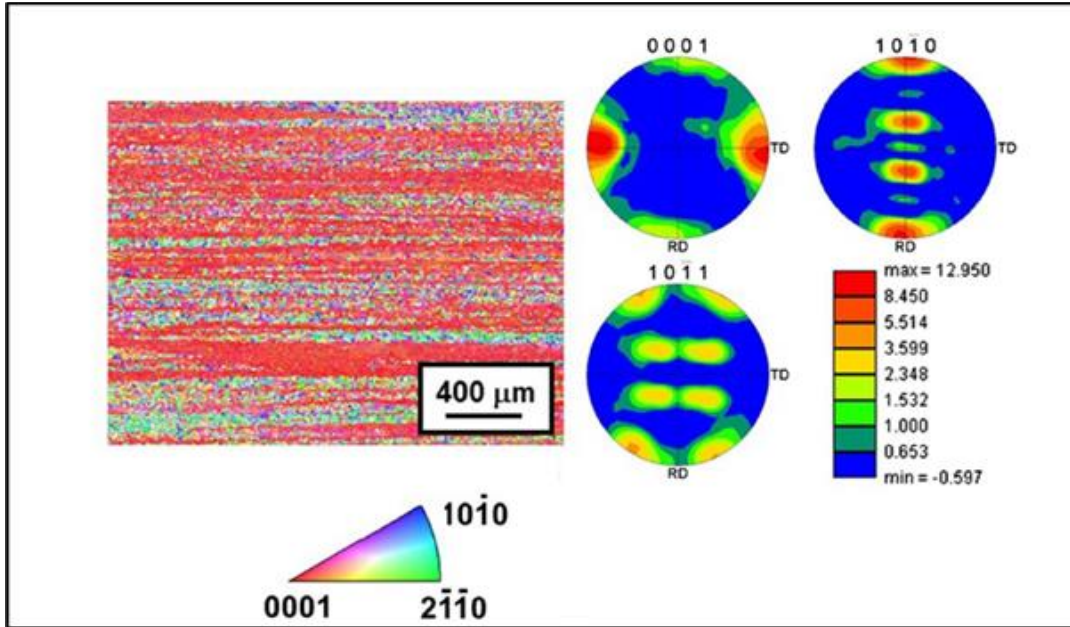
Figure 48. Transverse-direction inverse pole figure map and texture in 32-mm thick hot-rolled Ti-6-4 sheet
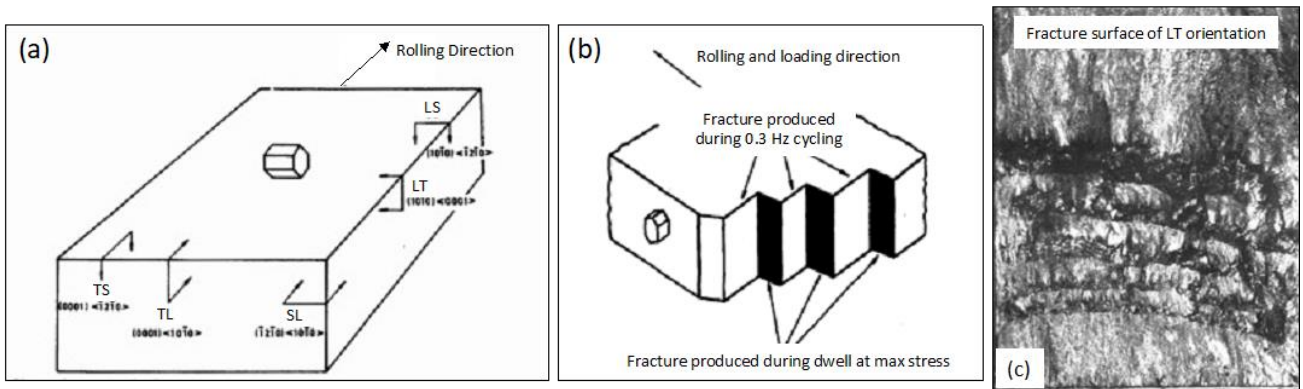
Figure 49. (a) Specimen orientations relative to crystallographic texture (b) schematic fracture surface of LT orientation (c) fracture surface of LT orientation
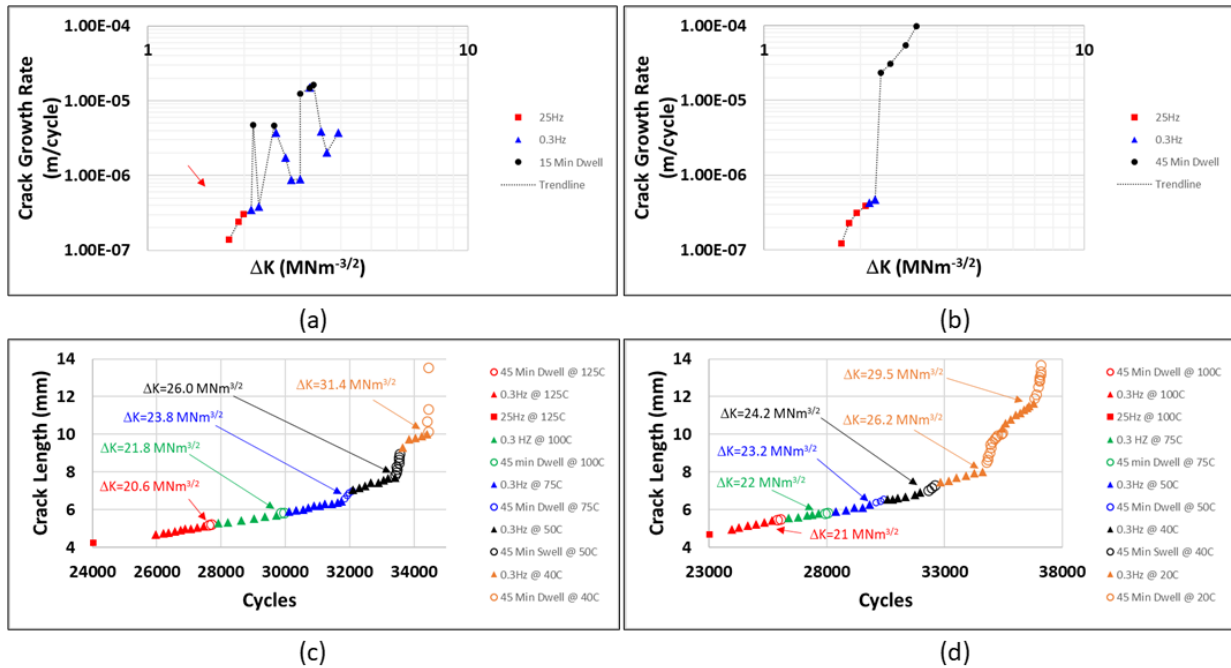
Figure 50. Fatigue crack growth rates in Ti-6-4
(a) 15 min and (b) 45 min dwell times, and crack length as a function of cycles for the (c) 700 °C annealed condition and (d) 985 °C + 2h 700 °C condition in the TS orientation

Several models have been proposed to address the microtexture-induced accelerated crack growth phenomenon. Pilchak (2014) developed a damage tolerance model that treated MTRs as elliptical features inside a volume of material. The initial flaw size was assumed to be of the order of the grain size and nucleate within the MTR. The location of each crack tip was tracked relative to the MTR domain and any crack tip that was inside of the MTR on a given iteration sampled crack growth rate data that included the MTR-induced acceleration. Once a crack tip exited the MTR, its growth rate was sampled from long crack data. The model was used to assess the effects of MTR size, shape, and location within a tested volume on damage tolerance lifetime. Later, James et al. (2022) expanded on this model to capture MTR attributes more explicitly including average (c-axis) orientation and density. In addition, the authors separated the contribution of hold time from the conventional fatigue cycle count such that different dwell times could be modeled without the need to capture additional experimental data. The MTR-induced small-crack acceleration was also incorporated through the use of El Haddad's (1979) intrinsic crack length correction, which adds a factor a_0 to the crack length that increases the driving force at small crack lengths and unifies the crack propagation between the small and long crack regions. The influence of a_0 diminishes with increasing crack length and the growth rate merges into the well-known Paris regime. Chan and Moody (2016) proposed a probabilistic

time-dependent crack growth model for cold dwell fatigue and incorporated it into DARWIN to model component-level performance. The model considered that accelerated crack propagation was based on the embrittling effect of internal hydrogen and explicitly incorporated orientation- and time-dependent crack growth rates.

5 Additional effects of microtexture on materials properties

5.1 Effect of microtexture on small crack growth

Szczepanski et al. (2014) investigated the effect of microtexture on small crack growth rates in Ti-6242 subjected to room temperature 0.5 Hz cyclic fatigue. Small 30 µm x 15 µm micronotches were machined into electropolished cylindrical samples using a dual-beam focused ion beam. Crack lengths were measured on 9 samples for material with low or high degrees of microtexture via acetate replication and the results are shown in Figure 51. The material was extracted from the same pancake forgings (#1 had low microtexture and #2 had high microtexture) used during the first part of the FAA-funded effort at The Ohio State University (Ghosh, et al., 2007). Both microstructural conditions led to the typical small crack effect whereby cracks grew at $\Delta K < \Delta K_{TH}$ and also propagated at faster rates at low ΔK compared to their long crack counterparts. Growth rates for the low microtexture condition quickly converged with the long crack data at $\Delta K \sim 6$ MPa m$^{1/2}$ while growth rates in the high microtexture condition remained above the baseline condition for essentially the entire range of ΔK investigated. Crack growth rates for the high microtexture condition were generally faster at $\Delta K < \sim 7$ MPa m$^{1/2}$ compared to the low microtexture condition and trended toward more constant da/dN with decreasing ΔK. Relative to long crack behavior, the low microtexture condition merged with the long crack data at $\Delta K \sim 6$ MPa m$^{1/2}$ whereas the high microtexture condition did not begin to merge with long crack data until well in the Paris regime at much higher ΔK (approaching 20 MPa m$^{1/2}$).
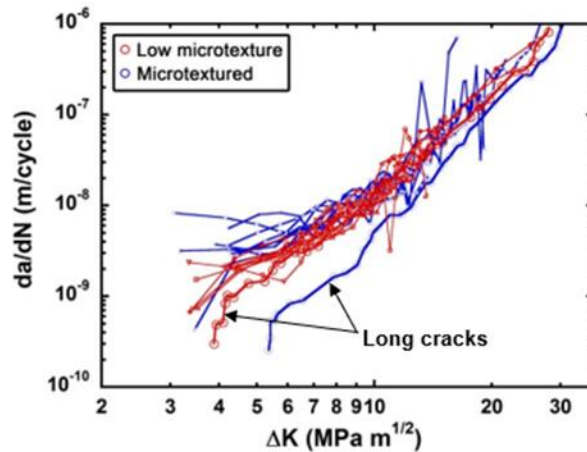
Figure 51. Effect of microtexture on long and small crack growth rates in Ti-6242

As noted earlier, the extent of the faceted growth mechanism depends strongly on the availability of hard oriented grains. Thus, the underlying MTR size and shape can result in the development of cracks that deviate significantly from thumbnail shaped cracks (i.e. a = c) often assumed for fracture mechanics calculations. For example, McBagonluri et al. (2005) have measured the aspect ratio of cracks in low, high, and transformed beta microstructures of Ti-6242 subjected to dwell fatigue. They found that the aspect ratio quickly deviated from near-ideal to an a/c ratio of ~0.4 indicating a strong preference for growth along the 'a' dimension (Figure 52). Note that the material used by McBagonluri et al. (2005) was "pancake 2" from Ghosh et al. (2007). Shaniavski and Losev (2003) made similar observations. These authors performed tests on material with high aspect ratio MTRs and noted a preference for accelerated growth along the long direction of the MTRs whether they were parallel or perpendicular to the specimen surface. These observations have implications on damage tolerance predictions because the MTRs may be larger than the assumed initial flaw size and also because the accelerated rate of growth can persist throughout the entire MTR (Pilchak & Williams, 2011).
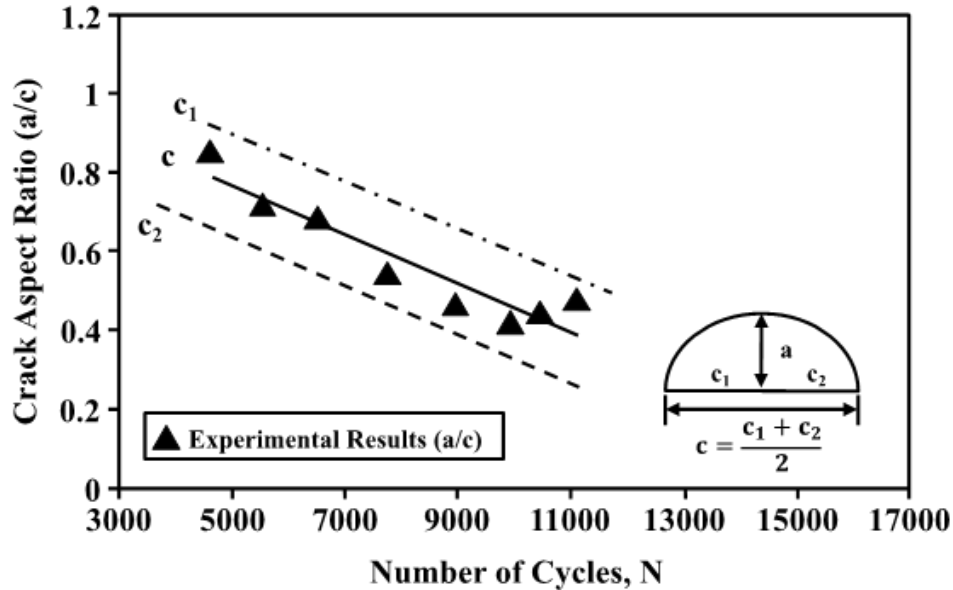
Figure 52. Crack aspect ratio as a function of cycles in highly microtextured material

5.2 Sustained load cracking

Before hydrogen content was easily measured by wet chemistry methods, the notch stress rupture test was used to assess whether a given lot of material had a suitably low hydrogen content. Samples with high hydrogen would fail quickly and show faceted initiation sites emanating from the machined notch. Under dwell fatigue conditions, a state of local triaxial stress created by "metallurgical notches" (i.e., stress fields caused by dislocation pileups, elastic/plastic interaction of MTRs, and load shedding) is a necessary condition for crack nucleation. Triaxial stress states are found at the roots of notches and hence it is possible that these tests could be used to assess sensitivity to MTRs without the high cycle counts needed for the natural development of triaxial stress states. Neal (1988) has pointed out that a sustained load test of this nature is effectively a prolonged single cycle dwell test and noted that fracture surfaces in 60° V-notch samples mirrored those observed on dwell fatigue specimens. The importance of texture and the availability of basal-oriented grains was also identified as a key factor in exciting a dwell effect during this type of test modeled after Neal (1988) (Figure 53). Thus, one obvious downside of this approach is that the machined notch may not intersect an MTR, which could give misleading results.
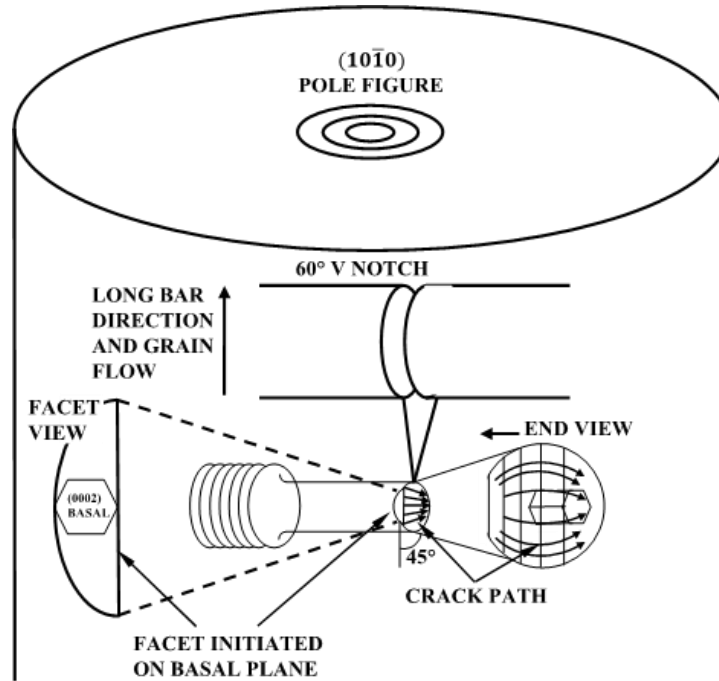
Figure 53. Schematic fracture mechanism for sustained load cracking of 60° V-notch specimen

Sustained load cracking (SLC) failure has been observed on non-rotating threaded parts machined from Ti-6Al-4V rolled plate material (AMS 4911) following application of a torque load used to secure the retaining nut. Separations occurred either immediately following engine acceptance testing or after a small number of engine cycles. Optical and SEM examination (Figure 54) of all SLC fractures revealed highly reflective, sub-surface faceted regions of fracture highlighting the presence of MTRs, similar to Ti-6242 dwell fatigue faceted failures.
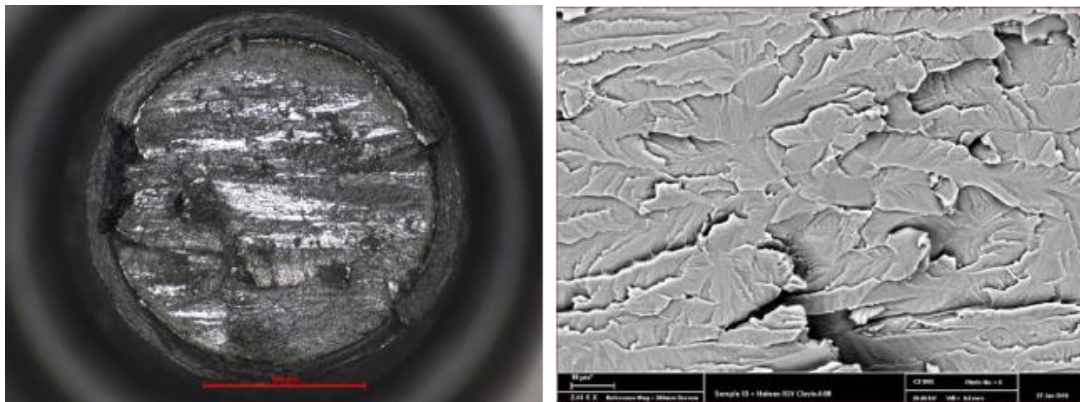
Figure 54. Fracture surface resulting from sustained load cracking of threaded Ti-6Al-4V part

5.3   High mean stress high cycle fatigue

High mean stresses during conventional fatigue testing may also induce a cold creep effect in titanium alloys leading to reduced lifetime and this effect may be especially pronounced as the loading frequency decreases. Oberwinkler (2016) pointed out that the Goodman diagram can be either overconservative or under conservative in predicting HCF behavior and the behavior is dependent on the underlying material microstructure and texture. Bandyopadhyay et al. (2019) have used digital image correlation and the crystal plasticity finite element method to investigate the mechanisms for the anomalous fatigue behavior at the relatively high load ratio of 0.6. The authors found that crack initiation occurred in regions of highly localized strain which were concentrated into deformation bands oriented at ~45° to the loading direction. Crystal plasticity finite element simulations revealed that the critical microstructure leading to nucleation was comprised of a soft-hard-soft grain combination wherein the soft grains deformed by both pyramidal and basal <a> slip and the hard grain experienced high normal stress relative to the basal plane. The simulations further showed that strain distributions were more heterogeneous as the load ratio increased. As R increased, a smaller number of grains experienced plastic deformation, but there was increased slip activity within each grain that included contributions from basal, prism, and pyramidal slip systems. In contrast, prismatic slip was preferred at lower load ratios and this was observed to occur in a larger number of grains.

Dod and Monavon (2024) have recently compared the fracture surface morphology in Ti-6Al-4V following dwell fatigue, creep, and R = 0.8 continuous cycling fatigue testing (Dod & Monavon, 2024). In all cases the authors observed cracks originating from alpha particles that produced very smooth, featureless facet morphology. Subsequent crack extension occurred on planes nominally perpendicular to the applied stress axis with surface morphologies consistent with prior observations of static and dwell fatigue loading (Pilchak & Williams, 2011). As a result of this investigation, Dod and Monavon (2024) concluded that creep strain accumulation under high mean stress at R = 0.8 at high applied stresses ($\geq$ 90% of yield strength in this work) resulted in stress redistribution and load shedding that caused fracture of hard-oriented MTRs. The fracture surfaces from dwell and R = 0.8 cyclic tests performed at 800 MPa (90% of the alloy yield strength) are shown in Figure 55.
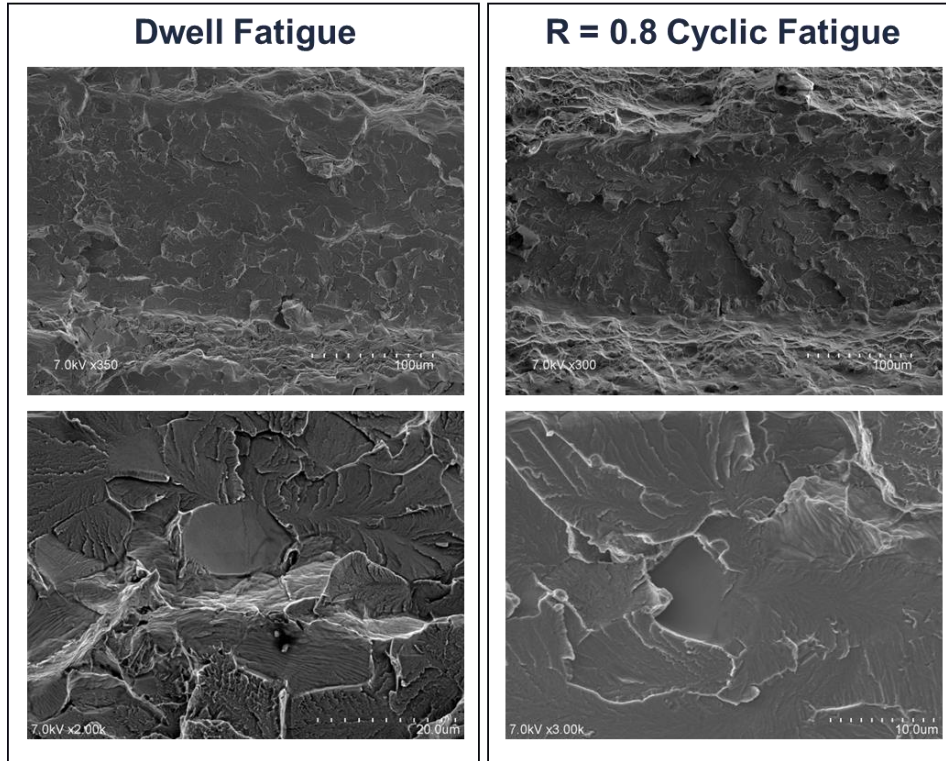
Figure 55. Comparison of Ti-6Al-4V fracture surfaces under cyclic and dwell fatigue loading

5.4 Impact on long crack growth rate under cyclic loading

While there has been no systematic investigation as to the role of MTRs on long crack growth rate during cyclic fatigue, the impact of these microstructural features can be inferred through the observations of multiple investigators. The long crack data in Figure 51 reveals a few important trends. The growth rates for the high microtexture condition are slower across the entire range of ΔK investigated, but the disparity is largest for values of $\Delta K < 10$ MPa m$^{1/2}$. In addition, the threshold crack stress intensity range (ΔK_{TH}) is higher for material containing microtexture compared to the low microtexture condition, i.e. ~5.5 MPa m$^{1/2}$ compared to ~4 MPa m$^{1/2}$. When considered in the context of the work of Bantounas et al. (2007), a plausible explanation for these observations may be related to crack growth arrest at hard-oriented MTRs leading to a complicated crack front geometry as well as roughness-induced and/or plasticity-induced closure effects. In particular, the authors showed that fracture mode is strongly influenced by the orientation of the underlying macrozone. The crack front progressed readily through regions well oriented for prismatic slip and temporarily arrested at hard-oriented regions leaving connected ligaments in the crack wake. These ligaments ultimately failed by more ductile failure modes,

which could contribute to the development of plasticity-and-roughness-induced closure effects that tend to decrease crack growth rate.

This premise is further supported by the work of Bowen (1975), who studied fatigue crack growth rates in strongly transverse textured Ti-6Al-4V plate material. An exhaustive investigation was performed to measure Paris law constants (C and m in the equation da/dN = $C\Delta K^m$) on this essentially "microtextured single crystal" material. The work is summarized in Figure 56 (Brandes, 2008) which shows Paris law behavior for cracks growing nominally parallel to a given (hkil) plane and along a particular [uvtw] direction. Bowen reported that deformation occurred symmetrically when there were prismatic slip systems readily available to satisfy the continuum plastic zone and fatigue cracking resulted in a relatively flat fracture surface oriented normal to the primary stress axis that was dominated by striation growth. Some mixed mode I and mode II growth was observed when the crack was growing on $\{11\bar{2}0\}$ resulting in a serrated crack path. When deformation was not symmetric about the crack tip, such as during propagation close to (0001), fracture topography was much more complex, and the crack sought out the most convenient crystallographic fracture modes. This resulted in a mix of fatigue and monotonic failure modes with striations at various angles relative to the overall crack propagation direction and a decrease in the overall growth rates. This result contrasts with the earlier comments regarding dwell fatigue crack growth, which occurs rapidly when (0001) is nearly perpendicular to the stress axis and highlights the difference in the underlying fracture mechanism. As a reminder, under pure cyclic loading fatigue, cracks growing via the faceted mechanism prefer basal planes inclined to the stress axis because crack extension occurs along the slip band whereas under dwell fatigue conditions the fracture plane is *inclined* to the basal plane and controlled more strongly by mode-I forces (Pilchak & Williams, 2010).
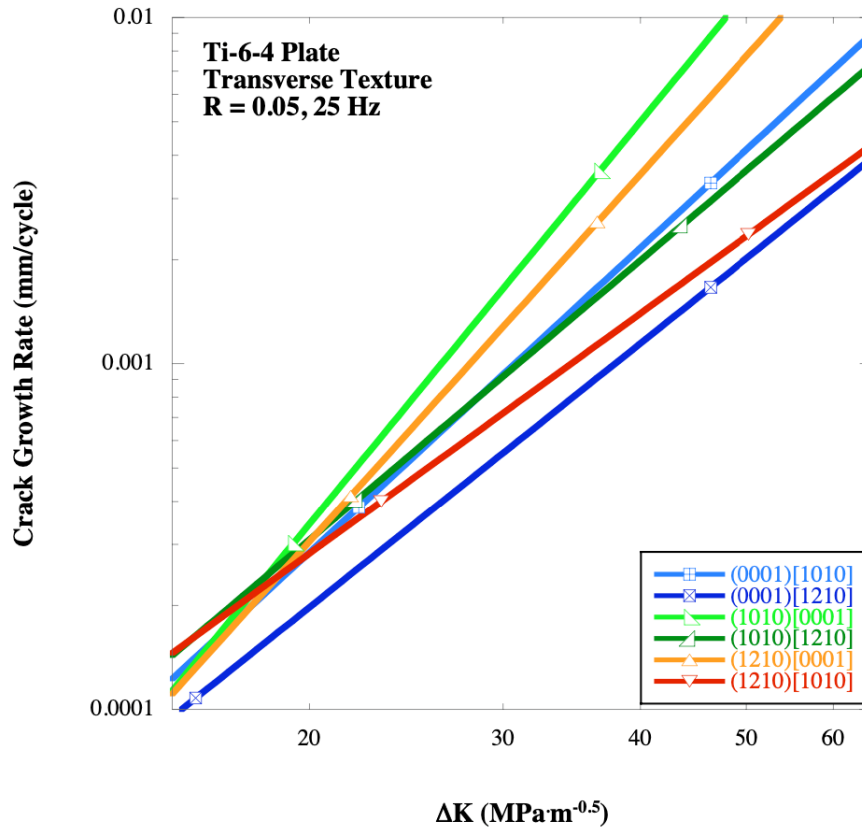
Figure 56. Effect of crystallographic orientation on stage II fatigue crack growth in Ti-6Al-4V

5.5   Stress corrosion cracking

The stress corrosion cracking (SCC) process has long been known to produce faceted failure in titanium alloys under static loading, though the sensitization does not occur without a stress concentration unless the native TiO_2 oxide layer is ruptured – a process which is enhanced by the presence of a notch or precrack (Blackburn, Smyrl, & Feeney, 1972). The fracture surfaces of samples that have failed by SCC have many similar characteristics to dwell fatigue fracture surfaces as shown by Pilchak and Williams (2011) and Pilchak et al. (2010). SCC samples prepared from Ti-8Al-1Mo-1V billet were tested under slow strain rate tension (e.g. ~10^{-6} to 10^{-7}/s) in 3.5% NaCl solution. The size and shape of the faceted region, the morphology of individual facet surfaces, the spatial orientation of the facets, and the crystallographic plane exposed to the fracture surface were nearly identical to those which failed under dwell fatigue. It was also demonstrated that the sensitivity to SCC was further enhanced by an aging treatment to produce alpha$_2$ precipitates, which reduced the time to failure from ~10 hours to less than two minutes. These observations, along with similar fracture surface morphology for compact tension specimens of alpha+beta alloys fractured in positive pressures of hydrogen gas (Yeh & Huang,

1997; 1998), provides insight into the potential mechanism for accelerated crack growth which may involve the hydrogen enhanced localized plasticity mechanism (Robertson, et al., 2015; Shih, Robertson, & Birnbaum, 1988) as proposed by Pilchak and Williams (2011).

Stubbington & Pearson (1978) made similar observations on Ti-6Al-4V with a bimodal microstructure. The authors introduced 3.5% NaCl solution to a growing fatigue crack and observed a strong waveform dependence on crack growth rate. For example, the crack growth rate immediately increased from 7.5×10^{-7} m/cycle to 5.8×10^{-6} m/cycle when changing from 25 Hz to 0.3 Hz at $\Delta K \sim 20$ MPa m$^{1/2}$. The authors next changed to 5-min dwell loads at $\Delta K \sim 26$ MPa m$^{1/2}$ and observed a further increase from 8×10^{-6} m/cycle to 3.4×10^{-4} m/cycle which resulted in failure in only 11 cycles.

6   Aspects of materials processing

Thermomechanical processing of titanium alloys is performed with the goal of controlling microstructure to optimize and balance quasistatic and dynamic material properties. The processing steps include casting an ingot, converting the ingot to billet, forging the billet into a component, and typically solution heat treating and stress relieving the component before machining to final dimensions. Titanium ingots may be produced via vacuum arc remelting (typically two or three times, depending on part criticality), cold hearth melting, or a combination of the two and solidified as large ingots (~36" diameter and weighing between 4,000 and 30,000 lbs.). This large volume of material is worked down to billet with multiple steps and intermediate reheats with typical billet diameters being between 6" and 14". The billet is cut into smaller pieces and machined into cylinders to produce forging stock, which are often referred to as mults.

The properties of titanium alloys have an incredibly strong dependence on the thermomechanical processing sequence used to produce them (Figure 57). This includes everything from the macrostructure of the initial cast ingot and all subsequent processing steps used to refine the ingot to billet, the subsequent processing steps used to forge the billet into a component, and the final heat treatment practices applied to the component. Although a significant amount of strain is imposed in multiple directions and the material is re-heated multiple times during processing, MTRs persist into the finished forging. Semiatin (2020) has summarized the key steps in the thermomechanical processing sequence and identified the relevant deformation mechanisms and microstructure evolution phenomena in each. These various steps cumulatively control the length scale and crystallographic orientation of the microstructural elements outlined in Figure 25. In this section, we describe the main factors that control microstructure evolution at various stages

of processing. The evolution of each feature, which includes the primary alpha, beta, and transformed beta phases, collectively impact the character of the MTRs.

The material presented in this section comes from a variety of sources including peer-reviewed literature, for which references are given, industrial internal research and development efforts, some details of which cannot be shared due to the proprietary nature of the work, and, finally, some aspects are inferred through an understanding of relevant metallurgical phenomena and the anticipated effect on material behavior. This final class are aspects that are believed to be true, but for which there is no clear validation and hence represent opportunities for further research.
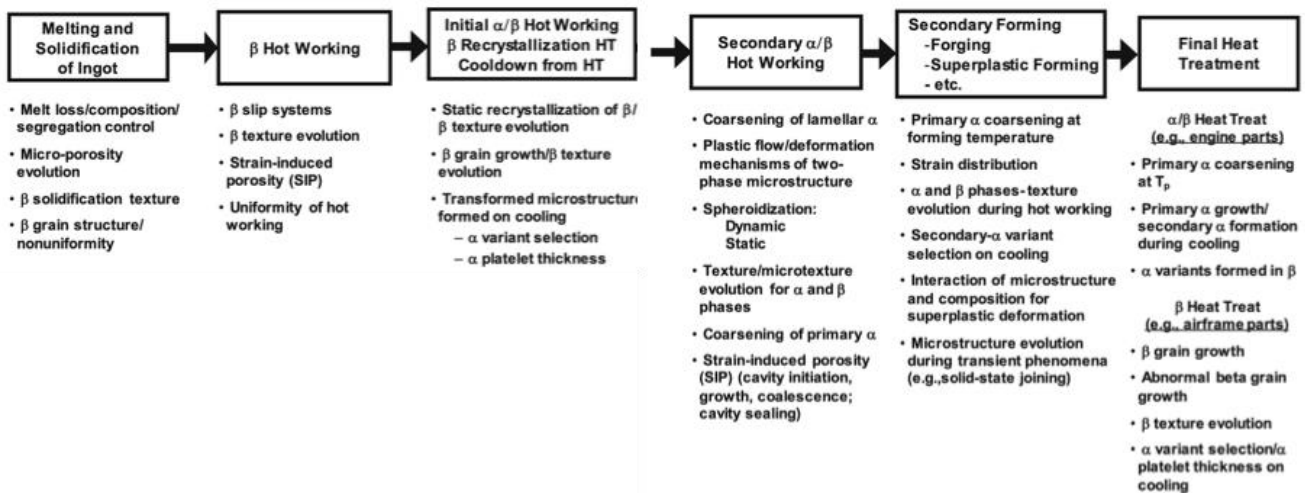
Figure 57. Key steps and microstructure evolution mechanisms during thermomechanical processing

6.1 Billet processing

Historically, conversion practice for alpha+beta processed and heat-treated materials has been to produce a smaller product form with a refined microstructure for use in subsequent forging operations. There was no regard for the presence of MTRs since they were not known to exist or play a detrimental role in CDF until the advent of automated EBSD in the early 1990's (Woodfield A. , Gorman, Corderman, Sutliff, & Yamrom, 1996; Woodfield A. , Gorman, Sutliff, & Corderman, 1999). However, an increasing emphasis on cost reduction and performance improvements of titanium alloys over the last three decades has driven the development and implementation of microstructure and damage models. Thermo-mechanical modeling of various primary production stages has been accomplished via the use of 2D and 3D finite element analysis (FEA) codes, which determine local state variables (e.g., strain, strain rate, temperature, etc.). These variables are subsequently linked through user routines to various microstructure and

critical damage models, which predict beta/alpha grain size, grain boundary alpha, alpha lath size, phase proportions, percent spheroidized alpha, and the onset of void initiation. These models, developed for Ti-6Al-4V, are being effectively utilized in the design of key process conditions (e.g., soak times, cooling rates, transfer times, die speeds, bites and drafts, resulting in improved yield and microstructure). Production titanium ingots are converted to billet by the careful control of process conditions such as temperature, strain levels, and strain rates of deformation, optimized and supported by 3D cogging modeling to minimize flow localization and damage, while maintaining uniform microstructure. These modeling approaches have also improved MTR characteristics over time.

6.1.1 Introduction

It has been reported (Semiatin S. , 2020; Tricot, 1988) that the billet conversion process for Ti alloys typically consists of (i) initial ingot breakdown above the beta transus, (ii) sub-transus working in alpha + beta phase field, (iii) heating above the beta transus to recrystallize and refine the beta grains, (iv) water quenching, and (v) final alpha + beta work to spheroidize the primary alpha particles. As a result of the allotropic transformation and limited by the relatively low thermal conductivity of titanium alloys, colonies of aligned alpha plates are formed in large-section billet products during step (iv). These colonies of aligned alpha plates are converted to MTRs during step (v). From our understanding of the physical metallurgy of titanium alloys, we note that:

- The recrystallized prior beta grain size will be determined by the effectiveness of steps (ii) and (iii) (Venkatesh & Wilson, 2007).

- The maximum theoretical size of the MTRs will be determined by the size of the alpha colonies within the prior beta grains that are formed during step (iii), although, as discussed later, variant selection during beta quenching may lead to regions of similarly oriented alpha on opposite sides of a prior beta grain boundary resulting in regions of near-constant orientation that may exceed the prior beta grain size.

- In principle, the MTR size is thus limited by the size of the prior beta grain, however, often colonies nucleate from opposite sides of the grain and grow inward. From this perspective, the colony size will be limited to approximately half the prior beta grain size, but additional possibilities are discussed below.

- The degree of randomization within an MTR will be determined by a combination of the cooling rate in the billet during step (iv), which sets the alpha lath thickness and colony

size, as well as the strain-path (Bieler & Semiatin, 2002) and amount of final alpha + beta work in step (v) (Semiatin S. , 2020; Woodfield & Lemaitre, 2020).

These concepts have been demonstrated by a full-scale, Ti-6242 billet conversion design of experiments that was performed by GE Aerospace with subsequent EBSD quantification of MTR size, volume fraction, and alignment on slices taken from the end and middle of billets (Woodfield, A. et al., 1995). The key findings of this work were that:

- Increased levels of final alpha + beta work (step v) reduced MTR size and intensity.

- Increasing the temperature of the final alpha + beta work (step v) reduced MTR intensity.

More recently, follow-on work on Ti-6Al-4V confirmed that MTR size and intensity correlated directly with the processing parameters utilized in billet processing steps (iii), (iv) and (v) as they did for Ti-6242.

Exact conversion processes are supplier-specific intellectual property and hence are proprietary. However, the general sequence has been described by Tricot (1988), later by Lutjering and Williams (2007), and more recently by Semiatin (2020). The information below is compiled from the information reported by these authors and is intended to show a high-level overview after which the various process steps will be discussed in more detail.

The simplest process involves rough working performed first in the beta phase field at a temperature between 1000 ºC and 1150 ºC to take advantage of the lower flow stress in this regime followed by air cooling. Following this initial breakdown, the material is subjected to alpha+beta working and typically reduced in size by a factor of 4 to 5 at a temperature ~50 ºC below the beta transus as shown in sequence 1 in Figure 58 (Tricot, 1988). There are variations of this basic process which can be used to elicit further macro-and-microstructural refinement, to reduce production times, or save on heating energy costs as shown in sequences 2 through 4 in Figure 58. For example, sequence 2 involves performing an intermediate beta anneal followed by rapid cooling before reheating for additional alpha+beta hot work. This helps provide additional refinement and control over macro- and microstructures. Sequence 3 is a variation of sequence 2 which reduces the total number of heating steps by going straight to alpha+beta hot working after the initial beta working thereby reducing time and cost. Sequence 4 is a variation on 3 where instead of fast cooling from above the beta transus, the material is worked continuously while cooling below the beta transus which is known to minimize grain boundary alpha (Tricot, 1988).
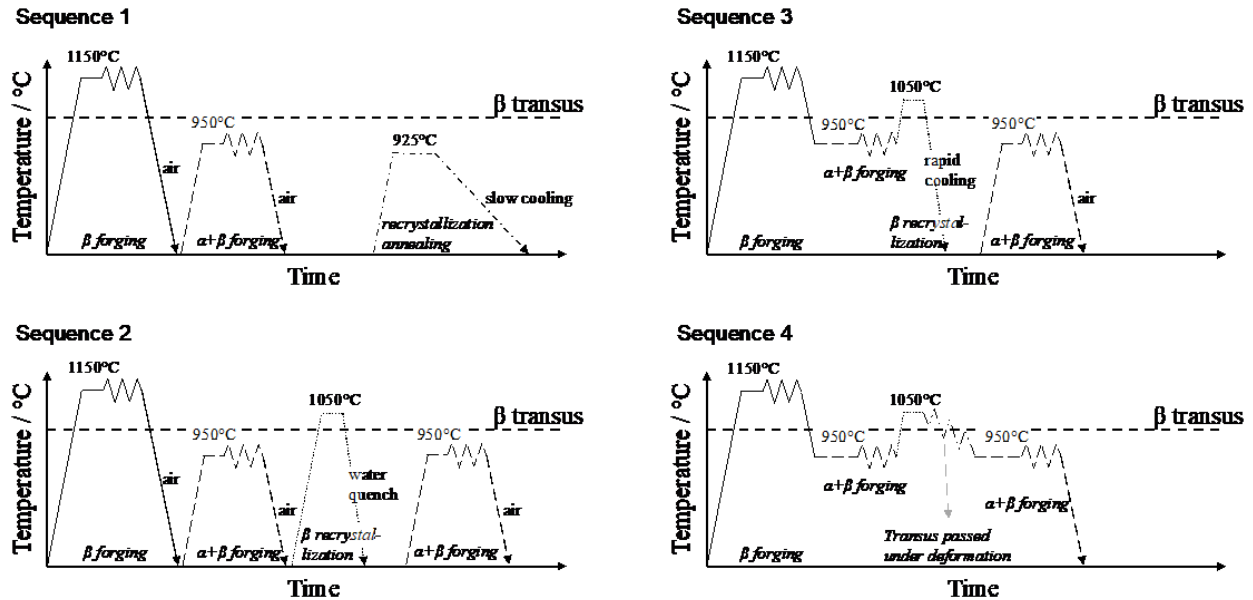
Figure 58. Schematic processing paths for titanium billet production

6.1.2 Step 1: Beta hot-working

Hot-working in the beta phase field is performed to reduce the diameter of the ingot while simultaneously breaking down the coarse, as-cast microstructure. As described by Lütjering and Williams (2007), the initial hot working is done on an open die forging press at a temperature well above the beta transus (e.g. T_{beta} + 150 °C). The high temperature results in lower flow stress (Tricot, 1988) and, along with concurrent deformation, serves to ensure a homogeneous distribution of alloying elements to produce microstructural uniformity in preparation for subsequent thermomechanical processing operations. Some highly beta stabilized alloys require a separate homogenization cycle. The amount of deformation imparted during this initial step depends on the alloy but is in the range of ~28-38% (Lütjering & Williams, 2007). As an example, an initially ~90 cm diameter ingot will be reduced to about 60~70 cm in diameter and may be converted to a square or round-cornered square (RCS) cross section during this stage. This process may include multiple upsets and drawing operations to reach the desired diameter.

In principle, beta hot working seems like a simple operation, but there are many nuances in practice which makes it difficult to control microstructural uniformity both along the billet axis as well as radially at a given location. The work of Glavicic et al. (2003) helps illustrate some of these complications. The authors have investigated the microstructure and texture of a 91.5 cm diameter vacuum arc remelted (VAR) ingot. They sectioned a large piece of material from the bottom of the ingot that spanned from the outer diameter to the center. A schematic partial cross

section of the ingot highlighting columnar grain growth direction and the equiaxed grain region is shown in Figure 59 (based on the work of Glavicic et al. (2003)).
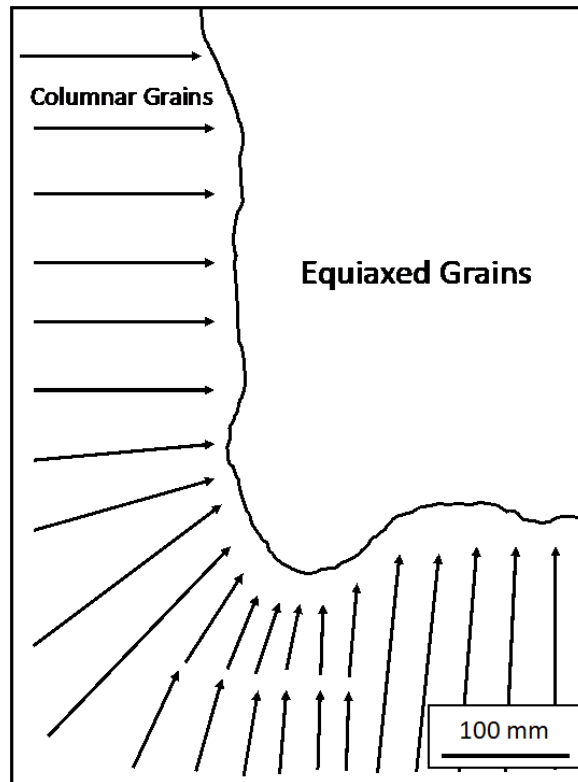
Figure 59. Columnar grain growth directions near the bottom section of Ti-6Al-4V VAR ingot

This image reveals that the large, columnar grains that are axially oriented at the bottom of the ingot, radially oriented on the side wall, and have a gradual transition between these two extremes. The center of the ingot contained nominally equiaxed beta grains. Glavicic et al. (2003) further sectioned this piece and performed large-area EBSD analysis at various locations in the center and exterior portions of the ingot. They found that the columnar grains consisted of strong <100> fiber textures where the fiber axis was parallel to the elongation direction. In contrast, the texture of the equiaxed grains were weaker and varied from location to location. Higher working temperatures coupled with slower strain rates tends to result in a more uniform development of subgrains (Banerjee, Pilchak, & Williams, 2012). However, it is noteworthy that slow strain rates and long processing times may lead to extensive heat loss due to radiation and may introduce undesirable axial variations in microstructural refinement and/or edge cracking.

6.1.3 Step 2: Alpha+beta hot working

Following the beta hot working step, an initial alpha+beta hot working step is performed. Because the material will again be heat treated above the beta transus, the primary purpose of this step is to impart sufficient strain to promote beta recrystallization during the following step. As mentioned by Venkatesh and Wilson (2007), while detailed studies of the effect of prior alpha+beta strain have not been published, it is clear that this along with temperature and time at temperature will have a strong impact on subsequent beta recrystallization kinetics. Lütjering and Williams (2007) suggest that a 30-40% reduction be applied during this step while Semiatin (2020) suggests that 15-30% reduction be applied at a temperature about 40 °C below the beta transus. In general, temperatures high in the alpha+beta phase field will provide a benefit in terms of workability due to the lower flow stress and lower volume fraction of beta phase, however, working too close to the beta transus can limit grain size refinement during subsequent beta annealing (Elagina, Gordienko, Evmenov, & Ivashko, 1982). These temperatures also allow more time on die since heat loss due to radiation will occur resulting in higher forging loads. Care must be taken, however, to not be too high in the two-phase field since large bites will result in local deformation heating which may cause transients above the beta transus.

With regard to microstructure evolution, the initially lamellar microstructure may undergo general reorientation, bending, or kinking depending on the initial orientation relative to the principal working direction. Kinking is observed when the laths are initially elongated in the compression direction while rotation and thinning of the alpha laths occurs for initially inclined laths (Perumal, Rist, Gungor, Brooks, & Fitzpatrick, 2016). Lattice rotations occur concurrently with these morphological changes. It is generally observed that subgrains are formed within the alpha lamellae that increase in misorientation with increasing strain. The subgrain misorientation is of the order of 5° following true strains of ~0.3 and increases to ~15° or more by strains of ~1.1 – 1.3 (Ito, Murakami, & Tsuji, 2017; Mironov, Murzinova, Zherebtsov, Salishchev, & Semiatin, 2009). These values represent local continuum scale strains, however, the morphological dependence and plastic anisotropy results in a strong orientation-dependent spheroidization phenomenon. Nicolaou and Semiatin (2007) analyzed spheroidization using EBSD and a self-consistent model that incorporated the strain partitioning phenomenon and concluded that soft orientations spheroidize readily by strains of ~1.5 whereas hard-oriented colonies require strains as high as ~3.5 under a torsion strain-path.

The flow stress depends strongly on the deformation temperature, the applied strain rate, and, to a far lesser extent, the initial thickness of the alpha lamellae (Figure 60) (Perumal, Rist, Gungor, Brooks, & Fitzpatrick, 2016). Flow stress increased with increasing strain rate but decreased with

temperature. Samples were preheated to the deformation temperature for 30-min followed by water quenching to observe the microstructure at the deformation temperature. Soaking at an elevated temperature of 950 ºC compared to 880 ºC resulted in slightly finer lath sizes, which aids in spheroidization kinetics. There was significant flow softening for all temperatures and strain rates investigated which is due to a combination of spheroidization and the morphological reorientation of the laths. The authors found that achievement of a steady-state flow stress correlated well with completion of lath reorientation to be nearly perpendicular to the stress axis as opposed to complete spheroidization. In addition to these processes, it has been reported that texture evolution may play an important role in the observed flow softening behavior (Miller, Bieler, & Semiatin, S. L., 1999; Semiatin & Bieler, 2001b).
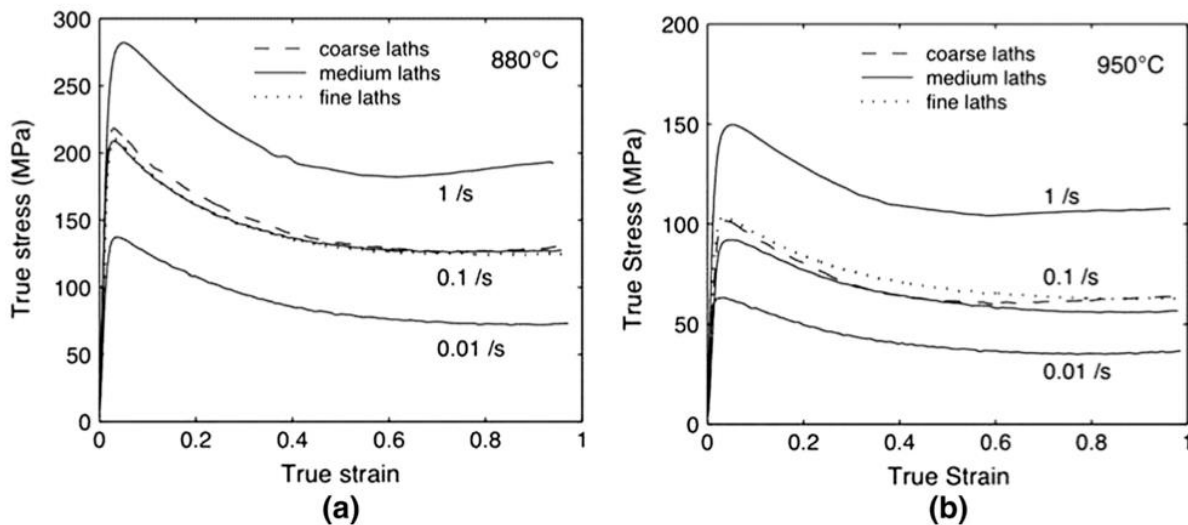
Figure 60. Flow stress of hot-worked Ti-6Al-4V with initially lamellar microstructure

6.1.4 Step 3: Beta recrystallization

The beta recrystallization step and subsequent cooling (Section 6.1.5) are key steps in the conversion process. This is because the alpha colonies formed at this stage will be the "nuclei" for MTRs that will persist through all subsequent working steps (for components that will be used in the alpha+beta processed condition). This step follows beta hot-working and alpha+beta hot-working, the former which refines the very coarse beta grains from the casting process and the latter which introduces stored strain energy that induces recrystallization during subsequent heat treatment above the beta transus. The beta recrystallization step is meant to produce a fine, uniformly small beta grain size in preparation for subsequent alpha+beta working (Section 6.1.6), but non-uniform strain and temperature distributions make this difficult to achieve in

practice. In addition to the prior alpha+beta prestrain, annealing temperature, and time at temperature, the heating rate is also an important consideration with respect to the final observed prior beta grain size. Moreover, the potential for variant selection mechanisms which result in similarly oriented alpha colonies on opposite sides of prior beta grain boundaries that have a common {110} plane (Bhattacharyya, Viswanathan, Denkenberger, Furrer, & Fraser, 2003) result in larger effective structural units that are difficult to break down during subsequent working operations. These may be the 'seeds' for the largest MTRs that remain following conversion, but to date there have been no direct observations of this.

Semiatin et al. (1996; 2001) investigated the kinetics of grain growth during the early stages of beta-annealing. The authors performed salt pot heat treatments on thin sheets of Ti-6Al-4V at temperatures of 1032 °C and 1088 °C (Semiatin, Soper, & Sukonnik, 1996). They found that grain size evolved rapidly with time and that the grain growth kinetics were well described by the classical growth law, $d^n - d_0^n = k(t - t_0)\exp\left(-\frac{Q}{RT}\right)$, with a grain growth exponent $n = 2.0$. The activation energy, Q, was determined to be 312 kJ/mol while the rate constant k was 1110 m^2/s. Based on the finding of $n = 2$ coupled with the activation energy led the authors to conclude that beta grain growth was controlled by diffusion. The finding of $n = 2$ is consistent with classical theories for ideal grain growth in pure metals, and hence, it is unique to observe such behavior in a substitutional solid solution alloy. In analyzing the short-time grain growth kinetics, it was essential to model the time associated with the subtransus transient during heating. Semiatin et al. (2001) also demonstrated that the initial beta phase texture also affected grain growth kinetics through a series of continuous annealing trials on two different lots of Ti-6Al-4V bar material. The investigation consisted of heating at constant rates of 1.4, 5.6, and 18 °C/s to maximum temperatures of 1150 °C and 1250 °C. The first lot of material (A) exhibited a cube texture with <001> aligned with the bar axis while the second lot (B) had a <110> partial fiber texture aligned with the bar axis. Following heat treatment, lot (A) exhibited consistently larger grain sizes at all heating rates than lot (B). For both lots of material and both peak temperatures it was found that grain size decreased with increasing heating rate. The grain growth exponents were similar for both lots, between 3.2 and 4.6, depending on material and peak temperature while the activation energies were 309 kJ/mol and 318 kJ/mol for Lot (A) and (B), respectively. The rate constants, on the other hand, were quite different with k = 28.5 x 10^{-4} and 5 x 10^{-4} m$^{3.7}$ s^{-1} for lots (A) and (B), respectively.

These observations underscore the importance of considering the beta phase texture at the time of annealing. The key parameters for consideration include the strain path during ingot conversion, which establishes the texture, the section thickness at the time of beta-

recrystallization, which influences the heating time, the peak temperature, and time at temperature. Based on the work of Semiatin et al. (1996; 2001), we can conclude that the heating rate should be maximized and the time and temperature above the beta transus should be minimized to maintain the smallest prior beta grain size.

6.1.5 Step 4: Post-beta-recrystallization cooling

The cooling rate following the beta recrystallization step is another critical aspect regarding the formation of MTRs during subsequent conversion and forging operations. The alpha colonies and laths formed during this step are the 'seeds' for the MTRs that will persist into the final billet. The cooling rate from above the beta transus step has a direct impact on the formation of grain boundary alpha, the size of the alpha colonies, and the alpha lath thickness. These factors will influence the spheroidization kinetics during subsequent alpha+beta working as discussed in Section 6.1.6. From this perspective fast cooling rates are desirable, but at this stage a typical billet may be ~ 50 cm (~20") in diameter and thus cooling rates will be limited by the relatively low thermal conductivity of titanium at these section thicknesses. There is a minor effect of the quench geometry on cooling rate as shown by Venkatesh and Wilson (2007) (Figure 61). Rapid cooling rates are also beneficial with respect to spheroidization kinetics during subsequent alpha+beta hot working steps (see Section 6.1.6). Fine, acicular microstructures respond readily and spheroidize or globularize at smaller strains compared to coarse or fine alpha colonies.
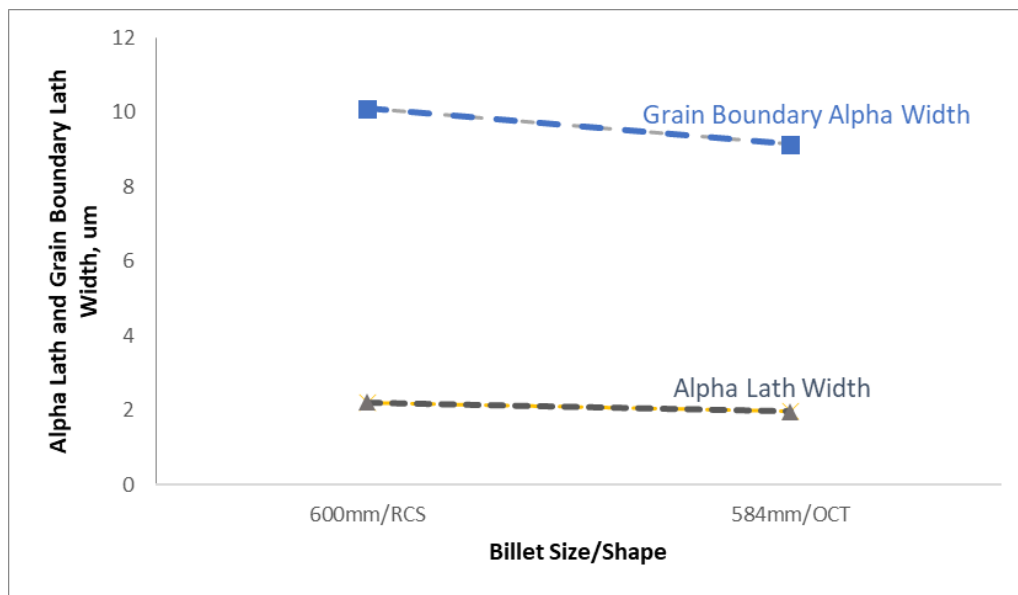
Figure 61. Effect of billet size and shape on microstructural features following quenching

Classical views of decomposition of the beta phase during the allotropic transformation indicate that alpha forms first at the prior beta grain boundaries established in the previous step after which alpha laths/colonies form and grow toward the interior of the grain until they impinge on one another near the center of the grain or there is sufficient undercooling for sympathetic nucleation of a new alpha orientation off of an existing one. The cooling rate through the beta transus has an important effect on grain boundary alpha thickness, which has been shown to follow an exponential relationship by Fox and Neal (1995) for Ti-6Al-4V, Figure 62. Gil et al. (2001) have shown that a similar relationship holds for alpha lath thickness. The cooling rate will be limited by the section thickness, which is typically quite large at this stage and thus the transformed structure assumes a colony morphology as opposed to basketweave. In general, the colonies will be of different orientation making the upper limit of the alpha colony size effectively half of the prior beta grain size. However, in some instances it may be possible that colonies of the same orientation may nucleate on opposing grain boundaries and meet in the middle making the prior beta grain size the upper limit to the colony size. As an additional point of note, it is worth recalling the observations of Bhattacharyya et al. (2003) who investigated variant selection at prior beta grain boundaries and alpha sideplate formation in Ti-6Al-2Sn-4Zr-6Mo. They analyzed a special case of two prior beta grains that shared a common {110} plane and observed that the alpha variant formed at the prior beta grain boundary was aligned (0001) with the common {110}. Furthermore, the alpha sideplates formed on both sides of the prior beta grain boundary also adopted the same {110} plane. This implies that a region of near-constant orientation may span more than one prior beta grain which, as mentioned above, can lead to larger effective structural units that may be among the largest MTRs in the finished mill product.
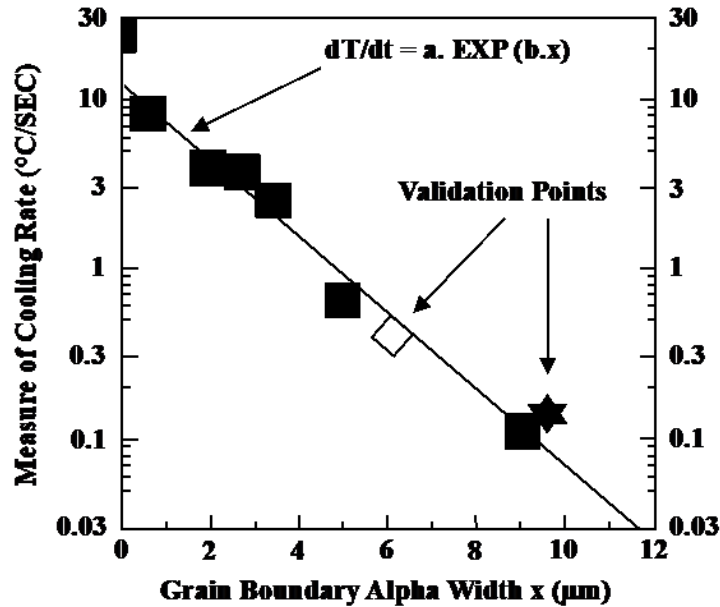
Figure 62. Empirical relationship between cooling rate through beta transus and grain boundary alpha thickness

6.1.6 Step 5: Final alpha/beta work

During the final alpha+beta working step, the material is reduced to a finished billet product that will be used for subsequent forging operations to produce a component. Typical billet diameters for rotating components are in the range of 10" to 14" for large aeroengine components and 4" to 8" for small engines. Historically, the goal has been to create spheroidized/equiaxed microstructure with a fine grain size, although processing routes have been augmented more recently in efforts to minimize the degree of microtexture that remains in the final product (Venkatesh & Wilson, 2007). Lütjering and Williams (2007) suggest at least a 65% reduction in this regime while Tricot (1988) recommends at least 75%. Gorman and Woodfield (USA Patent No. 6,332,935 B1, 2001) provide a slightly different perspective of the process aimed at decreasing ultrasonic inspection noise. They propose a final alpha beta working step involving a smaller reduction in area after the beta quench step which helps improve the ultrasonic inspectability of the billet. The degree of work suggested is between 5% and 40%, but reductions of 5% to 15% are highlighted as being the most effective in reducing ultrasonic noise (see Section 6.1.14 for additional discussion of ultrasonic testing). Multiple reheats may be required to reach these levels of reduction.

As evident from the discussion above, there are multiple strategies for billet conversion. While these serve as useful guidelines, processing routes should be carefully developed leveraging modeling and simulation techniques that are validated by full-scale trials. The total amount of

strain imposed during this step should be a function of the microstructure following the prior post-beta-recrystallization cooling. Shell and Semiatin (1999) studied the effect of initial microstructure on the flow behavior and spheroidization kinetics of Ti-6Al-4V. These included acicular alpha, fine colony, and coarse colony microstructures. The strain to complete the spheroidization process is also a function of the initial microstructure, and the microstructure evolution mechanisms in this step are the same as discussed in Section 6.1.3. As evident in Figure 63, acicular microstructures begin spheroidizing at strains just below ~0.5 while strains between 1.0 and 1.5 are needed to begin spheroidizing fine and coarse colony microstructures (Semiatin S. , 2020; Shell & Semiatin, 1999). Spheroidization may be completed by strains as low as 1.5 for fine acicular microstructures but may not complete even with strains exceeding ~2.5. Of course, spheroidization kinetics depend on temperature, which are addressed in more detail in Section 6.1.7.
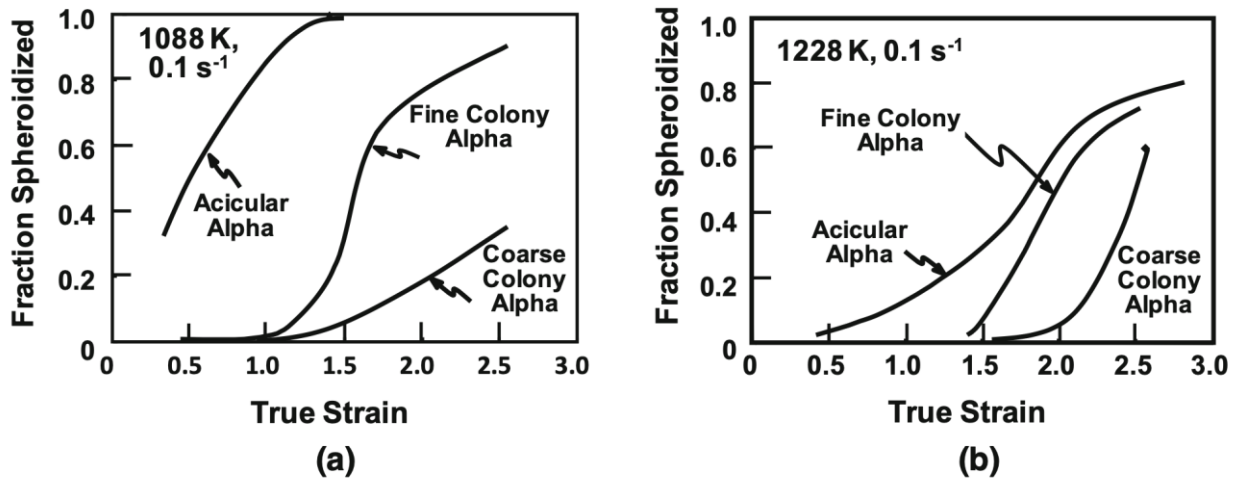
Figure 63. Effect of microstructure on dynamically spheroidized volume fraction: (a) 815°C (b) 955° C

The work of Mironov et al. (2009) provides further insight into the mechanism by which colonies are converted to equiaxed alpha grains. Figure 64 shows results from EBSD analysis of colony alpha compressed to various levels of reduction. In this image, the results are expressed as grain boundary misorientation maps where red indicates boundaries < 15º and black lines represent all other boundaries. Internal misorientation angles are shown as histograms while the angle/axis of misorientation are shown on inverse pole figures. Finally, representative alpha phase pole figures within a single colony in a sample upset to 50% demonstrates continuous lattice rotation and lack of classical recrystallization. As evident in the grain boundary misorientation maps and the corresponding misorientation distributions, low angle boundaries are developed inside of the colonies which tend to increase with misorientation with further

straining. At reductions of 50%, there was evidence of thinning and/or kinking of alpha laths as well as rotation perpendicular to the compression axis. Analysis of pole figures from individual colonies revealed that there were no new orientations formed via classical recrystallization mechanisms, but rather that strong orientation gradients were developed inside the colony.

These levels of strain may be difficult to achieve through-thickness in near-alpha and alpha+beta Ti alloys with larger cross section. As discussed in more detail in Section 6.1.10, this is related to the details of the forging and the type of press used for processing. In particular, radial variation in microstructural refinement in billet has been observed due to a combination of strain levels which are typically high near the surface and low in billet center as well as temperature gradients. The temperature near the center of the billet is usually maintained between reheats but the surface and mid-radial locations will see temperature gradients during processing. Venkatesh and Wilson (2007) predicted that temperatures around the surface regions drop by as much as 75 °C, while the rest of the billet was maintained at forging temperature. With respect to the axial direction, it was found that large forging bites produce surface undulations associated with flow around the die radii which leads to variations in longitudinal strain and spheroidized alpha fraction. In contrast, smaller bites (die increments) result in a larger and more uniform strain field and spheroidized alpha distribution for the same number of passes (Venkatesh & Wilson, 2007).
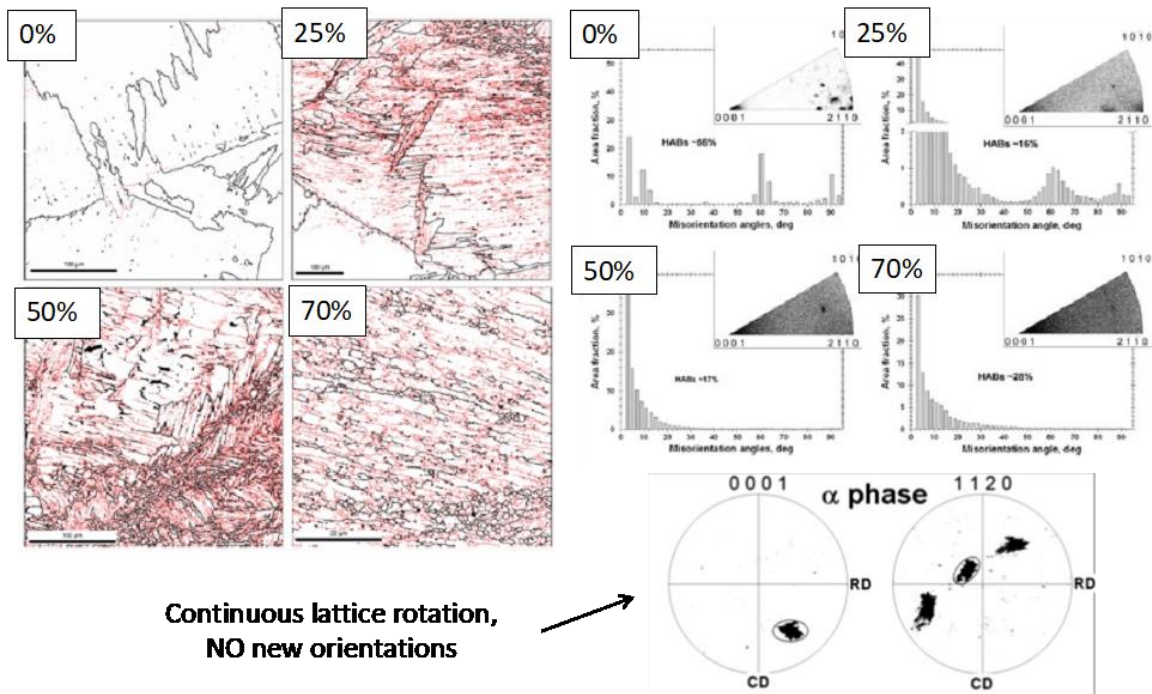
Figure 64. Effect of reduction on development of misorientations in alpha colonies in Ti-6Al-4V

6.1.7 Temperature of final alpha+beta work

The flow stress during final alpha+beta hot working at a given strain rate depends strongly on the deformation temperature. Flow stress is relatively uniform at temperatures just below the beta transus (e.g., 10 to 30 ºC or 20 to 55 ºF) (Tricot, 1988), but increases dramatically with decreasing temperature. For this reason, it is preferable to perform hot working at higher temperatures to reduce flow stress and decrease the force acting on the dies to prolong die life. The deformation temperature also has an important effect on the evolution of microstructure, macrotexture, and microtexture as a result of the strain-partitioning effect between the alpha and beta phases. At low temperature and high-volume fraction of alpha (e.g. 75%), the deformation is largely accommodated by the alpha phase and microtexture evolution is thought to be controlled by anisotropic plastic deformation in the alpha phase. In contrast, at high temperature where the volume fraction of alpha phase is small (e.g. $< 25\%$) the beta phase dominates the deformation behavior leading to a difference in microstructure and texture evolution kinetics. The strain-path during open die forging of a cylinder or round-cornered square is essentially a plane strain compression. Pilchak et al. (2020) and Levkulich et al. (2021) have reported on the *beta phase* texture evolution as a function of temperature/primary alpha volume fraction, but because the work focused on the role of beta phase texture on coarse grain growth (similar to abnormal grain growth but arising from a different mechanism) the alpha phase textures were not reported. Nevertheless, the effect of the temperature-dependent-strain-partitioning can be observed in the beta phase ODFs in Figure 65. At low forging temperature (high volume fraction primary alpha), we see orientation a predominantly distributed along the γ fiber with main texture components at {111}<110> and {111}<112>. At higher forging temperatures, the BCC orientations respond strongly to the plane strain compression and a pathway is formed along the α fiber permitting orientations to flow into the rotated cube {001}<110> orientation. These simulations are described in more detail inPilchak et al. (2020), but consisted *of* beta phase texture evolution after a true strain of 1.2 in plane strain compression from an initially randomly textured material. The Figure 65 schematic ODF on the left shows important texture components in these $\phi2 = 45$o sections of the ODF.
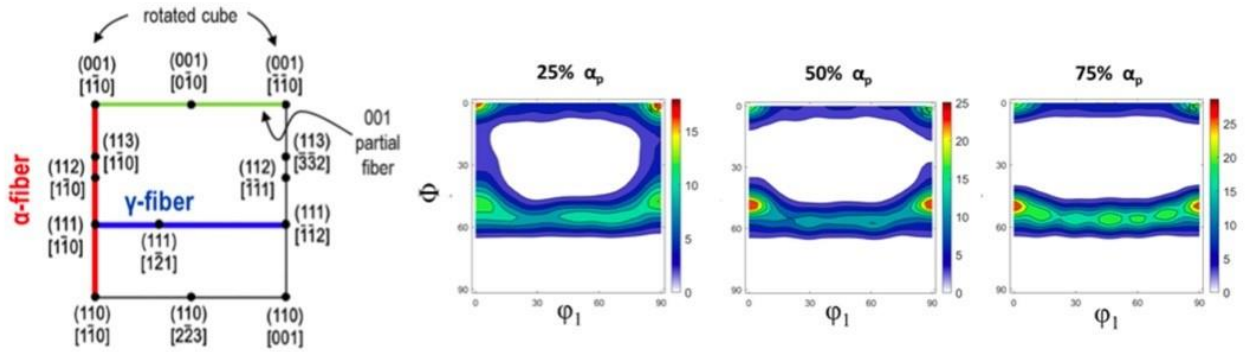
Figure 65. Effect of primary alpha volume fraction on beta phase texture evolution under plane strain compression ($\varphi_2 = 45°$)

Figure 63 referring again to the work of Semiatin and Shell (1999), we see the stark dependence of deformation temperature on fraction of dynamically spheroidized primary alpha. With respect to processing temperature for finishing production billets, Tricot (1988) suggests a finishing temperature ~90 °F (50 °C) below the beta transus.

Venkatesh et al. (2007) developed a processing route to produce a more uniform fine grain Ti-6Al-4V billet. Based on success with small-scale laboratory trials, the authors applied a similar approach to a production scale billet. By incrementally forging at 100 °C (180 °F) below the beta transus with slower press speeds, the authors were able to produce defect-free material with reduced texture, microtexture, and grain size. The strain-rate sensitivity was of the order of 0.3 at higher strain (>0.9) indicating the deformation mechanism may have transitioned to grain boundary sliding, which aided in randomizing crystallographic orientations. The alpha grain size was 3 to 7 µm smaller than in the conventionally processed material although the latter was processed to much higher strains.

6.1.8 Reheat time for final alpha/beta work

The primary microstructure evolution processes during reheat include conversion from alpha to beta phase upon heating with concurrent static spheroidization and finally primary alpha coarsening. Venkatesh and Wilson (2007) reported that the greater number of reheats (i.e., longer time at temperature) and increased levels of prior alpha+beta work for billets converted on hydraulic presses resulted in a greater degree of spheroidization. In contrast to open die forging, GFM-converted billets, which require fewer reheats had overall finer microstructures, but had a higher incidence of remnant aligned, elongated regions of primary alpha (Venkatesh & Wilson, 2007).

6.1.9 Redundant work for MTR break-up

Bieler and Semiatin (2002) demonstrated that crystallographic orientation of alpha colonies relative to the compression direction in Ti-6Al-4V had a strong impact on the potential for spheroidization. Colonies well aligned for basal and prismatic slip tended to spheroidize more readily and also produced more randomized alpha particle orientations at lower applied strains compared to orientations with the c-axis aligned with the primary deformation axis. The latter were more difficult to spheroidize due to the requirement for operating <c+a> slip systems. Based on this analysis, the authors suggested that strain-path changes would result in a more uniform structure since different slip systems would be preferred under each increment of imposed deformation.

Based on this understanding and building on the work of Salishchev et al. (1993), Zherebtsov et al. (2004) devised a multi-axial 'ABC' forging process to produce ultrafine grain (UFG) Ti-6Al-4V billet. Initially, small isothermal hot compression cylinders were analyzed to establish the effect of initial microstructure and temperature range required to produce the UFG material. The forging schedule consisted of three increments of strain imposed in three orthogonal directions (i.e., 'ABC'). These trials indicated that the UFG structure could be obtained by beginning with material in the basketweave or fully globular condition, but not with bi-modal microstructures. The initial work further indicated that the material should be warm-worked at a temperature not exceeding 700 $^{\circ}$C and a strain-rate of 10^{-3}/s. Furthermore, because of the sharp increase required for the onset of spheroidization at low temperature, it was recommended that cumulative strains should exceed 3.0 within the *entire volume* of material. Using these guidelines, the authors successfully scaled the laboratory process up to produce a 150 mm diameter x 200 mm long billet of Ti-6Al-4V with a primary alpha grain size of less than 0.5 µm with a high fraction of high angle boundaries (~75%). Later, Gigliotti et al. (2000) showed EBSD data from UFG Ti-6242 billet material which confirms the absence of MTRs (Figure 66). In this image, the orientations are colored according to where the facet normal of an icosahedra intersects the unit sphere and the legend is in the upper right.
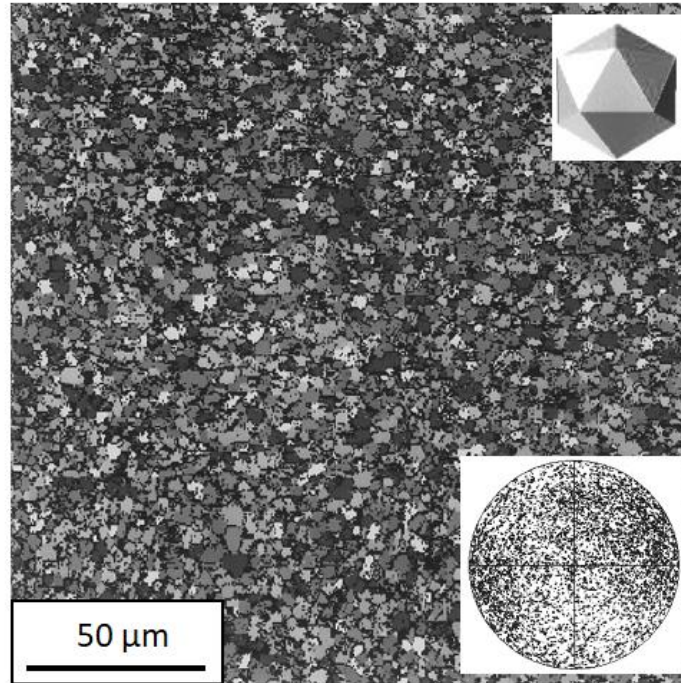
Figure 66. EBSD data presented in a greyscale icosahedral color map of UFG billet

While the scientific approach has been developed, there are a few challenges in implementing it for widespread production – all of which are related to increased cost. First, the low working temperature results in increases wear on hydraulic forging presses and dies resulting in increased maintenance. Second, the need for isothermal working conditions limits the availability of forging presses. Additionally, the increased time on die decreases throughput and increases cost and lead times. Finally, the scale-up work was demonstrated on 150 mm diameter billet, but many aeroengine disks are forged from larger diameter billet which requires higher load capacity.

Gorman and Woodfield (USA Patent No. 6,332,935 B1, 2001) have devised a process to reduce the noise in ultrasonic inspection of titanium billet, which arises primarily from the presence of microtexture (Gigliotti, Bewlay, Deaton, Gilmore, & Salishchev, 2000; Pilchak, Li, & Rokhlin, 2014a). The process involves four hot working steps. In the first, the material is beta forged about 30 °C above the beta transus followed by water quenching or another rapid cooling strategy. The second step consists of alpha+beta working at a temperature most preferably about 30° C below the beta transus where the cross-sectional area is reduced by at least 20%. The third step involves heating the material preferably to ~30 to 80° C above the beta transus again and reducing the cross section again by at least 20% followed by water quenching. If the product form requires an initially alpha+beta worked billet structure, an optional fourth step is used to

further work the material in the two-phase field again, preferably about 30°C below the transus and to a reduction of about 15%, but potentially as high as 40%. The resultant structure produces significantly lower noise during ultrasonic inspection, which is indicative of reduced MTR size and intensity.

6.1.10 Type of press work

Two types of presses are commonly used to convert titanium ingot to billet, namely, hydraulic two-die open-die forging presses and rotary forge presses. Some billets are converted entirely on open die presses while others may go through initial breakdown on open dies and subsequently be reduced in diameter via a general forging machine (GFM – sometimes called a gyrational forging machine, both of which are English recreations for an originally German acronym for Gesellschaft für Fertigungstechnik und Maschinenbau, which was the name of the company which Austrian engineer Bruno Kralowetz founded). The GFM utilizes a four-die open-die configuration. The four dies can move independently and there is a manipulator to advance the billet axially through the GFM while simultaneously rotating it between bites. There is a key difference in the strain path between two- and four-die systems. In particular, the two-die configuration imposes strain in only one direction which permits lateral spreading of the billet transverse to the forging direction but requires redundant working to achieve a reduced diameter with round-cornered square or octagonal cross section. In contrast, the GFM has two sets of opposing rams which constrains the material making it easier to create a uniform reduced cross section, but precludes the need for redundant working, which is known to contribute to the break-up of MTRs as discussed in Section 6.1.9. In addition, as a result of the limited lateral flow of the material, the GFM does not drive work into the interior of the billet as effectively as conventional two-die hydraulic presses (Figure 67). In addition, care must be taken to control process parameters in the GFM to avoid introducing extensive axial variation in the billet. Venkatesh and Wilson (2007) have shown qualitative strain profiles for billets converted using radial forging methods using both large and small drafts (Figure 68). The former produced larger axial variations in strain and surface undulations due to material flowing around the dies while the latter showed more uniform axial strain profiles.
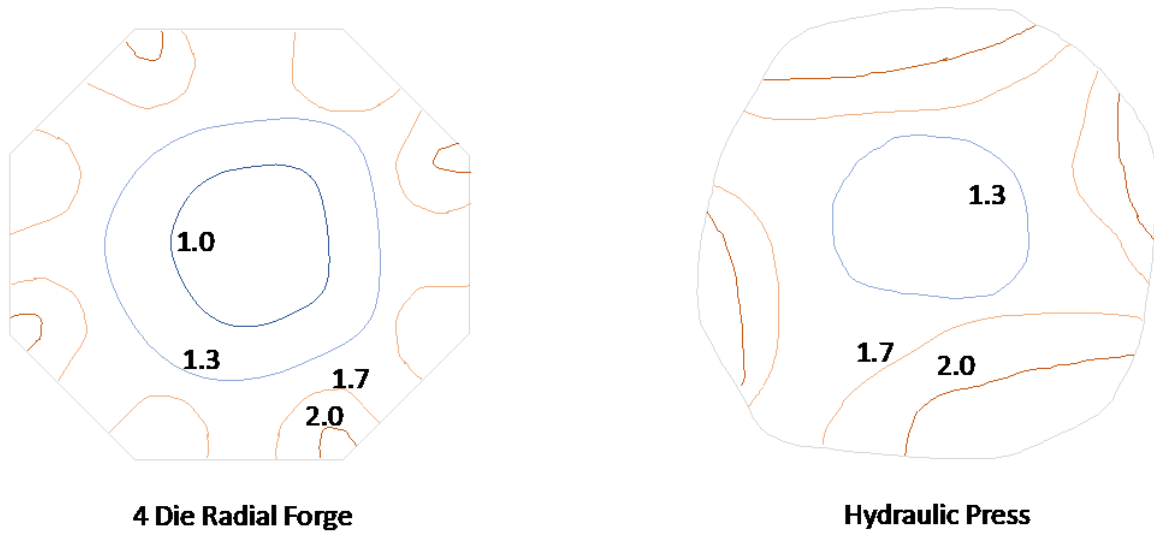
Figure 67. Transverse cross sections following final alpha+beta hot working of Ti-6Al-4V billet
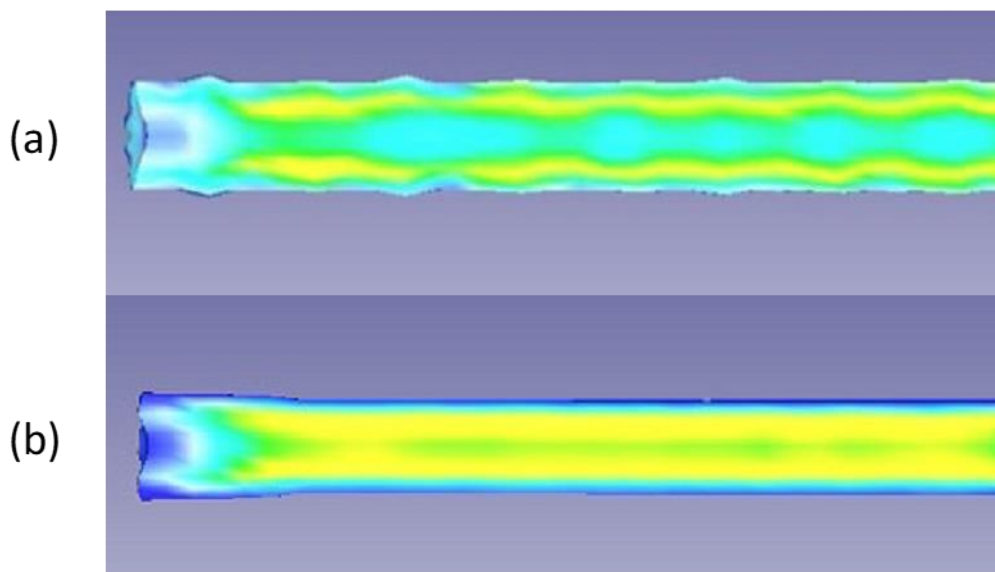
Figure 68. Axial strain profiles (blue=low; yellow=high) for Ti-6Al-4V billet converted via radial forging with (a) large drafts and (b) small drafts

6.1.11 Billet end effects

The local strain profiles at the extremities of billets result in lower work being imparted in these locations. In addition, the larger surface area at these locations results in enhanced heat loss through radiation. Both aspects decrease the driving force for the key microstructural evolution processes that control dynamic spheroidization during billet conversion.

Antolovich & Evans (2000) have also performed finite element modeling of the cogging process using 3D finite element modeling. While their work focused on nickel-base superalloys, similar processes are used in the production of titanium billets. For example, the conversion steps involve the selection of bites, drafts, and rotations. For the cases of open die forging and rotary forging (also called radial forging or GFM) the simulation results showed a 'dead zone' near the extremity of the billet which had lower volumetric strain compared to the near steady-state region of the billet, which is indirectly acknowledged when Antolovich & Evans (2000) cite the presence of 'end effects' in the billets. As a result, care should be taken to crop the ends of billets, and the selection of the crop length/weight should be based on careful process simulation and metallographic evaluation. The strain profiles from the work of Venkatesh & Wilson (2007) (Figure 68) also illustrate the significant end effects encountered in titanium billet conversion.

There is an additional complexity with titanium alloys in that the prior processing history greatly influences subsequent microstructure evolution. Depending on where the billet originates relative to the initial cast ingot, the location-specific macrostructure of the ingot will be oriented differently relative to the subsequent deformation imposed. A macro-etched cross section of the lower portion of a vacuum arc remelted ingot of Ti-6Al-4V is shown in Figure 59 (Glavicic, Kobryn, Spadafora, & Semiatin, 2003). From this figure, it is clear that the initial orientation of the prior beta grains in the original cast ingot varies spatially. As a result, the deformation and recrystallization behavior will vary as well, and hence particular attention should be paid to the bottom of the bottom billet of each ingot.

6.1.12 Degree of microtexture in billet used to manufacture parts

The degree of microtexture in billets used to manufacture parts varies considerably and depends on numerous factors including, but not limited to (1) the alloy composition, (2) the diameter of the billet, (3) the conversion route, including the type of press work, used by the supplier, and (4) the location where the MTRs are observed in the billet (axially, radially, and circumferentially). In addition, the degree of microtexture in billets of the same diameter produced by the same fixed conversion practice may also vary due to stochastic processes in microstructure evolution (beta grain growth, variant selection during cooling, neighborhood effects on MTR breakdown, etc.). The alloy composition is influential on MTRs for several reasons. First, from the perspective of alloy class, the more heavily beta-stabilized alloys tend to have less microtexture than the leaner alloys. This is because the heavier beta-stabilizing elements have slower diffusion rates that generally retard microstructure evolution processes and lower the allotropic (beta $\rightarrow$ alpha+beta) transformation temperature so that the secondary alpha phase tends to be finer in length scale and form with a larger number of variants per prior beta grain. In addition, in-

specification variations in composition can also influence the beta-transus. Since conversion sequences generally use fixed furnace temperatures, this can lead to working temperatures that vary relative to the beta transus. In heats with increased interstitial content (O, N, and C) that push the beta-transus to higher temperatures, this results in a greater delta from the beta-transus and increased volume fractions of primary alpha at the working temperature.

In general, the extent of microtexture decreases with billet diameter as a consequence of the increased level of strain imposed during conversion, however, titanium alloys have a strong thermomechanical history dependence and thus the MTRs present in the billet depend on all prior steps (i.e., the conversion sequence). The location-dependence of MTR characteristics results from the radial, axial, and circumferential variations in strain during conversion (see Section 6.1.10 and Figure 67 and Figure 68).

Several authors have reported on the texture/microtexture in titanium billet material, but these studies have been focused on 250-mm (10") diameter billet and smaller. Pilchak et al. (2013) documented radial variations in microtexture in 57-mm (2.25") and 152-mm (6") diameter bar and 210-mm diameter billet (8.25") of the near-alpha Ti-6242 alloy. The authors used backscattered electron imaging and EBSD analysis to analyze the volume fraction and size of primary alpha phase and crystallographic texture/microtexture, respectively, at the center, mid-radius, and outer diameter locations. The authors found that the primary alpha particle size decreased with billet/bar diameter from ~10 µm to ~7.5 µm to ~5 µm, though more significant radial variations were observed in the larger diameter product forms. The volume fraction of primary alpha also varied with location, but generally increased and became more homogeneous with decreasing diameter. The primary alpha aspect ratio, on the other hand, was greatest in the 57-mm bar and was highest at the outer diameter location (~3.5:1) and trended toward more equiaxed (~1.5:1) at the centerline. The macrotexture was generally weak for all diameters but trended toward a $\{10\bar{1}0\}$ partial fiber texture with decreasing diameter – consistent with increased levels of strain imposed under an axisymmetric extrusion-like process Figure 69 (the billet/bar axis is vertical in this image).
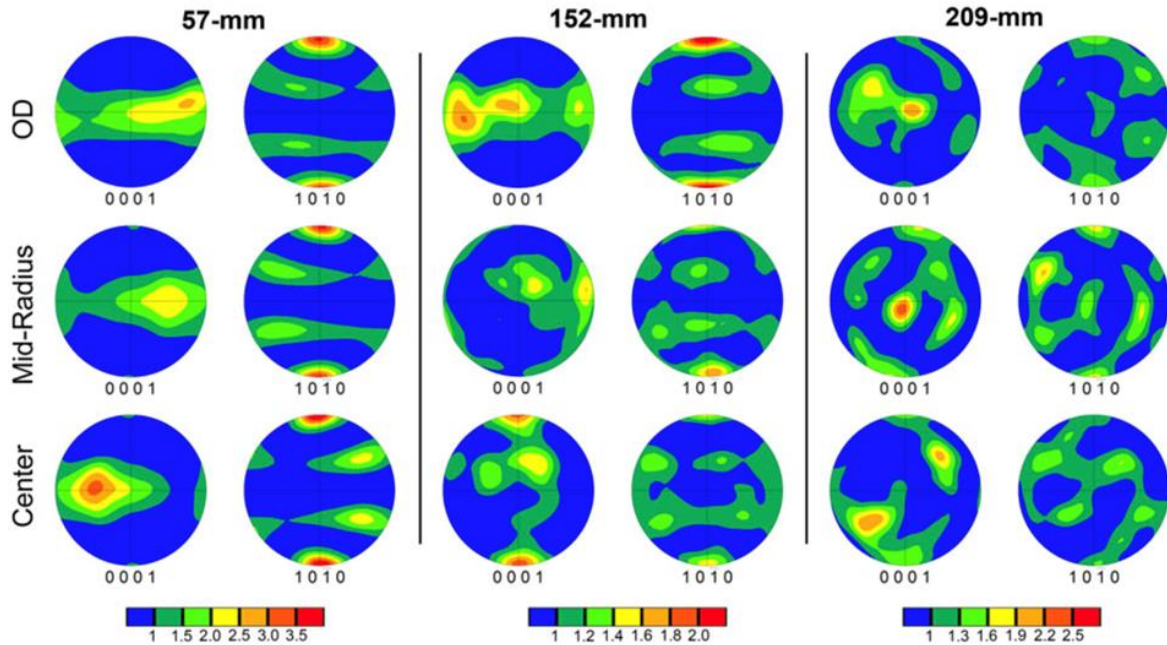
Figure 69. Macrotexture as a function of location in Ti-6242 bar/billet of various diameters

The microtexture in the material was characterized using two-point statistics and visualized in principal component space. In addition, one-point statistics were presented for the mean, median, max, and volume fraction of MTRs (Table 5). The results revealed a trend where the size and volume fraction of microtexture were reduced with increasing levels of reduction and became more homogeneous as a function of location within the billet/bar. The outer diameter position was a notable exception where similar MTR sizes were observed across all product sizes. For the 152-mm (6") and 209-mm (8.25") material, the mid-radius location had the largest MTR sizes. Representative EBSD scans (Figure 70) from the 209-mm (8.25") billet material show that the MTRs are relatively similar in the mid-radius and center locations, but that there is significant refinement near the other diameter. These maps reveal that there is a significant degree of elongation in the direction of the billet axis.

Table 5. One-point statistics quantifying MTR size in Ti-6242 billets and bar

Sample	Mean (Std. Dev) (μm)	Median (μm)	Max (μm)	MTR (V_f)
57-OD	94 (38)	87	162	0.10
57-Mid-Radius	82 (17)	84	120	0.16
57-Center	77 (20)	75	115	0.13
152-OD	71 (20)	72	135	0.10
152-Mid-Radius	264 (83)	260	496	0.20
152-Center	239 (84)	216	393	0.24
209-OD	184 (65)	174	537	0.36
209-Mid-Radius	821 (196)	840	1314	0.61
209-Center	377 (112)	351	672	0.49
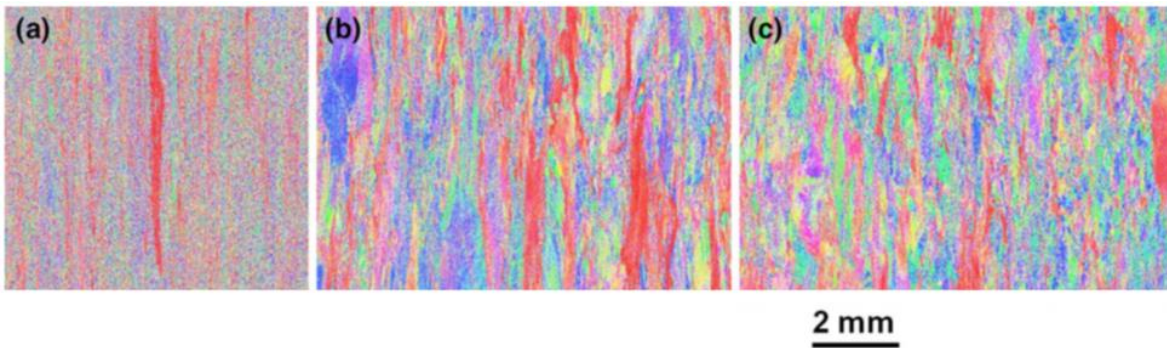
Figure 70. Inverse pole figure maps for longitudinal (vertical) / radial (horizontal) plane in Ti-6242 billet
(a) outer diameter, (b) mid-radius, (c) center location of a 209-mm (8.25")

Wynne et al. (2008) and Davies et al. (2018) used optical microscopy, neutron diffraction, and EBSD to investigate variations in texture/microtexture in a 250-mm diameter IMI-834 billet. The work was very comprehensive and interrogated many locations throughout the cross section (Figure 71 and Figure 72). Similar to the work of Pilchak et al. (2013), the authors found generally weak textures with maximum intensities of ~2-3x random. The authors noted that there were MTRs present at all locations and were either [0001] or $<10\bar{1}0>$ partial fiber textures with the fiber axis parallel to the billet axis. The latter type, of course, has [0001] perpendicular to the billet axis. Some MTRs with $<11\bar{2}0>$ parallel to the billet axis were also observed. The relative fraction of each texture component varied with location. The $<10\bar{1}0>$ fiber was strongest at the center of the billet and decreased in intensity with increasing radial position. The [0001] fiber displayed the opposite trend being strongest near the outer diameter and weakest near the center. The basal-axial MTRs tended to be the largest in size while the $<10\bar{1}0>$-axial MTRs were smaller, but generally had a tighter distribution of orientations.

119
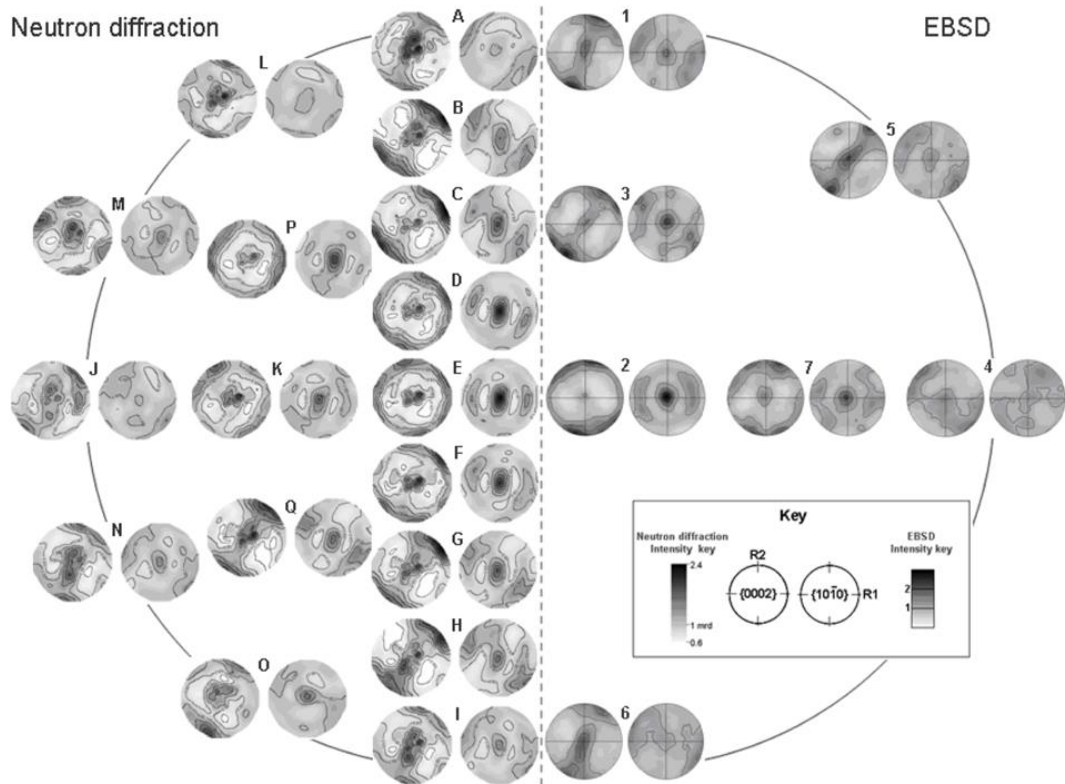
Figure 71. Distribution of crystallographic texture in 250-mm diameter IMI-834 billet
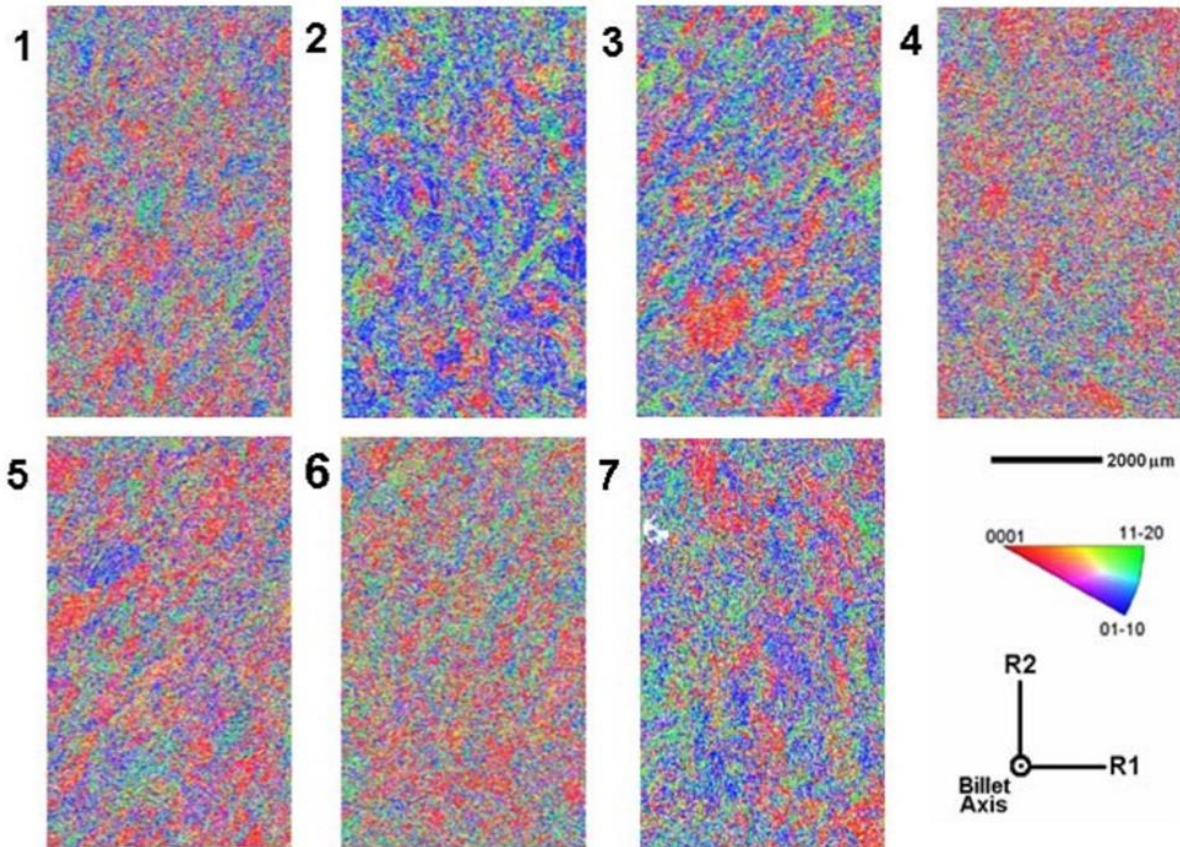
Figure 72. Inverse pole figure maps from a transverse cross section of 250-mm diameter IMI-834 billet

The numbers represent the location of scans in the billet cross section as shown in Figure 71

6.1.13 Pores in billet material

Pores are an undesirable feature of titanium alloy microstructures. Improvements in melt technology have largely eliminated pores, but nevertheless, they can persist into finished products and have sometimes been implicated in field (see Section 8.1.1), rig (see Section 8.2.1), and specimen failures. These so-called micropores are several micrometers in size and distinct from the large pores formed due to pipe shrinkage near the top of ingots. There are several opportunities for microporosity formation in billet material including ingot solidification (Eylon & Hall, 1977), the alpha+beta prestrain operation, and during the alpha+beta finishing operation. Eylon and Hall (1977) noted that ingot porosity may be gas filled, the internal pressure of which makes it difficult to seal them during thermomechanical processing without the application of very large strains.

The location of a pore relative to the microstructural features may provide insight into when it is formed during processing. In colony microstructures, voids have been observed to form at colony boundaries where c-axes are highly misoriented (e.g., 90° from one another) or at the

121

interface between a colony and a prior beta grain boundary (Bieler, Nicolaou, & Semiatin, 2005; Nicolaou & Semiatin, 2007). The colonies essentially act as hard/soft regions at the processing temperature and strain incompatibility at these locations can lead to void formation. During the alpha+beta processing of an already spheroidized microstructure, voids are observed to form primarily at alpha/beta interfaces, especially along the centerline of the billet which may experience less work and which may develop tensile stress components during hot working, especially with GFM processing. The following is speculation based on known mechanisms of pore formation during ingot solidification as well as in colony microstructures and subsequent microstructure evolution processes during alpha+beta hot working and reheating. Future work is needed to better understand pore formation and closure mechanisms as well as the role of chemistry on these effects. However, it is known that increased levels of alpha+beta work tends to reduce porosity (see Section 8.1.1). If a pore is observed in a part, the following factors may help identify its source, but significantly more work is needed to demonstrate this clearly.

- Residual ingot microporosity

   This type of pore will be subjected to five thermomechanical processing steps outlined in Sections 6.1.2 – 6.1.6. If a pore survives the beta recrystallization step, its small size makes it statistically unlikely that it will be associated with a prior beta grain boundary or a colony boundary since these features are considerably larger than the pore itself. During subsequent alpha+beta working the colonies will be converted to MTRs and the pore will likely be found internal to the MTR, well away from the boundary with neighboring MTRs. These pores may be elongated in the principal direction of deformation. Ingot microporosity may contain entrapped gas.

- Microporosity formed during alpha+beta prestrain

   These pores are most likely to form at alpha colony boundaries. As was the case with remnant ingot porosity discussed above, beta recrystallization and alpha colony formation during cooling from the beta phase field produces a situation where these pores will likely not be associated with MTR boundaries. Further, these pores may also be elongated in the primary working direction making them difficult to distinguish from residual ingot microporosity.

- Microporosity formed during final alpha+beta working

   Pores that form late in the conversion process during final alpha+beta working are likely to be found at or near the boundaries of highly incompatible MTRs (i.e., with highly

misaligned c-axes where one of the MTRs has a c-axis in a hard orientation). These pores may also be elongated in the principal working direction.

- Residual gas filled pores formed during ingot solidification

    These pores are present during the beta recrystallization step and thus are not expected to be associated with MTR boundaries present in the finished forging. However, the internal pressure of gas-filled pores makes them resistant to closure as well as shape change during thermomechanical processing and thus gas-filled pores may remain nearly spherical in billets and finished forgings.

A methodology for identifying safe and unsafe forging process regimes with respect to strain induced porosity during alpha+beta prestrain or final alpha+beta forging based on finite element analysis and a ductile fracture criterion was and validated for Ti-6Al-4V titanium, Ti-17 (Ti-5Al-2Sn-2Zr-4Mo) and Ti-10V-2Fe-3Al alloys under industrial process relevant conditions (Venkatesh & Fox, 2001b; 2001a). The methodology used to generate critical damage maps for crack prediction utilized the classic Cockcroft- Latham fracture criterion that is related to both maximum normal tensile stress and plastic strain. To begin, FEA simulations of hot tensile tests were conducted to compute critical damage values at the start of necking, usually associated with the initiation of cracking. Critical damage values, above which cracking or porosity is likely to occur, were determined as a function of strain rate, temperature, and microstructure and were used together with billet cogging models, to minimize the cracking potential during forging. Validation of the damage maps was successfully completed through a combination of tensile and compression tests; pancake forgings and FEA simulations determine the critical damage values. This method of generating critical damage maps via FEA simulations successfully demonstrated the potential for predicting cracking during various forging processes.

6.1.14 Ultrasonic inspection of billet products

As a matter of practice (Pardee, 1998), and in the interest of safety, premium quality titanium is inspected at the billet stage and again following forging where the part is machined into the so-called sonic shape, which facilitates ultrasonic inspection. The greatest sensitivity is achieved for forgings because of the smaller section thicknesses compared to billet materials, which often measure between 203 mm and 356 mm in diameter. Historically, the primary objective of these inspections was to identify the presence of any high-density inclusions or high interstitial inclusions (e.g., hard alpha or Type I inclusions), which are known to be detrimental to fatigue performance (Shamblen, Woodfield, Wayte, & Dibert, 2003; Woodfield & Lemaitre, 2020;

Woodfield & Shamblen, 2007) . These inspections are not capable of detecting the microporosity discussed in Section 6.1.13.

Inspections must be performed using an approved production inspection system which may utilize phased array or multizone technologies. Phased array systems have a series of piezoelectric transducers that can independently transmit and receive ultrasound. The timing of the pulse emitted from each element is selected to allow steering and focusing of the beam to target specific locations and depths in each billet. Multizone inspection systems utilize multiple transducers each focused at a different depth to enhance detection capabilities. Each of these modern inspection systems can analyze long lengths of billet (typically 3 to 6 meters) in an automated fashion. For billet material, ultrasonic energy is incident from a radial direction and the billets are rotated through an angle of 360° about the billet axis to ensure complete coverage.

Inspection is typically done using 5 MHz or 10 MHz longitudinal and shear waves. Longitudinal waves are effective for analyzing through-thickness while shear waves are used to enhance near-surface detection. At these frequencies, the wavelength of longitudinal waves is approximately 600 µm and 300 µm, respectively. As noted in Figure 25, this is situated within the range of sizes for MTRs in the material. This results in significant ultrasonic backscattering noise during these inspections (Panetta, Margetan, Yalda, & Thompson, 1997a), which increases the minimum detection threshold and can also lead to false calls (Margetan, Gigliotti, Brashe, & Leach, 2002). The Engine Titanium Consortium, commissioned by the FAA, optimized the frequency, focus diameters, and bandwidth to improve the sensitivity of these inspections. When the MTRs are larger than the incident elastic wave, geometric scattering can result in significant distortion of the wavefront (Panetta, Margetan, Yalda, & Thompson, 1997a) or mode-conversion from shear-to-longitudinal, for example (Blackshire, Na, & Daugherty, 2019). The absence of MTRs significantly improves the signal-to-noise ratio during ultrasonic inspection. In fact, for inspection frequencies of 5, 10, and 20 MHz, Gigilotti et al. (2000) demonstrated a 7.5x, 9x, and 8x improvement, respectively, for UFG Ti-6242 billet compared to conventional billet material. Thus, while inspection strategies can be optimized to a certain extent, the overall key to improving inspectability is related to microtexture control through the means outlined throughout Section 6.

The prior discussion of the impact of microtexture on backscattered noise and resulting sensitivity variation is best addressed by using a Signal-to-Noise Ratio (SNR) acceptance criterion. Historic acceptance criteria were based on amplitude thresholds. To avoid false positives, the thresholds would be elevated to accommodate the higher noise levels which occur, and therefore this approach does not fully exploit the higher sensitivity possible for low noise

billets. By changing the threshold to call out all features which have an ultrasonic response significantly higher than the surrounding material, more subtle anomalies can be found. While this SNR approach may not improve sensitivity for high noise billets, the lower noise billets will be inspected to the best sensitivity that the microstructure permits.

6.2   Component forging and heat treatment

6.2.1 Introduction

The processing route for components is shown schematically in Figure 73. The conversion from ingot to billet was discussed in detail in 6.1 while the subsequent steps, except for finish machining, are discussed here. There are three primary thermomechanical processing routes used to create fracture critical rotating components. All three begin with billet material in the alpha+beta processed condition and include:

- alpha+beta forging followed by beta heat treating

- beta forging followed by alpha/beta heat treating

- alpha+beta forging followed by alpha+beta heat treating

Different forging and heat treat practices can lead to very different degrees of microtexture in the finished component.
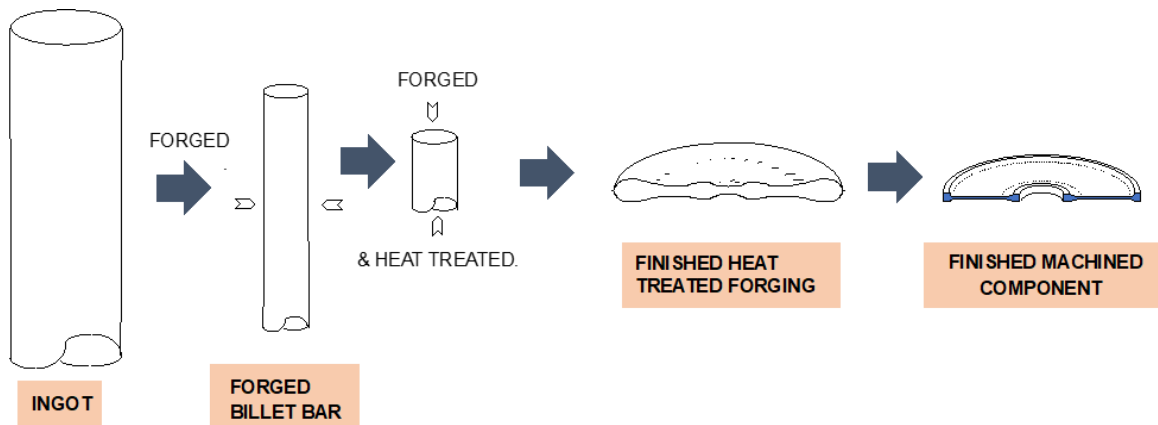
Figure 73. Schematic processing route for a rotating component

With respect to performance, Max et al. (2020) compared the properties of beta heat treated, beta forged, and alpha+beta forged Ti-6242 in the as-forged + heat treated and forged + heat treated + aged conditions. While the post-forge heat treatments were not described, the aging cycle consisted of 5,000 hours at 500 ºC (932 ºF). These conditions served as an instructive comparison of some properties for these three common processing routes. As shown in Figure 74

125

(Max et al., 2020), the bimodal condition has the highest strength and ductility in the forged/heat treated condition compared to beta heat treated and beta forged conditions. For both beta heat treated and beta forged conditions, additional aging resulted in a substantial decrease in ductility while the same was not true for the bimodal condition. Meanwhile, the tensile and ultimate strengths all increased with the low-temperature aging treatment, presumably due to the formation of α_2. The reduced ductility of the beta annealed and beta forged conditions is tolerable because of the increased damage tolerance capability of this heat treatment. Figure 75 shows the fracture toughness for these microstructures, which is much higher for the beta forged and beta annealed conditions compared to the bimodal. Crack growth rates (Figure 76) are also slower in the beta heat treated and beta forged conditions compared to bimodal (Max, Alexis, Larignon, & Perusin, 2020), which explains why this processing route may be chosen over alpha+beta processing for certain fracture-limited applications where high damage tolerance is required.
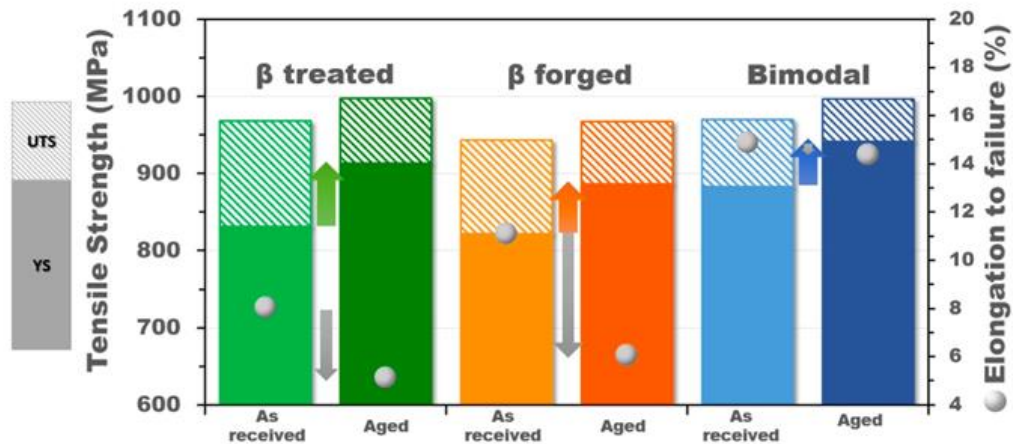
Figure 74. Effect of forging practice on the yield and ultimate strength and ductility of Ti-6242
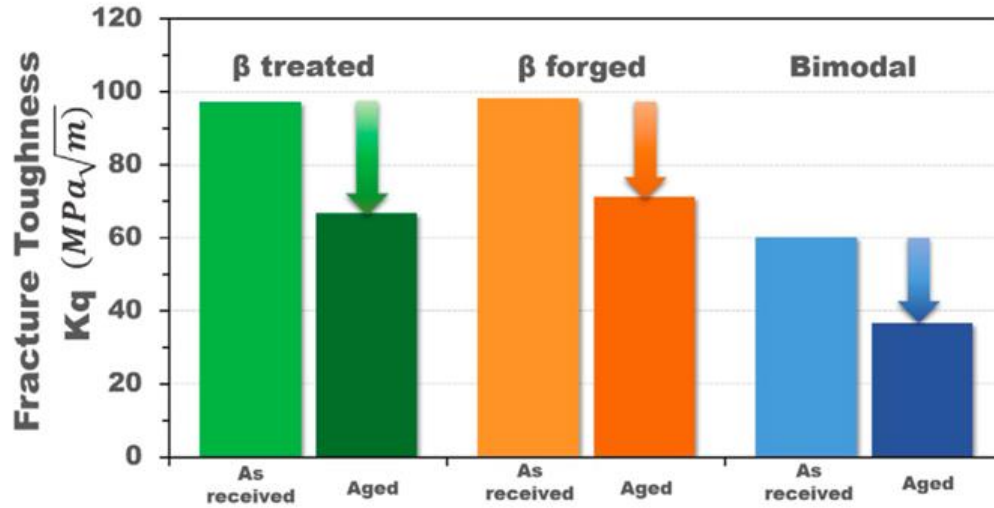
Figure 75. Effect of forging practice on fracture toughness of Ti-6242
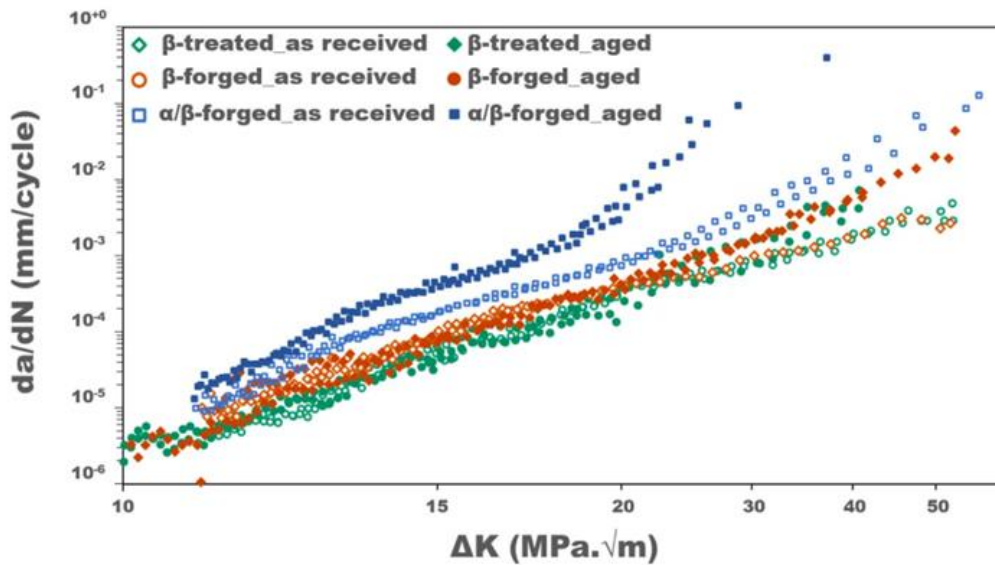
Figure 76. Effect of forging practice and aging on long fatigue crack growth rates of Ti-6242

6.2.2 Alpha+beta forging + alpha/beta heat treatment introduction

This route represents the process used to produce the largest portion of critical rotating parts. This condition has a good balance of strength, ductility, creep resistance, crack nucleation resistance, and crack growth resistance. This is a common process for alloys like Ti-6Al-4V, Ti-6242, Ti-834, Ti-829, and Ti-685. This route has a reasonably wide processing window to achieve the desired microstructure, however, it also has the strongest sensitivity to the state of

the MTRs in the billet used for the forging process. This is because the MTRs formed during the conversion process are carried into the forging, though the additional strain and thermal cycle alters the characteristics of the MTRs.

6.2.2.1 Forge strain, strain rate, and temperature

Gey et al. (2012) studied the effect of forging strain in different regions of a bimodal Ti-834 disk forging (Figure 77). They concluded that the texture in a 'dead zone' of the forging was essentially identical to that of the billet and the texture in a region which had undergone severe compressive plastic deformation exhibited no MTRs (macrozones). They also noted a dependence on strain path in the morphology of the macrozones with the most significant break-up of the macrozones occurring when the compression direction coincides with the previous elongation direction of the billet. This observation was also seen in work by Fernandez Silva et al. (2019) where double cone compression samples of Ti-834 were studied in terms of the effect of forging strain on microtextured region sizes (Figure 78 and Table 6). It was also seen that increased forging strain breaks up the high aspect ratio "ribbons" of MTRs typically seen at the billet stage. For the material investigated by the authors, significant breakup of MTRs was observed consistently beyond strains of ~2.1, but it should be noted that most disk forgings have a more complex geometry, and the strain-path is also known to be an important factor that influences the MTR condition after finishing forging.
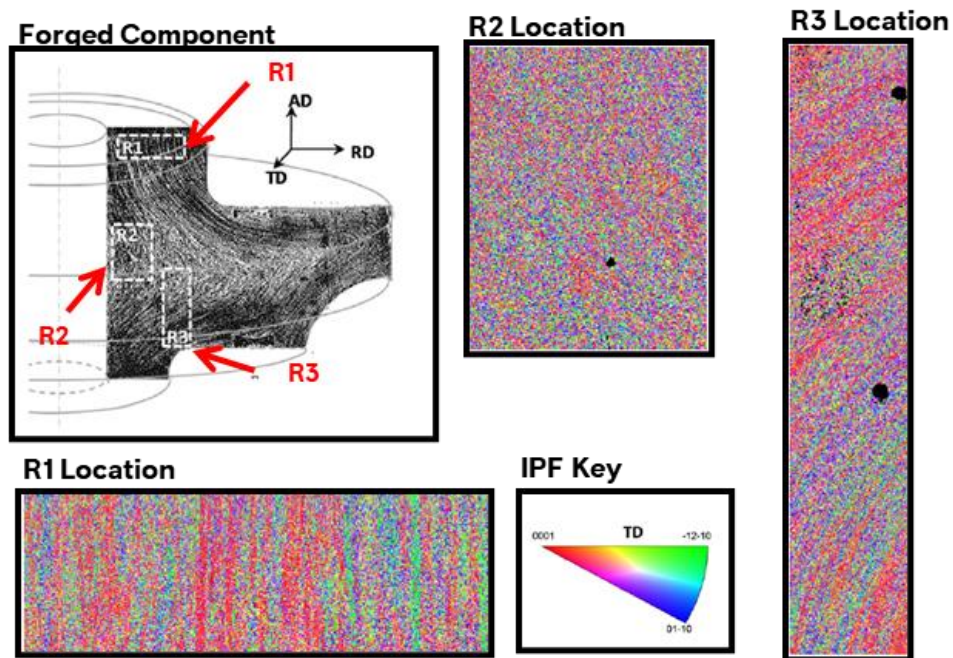
Figure 77. Effects of forging strain on MTR evolution in a closed die forging
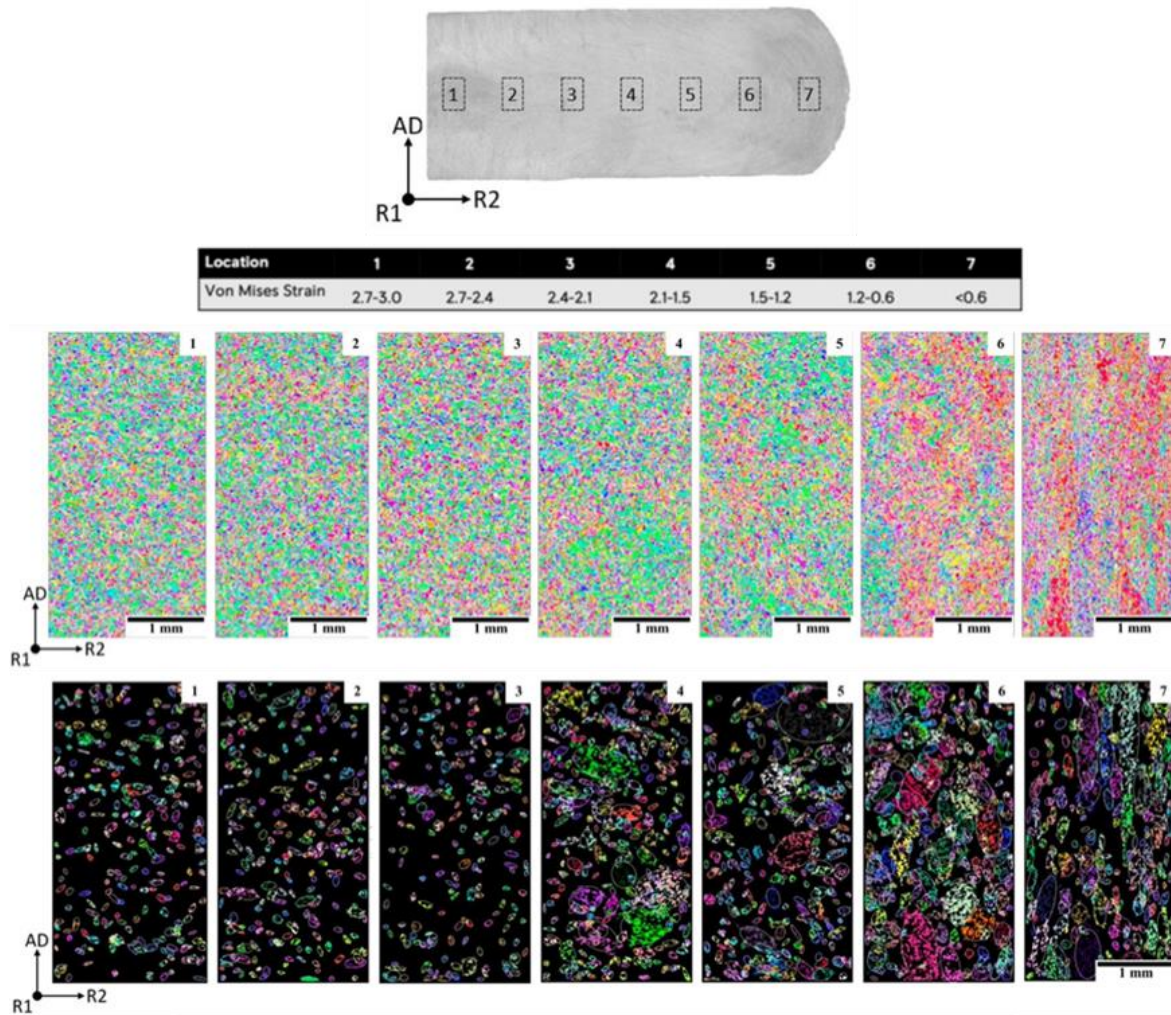
Figure 78. Effect of local strain on MTRs in Ti-834 forging

Table 6. MTR metrics on Ti-834 double cone compression samples

Location	1	2	3	4	5	6	7
Mean (μm)	77	79	78	109	112	143	135
Max (μm)	210	215	192	511	824	628	621
MTR Density %	11	11	9	21	19	31	24

While there have been no systematic studies on the effect of temperature on MTR evolution, the impact can be understood on the bases of crystal plasticity and phase transformations. At the simplest level, MTRs are groups of similarly oriented alpha phase, and therefore, both the primary and secondary alpha phases are important to their overall character. The details of the final microstructure are set during the heat treatment step (see Section 6.2) but forging represents an important intermediate step along the way. As titanium alloys do not undergo classical recrystallization processes during alpha+beta processing (i.e., formation and growth of high angle boundaries) the texture of each constituent phase at the end of this step has a strong influence on the final microstructure even though the material will still undergo solution heat treatment. During forging, the deformation textures of the primary alpha and beta phases will persist into the heat treatment step. This step will cause orientation changes due to crystallographic slip as well as rigid body rotations due to metal flow. This will result in changes in the primary alpha contribution to overall MTR density, orientation spread, size, shape, and intensity (see Section 3.1). The crystallographic rotations and recrystallization within the beta phase matrix in this step will establish the primary beta phase texture components that will persist into the finished forging, again, despite the fact that the material will still undergo a solution heat treatment. Thus, as noted in Figure 65 and the associated text in Section 6.1.7, the relative proportions of each phase during forging will have an impact on texture evolution. In general, working temperatures high in the alpha+beta phase field are desired to minimize the size of, and separate the similarly oriented primary alpha from one another, and also reduce the potential for shear band/deformation band formation in the alpha phase. This must be balanced with an understanding of the degree of deformation heating anticipated during forging so as to not locally exceed the beta transus in highly strained regions for an extended period of time which can result in the formation of a fully transformed (colony or basketweave) microstructure. Such anomalies are usually considered rejectable if observed during routine metallographic inspection of periodic cutups and may also give rise to rejectable ultrasonic indications as the large change in microstructural length scale can lead to strong ultrasonic backscatter reflections.

The effect of strain rate has also not been reported in great detail, but due to the strong rate sensitivity of titanium at hot-working temperatures, these two aspects are intimately related. Again, based on related published work and an understanding of deformation mechanisms and strain partitioning effects, we hypothesize regarding the role of strain rate on MTR evolution during hot working. The effect of strain rate on dynamic spheroidization of lamellar microstructures may give a first-order indicator of this effect on MTR evolution for typical billet material, which may contain a mixture of elongated and spheroidized alpha.

As shown in Figure 79 (Semiatin et al., 2000), temperature has a minor impact on the dynamically spheroidized fraction at slow working speeds while there is a significant effect at faster strain rates.
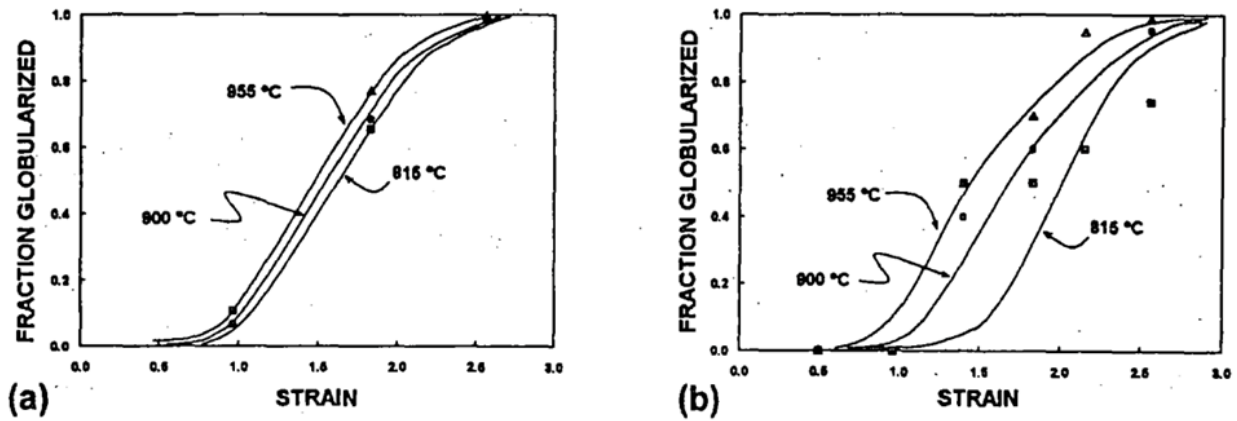
Figure 79. Kinetics of dynamic spheroidization in Ti-6Al-4V
With initial colony microstructure deformed in uniaxial compression at strain rates of (a) 0.001 s^{-1} and (b) 0.1 s^{-1}

Comparing the two strain rates, it is evident that faster strain rates tend to shift the curves to the right (i.e., more strain is required to achieve the same amount of spheroidization). This suggests that slower strain rates will result in more uniform deformation and randomization of MTRs. In contrast, higher working rates may tend to favor MTRs well oriented for easy slip thus requiring more strain for the same degree of crystallographic rotation.

Semiatin et al. (2002) have developed a self-consistent flow stress model to describe the flow behavior of wrought two-phase alloys under isothermal and nonisothermal hot-working conditions. The model considers the temperature-dependent and hence composition-dependent strength of the individual phases and predicts their contribution to overall flow stress. The model also predicts the average strain and strain rates in each constituent phase under the assumption that both phases have the same strain rate sensitivity exponent. The model predictions in Table 7 show the strain rates in each constituent phase ($\dot{\varepsilon}_i$) relative to the imposed average strain rate ($\dot{\varepsilon}_{ov}$) for various volume fractions of primary alpha (f_α). Across all temperature ranges, it is seen that the strain rates are lower in the alpha phase since it has a higher strength coefficient. The effect becomes more pronounced as the temperature approaches the beta transus. Glavicic et al. (2008) have used this model to partition strains obtained from FEM simulations to perform Taylor crystal plasticity calculations of alpha and beta phase texture evolution in Ti-6Al-4V pancakes and obtained reasonable agreement between the experimental and simulated texture components.

131

Table 7. Self-Consistent Model Predictions of the Strain Rates in the Alpha and Beta Phases of Ti-6Al-4V

Temperature (°C)	f_α	$\varepsilon_\alpha/\varepsilon_{ov}$	$\varepsilon_\beta/\varepsilon_{ov}$	$\varepsilon_\beta/\varepsilon_\alpha$
815	0.73	0.72	1.74	2.42
900	0.56	0.54	1.59	2.94
955	0.27	0.24	1.28	5.33

6.2.2.2 Flow localization

The strain, strain rate, and temperature of deformation has important consequences on the flow stress and microstructure evolution processes during forging. To a certain extent, the total strain is limited by the final part geometry because the primary purpose of the forging process is to produce the right shape from which the finished component can be machined. The choice of strain-rate and temperature have important consequences with respect to the uniformity of deformation and the potential for flow localization. The effect of strain on MTR evolution and breakup has been investigated and reported in the literature, but the role of temperature and strain rate have not been systematically investigated. Nevertheless, based on observations across various studies coupled with an understanding of the operative mechanisms and principles of physical metallurgy allow us to infer the effect of these variables on MTR evolution.

Figure 80. Extreme example of flow localization and shear band formation in Ti-6242 hot-worked at 850 °C (1562 °F)

Semiatin and Lahoti (1981; 1982) have analyzed flow localization in Ti-6242 across a range of microstructures (alpha+beta processed and beta-annealed), temperatures (816 °C to 954 °C or 1500 °F to 1750 °F), and strain-rates (10^{-3} s^{-1} to 10 s^{-1}) supplemented by finite element modeling. The authors investigated isothermal and nonisothermal conditions. The propensity for strain localization and shear band formation was found to depend primarily on the rate of flow

softening, which was a function of the aforementioned variables. An example of shear banding at the macro scales is shown in Figure 80 while Figure 81 shows a microscopic shear band. The authors proposed an instability criterion (flow localization parameter) which quantitatively predicted the onset of localization/shear banding. It was found that localization was promoted by lower temperatures (higher volume fraction of alpha) and higher strain rates for the alpha+beta processed microstructures. In contrast, shear bands were observed for essentially all temperatures and strain rates in the beta-annealed microstructures except for the slowest strain rate and highest temperature. The onset of strain localization occurred at true strains between 0.33 and 0.54. With respect to MTRs, flow localization events are found to occur readily within coarse colony microstructures. The strain within the band is high, which results in significant grain refinement and randomization of the local texture within the shear band. However, the surrounding colony does not get heavily deformed and shows evidence of bent/kinked lamellae with only small internal misorientations (Bieler & Semiatin, 2002).
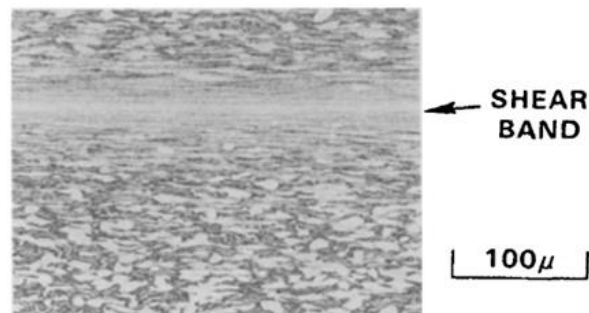
Figure 81. Micrograph of a shear band in Ti-6242 worked at 913 °C (1675 °F) at a local strain rate of ~ 30 s^{-1}

6.2.2.3 Orientation effects

Pilchak et al. (2016a; 2016b) published a data descriptor article (see (Ward, 2015)) for a definition of *data descriptor*) that investigated the effect of temperature and forging orientation on MTR evolution in Ti-6242. The authors characterized the microstructure and microtexture on three orthogonal faces at three locations in a 152-mm (6") diameter billet (center, mid-radius, and outer diameter). They further extracted cylinders for isothermal hot compression at 0°, 45°, and 90° relative to the billet axis. Hot compression tests were performed at 899 °C, 954 °C, and 982 °C at a constant true axial strain rate of 0.01 s^{-1} from which it was found that forging orientation had a relatively minor impact on the flow stress. The axial orientation had the highest flow stress compared to 45° and 90° for all temperatures, but the magnitude of the difference decreases with increasing temperature (Figure 82). At a temperature of 899 °C, the MTRs segmented using the DREAM.3D algorithm with noncontiguous grouping showed that MTR

sizes, as measured using the circle equivalent diameter method, was largest in the axial (0º) samples and smallest in the radial (90º) orientation. However, both off-axial forging directions resulted in high aspect ratio MTRs (~4:1) whereas the axial orientation was ~2:1. While the authors did not report it in the paper, the EBSD datasets published with the article would enable other researchers to explore other critical MTR parameters defined in Section 3.1.
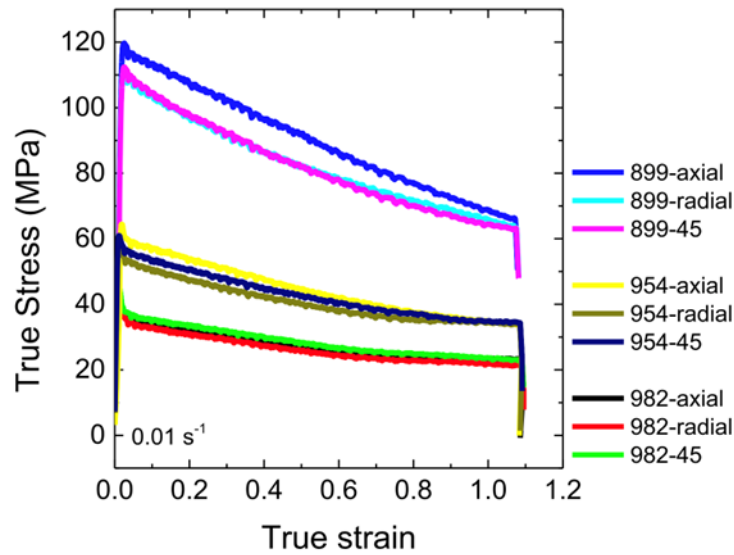
Figure 82. Effect of forging temperature and orientation relative to billet axis on flow stress of Ti-6242

Using the results from the data descriptor article of Pilchak et al. (2016a), Ma (2018) and Ma et al. (2018) used the crystal plasticity finite element method to investigate the role of MTR crystallography and morphological orientation on the breakdown of MTRs. Figure 83 shows a compilation of results from Ma (2018). Idealized MTR orientations relative to the compression direction are shown in Figure 83(a), Figure 83(b), and Figure 83(c), which correspond, respectively, to the equivalent plastic strain distributions shown in Figure 83(d), Figure 83(e), and Figure 83(f) following isothermal hot compression to a strain of 0.51 at 899 ºC (cross-section view on the mid-plane). Traces of the equivalent plastic strain are shown in Figure 83(g) while probability density functions representing the misorientation from the initial MTR orientation are shown for Figure 83(h) region 1 and (i) region 2. The simulations included three cases depicted in Figure 83(a-c). The authors investigated the distribution of plastic strains (Figure 83(d-h)), the extent of lattice rotation, and the development of internal misorientations as indicators for the effectiveness of MTR breakdown. Not unexpectedly, the first case where the c-axes were both perpendicular to the stress axis exhibited the most efficient breakdown due to the ease and multiplicity of prismatic <a> slip, which causes lattice rotations about the c-axis leading

134

to a wide distribution of orientations relative to the original orientation. However, in this case, the c-axes of regions 1 and 2 did not rotate significantly relative to the stress axis. For the second case (Figure 83(b)), simulations showed that the c-axes oriented at 45° to the stress axis rotated during compression, but that all particles co-rotated such that they stayed relatively aligned with one another. The third case (Figure 83(c)) was the first which had a c-axis parallel to the compression axis in a classic hard orientation. The spread in c-axes was greatest for the cases studied but was still limited by the high CRSS of the pyramidal slip systems. An important development of this work was the ability to perform large-strain simulations.
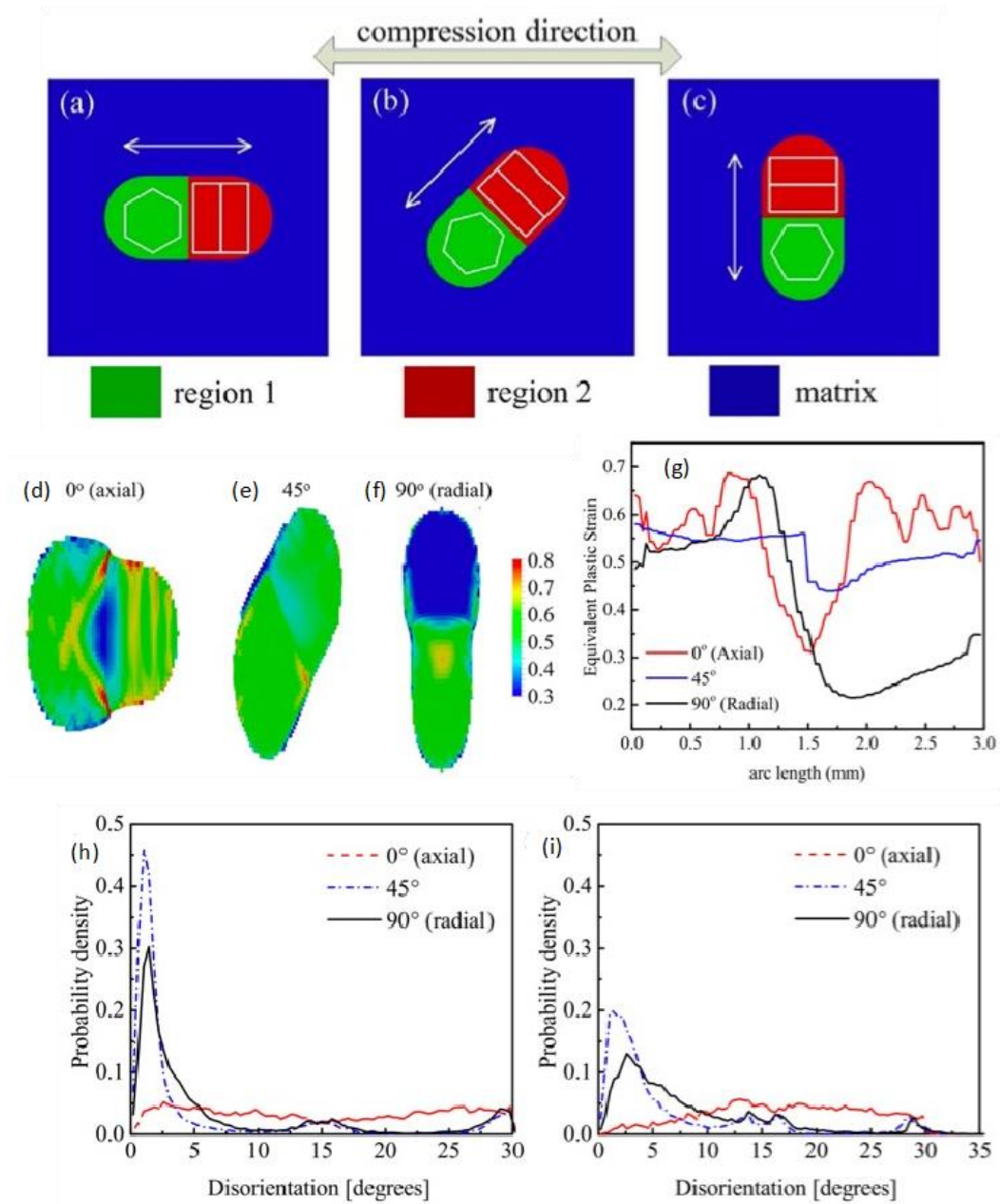
Figure 83. Effect of forging orientation on strain and misorientation distributions in MTRs

6.2.2.4 Number of reheats

While many forging operations can be completed in a single push, there are some components which require multiple operations to produce the desired shape. As a result, these components need to be reheated in between forging blows to ensure the flow stress is reasonable. Various restoration and microstructure evolution processes may be active including recovery, spheroidization, grain growth, and coarsening during the reheating operations. While recovery

and spheroidization are desirable, the time at temperature in the furnace should be carefully considered when designing forging operations in order to avoid excessive particle coarsening.

Semiatin et al. (2004) have analyzed the coarsening kinetics of Ti-6Al-4V subjected to heat treatments at various temperatures (843 $^\circ$C, 900 $^\circ$C, 955 $^\circ$C, and 982 $^\circ$C) for times ranging from 0.25 hours to 144 hours. The average coarsening kinetics were found to follow cubic kinetics with time, i.e. $r^3 - r_0^3$ vs $t - t_0$ where r is the t is time and the subscript 0 denotes initial particle radius and time. The authors analyzed the results using Lifshitz–Slyozov–Wagner (LSW) coarsening theory modified to consider the effect of volume fraction and the fact that the phases are not terminal solid solutions. They further compared the results to prior models and found that those which take into account the interactions of particles with one another (i.e., source and sink effects) provided the best description of the data.

6.2.2.5 Solution temperature, time, and cooling rate

The key microstructural features formed in the final heat treatment for alpha+beta processed alloys include the primary alpha particle size and volume fraction and the morphology and lath thickness of secondary alpha. The final heat treatment will also determine whether or not the ordering reaction that forms alpha2 (Ti$_3$Al) precipitates will occur. Tensile, fatigue, and dwell fatigue behavior are all impacted by these variables and hence they should be controlled during the production of critical components. Based on our understanding of the mechanisms that lead to poor dwell fatigue capability, we contend that the final heat treatment for alpha+beta processed alloys should be at a temperature sufficiently high in the two-phase field that the volume fraction of primary alpha particles is low so that most/all of the similarly oriented alpha particles are insulated from one another by transformed beta phase. This temperature should be no lower than the forging temperature and the time should be long enough to ensure that spheroidization completes and the primary alpha aspect ratio is reduced to below ~2:1.

Woodfield et al. (1996; 1999) cited primary alpha size and volume fraction as important factors in their regression model for dwell fatigue capability of Ti-6242 but did not report specific details regarding the magnitude of the effect at the time. Later, Kassner et al. (1999) investigated the effect of primary alpha volume fraction in the range from 5% to 60% on dwell fatigue performance of Ti-6242. From a limited number of samples for each condition tested at the same stress level, and thus different fractions of their yield and ultimate strengths, the authors observed that the longest lifetimes for the lowest volume fraction (highest solution heat treat temperature) despite it having the lowest yield stress. Fractography revealed that 9 out of 10 subsurface initiated cracks in these samples initiated in the transformed beta regions, presumably due to the longer slip lengths in the alpha colonies.

Gorman et al. (USA Patent No. 6,284,070 B1, 2001) describe an approach to heat treat two-phase titanium alloys to a microstructural condition that maximizes resistance to dwell fatigue which is applicable to near-alpha and alpha+beta alloys. The alloy is first heat treated at a temperature about 40 °C (~70 °F) below the beta transus targeting a volume fraction of primary alpha of ~30%, held for 30 minutes to 4 hours depending on the size of the component, and then rapidly quenched to room temperature at a rate greater than ~40 °C/min (~200 °F/min). The rapid quenching ensures that the nucleation is favored over growth and the transformed beta assumes a basketweave (Widmanstätten) microstructure. The multiple variants in the transformed beta inhibits transgranular facet growth thereby decreasing crack growth rate in the early stages of crack formation when it is most important.

Rapid cooling rates are known to increase strength; however, they also reduce ductility and toughness and promote residual stress. Consequently, the material is subjected to a second heat treatment to serve as a stress relief and to restore some ductility. This is done for the same amount of time as the solution heat treat (0.5 to 4 hours) at a temperature between 55 °C and 220 °C (100 °F and 400 °F) below the beta transus, generally favoring the high side of this range. This temperature causes slight coarsening of the transformed beta phase but does not result in further coarsening of the primary alpha. The kinetics of primary alpha coarsening were addressed in Section 6.2.2.4. Following this step, the material is cooled at a fast enough rate to avoid the formation of Ti_3Al, which can diminish strength, ductility, and fatigue performance.

The above strategy works well for the majority of components, but in pursuit of the microstructural weakest link, it is worth mentioning two factors at this stage, namely, beta microtexture and variant selection. In many MTRs, the beta phase orientations underlying adjacent packets of transformed beta have high angle grain boundaries due to deformation texture formation and recrystallization processes that occur during prior thermomechanical processing. In rare instances, however, there may be similar beta phase orientations (i.e., beta phase microtexture (Figure 25)), underneath each packet of transformed beta (Germain, Gey, Humbert, Bocher, & Jahazi, 2005). In certain MTRs, there may be {110} beta phase planes closely aligned with the (0001) alpha planes of the primary alpha grains, and Germain et al. (2005) have shown that this can lead to preferred variant selection of secondary alpha, especially when the angle between [0001] and the adjacent <110> is less than 5°, but also up to angles of 10°. An example of this phenomenon is shown in Figure 84. As discussed in Section 4.2, the critical grain pair observed at crack initiation sites consist of grains well oriented for basal slip adjacent to grains unsuitably oriented for easy slip on any <a>-type slip system. If this line of thinking is extended to a presumed underlying BCC orientation, a grain with <110> aligned / nearly aligned with the stress axis would be consistent with both criteria. Of course, the basal

planes that transform onto the {110} perpendicular to the stress axis would constitute hard grains while the other (0001) transformed onto four of the other five {110} would be well oriented for basal slip. If variant selection occurs in this way, the transformed beta can effectively "restore" the microtexture that was intended to be eliminated by the high alpha/beta solution heat treat temperature.
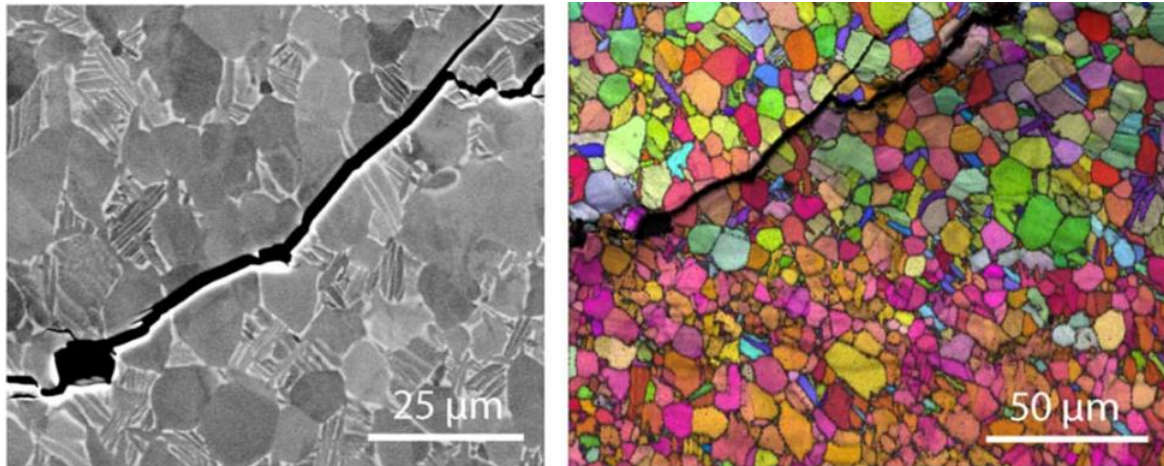
Figure 84. Example of closely aligned primary and secondary alpha orientations

Harr et al. (2021) have produced a schematic to illustrate the potential weak link microstructural configuration that considers the variant selection phenomena. There are a total of five deformation pathways illustrated in Figure 85. Long continuous (0001) traces that could contribute to dislocation pileups occur through regions of similarly oriented primary α. Long-range slip is inhibited by primary α of a different orientation, β phase, and basketweave microstructures. The first, connecting point A to A', is the critical arrangement that would allow development of a large slip band that creates a pileup of appreciable strength. It is bounded on both ends by obstacles to further dislocation motion (i.e., basketweave secondary α on top and a highly misoriented "hard grain" on the bottom). The large slip length is possible due to the similar orientation of the primary alpha grains as well as the spatial arrangement that aligns the basal slip traces of the interconnected alpha. The adjacent, similarly oriented colony alpha then provides an easy small crack propagation pathway following nucleation due to the variant selection phenomenon caused by the underlying similarly oriented beta phase. The details of the remaining deformation pathways are discussed in detail in (Harr, Pilchak, & Semiatin, 2021). Indeed, Evans (1998) showed the impact of this alignment on CDF behavior. Figure 86 shows the impact of dwell fatigue relative to cyclic fatigue for bar and disk material both with ~15% primary alpha in a matrix of transformed beta. The higher degree of work in the bar material was found to refine the prior beta grain structure while it remained more intact in the forged disk

material which set up a condition where long range alignment of primary and secondary alpha was possible.
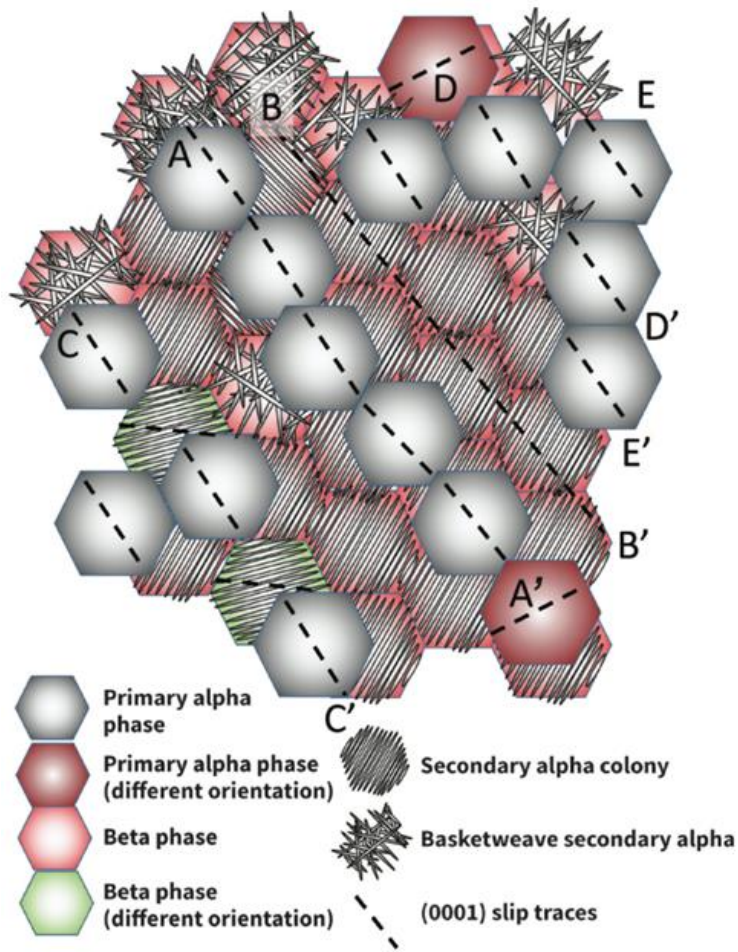
Figure 85. Schematic bimodal microstructure of an α/β titanium alloy with representative (0001) slip traces
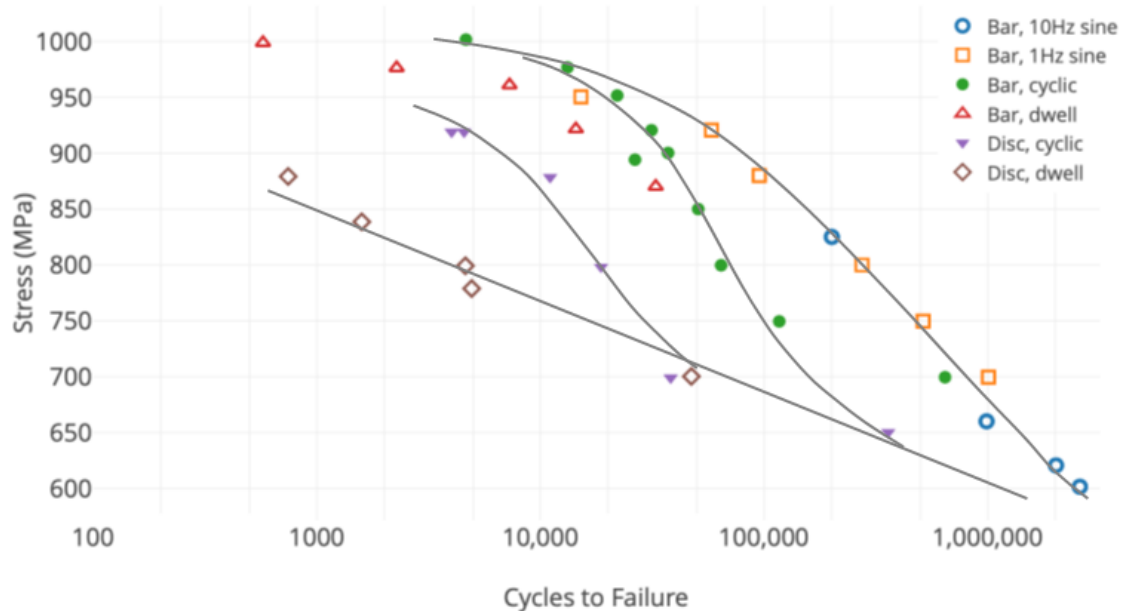
Figure 86. Comparison of dwell and cyclic response for bar and disk material in Ti-834

6.2.3 Alpha+beta forging + beta heat treatment introduction

Alpha+beta forging followed by beta heat treatment is used when designers want the best creep resistance, damage tolerance, and fatigue crack growth properties. These come at the expense of ductility and low cycle fatigue performance. The crack growth resistance is derived from the roughness induced closure effect by which asperities on adjacent halves of the fracture surface contact each other before the minimum stress is reached. This has a beneficial effect of shielding and reducing the effective stress intensity range on the crack tip. The roughness in colony microstructures is a direct result of crack tip deflection at colony boundaries leading to a tortuous crack path. The type of microtexture formed during this process are actually alpha colonies (aligned laths) which tend to form most readily off of prior beta grain boundaries during cooling from the beta heat treatment. These features are distinct from MTRs and hence we recommend not using the terms interchangeably. The component is taken into the single-phase field which dissolves all primary alpha present in the mill product and therefore, the state of the MTRs in the billet material is not considered an important factor. Instead, the cooling rate from beta heat treatment is the primary factor controlling the microstructural dimensions in the finished product. An additional factor to consider is the size of the prior beta grains. They generally represent the upper limiting dimension of the alpha colonies that can form aside from a special circumstance where two colonies on opposite sides of a prior beta grain boundary can share a common orientation.

141

6.2.3.1 Forge strain, strain rate, and temperature

There has been a very limited amount of work related to the effect of forging strain, strain rate, and temperature on the recrystallized prior beta grain size. A notable exception is the work of Postans and Jeal (1980).

They measured a periodic fluctuation in prior beta grain size following forging in the alpha+beta phase field at strain rates ranging from 10^{-3} s^{-1} to 10^{-1} s^{-1} (Figure 87). Based on observing similar effects on grain size during forging at the beta transus, they posit that recovery processes occur during forging at the two slower strain rates which prevents the storage of significant strain energy to drive recrystallization during subsequent beta annealing. In contrast, dynamic recrystallization occurs during forging at 10^{-2} s^{-1} leading to an initially fine prior beta grain size such that the grain size remains small following beta heat treatment. As strain rate is further increased, dynamic recrystallization occurs more readily resulting in the formation of new grains at deformed prior beta grain boundaries. Grain growth during subsequent beta heat treatment then involves a competition between nucleation of statically recrystallized grains and growth of the dynamically recrystallized grains. The fraction of dynamically recrystallized grains was greatest at the highest strain rate leading to the largest grain sizes for the range of strain rates over which this mechanism was active.
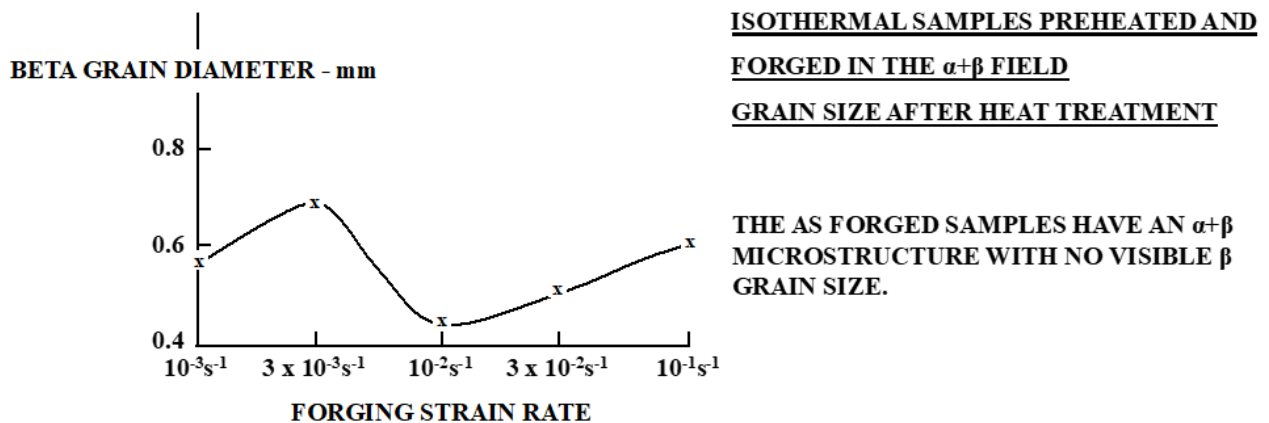
Figure 87. Effect of strain rate on prior beta grain size in Ti-829 following beta heat treatment

Postans and Jeal (1980) also forged multiple disks out of the Ti-829 alloy using hammer and screw presses. All forgings were given an initial beta upset followed by finishing at various temperatures in the alpha+beta phase field. The disks were then beta heat treated 1040 ºC – 1050 ºC, oil quenched, and then aged.

The following observations were made (Figure 88) (Postans & Jeal, 1980):

- **Disk 1:** Screw press forging first in the beta phase field resulted in dynamic recrystallization. Subsequent finishing at the highest temperature in the alpha+beta phase field resulted in deformation heating above the beta transus that promoted a uniform as-forged structure consisting of slightly elongated prior beta grains.

    o Recovery processes active during deformation prevented significant amounts of stored work which inhibited recrystallization during beta heat treatment.

- **Disk 2:** Screw press forging at an intermediate temperature in the alpha+beta phase field (following beta upset) resulted in larger variations in strain within the forging due to die chill and friction effects which resulted in the highest strain in the center of the forging.

    o During beta heat treatment, the highly strained center of the forging recrystallized readily and produced a fine beta grain size; in contrast, lower stored work at the outer areas of the forging resulted in fewer nuclei and the grains which formed early grew rapidly into the deformed structure resulting in a larger prior beta grain size.

- **Disk 3:** Screw press forging at an even lower temperature in the alpha+beta phase field (again, following a beta upset), despite reducing the extent of recovery and leading to more stored work, did not lead to further reductions in beta grain size following beta heat treatment.

- **Disk 4:** Hammer forging in the beta phase field as the temperature cooled below the beta transus resulted in insufficient work for recrystallization to occur; recovery during heating to forging temperature in the alpha+beta phase field resulted in recovery; work was concentrated near the center of the forging as observed previously.

    o Static recrystallization occurred during beta heat treatment, but resulted in a coarser beta grain size since this was the first recrystallization step and all prior disks had the benefit of dynamic recrystallization during beta upsetting.

DISC FORGING ROUTE	HEAT TREATED GRAIN SIZE IN THE DISC BORE AREA
DISC 1 UPSET WITH 2β PREHEATS. FORGED WITH HIGH α+β PREHEAT (WENT INTO β FIELD DUE TO KINETIC HEATING) SCREW PRESS FORGED AT DANIEL DONCASTER	β GRAIN DIAMETER, mm 1.0 0.5
DISC 2 UPSET WITH β PREHEAT FORGED WITH LOWER α+β PREHEAT SCREW PRESS FORGED AT DANIEL DONCASTER	β GRAIN DIAMETER, mm 1.0 0.5
DISC 3 UPSET WITH β PREHEAT FORGED WITH LOWEST α+β PREHEAT SCREW PRESS FORGED AT DANIEL DONCASTER	β GRAIN DIAMETER, mm 1.0 0.5
DISC 4 UPSET WITH β PREHEAT FORGED α+β PREHEAT HAMMER FORGED AT SMITH CLAYTON	1.0 β GRAIN DIAMETER, mm 0.5 DISC FRONT FACE 20 40 60 DISC REAR FACE DISTANCE - mm

Figure 88. Effect of forging practice on prior beta grain following beta annealing in Ti-829

6.2.3.2 Solution temperature, time, and post-solution cooling rate

Provided that sufficient strain is imparted to create a fine and uniform grain size, the microstructure of alpha+beta forged and beta heat treated components is primarily controlled by the details of the heat treatment. The solution temperature and time will control the prior beta grain size while the cooling rate governs the morphology of the alpha phase (i.e., colony or basketweave) and the thickness of the alpha laths. Ideally, the cooling rate should be as fast as possible to form a basketweave microstructure and avoid the formation of large alpha colonies. The cooling rate will be limited by section thickness and the cooling rates required to form the basketweave microstructure are a function of alloy content. With increasing beta stabilizer content, the beta transus is suppressed and the phase transformation occurs at lower temperatures

144

which limits the time and rate of diffusional growth of alpha phase. As a result, it is easier to form the basketweave structure across greater section thicknesses for these alloys compared to near-alpha alloys, for example. This effect is illustrated for the more heavily beta stabilized Ti-17 alloy by the work of Bruneseaux (2008) (Figure 89). For leaner alloys, faster cooling rates are required to achieve similar refinement. This is evident in the work of Lee (2004) who investigated the Ti-550 alloy (Figure 90).
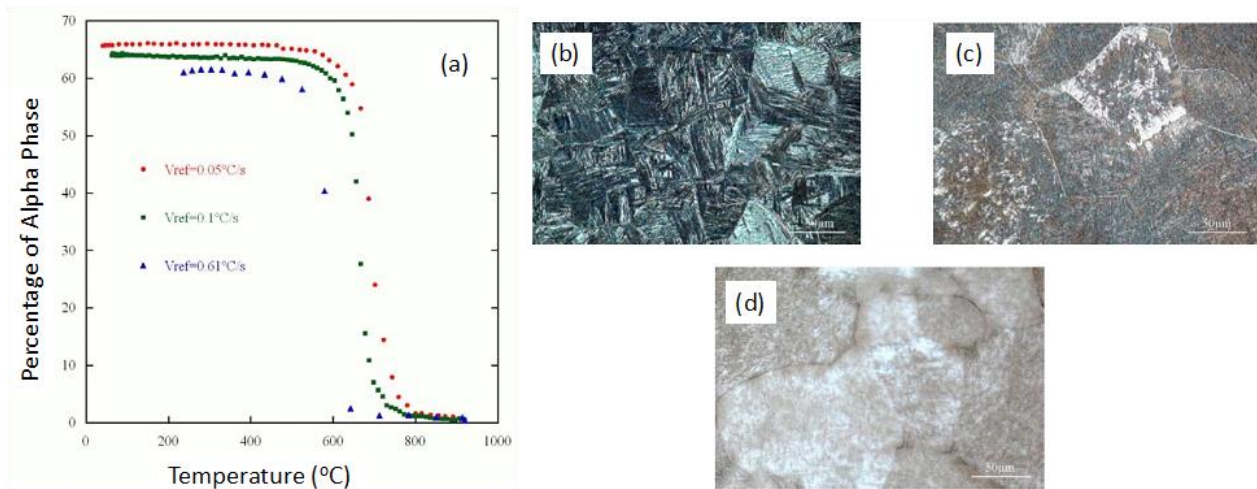
Figure 89. (a) Effect of cooling rate on phase fraction of Ti-17 and impacts on microstructure for cooling rates of (b) 0.05 ºC/s (c) 0.1 ºC/s (d) 0.61 ºC/s
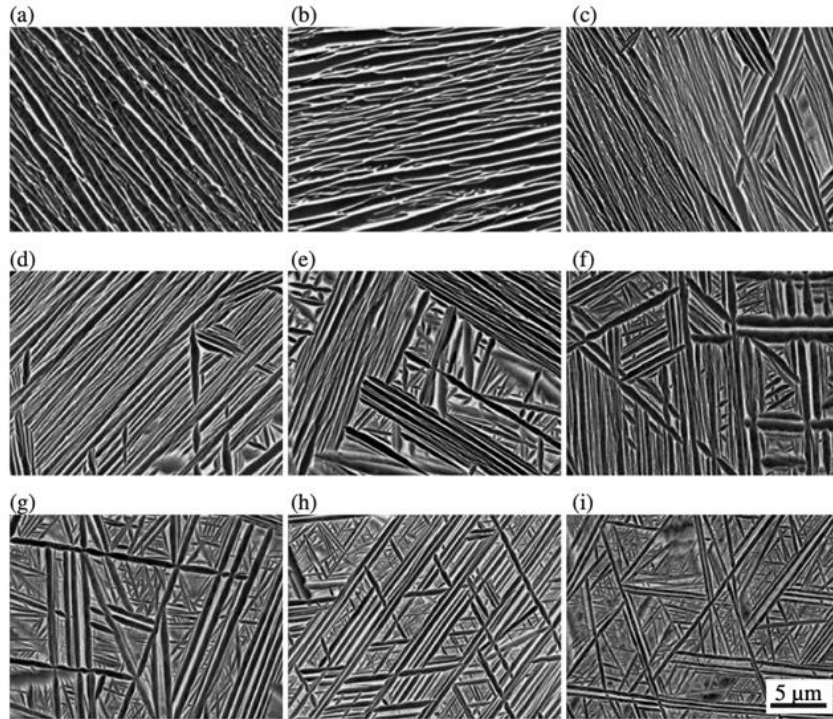
Figure 90. Effect of cooling rate from supertransus heat treatment at 1005 ºC for Ti-550 alloy *(a) 0.276 ◦C/s, (b) 0.4 ºC/s, (c) 0.6 ºC/s, (d) 0.8 ºC/s, (e) 1.0 ºC/s, (f) 1.5 ºC/s, (g) 2.0 ºC/s, (h) 2.76 ºC/s, and (i) 15 ºC/s*

With respect to impact on dwell fatigue, Evans (1987b) investigated the difference in creep and dwell fatigue strength in Ti-685 material specimens having aligned colony structures and basketweave structures. The specimens were created by cooling 16 mm diameter Ti-685 bar at different rates from the beta heat treatment (the aligned structure was produced by furnace cooling and the basketweave structure by air cooling) followed by an anneal of 24 hours as 577°C. High rates of strain accumulation and faceted initiation sites inclined to the stress axis were observed at all stress levels investigated for the basketweave material and at high stresses for the colony material (i.e., strain-dominated failures). At lower stress levels, the colony microstructure exhibited classical orthogonal faceting (i.e., stress-dominated failures). The basketweave microstructures significantly outperformed the colony microstructure with the former tolerating stresses nearly 150 MPa higher at similar lifetime. This may be attributable to the smaller slip lengths in the basketweave microstructure, which increased strength as well as resistance to small crack growth afforded by the same microstructure.

6.2.4 Beta forging + alpha+beta heat treatment

For certain applications beta-forging is utilized to meet the required properties. As discussed in Section 6.1.4, grain growth is rapid above the beta transus and hence careful process controls are

146

required for this forging practice. However, due to the additional excursion above the beta transus, which dissolves all of the primary alpha present in the billet, the state of the MTRs in the billet has limited impact on the degree of microtexture in the final part. The microstructures formed during cooling from the beta forging temperature are most accurately described as alpha colonies. The effective structural unit in this case is the alpha colony dimension because all of the laths in each colony have the same crystallographic orientation and slip can traverse the alpha/beta interfaces due to the preferential alignment of slip systems due to the Burgers orientation relationship. This forging practice is common for more heavily stabilized alloys like Ti-6246 and Ti-17. To a lesser extent, Ti-6242 is also used in the beta forged condition.

6.2.4.1 Forge strain, strain rate, and temperature and post-forge cooling rate
Safran Aircraft Engines has performed an internal investigation on small, beta-forged Ti-6242 pancakes to understand the role of strain (during the β forging operation) and cooling rate effect (after the beta forging operation and also during subsequent heat treatment in the alpha+beta phase field) on dwell fatigue capability. The samples were subjected to the same cooling rate from the forging and alpha+beta solution heat treat steps. Larger strains (ε) and faster cooling rates (*Vr*) from the forging temperature promoted a finer microstructure that reduced the tendency for the formation of large alpha colonies which, because of the alignment of slip systems due to the BOR (see Section 2.3), have large slip lengths that lead to transgranular cracking and thus have a very similar effect as MTRs. Various alpha phase morphologies are observed as a function of cooling rate, which includes alpha laths and grain boundary alpha as illustrated in Figure 91 (Microstructure 1) with lath widths of 5 microns at higher strains and cooling rates. At lower strains and cooling rates, the alpha phase morphology consisted of longer and thicker laths giving rise to larger alpha colonies (Microstructure 4 in Figure 91).

Safran Aircraft Engines performed dwell tests (20°C with 40 second dwells at 90% of the yield strength) on the four different microstructures shown in Figure 91 and it was found that dwell capability was greatest with a finer microstructure resulting from more forging strain and a faster cooling rate (Figure 92). Further details on microstructure evolution for beta-forged Ti-6242 can be found in (Appolaire, Aeby-Gautier, Da Costa-Teixeira, Hericher, & Denis, 2011; Gautier, et al., 2006).
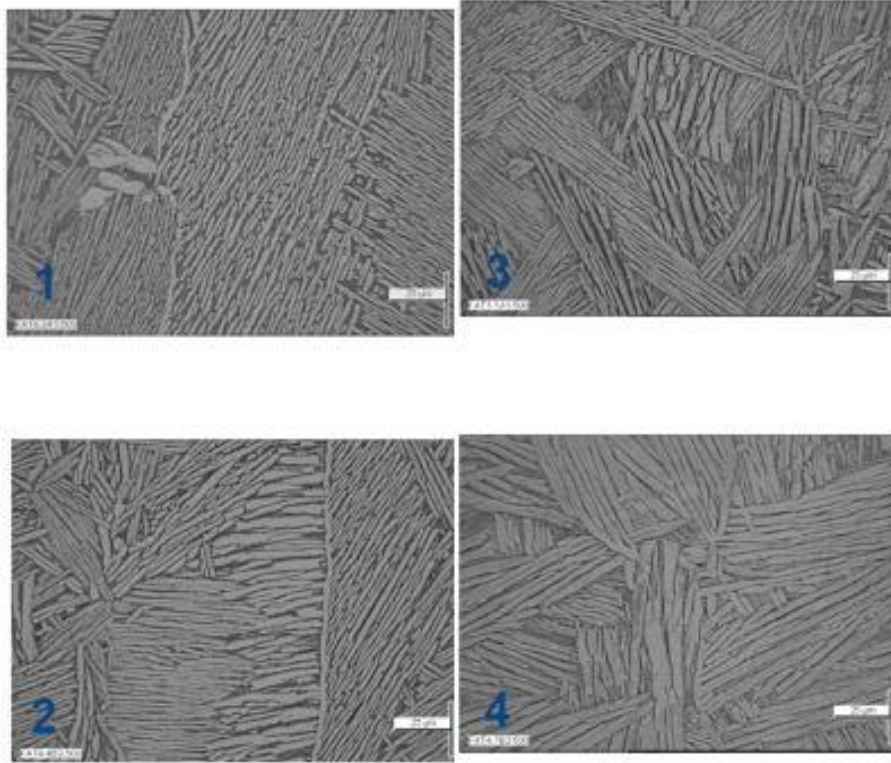
Figure 91. Effect of cooling rate following beta forging of Ti-6242
Cooling rate is highest in micrograph 1 and decreases toward micrograph 4

Postans and Jeal (1980) have looked at the role of strain rate on microstructure evolution during beta forging of Ti-829. Forging at slower strain rates (e.g., 10^{-3} s^{-1} and 3×10^{-3} s^{-1}) allowed time for recovery processes to occur within the existing prior beta grains that accommodated strain which otherwise would lead to recrystallization. The grains were elongated perpendicular to the forging direction and were also observed to grow concurrent with deformation. A small amount of recrystallization occurred at prior beta grain boundaries leading to a bimodal grain size distribution. At a slightly faster strain rate of 10^{-2} s^{-1} there is less time for recovery and complete recrystallization occurs near the end of the forging process. Finally, recrystallization occurred readily and early during the forging process under the fastest strain rates (3×10^{-2} s^{-1} and 10^{-1} s^{-1}). These dynamically recrystallized grains were lightly deformed through the rest of the forging process, but this did not result in significant elongation of the prior beta grains.
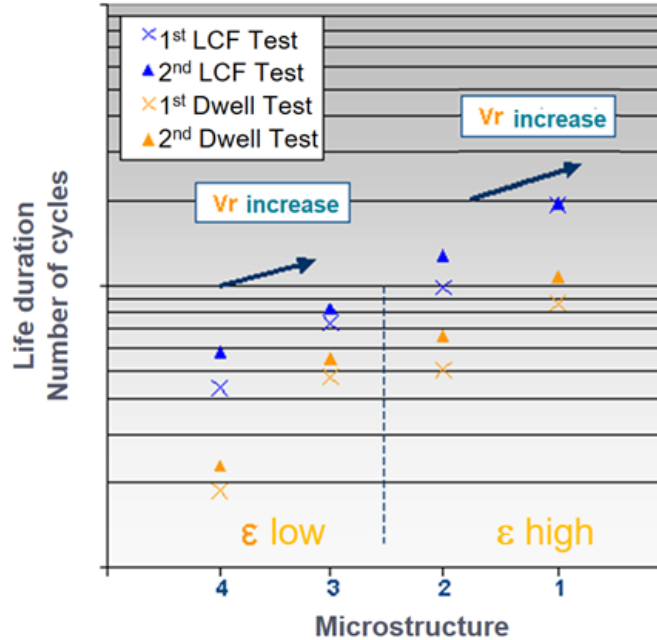
Figure 92. Comparison between LCF and Dwell tests as a function of strain and cooling rate
Microstructures 1 through 4 correspond to those in Figure 91

6.2.4.2 Solution temperature, time, and post-solution cooling rate

Consistent with the other component forging routes, the solution temperature, time, and post-solution cooling rate have an important effect on the final properties. Semiatin (2020) reported that alpha lath coarsening kinetics follow a parabolic law such that the average thickness is proportional to t^{n_c} where n_c is a rate constant in the range of 0.05 to 2 for Ti-6Al-4V (Figure 93). The rate limiting mechanism for lath coarsening is solute diffusion through the beta phase. Higher temperature permits more rapid diffusion and hence, coarsening rates are increased. Coarsening rates are initially higher for thin alpha laths which can more than double in size in less than an hour at the highest temperature. For this reason, the solution heat treatment should be done at moderate temperature in the alpha+beta phase field to avoid significant coarsening.
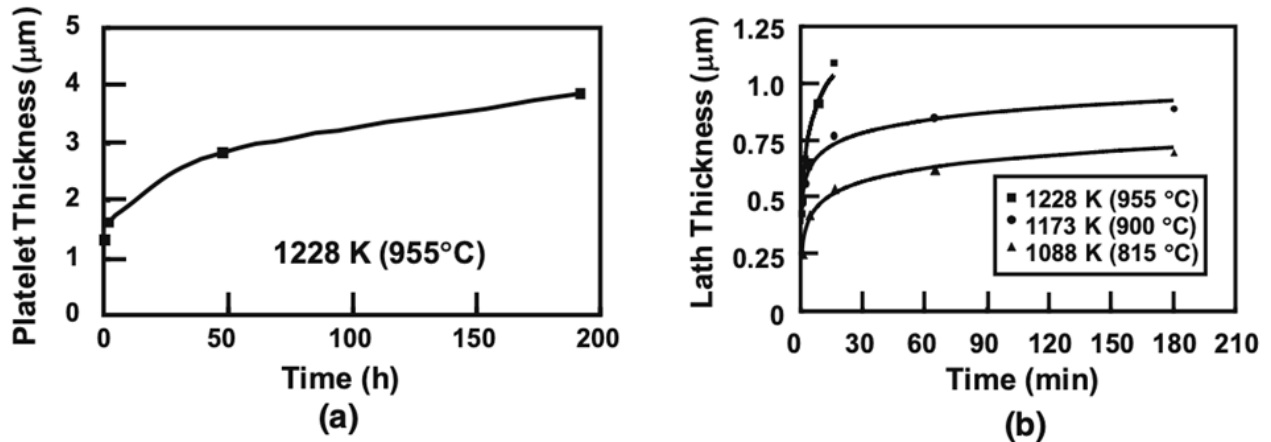
Figure 93. Effect of time and temperature on lath coarsening kinetics of Ti-6Al-4V in (a) colony and (b) basketweave conditions

While the authors are unaware of a study isolating the effects of solution temperature and cooling rate on the microstructure and properties of beta forged and alpha+beta heat treated titanium alloys, the combined effect is contained within the work of Safran Aircraft Engines discussed in Section 6.2.4.1. The cooling rates used following alpha+beta heat treatment mirrored those used from the forging operation. The micrographs (Figure 91) show evidence of fine secondary alpha between the coarser alpha laths that were established during cooling from the forging temperature. These secondary alpha laths are thickest with the slow cooling rate and decrease in size until they become indistinguishable with the fastest cooling rate. A very fine distribution of laths is presumably present in this case, but not resolvable at the magnification used.

Brandes (2008) used various heat treatments to control the secondary alpha laths in beta-forged, heat treated, and annealed Ti-6242 pancake (pancake 3 from (Ghosh, et al., 2007)). The heat treatments (outlined inTable 8) produced the microstructures shown in Figure 94. The corresponding tensile properties are shown inTable 9 where n and m are the strain and strain rate sensitivity exponents, and the static response is characterized by the time constant a obtained by fitting creep data (Figure 95) to a power law. The creep behavior of these alloys is shown in Figure 95. The highest strengths were observed in the as-received and solution quenched conditions. In general, creep behavior was improved in heat treatments that resulted in lower strain rate sensitivity and increased strain hardening response. The best creep resistance was observed in the as-received and annealed conditions which contained the coarsest secondary alpha laths as compared to those with fine secondary alpha laths (i.e., furnace cooled and annealed). The microstructure lacking secondary alpha precipitates (i.e., the furnace cooled and solution quenched condition) showed the highest transient creep strain accumulation rates, which

was attributed to the reduced strain hardening rate. The results were rationalized on the basis of the lath size and morphology as well as the distribution of alloying elements between the primary alpha and secondary alpha laths. In the as-received condition, the secondary alpha is formed at a higher temperature which led to a more heterogeneous distribution of Al and Mo as compared to the furnace cooled and annealed condition.

Table 8. Heat treatments to manipulate secondary alpha lath morphology in beta-forged Ti-6242

Condition	Heat treatment
As-received	Forged to 89% reduction at T_{beta} + 28 ºC; solution treated at T_{beta} − 20 ºC / 1h / oil quenched; aged at 593 ºC / 8 hr / air cooled
Annealed	Solution treated T_{beta} − 95 ºC / 10 min / water quench
Furnace cooled	Solution treated T_{beta} − 95 ºC / 60 min / furnace cooled
Furnace cooled and annealed	Solution treated T_{beta} − 95 ºC / 60 min / furnace cooled to room temperature then annealed at T_{beta} − 65 ºC / 10 min / water quench
Solution quenched	Solution treated T_{beta} − 10 ºC / 60 min then quenched to T_{beta} − 120 ºC / 60 min / water quenched
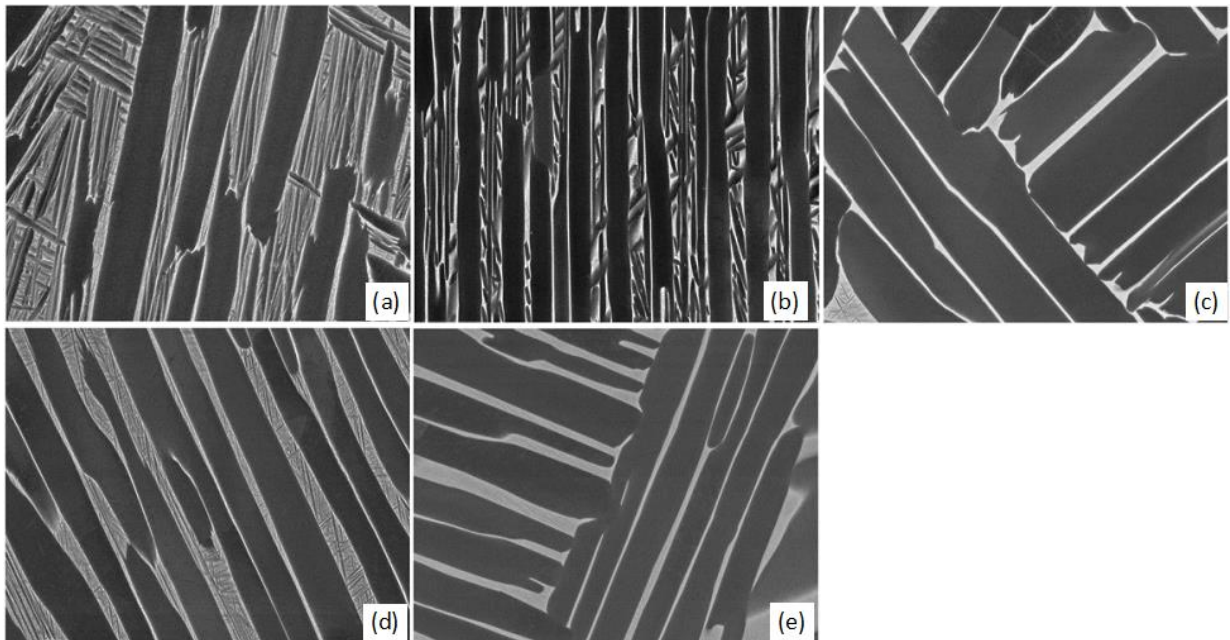
Figure 94. Secondary alpha lath morphologies in beta-forged and alpha+beta heat treated Ti-6242 *(a) as-received (b) annealed (c) furnace cooled (d) furnace cooled + annealed (e) solution quenched conditions*

Table 9. Quasi-static response of the various Ti-6242 microstructures investigated by Brandes

Material	Microstructure	Stress State	σ_{ys} (MPa)	m	n	a
Ti-6-2-4-2	AR	Comp	1037	0.011	0.131	0.155
		Ten	960	0.014	0.075	0.221
	AN	Comp	952	0.011	0.103	0.158
		Ten	890	0.015	0.068	0.248
	SQ	Comp	1012	0.011	0.100	0.182
		Ten	930	0.016	0.062	0.29
	FC	Comp	933	0.013	0.081	0.195
		Ten	837	0.020	0.046	0.37
	FC+An	Comp	945	0.012	0.096	0.157
		Ten	880	0.014	0.067	0.242

σ_{ys} determined at $\dot{\varepsilon} = 10^{-4}\ s^{-1}$ m determined by rate jumps, $\dot{\varepsilon} = 10^{-4} \rightarrow 50^{-4}\ s^{-1}$
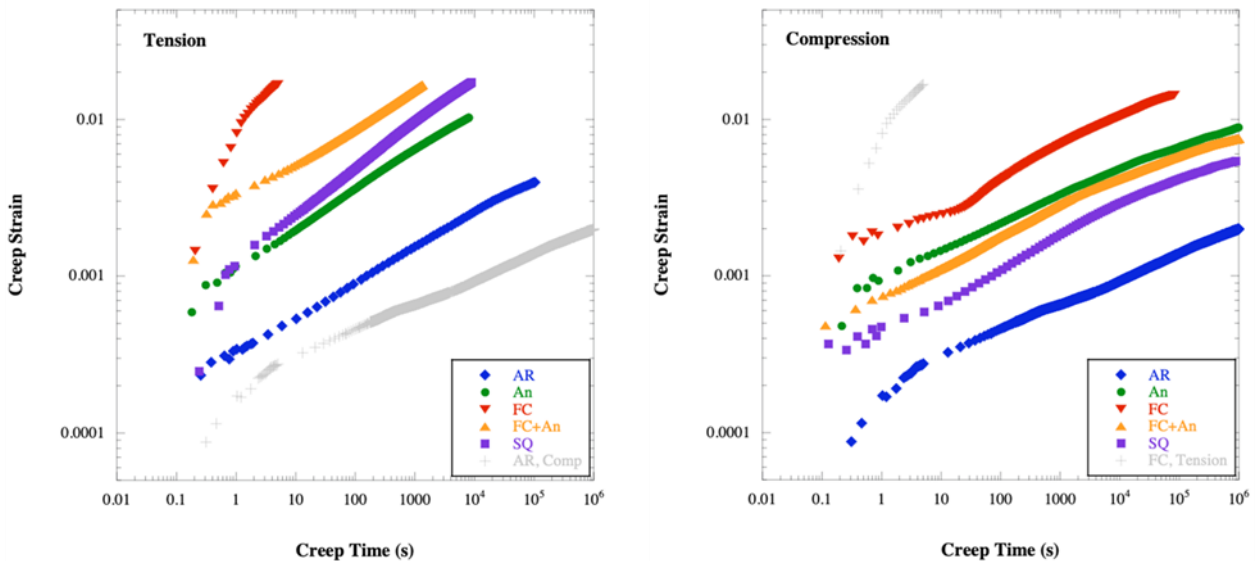
Figure 95. Room temperature tension and compression creep response of Ti-6242 with various secondary alpha lath morphologies at 950 MPa

6.2.5 Pore formation during forge processing

As briefly mentioned in Section 6.1.13, pores may form at prior beta grain boundaries or colony boundaries during billet conversion due to strain incompatibility between adjacent hard/soft-oriented regions with respect to the deformation axis. The same process may occur during alpha+beta forging, although these pores are speculated to be at MTR boundaries as opposed to being internal to the MTR. While the published literature related to cavity formation has all been performed on colony microstructures (Bieler, Nicolaou, & Semiatin, 2005; Nicolaou & Semiatin, 2007), the Air Force Research Laboratory (AFRL) performed detailed investigation of the Ti-

6242 hot compression samples discussed in Pilchak et al. (2016a; 2016b) and noted cavity formation at the interfaces between primary alpha grains and adjacent beta phase (Nicolaou, Semiatin, & Pilchak, 2019). Cavities were observed primarily at the midplane of the compression samples near the outer diameter of the forging in the barreled region where FE models predicted large tensile stresses were developed. The propensity for cavities increased with decreasing forging temperature.

6.2.6 Concluding thoughts on microstructural length scales resulting from various processing routes

The length scale of microstructural constituents formed by the three processing routes discussed above decreases in the order of (i) alpha+beta forged and beta heat treated, (ii) beta forged and alpha+beta heat treated, (iii) alpha+beta forged and alpha+beta heat treated. However, due to the impact of microtexture, the slip lengths in route (iii) may actually exceed those of (i) and (ii) if prior thermomechanical processing steps are not well controlled. Said differently, just because the microstructure appears finer via optical or SEM imaging, it will not automatically lead to improved properties. For this reason, characterization techniques sensitive to crystallographic orientation like EBSD and polarized light microscopy are needed for a complete characterization.

Colony microstructures, such as those formed during beta forging or beta heat treatment, are distinct from MTRs in terms of the length scale of microstructural features which represent obstacles to dislocations as well as the partitioning of alloying elements between the constituent phases. MTRs are comprised of alpha particles with typical sizes in the range of 10 ~ 20 µm that may or may not be separated by transformed beta or retained beta ribs. The size of the transformed beta regions is generally of the same order as the primary alpha particles, although this depends on the volume fraction of primary alpha. Lower volume fractions of primary alpha will result in larger underlying beta grains and hence larger packets of transformed beta. Further, grain boundary alpha may be present between two adjacent transformed beta regions with different underlying beta grain orientations. All of these features represent potential barriers to slip in the MTR (Harr, Pilchak, & Semiatin, 2021) and also represent sites where slight or significant differences in crystallographic orientation can lead to crack-tip deflection in the event a crack is initiated. Increased microscopic crack path tortuosity (roughness) reduces crack growth rates in the early stages of crack formation compared to cases of highly aligned grains that have minimal resistance to crack propagation.

In contrast, there are only two primary barriers to slip in colony microstructures. The strongest barriers are high angle colony boundaries (i.e., any colony boundary other than the 10.5º about

[0001] boundary, see Section 2.3 for more details). The size of the colonies in beta-forged microstructures is a strong function of cooling rate, but it generally exceeds the length scale of the microstructural features in MTRs by about an order of magnitude for typical microstructures observed in large forgings. As discussed in Section 2.3, the alpha/beta lath interfaces represent relatively weak barriers to slip (compared to high angle boundaries), but residual dislocations are left at the interphase boundary as dislocations propagate through colony microstructures. Although these offer a limited Hall-Petch strengthening effect, these do represent a series of closely spaced obstacles on the slip plane which can temporarily pin dislocations leading to more homogeneously distributed dislocations along the slip plane. This has the effect of reducing the rate sensitivity compared to the case of a pure alpha phase constituent (Waheed, S., Zheng, Balint, & Dunne, 2019; Zheng, Balint, & Dunne, 2017).

In addition to differences in microstructure morphology, there are also differences in the composition of each constituent. Alpha stabilizing elements (e.g., Al, O) partition to the primary alpha while beta-stabilizing elements partition to the beta phase at the deformation temperature during alpha+beta processing. This results in the transformed beta regions being lean in alpha stabilizers, which has important implications on the strength and slip character. Elements like Al and O tend to promote planar slip (Williams, Sommer, & Tung, 1972) which is thus enhanced in the primary alpha particles compared to the transformed beta leading to strong dislocation pileups, load shedding, and facet formation in the primary alpha phase. In contrast, the alpha laths in colony microstructures that form during cooling following beta-forging have a higher concentration of alpha stabilizing elements. With respect to composition, more heavily beta stabilized alloys will result in refined alpha laths, which have the effect of reducing strain rate sensitivity and load shedding (Waheed, S., Zheng, Balint, & Dunne, 2019).

It is noteworthy that although there are distinct differences between alpha colonies and MTRs, the net effect is similar and there can be significant slip lengths, dislocation pileups, and stress redistribution in either microstructural condition.

7   Characterization of mechanical properties

A commonly used test to assess cold dwell sensitivity of titanium alloys has historically been a smooth load-controlled uniaxial fatigue test with an extended dwell at the peak load condition. Typical dwell times in the literature are between 30 and 120 seconds, and this is normally compared to a 'fast cycle' with either no dwell or a very short dwell at maximum load. The ratio of lifetimes $N_{f,cyclic}/N_{f,dwell}$ is termed the dwell debit. In practice, these pairs of specimens should be extracted from adjacent locations in the forging to minimize variations due to differences in

forging strain and cooling rate to the extent possible. Tensile testing is commonly performed from samples extracted from adjacent locations and used to aid in fatigue stress selection. Test stresses are commonly selected as a function of the 0.2% yield stress and using "typical" 0.2% yield stress rather than an "actual" 0.2% yield stress from the material of interest can lead to significant errors. Furthermore, these tests are usually performed on samples with shot peened gages in order to suppress surface initiation and promote initiation sites consistent with those observed on components. In general, a debit greater than 3x accompanied by internal crack nucleation and an associated faceted initiation site is cause for more extended and thorough investigation. This is because all Ti alloys will generally exhibit a 2~3x dwell debit at a given stress level even without the presence of hard-oriented grains leading to internal faceting (Brandes, Mills, & Williams, 2010). However, care must be taken in interpreting specimen test results for two reasons:

1. Uniaxial load-controlled testing at high stress levels (at or above ~95% of the 0.2% proof stress) can cause gross plasticity and therefore a debit in life may occur but not necessarily by the same failure mode as cold dwell fatigue. See Figure 96, for example, which shows pockets of isolated facets separated by ductile fracture under high stress dwell testing (Stress = 865 MPa, R = 0.05, T = 66 ºC / 150 ºF, N_f = 1,001, dwell time = 150 sec).

2. There have been multiple observations confirming that components can perform less well than specimens at the same applied stress levels (Evans & Bache, 1994; Harrison, Trantner, Winstone, & Evans, 1986).
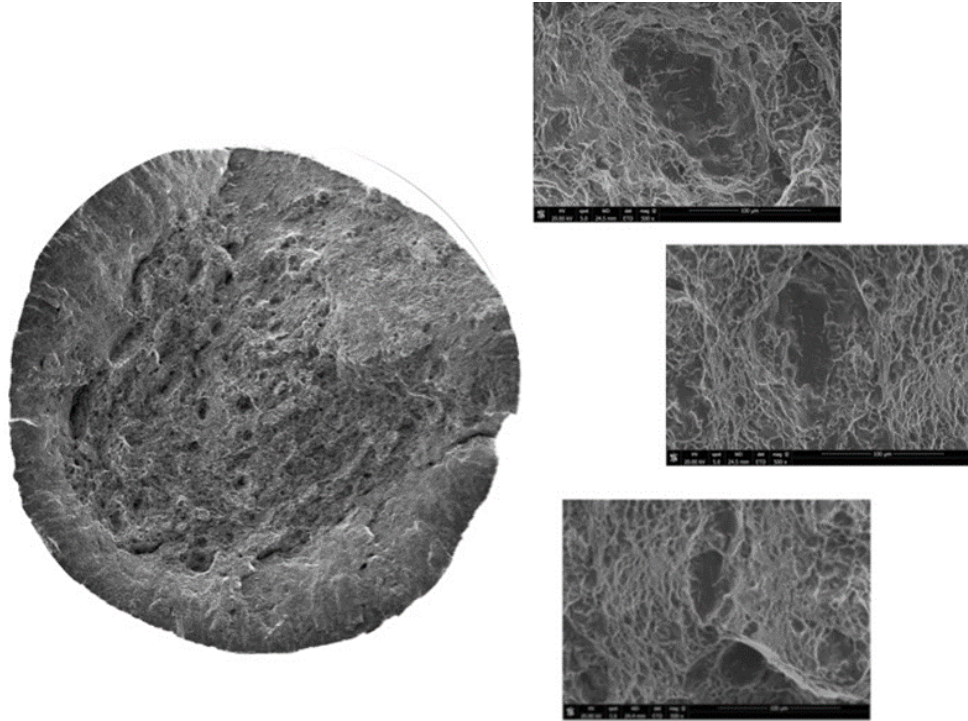
Figure 96. Example of a Ti-6Al-4V dwell fatigue fracture surface

Multiple factors are known to influence the dwell debit. These include alloy composition (major alloying elements and interstitials), microstructure, microtexture, macrotexture, stress and stress state, dwell time, load ratio, loading rate, control mode (i.e., stress vs. strain control), and temperature. Several of these have been addressed elsewhere in the report. In addition, Wu et al. (2022) have also recently published a review article which summarizes some of these aspects. In this section, for the sake of thoroughness, each factor will be briefly summarized and cross-linked to other locations where they are discussed as appropriate. Following this, we highlight a few considerations for interpreting the results of spin pit testing and then conclude with a discussion of potential accelerated and more affordable tests for dwell sensitivity.

7.1   Laboratory coupon testing

7.1.1 Stress level

The current understanding of cold dwell fatigue behavior is that the initiation mechanism is dependent on localized deformation behavior at the size scale of the effective structural units (i.e., microtextured regions/macrozones) or smaller where material can accumulate strain in regions preferentially oriented for slip, which depends strongly on the stress level. In lab scale specimens, cold dwell fatigue behavior is generally only seen at relatively high fractions of the

0.2% yield stress (Neal, 1988; Venkatesh, et al., 2020), but component experience has shown that the mechanism can operate at lower stresses even down to below the cyclic yield stress. In load-controlled laboratory coupon testing with a dwell, failure in a reasonable time and number of cycles (e.g. $N_f \sim 10,000$) generally requires testing at stresses $\geq \sim 90\%$ of the monotonic yield stress (Neal, 1988; Venkatesh, et al., 2020). Such high stresses are generally required to activate the dwell mechanism in specimens, which contain a much smaller number of MTRs as compared to components, and hence have a lower probability of containing the critical combination of microstructural features (crystallographic orientation and size, etc.). In general, the dwell debit diminishes as the applied stress is reduced and a point will be reached where the scatter in dwell fatigue and standard fatigue testing will overlap. This crossover point will be a function of the usual factors including composition, microstructure, macro- and microtexture. The crossover stress tends to increase with increasing beta stabilizer concentration which is evident by comparing the alpha+beta alloy Ti-6Al-4V with the near-alpha alloy Ti-834 in Figure 97 (data from Bache (2003) and figure from Wu et al. (2022)) and Figure 98 (Bache, Cope, Davies, Evans, & Harrison, 1997), respectively.
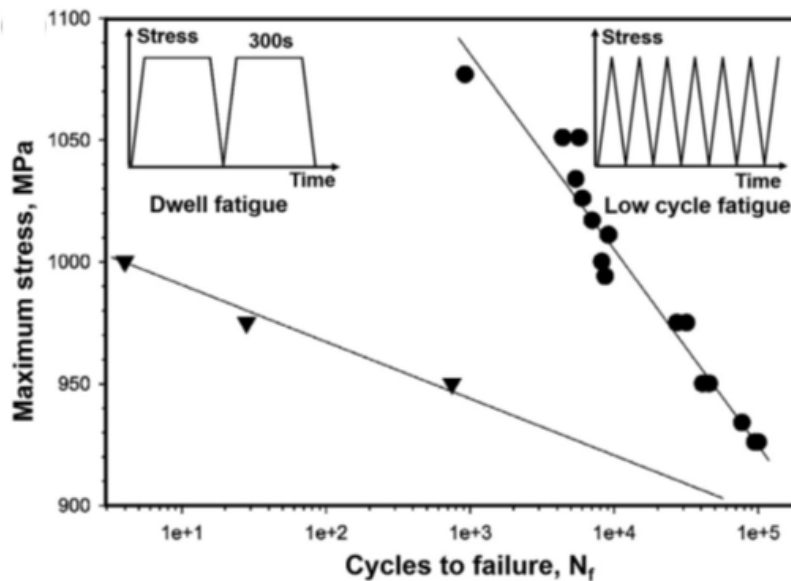
Figure 97. Comparison of cyclic and dwell response of beta-annealed Ti-6Al-4V
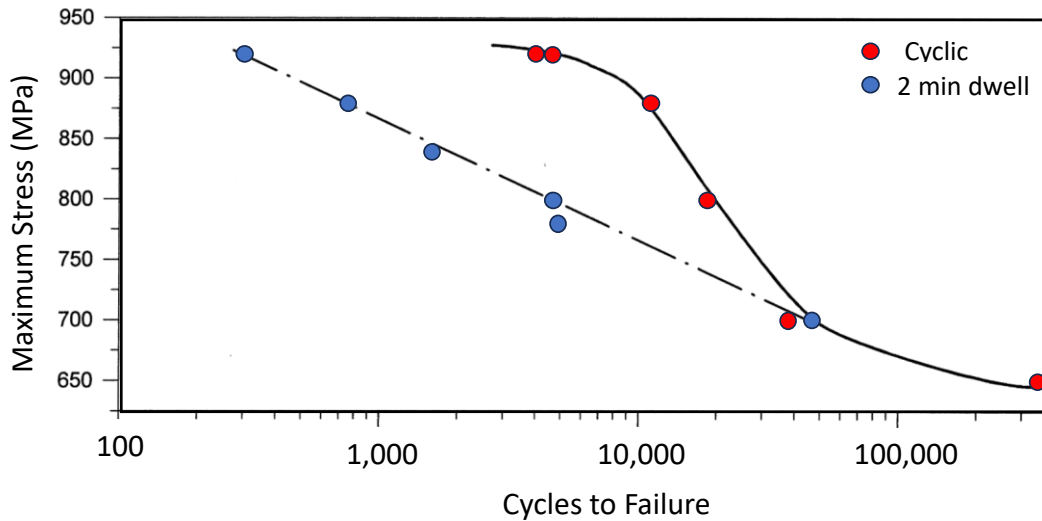
Figure 98. Comparison of LCF and dwell behavior of Ti-834

Significant dwell debits (i.e., >3x) have been reported in lab specimen/coupon tests in commercial alloys Ti-6Al-4V, Ti-685, Ti-829, Ti-834, Ti-811, and Ti-6242 (in both the alpha+beta and beta forged conditions). In Ti-6246, minor life debits are observed in specimens tested at very high stresses (above ~90% of ultimate tensile strength), but there are no attendant large, faceted initiations sites observed on the fracture surfaces (Spence, Evans, & Cope, 1997).

Early work by Evans (1987b) classified fractures in Ti-685 with a colony microstructure into two different classes based on the angle of the facets with respect to the stress axis. Strain-dominated failures with facets near 45° to the stress axis were observed at high stresses (above 90% of the tensile strength) while facet-dominated failures were oriented near perpendicular to the stress axis. In higher strength materials with bimodal microstructures, orthogonal facets are still readily observed at stresses near 95% of the yield strength and these give way to ductile overload fracture mechanisms at stresses exceeding the yield strength. In general, samples that fail with isolated facets do not show a strong dwell debit whereas those with significant clustering of facets do.

Depending on the applied stress level there may be a reasonable amount of scatter present in the dwell test data. As with conventional fatigue, scatter decreases as the peak test stress is increased. Very few studies in the open literature discuss variability under constant test conditions. An exception to this is the work of Toubal et al. (2009) who performed 10 repeat tests on Ti-834 under identical conditions (824 MPa peak stress or 90% of the yield strength, 30 second dwell, and R = 0) on specimens extracted from various locations in a forging. The authors observed a 6x difference in life between the longest and shortest and also differences in strain-

time response as summarized in Figure 99 (Toubal, Bocher, & Moreau, 2009). The authors represented the data as a cumulative distribution and found that it was suitably fit by the Weibull distribution, which is widely used to analyze "weakest link" failure phenomena in brittle materials. There was a limited degree of correlation between strain accumulation and dwell life. For example, samples 1, 2, 4, 6 and 9 all exhibited very similar strain history, but varied in life by about 2.5x. Sample 7 accumulated strain at a faster rate than sample 2, but the latter failed earlier than the former. Sample 10 had the highest strain accumulation rates of all specimens tested but three samples (3, 5, and 8) failed at lower cycle counts. These observations are likely related to differences in the fraction of soft-oriented material which is the primary driver of creep damage and distribution of hard-oriented MTRs which support faceted crack propagation.
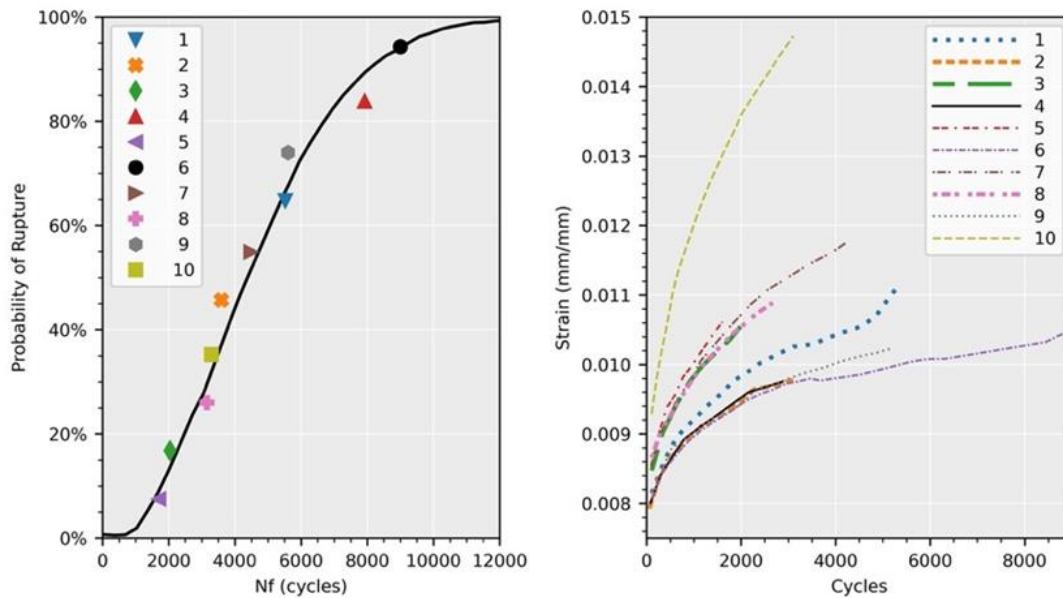
Figure 99. Dwell fatigue lifetime variability and strain accumulation in Ti-834

7.1.2 Stress state

The majority of laboratory specimen testing has been conducted on uniaxial stressed plain load-controlled specimens, but full-scale rig tests and engine components may be subject to more multiaxial stress states due to the part geometry, presence of bulk residual stresses, and thermal stresses, among other things. A limited amount of work exists in the literature examining the effect of multiaxiality on cold dwell behavior, which is reviewed here.

Evans and Bache (1994; Bache & Evans, 1993) investigated tension-torsion loading of tubular specimens in Ti-685 alloy cut from 30 mm diameter bar with a 1.1 mm wall thickness. The fatigue cycle consisted of a 2 second load, 1 second hold at peak stress, and a 2 second ramp

down and no hold at minimum load. The dwell fatigue cycle was the same loading and unloading times but incorporated a 120 second hold at peak load. The R ratio was 0.1. The tests showed a debit in fatigue life under uniaxial conditions, but results did not show a significant difference between solid tension and tubular torsion performance in dwell.

Doquet and De Greef (2012) investigated multiaxial stress state effects on dwell fatigue using tubular specimens cut from 40 mm diameter bar Ti-6Al-4V bar with a wall thickness of 1.1mm. The specimens were tested at R = 0 under uniaxial and biaxial stress states. The conventional fatigue cycle was a triangular waveform with 1 second loading and 1 second unloading whereas the dwell cycle was a trapezoidal waveform with an 80 second dwell period at peak load and 1 second ramps to maximum and minimum stress. The work found that introducing a biaxial stress field increased the fatigue life by ~23% on average, but no definitive conclusion could be drawn regarding the influence of biaxial loading on dwell fatigue life.

Hommer (2018) developed an in-situ planar biaxial loading experiment and utilized synchrotron x-ray diffraction and normalized resolved shear stress composite pole figures to analyze the proportional and non-proportional dwell fatigue behavior of the Ti-7Al alloy. The work suggested that the region of orientation space that could be classified as "hard" was reduced under non-proportional biaxial loading which prevented classical load shedding observed under uniaxial tension. As a special case for the thin planar cruciform specimens investigated, the out of plane Poisson contraction caused the hard grain to exert a tensile force on the adjacent soft grain leading to increased triaxiality.

Maloth et al. (2020) modelled the Ti-7Al cruciform specimens from Hommer's thesis (Hommer, 2018) using an uncertainty-quantified, parametrically homogenized constitutive model (UQ-PHCM). The source material was cast, HIPed twice and then subjected to extrusion and cross-rolling to form the cruciform specimen. Two biaxial stress states were investigated (X:Y load ratios of 1:1 and 1:2. DIC was used to measure the surface strain evolution. Dwell times were a minimum of 2 minutes with data collection times of at least 25 minutes per cycle (the 1st, 5th, and 50th cycles were monitored). It was found that the UQ-PCHM predicted the gauge strain evolution shown in the DIC measurements satisfactorily and also reproduced the experimentally measured elastic strain distribution. The latter was only possible after instantiating the experimentally determined grain-scale residual stress state in the UQ-PHCM prior to simulating the experiment.

Cuddihy et al. (2017) used crystal plasticity modeling to understand multiaxial stress states in an effort to interpret cold dwell fatigue failure in Ti-834 component spin pit tests (this work is addressed in more detail in Section 8.2.1). They observed that the hoop stresses dominated but

that relatively large radial stresses were carried by the diaphragm web section of the disk. In fact, the radial stress was almost 40% of the hoop stress for that region. Crack initiation sites in a number of spinning rig tests were then examined and it was concluded that no faceting is observed when the normalized hoop stress is less than 0.58 with the majority of faceting occurring when the hoop stress normalized by the yield strength is greater than 0.66. Further calculations of the stress triaxiality across the bore showed that triaxiality (i.e., the ratio of hydrostatic mean stress and the von Mises effective stress) was less than 0.37 in these locations. The authors then applied a crystal plasticity finite element approach which had been developed previously and modelled a 'rogue' hard/soft orientated grain pair under different levels of biaxiality (Figure 100 (Cuddihy, 2016)). The predictions indicated that equi-biaxial loading would give a longer dwell fatigue life than uniaxial loading and occurred at a CRSS value > 1 when normalized against the threshold value for slip in Ti-6Al.
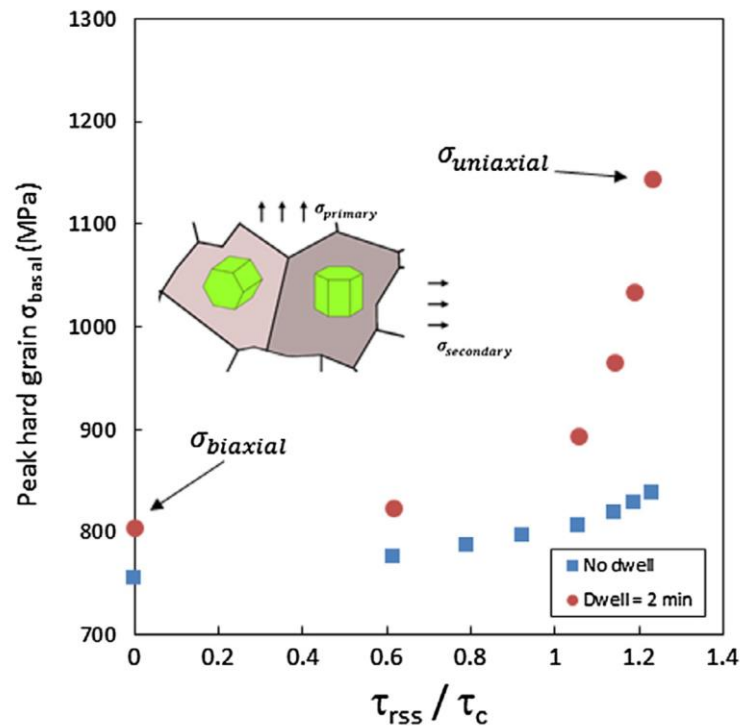
Figure 100. Effect of stress state and dwell on hard grain stresses from CPFEM simulation

7.1.3 Dwell time

The dwell time selected for the test has an important effect on total dwell fatigue lifetime. Early work investigated the effect of hold times on crack propagation, which is covered elsewhere (see Section 4.3). With respect to total dwell fatigue life, Bache et al. (1997) investigated hold times ranging from 15 seconds to 5 minutes and found that the dwell debit increased with increasing

hold time (Figure 101) for isothermally forged Ti-834 disk material which contained microtexture (Bache, Cope, Davies, Evans, & Harrison, 1997). The authors also noted that longer dwell times correlated to increased strain accumulation. Evans (2004) reported additional data from the same material with dwell times between 1 and 500 seconds (Figure 102, modeled after Evans (2004)). A minor debit was found between the non-dwell and 1 second dwell conditions at stresses just over 900 MPa. A more significant debit was observed for 15 second dwells and this debit increased with increasing hold time up to five minutes. Drawing on the subsequent work of Zheng et al. (2017), longer dwell times offer increased chances for thermally activated dislocation escape from obstacles on the slip plane and hence can lead to stronger pileups.
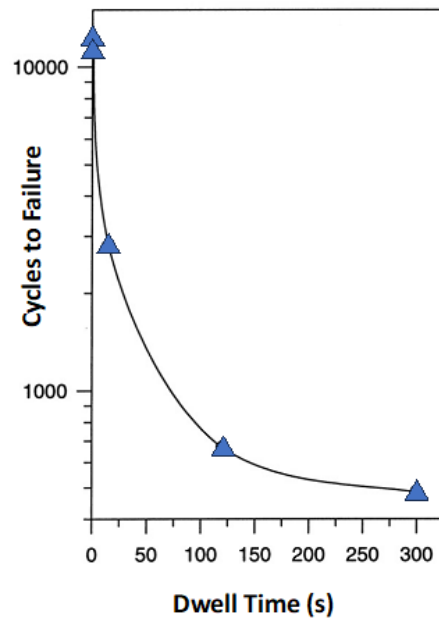
Figure 101. Effect of dwell time on fatigue life of Ti-834 disk material (880 MPa, R = 0.1)
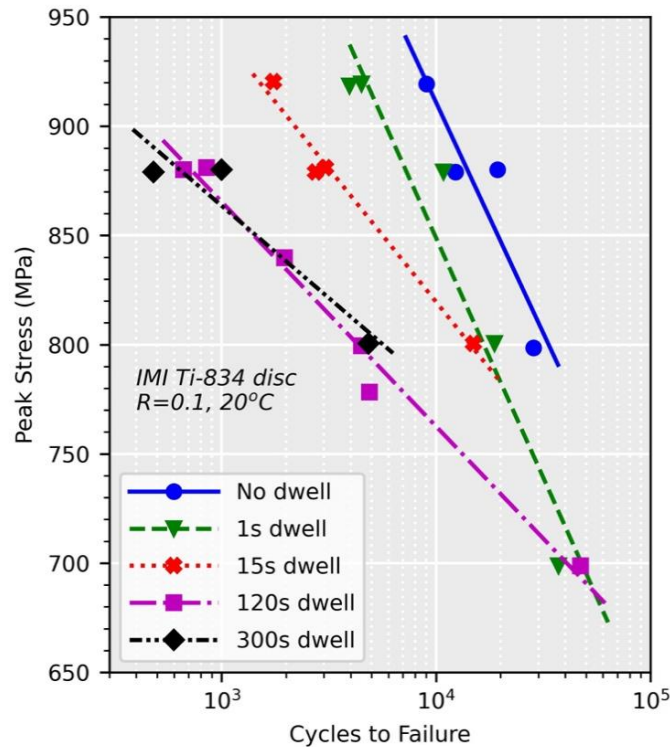
Figure 102. Effect of hold time on dwell fatigue behavior of Ti-834 disk material

More recently, You et al. (2022) reported a variation in dwell sensitivity as a function of hold time and position within an Ti-834 forging (Figure 103). The maximum stress was 830 MPa (88% of yield strength) with 1 second ramp rates to and from peak stress with a load ratio of 0.05. Sample A1 was a conventional fatigue sample with no dwell, samples B2 and B3 had 120 sec hold times, and samples C2 and C3 had 300 sec hold times. The authors noted that the spatial variation in microstructure led to differences in apparent dwell sensitivity to hold time. They further found through x-ray computed tomography that the high sensitivity microstructure, which contained a higher degree of microtexture, had a larger number of internal cracks distributed throughout the gauge section as compared to the low sensitivity regions. Xi et al. (2020) investigated the impact of short dwell times (1 and 10 seconds) on strain accumulation and dwell fatigue (Figure 104). Hold times as short as 1 second resulted in an appreciable increase in plastic strain accumulation and a corresponding reduction in lifetime, though the debit in terms of cycle count was relatively small (~1.25x debit). Increasing the hold time to 10 seconds resulted in an additional ~2% plastic strain over the lifetime of the test with a corresponding increase in the dwell debit to ~1.8x.

163
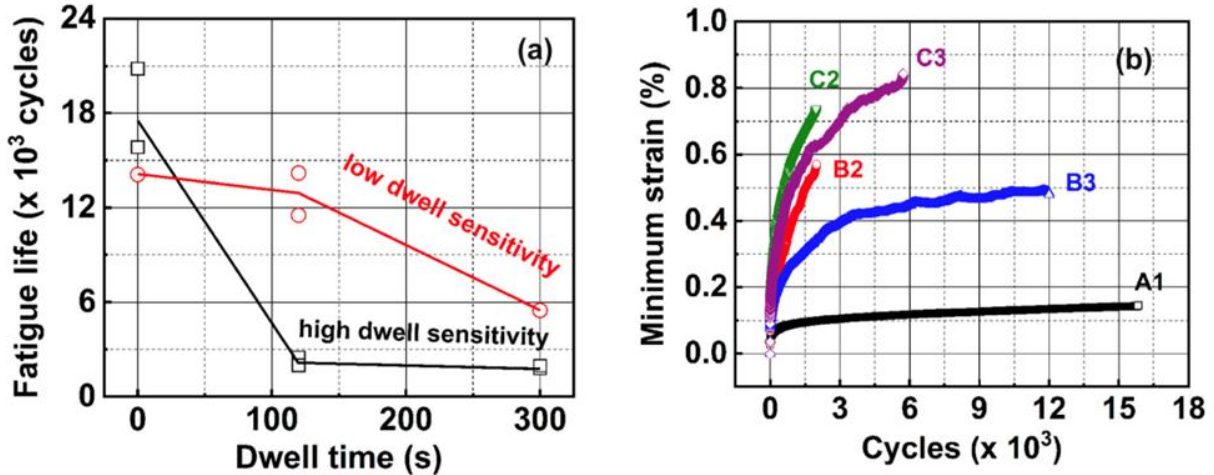
Figure 103. Effect of hold time on dwell sensitivity and strain accumulation in Ti-834
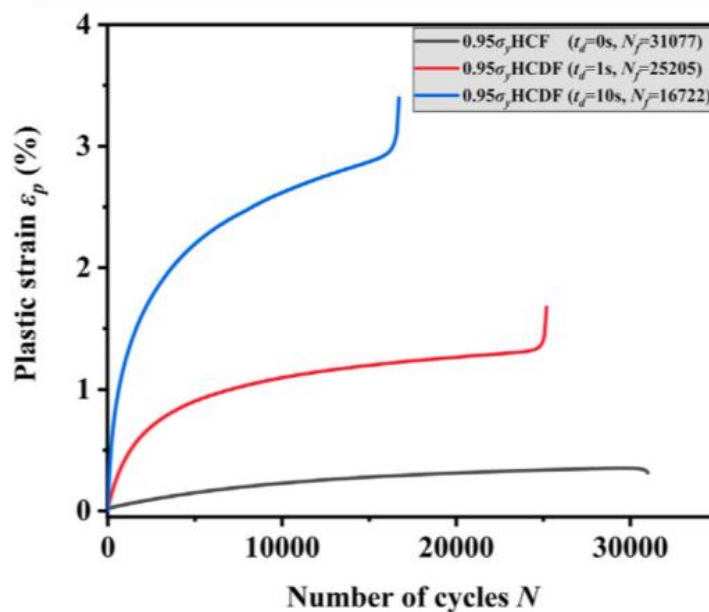
Figure 104. Effect of short dwell periods on strain accumulation in Ti-6Al-4V (R = 0)

7.1.4 Stressed volume

The general understanding of the mechanism of cold dwell fatigue is that the initiation events depend on a number of factors including a preferred orientation between microstructural units to create the maximum offloading from weak to strong features. These factors make the initiation event itself probabilistic in nature and this is cited as one of the reasons why components (which have a large-stressed volume) can initiate and fail in cold dwell fatigue at lower stresses than is generally seen in coupon tests (with a relatively small-stressed volume). The expectation is that

the larger the volume of material is more likely to contain the 'worst case' combination of features responsible for crack formation. The volume of interest for the component is typically taken as the volume above a critically stressed volume where dwell fatigue is of concern. The magnitude of this stress should be determined experimentally using laboratory coupons and validated through spin pit testing. The actual stress level depends heavily on the alloy composition and microstructural (MTR) condition.

Song and Hoeppner (1989) investigated Ti-829 in the beta heat treated condition with an average grain size of ~0.6 mm. The authors tested smooth cylindrical specimens with three different gauge diameters (17.5, 12.7, and 6.4 mm) in Ti-829 using waveforms with and without a dwell at maximum stress. The smaller diameter dwell tests performed the worst of all three specimen types both in terms of plastic strain accumulation and in lower lives in both fast cycle and dwell tests. The explanation given in the paper invoked a texture effect for this observation. The smaller specimens had fewer prior beta grains in the gauge section and therefore they were less likely to have a strong orientation (c-axis parallel to the stress axis) within the gauge section. This was evident by the more rapid strain accumulation in soft-oriented regions which we suggest contributed to higher degrees of load shedding leading to early failure. In addition, Song and Hoeppner (1989) also suggest that the larger specimens will be subject to higher triaxial stresses and that this may be more favorable in creating facets. This result is highly unexpected considering other work in this area, particularly in alpha+beta processed materials, but is included here in order to capture all of the possible scenarios. Evans and Bache (1994) later noted that the range of specimen volumes tested by Song and Hoeppner was less than an order of magnitude which might imply that the typical variability in specimen testing may have confounded the results.

Harrison et al. (1986) also investigated Ti-829 in the alpha+beta forged, beta heat treated, and oil quenched condition. The majority of the material had a basketweave microstructure, though it was noted that a few locations in the disks had aligned colony structure due to slower cooling rates in thicker sections. The authors compared results from laboratory coupon and spin pit testing. Two different simplified disk geometries were tested which had approximately 1,000 and 10,000 times the volume of the specimens. As shown in Figure 105, dwell lifetime decreased with increasing stressed volume. Harrison et al. (1986) applied extreme value statistics (EVS) to estimate the component lifetime based on the specimen test results (Figure 105(b)).
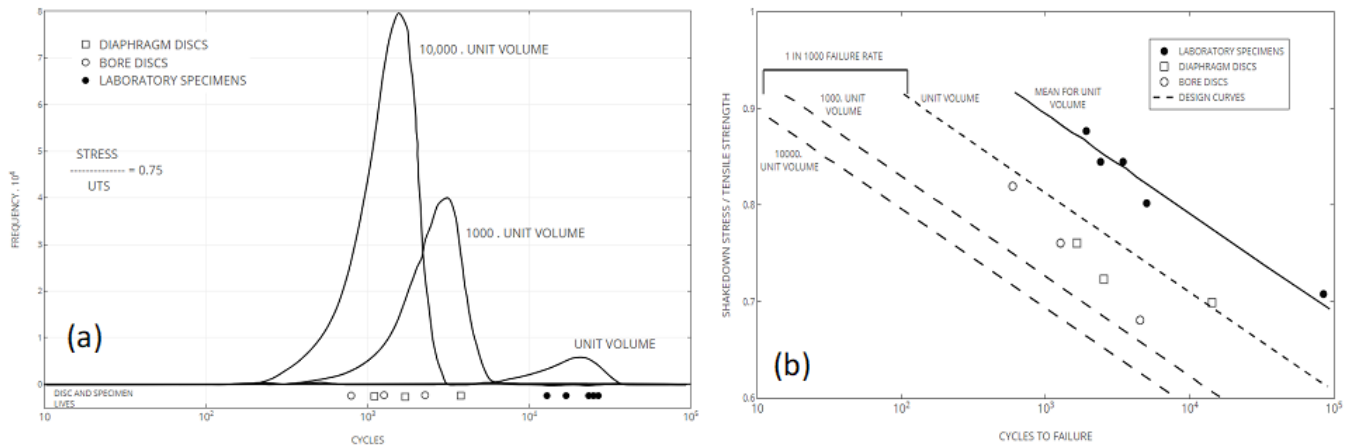
Figure 105. Effect of stressed volume on dwell fatigue lifetimes of Ti-829
(a) lifetime distributions (b) comparison of test results with failure lifetime predictions for different volumes of critically stressed material

The authors fit a set of Ti-685 dwell specimen test data (applied stress / UTS = 0.75) to a two-parameter Weibull distribution and applied EVS to estimate the B0.1 (1/1000 probability of failure) lifetimes of bore and diaphragm spin pit components. The specimen lifetimes were consistent with prediction distributions for 1,000 and 10,000 times the volume of a specimen for diaphragm and bore discs, respectively. Stress analysis suggested that the volume of material above an unspecified critical stress level would be closer to 500 and 3,000 times suggesting that volume alone could not account for the observed effects. Nevertheless, the predicted safe-life limits were conservative relative to the spin pit data. It's worth noting that elastic-plastic stress analysis was employed utilizing cyclic stress-strain data and that bulk residual stresses also needed to be considered. The use of elastic-plastic analysis shifted the location of the peak stress within the disk and this location correlated well with the location of faceted initiation sites. Furthermore, the position of peak stress and initiation location also varied with the speed of the disk in a predictable manner when the cyclic stress-strain response was considered. Harrison et al. (1986) describe the process for obtaining a cyclic stress-strain curve in detail. Briefly, this involves performing strain control fatigue testing at various strain amplitudes until the cyclic hysteresis loops stabilizes (typically at half-life) and then fitting the maximum stress versus strain amplitude data to obtain the cyclic stress-strain curve. Glinka has also posted a useful set of charts on this topic (Glinka, 2010).

Dwell initiation in components have typically been seen in smooth features such as bores, diaphragms and circumferential slots and have only occasionally been seen at stress concentrating features with low stress concentration factors (k_t). Crack origins at the root of low k_t notches also exhibit classical faceted initiation sites, which has been previously reported by

166

Evans (1987a) who also pointed out that notches have varying degrees of biaxiality that can lead to an ameliorating effect on dwell (Cuddihy, Stapleton, Williams, & Dunne, 2017). Several examples are shown in Figure 106 and Figure 107 where the test conditions include a maximum stress of 865 MPa, R = 0.05, T = 66 °C (150 °F), and a dwell time of 2.5 min. In both cases, nucleation occurs slightly subsurface but the MTR in Figure 106 is not surface connected resulting in the crack tunneling internally following the easy propagation path in the hard-oriented MTR. Figure 107 shows a similar subsurface nucleation and faceted crack propagation to the surface. From a continuum mechanics perspective, classical theories suggest that notched locations can be lifed using the results from smooth bar strain control fatigue testing (Glinka, 2010). Recall that faceted nucleation and dwell debits are generally not observed under strain control dwell fatigue loading (see Section 7.1.7) and thus the fact that the fracture surface is consistent with those routinely seen on smooth load-control samples has important implications on design and lifing strategies. A probabilistic argument has also been used to explain the effect of stress concentrations on cold dwell fatigue, in that, for high k_t features, there is only a small volume of material subject to high stresses and therefore it is highly improbable that the worst-case combination of microstructure would be present in the high stress region. The stress gradient itself is likely to be important, since a low gradient will result in a higher volume being under significant stress and therefore more microstructural units being sampled, although this also depends on how big the microstructural units are in the pedigree of material of interest. It would therefore be expected that a low k_t feature at a given peak stress would be more likely to show cold dwell fatigue behavior than a high k_t feature at the same peak stress.
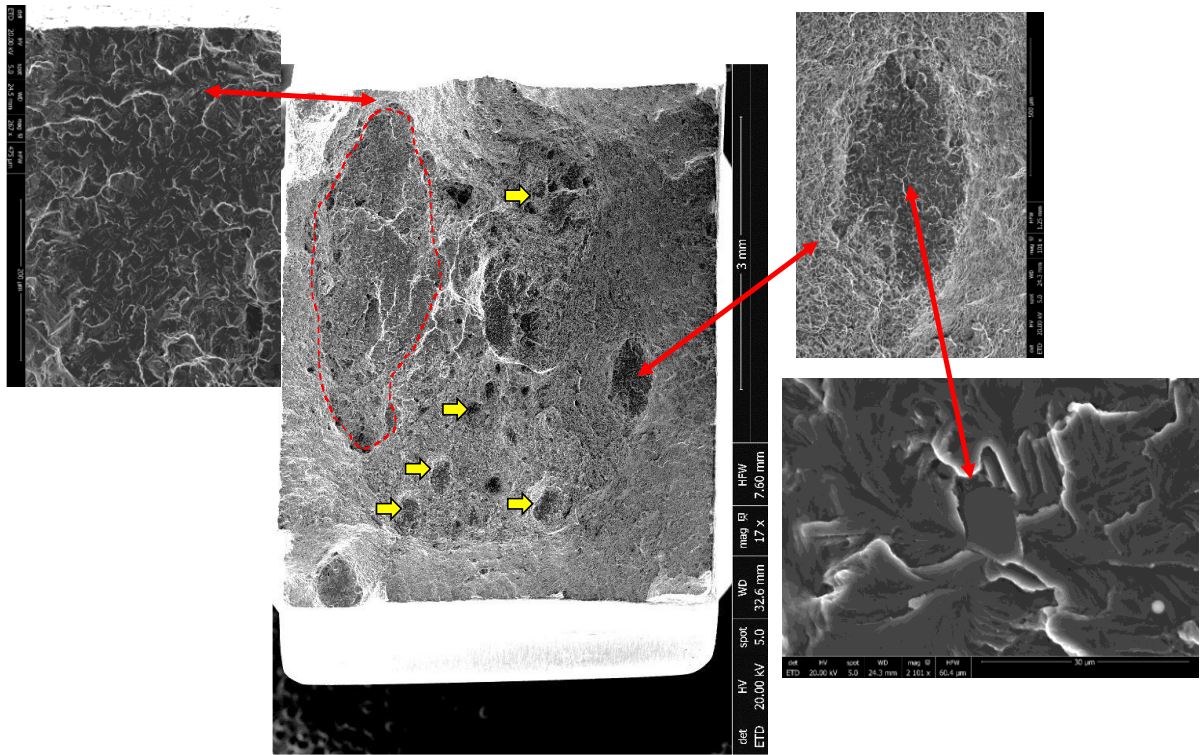
Figure 106. Fracture surface of a low kt notched Ti-6Al-4V specimen
Yellow arrows indicate additional pockets of nucleation
Photo credit: Air Force Research Laboratory
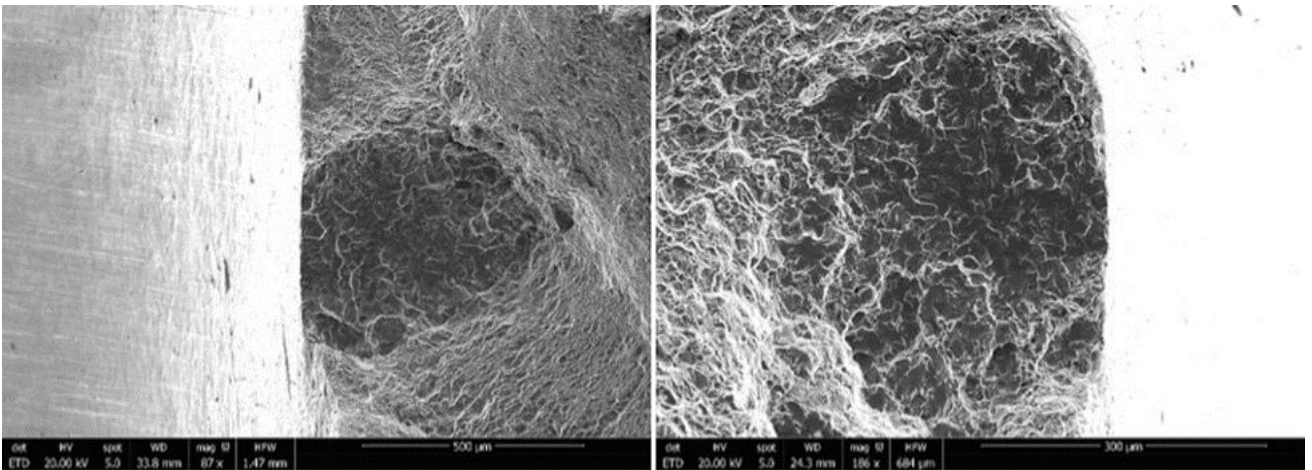
Figure 107. Fracture surfaces of low k_t notched Ti-6Al-4V specimens
Photo credit: Air Force Research Laboratory

Pilchak et al. (2017) and Tucker et al. (2016) have devised a simulation method to estimate the rate of occurrence of critical features in a given volume of material that is capable of considering the material macrotexture as well as the MTR volume fraction, MTR size distribution, MTR neighborhood distribution, and MTR aspect ratio. The authors ported DREAM.3D to the Department of Defense supercomputer 'Predator' and ran it in what is known in supercomputing literature as embarrassingly parallel mode (i.e., where each iteration of the code is not influenced by the others) to simulate 2637.6 cm^3 (160.9 in^3) of digital material. The study assumed a highly simplified microstructure with a random texture, equiaxed grains, and a quasi-unimodal grain size distribution with a mean centered at 1.5 mm diameter. Each volume was segmented into hard or soft regions with c-axes less than or equal to 20° from the stress axis and 70°-90° to the stress axis, respectively. Since the simulation was at the MTR scale and individual alpha particles were not simulated, it was assumed that each of these features contained an 'initiator grain' with the basal pole oriented near 45° to be consistent with fractographic observations (Pilchak & Williams, 2011). Simulated volumes with MTR volume fractions of 25, 50, 75, and 100% were prepared. The segmented volumes were sectioned perpendicular to an applied stress axis and the grains in each slice were analyzed to determine if there were adjacent hard/soft grain pairs as depicted in Figure 108 and the statistics across all simulated 100^3 voxel volumes were aggregated for analysis.
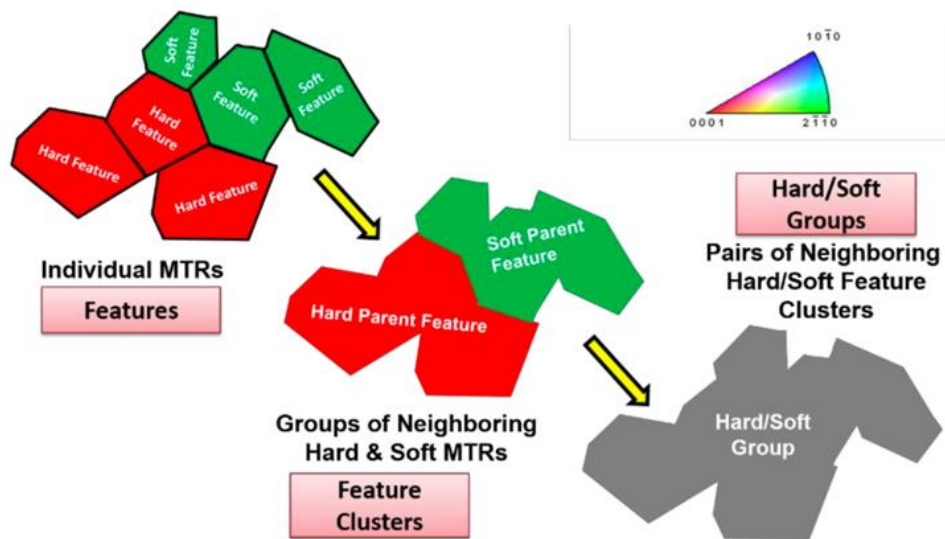
Figure 108. Grouping methodology for analyzing dwell-susceptible simulated microstructures

A second set of simulations applied the same approach to investigate volumes of 500^3 voxels. Scatter plots were used to depict the number of hard/soft pairs in each set of simulated

microstructures and the associated hard and soft MTR sizes (Figure 109). Here, each marker represents a hard/soft pair for either (a) 100^3 or (b) 500^3 digital microstructures. The marker size is proportional to shared surface area in (a), while the color corresponds to specific MTR volume fractions. The color in (b) corresponds to shared surface area with higher 'heat' indicating more shared surface area (Pilchak, Tucker, & Weihing, 2017). The authors discussed strategies to filter the data based on hard or soft MTR size, local elastic modulus, MTR intensity, and shared surface area. These filters were applied to estimate the critical number of 'weak links' present per unit volume.
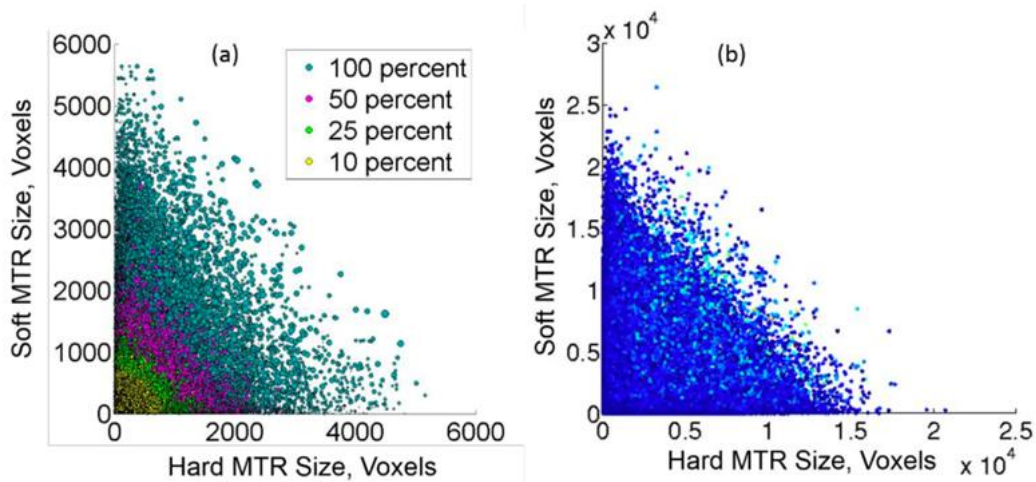
Figure 109. Scatter plot of hard grain size versus soft grain size MTR

One challenge associated with understanding the dwell fatigue capability of a particular processing route is related to the difficulty in characterizing the upper tail of the MTR distribution since large, well aligned MTRs are typically observed at crack initiation sites. EBSD analysis of random sections of the microstructure are unlikely to reveal the worst-case MTRs. An alternate approach would be to estimate the upper tail of the MTR distribution based on measured MTR sizes using one of the two prevailing extreme value statistics methods (i.e., block maxima or peaks-over-threshold). Both methods have been reviewed and are presented in an easily understood manner by Atkinson and Shi (2003).

The block maxima approach was originally applied to materials by Murakami (2019) to estimate the largest inclusion size in steel samples. In this method, a standard and constant inspection area is defined and the largest of the features of interest is obtained across multiple images. The two-dimensional area is converted to an effective three-dimensional volume based on the average size of the measured max sizes. These data are fit to a distribution and used to calculate the return period, which effectively extrapolates the distribution to the expected value that would be observed for an arbitrary number of desired inspection volumes. A downfall to this approach,

however, is that there is no upper bound to the extrapolation and thus the max size increases continuously with simulated inspection volume. With respect to cold dwell fatigue, this approach does not account for the prior beta grain size, which acts as a limiting parameter for the upper size of MTR. As discussed in Section 6, MTRs arise from the prior beta grains present in billet prior to final alpha beta work. The size of these prior beta grains represents a potential limiting parameter that will effectively restrict the maximum size of MTRs although we note that special grain boundaries sharing a common {110} plane may lead to common alpha colony orientations spanning multiple prior beta grains. To date, however, the authors are not aware of any observations that show MTR sizes that exceed the prior beta grain size from earlier stages of conversion.

The block maxima approach was applied to max MTR size prediction in the work of Pilchak et al. (2017). A bootstrapping approach was applied to subsets of the 500^3 voxel microstructures (subset sizes were 50^3, 100^3, and 250^3) until a converged set of parameters were obtained for the Generalized Extreme Value Distribution. These were used as the basis for estimating the MTR sizes in larger volumes of material (individually) as shown in Figure 110. In general, all of the predictions were reasonable, but the error estimates reduced substantially with increasing number of subsets. The top 25 largest MTRs from all 1,000 simulated 500^3 structures are plotted as well for comparison. All predictions were conservative except for a single data point at ~21,000 voxels. Later inspection revealed that this was two large MTRs in a given slice connected by a small number of voxels.
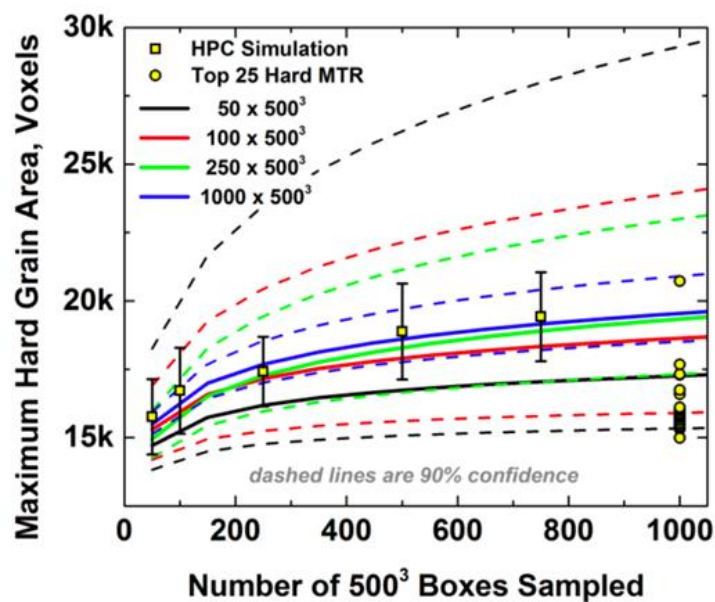
Figure 110. Extreme value statistical extrapolation for dwell-susceptible microstructures

While not utilized in the papers by Pilchak et al. (2017) and Tucker et al. (2016), the peaks over threshold approach may actually be a more suitable way to estimate the tail of MTR sizes (or other MTR metrics of interest). Atkinson and Shi (2003) were the first to apply this method to material to improve on the characterization of inclusions in clean steels. Donegan et al. (2013) have also applied this method to analyze the tail of grain size distributions and has a clear and easily understood description of the method. Further, there are packages available for Python and the statistical computing software R (The R Foundation, 2023) to perform this analysis readily. The main benefit is that all data from the measured feature of interest is used as opposed to only the maxima. Thus, more information is obtained from each set of characterization data and no large sizes are excluded due to being in close proximity to another large feature. The approach involves plotting the distribution of data, u, and selecting a threshold value x_i and fitting all data $u \geq x_i$ to the Generalized Pareto Distribution (GPD). The fit parameters are stored in an array and then the smallest datapoint is exchanged for x_{i+1} and the data are fit again, and the parameters stored. This is repeated until there are very few data points remaining in the tail and the reliability of the fit is poor. The scale parameter is transformed into a modified scale parameter and this along with the shape parameter and mean excess values above the threshold are plotted against the threshold value to produce so-called diagnostic plots (Figure 111, modeled after Donegan et al. (2013)). The threshold choice is made by analyzing the diagnostic plots for a region where the modified scale and shape parameters are relatively stable with threshold, the mean excesses are minimized, and the error bounds on these parameters remain small. The set of fit parameters for this threshold can then be used to calculate the return period. A major benefit of the peaks over threshold method is that when the shape parameter is positive it asymptotically approaches an upper limit. For MTRs, it is reasonable to assume that there is an upper limit which is related to the size of the alpha colonies following beta quenching of the billet during conversion. For the reader interested in extreme value theory, Beretta's recent review article is a good starting point (Beretta, 2021) in addition to the other papers referenced in this section.
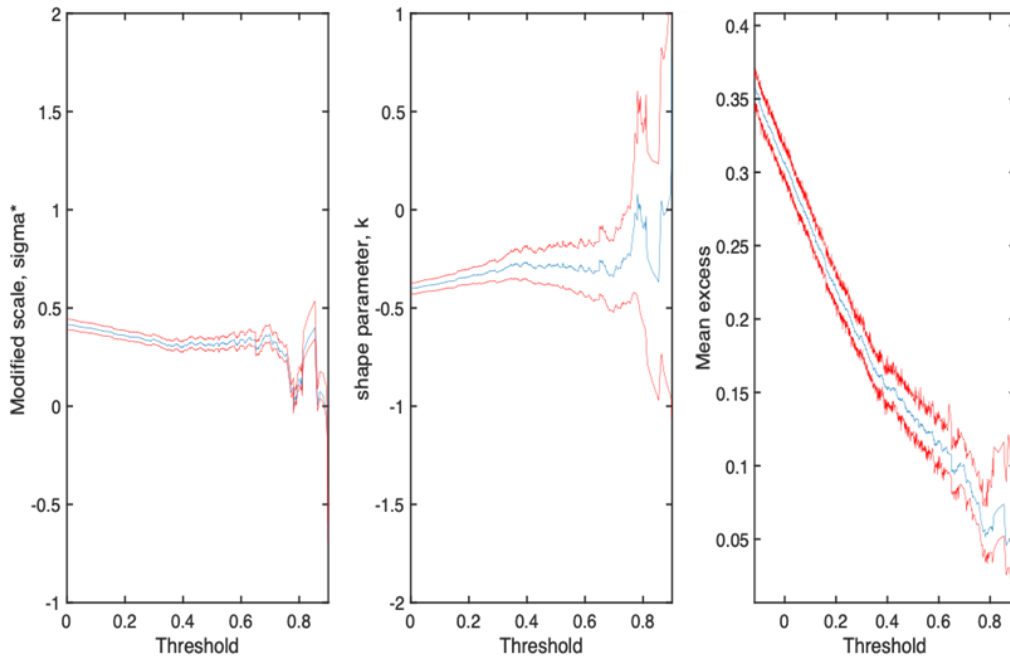
Figure 111. Example diagnostic plots for the peaks over threshold method

7.1.5 Load ratio

A very limited amount of work has been published related to load ratio effects on dwell performance. Bache et al. (1997) have reported a small amount of data on alpha+beta forged Ti-834. Tests were performed at R = -0.5, 0.1, and 0.5 at maximum applied stress levels of ~94% and 100% of the monotonic yield strength. In contrast to classical views on fatigue, where stress range is the primary driver of lifetime, the authors observed a *decrease* in life for R = 0.5 tests (i.e., increased mean stress) compared to R = 0.1 while tests performed at R = -0.5 increased the lifetimes (Figure 112, modeled after Bache et al. (1997)). This was attributed to the continuous application of a mean stress which encouraged strain accumulation and load shedding whereas the lower R tests promoted slip reversal, potentially dislocation annihilation, and stress relaxation. Evans (1998) later reported additional data illustrating the effect of hold time and load ratio (Figure 113) and the same trends were found. In a separate study on the single-phase Ti-7Al alloy, Brandes (2008) and Mills et al. (2018) obtained conflicting results. The total strain to failure and dwell fatigue lifetime was observed to scale with the absolute value of the load ratio. The authors acknowledged the data of Bache et al. (1997) and were unable to identify the source of the discrepancy.

However, the work on Ti-7Al resulted in relatively short lifetimes (e.g., < 1,000 cycles) and hence the contribution of crack growth to total lifetime was likely more important in this case.

This is an area that warrants further investigation, especially as it relates to the susceptibility of fan and compressor blade components which may experience an elevated mean stress.
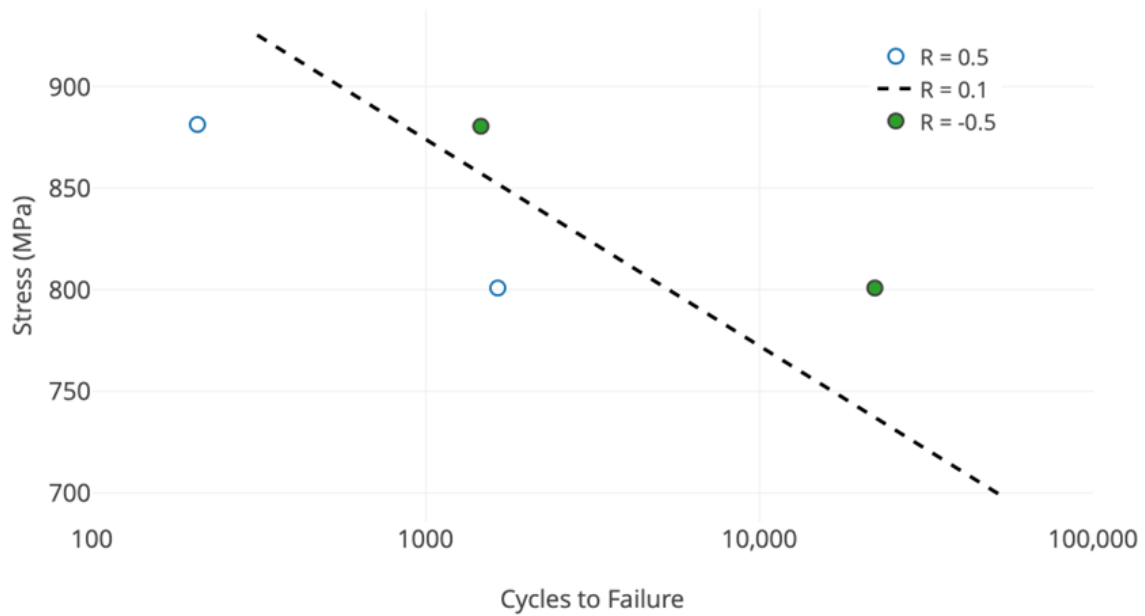
Figure 112. Effect of load ratio on dwell fatigue of Ti-834 bar with bimodal microstructure
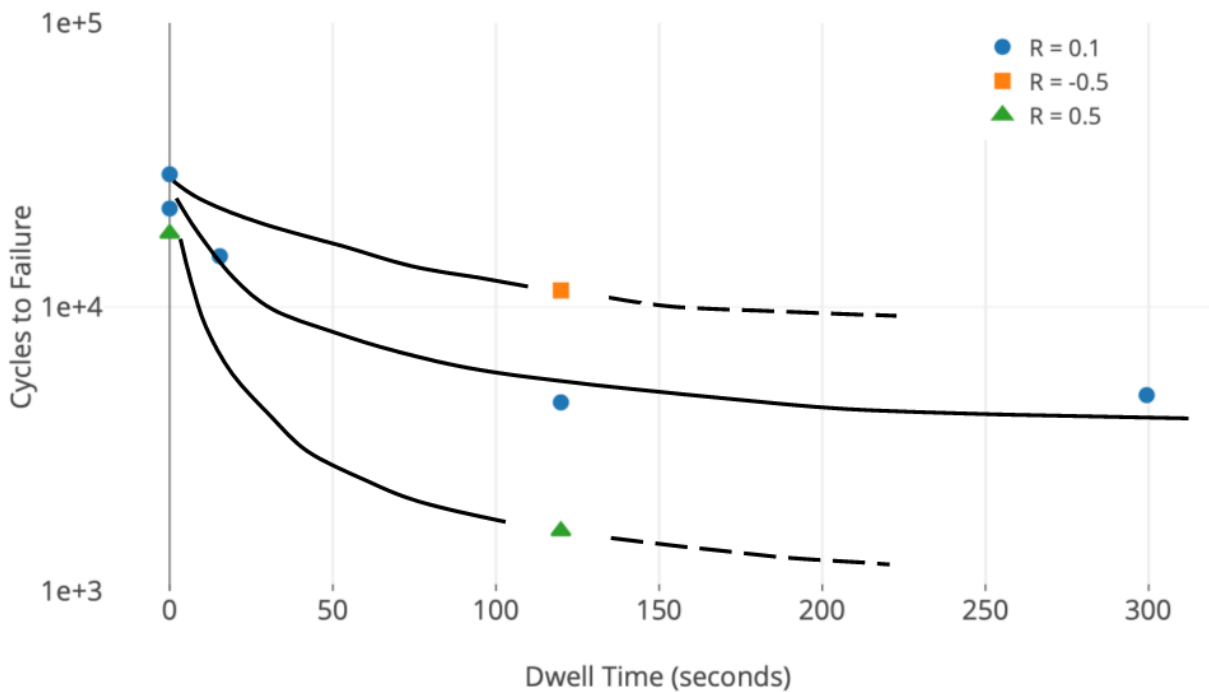
Figure 113. Effect of hold time and load ratio on dwell fatigue of Ti-834 disk material

7.1.6 Loading rate

Review of the literature reveals a range of ramp rates used to achieve the peak stress value. Most studies utilize a 1, 2, or 3 second ramp rate, but a wide range of values have been utilized (e.g., 0.05 seconds (Xi, G.; Lei, J.; Qiu, J.; Ma, Y.; Yang, R.;, 2020) to 200 seconds (Song, Li, Wang, Huang, & Sun, 2019)) which have been summarized by Zheng et al. (2022) (Figure 114). This effectively results in a variable strain rate for tests performed on the same material but tested at different stress levels. As discussed, titanium exhibits room-and-low-temperature rate-sensitivity and hence these tests are actually being performed at different fractions of the yield strength. The tensile tests used to establish monotonic response which is used in selecting peak dwell stresses are typically performed in the $10^{-4} \sim 5 \times 10^{-3}$ s^{-1} range so care must be taken to ensure that the loading rates during dwell testing do not deviate significantly from the values used to establish yield behavior. To this end, Figure 115 highlights the strain rate as a function of peak stress for various reported ramp rates assuming an elastic modulus of 116 GPa. In general, 1 second ramp rates are on the high side of typical tensile test strain rates while slightly slower rates in the 2 ~ 5 second range are more commensurate with common tensile test strain rates. Future work should strive to use identical loading rates for tensile and dwell tests and the strain-rate should closely mirror that found in components.
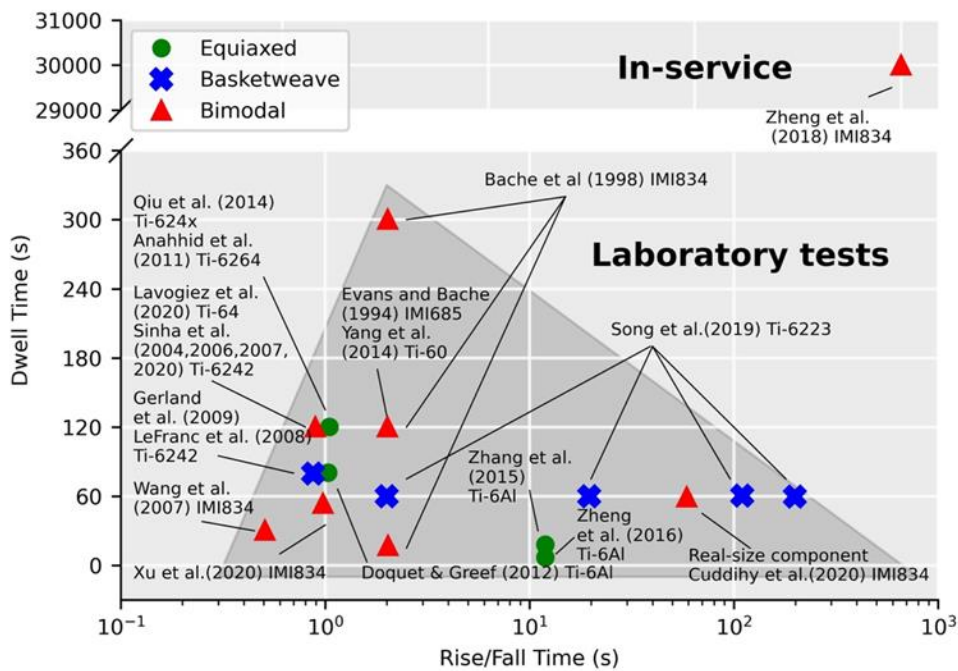
Figure 114. Summary of dwell times as a function of rise and fall times

As discussed in Section 2.3, each family of slip systems exhibits its own rate dependence, and the basal slip system shows the highest rate sensitivity of all in tension (May, 2010). Given that this is the critical orientation with respect to crack nucleation, the loading rate should be an important factor in dwell fatigue capability. Song et al. (2019) were the first to report the effect of loading rate on the dwell fatigue response based on testing of the Ti-6Al-2Sn-2Zr-3Mo alloy with a basketweave microstructure. The authors investigated loading/unloading times of 2, 20, 110, and 200 seconds under fully reversed loading at a stress level of 95% of the yield strength. Unfortunately, the loading rate for the tensile tests were not reported. However, dwell fatigue testing revealed a ~25% decrease in average lifetime for the longest loading time compared to the shortest. While not discussed by the authors, the underlying cause of this debit is related to the rate-sensitivity of the yield strength. Slow loading rates suppress the proportional limit and yield strength resulting in deformation earlier in the cycle during the ramp to peak stress which may result in increased strain accumulation in the soft grains thereby enhancing the degree of load shedding. Further, differences in strain rate will also impact the number of active dislocation sources and potentially the number of active slip systems. It is worth noting that the cycle counts reported in the study by Song et al. (2019) were relatively short (~500 cycles to ~1300) cycles and thus a significant portion of the specimen lifetime was consumed by crack propagation. Hence, future efforts should focus on lower applied stress levels or shorter dwell times as well as under zero or slightly positive load ratio.
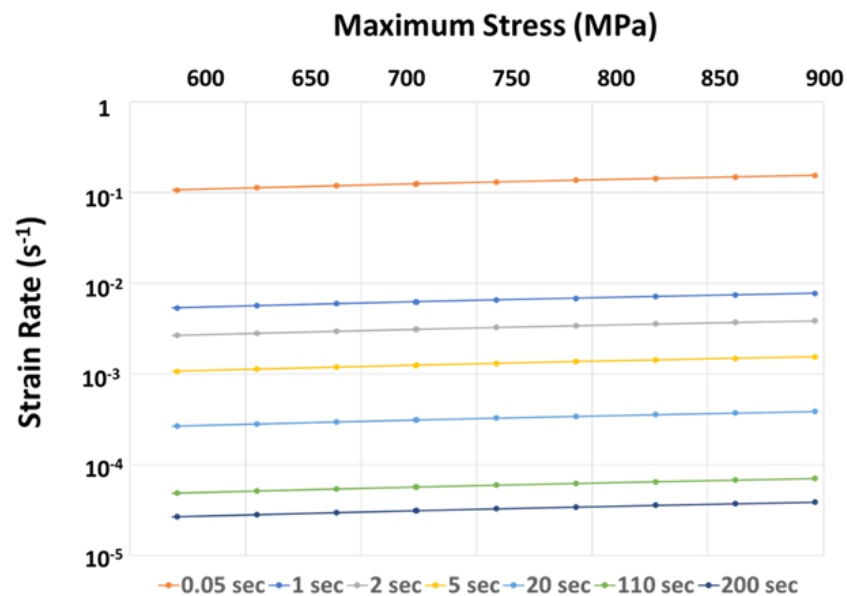
Figure 115. Correlation between peak stress, ramp rate to max stress, and applied strain rate

We note that there is also likely a stress-level dependence to the loading rate effect. Lerch and Arnold (2014) have noted that the slower loading rates will lead to increased strain accumulation rates under creep conditions for cases where the material exceeds the temperature-and-rate dependent 0.02% offset yield strength. If the peak applied stress is below this value, it would be expected that creep rates would be lower and thus we surmise that a loading-rate impact to the dwell debit may not be observed.

7.1.7 Load control vs. strain control

The question of whether to run load control or strain control tests to inform low cycle fatigue lifing methods is often one of design philosophy and applied stress level. For low cycle fatigue, design engineers often prefer strain control whereas in the HCF regime load control tests are preferred. The choice is also dependent on the details of the loading that will be encountered by the component in service. Classical approaches often employ strain control testing of smooth bars for notched locations where one anticipates local deformation that is surrounded by a nominally elastic body, whereas smooth locations, like the bore of a disk where stresses are intentionally kept low, are often lifed using load control specimen test data. While these approaches have generally worked well in the past, the potential for cold dwell fatigue failure necessitates alternate approaches that may be unfamiliar to classically trained design engineers. The key here is ensuring that the fracture surface features observed during specimen testing matches the fracture surface observed on components that have fractured due to dwell fatigue (see Section 7.1.11). Strain control specimens generally do not show appreciable dwell debits and do not produce faithful fracture surfaces.

In this context, it is noteworthy that strain-controlled testing at temperatures considered to be in the cold dwell regime have not shown the debit in life associated with the dwell cycle (Winstone & Weaver, 1985). This is because stresses relax during the hold under strain control, which precludes the development of intense dislocation pileups that result in early crack nucleation. The application of a strain-control dwell hold is found to slightly increase the inelastic strain range (i.e., the width of the hysteresis loop), but lives are found to be long because stresses relax quickly early in the test and significant compressive residual stresses are developed in order to reach zero displacement.

With regard to stress analysis of components, it is worth reiterating that Harrison et al. (1986) advocate for the use of dynamic stress-strain curves (i.e., cyclic stress strain curves) to describe the constitutive response of the material. This is due to the fact that titanium alloys generally exhibit cyclic softening (Figure 116) (Chesnutt, Thompson, & Williams, 1978; Evans W. , 1998) although certain combinations of microstructure, texture, and strain-path may lead to cyclic

hardening as well (Chesnutt, Thompson, & Williams, 1978). As a result, it is best practice to establish the constitutive response for a particular alloy and processing route for use in finite element analysis.
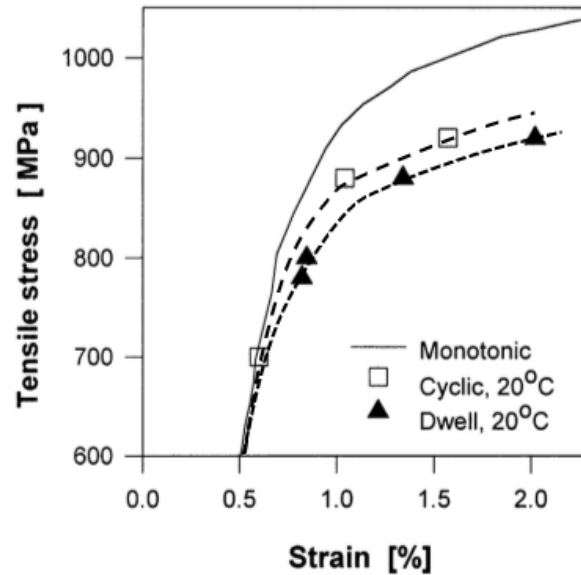
Figure 116. Comparison of monotonic, cyclic, and dwell stress-strain response

Dunne et al. (2007) have also addressed load and strain control from a modeling perspective using CPFEM. The authors report that load shedding is maximized under load-control dwell conditions whereas stress relaxation occurs in the soft grain under strain control. Zhang et al. (2015) investigated this effect in more detail and showed that the degree of strain accumulation, stress relaxation, and hence load shedding onto the hard grain is significantly reduced under strain control loading. However, isolated facets with characteristics (spatial orientation, crystallographic nature, and surface topography) similar to those observed on dwell fatigue fracture surfaces have been observed following stress relaxation testing (Evans W. , 1987a) indicating the possibility of initiating by a similar mechanism under strain control conditions. In this case, the improved lifetime under strain control dwell conditions may be at least partially attributable to the decreased stress range imposed on the crack due to the compressive residual stresses developed in the material when it is returned to zero displacement.

7.1.8 Temperature

Life debits due to cold dwell fatigue are generally seen at temperatures below ~200 °C (400 °F) (Neal, 1988), which has been realized through mechanical test programs as well as modeling and simulation. Below this temperature, however, the temperature at which the maximum dwell debit occurs appears to vary by alloy type with some more heavily beta-stabilized alloys showing no

178

major effect at all. There have been several reports in the literature that the dwell debit increases just above room temperature. These trends are illustrated schematically in Figure 117 which shows the dwell debit as a function of temperature and various intrinsic factors including the degree of microtexture as well as other microstructure variables (primary alpha, transformed beta morphology, etc.) and variations in chemistry. Based on the significantly lower rate of occurrence of component dwell experience in alpha + beta alloys, it is surmised that the intrinsic factors have a smaller effect compared to near-alpha alloys. In general, there has been little published work on elevated temperature effects as compared to room temperature and this area needs significant further investigation. It is important to focus these studies on temperatures up to about ~200 °C (~400 °F) (Neal, 1988).
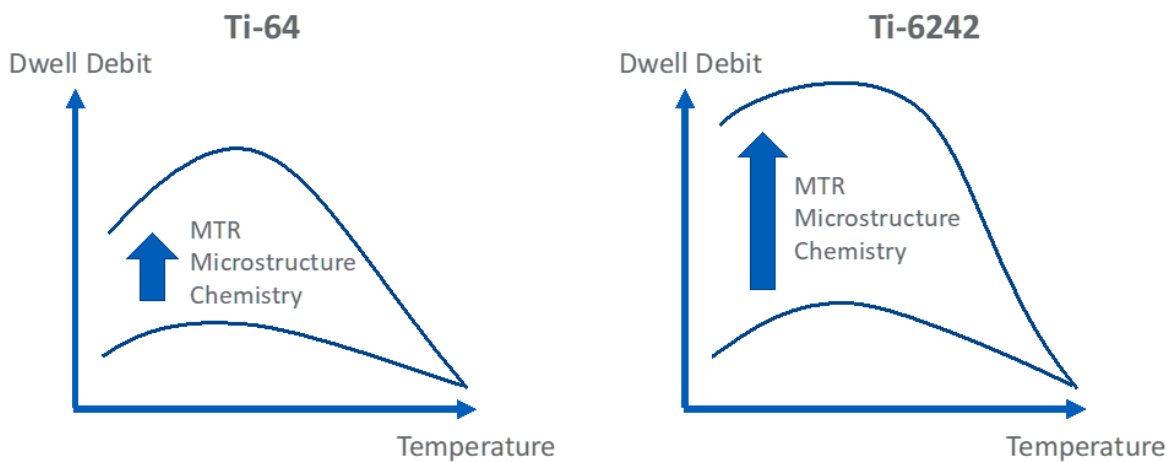
Figure 117. Schematic effect of temperature on dwell fatigue debit for Ti-6Al-4V and Ti-6242

Winstone and Weaver (1985) investigated the *strain-control* dwell fatigue behavior of the near-alpha alloy Ti-829 in the beta-annealed and aged condition in the temperature range of 20 °C to 300 °C. The authors observed that a 120 second hold at 20 °C and 80 °C increased the inelastic strain range for a given cyclic life whereas the relationship was unchanged at 120 °C and 300 °C. Creep-induced stress relaxation occurred at the two lower temperatures investigated which resulted in a small cyclic stress range that increased the life for a given inelastic strain.

Spence et al. (1997) investigated the temperature dependence of dwell fatigue in Ti-6246 in the beta forged and heat-treated condition and observed no significant debits at 20, 80, and 150 °C on a UTS-normalized basis (Figure 118). This was attributed to the finer scale of the transformation product and the lack of large regions of aligned alpha phase that typically led to the formation of large slip bands and strong dislocation pileups that induce load-shedding. In addition, the lack of crystallographically aligned alpha eliminates the potential for the formation

of large, faceted initiation sites, which significantly reduces crack growth rates during the early stages of crack growth.

The effect of thermal soaks at temperatures greater than 200°C following exposure to cold dwell conditions has also been investigated (Xu, Fox, Rugg, & Dunne, 2020). This showed experimental data in Ti-834 alloy whereby strain accumulation under cold dwell loading is significantly reduced by introducing a second lower load and also by incorporating a higher temperature soak on every loading cycle. This phenomenon was predicted using a temperature-coupled discrete dislocation dynamics modeling approach and appears to be due to negative creep occurring during both the lower stress hold and in the thermal soak.
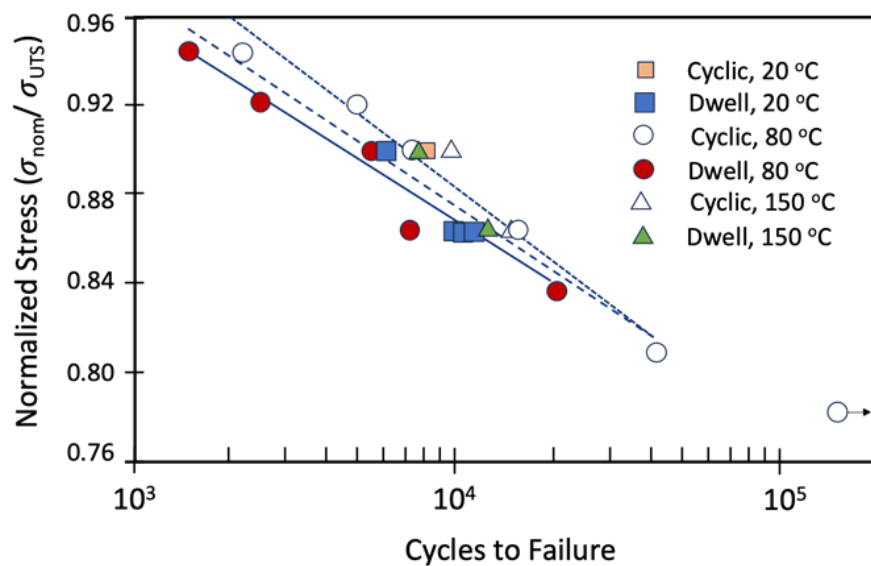
Figure 118. Effect of temperature and waveform on fatigue response of Ti-6246

Zhang et al. (2015) have analyzed the role of temperature on dwell fatigue using CPFEM and Ti-6Al as a model material system. The authors reported that the strongest stress redistribution was observed at 120 °C under load control dwell conditions and this was related to a coupling between the crystallographic slip rate and slip system dislocation hardening. At high temperatures (e.g. ~230 °C), grain-scale load shedding was significantly diminished as a result of more rapid stress relaxation during the dwell hold.

The mechanistic basis for the temperature dependence of dwell fatigue has been addressed by Zheng et al. (2017) using a discrete dislocation plasticity model that incorporates both thermally activated dislocation escape from obstacles and slip transfer across grain boundaries. The authors analyzed a wide range of temperatures for the Ti-6242 and Ti-6246 alloys. The key parameters in the model included the time constant associated with thermally activated dislocation escape from

obstacles and the dwell time. The time constant is defined as the inverse of the successful dislocation jump frequency. They analyzed several combinations of these parameters and arrived at the following conclusions:

- Low temperature or high activation energy reduces dwell sensitivity because dislocations are pinned on the slip plane leading to backstress that inhibits further dislocation nucleation from the original source. In this case no significant load shedding is observed.

- High temperature or low activation energy leads to rapid escape from obstacles and eventual pileup against grain boundaries. While strong slip bands are formed, the system saturates quickly before the stress hold begins leading to intermediate stresses at the hard-soft grain interface, but no further stress redistribution occurs during the dwell period.

- In the intermediate regime, where the time constant associated with dislocation escape is similar to the time of the dwell period, it is possible for dislocations to be pinned and escape during the ramp to peak stress and also during the hold at peak stress. When dislocations escape from obstacles, they glide to the grain boundary thereby relieving backstress on the slip plane allowing additional nucleation. The new dislocations again can be pinned, escape, and enter the pileup during the dwell period resulting in significant load shedding during the dwell period. This process is shown schematically in Figure 119 for the case where temperature and activation energy are such that the time constant associated with thermally activated dislocation escape is similar to the time associated with dwell loading.
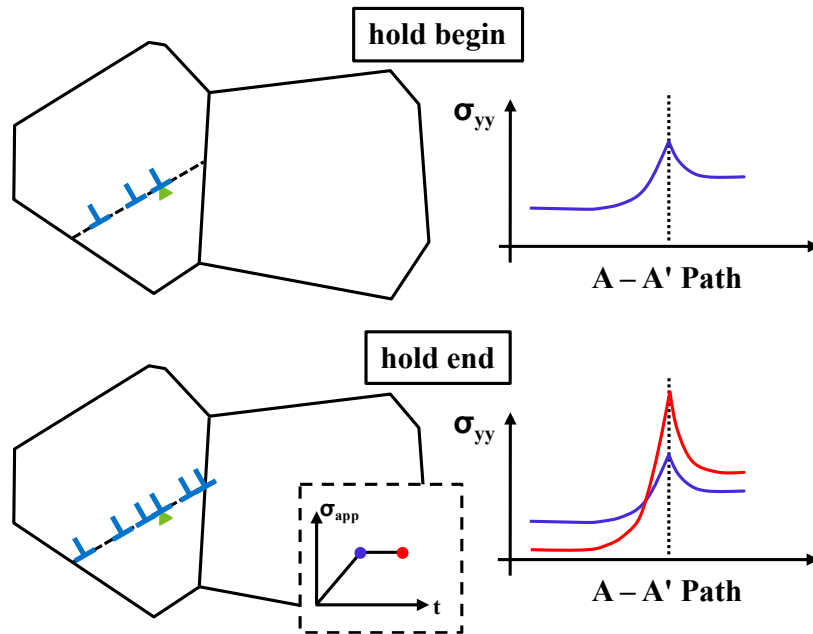
Figure 119. Schematic representation of dislocation-obstacle interaction

7.1.9 Pre-straining or pre-cycling

Several investigators have looked at the effect of prestrain on subsequent creep or dwell fatigue behavior. While this is an area that would benefit from further research, there are a few things that can be gleaned from the existing literature. First, the amount of prestrain can either increase, decrease, or not affect the dwell debit. Second, the method by which the prestrain is introduced (i.e., tensile vs creep vs fatigue) apparently has an impact on subsequent material behavior.

Odegard and Thompson (1974) prestrained Ti-6Al-4V samples to various degrees of strain at 95% of the alloy yield strength and subsequently unloaded them and performed additional creep tests at 70, 80, or 90% of the yield strength. In general, the prestrain reduced subsequent creep rates, though a critical strain of 5 x 10^{-3} was required to induce the effect for 90% subsequent creep loading. The prestrain effectively shut down subsequent creep upon reloading to 70% of the yield strength for the smallest two prestrains (2.5 x 10^{-4} and 10^{-3}) and negative creep was observed for the prestrain of 5 x 10^{-3}. The authors hypothesized that this was due to exhaustion of dislocation sources during creep loading at the initially higher applied stress.

Whittaker and Evans (2009) investigated the effect of prestrain introduced via quasi-static loading at a rate of 0.005 s^{-1} in tension and compression on creep strain accumulation in Ti-834. For prestrains of +2% and -2%, there was an increase in strain rate and a reduction in the time to failure compared to the baseline material. Prestrains of 8%, however, introduced sufficient

dislocation content to present enough barriers that strain accumulation was significantly reduced during subsequent creep testing.

Finally, von Thungen (2017) has investigated the effect of precycling on the dwell fatigue response of beta-processed Ti-6242. The strain-time history of virgin material was compared to that of material that was precycled under constant amplitude, continuous cycling fatigue. The precycling consisted of applying fatigue cycles corresponding to ~1/3 of the anticipated dwell fatigue lifetime for the applied stress level, which was at the 0.2% offset yield strength for the condition studied. The strain accumulation of virgin samples subjected to 2-min dwell cycles at room temperature was much higher than that for pure fatigue cycling (Samples D1 and D11 versus sample D13 in Figure 120).
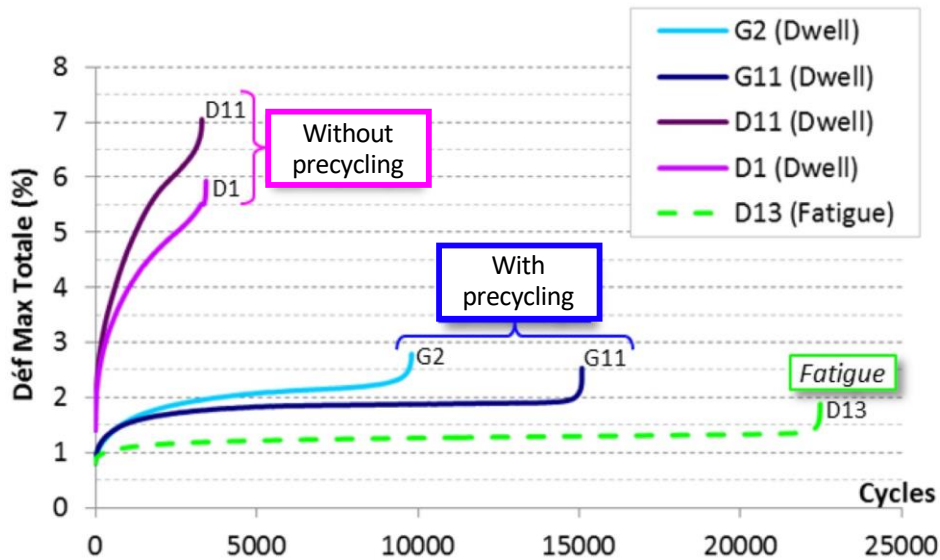
Figure 120. Effect of precycling on strain accumulation under dwell fatigue loading of beta-processed Ti-6242

By comparison, samples G2 and G11, which were precycled for ~1/3 of the anticipated fatigue lifetime (~7000 cycles), exhibited much smaller strain accumulation rates than virgin samples following a brief transient regime. Overall, the lifetimes were of the order of 2.5 ~ 3.5 longer. It is worth noting that the cycle count in Figure 120 does not include those incurred during precycling. The beta-processed microstructure investigated had aligned colonies and thus it may be hypothesized that the precycling under cyclic fatigue developed dislocation debris at alpha/beta interfaces. This in turn may have provided a series of closely spaced obstacles which could diminish the strength of the pileup formed during subsequent dwell loading. Again, this is another area for future investigation that has important implications on fielded components.

183

7.1.10 Bulk residual stress

Evidence from component testing (see Section 8) indicates that accounting for bulk residual stress is necessary to accurately predict failure locations and therefore the failure mechanism itself. Residual stresses can be predicted with good accuracy using commercial finite element process modeling codes like DEFORM™ and Simufact™ provided that accurate flow stress and thermal boundary conditions are utilized. Such data includes accurate elastic and thermophysical properties, elastic-plastic response obtained from concurrent cooling/straining tests (Semiatin, Fagin, Goetz, Furrer, & Dutton, 2015) as well as accurate processing information (transfer times, cooling rate, etc.). Glavicic et al. (2010) have discussed the formation of residual stresses and have briefly discussed the importance of bulk residual stresses as they relate to cold dwell susceptibility. Figure 121 shows the residual stress profiles around a critical feature on a component for two different forging and heat treat sizes, '1' and '2' in the as machined and shot peened conditions. Route '1' produces compressive bulk residual stresses at the critical location whereas Route '2' shows a moderate sized zone of bulk tensile residual stress. While the application of shot peening creates a compressive surface residual stress in both cases, this must be balanced by subsurface tensile residual stresses. The magnitude and size of the tensile stressed region, however, is substantially different. Route '1' produces a lower maximum tensile stress over a very small region of material while Route '2' leads to residual stresses about two times greater that cover a significantly larger volume of subsurface material. This work emphasizes the importance of process modeling to understand and manage the effects of residual stresses on dwell fatigue susceptibility. While shot-peening-induced residual stresses can delay surface-initiated low cycle fatigue, it may be detrimental to dwell fatigue capability in instances where large volumes of tensile residual stresses are developed. This, of course, also depends on the applied stresses during service.
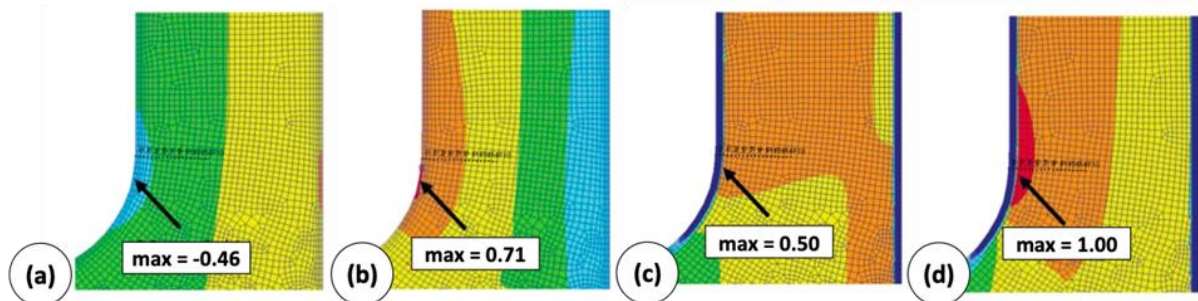
Figure 121. Residual stress prediction for a component feature for two different processing routes *(a) and (b) show Route '1' and Route '2' in the as-machined condition while (c) and (d) show Route '1' and Route '2' after a supplemental shot peening procedure*

7.1.11 Importance of fractography

It is suggested that fractography and metallographic analysis immediately below the fracture surface, including an assessment of MTRs via EBSD, be performed on all fatigue and dwell fatigue specimens. This will help rationalize differences in lifetime among a group of specimens tested from the same lot of material or across different heats/lots. Key features of interest include:

- number of initiation sites

- location of each initiation site (i.e., surface vs. subsurface) and fractional radial position for subsurface

- presence of any pores or melt-related anomalies at the origin

- size and aspect ratio of the MTR(s) at each crack origin and whether or not they intersect the free surface (this can be estimated from the fracture surface, but metallographic preparation and EBSD is the preferred route)

- morphology of fracture surface in secondary alpha phase for bimodal microstructures

- presence or absence of classical fatigue striations

- crack aspect ratio

- final crack length

- fraction of ductile overload, especially for samples with lifetimes below ~1,000 cycles; this gives an indication of whether or not the specimen-specific yield strength was exceeded during testing; specimens with no faceted initiation sites or with a significant fraction of ductile overload near the origin should be excluded from analysis on a lack of similarity to the mechanism which represents component behavior

With relatively small total cycle counts for coupon testing, crack growth may constitute a sizable fraction of the lifetime. For example, using a simple model based on linear elastic fracture mechanics where crack growth was accelerated by a factor of 10x inside the initiating MTR, Pilchak (2014) showed that lifetime could vary by ~1/3 depending on the location of the crack initiation site for the constant MTR size and aspect ratio used in the simulations. Near-surface-initiated cracks had lower lifetime compared to subsurface initiated cracks due to the step-increase in K_{max} and ΔK (i.e., driving force for MTR-assisted small and long crack growth, respectively) when the former breaks through to the surface at a smaller cycle count than the latter (Figure 122).
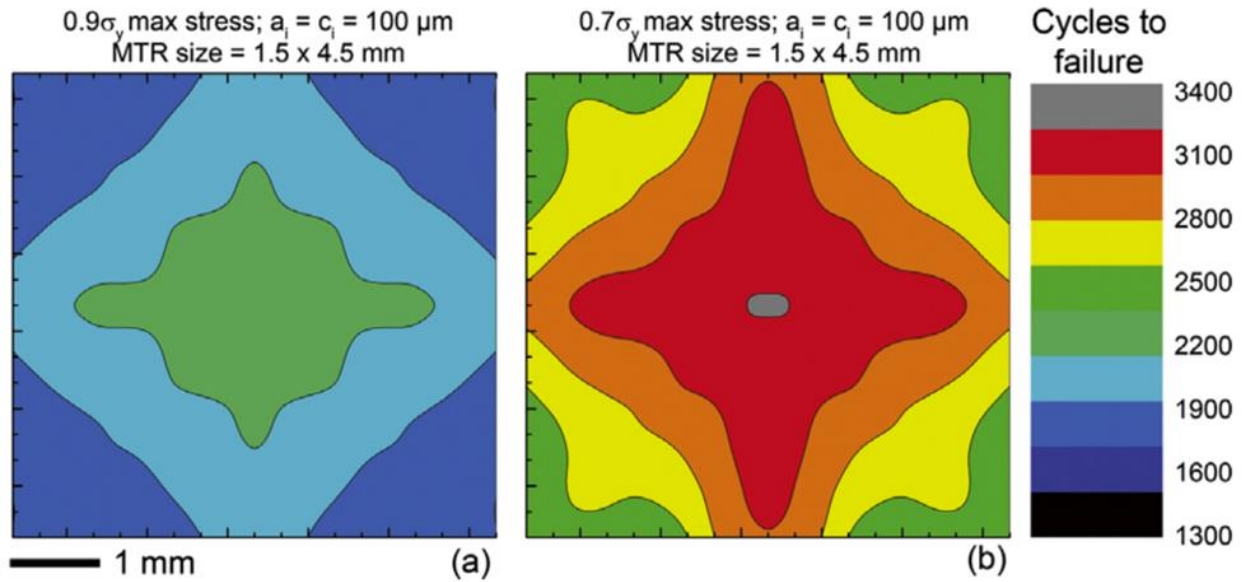
Figure 122. Effect of crack initiation position on dwell lifetime at (a) high and (b) low stress

7.2 Accelerated tests for dwell sensitivity

Dwell fatigue testing on servohydraulic test frames is expensive compared to standard fatigue testing due to the long cycle times for the typical two-minute dwell tests. For example, a standard LCF test at 0.5 Hz will accumulate 10,000 cycles in 5.5 hours, while a dwell fatigue test with a 120s hold requires approximately 14 days to accumulate 10,000 cycles. Consequently, there is great interest in the industry to develop low-cost test strategies and accelerated tests for dwell sensitivity. Such tests could be used for rapid screening when developing new processing strategies or understanding the impact of process deviations. While there are no industry-standard or American Society for Testing and Materials (ASTM) accelerated tests, there are several promising approaches.

Since strain accumulation at max stress is an essential part of the dwell fatigue failure mechanism, creep testing represents one possible proxy test for dwell fatigue that can be performed for lower cost and without the use of servohydraulic frames. The fracture surfaces of creep specimens show striking similarities to dwell fatigue fracture surfaces when tested at the same maximum stress level (Pilchak & Williams, 2011). These similarities include subsurface faceted nucleation and extensive faceted growth where the individual facets have similar spatial, crystallographic, and morphological characteristics. Since dwell fatigue crack initiation is a local phenomenon, comparison of macroscopic creep behavior can provide directional guidance, but care must be taken in interpreting the results as there can be significant scatter in creep response for samples tested under identical conditions, especially when large MTRs are present. In most

186

cases, there is good inverse correlation between creep rupture time and total strain to failure, but this trend does not always hold. Work performed by AFRL (Pilchak, John, Larsen, Jha, & Jha, 2020) showed a strong correlation between the *transient* creep behavior and dwell fatigue lifetime. Figure 123 shows the results from dwell fatigue tests at a range of stresses for Ti-6Al-4V between 750 and 900 MPa. Creep strain was measured by way of an extensometer during these tests and a strong correlation was found between the total strain at the end of the first 2.5-minute dwell cycle and cycles to failure. This correlation suggests that the relative dwell fatigue susceptibility for samples from various processing routes and/or microstructures could be compared by running a small number of dwell fatigue cycles while monitoring strain without necessarily fracturing the samples. This approach may be a better proxy for dwell susceptibility than generating creep curves to failure since creep strain accumulation rates at longer times can be impacted by the number of cracks that form in the gauge section. While showing initial promise, this approach requires further validation.
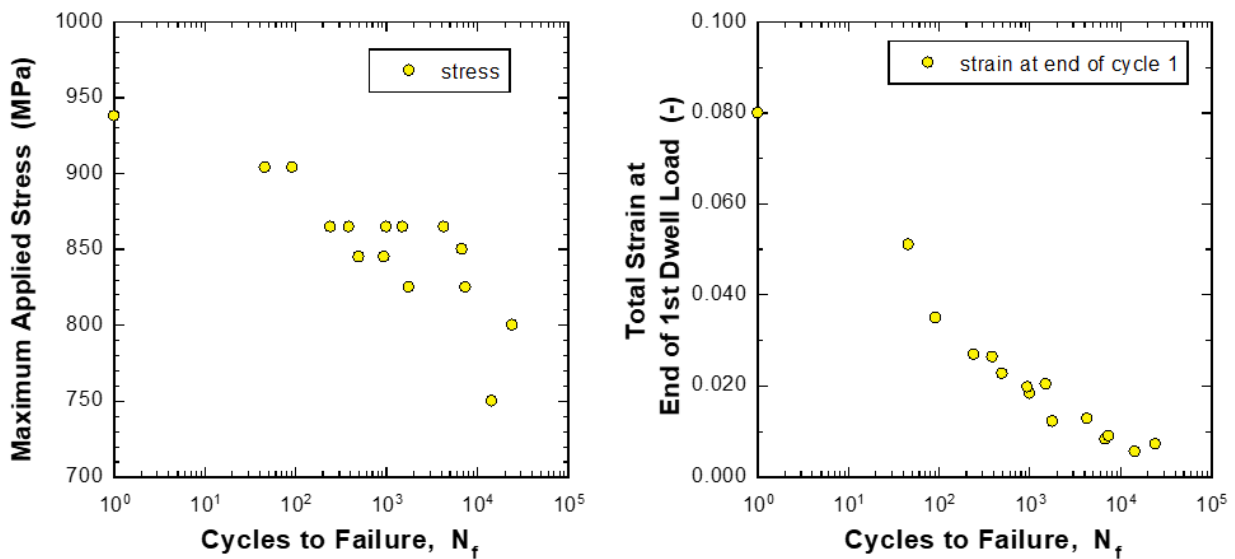
Figure 123. Results from smooth bar load control dwell tests of Ti-6Al-4V (left) Correlation between total strain at the end of the first dwell cycle and cycles to failure (right)

GE has developed and patented a method to apply cyclic loading to a sample using a creep-rupture frame. The creep frame is modified to use a fluidic "muscle" that expands and contracts to apply the load to a specimen (U.S. Patent No. 20,090,314,100, 2009). This approach may provide a less expensive alternative to servohydraulic testing.

As discussed in Section 5.2, sustained load cracking of 60º V-notched specimens has been shown to induce a dwell effect and produce the correct fracture features in Ti-6Al-4V (Neal, 1988). As

shown in Figure 53, the material must have suitable texture with basal poles approximately normal to the stress axis in order to induce the effect. Thus, one obvious downside of this approach is that the machined notch may not intersect an MTR, which could give misleading results for forged material which exhibit wide variations in microstructure and microtexture.

The fracture surface of samples that have failed by SCC in 3.5% NaCl solution also show very similar characteristics to dwell fatigue fracture surfaces (Pilchak, Young, & Williams, 2010; Pilchak & Williams, 2011). Similar to observations during creep testing, SCC samples also exhibit large, faceted regions through suitably oriented MTRs with all of the same characteristics in terms of spatial and crystallographic orientations as well as facet surface morphology. Thus, SCC tests performed either under constant load or under slow strain rate tension (strain rates of 10^{-6} to 10^{-7} s^{-1}) may provide a quick and affordable screening test to compare dwell susceptibility of different processing routes or alloy compositions as they take considerably less time (minutes to hours) than dwell fatigue testing. Similarly, Shaniavski and Losev (2003) noted a loose correlation between the area fraction of faceted features on the fracture surface and fracture energy as assessed by Charpy impact testing. The authors investigated two different titanium alloys with several repeats of each (Table 10). While there were inconsistencies within each alloy, the average behavior between the two alloys is evident from this approach. Thus, it may be useful as a coarse, first-order screening method when developing new alloy compositions.

Table 10. Correlation between fracture surface appearance (% faceted) and Charpy impact energy

Ti-alloys	VT3-1				VT8		
FECT, J/cm^2	3.8	4.9	8.2	11	10.2	15	19.1
Percent of facetted pattern of fracture surface	95%	40%	80%	5%	5%	5%	80%

7.3   Specimen versus component behavior

Experience with component testing indicates that components can fail at lower net stresses that would be expected based on lab coupon results (Section 7.1). Potential reasons for this have

been investigated by a number of research groups and include the difference in stress state (Section 7.1.2), the difference in the stressed volume (Section 7.1.4), and the difference in residual stress state (Section 7.1.10). Harrison et al. (1986) (Figure 105) and Evans and Bache (1994) (Figure 124) have published representative data illustrating this effect.
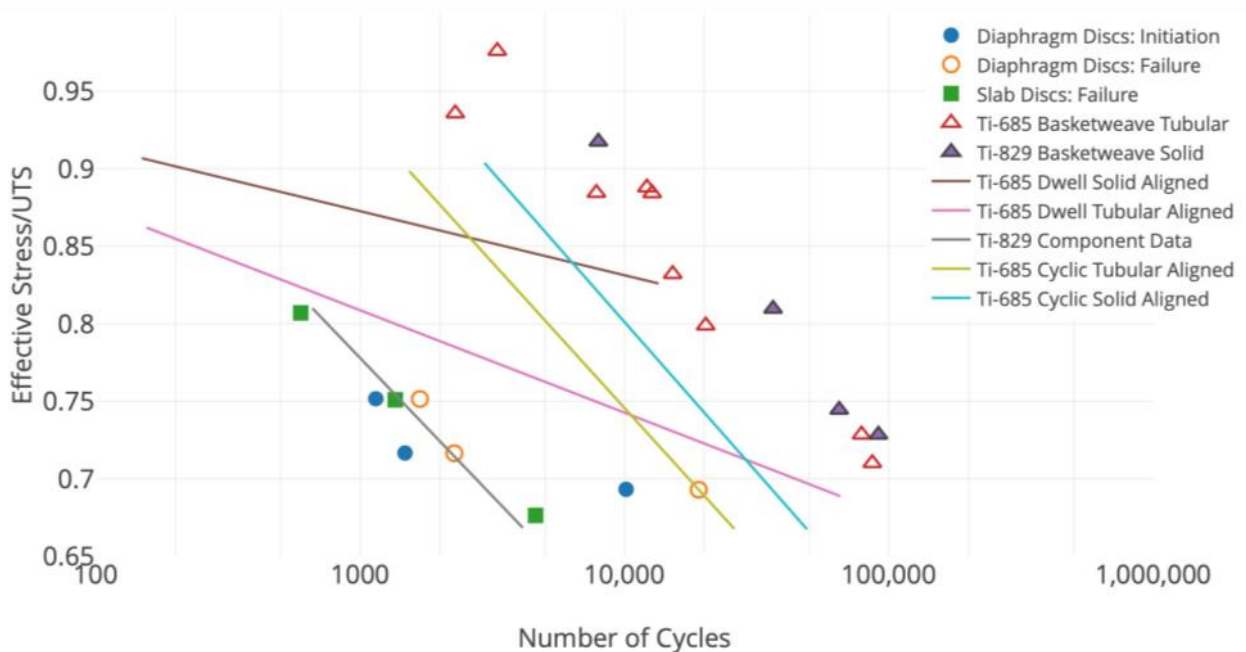
Figure 124. Comparison of component and specimen data

8   Industry experience

Industry component experience with cold dwell fatigue is summarized in this section, however, before delving into the limited number of events on record, we note that turbine engines have been utilized for more than six decades using many of the alloys mentioned above. Many of the components were produced before MTRs were acknowledged and nevertheless flew successfully and were retired without any issues related to dwell. Trends in engine size to support increasingly large commercial aircraft coupled with cost-and-weight reduction efforts have pushed existing alloys nearer to their limits and hence this review should serve as a timely reminder to pay careful attention to processing routes to ensure material *quality* over and above all else.

8.1 Industry learnings from metallurgical investigations of field events

8.1.1 1980's-1990's Ti-6242 CF6 compressor spools

In GE's investigation of the CF6 separation events (Section 1.3.2), cracks were confirmed to originate from MTRs with their [0001] close to parallel to the hoop direction. The 16" billet 3-9 spool population had the highest cracking rate, with each crack initiating sub-surface from a large MTR containing a small micropore (<0.001"). Cracks in the smaller diameter billet populations were found not to initiate from a pore. EBSD analysis of a crack cross-section from 10" billet population confirmed the crack fracture plane was normal to the hoop direction and close to (0001) (hard orientation) and that the adjacent MTRs, acting as the 'soft orientation' had their (0001) planes nominally 45 degrees away from the hoop direction as shown in Figure 125. In this figure, the pole figures show the orientation of the 'hard' and 'soft' MTRs at the origin and note that the 'soft' MTRs are well oriented for basal slip while the crack-containing MTR has [0001] aligned with the stress axis.
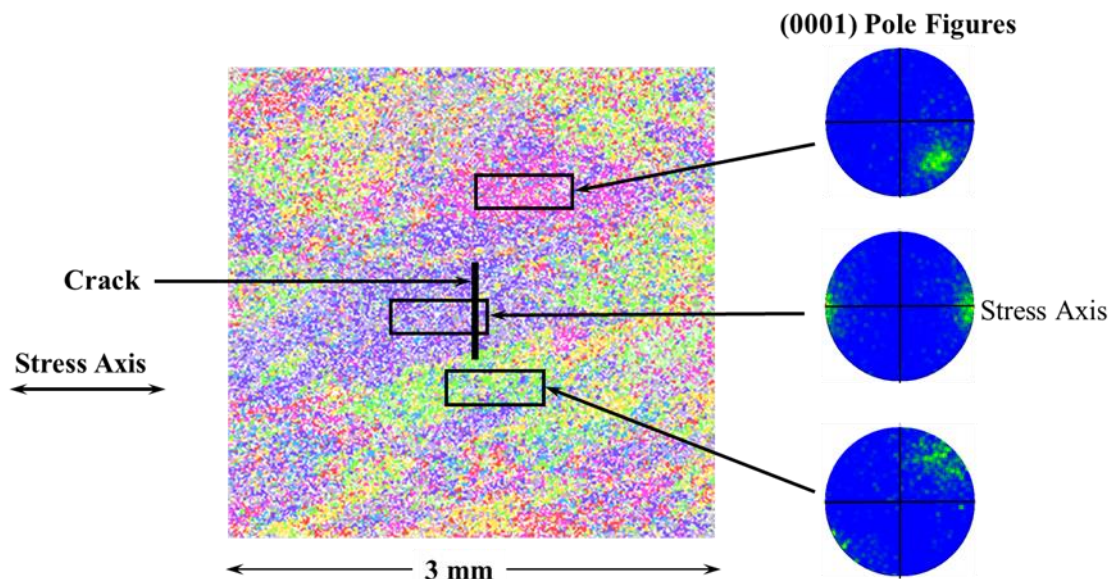
Figure 125. Cross-section through a dwell fatigue crack initiation site from a CF6 engine

In response to these field events, GE improved the 3-9 spool manufacturing process to reduce the tendency for CDF. In particular, in 1995 GE's suppliers moved to using of smaller diameter billet (8") with increased levels of final alpha + beta billet work and alpha + beta component forging work as well as a more rapid cooling rate from a solution heat treat temperature closer to the beta transus. Figure 126 shows an orientation image using an icosahedral color scheme (Yamrom, Sutliff, & Woodfield, 1994), comparing the large diameter billet (old) forge process

versus the absence of MTRs in the new process. The orientation images were produced by mapping each [0001] to an icosahedral color scheme (Figure 127). Figure 128 shows orientation images with examples from the full-scale, design of experiments Ti-6242 billet conversion study to optimize billet conversion for the minimization of MTRs. This work showed that increased levels of final alpha/beta billet work and a higher temperature for the final alpha/beta work were found to be important to minimize MTR size and intensity.
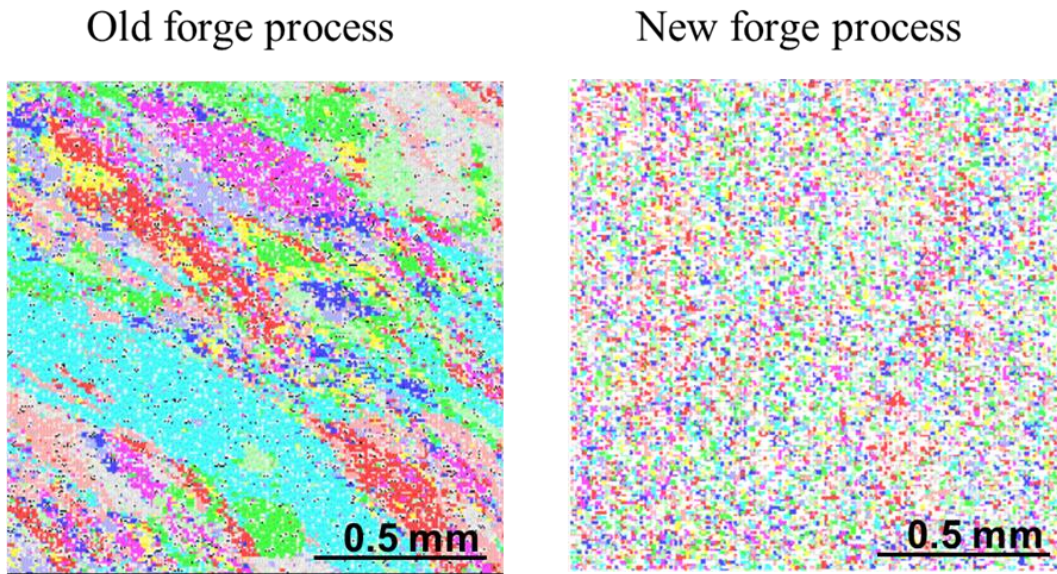
Figure 126. Orientation images of the bore location in CF6 3-9 spool for old (left) and new (right) forge processes
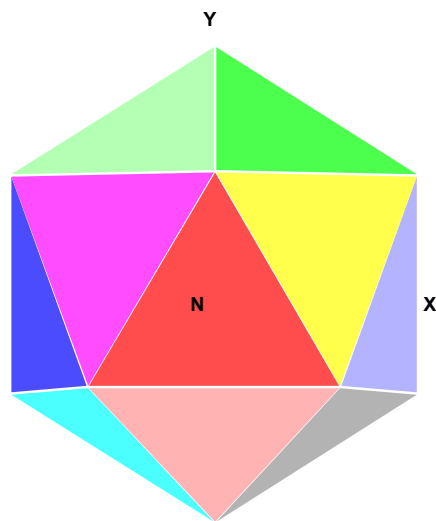
Figure 127. Icosahedral color mapping for EBSD data

Standard	Beta process	Special
Small	Beta quench diameter	Small
Large	Final diameter	Small
Fewer	Number of alpha/beta steps	Fewer
Lower	Alpha/beta temperature	Higher
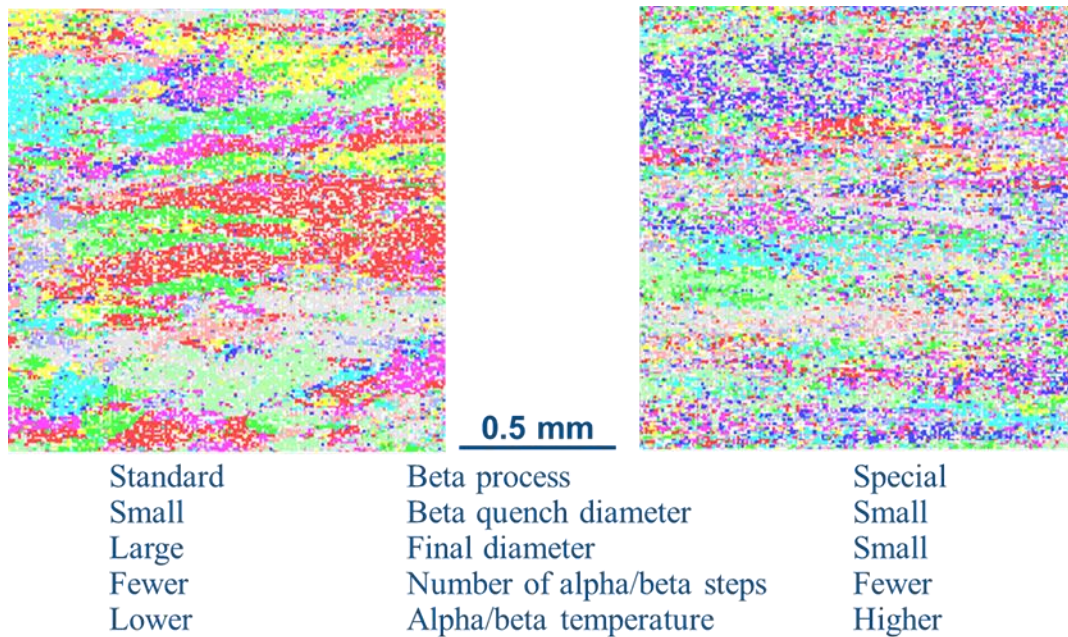
Figure 128. Full-scale Ti-6242 billet conversion design of experiments study showing billet with (left) large, strongly aligned MTRs, and (right) smaller, more randomized MTRs

The importance of primary alpha volume fraction on dwell fatigue behavior of material containing large MTRs is shown in Figure 129. Dwell LCF specimen blanks were removed from a large 3-9 spool forging from a population known to contain large MTRs, and then re-solution heat treated and cooled using carefully controlled cooling methods. The resulting 2-minute dwell fatigue lives and fracture surfaces from these specimens are shown in Figure 129. At low cooling rates (~11 °C/min or ~20 °F/min) from the re-solution temperature, the 869 MPa (126 ksi) dwell life is < 2,000 cycles and large, internally initiated faceted regions are observed. At a much faster cooling rate (~208 °C/min or 375 °F/min) from the re-solution temperature, the dwell life is an order of magnitude higher and there is an almost total absence of large, internally initiated faceted regions. Because all samples were cut from the same forging, they initially had the same underlying MTR characteristics subject to the caveat of location-to-location and thus specimen-to-specimen variability. The difference in cooling rate from the re-solution temperature resulted in a significant higher primary alpha volume fraction in the slower cooled samples compared to the fast cooled ones. The change in secondary alpha morphology also would have increased the 0.2% yield strength in the fast cooled samples. Since moving to the improved manufacturing process, many thousands of spools have been produced and subsequently retired at full life with no indication of any dwell fatigue cracks indicating that the improved manufacturing process has led to the elimination of dwell fatigue cracks in this component.
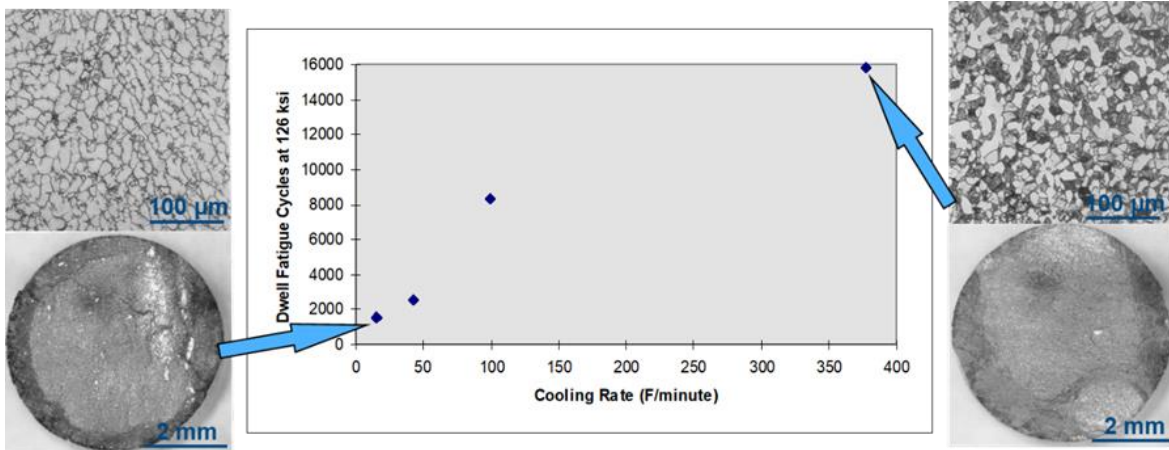
Figure 129. Effect of re-solution heat treatment cooling rate on 869 MPa (126 ksi) dwell fatigue life and fracture surface

An empirical model was developed to predict dwell fatigue lifetime as a function of applied stress during the dwell, microstructure, and MTR features was developed (Woodfield A. , Gorman, Corderman, Sutliff, & Yamrom, 1996; Woodfield A. , Gorman, Sutliff, & Corderman, 1999). Key MTR and microstructural parameters that were statistically significant included MTR (or colony) size, MTR volume fraction and orientation spread (alignment) as well as primary alpha grain size and volume fraction. An adjusted R^2 of 0.75 was obtained with the model as shown in Figure 130 that also includes separation of the points into test stresses of 785, 827, and 869 MPa (114, 120 and 126 ksi). Figure 131 shows the test data as well as results from test bars extracted from disks that had cracked. As can be seen from Figure 131, test bars from cracked disks generally had larger/more aligned MTRs and/or larger primary alpha volume fractions/grain sizes resulting in lower predicted dwell lives.
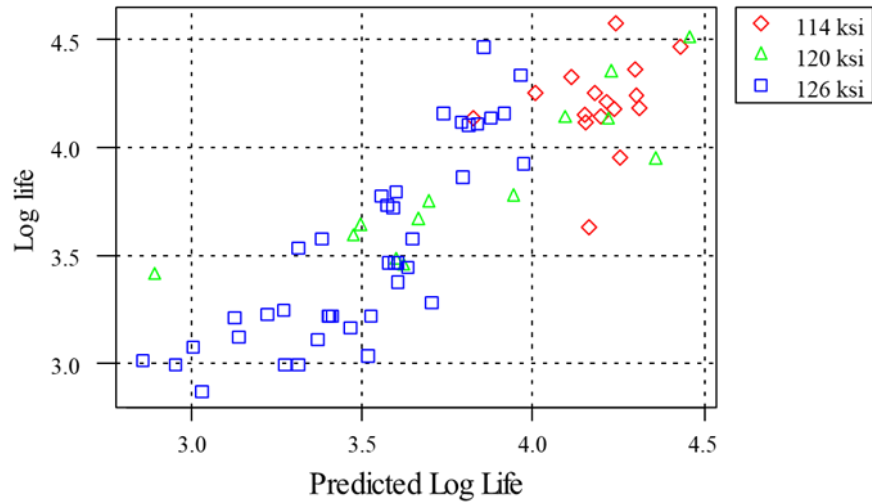
Figure 130. Predicted versus actual dwell life from empirical model, separated by test stress
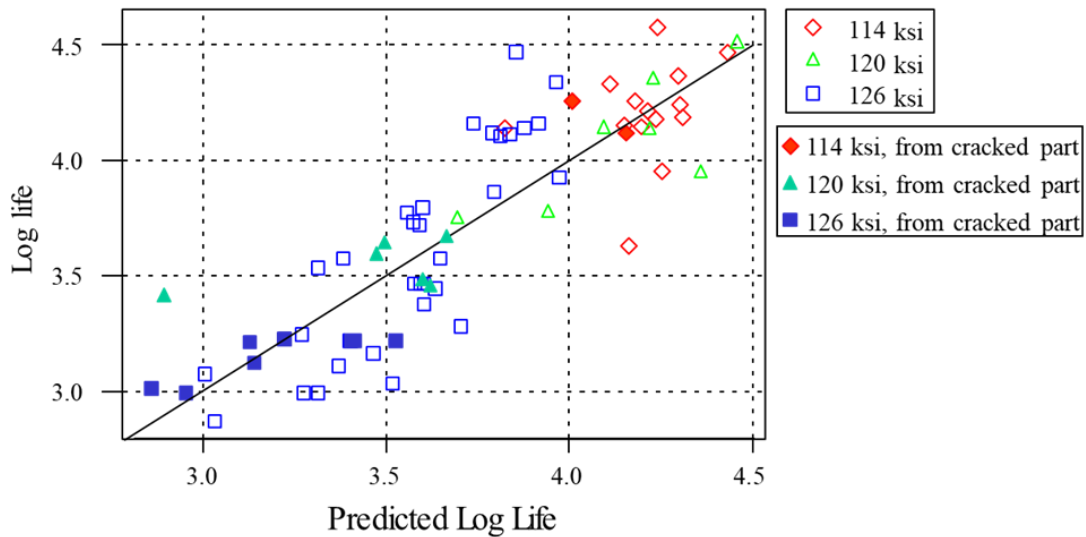
Figure 131. Data from Figure 130 with test bar data obtained from cracked parts
Showing cracked parts tended to have shorter dwell lives than non-cracked parts

8.1.2 1998 Ti-6242 Impeller

Honeywell performed EBSD analysis of the primary and secondary fatigue crack initiation sites in collaboration with engineers from GE Aviation after the release of the NTSB report. Figure 132 shows the cross section through the faceted initiation site from the primary fracture origin. Regions 1 and 2 identify the MTRs beneath the primary origin had c-axes generally aligned with the principal stress direction. Regions 3 and 4 indicate that the hard-oriented MTRs were surrounded by soft MTRs with c-axes oriented 90-degrees to the hard MTR and the primary

stress axis. This is a noteworthy difference from the event discussed in Section 8.1.1, which indicates that MTRs oriented for either basal or prism slip may provide sufficient strain accumulation under cold creep conditions to cause load-shedding and crack nucleation as discussed in more detail in Section 4.1. Analysis beneath the faceted initiation site of a secondary origin that did not propagate to failure (not reproduced here) yielded similar results.

With this new information, Honeywell reclassified the failure as a CDF event. This is a notable event because it occurred on a product forged from 8" diameter billet. Prior and subsequent events involved larger diameter billets 10-16", which receive less strain during alpha+beta working and hence typically have much larger MTRs. It is worth mentioning that the billet was converted from a double vacuum arc remelted ingot that was produced in 1977 and so it was not processed with more modern conversion techniques which are designed to limit the extent of microtexture.
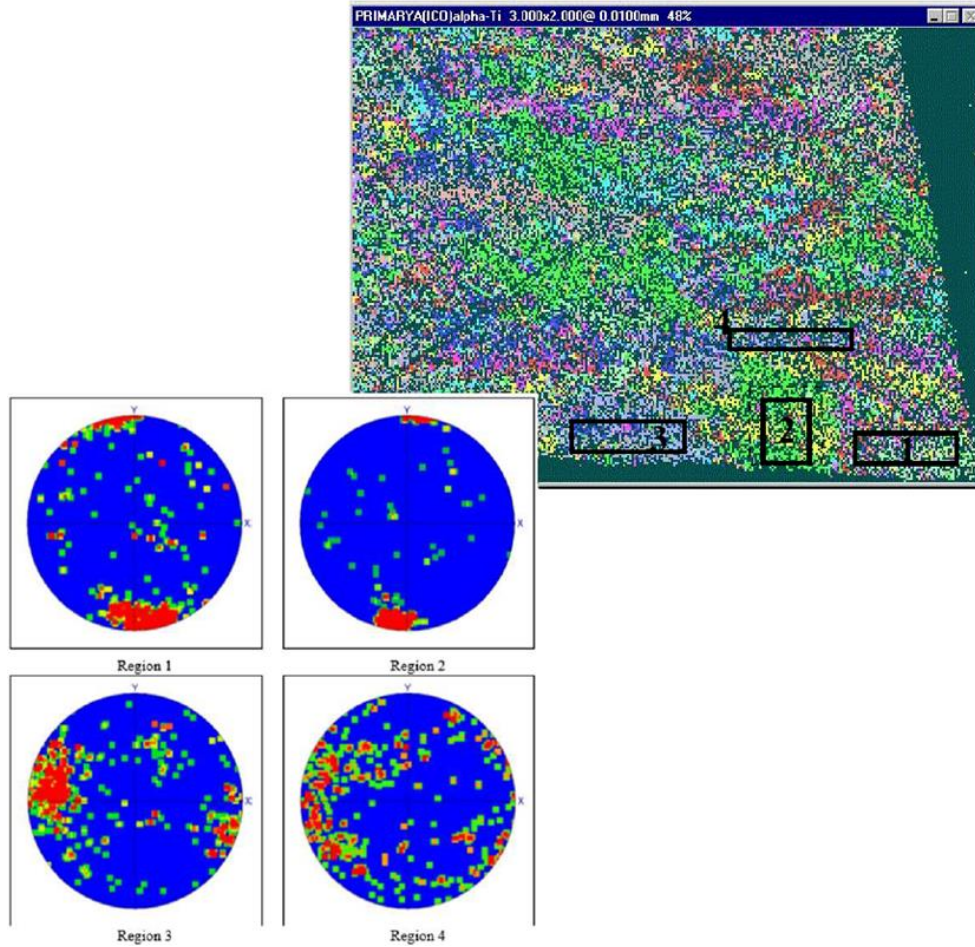
Figure 132. Crystal orientation map and corresponding pole figures for regions around primary origin from Ti-6242 impeller crack nucleation site

8.1.3 2017 GP7270 Ti-6Al-4V fan disk

Analysis of the fracture surface (BEA, 2020) revealed the initiation site was 1.4 mm subsurface and was situated in a large microtextured region (Figure 133). In this figure, the yellow dashed line indicates the extent of the primary faceted origin while blue lines indicate regions of predominantly striation growth. The component was manufactured from 14" diameter billet. The fracture occurred predominantly by faceted growth in both primary and secondary alpha with infrequent striations. At longer crack lengths, the fraction of striations increased making it easier to estimate local crack growth rates. From this analysis, the propagation lifetime was determined to be ~1,642 cycles of which approximately half occurred when the crack was completely subsurface.
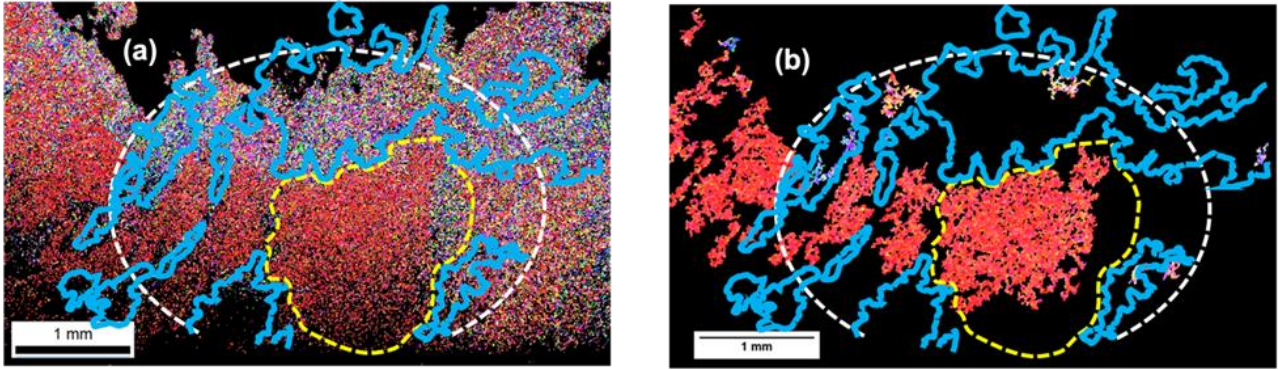
Figure 133. (a) Crystal orientation map following light polishing into faceted initiation site from GP7270 event rotor and (b) segmented MTRs

8.1.4 2018 Ti-6Al-4V fan blade event

Evaluation of the fracture surface (Figure 134) revealed high aspect ratio bands of extensive faceted growth from the origin, consistent with the size and shape of the underlying microtextured regions in the material (Figure 135). The crack nucleated in an area of rough machining marks and dwell fatigue was not suspected to play a role in this process. However, investigators performed EBSD directly on the fracture surface to ascertain the orientation of grains which exhibited faceted and striated growth (Figure 136). In all, 38 facets were analyzed. It was found that grains with c-axes >50° from the principal stress direction exhibited striated growth while grains below this threshold tended to exhibit faceted growth. It is noteworthy that there were many facets with c-axes greater than what is typically observed for classic dwell fatigue failures, however, some of the facet orientations and surface morphologies were consistent with dwell crack propagation. This was especially true at longer crack lengths (i.e., in the region identified as mixed faceted/striated with dimple rupture in Figure 134) which were consistent with those observed on dwell fatigue fracture surfaces of specimens tested from the same material. This event illustrates that cracks initiated in blades in the absence of a dwell contribution can propagate by a dwell fatigue mechanism.
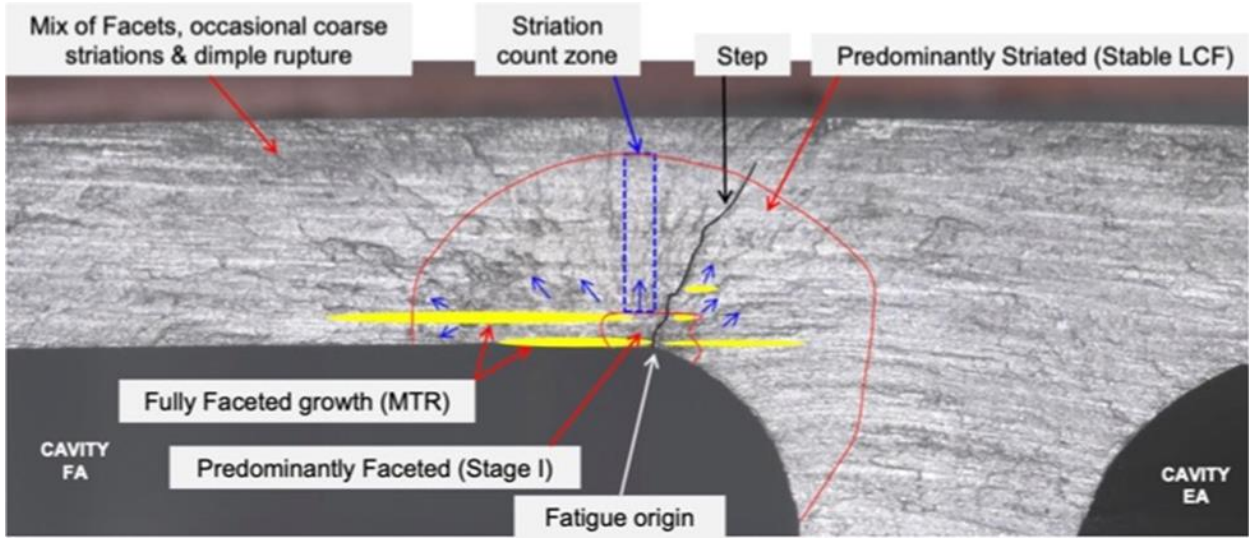
Figure 134. Fracture surface from PW4077 fan blade out event
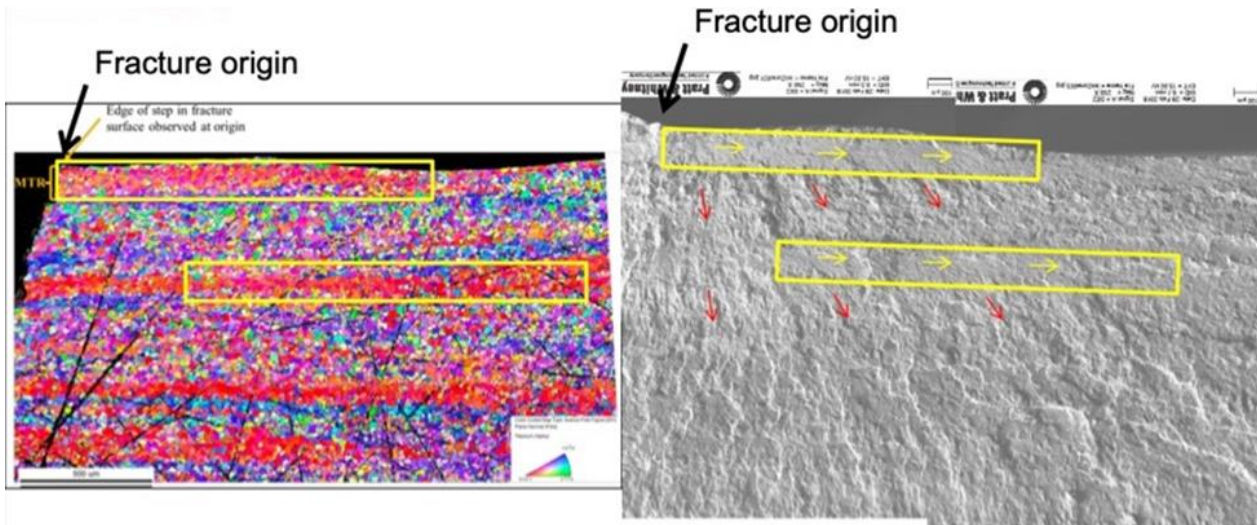
Figure 135. Crystal orientation map (EBSD) and fracture surface of PW4077 fan blade
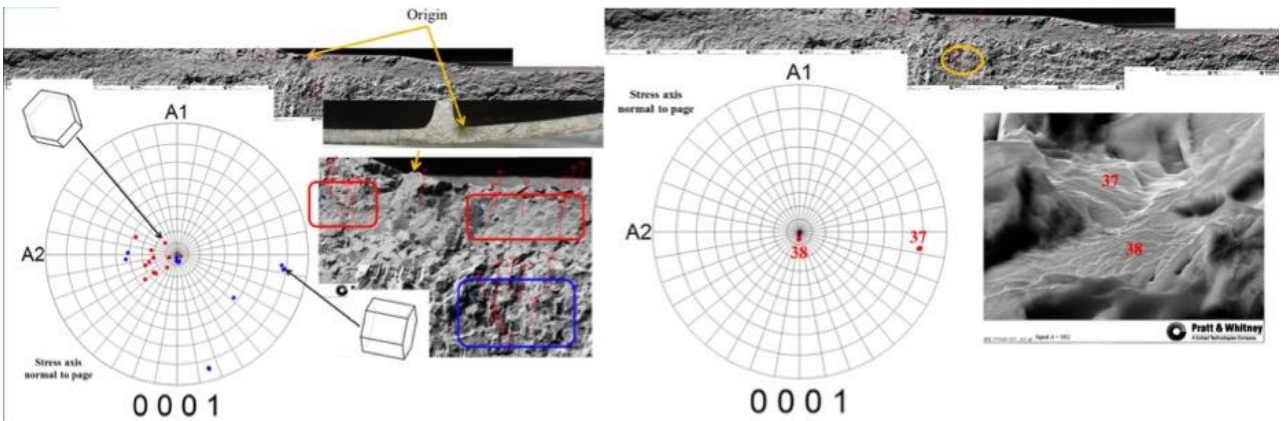
Figure 136. EBSD analysis directly on fracture surface of PW4077 fan blade out event

8.1.5 2006 Ti-8Al-1Mo-1V fan blade event

The investigation revealed (i) presence of large, intense MTRs associated with the fatigue crack initiation site, with these MTRs related to the lower level of bar and blade forging work, and (ii) maximum permissible aluminum content in the failed blade.

8.1.6 Additional data from literature

Shaniavski and Losev (2003) described a number of in-service failures of high-pressure compressor disks from the D-30 (low bypass) and D-30KU (higher bypass variant) engines manufactured from the VT8 (Ti-6.5Al-3.3Mo-0.3Si) and VT3-1 (Ti–6Al–1.5Cr–2.5Mo– 0.5Fe–0.3Si) alloys with lamellar microstructures. They report a distribution of lifetimes for many disks which exhibit two peaks. The first peak, centered around 8000 hours of operation, is due to a reduced nucleation lifetime associated with initiation from inclusions in the material (likely hard alpha). The second peak, centered around 12,000 hours, is due to sensitivity to in-service loading conditions including holds at peak stress. In both cases, the fracture surface morphology at the nucleation site is faceted in nature. The authors report a strong sensitivity of crack growth rate on the underlying microstructure and preferential 'tunneling' of the crack along "filament" (i.e., microtextured) regions of the microstructure.

8.2   Industry full-scale component spin rig experience

In addition to the field events described above, the industry has experience that provides further insight into the cold dwell fatigue mechanism from a number of spin rig tests.

8.2.1 Rolls-Royce full-scale component rig spin tests including dwell time from early 1970's onwards

Learning from the RB211 fan disk failures in Ti-I685 in the early 1970s (Section 1.3.1) led to the incorporation of a dwell at maximum rotational speed into full scale component spin rig testing as part of the standardization of new titanium alloys in Rolls-Royce in large civil engines. Dwell spin rig tests have been run in a number of Ti disk alloys including Ti6Al-4V, Ti-829, Ti-685, Ti-834 and Ti-6246.

Full scale component spin testing has been used to inform the derivation of cold dwell design limits for the relevant components in each titanium alloy and have also led to a significant level of understanding of component behavior in the cold dwell. The results from spin pit testing of Ti-829, Ti-685 and Ti-834 are shown in Figure 137. Lab specimen coupon test results are also indicated on the same plot – 15cpm is a trapezoidal 1s-1s-1s-1s waveform vs a trapezoidal 1s-120s-1s-1s waveform with 120 s being the peak load condition (1 sec rest at minimum stress). Lab specimen tests are assumed to have 0 MPa bulk residual stress due to their relatively small size.
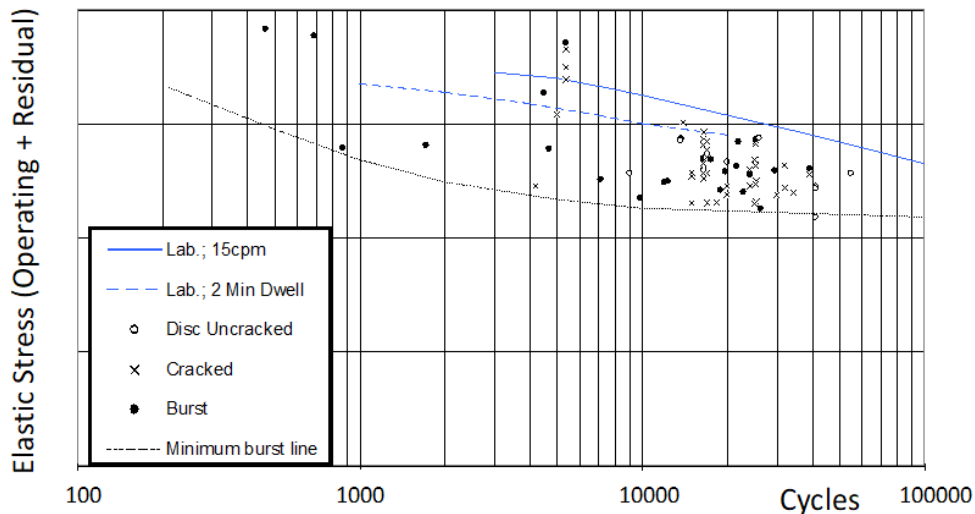
Figure 137. Component spin dwell test results for Ti-829, Ti-685 and Ti-834 expressed as net stress
Operating stress plus bulk residual stress against life in cycles

Full scale dwell rig tests fail at significantly lower stresses than lab-scale coupon dwell tests even when accounting for the effect of the bulk residual stresses present in the components. Life scatter at a given stress tends to be relatively high and it can be seen that the minimum burst line is very flat beyond ~10,000 cycles and thus cold dwell can be treated as a threshold-type behavior.

Failure origins in rig tests were generally in bore cob and diaphragm (web) features and were usually (but not always) considerably sub surface. The initiation sites typically showed quasi-cleavage faceting. Examination of cracked and failed locations on dwell spin tests showed that these locations are best predicted by considering the peak net stress (operating stress + bulk residual stress) although the microtextural characteristics of the part are considered to be important.

Laboratory specimen and component spin tests were carried out in the 1980s by the RAE at Farnborough in conjunction with the University of Swansea, UK. Component spin test results from two discs in the near alpha Ti-829 alloy are reported in Harrison et al. (1986). Two disk designs were tested, a 'diaphragm' disk and a larger 'bore disk,' and failures were observed at stresses down to below 70% of the UTS. They noted that the failure origins were not well predicted by elastic stress only. Additional work was undertaken where strain-controlled specimen testing was completed at a representative R ratio to determine a 'dynamic' or 'cyclic' yield stress/strain curve. These data were used to recalculate the discs stress distribution which gave a good prediction of the crack initiation location. They postulated that the lower strength of the dwell spin test components compared to dwell specimens was due to the larger volume under test in the rig discs being more likely to expose 'weak links' in the structure (e.g., aligned alpha laths). This is discussed in more detail in Section 7.1.4.

An example of a completed Ti-6Al-4V dwell spin rig test is shown in Figure 138(a). In this example, the single initiation site was slightly sub-surface in a region in which two large bright facets of about 1-and 1.4-mm length can be seen optically on the fracture surface Figure 138 (b). Figure 139 (Images courtesy C. Pleydell-Pearce and M.R. Bache, Swansea) shows secondary electron imaging of the area considered to be the initiation site.
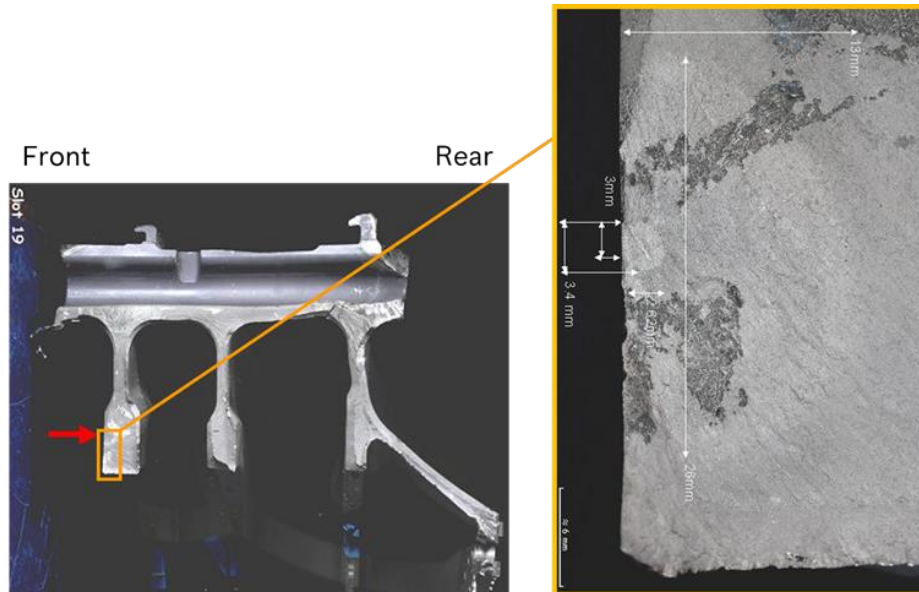
Figure 138. Optical images of Ti64 spinning compressor disk rig test showing an overview and primary origin in front bore cob
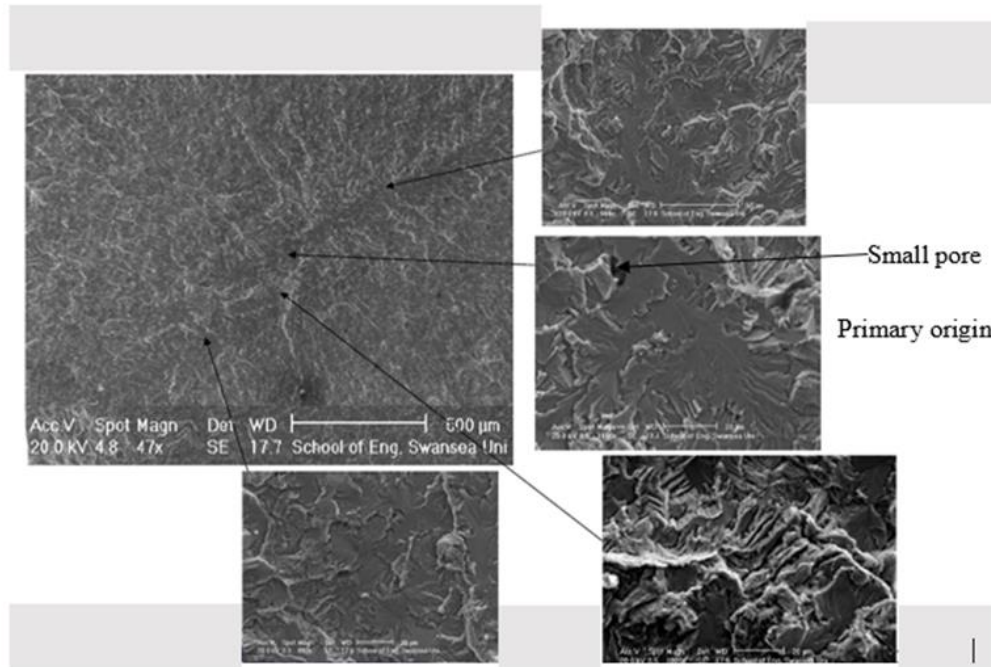
Figure 139. Secondary electron images showing microfacets facets and a small pore at initiation site of a Ti-6Al-4V compressor spin rig test

Under the auspices of the HexMat program (see Appendix A), Rolls Royce worked closely with Imperial College to analyze faceted fatigue initiation sites on spin rig tests of Ti-834 (Figure 140). It was found that the fatigue location of the origins did not correlate well with the hoop, radial, or axial principal stresses. However, when overlaid with stress triaxiality, it was found that the faceted origins occurred in regions of relatively high hoop stress (Figure 140(b)) where stress triaxiality was relatively low (Figure 140(c)). The dots in (b) and (c) correspond to faceted nucleation site locations. The authors further analyzed the initiation sites using a crystal plasticity model that utilized the boundary conditions from the component simulation and a microscale facet nucleation model.
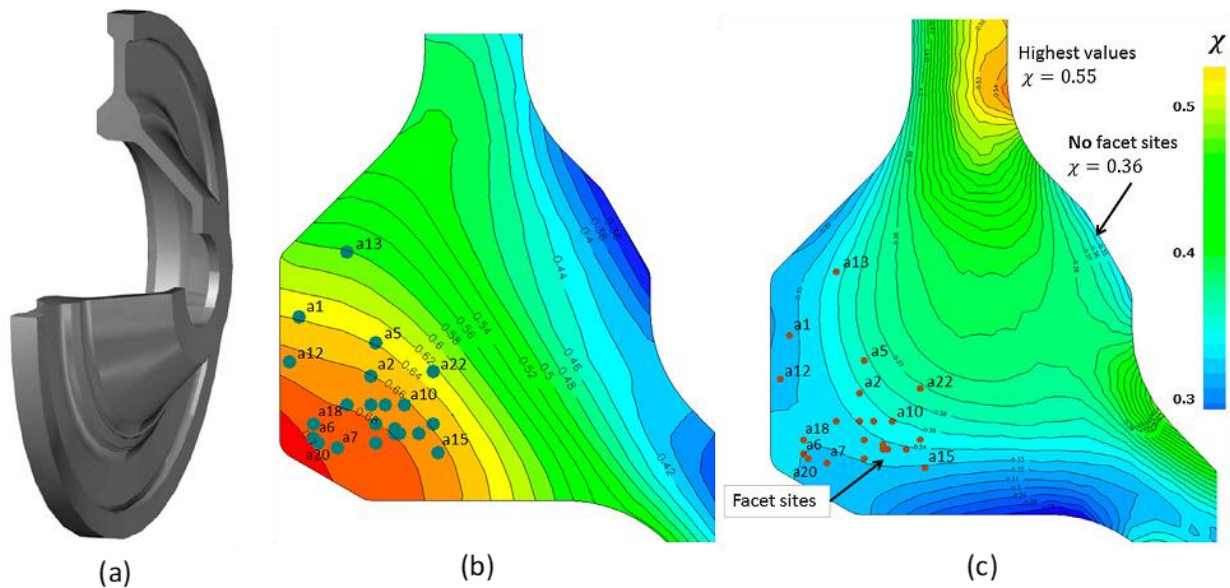
Figure 140. (a) Component spin rig geometry (b) normalized hoop stress (c) stress triaxiality

8.2.2 2006 Ti-6242 beta-forged compressor disk

Safran Aircraft Engines (SAE) performed spin rig tests on beta-forged Ti-6242 compressor disks to investigate the behavior of components running at higher stresses than are currently used in operational engines. During one of these tests, cracks were observed in both the bore and web locations. Subsequent investigation revealed faceted initiation sites initiating from fully lamellar colonies. The alternating alpha/beta lamellae gave the facets a 'featherlike' appearance as shown in Figure 141 and Figure 142. The initiation sites were both subsurface, though one facet at the bore location extended nearly to the free surface. The orientations and morphological appearance of the facets closely mirrored those observed at dwell fatigue crack origins under controlled laboratory testing on similar material in (Freiherr von Thungen, 2017) and hence are linked to

the dwell effect. Finite element calculations (Figure 143) were performed to understand the preference for cracking in these locations. These calculations considered residual stresses from manufacturing as well as those induced by loading. The work emphasized the need to consider bulk residual stresses resulting from the manufacturing process in order to explain the location of the cracks.
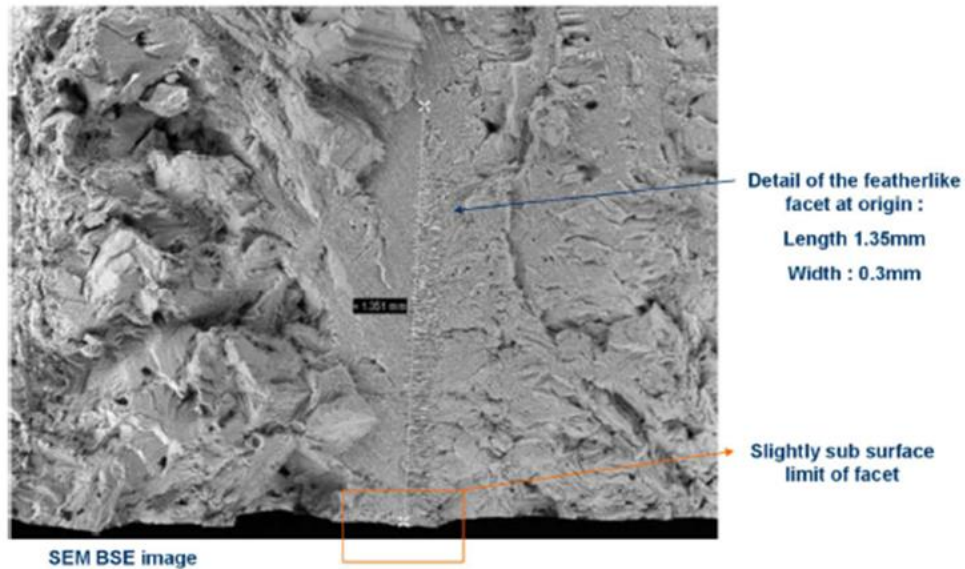
Figure 141. Illustration of faceted initiation site at bore location of a beta-forged Ti-6242 spin rig initiation site
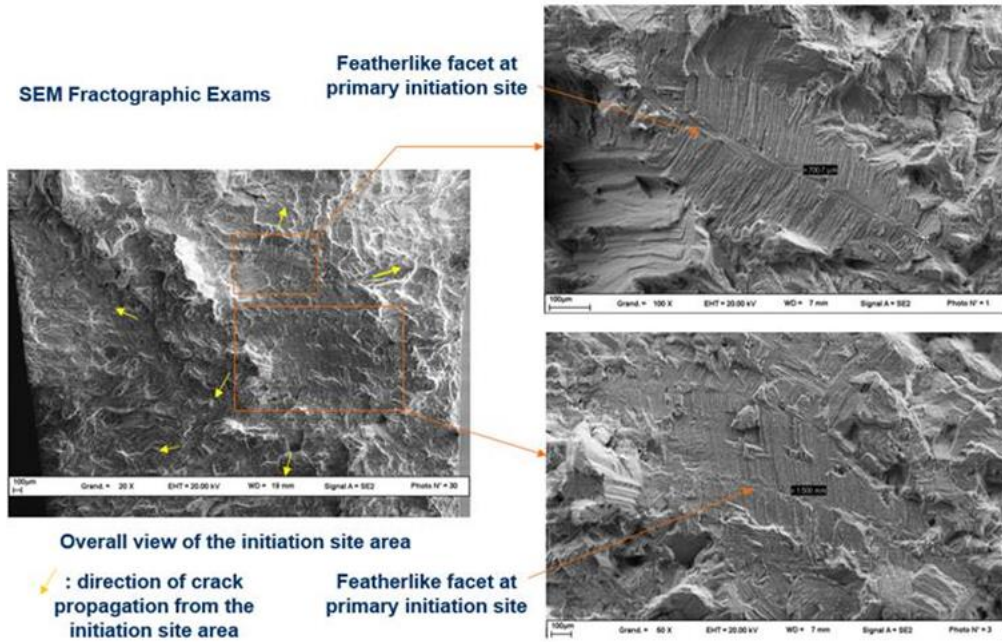
Figure 142. Fracture surface images from rim location of beta-forged Ti-6242 spin rig test
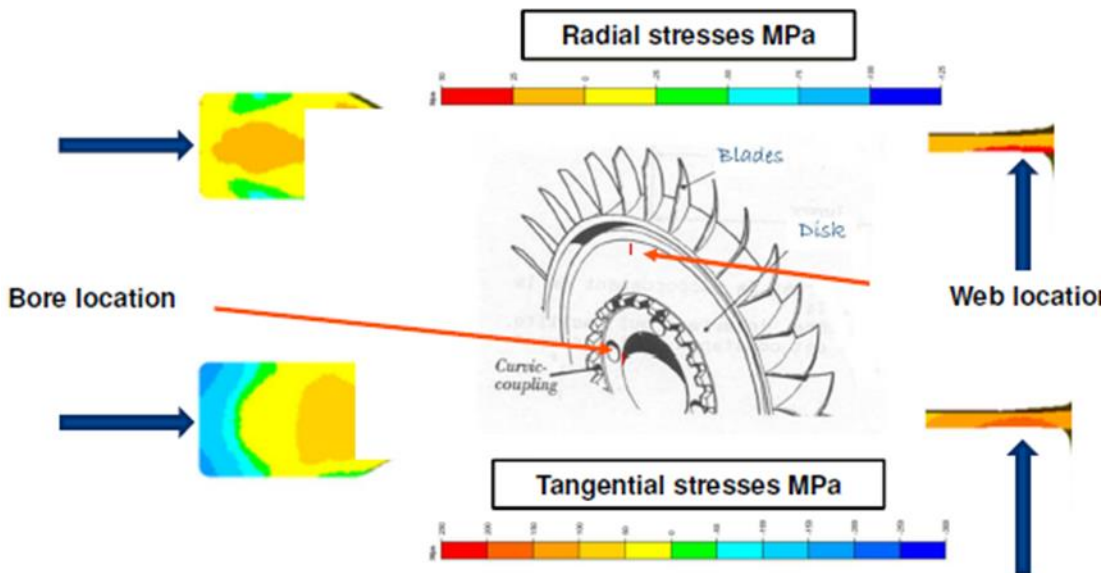
Figure 143. Finite element stress calculations relative to positions of cracks and net stresses on beta-forged Ti-6242 rig test

8.2.3 Alpha+beta processed and heat-treated Ti-834

Pratt & Whitney Canada (PWC) has investigated the dwell fatigue performance of a range of alpha+beta processed and heat-treated titanium alloys including Ti-6Al-4V, Ti-6242, and Ti-834. Specimen testing was used to explore the stress and temperature dependence of the dwell debit

for dwell times up to two minutes (Table 11). Of these alloys, PWC has performed multiple component spin pit tests on various components at a variety of temperatures as high as 200 ºC (400 ºF).

Table 11. Pratt & Whitney Canada dwell fatigue test experience

TEST TYPE	ALLOY	TEMPERATURE (°F)	STRESS (%YS)	DWELL TIME (minutes)
SPECIMEN, COLD DWELL FATIGUE (Extracted from forgings)	Ti-64	75	~95 to ~100	≤ 2
	Ti-6242	75 to 200	~80 to ~100	≤ 2
	Ti-834	75 to 400	~80 to ~100	≤ 2
COMPONENT SPIN PIT, COLD DWELL FATIGUE	Ti-64	-	-	-
	Ti-6242	-	-	-
	Ti-834	Up to ~400	various	various

An example fracture surface from one of the spin pit tests showing subsurface crack nucleation is shown in Figure 144. The initiation site was flat and shiny when inspected visually, which is characteristic of dwell fatigue. Electron microscopy analysis revealed the presence of multiple interconnected facets at the origin with river lines emanating away from it towards the surface and into the part.
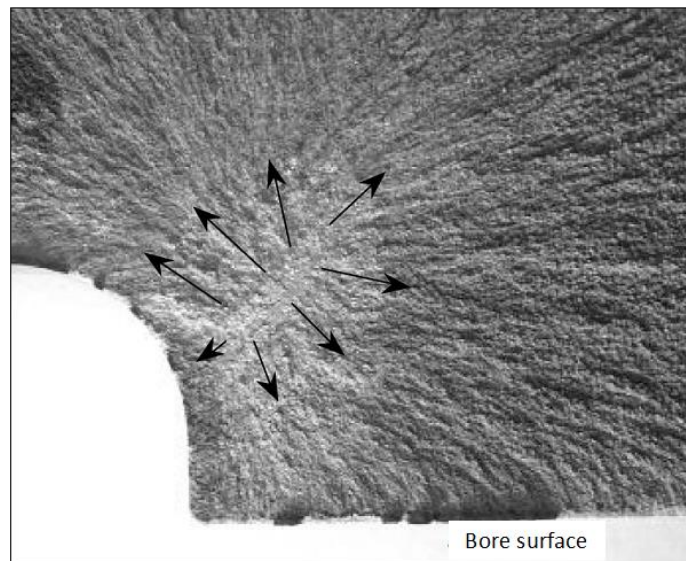
Figure 144. Fracture surface of a Ti-834 spin rig component

8.2.4 2019 alpha+beta forged structural component high cycle fatigue

The IHI Corporation performed a rig test to characterize the HCF behavior of a Ti-6Al-4V structural component. The test was simulating engine operating conditions. A crack was formed during testing and the origin was analyzed using optical and scanning electron microscopy. An overview of the fracture surface is shown in Figure 145. Electron fractography revealed that part of the origin was damaged (Figure 146), presumably due to the slightly negative load ratio of -0.14 at this location despite there being a positive mean stress (note that residual stresses were not considered in the calculation of load ratio). A series of facets, including some elongated facets, were observed in the vicinity of the suspected origin (Figure 147). Additional propagation facets were observed in the undamaged region of the fracture surface (Figure 148) which led into the larger faceted region running vertically in Figure 146. Following this event, the forging process for the component was revised to enhance break up of MTRs in the billet material, which required considerable effort and cost, but provided improved performance.
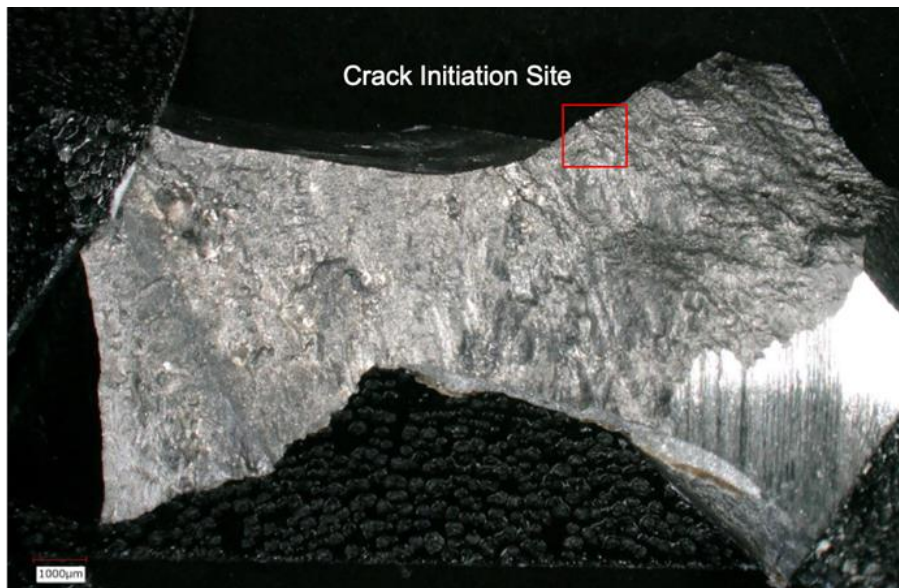
Figure 145. Fracture surface from component high cycle fatigue test

Fracture surface smeared during
testing due to negative load ratio
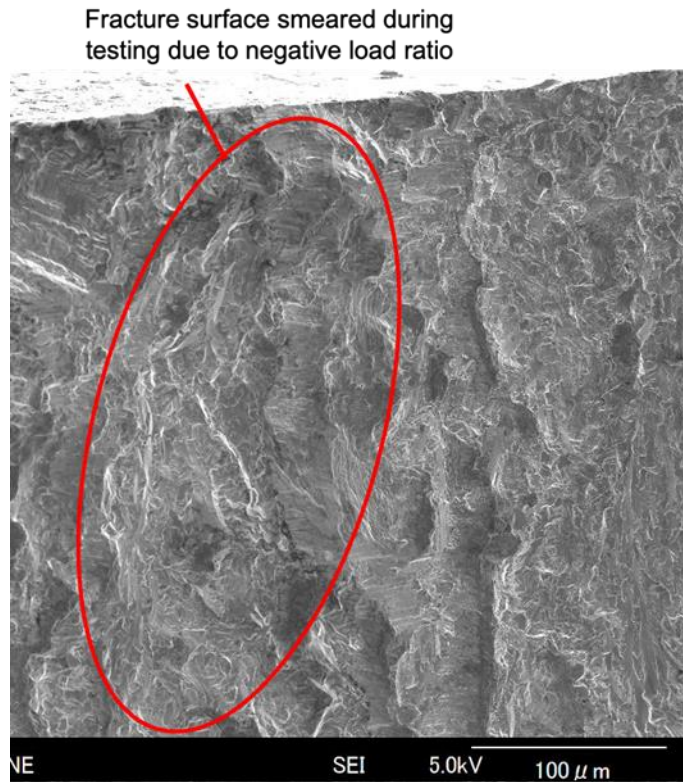
Figure 146. Secondary electron image near the fracture origin from the HCF rig test
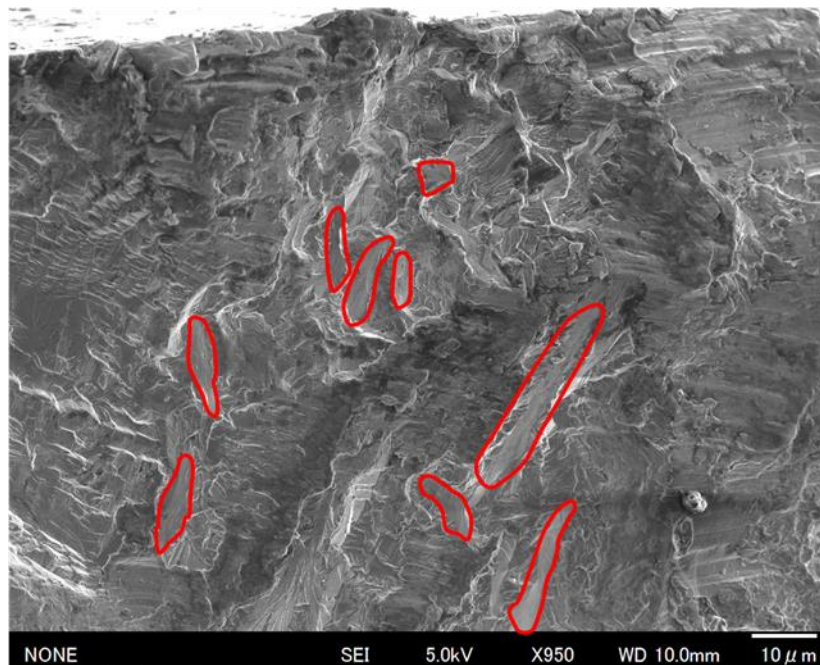
Figure 147. Facets found near origin despite damage to the fracture surface
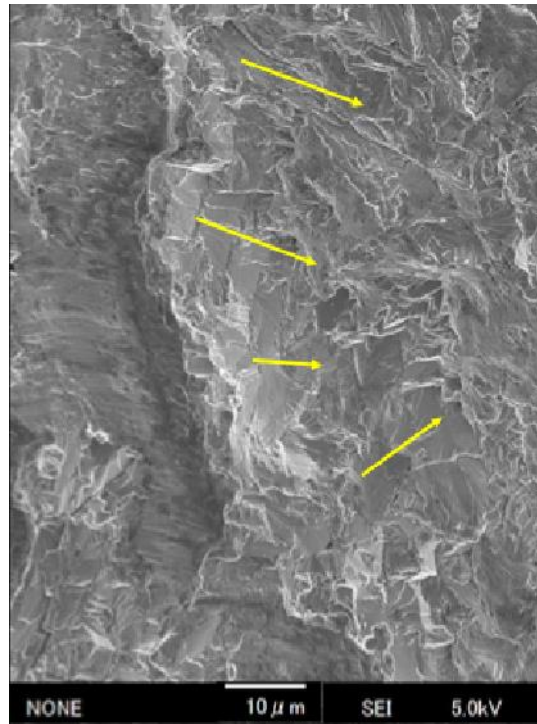
Figure 148. Faceted crack propagation in the HCF rig test

9 Mitigating the risk of cold dwell fatigue failure

The preceding sections have highlighted the importance of composition, thermomechanical processing history, microstructure, and loading conditions on dwell fatigue behavior of titanium alloys. Reducing the risk of CDF component failure requires careful attention to these aspects, but they must be considered in conjunction with component design practice and nondestructive evaluation.

9.1 Pathways to root cause

From the prior discussion, it is clear that CDF is a complex phenomenon and there are multiple factors that may contribute to anomalous microstructures that are susceptible to this failure mechanism. Further, there are interactions among these processing steps, which span all the way from the melt practice (composition control, ingot macrostructure, ingot porosity) through billet conversion, forging, heat treatment (spheroidization of primary alpha; development of macro- and microtexture; bulk residual stresses), and finish machining (probability and location of MTRs relative to critically stressed volumes). On top of this, the imposed stresses and duty cycles (max stresses, cyclic stresses, dwell times, and temperature) may make the same microstructure benign in one application, but susceptible in another.

In an effort to capture this complexity, tree diagrams summarizing the various pathways to the root cause for a dwell fatigue failure in a component in service or a significant dwell debit observed during specimen testing have been developed for various processing routes used to produce rotating hardware. These include alpha+beta forging followed by alpha+beta heat treat (e.g., Ti-6-4, Ti-6242, Ti-834 (Figure 149)), beta forging followed by alpha+beta heat treatment (e.g., Ti-6242 (Figure 150)), and alpha+beta forging followed by beta heat treatment (e.g., Ti-685, Ti-5331s (Figure 151)). In these figures, several acronyms are used: AR = aspect ratio; CR = cooling rate; HT = heat treat; Rx = recrystallization; Soln. = solution; WQ = water quench. These diagrams represent the distillation of decades worth of literature and industry experience into a concise format. These have been color coded according to whether these factors have been determined to be influential in a field event, rig event, early specimen failure, or represent a possible contributor to such an event. One or more of these pathways may be active depending on the circumstance surrounding the event of interest. In addition to helping interested organizations in ascertaining the root cause of a CDF-related event, the roadmaps are also useful for illustrating the interconnectivity among the various sections in this report. The relative importance of these factors is addressed in more detail below.

The first-tier factors for all three processing routes are the alloy composition, microstructure, and the duty cycle. The alloy composition is the first order factor controlling strength, aspects of microstructure evolution, and the ability of the alloy to store/relieve residual stress. The duty cycle, which may be very different for test specimens compared to components, includes the applied stress, temperature, and the hold time at peak stress. Microstructure includes the size, shape, and spatial distribution of primary and secondary alpha as well as both macro- and microtexture. These factors depend strongly on the billet and forging processes. Additionally clean voids (i.e., large pores) or micropores/cavities from billet conversion are rarely occurring features of titanium alloy microstructures, but these represent potential nucleation sites for dwell fatigue cracks, especially if they are situated within a large MTR. Such a case has been encountered in several field failures (Sections 1.3.1 and 8.1.1) and spin rig tests (Section 8.2.1).
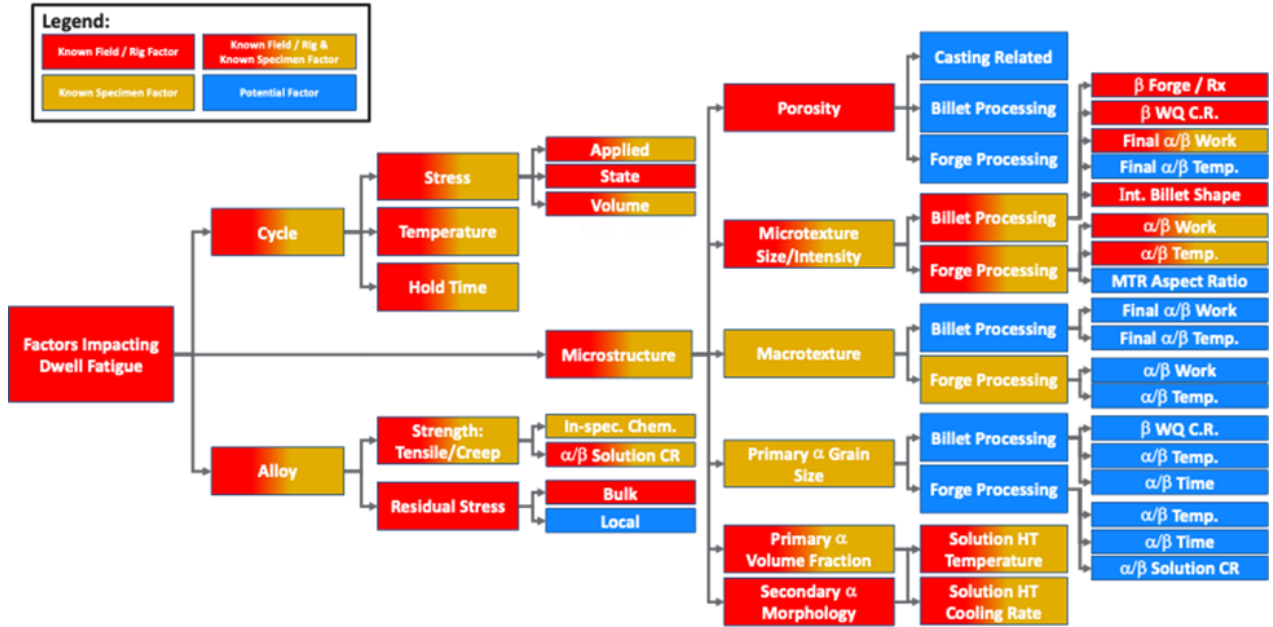
Figure 149. Root cause tree diagram for alpha+beta forged and alpha+beta heat treated alloys
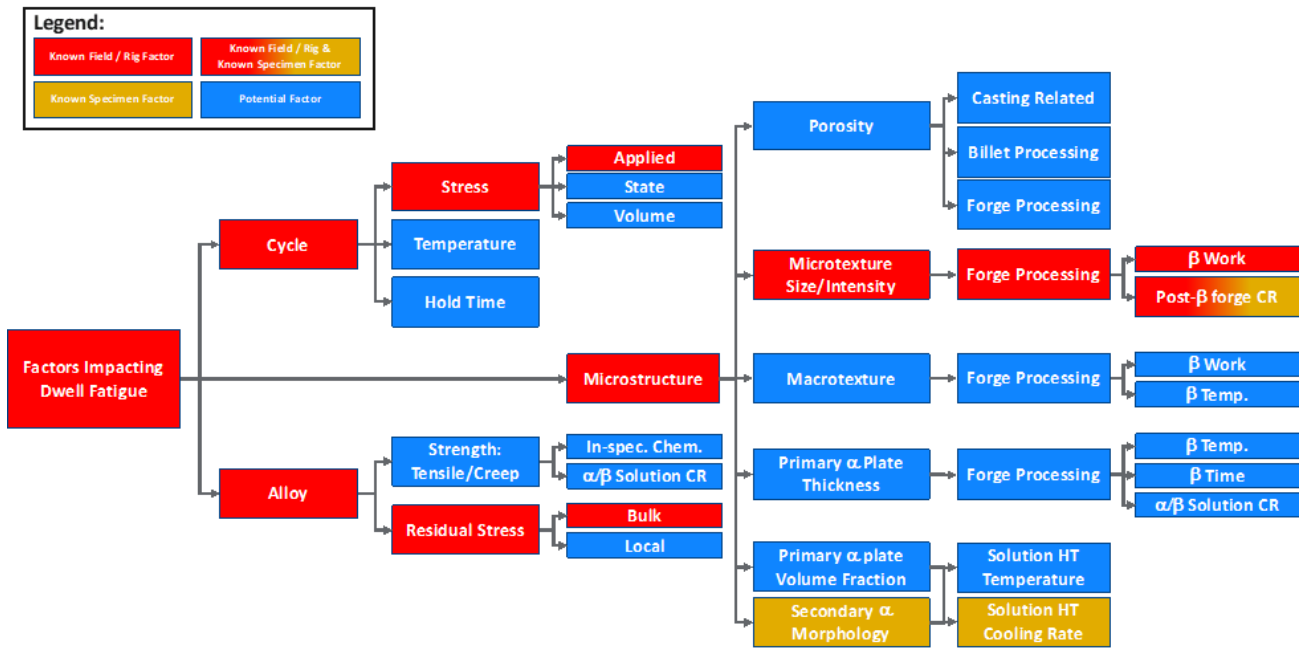
Figure 150. Root cause tree diagram for beta forged and alpha+beta heat treated alloys
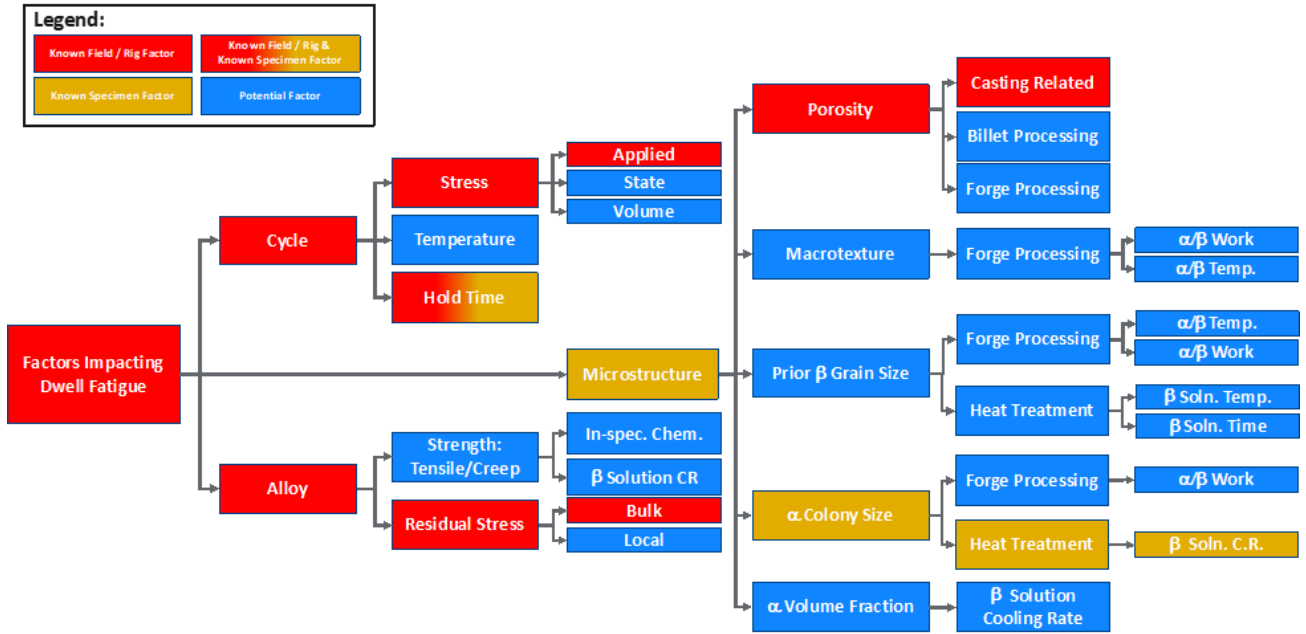
Figure 151. Root cause tree diagram for alpha+beta forged and beta heat treated alloys

A similar root cause diagram summarizing the mechanisms leading to reduced fatigue behavior due to the cold dwell cycle are further illustrated in Figure 152. In this figure, acronyms include: CPM = cycle per minute; GS = grain size; th = thickness; OR = orientation relationship; Vf = volume fraction. At the top level, low dwell fatigue lifetime is usually caused by a combination of early crack nucleation and rapid initial crack propagation. The long crack growth portion of the fatigue and fracture process has a negligible effect on the overall reduction in cycles to failure over continuous cycling. Early crack nucleation may result from any number of events. A small pore or cavity in the material adjacent to a suitably oriented grain can provide sufficient stress concentration to act as a nucleation site leading to faceted propagation through hard-oriented grains if the pore is preferentially located within an MTR. One mechanism for pore formation occurs during processing when adjacent colonies have c-axes at ~90° to one another and one of the colonies has the c-axis aligned with locally developed tensile stresses. The constraint of the hard orientations and the strongly incompatible anisotropic deformation by prism and basal slip in the softer orientations appeared to facilitate cavity nucleation and growth in these local regions (Bieler, Nicolaou, & Semiatin, 2005; Nicolaou & Semiatin, 2007). Additionally, it is known that localized plastic flow of soft-oriented microtextured regions leads to load shedding and early (typically) subsurface crack nucleation due to the enhanced stresses at the micromechanical scale. Both mechanisms can be exacerbated by the cycle conditions or the alloy composition. Alloy composition is known to affect yield strength as well as slip character, (i.e., the degree of slip planarity) and hence propensity for localization. Details of the

microstructure as well as MTRs like the size, shape, aspect ratio, and internal misorientations, which are discussed in more detail in Section 3, are also strong factors. The connection linking the Alloy/Chemistry branch and microstructural features in Figure 152 emphasizes the fact that rate sensitivity, an important material property with respect to stress relaxation, is dependent on both composition *and* the length scale and spatial arrangement of microstructural features (Waheed, S., Zheng, Balint, & Dunne, 2019).

Once initiated, cracks tend to grow rapidly through suitably hard-oriented MTRs which again depends on the applied cycle as well as the microstructure and alloy composition. This early MTR-assisted crack growth may occur from a single initiation site in a single MTR, or it may result from multiple nucleation sites within a single MTR which coalesce during growth, or nucleation may occur within multiple nearby MTRs. More work is needed to understand the magnitude of the debit in fatigue life associated with each of these events. Once the crack is sufficiently large and has grown out of the initiating MTR, the impact of the dwell cycle is diminished and the measured growth rates approach those which are measured from conventional crack growth tests on compact tension specimens, though for some microstructures and macrotextures the dwell cycle may continue to have an impact as discussed in Section 4.3.
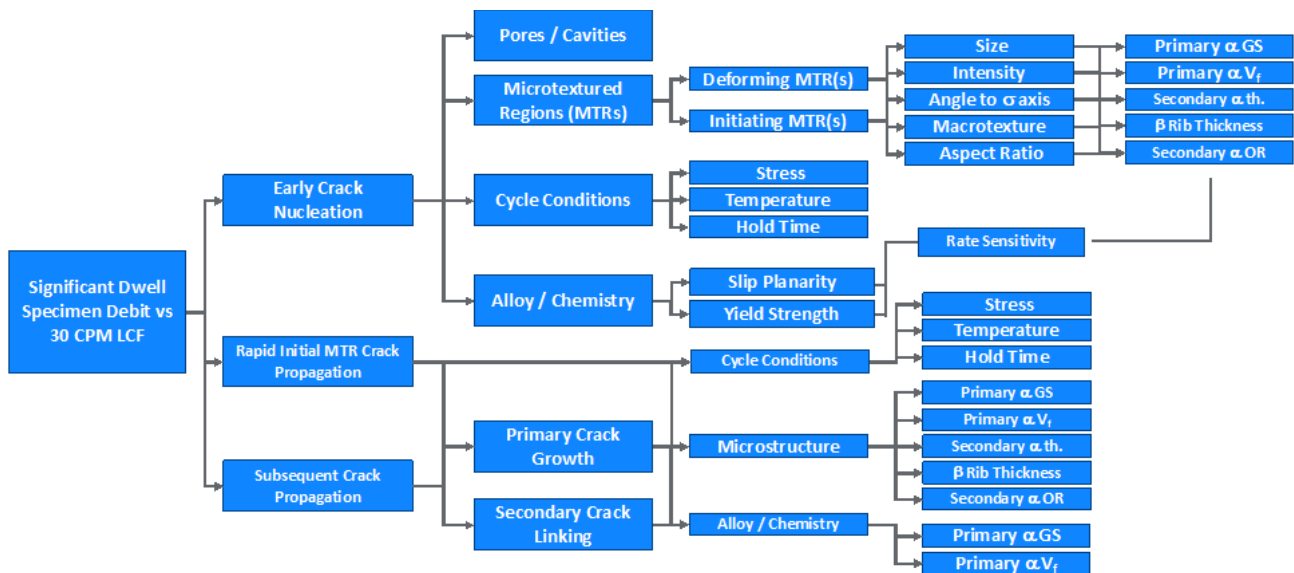
Figure 152. Roadmap of potential microstructure-and-mechanism-based root cause contributors for materials exhibiting a significant dwell debit

9.2　Alloy sensitivity

Neal (1988) investigated the dwell sensitivity of several titanium alloys including Ti-6Al-4V, Ti-550 (Ti-4Al-4Mo-2Sn-0.5Si), Ti-679 (Ti-11Sn-5Zr-2.25Al-1Mo-0.25Si), Ti-685 (Ti-6Al-5Zr-0.5Mo-0.25Si), Ti-6242, and Ti-829 (Ti-5.5Al-3.5Sn-3Zr-1Nb-0.25Mo-0.3Si) at room temperature and at 200 ºC (400 ºF). In all cases, there was no dwell effect observed at elevated temperature, however the alloys exhibited different degrees of sensitivity at room temperature. The results are summarized in Table 12 in terms of the percentage of life lost due to a 120 second hold at a peak stress that produced lifetimes of ~15,000 cycles under conventional low cycle fatigue testing. The results demonstrate a strong effect of alloy composition and shows a correlation between dwell sensitivity and the Al and Mo equivalencies. Ti-550 with low Al_{EQ} and high Mo_{EQ} (see Section 2.1) shows no sensitivity while Ti-685 and Ti-829 with higher Al_{EQ} and much lower Mo_{EQ} show relatively high sensitivity. This trend is not absolute, however, as Ti-6242 has only a marginally higher Al_{EQ} with $Mo_{EQ} = 2$ and shows the largest life debit of all. This illustrates clearly that other factors like processing route and microstructure also play an important role. Wu et al. (2022) have summarized additional experimental observations of alloy sensitivity (Table 13) but note that this is not an exhaustive list of all experimental data.

While Neal did not observe a strong dwell debit in Ti-6-4, Evans looked into the stress dependence of the dwell debit (Figure 97) and noted high levels of stress very near or above the yield strength induced a dwell effect during specimen testing of this alloy (Evans W. , 1987a). This is the earliest known report of the susceptibility of Ti-6-4 and two microstructural conditions were investigated. The first was a typical alpha+beta processed and alpha+beta heat treated with a bimodal microstructure while the second was a typical transformed beta microstructure consisting of alpha colonies. In this work, a conventional LCF cycle was compared with a 300 sec dwell at maximum load and indicated clear evidence of the susceptibility of Ti-6-4 (Figure 153) (Evans W. , 1987a). This paper may be less frequently cited in this context as it refers to CDF as creep-fatigue and cold-creep and was also published in a conference proceedings predating the advent of the internet and thus it is not widely available through the convenience of today's web searches. However, more recent observations confirming the effect of CDF on Ti-6-4 can be found in Tympel et al. (2016), Wang and Cui (2015), Venkatesh et al. (2020), and Pilchak, Hutson et al. (2016b).

Table 12. Effect of alloy composition on the percentage of life lost

Alloy	% Life Loss at Room Temperature	Aluminum Equivalence (Al_{EQ})*	Molybdenum Equivalence (Mo_{EQ})*	Max Stress (MPa)
Ti-550	0	6.42	4.00	935
Ti-6Al-4V	16	8.30	3.00	942
Ti-679	37	8.23	1.00	985
Ti-685	43	8.27	0.5	860
Ti-829	43	8.37	0.75	860
Ti-6242	65	8.66	2.00	not reported

*In Neal's work, $AlEQ = Al + Sn/3 + Zr/6 +10O$ and $MoEQ = Mo + 0.75V + 0.5Nb$; alternative definitions which consider a wider range of alloying elements are given in Section 2.1.
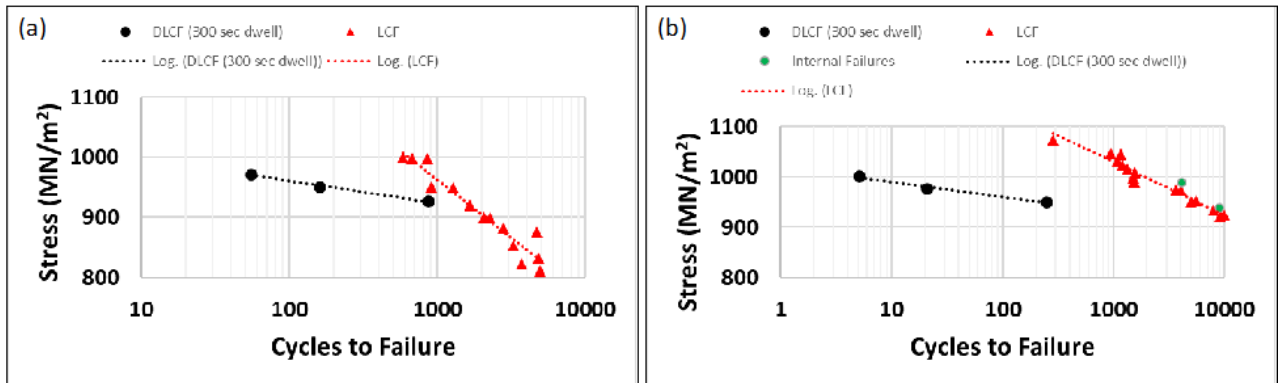
Figure 153. Fatigue test results for (a) bimodal microstructure and (b) transformed beta microstructure in Ti-6Al-4V

Table 13. Comparison of the dwell debit for various titanium alloys

Alloy	α_p grain size (μm)	α_p area fraction (%)	Loading waveforms	Stress ratio	Peak stress	LCF life (cycle)	Dwell-fatigue life (cycle)	Dwell debit
IMI 829 [13]	–	0	1-0 (120)-1	0	750 MPa	29,576	1983	14.91
					810 MPa	13,150	926	14.20
					827 MPa	10,477	232	45.16
IMI 834 bar stock material [15]	–	15	2-1 (120)-2	0.1	~0.78UTS	~31,000	~13,000	~2.38
					~0.83UTS	~12,000	~2200	~5.45
					~0.85UTS	~4800	~600	~8
IMI 834 disk material [15]	–	–	2-1 (120)-2	0.1	~0.69UTS	~39,000	~49,000	~0.80
					~0.76UTS	~19,000	~4800	~3.96
					~0.84UTS	~11,000	~780	~14.10
					~0.88UTS	~4500	~300	~15
Ti60 [18]	–	20	2-1 (120)-2	0.1	~0.90 YS	9790	4964	1.97
					~0.90 YS	9729	1870	5.20
					~0.96 YS	5800	1945	2.98
Ti–6Al–4V [97]	13	36	1-1 (120)-1-1	0.1	0.90 YS	~10,800	~3700	2.92
Ti6242Si [17]	–	64	1-1 (120)-1-1	0.05	0.95 YS	13,359	8655	1.54
Ti6242s [102]	21.5	25	1-0 (120)-1	0	0.99 YS	13,089	4871	2.69
Ti6242 [6]	~13.6	~90	1-1; 1-120-1-1	0	0.95 YS	–	–	7.9
Ti6243 [6]	~11.7	~85	1-1; 1-120-1-1	0	0.95 YS	–	–	~3.9
Ti6244 [6]	~9.6	~80	1-1; 1-120-1-1	0	0.95 YS	–	–	~3.5
Ti6245 [6]	–	–	1-1; 1-120-1-1	0	0.95 YS	–	–	~2.8
Ti6246 [6]	~5.3	~60	1-1; 1-120-1-1	0	0.95 YS	–	–	~2.9
TIMETAL® 575 [120]	–	15–18	1-1 (120)-1-1	0	~0.91 YS	~30,000	~19,000	~1.58
					~0.96 YS	~13,000	~6000	~2.17
					~100%YS	~6000	~2000	~3.0

1-1, a triangular waveform with 1 s rise and fall between peak and minimum stress; 1-120-1, a trapezoidal waveform with a rise/down time of 1 s, dwell time of 120 s; 1-1(120)-1-1, 1 s linear rise, 1 or 120 s hold at peak stress, 1 s fall and 1 s hold at minimum stress; UTS, ultimate tensile strength; YS, yield strength.

Based on their high aluminum equivalence and additional testing since Neal's efforts (1988), near-alpha titanium alloys such as Ti-834, Ti-829, Ti-685, and Ti-6242 are generally considered to be more cold dwell susceptible than alpha+beta titanium alloys. The reasons for this are still to be fully understood, but there are significant effects of alloying elements such as aluminium and oxygen on strain rate sensitivity and slip planarity as well as the effect of heavier beta stabilizing elements on microstructure evolution kinetics resulting in finer primary alpha grain size and transformed beta morphology (i.e., easier to form a basketweave microstructure with thinner lamellae). This is evident from the work of Spence et al. (1997) and Bache et al. (2007) who reported on coupon tests of Ti-6246 in the beta forged and beta heat treated condition as well beta forged and alpha+beta and water quenched condition. Both papers concluded that there was evidence that an applied dwell period shortens at very high applied stresses (90-95% UTS). There was also some evidence of planar slip extending over significant distances, however, there was no evidence of classic dwell facet formation on the fracture surface, which is indicative of the CDF failure mechanism. The absence of CDF susceptibility was attributed to the random orientations and extremely fine scale transformation product.

Qiu et al. (2014) investigated a series of alloys that spanned Ti-6242 to Ti-6246 in an effort to understand the role of Mo on dwell fatigue behavior. The authors investigated Ti-6Al-2Sn-4Zr-

*x*Mo with *x* = 2 to 6 and analyzed the life debit between a 'fast cycle' (1 second triangular wave form) fatigue and dwell fatigue (1-120-1 trapezoidal waveform with a 1 second dwell at minimum stress). The tests were performed at 95% of the 0.2% yield strength at room temperature with a load ratio of 0. The work showed that the dwell debit decreases rapidly as Mo content is increased and then changes slowly above 4% Mo (Figure 154). The alloys with low Mo content and higher dwell debits also showed higher rates of strain accumulation and more extensive secondary cracking as compared to the more heavily stabilized alloys. These effects were attributed to the effect of Mo in promoting nucleation of multiple variants of secondary alpha during cooling following forging as well as in slowing alpha grain growth. Finer alpha grains were found to promote finer slip band spacings implying strain was more homogeneously distributed across the alpha particles which reduced the intensity of the pileup on any one individual slip band.
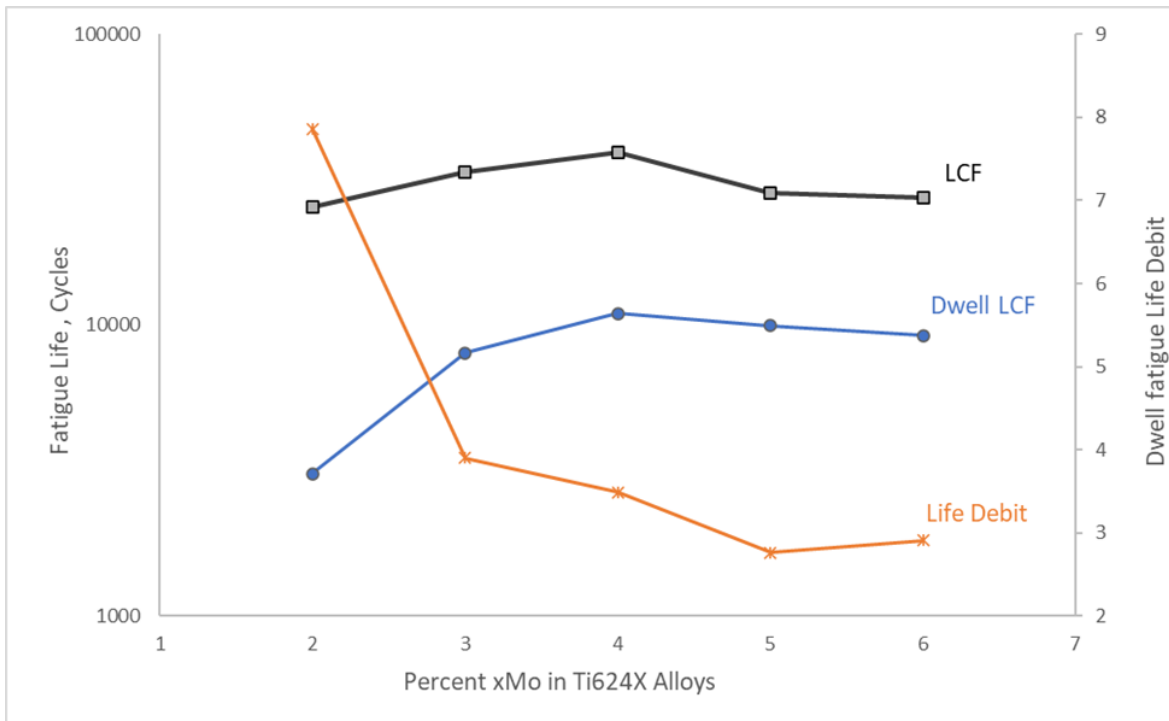
Figure 154. Effect of Mo on low cycle fatigue and dwell fatigue response of a Ti-6Al-2Sn-4Zr-xMo base alloy

Ready et al. (2017) complemented the work of Qiu et al. (2014) by using density functional theory to investigate the hypothesis that in Ti-6246 substitutional Mo-atoms in alpha-Ti grains trap vacancies therefore limiting creep relaxation and reducing sensitivity to the cold dwell fatigue failure mode. They calculated formation and binding energies between Mo-atoms and vacancies and concluded that this did not support the hypothesis thereby providing further

217

evidence that microstructural differences are one of the primary factors explaining why Ti-6246 has lower cold dwell susceptibility than Ti-6242. Another likely important factor may be related to the increased volume fraction of beta phase at room temperature. The BCC beta phase deforms more homogeneously due to the availability of 48 slip systems (e.g., {110}, {112}, and {123}) all gliding in <111> directions. This may help distribute slip more uniformly throughout the microstructure. Furthermore, Pilchak and Williams (2011) have noted the strong correspondence between the fracture morphology of samples under dwell fatigue and those that have failed under static loading in hydrogen gas. They argued in favor of the hydrogen enhanced localized plasticity mechanism (Robertson, et al., 2015; Shih, Robertson, & Birnbaum, 1988) by which the presence of hydrogen atmospheres can lower the barrier to dislocation nucleation, reduce the stress to move dislocations, and lowers the work to create two fracture surfaces (Kirchheim, Somerday, & Sofronis, 2015). While macroscopic testing regarding the role of hydrogen has been inconclusive, hydrogen is mobile at room temperature and is known to diffuse to regions of high stress. Since the beta phase has a much higher affinity and tolerance to hydrogen than the alpha phase, it is plausible that more heavily beta stabilized alloys can act as a sink for this hydrogen. Further work is needed in this area, however, especially first principles calculations.

Zheng et al. (2016) investigated the phenomenon of the difference in cold dwell fatigue behavior between Ti-6242 and Ti-6246 using a discrete dislocation model that includes the thermally activated escape of dislocations pinned by obstacles on the slip plane. It was predicted that Ti-6242 has a strong crystallographic and orientation-dependent rate sensitivity where Ti-6246 does not. These predictions agreed well with experimental measurements from nano-indentation tests (Jun, Armstrong, & Britton, 2016). The discrete dislocation model predicted significant amounts of load shedding and stress redistribution leading to very high basal stresses on poorly oriented hard/soft grain combinations in Ti-6242 that were potentially high enough to cause faceted nucleation. Ti-2646, on the other hand, because of its higher activation energy for dislocation escape, shows negligible stress redistribution and hence load shedding. This is in addition to the microstructure effects discussed by Qiu (2014).

The prime gas turbine engine manufacturers have reviewed the literature and their internal knowledge of dwell sensitivity of titanium alloys used for critical rotating parts and have collectively, and qualitatively summarized dwell sensitivity by alloy in Table 14.

Table 14. Current understanding of dwell sensitivity based on review by members of JETQC

Alloy	Forging	Heat Treat	Experience of cold dwell in field?	Experience of cold dwell in Rig testing?	Cold Dwell Sensitivity*	Temperature Limit for cold dwell susceptibility?	Potential to minimize sensitivity by processing
Ti-834	α/β	α/β	No	Yes	High	~400F	Unknown
Ti-829	α/β	β	No	Yes	High	~400F	Unknown
Ti-685	α/β	β	Yes	Yes	High	~400F	Unknown
Ti-6242	α/β	α/β	Yes	No	High	~400F	Yes
Ti-6242	β	α/β	No	Yes	High	~400F	No
Ti-64**	α/β	α/β	Yes	Yes	Medium	~400F	Yes
Ti-6246	β	α/β	No	No	Low	Not applicable	Not applicable
Ti-17	β	α/β	No	No	Low	Not applicable	Not applicable

* Based on material's current design space (field application) and current experience (specimen, rig, and field)

**Ti-6-4: 10x volume compared to other Ti alloys, but took many decades to show an issue in the field

This table also includes columns to depict whether the alloy has shown dwell sensitivity in fielded components or spin rig tests as well as upper temperature limits for cold dwell fatigue. Finally, the potential to minimize sensitivity by carefully controlling the thermomechanical processing is also captured. It is emphasized that this table is a summary of the current state of understanding and does not guarantee anything regarding the susceptibility of a given alloy to cold dwell fatigue in fielded components or rig tests. As discussed extensively throughout this document, there are many factors which can lead to a substantial dwell debit.

9.3 Processing and microstructure

With respect to thermomechanical processing, many variables were discussed for billet conversion, forging, and heat treatment in Section 6. However, some of these factors exert a stronger influence on finished component properties than others. A JETQC subcommittee was convened to collect decades worth of combined experience to rank the relative importance of these process parameters. It is noted that this is a qualitative assessment of the most critical elements based on today's state of combined industry knowledge, and a quantitative assessment of these factors is not well understood. This exercise took a holistic view of the processes used to manufacture rotating components and included billet conversion as well as component forging and heat treatment. Each JETQC member received a specific number of votes they could assign

to various processing steps and from this a qualitative assessment a ranking between 1 (most important) and 5 (least important) were compiled in Table 15.

Table 15. Critical process parameters leading to MTRs in components

Critical Process Parameter Leading to MTRs in Components		Rank
Billet Processing	α/β pre-strain parameters (strain, strain rate, temperature, time)	5
	β recrystallization parameters (time, temperature)	4
	β forge conditions (strain, strain rate, temperature, time)	3
	β quench conditions (section size, time to tank, water temperature, agitation)	2
	Final α/β work (strain)	1
	Final α/β work (upset & draw vs. draw only)	5
	Final α/β work (temperature)	3
	Final α/β soak time post-α/β work for recrystallization	4
	Final α/β work (shape)	3
	Billet end effects	5
	Press type	4
Forging and Heat Treatment	α/β or β forge (strain levels with multiple strain components)	2
	α/β forge (temperature and strain rate)	4
	Post-β forge or post-β heat treatment cooling rate	4
	Solution relative to transus to control primary α volume fraction	3
	Post-solution cooling rate to control epitaxial re-growth of primary α grains/plates and/or control secondary α plate size and morphology	3

It is worth emphasizing that all steps are important and those that ranked low, such as alpha/beta prestrain parameters, for example, generally reflect that the premium quality supply chain has developed a sufficient practice over the years and hence does not need significant attention. A lower ranking may also reflect the relative number of OEMs which use a particular forging practice (e.g., beta forging + alpha/beta heat treat or beta forging + beta heat treatment). With this in mind, the most influential factors were the final alpha+beta work and the beta quench conditions during billet processing followed by the strain imposed during finish forging. These were followed by various parameters for billet conversion (beta forging conditions, temperature of final alpha+beta work, and shape of the finished product) and heat treatment (solution temperature and cooling rate). The fourth most influential factors included the beta

recrystallization parameters, the final alpha+beta soak time, and the press type (open die vs. GFM) during conversion. The alpha+beta forging temperature and strain rate as well as the post-beta-forge and post-beta heat treat cooling rates ranked similarly for the finished forging.

9.4   Design

The precise conditions under which cold dwell fatigue presents a risk to components are not fully understood but are generally considered to be a function of the:

- alloy composition, including major alloying elements and interstitials,

- stress state (including stress level, stressed volume above a critical stress level, degree of multi-axiality, bulk residual stress, and the degree of load vs strain control),

- dwell time at a significant stress,

- thermal cycle under which dwell occurs (cold dwell is generally considered to occur at temperatures below 200 °C or 400 ºF), and

- the microstructure and macro/microtexture in the region of the component operating under cold dwell conditions (this will be dependent on both the alloy and the full thermomechanical processing route by which the component has been produced, see Section 6 for details).

In short, there is no specific stress limit that can be applied to a given alloy to ensure safety from cold dwell fatigue – the situation is much more complicated. Design of components and the processing routes to produce them need to be intimately related. As discussed in Section 7.1.1, the dwell debit decreases with stress level until a point at which the scatter associated with conventional fatigue and dwell fatigue overlap. The magnitude of this stress depends strongly on the state of the MTRs and other microstructure attributes in the material. Forgings produced from smaller diameter billet (with higher amounts of alpha+beta work) *may* be able to tolerate higher levels of stress. However, it is noted that variations in conversion practice and forging practice can obfuscate this correlation. For example, a forging produced from a well-converted 12" diameter billet and a well-designed forging practice can outperform a forging produced from a poorly converted 10" diameter billet with a poor forging practice.

As emphasized in Sections 7.1.4, 8.2.1, and 8.2.2, bulk residual stresses from the forging process must be considered, especially in creep-resistant near-alpha alloys. Although most components are shot-peened, initiation sites are typically well below the compressive residual stress layer associated with this process and hence, cannot be considered to provide any protection against

CDF crack nucleation. Furthermore, while classical design methodologies suggest the use of strain-control fatigue testing to life notched locations, early initiation due to CDF is generally not seen under strain control specimen testing. However, Section 7.1.4 demonstrated that low k_t notched specimens tested under load control exhibit crack initiation sites that are identical to those generated from load-control dwell tests performed on smooth cylindrical specimens. This implies that load-control failure processes are occurring in historically "strain-controlled" locations and thus these locations must not be assumed to be immune to CDF.

Finite element analysis is routinely used to predict the stress levels of components. Linear elastic analysis is relatively quick and easy but fails to accurately predict macroscopic stress redistribution within components. Thus, Harrison et al. (1986) advocated for the use of non-linear elastic (commonly referred to as "elastic plastic") analysis to predict component behavior. The constitutive response for such an analysis should be generated using a series of cyclic stress-strain tests (Glinka, 2010). The stressed volume that remains above a critical stress level (which is a function of the processing route) constitutes the risk volume of the component and this value multiplied by the total number of components constitutes the fleet risk volume. Since the mechanism of cold dwell is highly probabilistic in nature, there is potential for a relatively small subset of a population of parts to be subject to the conditions required to initiate and propagate a crack. Therefore, any sampling inspection of a limited number of parts or inspections concentrating on high life parts only may not indicate the level of risk in the total population as subtle differences in engine operating conditions and relatively minor variations in chemistry, billet/forge processing, and heat treatment conditions have the potential to change the overall population risk level.

9.5 Nondestructive inspection

9.5.1 Crack detection

Locating cracks developed in the manufacturing process or during service is a critical part of managing risk to rotating components and a variety of nondestructive inspection methods are used for this purpose. These include fluorescent penetrant inspection (FPI), eddy current inspection (ECI), and ultrasonic testing (UT) which may utilize longitudinal or shear wave inspections. Other techniques, like thermal acoustic imaging, are also utilized for specialized inspection of hollow-core fan blades. Each of these methodologies have different capabilities in terms of minimum detectable flaw sizes, probability of detection (POD) curves, and the locations of cracks that they can detect. For example, FPI and ECI are capable of detecting surface flaws although ECI is far more sensitive than FPI. Automated ECI systems can reliably detect cracks

as small as ~375 μm x 750 μm (depth x surface length), or 0.015" x 0.030", 90% of the time at 95% confidence (i.e. 90/95). FPI, on the other hand, is strongly dependent on local component geometry and access of the inspector, but, for the sake of comparison, NASA has reported a 90/95 value of ~1.91 mm x 3.82 mm (0.075" x 0.15") (NASA, 2019). In practice, better capability can be achieved with focused FPI at critical locations by well-trained inspectors and FPI can potentially detect cracks as small as 0.5 mm x 1 mm using automated systems (Harding & Hugo, 2011).

UT is the preferred method for interrogating for subsurface cracks and its 90/95 detectability is only marginally worse than ECI. The exact number, again, depends on component geometry, including section thickness, as well as the degree of microtexture in the component which can introduce significant backscattering noise during inspection. Cracks are typically driven by hoop stress in components and therefore oriented in the axial/radial plane which makes them difficult to detect with normal incidence inspection. As a result, shear wave inspections may be necessary for highly stressed locations.

Linear elastic fracture mechanics (LEFM) based crack propagation lifetimes are commonly used to help set inspection intervals as illustrated in Figure 155. These calculations assume an initial crack size that is consistent with the inspection method applied to the component and uses long crack growth data to estimate the propagation lifetime to a condition where the maximum stress intensity factor (K_{max}) equals or exceeds the plane strain fracture toughness (K_{IC}).
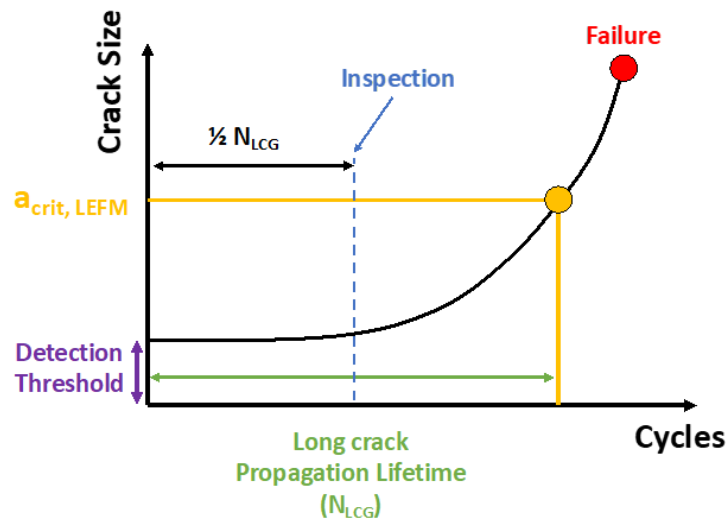

Figure 155. Schematic representation of a typical inspection methodology

In reality, cracks can grow to sizes larger than this value prior to complete separation of a component, but the growth rates are so fast that they are not managed this way. The inspection intervals are thus commonly set to be half of the calculated long crack propagation lifetime in order to give two chances to detect a potential flaw. This methodology works well for conventional low cycle fatigue (i.e., in the absence of dwell effects) because small crack effects are exhausted before the minimum detectable flaw size. Under dwell fatigue conditions, however, small crack effects persist throughout the entire initiating MTR and, depending on processing conditions, these MTRs may exceed the minimum detectable flaw size. Therefore, inspection intervals should be set more conservatively for locations where dwell fatigue is a potential concern. For more accurate predictions, modeling approaches which consider crack acceleration in and through the MTR can be considered (Chan & Moody, 2016; James, et al., 2022; Pilchak A. , 2014). If there is a concern about components operating in the cold dwell fatigue regime, the application of nondestructive inspections should be carefully considered.

9.5.2 Multizone inspection

Placing the focal spot of the transducer's sound beam subsurface is an inspection strategy which can boost signal strength for increased sensitivity. By pushing the focus subsurface, the ultrasound energy is intensified for the deep targets, increasing detection capability. This benefit was demonstrated by the ETC for use in titanium billets. Note that this effect should not be generalized to all angle scans because subsurface focusing of angled beam can lead to unpredictable and undesirable levels of defocus.

The depth of field of the 5 MHz, 6 inch (152 mm) focal length transducer allows for a single scan to cover a depth range of 1 inch (25 mm). Historic inspection practices have demonstrated that using this transducer at a 6-inch (152 mm) water path is effective at inspecting the volume from near front surface to 1 inch (25 mm) depth. It offers significant sensitivity beyond that depth, but superior sensitivity can be achieved for the 1-inch (25 mm) to 2 inch (51 mm) range of depths by reducing the water path to 2 inch (51 mm).

Curvature of the region also needs consideration when selecting the zones. The reduced water path of the second zone has an interaction with surface geometry which disrupts the focus. Regions with a concave diameter less than 20 inch (508 mm) should be viewed as problematic. Zone 2 scans may offer less sensitivity than using a Zone 1 water path with a zone 2 data gate.

9.5.3 Nondestructive evaluation of MTRs

While EBSD methods are the current 'gold standard' for MTR characterization, they are expensive, time consuming, and can only sample a limited area. It is clear from discussions

throughout this document that dwell fatigue failure is a rare event phenomenon involving critical pairs of MTRs with specific characteristics. Stochastic variations in the conversion process result in axial, radial, and circumferential differences in the MTRs along a billet which are carried into the forging process. Thus, forgings selected for periodic cutups, particular slices of these forgings, and the specific locations on these slices selected for EBSD analysis may not provide a complete picture of the dwell fatigue susceptibility of a given component with a nominally fixed processing route.

These realities underscore the need for the immediate development of nondestructive tools that can be used to rapidly scan large areas of metallographically prepared surfaces (e.g., billet or forging cross sections) or finished component surfaces as well as the eventual development of complete volumetric inspection technologies that can be used as a routine quality control tool to assess for process deviations. Fortunately, there has been significant research and development toward these goals which are outlined in Figure 26 and discussed in detail in Appendix C. Approaches based on ultrasonics (bulk and surface waves) and eddy current inspection are showing great promise toward these goals and there are ongoing programs to further mature these technologies.

10 Unknowns, open questions, and directions for further research

10.1 Material characterization

EBSD characterization of MTRs is well on its way to becoming a standard practice, however, the limited amount of material that can be characterized and the associated time and cost presents a challenge to implementing it as a routine quality control tool. As a result, there should be continued focus on developing alternative methods to scan larger areas more quickly and at lower cost.

Polarized light technologies (see Section 3.2 and Appendix B) have enormous potential for quantitative MTR characterization, however, there are several challenges that remain. These include understanding the impact of the optically isotropic beta phase on local c-axis orientation estimates, developing scanning protocols for components and curved surfaces, and developing methods tolerant to finish machined and shot peened components. Additionally, the plunge angle (angle between c-axis and surface normal) appears to be particularly challenging to determine accurately and quantitatively. Further work is also needed for segmentation and quantification protocols in order to obtain the MTR metrics outlined in Section 3.2.5.

Additional work on MTR characterization methods is needed to better understand critical microstructural neighborhoods and move beyond the classic hard/soft grain model. This should include the development of 3D datasets covering large volumes of material as well as continued development and industrialization of surface and volumetric nondestructive evaluation techniques. Further refinement and weighting the importance of key MTR characteristics outlined in Section 3.1 would also be beneficial.

10.2 Processing

As illustrated by Table 15, there are critical steps during billet processing, forging, and heat treatment that are believed to be most influential on MTR formation. Conversion and forging practices are typically supplier proprietary and hence OEMs and regulators do not have great insight into the steps in the process where seemingly subtle process deviations may potentially give rise to the formation of large MTRs. Thus, there is a need to track processes carefully and couple this with routine material characterization for MTRs. With the emergence of Industry 4.0 concepts which include increased connectivity of machines, automation/robotics, and the application of machine learning tools, among other things, there is an opportunity to better document all stages of the metal working processes used to manufacture critical components. One example may be identifying critical locations in the process leading to the formation of microporosity. Storage and analysis of such data is also beneficial for suppliers who can use it to optimize processes for increased productivity and yield.

10.2.1 Billet processing

Section 6.2.2.5 discusses a unique condition whereby large regions of similarly oriented beta phase can be present within certain MTRs. If the [0001] of the alpha phase in the MTR is close to a {110} plane in the beta phase, this sets up a condition where the variant selection processes during the allotropic transformation can lead to close alignment between [0001] in the primary and secondary alpha. Further, if these {110} || [0001] are also parallel to the hoop (max stress) direction in the disk (i.e., in hard orientations) they serve as the potential weak link in the microstructure. At present, it is unclear how these regions form, and further work is needed to ascertain the mechanisms of beta phase recrystallization during alpha+beta forging and heat treatment. They may be unrecrystallized grains from the final beta quench that are in near-ideal orientations relative to the strain path imposed during the rest of the forming operations, or they may originate from a preferred nucleation of preferred growth process either during alpha+beta forging or during solution heat treatment. Future work should focus on establishing the origin of beta microtexture which may involve characterizing the beta phase texture and presence of beta

microtexture within billet at various stages of the conversion process as well as careful analysis during solution heat treatment. Regardless of the origin, strategies should be developed to ensure that the beta phase fully recrystallizes and high angle beta grain boundaries are present beneath adjacent packets of transformed beta. This work may involve viscoplastic self-consistent crystal plasticity simulations similar to the work of Begley et al. (2020) who looked whether initially Burgers-related alpha would co-rotate in the same direction, rotate in opposite directions, or remain stable relative to axisymmetric compression. A similar analysis could be performed for a more complex strain path that mirrors the end of the conversion sequence and the forging operation. This should look for orientations that are in so-called ideal orientations or stable orientations relative to the imposed strain path. These orientations do not develop strong orientation gradients within them during hot working and hence have lower amounts of stored work and thus, do not recrystallize readily (Pilchak, et al., 2020).

10.2.2 Forging and heat treatment

Alpha+beta forging and alpha+beta heat treatment has been studied extensively, especially for the Ti-6Al-4V alloy. Considerably less attention has been given to the beta forging and alpha+beta heat treatment and the alpha+beta forging and beta heat treatment routes. Future studies can investigate the role of strain, strain rate, and temperature on microstructure evolution. In particular, the development of forging models that can predict MTR size and shape along with the MTR descriptors outlined in Section 3.1 would also be useful.

10.3 Mechanical properties

Despite several decades of research into cold dwell fatigue, there are still mechanical test variables that require further exploration. Any future work should be performed on material with known and carefully controlled thermomechanical processing to isolate the effects of specific microstructural variables. These include:

- **Alloying effects:** Alloy composition is one of the major factors in dwell susceptibility. It is known that alloy content influences rate sensitivity which significantly influences an alloys tendency to creep during the dwell period. The work of Qiu et al. (2014) provided great insight into composition effects on dwell fatigue spanning from near-alpha Ti-6242 to near-beta Ti-6246, however, the microstructures had differences in grain size and secondary alpha morphology. Another investigation could be performed to complement this foundational work which could utilize additional heat treatment steps and controlled cooling rates to produce equivalent microstructures to further the understanding of alloying element effects. There have been a few papers, including a recent one on the

227

binary Ti-7Al system (Worsnop, et al., 2022), that have elucidated the role of Ti$_3$Al (alpha2) on slip behavior and strain accumulation under creep conditions. Further work is needed in this area to understand the role of Ti$_3$Al during the unloading event and also the magnitude of the impact in commercial alloys. With the understanding of mechanisms leading to dwell fatigue failure, suppliers are beginning to offer new titanium alloys designed to be more tolerant to dwell fatigue. These generally involve increasing beta stabilizer content, which is known to increase strength at the expense of ballistic (i.e., bird strike) performance. Thus, ongoing and future alloy development efforts should consider ballistic resistance of the material early during the program. In addition, subtle variation in alloying elements within specification limits may also be important. For example, alloys with low Al and low O may have decreased strength compared to alloys on the other end of the spectrum. While there has been reasonable attention given to the role of oxygen on strength and damage tolerance characteristics, the role of other interstitials like C and N should also be explored.

- **Complex loading:** Most investigations have utilized very simple dwell cycles consisting of loading to high stress at a rapid rate (e.g., ~1 sec) followed by a long dwell period (~0.5 to 2 min) typically at a load ratio near zero (e.g. R = 0 ~ 0.1). Components in engines may experience a combination of low cycle fatigue without a significant dwell, low cycle fatigue with a dwell hold, and dwell holds with superimposed high-R HCF cycles. Additionally, high peak stresses may be encountered during climb followed by a significantly lower stress dwell during cruise. Certain locations may also experience different load ratios due to shakedown processes at low k$_t$ notches, for example. The interaction between these various types of loading may result in exhaustion of dislocation sources or differences in the dislocation structures. Thus, future work should consider the role of complex loading cycles to include variable stress cycles (e.g., high stress dwell followed by lower stress, longer duration dwell), variable R, as well as combined LCF/dwell/HCF cycles.

- **Load ratio effects:** As highlighted in Section 7.1.5, there is very limited data exploring the effect of load ratio on dwell fatigue performance and there are conflicting results among these reports (Section 7.1.5). Additional work should be undertaken to look at the impact of load ratio as a function of microstructural condition, stress, and temperature.

- **Loading rate effects:** Titanium alloys exhibit moderate rate-dependence at room and slightly elevated temperature. As a result, different loading rates to the peak stress will result in variations in the yield behavior of the material. Dwell test stresses are often

established and reported as fractions of the 0.2% yield strength or UTS, however, subsequent dwell tests are often done at a faster loading rate (e.g., ~1 second) meaning that the test is being performed at a different fraction of the rate-dependent yield strength. This has implications on specimen testing, spin rig testing, and fielded components. There are very few papers addressing this topic at this time and thus targeted investigations exploring different loading rates as a function of alloy composition and microstructural arrangement would be beneficial. This work should also attempt to isolate the role of loading rate on crack nucleation and the early stages of MTR-influenced crack propagation.

- **Other effects of microtexture:** It has been well established that MTRs affect cold dwell fatigue. The role of MTRs on other types of fatigue loading, including low cycle fatigue, high cycle fatigue, and very high cycle fatigue, remain less clear. Section 5 has covered some aspects which included the potential for creep during cycling at high load ratios, increased small crack growth rates, and increased variability in specimen testing. However, there have been no systematic investigations to quantify the magnitude of these effects.

- **Small crack effects:** It is well known that small crack effects exist under conventional cyclic fatigue loading, but most data in the literature is focused on low load ratios (R ≤ ~0.1) at high peak stress consistent with the LCF regime. Pilchak et al. (Pilchak A. , Hutson, Porter, Buchanan, & John, 2016b) have measured accelerated small crack growth rates under dwell fatigue conditions at room temperature inside of large MTRs in Ti-6-4. Thus, it is likely that there may be an additional acceleration of small cracks in the low stress, high-R HCF regime due to a combined creep-fatigue interaction. Experiments elucidating this mechanism would be beneficial.

- **Temperature effects:** While it is now well known that dwell sensitivity is worse at temperatures slightly above ambient, many investigations still rely on room temperature testing leading to a gap of relevant data in the literature. There is also increasing evidence that peak dwell sensitivity scales with the temperature dependence of the rate sensitivity as shown schematically in Figure 117. The peak value of the rate sensitivity as a function of temperature depends on alloy composition as well as microstructural arrangement. Further studies on the interaction of these two factors would be useful.

- **Thermomechanical fatigue:** Most academic and industrial studies to date have focused on testing samples to failure using 0.5 ~ 2 min dwell cycles, however, actual engine operating conditions are far more complex. Future work should focus on understanding

the effects of engine-relevant operating conditions, which include thermal transients, on dwell fatigue capability. Zheng et al. (2018) have shown that isothermal spin rig tests of Ti-834 are more damaging than disks in operation, however, these components also experience temperatures in excess of 200 ºC (400 ºF) which leads to a thermal alleviation effect. Additional work focused on combinations of stress and varying thermal history below 200 ºC would also be useful.

10.4 Basic research & fundamental mechanisms

▪ **Prestraining/precycling:** Early work by Odegard and Thompson (1974) demonstrated the beneficial effects of prestrain on reducing strain accumulation upon reloading the material at a lower stress level. More recent work by von Thüngen (2017) has demonstrated that precycling in conventional fatigue results in significant reductions in strain accumulation during subsequent dwell fatigue cycling of beta forged and alpha+beta heat treated Ti-6242. There were a limited number of tests performed, however, and the tests were at the 0.2% yield strength. Due to the potential importance of this effect in mitigating risk due to dwell fatigue via prespinning components, for example, this concept should be researched to look at variables such as the magnitude of prestrain and the method for imposing it (LCF vs. creep), the stress-dependence of the effect (i.e., at what stress level must the prestrain be applied in order to exhaust subsequent creep strain accumulation at a lower fraction of that applied stress), the temperature dependence of the effect, and the role of microstructure (bi-modal vs. basketweave vs. colony) on all of these factors.

▪ **Stress state:** Several authors have discussed the beneficial effect of biaxial stress states (Cuddihy, 2016; Cuddihy, Stapleton, Williams, & Dunne, 2017; Doquet & De Greef, 2012; Hommer, 2018) in reducing the dwell debit. In contrast, Evans and Bache (1994) found that positive biaxial ratios (under tension-torsion testing) may accelerate the failure process. These studies were generally based on a limited number of samples with small-stressed volumes. While these observations are useful, they are difficult to use in assessing the risk to component failure. Future work should be focused on samples with larger stressed volumes tested at various stress levels, load ratios, temperatures, and degrees of multiaxiality.

▪ **Stress vs. Strain control:** The local state at component features surrounded by large volumes of elastic material is generally treated with strain-life theories of fatigue. Nevertheless, fracture surfaces on components in these strain-controlled locations exhibit

features identical to those observed on load-control specimen tests. Strain control specimen testing fails to replicate these features although isolated facets have been observed during stress relaxation testing (Evans W. , 1987a). Additional testing is needed to rationalize these seemingly conflicting results. Such tests may explore the role of initial stress relaxation followed by periods of sustained dwell at smaller stress ranges or tests that use cycles with combined strain-and-stress-control such as those described in (Sonntag, Jürgens, Skrotzki, & Olbricht, 2023; Zhang, et al., 2020).

- **Room temperature recovery:** Creep and dwell fatigue tests typically show a strong initial creep transient followed by near steady state strain accumulation rates before accelerating again to failure. Savage et al. (2002) and Brandes and Mills (2004) conducted creep tests on samples of single-phase Ti-6Al, polycrystalline Ti-6242, and single colonies of Ti-6242 until the steady state creep regime and then unloaded them for times ranging between 1 minute and 11 months. The authors found that the macroscopic strain remained on the sample, but room temperature recovery processes that occurred during the period of unloading essentially "reset" the creep behavior such that an initial transient of rapid strain accumulation is present during subsequent loading. In operation or during engine overhaul or maintenance, there are potentially long periods of time where the engine is not under stress. From this perspective, components should experience multiple creep transients throughout the service life leading to increased strain accumulation and early failure. Based on the relatively few engine events documented, however, this is clearly not the case. Additional work is needed to understand the role of recovery processes on dwell fatigue capability. For example, do multiple unloading/recovery events followed by several creep transients eventually lead to exhaustion of dislocation sources at small cycle counts which diminishes strain accumulation for the rest of the service life?

- **Hydrogen:** The role of hydrogen on dwell fatigue remains largely clouded in the literature. Some authors advocate that it has an important role while others disagree. It is undeniable, however, that the fracture surfaces of dwell fatigue samples closely mirror those that are known to have fractured in hydrogen-containing environments (e.g., samples fractured in 3.5% NaCl solution and hydrogen gas environments). It is also known that hydrogen diffuses readily at room temperature to regions of high internal stress (such as crack tips) which implies that even small amounts of internal hydrogen in degassed samples may provide a sufficient concentration to induce the hydrogen enhanced localized plasticity (HELP) mechanism (Kirchheim, Somerday, & Sofronis, 2015; Robertson, et al., 2015; Shih, Robertson, & Birnbaum, 1988). Future theoretical

work utilizing density functional theory and experimental work can expand on the understanding of the role hydrogen potentially plays in both crack nucleation and crack propagation. Evidence to date suggests that hydrogen may likely play a role at the dislocation scale, but from specimen (Ghosh, et al., 2007; Sinha, Schwarz, Mills, & Williams, 2020) and field experience, there is no evidence that bulk hydrogen levels are related to specific failures.

10.4.1 Nondestructive evaluation of microtextured regions

Given the prior discussion on MTR variability during processing there are significant questions that remain regarding the contribution of individual thermomechanical processing steps to final MTR characteristics. From a practical perspective, the biggest need is to develop rapid and affordable volumetric scanning techniques to identify potential weaknesses in billet, forging, and heat treat processes. Until this happens, it will be difficult to isolate the key process variables leading to major deviations in MTR characteristics and provide meaningful feedback to improve processing sequences. Such tools will help to better understand these variables so that processing sequences can be modified to minimize the influence of MTRs on cold dwell fatigue.

Development of ultrasonic characterization of MTRs has been advanced significantly over the past 25 years (Appendix C). Most of this academic work has been performed with single element transducers in highly specialized laboratories on lab-scale coupons with normal incidences. Future studies should focus on the extension of these theories to phased array and multizone inspection systems as well as angled beams. Additionally, based on preliminary indications that mode-conversion at MTR boundaries results in backscattered shear-waves, additional work should continue to focus on developing new techniques for MTR-inversion using shear waves. In addition, development of production ready techniques for routine inspection and acceptance of billet and forgings would be highly useful in determining process deviations that lead to the formation of large MTRs. On-wing inspection technologies would also be useful for risk management strategies following uncontained engine events.

There are two key aspects that should be further explored. These include development of methods for the volume-averaged response of the material as well as techniques to identify discrete reflections from large MTRs. The former may be useful as a quality control tool that could be routinely performed on billets and forgings while the latter may be useful for identifying potential critical weak links within a nominally fixed processing practice. Recall that the allowable stress level in a component depends strongly on the state of the MTRs. Thus, if these tools could be used to verify the consistency of process improvements to reduce the

occurrence and deleterious aspects of MTRs, it would be possible to increase the maximum stress levels when designing future components.

An additional opportunity for further research toward improved inspectability lies in connecting the output of forge process modeling with UT inspection plans. As discussed in Appendix C, ultrasonic backscattering of longitudinal waves is minimized when the incident wave is parallel to the long axis of MTRs. Finite element analysis can predict forging flowlines during metal working processes and the long axes of the MTRs tend to line up with these (Pilchak, et al., 2016a). Sonic shapes and UT scanning strategies could be designed to guide inspections along directions where backscattering would be minimized to lower the noise level and enhance flaw detection.

11 Concluding comments and recommendations

Although there has been well over 10 billion component flight cycles across the major engine OEMs equating to a significant amount of successful experience with very few events, dwell fatigue still represents an important area to consider in the design and management of rotating components, especially with trends in engine size.

The work here shows that managing the risk of cold dwell fatigue is a multidisciplinary task involving design, materials, manufacturing, quality assurance, and sustainment. In this document, we have attempted to collect and collate industry knowledge on the subject supplemented by supporting literature. This was not intended to be a comprehensive review of all topics related to cold dwell fatigue and there are many more papers relevant to this topic that were not covered in detail here. In particular, the extensive modeling efforts of Somnath Ghosh (Johns Hopkins University) and Fionn Dunne (Imperial College) over the past 20 years were not adequately represented. This is not a reflection of the quality of the work, but rather a consequence of the broad scope of this effort. Several of their papers are referenced throughout this document and can serve as a starting point for a more thorough literature review on modeling and simulation approaches to understanding cold dwell fatigue.

At present, the FAA is considering updating Advisory Circular 33-15.1 and our intent is that this document provides substantiation behind the recommendations made therein. To mitigate the risk associated with cold dwell fatigue, JETQC recommends pursuing the following to reduce risks of future field failures due to influences of dwell fatigue and to ensure continued safe operations:

- Modify existing design and lifing practices to provide improved protection from CDF in titanium, including defining acceptable limits of MTRs or colony microstructures in rotating components.

- Develop improved billet, forging, and heat treat practices that limit the degree of microtexture and improve the consistency of materials used for rotating parts.

- Develop standard methods for characterizing microtexture from electron backscatter diffraction data and develop correlations between this and other destructive techniques including polarized light.

- Develop and industrialize non-destructive methods to characterize components with large colony or MTRs that do not meet design life intent due to potential reductions from dwell fatigue.

- Develop and apply models able to simulate behaviors in full scale components that are difficult to examine using specimen testing, for example, residual stress and stressed volume effects.

- Develop high fidelity, mechanism-based models that consider the role of composition, processing, and microstructure/defects on material performance. These models should be developed using highly characterized materials with well-known and intentionally varied processing pedigree. The breadth of material conditions should be wide enough to cover currently understood variations in production quality materials, including in-specification variations in alloy composition.

- Develop new rotor-grade, premium quality titanium alloys that consider the decades worth of composition and processing considerations summarized in this report and other associated literature that result in low susceptibility to cold dwell fatigue.

12   References

Advanced Optical Technologies. (2022). CrystalView CPCI Overview. Retrieved from
https://advanced-optical.com/products/crystalview-cpci

Ales, T., & Collins, P. (2020). A New Characterization Tool for 3D Orientation Microscopy at
Mesostructure Length Scales. *TMS Annual Meeting*.

Antolovich, B., & Evans, M. (2000). Predicting grain size evolution of UDIMET alloy 718
during the "cogging" process through the use of numerical analysis. *Ninth International
Symposium on Superalloys*, (pp. 39–47).

Appolaire, B., Aeby-Gautier, E., Da Costa-Teixeira, J., Hericher, L., & Denis, S. (2011).
Formation des microstructures issues des transformations à l'état solide dans les alliages
de titane. *Traitements & Matériaux, 408*, pp. 34–40.

Ari-Gur, P., & Semiatin, S. (1998). Evolution of microstructure, macrotexture and microtexture
during hot rolling of Ti-6A1-4V. *Materials Science and Engineering: A, 257*(1), 118–
127. doi:https://doi.org/10.1016/S0921-5093(98)00829-6

Atkinson, H., & Shi, G. (2003). Characterization of inclusions in clean steels: a review including
the statistics of extremes methods. *Progress in Materials Science, 48*(5), 457–520.
doi:https://doi.org/10.1016/S0079-6425(02)00014-2

Bache, M. (2003). A review of dwell sensitive fatigue in titanium alloys: The role of
microstructure, texture and operating conditions. *International Journal of Fatigue, 25*(9-
11), 1079–1087. doi:https://doi.org/10.1016/S0142-1123(03)00145-2

Bache, M., & Evans, W. (1993). Fatigue Under Tension / Torsion Loading in IMI685. *Ti'92:
Science & Technology, 1765*.

Bache, M., Cope, M., Davies, H., Evans, W., & Harrison, G. (1997). Dwell sensitive fatigue in a
near alpha titanium alloy at ambient temperature. *International Journal of Fatigue,
19*(93), 83–88. doi:https://doi.org/10.1016/S0142-1123(97)00020-0

Bache, M., Davies, H., & Evans, W. (1996). A Model for Fatigue Crack Initiation in Titanium
Alloys. In P. Blenkinsop, W. Evans, & H. Flower (Eds.), *Ti'95: Science and Technology*
(pp. 1347–1354). The Institute of Materials.

Bache, M., Germain, L., Jackson, T., & Walker, A. (2007). Mechanical and Texture Evaluations of Ti 6246 as a Dwell Fatigue Tolerant Alloy. *Ti-2007 Science and Technologie: Proceedings of the 11th World Conference on Titanium*, (pp. 523–526). Retrieved from https://www.researchgate.net/publication/272739532

Bandyopadhyay, R., Mello, A., Kapoor, K., Reinhold, M., Broderick, T., & Sangid, M. (2019). On the crack initiation and heterogeneous deformation of Ti-6Al-4V during high cycle fatigue at high R ratios. *Journal of the Mechanics and Physics of Solids, 129*, 61–82. doi:https://doi.org/10.1016/j.jmps.2019.04.017

Banerjee, D., Pilchak, A., & Williams, J. (2012). Processing, Structure, Texture and Microtexture in Titanium Alloys. *Materials Science Forum, 710*, 66–84. doi:https://doi.org/10.4028/www.scientific.net/MSF.710.66

Bantounas, I., Lindley, T., Rugg, D., & Dye, D. (2007). Effect of microtexture on fatigue cracking in Ti–6Al–4V. *Acta Materialia, 55*(16), 5655–5665. doi:https://doi.org/10.1016/j.actamat.2007.06.034

Bayha, T., Evans, D., & Furrer, D. (2002). Metals Afford Ability Initiative Consortium: the purpose of the Metals Affordability Initiative (MAI) is to improve the efficiency and reduce the costs of the methods by which metal parts are manufactured for aerospace applications. *Advanced Materials & Processes, 30*.

BEA. (2019). *Accident to the Airbus A380 registered F-HPJE and operated by Air France on 30/09/2017 en route over Greenland.* Retrieved from https://bea.aero/uploads/tx_elyextendttnews/F-HPJE_TECHNICAL_REPORT_05.pdf

BEA. (2020). *BEA2017-0568: Investigation Report: Accident to the AIRBUS A380-861 equipped with Engine Alliance GP7270 engines registered F-HPJE operated by Air France on 30 September 2017 in cruise over Greenland (Denmark).* Bureau d'Enquêtes et d'Analyses pour la sécurité de l'aviation civile. Retrieved from https://bea.aero/uploads/tx_elydbrapports/BEA2017-0568.en.pdf

Begley, B., Markham, K., Mizak, M., Pilchak, A., & Miller, V. (2020). Prediction of relative globularization rates in α + β titanium alloys as a function of initial crystal orientation. *Journal of Materials Research, 35*(8), 1113–1120. doi:https://doi.org/10.1557/jmr.2020.54

Beretta, S. (2021). More than 25 years of extreme value statistics for defects: Fundamentals, historical developments, recent applications. *International Journal of Fatigue, 151, 106407*. doi:https://doi.org/10.1016/j.ijfatigue.2021.106407

Bernier, J., Park, J.-S., Pilchak, A., Glavicic, M., & Miller, M. (2008). Measuring Stress Distributions in Ti-6Al-4V Using Synchrotron X-Ray Diffraction. *Metallurgical and Materials Transactions A, 39*(13), 3120–3133. doi:https://doi.org/10.1007/s11661-008-9639-6

Bernier, J., Suter, R., Rollett, A., & Almer, J. (2020). High-Energy X-Ray Diffraction Microscopy in Materials Science. *Annual Review of Materials Research, 50*(1), 395–436. doi:https://doi.org/10.1146/annurev-matsci-070616-124125

Bhattacharjee, A., Pilchak, A., Lobkis, O., Foltz, J., Rokhlin, S., & Williams, J. (2011). Correlating ultrasonic attenuation and microtexture in a near-alpha titanium alloy. *Metallurgical and Materials Transactions A: Physical Metallurgy and Materials Science, 42*(8), 2358–2372. doi:https://doi.org/10.1007/s11661-011-0619-x

Bhattacharyya, D., Viswanathan, G., Denkenberger, R., Furrer, D., & Fraser, H. (2003). The role of crystallographic and geometrical relationships between α and β phases in an α/β titanium alloy. *Acta Materialia, 51*(16), 4679–4691. doi:https://doi.org/10.1016/S1359-6454(03)00179-4

Bieler, T., & Semiatin, S. (2002). The origins of heterogeneous deformation during primary hot working of Ti–6Al–4V. *International Journal of Plasticity, 18*(9), 1165–1189. doi:https://doi.org/10.1016/S0749-6419(01)00057-2

Bieler, T., Nicolaou, P., & Semiatin, S. (2005). An experimental and theoretical investigation of the effect of local colony orientations and misorientation on cavitation during hot working of Ti-6Al-4V. *Metallurgical and Materials Transactions A, 36*(1), 129–140. doi:https://doi.org/10.1007/s11661-005-0145-9

Bingham, M., Lograsso, B., & Laabs, F. (2010). A statistical analysis of the variation in measured crystal orientations obtained through electron backscatter diffraction. *Ultramicroscopy, 110*(10), 1312–1319. doi:https://doi.org/10.1016/j.ultramic.2010.06.001

Blackburn, M., Smyrl, W., & Feeney, J. (1972). *Titanium Alloys In B. F. Brown (Ed.), Stress-corrosion cracking in high strength steels and in titanium and aluminum alloys.* Naval Research Laboratory. Retrieved from https://lccn.loc.gov/72600053

Blackshire, J., Na, J., & Daugherty, K. (2019). Coherent ultrasonic backscatter within a textured titanium alloy. *AIP Conference Proceedings*, *2102*. doi:https://doi.org/10.1063/1.5099725

Blodgett, M., & Eylon, D. (2001). The Influence of Texture and Phase Distortion on Ultrasonic Attenuation in Ti-6Al-4V. *Journal of Nondestructive Evaluation, 20*(1), 1–16. doi:https://doi.org/10.1023/A:1010611829059

Böhme, L., Morales-Rivas, L., Diederichs, S., & Kerscher, E. (2018). Crystal c-axis mapping of hcp metals by conventional reflected polarized light microscopy: Application to untextured and textured cp-Titanium. *Materials Characterization, 145*, 573–581. doi:https://doi.org/10.1016/j.matchar.2018.09.024

Bowen, A. (1975). The influence of crystallographic orientation on fatigue crack growth in strongly textured Ti-6A1-4V. *Acta Metallurgica, 23*(11), 1401–1409. doi:https://doi.org/10.1016/0001-6160(75)90149-2

Brandes, M. (2008). *Creep, Fatigue, And Deformation Of Alpha And Alpha-Beta Titanium Alloys At Ambient Temperature.* [Ph.D., The Ohio State University]. Retrieved from http://rave.ohiolink.edu/etdc/view?acc_num=osu1221848896

Brandes, M., & Mills, M. (2004). Static recovery in titanium alloys at lower temperatures. *Materials Science and Engineering: A, 387–389*, 570–575. doi:https://doi.org/10.1016/j.msea.2004.03.094

Brandes, M., Mills, M., & Williams, J. (2010). The influence of slip character on the creep and fatigue fracture of an α Ti-Al alloy. *Metallurgical and Materials Transactions A: Physical Metallurgy and Materials Science, 41*(13), 3463–3472. doi:https://doi.org/10.1007/s11661-010-0407-z

Bridier, F. (2006). *Analyse expérimentale des modes de déformation et d'endommagement par fatigue à 20°C d'alliage de titane: aspects cristallographiques à différentes échelles.* Retrieved from https://www.theses.fr/2006POIT2272. https://www.theses.fr/2006POIT2272

Brown, C., & Hicks, M. (1983). A study of short fatigue crack growth behaviour in titanium alloy IMI 685. *Fatigue & Fracture of Engineering Materials & Structures, 6*(1), 67–76. doi:https://doi.org/10.1111/j.1460-2695.1983.tb01139.x

Bruneseaux, F. (2008). *Apport de la diffraction des rayons X à haute énergie sur les transformations de phases, application aux alliages de titanes.* Institut National Polytechnique de Lorraine. Retrieved from https://hal.univ-lorraine.fr/tel-01748686

Bunge, H. (1982). *Texture Analysis in Materials Science.* Elsevier.
doi:https://doi.org/10.1016/C2013-0-11769-2

Burgers, W. (1934). On the process of transition of the cubic-body-centered modification into the
hexagonal-close-packed modification of zirconium. *Physica, 1*(7-12), 561–586.
doi:https://doi.org/10.1016/S0031-8914(34)80244-3

Burlatsky, S., Furrer, D., Venkatesh, V., Noraas, R., & Barker, S. (2023). Probabilistic Dwell
Fatigue Modeling of Titanium Components. *Proceedings of the 15th World Conference
on Titanium (Ti-2023), IOM3.*

Carr, R., Parinaud, H., Tritz, T., Winters, V., Alves, T., Knife, S., . . . Zabawa, D. (2010). *AIA
Project Report on High Bypass Ratio Turbine Engine Uncontained Rotor Events and
Small Fragment Threat Characterization 1969-2006.* Retrieved from
https://www.faa.gov/regulations_policies/rulemaking/committees/documents/media/App
%20B%20-
%20Vol1%20AIA%20Rotor%20Burst%20Small%20Fragment%20Committeee%20Rep
ort%20Fina%20r1%20(2).pdf

Castany, P., Pettinari-Sturmel, F., Crestou, J., Douin, J., & Coujou, A. (2007). Experimental
study of dislocation mobility in a Ti–6Al–4V alloy. *Acta Materialia, 55*(18), 6284–6291.
doi:https://doi.org/10.1016/j.actamat.2007.07.032

Chan, K., & Moody, J. (2016). A Hydrogen-Induced Decohesion Model for Treating Cold Dwell
Fatigue in Titanium-Based Alloys. *Metallurgical and Materials Transactions A, 47*(5),
2058–2072. doi:https://doi.org/10.1007/s11661-016-3367-0

Chatterjee, K., Ko, J., Weiss, J., Philipp, H., Becker, J., Purohit, P., . . . Beaudoin, A. (2017).
Study of residual stresses in Ti-7Al using theory and experiments. *Journal of the
Mechanics and Physics of Solids, 109*, 95–116.
doi:https://doi.org/10.1016/j.jmps.2017.08.008

Chatterjee, K., Venkataraman, A., Garbaciak, T., Rotella, J., Sangid, M., Beaudoin, A., . . .
Pilchak, A. (2016). Study of grain-level deformation and residual stresses in Ti-7Al under
combined bending and tension using high energy diffraction microscopy (HEDM).
International Journal of Solids and Structures, 94–95, 35–49.
doi:https://doi.org/10.1016/j.ijsolstr.2016.05.010

Cherry, M., Sathish, S., Mooers, R., & Pilchak, A. (2016). Progress in model development for
eddy current response in the presence of small conductivity changes. *42nd Annual*

Review of Progress in Quantitative Nondestructive Evaluation, 090019. doi:https://doi.org/10.1063/1.4940556

Cherry, M., Sathish, S., Pilchak, A., Cherry, A., & Blodgett, M. (2014). Characterization of microstructure with low frequency electromagnetic techniques. *40th Annual Review of Progress in Quantitative Nondestructive Evaluation*, 1456–1462. doi:https://doi.org/10.1063/1.4864993

Chesnutt, J., & Paton, N. (1980). Hold Time Effects on Fatigue Crack Propagation in Ti-6Al and Ti-6Al-4V. In K. &. (Eds.) (Ed.), *Ti'80 Science and Technology: Proceedings of the fourth international conference on titanium* (pp. 1855–1863). Metallurgical Society of AIME.

Chesnutt, J., Thompson, A., & Williams, J. (1978). *Influence of metallurgical factors on the fatigue crack growth rate in alpha-beta titanium alloys.* AFML-TR-78-68. Retrieved from https://apps.dtic.mil/sti/citations/ADA063404

Clark, M., Clare, A., Dryburgh, P., Li, W., Patel, R., Pieris, D., . . . Smith, R. (2019). Spatially resolved acoustic spectroscopy (SRAS) microstructural imaging. *45th Annual Review of Progress in Quantitative Nondestructive Evaluation*, 1–7. doi:https://doi.org/10.1063/1.5099705

Collins, P., & Ales, T. (2022, April 4). Iowa State University Center for Nondestructive Evaluation Post-IAB Seminar Part I.

Crispin, R., Jackson, E., Cummins, M., & Mecalo, J. (2000). *NTSB Final Report LAX98IA158.* National Transportation Safety Board. Retrieved from https://app.ntsb.gov/pdfgenerator/ReportGeneratorFile.ashx?EventID=20001211X10122&AKey=1&RType=Final&IType=IA

Cuddihy, M. (2016). *Cold Dwell Facet Nucleation in Titanium Alloy Aero-Engine Components.* PhD, Imperial College. Retrieved from https://spiral.imperial.ac.uk/bitstream/10044/1/68386/3/Cuddihy-M-2019-PhD-Thesis.pdf. https://spiral.imperial.ac.uk/bitstream/10044/1/68386/3/Cuddihy-M-2019-PhD-Thesis.pdf

Cuddihy, M., Stapleton, A., Williams, S., & Dunne, F. (2017). On cold dwell facet fatigue in titanium alloy aero-engine components. *International Journal of Fatigue, 97*, 177–189. doi:https://doi.org/10.1016/j.ijfatigue.2016.11.034

Davidson, D., & Eylon, D. (1980). Titanium Alloy Fatigue Fracture Facet Investigation by Selected Area Electron Channeling. *Metallurgical Transactions A, 11*(5), 837–843.

Davies, P., Wynne, B., Thomas, M., & Rainforth, W. (2018). Quantifying Crystallographic Texture Variation in a Titanium Billet. *IOP Conference Series: Materials Science and Engineering, 375, 012019*. doi:https://doi.org/10.1088/1757-899X/375/1/012019

Delfosse, J. (2005). *Forgeage β du Ti17: propriétés en fatigue [Encole Centrale de Paris].* Retrieved from https://www.theses.fr/2005ECAP0978

Dod, B., & Monavon, G. (2024). Room Temperature Creep Fracture Surface Morphology of Ti-6Al-4V Titanium Alloy and Comparison with Dwell and High R Ratio Cyclic Loading. *Proceedings of 15th World Conference on Titanium (Ti-2023).*

Doherty, R., Hughes, D., Humphreys, F., Jonas, J., Juul Jensen, D., Kassner, M., . . . Rollett, A. (1998). Current issues in recrystallization: A review. *Materials Today, 1*(2), 14–15. doi:https://doi.org/10.1016/S1369-7021(98)80046-1

Donegan, S., Tucker, J., Rollett, A., Barmak, K., & Groeber, M. (2013). Extreme value analysis of tail departure from log-normality in experimental and simulated grain size distributions. *Acta Materialia, 61*(15), 5595–5604. doi:https://doi.org/10.1016/j.actamat.2013.06.001

Doquet, V., & De Greef, V. (2012). Dwell-fatigue of a titanium alloy at room temperature under uniaxial or biaxial tension. *International Journal of Fatigue, 38*, pp. 118–129. doi:https://doi.org/10.1016/j.ijfatigue.2011.12.007

Dryburgh, P., Smith, R., Marrow, P., Lainé, S., Sharples, S., Clark, M., & Li, W. (2020). Determining the crystallographic orientation of hexagonal crystal structure materials with surface acoustic wave velocity measurements. *Ultrasonics, 108*, 106171. doi:https://doi.org/10.1016/j.ultras.2020.106171

Du, X., & Zhao, J.-C. (2017). Facile measurement of single-crystal elastic constants from polycrystalline samples. *Npj Computational Materials, 3*(1), 17. doi:https://doi.org/10.1038/s41524-017-0019-x

Dunne, F., Rugg, D., & Walker, A. (2007). Lengthscale-dependent, elastically anisotropic, physically-based hcp crystal plasticity: Application to cold-dwell fatigue in Ti alloys. *International Journal of Plasticity, 23*(6), 1061–1083. doi:https://doi.org/10.1016/j.ijplas.2006.10.013

El Haddad, M., Topper, T., & Smith, K. (1979). Prediction of non propagating cracks. *Engineering Fracture Mechanics, 11*(3), 573–584. doi:https://doi.org/10.1016/0013-7944(79)90081-X

Elagina, L., Gordienko, A., Evmenov, O., & Ivashko, V. (1982). J. C. Williams & A. F. Belov (Eds.), Titanium and Titanium Alloys: Scientific and Technological Aspects. In *Methods of Refining Coarse-grained Structures of Titanium Alloys* (pp. 1789–1798). Plenum Press.

Evans, W. (1987a). Creep-Fatigue Interactions in Ti-6Al-4V at Ambient Temperatures. *Creep and Fracture of Engineering Materials and Structures*, 603–613.

Evans, W. (1987b). The influence of microstructure on dwell sensitive fatigue in a near alpha titanium alloy. *Scripta Metallurgica*, 469–474. doi:https://doi.org/10.1016/0036-9748(87)90183-9

Evans, W. (1998). Optimising mechanical properties in alpha+beta titanium alloys. *Materials Science and Engineering: A, 243*(1-2), 89–96. doi:https://doi.org/10.1016/S0921-5093(97)00784-3

Evans, W. (2004). Time dependent effects in fatigue of titanium and nickel alloys. *Fatigue & Fracture of Engineering Materials & Structures, 27*(7), 543–557. doi:https://doi.org/10.1111/j.1460-2695.2004.00793.x

Evans, W., & Bache, M. (1994). Dwell-sensitive fatigue under biaxial loads in the near-alpha titanium alloy IMI685. *International Journal of Fatigue, 16*(7), 443–452. doi:https://doi.org/10.1016/0142-1123(94)90194-5

Evans, W., & Gostelow, C. (1979). The effect of hold time on the fatigue properties of a β-processed titanium alloy. *Metallurgical Transactions A, 10*(12), 1837–1846. doi:https://doi.org/10.1007/BF02811727

Eylon, D., & Hall, J. (1977). Fatigue behavior of beta processed titanium alloy IMI 685. *Metallurgical Transactions A, 8*(6), 981–990. doi:https://doi.org/10.1007/BF02661583

Fernandez Silva, B., Wynne, B., Jackson, M., Bodie, M., & Fox, K. (2019). Microtexture analysis of near-alpha titanium alloy Timetal 834 with varying macrozone sizes. *In Presentation at the 19th International Conference on Texture of Materials (ICOTOM 2019).*

Fernandez, S. B. (2021). *The Effect of Thermomechanical Processing on Texture, Macrozones and Cold Dwell Fatigue Performance in a Ti834 Compressor Disc Alloy.* [PhD, The University of Sheffield]. Retrieved from https://etheses.whiterose.ac.uk/29801/

Fernández, S. B., Jackson, M., Fox, K., & Wynne, B. (2023). Tool for automatic macrozone characterization from EBSD data sets of titanium alloys. *Journal of Applied Crystallography, 56*(3). doi:https://doi.org/10.1107/S1600576723003862

Fox, S., & Neal, D. (1995). The role of computer modelling in the development of large scale primary forging of titanium alloys. *Ti'95: Science and Technology*, 628–635.

Freiherr von Thungen, I. (2017). *Effet dwell: relation microstructure-microtexture-propriétés mécaniques de l'alliage de titane Ti6242.* Retrieved from https://theses.hal.science/tel-01486574/

Froes, F. (2015). *Titanium : physical metallurgy, processing, and applications.* ASTM International. doi:https://doi.org/10.31399/asm.tb.tpmpa.9781627083188

Garvey, J. (2000). *Safety Recommendation A-00-104.* Retrieved from https://www.ntsb.gov/safety/safety-recs/recletters/A00_104.pdf

Gautier, E., Bonina, D., Bruneseaux, F., Lamendin, A., Khelifa, M., & Lazaro, S. (2006). *TBD - Etude du comportement en fatigue fluage (Dwell) à 200°C de l'alliage Ti6242 - Evolution des microstructures et propriétés.*

Germain, L., Gey, N., Humbert, M., Bocher, P., & Jahazi, M. (2005). β→αs; Variant Selection in Sharp hcp Textured Regions of a Bimodal IMI834 Billet. *Materials Science Forum*, 495–497, 663–668. doi:https://doi.org/10.4028/www.scientific.net/MSF.495-497.663

Germain, L., Gey, N., Humbert, M., Vo, P., Jahazi, M., & Bocher, P. (2008). Texture heterogeneities induced by subtransus processing of near α titanium alloys. *Acta Materialia, 56*(16), 4298–4308. doi:https://doi.org/10.1016/j.actamat.2008.04.065

Germain, L., Samih, Y., Delaleau, P., Gilgert, J., & Gey, N. (2020). Analysis of Cold Dwell Fatigue Crack Initiation Site in a β-Forged Ti-6242 Disk in Relation with Local Texture. *Metals, 10*(7), 951. doi:https://doi.org/10.3390/met10070951

Gey, N., Bocher, P., Uta, E., Germain, L., & Humbert, M. (2012). Texture and microtexture variations in a near-α titanium forged disk of bimodal microstructure. *Acta Materialia, 60*(6-7), 2647–2655. doi:https://doi.org/10.1016/j.actamat.2012.01.031

Ghosh, S., Mills, M., Rokhlin, S., Sinha, V., Soboyejo, W., & William, J. (2007). *The Evaluation of Cold Dwell Fatigue in Ti-6242.* DOT/FAA/AR-06/24, FAA. Retrieved from https://www.tc.faa.gov/its/worldpac/techrpt/ar0624main.pdf.

Gigliotti, M., Bewlay, B., Deaton, J., Gilmore, R., & Salishchev, G. (2000). Microstructure-ultrasonic inspectability relationships in Ti6242: Signal-to-noise in fine-grain-processed Ti6242. *Metallurgical and Materials Transactions A, 31*(9), 2119–2125. doi:https://doi.org/10.1007/s11661-000-0129-8

Gil, F., Ginebra, M., Manero, J., & Planell, J. (2001). Formation of α-Widmanstätten structure: effects of grain size and cooling rate on the Widmanstätten morphologies and on the mechanical properties in Ti6Al4V alloy. *Journal of Alloys and Compounds, 329*(1-2), 142–152. doi:https://doi.org/10.1016/S0925-8388(01)01571-7

Ginty, B., Hallam, P., Hammond, C., Jackson, G., & Robb, C. (1980). The Influence of Microstructure on Ultrasonic Response in a Titanium Alloy Forging. In H. Kimura, & O. Izumi (Ed.), *Ti'80 Science and Technology: Proceedings of the fourth international conference on titanium* (pp. 2095–2103). Metallurgical Society of AIME.

Glavicic, M., Furrer, D., & Shen, G. (2010). A Rolls-Royce Corporation industrial perspective of titanium process modelling and optimization: current capabilities and future needs. *Journal of Strain Analysis for Engineering Design, 45*(5), 329–335. doi:https://doi.org/10.1243/03093247JSA577

Glavicic, M., Goetz, R., Barker, D., Shen, G., Furrer, D., Woodfield, A., & Semiatin, S. (2008). Modeling of Texture Evolution during Hot Forging of Alpha/Beta Titanium Alloys. *Metallurgical and Materials Transactions A, 39*(4), 887–896. doi:https://doi.org/10.1007/s11661-007-9376-2

Glavicic, M., Kobryn, P., Spadafora, F., & Semiatin, S. (2003). Texture evolution in vacuum arc remelted ingots of Ti-6Al-4V. *Materials Science and Engineering: A, 346*(1-2), 8–18. doi:https://doi.org/10.1016/S0921-5093(02)00525-7

Glavicic, M., Morton, T., Broderick, T., Venkatesh, V., Zhang, F., Boyce, D., . . . Semiatin, S. (2016). Progress in the Advanced Titanium Microstructure and Modeling Program. *Proceedings of the 13th World Conference on Titanium*, (pp. 1863–1873). doi:https://doi.org/10.1002/9781119296126.ch312

Glinka, G. (2010). *The Local Stress-Strain Fatigue Method.* Retrieved from https://www.efatigue.com/training/Strain_Life_Method.pdf

Gorman, M., & Woodfield, A. (2001). *USA Patent No. 6,332,935 B1.* Retrieved from
https://patents.google.com/patent/US6332935B1

Gorman, M., Woodfield, A., & Link, B. (2001). *USA Patent No. 6,284,070 B1.* Retrieved from
https://patents.google.com/patent/US6284070B1/en

Gourbesville, O. (2000). *Caractérisation par drx de la microstructure d'alliages à base de nickel
(718) et à base de titane (ti-17) forges et traites prévision des propriétés mécaniques
[ENSAM].* Retrieved from https://www.theses.fr/2000ENAM0035.
https://www.theses.fr/2000ENAM0035

Groeber, M., & Jackson, M. (2014). DREAM.3D: A Digital Representation Environment for the
Analysis of Microstructure in 3D. *Integrating Materials and Manufacturing Innovation,
3*(1), 56–72. doi:https://doi.org/10.1186/2193-9772-3-5

Hall, J., & Garvey, J. (1998). *NTSB: Safety Board Recommendation A-98-27.* Retrieved from
https://www.ntsb.gov/safety/safety-recs/recletters/A98_27_33.pdf

Hall, J., & Garvey, J. (2000). *NTSB: Safety Recommendation A-00-104.* Retrieved from
https://www.ntsb.gov/safety/safety-recs/recletters/A00_104.pdf

Han, Y., & Thompson, R. (1997). Ultrasonic backscattering in duplex microstructures: Theory
and application to titanium alloys. *Metallurgical and Materials Transactions A, 28*(1),
91–104. doi:https://doi.org/10.1007/s11661-997-0085-7

Harding, C., & Hugo, G. (2011). *DSTO-TR-2623: Review of Literature on Probability of
Detection for Liquid Penetrant Nondestructive Testing.* Retrieved from
https://apps.dtic.mil/sti/pdfs/ADA560011.pdf

Harper, M., Kosaka, Y., & Fox, S. (2007). Titanium Metallography Using Heat Tinting. In N.
Gakkai, & M. Niinomi (Ed.), *Ti-2007 Science and Technology: Proceedings of the 11th
World Conference on Titanium* (pp. 785–788). Japan Institute of Metals.

Harr, M., Daly, S., & Pilchak, A. (2021). The effect of temperature on slip in microtextured Ti-
6Al-2Sn-4Zr-2Mo under dwell fatigue. *International Journal of Fatigue, 147*, 106173.
doi:https://doi.org/10.1016/j.ijfatigue.2021.106173

Harr, M., Pilchak, A., & Semiatin, S. (2021). Titanium Microtexture 101 - Part II. *Advanced
Materials and Processes, 179*(6), 13–16.

Harrison, G., & Winstone, M. (1996). Modelling and lifing of structural materials for future aeroengine components. *Advanced Performance Materials, 3*(3-4), 263–278. doi:https://doi.org/10.1007/BF00136791

Harrison, G., Trantner, P., Winstone, M., & Evans, W. (1986). Designing for dwell-sensitive fatigue in near-alpha titanium alloys. *Designing with Titanium*, pp. 198–204.

Hasija, V., Ghosh, S., Mills, M., & Joseph, D. (2003). Deformation and creep modeling in polycrystalline Ti–6Al alloys. *Acta Materialia, 51*(15), 4533–4549. doi:https://doi.org/10.1016/S1359-6454(03)00289-1

Hémery, S., Stinville, J., Wang, F., Charpagne, M., Emigh, M., Pollock, T., & Valle, V. (2021). Strain localization and fatigue crack formation at (0001) twist boundaries in titanium alloys. *Acta Materialia, 219*, 117227. doi:https://doi.org/10.1016/j.actamat.2021.117227

Hémery, S., Villechaise, P., & Banerjee, D. (2020). Microplasticity at Room Temperature in α/β Titanium Alloys. *Metallurgical and Materials Transactions A, 51*(10), 4931–4969.

Hertzberg, R., Vinci, R., & Hertberg, J. (2012). *Deformation and Fracture Mechanics of Engineering Materials (5th ed.).* Wiley.

Hijazi, F., Srinivasan, D., Roy, B., Kumar, P., & Jayaram, V. (2022). Micro-texture regions in rolled Ti-6Al-4V under polarized light. *Scripta Materialia, 213*, 114588. doi:https://doi.org/10.1016/j.scriptamat.2022.114588

Homa, L., Cherry, M., & Wertz, J. (2021). Estimation of microtexture region orientation distribution functions using eddy current data. *Inverse Problems, 37*(6), 065004. doi:https://doi.org/10.1088/1361-6420/abfb7e

Homa, L., Cherry, M., & Wertz, J. (2022). Estimation of Realistic Microtexture Region Orientation Distribution Functions Using Eddy Current Data. *JOM, 74*(10), 3693–3708. doi:https://doi.org/10.1007/s11837-022-05360-7

Hommer, G. (2018). *Mechanism of dwell fatigue crack initiation in Ti-7Al under biaxial tension-tension loads.* PhD, Colorado School of Mines. Retrieved from https://www.proquest.com/openview/5da5a44b0ed6331bfd408a2d3b59e825/1?pq-origsite=gscholar&cbl=18750

Hoover, B., Turner, J., & Ornelas-Rascon, C. (2021). Electrodynamic solution for polarized reflectivity and wide-field orientation imaging of uniaxial metals. *Journal of the Optical Society of America A, 38*(12), 1752. doi:https://doi.org/10.1364/JOSAA.435617

Hoover, B., Turner, J., Ritter, B., Michael, J., & Uchic, M. (2018). Polarized reflectivity for quantitative crystallography of alpha-titanium. In L. Hanssen (Ed.), *Reflection, Scattering, and Diffraction from Surfaces VI* (p. 12). SPIE. doi:https://doi.org/10.1117/12.2321601

Hoover, B., Turner, J., Ritter, B., Michael, J., & Uchic, M. (2018b). *Polarized Reflectivity for Quantitative Crystallography of alpha-Titanium.* Retrieved from https://www.osti.gov/servlets/purl/1576212

Humbert, M., Moreau, A., Uta, E., Gey, N., Bocher, P., & Bescond, C. (2009). Analysis of backscattered ultrasound amplitude of Ti–5.8Al–4Sn–3.5Zr–0.7Nb–0.5Mo–0.3Si samples in terms of their microstructures and local textures. *Acta Materialia, 57*(3), 708–714. doi:https://doi.org/10.1016/j.actamat.2008.10.012

Imperial College London. (2023). Retrieved from HexMat Website: Https://www.Imperial.Ac.Uk/Hexmat/. https://www.imperial.ac.uk/hexmat/

Iowa State University, & Center for Nondestructive Evaluation. (2022). *Nondestructive Testing and Evaluation (NDT&E) Education.* Retrieved from https://nde-ed.org

Ito, Y., Murakami, S., & Tsuji, N. (2017). SEM/EBSD Analysis on Globularization Behavior of Lamellar Microstructure in Ti-6Al-4V During Hot Deformation and Annealing. *Metallurgical and Materials Transactions A, 48*(9), 4237–4246. doi:https://doi.org/10.1007/s11661-017-4180-0

Ivasishin, O., Semiatin, S., Markovsky, P., Shevchenko, S., & Ulshin, S. (2002). Grain growth and texture evolution in Ti–6Al–4V during beta annealing under continuous heating conditions. *Materials Science and Engineering: A, 337*(1-2), 88-96. doi:https://doi.org/10.1016/S0921-5093(01)01990-6

Jackson, M. (2023). Bluequartz Software. http://www.bluequartz.net.

James, J., John, R., Jha, S., Pilchak, A., Arroyave, R., & Payton, E. J., E. (2022). Effect of Microtextured Region Stereology on Crack Growth Lifetime Predictions in Ti-6Al-4V. *JOM: Journal of the Minerals, Metals, and Materials Society, 74*(10), 3720–3732. doi:https://doi.org/10.1007/s11837-022-05462-2

Jin, K.-W., & De Graef, M. (2020). c-Axis orientation determination of α-titanium using Computational Polarized Light Microscopy. *Materials Characterization, 167*, 110503. doi:https://doi.org/10.1016/j.matchar.2020.110503

Joseph, S., Joseph, K., Lindley, T., & Dye, D. (2020). The role of dwell hold on the dislocation mechanisms of fatigue in a near alpha titanium alloy. *International Journal of Plasticity, 131*, 102743. doi:https://doi.org/10.1016/j.ijplas.2020.102743

Joseph, S., Lindley, T., & Dye, D. (2018). Dislocation interactions and crack nucleation in a fatigued near-alpha titanium alloy. *International Journal of Plasticity, 110*, 38–56. doi:https://doi.org/10.1016/j.ijplas.2018.06.009

Jousset, H. (2008). *Viscoplasticité et microstructures d'un alliage de titane: effets de la température et de la vitesse de sollicitation [École Nationale Supérieure des Mines de Paris].* Retrieved from https://pastel.archives-ouvertes.fr/tel-00428968

Jun, T.-S., Armstrong, D., & Britton, T. (2016). A nanoindentation investigation of local strain rate sensitivity in dual-phase Ti alloys. *Journal of Alloys and Compounds, 672*, 282–291. doi:https://doi.org/10.1016/j.jallcom.2016.02.146

Kassner, M., Kosaka, Y., & Hall, J. (1999). Low-cycle dwell-time fatigue in Ti-6242. *Metallurgical and Materials Transactions A, 30*(9), 2383–2389. doi:https://doi.org/10.1007/s11661-999-0246-y

Keller, M., Patton, T., Degtyar, A., Umbach, J., Hassan, W., Kinney, A., . . . Brasche, L. (2005). *Inspection Development for Titanium Billet - Engine Titanium Consortium Phase II.* DOT/FAA/AR-05/30. Retrieved from https://www.tc.faa.gov/its/worldpac/techrpt/ar05-30.pdf

Kim, J.-Y., & Rokhlin, S. (2009). Determination of elastic constants of generally anisotropic inclined lamellar structure using line-focus acoustic microscopy. *The Journal of the Acoustical Society of America, 126*(6), 2998–3007. doi:https://doi.org/10.1121/1.3245032

Kim, J.-Y., Yakolev, V., & Rokhlin, S. (2002). Line-focus acoustic microscopy of Ti-6242 α/β single colony: determination of elastic constants. *AIP Conference Proceedings*, *Vol. 615, No. 1*, pp. 1118–1125. doi:https://doi.org/10.1063/1.1472920

Kirchheim, R., Somerday, B., & Sofronis, P. (2015). Chemomechanical effects on the separation of interfaces occurring during fracture with emphasis on the hydrogen-iron and hydrogen-nickel system. *Acta Materialia, 99*, 87–98. doi:https://doi.org/10.1016/j.actamat.2015.07.057

Klaassen et al. (2023). New Inspection Method to Rapidly Detect Microtexture in Ti Alloys. In M. J. (Ed.) (Ed.), *15th World Conference on Titanium.* IOM3.

Korsunsky, A., Wells, K., & Withers, P. (1998). Mapping two-dimensional state of strain using synchrotonsynchrotron X-ray diffraction. *Scripta Materialia, 39*(12), 1705–1712. doi:https://doi.org/10.1016/S1359-6462(98)00385-6

Kotha, S., Ozturk, D., & Ghosh, S. (2020). Uncertainty-quantified parametrically homogenized constitutive models (UQ-PHCMs) for dual-phase α/β titanium alloys. *Npj Computational Materials, 6*(1), 117. doi:https://doi.org/10.1038/s41524-020-00379-3

Kuzmenkov, K. (2012). *Study of dwell-effect on behaviour and fracture of the alloy Ti-6242.* Retrieved from https://pastel.archives-ouvertes.fr/pastel-00745834/

Lan, B., Lowe, M., & Dunne, F. (2014). Experimental and computational studies of ultrasound wave propagation in hexagonal close-packed polycrystals for texture detection. *Acta Materialia, 63*, 107–122. doi:https://doi.org/10.1016/j.actamat.2013.10.012

Lan, B., Lowe, M., & Dunne, F. (2015). A spherical harmonic approach for the determination of HCP texture from ultrasound: A solution to the inverse problem. *Journal of the Mechanics and Physics of Solids, 83*, 179–198. doi:https://doi.org/10.1016/j.jmps.2015.06.014

Lavogiez, C. (2020). *Étude de l'effet « dwell » dans le Ti-6Al-4V: mécanismes de déformation et d'amorçage de fissures en relation avec l'orientation cristallographique locale de la phase αp.* Retrieved from https://www.theses.fr/2020ESMA0004

Lavogiez, C., Hémery, S., & Villechaise, P. (2020a). Analysis of deformation mechanisms operating under fatigue and dwell-fatigue loadings in an α/β titanium alloy. *International Journal of Fatigue, 131*. doi:https://doi.org/10.1016/j.ijfatigue.2019.105341

Lavogiez, C., Hémery, S., & Villechaise, P., P. (2020b). On the mechanism of fatigue and dwell-fatigue crack initiation in Ti-6Al-4V. *Scripta Materialia, 183*, 117–121. doi:https://doi.org/10.1016/j.scriptamat.2020.03.031

Le Biavant-Guerrier, K. (2000). *Etude de l'amorçage de fissures de fatigue dans le Ti-6Al-4V [Encole Centrale de Paris].* Retrieved from https://theses.hal.science/tel-00466425/

Lee, E. (2004). *Microstructure evolution and microstructure/mechanical properties relationships in α+β titanium alloys.* PhD, The Ohio State University. Retrieved from https://etd.ohiolink.edu/apexprod/rws_etd/send_file/send?accession=osu1092756139&disposition=inline

Lefranc, P. (2008). *Endommagement sous chargement cyclique avec temps de maintien de l'alliage de titane Ti-6242: rôle de l'hydrogène interne.* Retrieved from https://www.theses.fr/2008POIT2265

Lefranc, P., Doquet, V., Gerland, M., & Sarrazin-Baudoux, C. (2008). Nucleation of cracks from shear-induced cavities in an α/β titanium alloy in fatigue, room-temperature creep and dwell-fatigue. *Acta Materialia, 56*(16), 4450–4457. doi:https://doi.org/10.1016/j.actamat.2008.04.060

Lerch, B., & Arnold, S. (2014). *Viscoelastic Response of the Titanium Alloy Ti-6-4: Experimental Identification of Time- and Rate-Dependent Reversible and Irreversible Deformation Regions.* Retrieved from https://ntrs.nasa.gov/citations/20140008853

Levkulich, N., Semiatin, S., Payton, E., Srivatsa, S., & Pilchak, A. (2021). An Investigation of the Development of Coarse Grains During β Annealing of Hot-Forged Ti-6Al-4V. *Metallurgical and Materials Transactions A*, 1353–1367. doi:https://doi.org/10.1007/s11661-021-06158-z

Li, J., & Rokhlin, S. (2016). Elastic wave scattering in random anisotropic solids. *International Journal of Solids and Structures, 78–79*, 110–124. doi:https://doi.org/10.1016/j.ijsolstr.2015.09.011

Li, J., Lobkis, O., Yang, L., & Rokhlin, S. (2012). Integrated method of ultrasonic attenuation and backscattering for characterization of microstructures in polycrystals. *AIP Conference Proceedings*, *1430*, pp. 1397–1404. doi:https://doi.org/10.1063/1.4716380

Li, J., Yang, L., & Rokhlin, S. (2014). Effect of texture and grain shape on ultrasonic backscattering in polycrystals. *Ultrasonics, 54*(7), 1789–1803. doi:https://doi.org/10.1016/j.ultras.2014.02.020

Liu, C., Xu, X., Sun, T., Thomas, R., da Fonseca, J., & Preuss, M. (2023). Microstructural effects on fatigue crack initiation mechanisms in a near-alpha titanium alloy. *Acta Materialia, 253*, 118957. doi:https://doi.org/10.1016/j.actamat.2023.118957

Liu, Y., & Dunne, F. (2021). The mechanistic link between macrozones and dwell fatigue in titanium alloys. *International Journal of Fatigue, 142*, 105971. doi:https://doi.org/10.1016/j.ijfatigue.2020.105971

Livings, R., Mayes, A., Biedermann, E., Heffernan, J., Jauriqui, L., & Mazdiyasni, S. (2019). Detection of microtexture regions in titanium turbine engine disks using process

compensated resonance testing: A modeling study. 020022. doi:https://doi.org/10.1063/1.5099726

Lobkis, O., & Rokhlin, S. (2010). Characterization of polycrystals with elongated duplex microstructure by inversion of ultrasonic backscattering data. *Applied Physics Letters, 96*(16), 161905. doi:https://doi.org/10.1063/1.3416910

Lobkis, O., Yang, L., Li, J., & Rokhlin, S. (2012). Ultrasonic backscattering in polycrystals with elongated single phase and duplex microstructures. *Ultrasonics, 52*(6), 694–705. doi:https://doi.org/10.1016/j.ultras.2011.12.002

Lunt, D., Quinta da Fonseca, J., Rugg, D., & Preuss, M. (2017). Microscopic strain localisation in Ti-6Al-4V during uniaxial tensile loading. *Materials Science and Engineering: A, 680*, 444–453. doi:https://doi.org/10.1016/j.msea.2016.10.099

Lütjering, G., & Williams, J. (2007). *Titanium (2nd ed., Vol. 2).* Berlin: Springer. doi:https://doi.org/10.1007/978-3-540-73036-1

Ma, R. (2018). *Investigating the evolution of microtextured region in Ti-6242 using FE-FFT multiscale modeling method.* Retrieved from https://trace.tennessee.edu/utk_graddiss

Ma, R., Pilchak, A., Semiatin, S., & Truster, T. (2018). Modeling the evolution of microtextured regions during α/β processing using the crystal plasticity finite element method. *International Journal of Plasticity, 107*, 189–206. doi:https://doi.org/10.1016/j.ijplas.2018.04.004

Maloth, T., Ozturk, D., Hommer, G., Pilchak, A., Stebner, A., & Ghosh, S. (2020). Multiscale modeling of cruciform dwell tests with the uncertainty-quantified parametrically homogenized constitutive model. *Acta Materialia, 200*, 893–907. doi:https://doi.org/10.1016/j.actamat.2020.09.037

Margetan, F., Gigliotti, M., Brashe, L., & Leach, W. (2002). *Fundamental Studies: Inspection Properties for Engine Titanium Alloys.* DOT/FAA/AR-02/114, FAA. Retrieved from http://www.tc.faa.gov/its/worldpac/techrpt/ar02-114.pdf

Margetan, F., Nieters, E., Haldipur, P., Brasche, L., Chiou, T., Keller, M., . . . Smith, K. (2005). *Fundamental Studies of Nickel Billet Materials - Engine Titanium Consortium Phase II.* DOT/FAA/AR-05/17, FAA. Retrieved from https://www.tc.faa.gov/its/worldpac/techrpt/ar05-17.pdf

Margetan, F., Thompson, R., & Yalda-Mooshabad, I. (1994). Backscattered microstructural noise in ultrasonic toneburst inspections. *Journal of Nondestructive Evaluation, 13*(3), 111–136. doi:https://doi.org/10.1007/BF00728250

Martin, R., & Evans, D. (2000). Reducing costs in aircraft: The metals affordability initiative consortium. *JOM: The Journal of Minerals, Metals, & Materials Society, 52*(3), 24–28. doi:https://doi.org/10.1007/s11837-000-0096-y

Max, B., Alexis, J., Larignon, C., & Perusin, S. (2020). Titanium alloy Ti-6242 for high temperature structural application . *Static and dynamic mechanical properties and impact of ageing , 321*. doi:https://doi.org/10.1051/matecconf/202032111089

May, K. (2010). *Small Scale Tensile Testing of Titanium Alloys.* [Master Thesis, Ohio State University]. Retrieved from http://rave.ohiolink.edu/etdc/view?acc_num=osu1282099780

McBagonluri, F., Akpan, E., Mercer, C., Shen, W., & Soboyejo, W. (2005). An investigation of the effects of microstructure on dwell fatigue crack growth in Ti-6242. *Materials Science and Engineering: A, 405*(1-2), 111–134. doi:https://doi.org/10.1016/j.msea.2005.05.097

Miller, M., Bernier, J., Park, J.-S., & Kazimirov, A. (2005). Experimental measurement of lattice strain pole figures using synchrotron x rays. *Review of Scientific Instruments, 76*(11), 113903. doi:https://doi.org/10.1063/1.2130668

Miller, R., Bieler, T., & Semiatin, S. L., S. (1999). Flow softening during hot working of Ti-6Al-4V with a lamellar colony microstructure. *Scripta Materialia, 40*(12), 1387–1393. doi:https://doi.org/10.1016/S1359-6462(99)00061-5

Mills, M., Ghosh, S., Rokhlin, S., Brandes, M., Pilchak, A., & Williams, J. (2018). *The Evaluation of Cold Dwell Fatigue in Ti-6242.* DOT/FAA/TC-17/57, FAA. Retrieved from https://www.tc.faa.gov/its/worldpac/techrpt/tc17-57.pdf

Ministerio Detransportes: Movilidad Y Agenda Urbana. (2006). Retrieved from https://www.mitma.gob.es/recursos_mfom/2006_045_in_eng.pdf

Mironov, S., Murzinova, M., Zherebtsov, S., Salishchev, G., & Semiatin, S. (2009). Microstructure evolution during warm working of Ti–6Al–4V with a colony-α microstructure. *Acta Materialia, 57*(8), 2470–2481. doi:https://doi.org/10.1016/j.actamat.2009.02.016

Morales-Rivas, L., Böhme, L., & Kerscher, E. (2020). Orientation mapping of cp-Ti by reflected polarized light microscopy. *MATEC Web of Conferences, 321*, 11096. doi:https://doi.org/10.1051/matecconf/202032111096

Murakami, Y. (2019). *Metal Fatigue: Effects of Small Defects and Nonmetallic Inclusions, 2nd ed.* Elsevier. doi:https://doi.org/10.1016/C2016-0-05272-5

Murakami, Y., Y. (1994). Inclusion rating by statistics of extreme values and its application to fatigue strength prediction and quality control of materials. *Journal of Research of the National Institute of Standards and Technology, 99*(4), 345. doi:https://doi.org/10.6028/jres.099.032

Myers, J., & General Electric Co. (2009). *U.S. Patent No. 20,090,314,100.* Retrieved from https://patents.google.com/patent/US20090314100

Neal, D. (1988). Creep Fatigue Interactions in Titanium Alloys. *Sixth World Conference on Titanium*, (pp. 175–180).

Newton, C., & Vacherm, H. (1954). Correlation of Polarized Light Phenomena With the Orientation of Some Metal Crystals. *Journal of Research of the National Bureau of Standards, 53*(1). Retrieved from https://nvlpubs.nist.gov/nistpubs/jres/53/jresv53n1p1_A1b.pdf

Nicolaou, P., & Semiatin, S. (2007). Effect of Strain-Path Reversal on Microstructure Evolution and Cavitation during Hot Torsion Testing of Ti-6Al-4V. *Metallurgical and Materials Transactions A, 38*(12), 3023–3031. doi:https://doi.org/10.1007/s11661-007-9343-y

Nicolaou, P., Semiatin, S., & Pilchak, A. (2019). *Investigation of cavitation during isothermal hot compression of Ti-6242.* Air Force Research Laboratory.

Nishikawa, S., & Kikuchi, S. (1928). Diffraction of Cathode Rays by Mica. *Nature, 121*(3061), 1019–1020. doi:https://doi.org/10.1038/1211019a0

Nolze, G. (2007). Image distortions in SEM and their influences on EBSD measurements. *Ultramicroscopy, 107*(2-3), 172–183. doi:https://doi.org/10.1016/j.ultramic.2006.07.003

NTSB, N. T. (1990). *NTSB/AAR-90/06: Aircraft Accident Report United Airlines Flight 232, McDonnell Douglas DC-10, Sioux Gateway Airport, Sioux City, Iowa, July 19, 1989.* Retrieved from https://www.ntsb.gov/investigations/accidentreports/reports/aar-90-06.pdf

Oberwinkler, B. (2016). On the anomalous mean stress sensitivity of Ti-6Al-4V and its consideration in high cycle fatigue lifetime analysis. *International Journal of Fatigue, 92*, 368–381. doi:https://doi.org/10.1016/j.ijfatigue.2016.07.010

Odegard, B., & Thompson, A. (1974). Low temperature creep of Ti-6Al-4V. *Metallurgical and Materials Transactions B, 5*(5), 1207–1213. doi:https://doi.org/10.1007/BF02644335

Okawa, S., & Watanabe, K. (2009). Chemical mechanical polishing of titanium with colloidal silica containing hydrogen peroxide-mirror polishing and surface properties. *Dental Materials Journal, 28*(1), 68–74. doi:https://doi.org/10.4012/dmj.28.68

Ozturk, D., Pilchak, A., & Ghosh, S. (2017). Experimentally validated dwell and cyclic fatigue crack nucleation model for α–titanium alloys. *Scripta Materialia, 127*, 15–18. doi:https://doi.org/10.1016/j.scriptamat.2016.08.031

Pagan, D., Shade, P., Barton, N., Park, J.-S., Kenesei, P., Menasche, D., & Bernier, J. (2017). Modeling slip system strength evolution in Ti-7Al informed by in-situ grain stress measurements. *Acta Materialia, 128*, 406–417. doi:https://doi.org/10.1016/j.actamat.2017.02.042

Pan, J., Shong, S., & Li, J. (1990). Influence of different forging processes on the ultrasonic response in titanium alloys TC6 and TC11. *NDT International, 23*(2), 103–106. doi:https://doi.org/10.1016/0308-9126(90)91894-Y

Panetta, P., Margetan, F., Yalda, I., & Thompson, R. (1997a). Observation and Interpretation of Microstructurally Induced Fluctuations of Back-Surface Signals and Ultrasonic Attenuation in Titanium Alloys. *In Review of Progress in Quantitative Nondestructive Evaluation*, pp. 1547–1554. doi:https://doi.org/10.1007/978-1-4615-5947-4_202

Panetta, P., Margetan, F., Yalda, I., & Thompson, R. (1997b). Observation and Interpretation of Microstructurally Induced Fluctuations of Back-Surface Signals and Ultrasonic Attenuation in Titanium Alloys. In *Review of Progress in Quantitative Nondestructive Evaluation* (pp. 1547–1554). Springer US. doi:https://doi.org/10.1007/978-1-4615-5947-4_202

Pardee, J. (1998). *Manufacturing Process of Premium Quality Titanium Alloy Rotating Engine Components.* AC 33-15.1, FAA. Retrieved from https://www.faa.gov/documentLibrary/media/Advisory_Circular/AC_33_15-1.pdf

Partridge, P. (1967). The crystallography and deformation modes of hexagonal close-packed metals. *Metallurgical Reviews, 12*(1), 169–194. doi:https://doi.org/10.1179/mtlr.1967.12.1.169

Perumal, B., Rist, M., Gungor, S., Brooks, J., & Fitzpatrick, M. (2016). The Effect of Hot Deformation Parameters on Microstructure Evolution of the α-Phase in Ti-6Al-4V. *Metallurgical and Materials Transactions A, 47*(8), 4128–4136. doi:https://doi.org/10.1007/s11661-016-3552-1

Pilchak, A. (2013). Fatigue crack growth rates in alpha titanium: Faceted vs. striation growth. *Scripta Materialia, 68*(5), 277–280. doi:https://doi.org/10.1016/j.scriptamat.2012.10.041

Pilchak, A. (2014). A simple model to account for the role of microtexture on fatigue and dwell fatigue lifetimes of titanium alloys. *Scripta Materialia, 74*, 68–71. doi:https://doi.org/10.1016/j.scriptamat.2013.10.024

Pilchak, A., & Williams, J. (2010). Clarification of the Fracture Plane of Dwell Fatigue Cracks in Titanium Alloys. *In Fatigue of Materials*, pp. 327–337. doi:https://doi.org/10.1002/9781118013373.ch21

Pilchak, A., & Williams, J. (2011). Observations of Facet Formation in Near-α Titanium and Comments on the Role of Hydrogen. *Metallurgical and Materials Transactions A, 42*(4), 1000–1027. doi:https://doi.org/10.1007/s11661-010-0507-9

Pilchak, A., Banerjee, D., & Williams, J. (2016). Grain Boundary α and β Grain Boundary Orientation in Titanium Alloys. *Proceedings of the 13th World Conference on Titanium* (pp. 425–430). John Wiley & Sons, Inc. doi:https://doi.org/10.1002/9781119296126.ch66

Pilchak, A., Beaudoin, A., Pagan, D., Chatterjee, K., Swartz, K., Budrow, C., . . . Sinha, V. (2020). Combining Fractography with High-Energy x-Ray Diffraction to Study Fatigue Crack Growth in Ti-6Al-4V. *JOM: Journal of the Minerals, Metals, and Materials Society, 72*(1), 91–100. doi:https://doi.org/10.1007/s11837-019-03826-9

Pilchak, A., Brandes, M., Williams, R., & Williams, J. (2012). Investigation of faceted crack initiation and propagation in near-alpha titanium alloys. *Ti-2011: Proceedings of the 12th World Conference on Titanium*, (pp. 993–997).

Pilchak, A., Hutson, A., Porter, W. J., W., Buchanan, D., & John, R. (2016a). On the Cyclic Fatigue and Dwell Fatigue Crack Growth Response of Ti-6Al-4V. *Proceedings of the 13th World Conference on Titanium* (pp. 993–998). John Wiley & Sons, Inc. doi:https://doi.org/10.1002/9781119296126.ch169

Pilchak, A., Hutson, A., Porter, W., Buchanan, D., & John, R. (2016b). On the Cyclic Fatigue and Dwell Fatigue Crack Growth Response of Ti-6Al-4V. *Proceedings of the 13th World Conference on Titanium* (pp. 993–998). John Wiley & Sons, Inc. doi:https://doi.org/10.1002/9781119296126.ch169

Pilchak, A., John, R., Larsen, J., Jha, S., & Jha, S. (2020). Unpublished research.

Pilchak, A., Li, J., & Rokhlin, S. (2014a). Quantitative comparison of microtexture in near-alpha titanium measured by ultrasonic scattering and electron backscatter diffraction. *Metallurgical and Materials Transactions A: Physical Metallurgy and Materials Science, 45*(10), 4679–4697. doi:https://doi.org/10.1007/s11661-014-2367-1

Pilchak, A., Li, J., & Rokhlin, S. (2014b). Quantitative comparison of microtexture in near-alpha titanium measured by ultrasonic scattering and electron backscatter diffraction. *Metallurgical and Materials Transactions A: Physical Metallurgy and Materials Science, 45*(10), 4679–4697. doi:https://doi.org/10.1007/s11661-014-2367-1

Pilchak, A., Shank, J., Tucker, J., Srivatsa, S., Fagin, P., & Semiatin, S. (2016a). A dataset for the development, verification and validation of microstructure-sensitive process models for near-alpha titanium alloys. *Integrating Materials and Manufacturing Innovation, 5*(1), 259–276. doi:https://doi.org/10.1186/s40192-016-0056-1

Pilchak, A., Shank, J., Tucker, J., Srivatsa, S., Fagin, P., & Semiatin, S. (2016b). *A Dataset for the Development, Verification and Validation of Microstructure-sensitive Process Models in Near-alpha Titanium Alloys.* NIST Materials Data Repository. Retrieved from http://hdl.handle.net/11256/647

Pilchak, A., Sherman, G., Safriet, S., & Rosenberger, A. (2012). *Dwell fatigue crack growth in beta-forged Ti-6242.* Air Force Research Laboratory.

Pilchak, A., Shiveley, A., Shade, P., Tiley, J., & Ballard, D. (2012). Using cross-correlation for automated stitching of two-dimensional multi-tile electron backscatter diffraction data. *Journal of Microscopy, 248*(2), 172–186. doi:https://doi.org/10.1111/j.1365-2818.2012.03661.x

Pilchak, A., Shiveley, A., Tiley, J., & Ballard, D. (2011). AnyStitch: a tool for combining electron backscatter diffraction data sets. *Journal of Microscopy, 244*(1), 38–44. doi:https://doi.org/10.1111/j.1365-2818.2011.03496.x

Pilchak, A., Srivatsa, S., Levkulich, N., Sinha, V., Payton, E., & Semiatin, S. (2020). Characterizing and Modeling the Precursors to Coarse Grain Formation during Beta-

Annealing of Ti-6Al-4V. *MATEC Web of Conferences*, *321*, p. 12007. doi:https://doi.org/10.1051/matecconf/202032112007

Pilchak, A., Szczepanski, C., Shaffer, J., Salem, A., & Semiatin, S. (2013). Characterization of Microstructure, Texture, and Microtexture in Near-Alpha Titanium Mill Products. *Metallurgical and Materials Transactions A, 44*(11), 4881–4890. doi:https://doi.org/10.1007/s11661-013-1804-x

Pilchak, A., Tucker, J., & Weihing, T. (2017). Determining the Probability of Occurrence of Rarely Occurring Microstructural Configurations for Titanium Dwell Fatigue. In *From Microstructure Investigations to Multiscale Modeling* (pp. 41–66). John Wiley & Sons, Inc. doi:https://doi.org/10.1002/9781119476757.ch2

Pilchak, A., Young, A., & Williams, J. (2010). Stress corrosion cracking facet crystallography of Ti–8Al–1Mo–1V. *Corrosion Science, 52*(10), 3287–3296. doi:https://doi.org/10.1016/j.corsci.2010.05.046

Postans, P., & Jeal, R. (1978). Dependence of Crack Growth Performance Upon Structure in Beta Processed Titanium Alloys. *Proceedings Forging and Properties of Aerospace Materials*, (pp. 192–198).

Postans, P., & Jeal, R. (1980). The Influence of Forging Route and Heat Treatments on the Recrystallization of a Commercial Titanium Alloy. In H. Kimura, & O. Izumi (Ed.), *Ti'80 Science and Technology: Proceedings of the fourth international conference on titanium* (pp. 441–455). The Metallurgical Society of AIME.

Poulsen, H., Nielsen, S., Lauridsen, E., Schmidt, S., Suter, R., Lienert, U., . . . Juul Jensen, D. (2001). Three-dimensional maps of grain boundaries and the stress state of individual grains in polycrystals and powders. *Journal of Applied Crystallography, 34*(6), 751–756. doi:https://doi.org/10.1107/S0021889801014273

Pratt & Whitney. (2018). *NTSB: Metallurgical Investigation Final Report of Fan Blades No. 11 and No. 10 from PW4077 Engine 777049.* Materials & Processes Engineering. Retrieved from https://data.ntsb.gov/Docket?ProjectID=96738. https://data.ntsb.gov/Docket?ProjectID=96738

Pugh, P. (2001). The Magic of a Name: The Rolls-Royce Story, Part 2: The Power Behind the Jets. *Vol 1*.

Qiu, J., Ma, Y., Lei, J., Liu, Y., Huang, A., Rugg, D., & Yang, R. (2014). A Comparative Study on Dwell Fatigue of Ti-6Al-2Sn-4Zr-xMo (x = 2 to 6) Alloys on a Microstructure-

Normalized Basis. *Metallurgical and Materials Transactions A, 45*(13), 6075–6087. doi:https://doi.org/10.1007/s11661-014-2541-5

Ready, A., Haynes, P., Grabowski, B., Rugg, D., & Sutton, A. (2017). The role of molybdenum in suppressing cold dwell fatigue in titanium alloys. *Proceedings of the Royal Society A: Mathematical, Physical and Engineering Sciences*. doi:https://doi.org/10.1098/rspa.2017.0189

Robertson, I., Sofronis, P., Nagao, A., Martin, M., Wang, S., Gross, D., & Nygren, K. (2015). Hydrogen Embrittlement Understood. *Metallurgical and Materials Transactions B, 46*(3), 1085–1103. doi:https://doi.org/10.1007/s11663-015-0325-y

Rokhlin, S., Li, J., & Sha, G. (2015). Far-field scattering model for wave propagation in random media. *The Journal of the Acoustical Society of America, 137*(5), 2655–2669. doi:https://doi.org/10.1121/1.4919333

Rokhlin, S., Sha, G., Li, J., & Pilchak, A. (2021). Inversion methodology for ultrasonic characterization of polycrystals with clusters of preferentially oriented grains. *Ultrasonics, 115*, 106433. doi:https://doi.org/10.1016/j.ultras.2021.106433

Rollett, A. (2020). *Texture Components and Euler Angles.* Retrieved from http://pajarito.materials.cmu.edu/lectures/Components_EulerAngles-14Jan20.pdf

Rose, J. (1992). Ultrasonic backscatter from microstructure. *Review of Progress in Quantitative Nondestructive Evaluation, 11*, 1677–1684.

Rosenker, M. (2008). *National Transportation Safety Board Safety Recommendation.* Retrieved from http://www.ntsb.gov/safety/safety-recs/recletters/A08_4_9.pdf

Ruffles, P. (1995). Aerospace structural materials: present and future. *Materials World, 3*(10), 469–470.

Rugg, D., Dixon, M., & Dunne, F. (2007). Effective structural unit size in titanium alloys. *The Journal of Strain Analysis for Engineering Design, 42*(4), 269–279. doi:https://doi.org/10.1243/03093247JSA273

Russ, J., & Neal, F. (2018). *The Image Processing Handbook.* CRC Press. doi:https://doi.org/10.1201/b18983

Sackett, E., Germain, L., & Bache, M. (2007). Crystal plasticity, fatigue crack initiation and fatigue performance of advanced titanium alloys. *International Journal of Fatigue, 29*(9-11), 2015–2021. doi:https://doi.org/10.1016/j.ijfatigue.2006.12.011

Safaie, H., Mitchell, R., Johnston, R., Russell, J., & Pleydell-Pearce, C. (2018). An Assessment of Polarized Light Microscopy for the Quantification of Grain Size and Orientation in Titanium Alloys via Microanalytical Correlative Light to Electron Microscopy (CLEM). *Microscopy and Microanalysis, 24*(S1), 400–401. doi:https://doi.org/10.1017/S1431927618002490

Salem, A., Shaffer, J., Kublik, R., Wuertemberger, L., & Satko, D. (2017). Microstructure-Informed Cloud Computing for Interoperability of Materials Databases and Computational Models: Microtextured Regions in Ti Alloys. *Integrating Materials and Manufacturing Innovation, 6*(1), 111–126. doi:https://doi.org/10.1007/s40192-017-0090-7

Salishchev, G., Valiakhmetov, O., & Galeyev, R. M. (1993). Formation of submicrocrystalline structure in the titanium alloy VT8 and its influence on mechanical properties. *Journal of Materials Science, 28*(11), 2898–2902. doi:https://doi.org/10.1007/BF00354692

Sargent, G., Kinsel, K., Pilchak, A., Salem, A., & Semiatin, S. (2012). Variant Selection During Cooling after Beta Annealing of Ti-6Al-4V Ingot Material. *Metallurgical and Materials Transactions A, 43*(10), 3570–3585. doi:https://doi.org/10.1007/s11661-012-1245-y

Sathish, S., & Martin, R. (2002). Quantitative Imaging of Rayleigh Wave Velocity with a Scanning Acoustic Microscope. *IEEE Transactions on Ultrasonics, Ferroelectrics, and Frequency Control, 49*(5), 550–557. doi:https://doi.org/10.1109/TUFFC.2002.1002453

Savage, M., Neeraj, T., & Mills, M. (2002). Observations of room-temperature creep recovery in titanium alloys. *Metallurgical and Materials Transactions A, 33*(13), 891–898. doi:https://doi.org/10.1007/s11661-002-1022-4

Savage, M., Tatalovich, J., & Mills, M. (2004). *Role of the α/β Interface in the Plastic Anisotropy of Single Colony Crystals in Titanium Alloys.* MRS Proceedings, 819, N1.6. doi:https://doi.org/10.1557/PROC-819-N1.6

SBIR STTR America's Seed Fund powered by SBA. (2017a). Adaptive Data Collection for Optical Quantification of Microtextured Regions. Retrieved from https://beta.www.sbir.gov/awards/166883

SBIR STTR America's Seed Fund powered by SBA. (2017b). AF171-098 Quantification of microtexture regions in titanium alloy using optical sensing methods. Retrieved from https://www.sbir.gov/node/1208215

SBIR STTR America's Seed Fund powered by SBA. (2017d). Laser Polarimeter for Mapping and Assessment of Microtextures in Titanium Alloys - Phase II. Retrieved from https://www.sbir.gov/node/1597817

SBIR STTR America's Seed Fund powered by SBA. (2021). Crystallographic orientation mapping of minimally prepared large nonplanar surfaces. Retrieved from https://www.sbir.gov/sbirsearch/detail/2178573

SBIR STTR America's Seed Fund powered by SBA. (2017c). Laser Polarimeter for Mapping and Assessment of Microtextures in Titanium Alloys - Phase I. Retrieved from https://www.sbir.gov/node/1487385

Schindelin, J., Arganda-Carreras, I., Frise, E., Kaynig, V., Longair, M., Pietzsch, T., . . . Cardona, A. (2012). Fiji: an open-source platform for biological-image analysis. *Nature Methods, 9*(7), 676–682. doi:https://doi.org/10.1038/nmeth.2019

Searles, T., Tiley, J., Tanner, A., Williams, R., Rollins, B., Lee, E., . . . Fraser, H. (2005). Rapid characterization of titanium microstructural features for specific modelling of mechanical properties. *Measurement Science and Technology, 16*(1), 60–69. doi:https://doi.org/10.1088/0957-0233/16/1/009

Semiatin, S. (2020). An Overview of the Thermomechanical Processing of α/β Titanium Alloys: Current Status and Future Research Opportunities. *Metallurgical and Materials Transactions A: Physical Metallurgy and Materials Science, 51*(6), 2593–2625. doi:https://doi.org/10.1007/s11661-020-05625-3

Semiatin, S., & Bieler, T. (2001a). Effect of texture and slip mode on the anisotropy of plastic flow and flow softening during hot working of Ti-6Al-4V. *Metallurgical and Materials Transactions A, 32*(7), 1787–1799. doi:https://doi.org/10.1007/s11661-001-0155-1

Semiatin, S., & Bieler, T. (2001b). Effect of texture changes on flow softening during hot working of Ti-6Al-4V. *Metallurgical and Materials Transactions A, 32*(7), 1871–1875. doi:https://doi.org/10.1007/s11661-001-0166-y

Semiatin, S., & Furrer, D. (2009). Modeling of Microstructure Evolution during the Thermomechanical Processing of Titanium Alloys. In *ASM Handbook Volume 22A: Fundamentals of Modeling for Metals Processing* (pp. 522–533). ASM International.

Semiatin, S., & Lahoti, G. (1981). Deformation and unstable flow in hot torsion of Ti-6Ai-2Sn-4Zr-2Mo-0.1Si. *Metallurgical Transactions A, 12*(10), 1719–1728. doi:https://doi.org/10.1007/BF02643754

Semiatin, S., & Lahoti, G. (1982). The occurrence of shear bands in isothermal, hot forging. *Metallurgical Transactions A, 13*(2), 275–288. doi:https://doi.org/10.1007/BF02643318

Semiatin, S., Fagin, P., Glavicic, M., Sukonnik, I., & Ivasishin, O. (2001). Influence on texture on beta grain growth during continuous annealing of Ti–6Al–4V. *Materials Science and Engineering: A, 299*(1-2), 225–234. doi:https://doi.org/10.1016/S0921-5093(00)01371-X

Semiatin, S., Fagin, P., Goetz, R., Furrer, D., & Dutton, R. (2015). Characterization of Plastic Flow Pertinent to the Evolution of Bulk Residual Stress in Powder-Metallurgy, Nickel-Base Superalloys. *Metallurgical and Materials Transactions A, 46*(9), 3943–3959. doi:https://doi.org/10.1007/s11661-015-3033-y

Semiatin, S., Kirby, B., & Salishchev, G. (2004). Coarsening behavior of an alpha-beta titanium alloy. *Metallurgical and Materials Transactions A, 35*(9), 2809–2819. doi:https://doi.org/10.1007/s11661-004-0228-z

Semiatin, S., Levkulich, N., Payton, E., & Pilchak, A. (2022). A Heat Treatment to Produce a Coarse-α-Particle Size in Ti–6Al–4V. *Metallurgical and Materials Transactions A, 53*(11), 3823–3826. doi:https://doi.org/10.1007/s11661-022-06810-2

Semiatin, S., Montheillet, F., Shen, G., & Jonas, J. (2002). Self-consistent modeling of the flow behavior of wrought alpha/beta titanium alloys under isothermal and nonisothermal hot-working conditions. *Metallurgical and Materials Transactions A, 33*(8), 2719–2727. doi:https://doi.org/10.1007/s11661-002-0394-9

Semiatin, S., Soper, J., & Sukonnik, I. (1996). Short-time beta grain growth kinetics for a conventional titanium alloy. *Acta Materialia, 44*(5), 1979–1986. Retrieved from https://doi.org/10.1016/1359-6454(95)00311-8

Shamblen, C., Woodfield, A., Wayte, P., & Dibert, G. (2003). Titanium Industry Quality Improvements. *Proceedings of the 10th World Conference on Titanium*, (pp. 2737–2744).

Shaniavski, A., & Losev, A. (2003). The effects of loading waveform and microstructure on the fatigue response of titanium aero-engine compressor disk alloys. *Fatigue & Fracture of Engineering Materials & Structures, 26*(4), 329–342. doi:https://doi.org/10.1046/j.1460-2695.2003.00589.x

Sharples, S., Clark, M., & Somekh, M. (2006). Spatially resolved acoustic spectroscopy for fast noncontact imaging of material microstructure. *Optics Express, 14*(22), 10435–10440. doi:https://doi.org/10.1364/OE.14.010435

Sharples, S., Clark, M., Li, W., & Somekh, M. (2008). Rapid Imaging of Microstructure using Spatially Resolved Acoustic Spectroscopy. *Proceedings of the 1st International Symposium on Laser Ultrasonics: Science, Technology and Applications*. Retrieved from https://www.researchgate.net/profile/Mike-Somekh/publication/228552904_Rapid_Imaging_of_Microstructure_using_Spatially_Resolved_Acoustic_Spectroscopy/links/00b7d51911348c9c04000000/Rapid-Imaging-of-Microstructure-using-Spatially-Resolved-Acoustic-Spectros

Shell, E., & Semiatin, S. (1999). Effect of initial microstructure on plastic flow and dynamic globularization during hot working of Ti-6Al-4V. *Metallurgical and Materials Transactions A, 30*(12), 3219–3229. doi:https://doi.org/10.1007/s11661-999-0232-4

Shen, W., Soboyejo, W., & Soboyejo, A. (2004a). An investigation on fatigue and dwell-fatigue crack growth in Ti–6Al–2Sn–4Zr–2Mo–0.1Si. *Mechanics of Materials, 36*(1-2), 117–140. doi:https://doi.org/10.1016/S0167-6636(03)00035-8

Shen, W., Soboyejo, W., & Soboyejo, A. (2004b). Microstructural effects on fatigue and dwell-fatigue crack growth in α/β Ti-6Al-2Sn-4Zr-2Mo-0.1Si. *Metallurgical and Materials Transactions A, 35*(1), 163–187. doi:https://doi.org/10.1007/s11661-004-0119-3

Shi, R. (2014). *Variant Selection during Alpha Precipitation in Titanium Alloys- A Simulation Study.* [PhD, The Ohio State University].

Shih, D., Robertson, I., & Birnbaum, H. (1988). Hydrogen embrittlement of α titanium: In situ tem studies. *Acta Metallurgica, 36*(1), 111–124. doi:https://doi.org/10.1016/0001-6160(88)90032-6

Sinha, V., Mills, M., & Williams, J. (2004). Understanding the contributions of normal-fatigue and static loading to the dwell fatigue in a near-alpha titanium alloy. *Metallurgical and Materials Transactions A, 35*(10), 3141–3148. doi:https://doi.org/10.1007/s11661-004-0058-z

Sinha, V., Mills, M., & Williams, J. (2006). Crystallography of fracture facets in a near-alpha titanium alloy. *Metallurgical and Materials Transactions A, 37*(6), 2015–2026.

Sinha, V., Mills, M., & Williams, J. (2007). Determination of crystallographic orientation of dwell-fatigue fracture facets in Ti-6242 alloy. *Journal of Materials Science, 42*(19), 8334–8341. doi:https://doi.org/10.1007/s10853-006-0252-z

Sinha, V., Schwarz, R., Mills, M., & Williams, J. (2020). Influence of hydrogen on dwell-fatigue response of near-alpha titanium alloys. *Acta Materialia, 188*, 315–327. doi:https://doi.org/10.1016/j.actamat.2019.12.025

Sinha, V., Spowart, J., Mills, M., & Williams, J. (2006). Observations on the faceted initiation site in the dwell-fatigue tested ti-6242 alloy: Crystallographic orientation and size effects. *Metallurgical and Materials Transactions A, 37*(5), 1507–1518. doi:https://doi.org/10.1007/s11661-006-0095-x

Smith, R., Li, W., Coulson, J., Clark, M., Somekh, M., & Sharples, S. (2014). Spatially resolved acoustic spectroscopy for rapid imaging of material microstructure and grain orientation. *Measurement Science and Technology, 25*(5), 055902. doi:https://doi.org/10.1088/0957-0233/25/5/055902

Sommer, A., & Eylon, D. (1983). On fatigue crack propagation of titanium alloys under dwell time conditions. *Metallurgical Transactions A, 14*(10), 2178–2181. doi:https://doi.org/10.1007/BF02662386

Song, Q., Li, Y., Wang, L., Huang, R., & Sun, C. (2019). Effect of rise and fall time on dwell fatigue behavior of a high strength titanium alloy. *Metals, 9*(8). doi:https://doi.org/10.3390/met9080914

Song, Z., & Hoeppner, D. (1989). Size effect on the fatigue behaviour of IMI 829 titanium alloy under dwell conditions. *International Journal of Fatigue, 11*(2), 85–90. doi:https://doi.org/10.1016/0142-1123(89)90002-9

Sonntag, N., Jürgens, M., Skrotzki, B., & Olbricht, J. (2023). Creep-fatigue of P92 in service-like tests with combined stress- and strain-controlled dwell times. *International Journal of Fatigue, 168*, 107381. doi:https://doi.org/10.1016/j.ijfatigue.2022.107381

Sosa, J., Huber, D., Welk, B., & Fraser, H. (2014). Development and application of MIPARTM: a novel software package for two- and three-dimensional microstructural characterization. *Integrating Materials and Manufacturing Innovation, 3*(1), 123–140. doi:https://doi.org/10.1186/2193-9772-3-10

Spence, S., Evans, W., & Cope, M. (1997). *Dwell fatigue on Ti 6246 at near ambient temperatures.* ICF 9., 3,.

Stanke, F., & Kino, G. (1984). A unified theory for elastic wave propagation in polycrystalline materials. *The Journal of the Acoustical Society of America, 75*(3), 665–681. doi:https://doi.org/10.1121/1.390577

Stapleton, A., Raghunathan, S., Bantounas, I., Stone, H., Lindley, T., & Dye, D. (2008). Evolution of lattice strain in Ti–6Al–4V during tensile loading at room temperature. *Acta Materialia, 56*(20), 6186–6196. doi:https://doi.org/10.1016/j.actamat.2008.08.030

Stroh, A. (1954). The formation of cracks as a result of plastic flow. Proceedings of the Royal Society of London. Series A. *Mathematical and Physical Sciences, 223*(1154), 404–414. doi:https://doi.org/10.1098/rspa.1954.0124

Stubbington, C., & Pearson, S. (1978). Effect of dwell on the growth of fatigue cracks in Ti-6Al-4V alloy bar. *Engineering Fracture Mechanics, 10*(4), 723–756. doi:https://doi.org/10.1016/0013-7944(78)90030-9

Suresh, S. (1998). *Fatigue of Materials.* Cambridge University Press. doi:https://doi.org/10.1017/CBO9780511806575

Suri, S., Viswanathan, G., Neeraj, T., Hou, D.-H., & Mills, M. (1999). Room temperature deformation and mechanisms of slip transmission in oriented single-colony crystals of an α/β titanium alloy. *Acta Materialia*, 1019–1034. doi:https://doi.org/10.1016/S1359-6454(98)00364-4

Suter, R., Hennessy, D., Xiao, C., & Lienert, U. (2006). Forward modeling method for microstructure reconstruction using x-ray diffraction microscopy: Single-crystal verification. *Review of Scientific Instruments, 77*(12), 123905. doi:https://doi.org/10.1063/1.2400017

Szczepanski, C., Pilchak, A., Jha, S., Harr, M., John, R., & Larsen, J. (2014). Combined Experimental and Computational Modeling to Understand the Role of Micro- structure on Fatigue Behavior of Ti-6Al-2Sn-4Zr-2Mo-0.08Si. In Presentation at 2014 TMS Annual Meeting.

Tanaka, H., Yamada, T., Sato, E., & Jimbo, I. (2006). Distinguishing the ambient-temperature creep region in a deformation mechanism map of annealed CP-Ti. *Scripta Materialia, 54*(1), 121–124. doi:https://doi.org/10.1016/j.scriptamat.2005.08.045

The R Foundation. (2023). *The R Project for Statistical Computing*. Retrieved from https://www.r-Project.Org/. https://www.r-project.org

TIMET. (n.d.). Retrieved from https://www.timet.com/products/ingot.html

Torquato, S. (2002). *Random Heterogeneous Materials* (Vol. 16). Springer New York. doi:https://doi.org/10.1007/978-1-4757-6355-3

Toubal, L., Bocher, P., & Moreau, A. (2009). Dwell-fatigue life dispersion of a near alpha titanium alloy. *International Journal of Fatigue, 31*(3), 601–605. doi:https://doi.org/10.1016/j.ijfatigue.2008.09.010

Toubal, L., Bocher, P., Moreau, A., & Lévesque, D. (2010). Macroregion Size Measurements in Bimodal Titanium Forgings Using Two-Dimensional Autocorrelation Method. *Metallurgical and Materials Transactions A, 41*(3), 744–750. doi:https://doi.org/10.1007/s11661-009-0128-3

Triantafyllou, C., Pagan, D., & McBride, A. (2022). Quantifying the effect of macrozones on the cold-dwell fatigue response of UD-rolled Ti-6Al-4V using high-energy X-ray diffraction. *Materials Science and Engineering: A, 834*, 142498. doi:https://doi.org/10.1016/j.msea.2021.142498

Tricot, R. (1988). Thermomechanical processing of titanium alloys. *Ti'88: Proceedings of the Sixth World Conference on Titanium 1988*, *86(10)*, pp. 23–35.

Tsukada, M., Yamada, N., Inagaki, K., Kawata, I., Hamaguchi, T., Yasuda, S., . . . Nishikiori, S. (2024). Development of Methods for Microtexture Characterization and Dwell Fatigue Life Prediction of Dual Phase Titanium Alloys. In M. Jackson (Ed.), *Proc. 15th World Conference on Titanium (Ti-2023), IOM3*.

Tucker, J., Groeber, M., Semiatin, S., & Pilchak, A. (2016). Synthetic Building and Targeted Analysis of Life-Limiting Microtextured Regions. *Proceedings of the 13th World Conference on Titanium*, (pp. 1913–1918). doi:https://doi.org/10.1002/9781119296126.ch320

Turner, T., Shade, P., Bernier, J., Li, S., Schuren, J., Kenesei, P., . . . Almer, J. (2017). Crystal Plasticity Model Validation Using Combined High-Energy Diffraction Microscopy Data for a Ti-7Al Specimen. *Metallurgical and Materials Transactions A, 48*(2), 627–647. doi:https://doi.org/10.1007/s11661-016-3868-x

Turner, T., Shade, P., Bernier, J., Li, S., Schuren, J., Lind, J., . . . Almer, J. (2016). Combined near- and far-field high-energy diffraction microscopy dataset for Ti-7Al tensile specimen elastically loaded in situ. *Integrating Materials and Manufacturing Innovation, 5*(1), 94–102. doi:https://doi.org/10.1186/s40192-016-0048-1

Tympel, P., Lindley, T., Saunders, E., Dixon, M., & Dye, D. (2016). Influence of complex LCF and dwell load regimes on fatigue of Ti-6Al-4V. *Acta Materialia,*

https://doi.org/10.1016/j.actamat.2015.09.014, 77–88.
doi:https://doi.org/10.1016/j.actamat.2015.09.014

Uchic, M., Groeber, M., Woodward, C., Dimiduk, D., & Pilchak, A. (2015). *Unpublished research.* Air Force Research Laboratory.

UES Inc. (2023). Robo-Met.3D. Retrieved from https://www.ues.com/robomet

Venkatesh, V., & Fox, S. (2001a). Development of Damage Maps for Ti-6Al-4V. In R. Srinivasan, S. Semiatin, A. Beaudoin, S. Fox, & Z. Jin (Eds.), *Microstructure Modeling and Prediction during Thermomechanical Processing* (pp. 147–156). TMS.

Venkatesh, V., & Fox, S. (2001b). Use of FEA Modeling to Evaluate the Hot Workability of Titanium Alloys. *J. Mater. Process. Technol., 117*(3).

Venkatesh, V., & Wilson, A. (2007). Application of Microstructure and Damage Models in the Primary Conversion of Ti-6-4. *Ti-2007 Science and Technologie: Proceedings of the 11th World Conference on Titanium*, (pp. 865–868).

Venkatesh, V., McDaniel, C., Harper, M., Kosaka, Y., & Fox, S. (2007). Processing and Properties of Uniform Fine Grain Ti 6-4 Billt. *Ti-2007 Science and Technologie: Proceedings of the 11th World Conference on Titanium*, 957–960. doi:https://cdn.ymaws.com/titanium.org/resource/resmgr/ZZ-WCTP2007-VOL2/2007_Vol_2_Pres_25.pdf

Venkatesh, V., Noraas, R., Pilchak, A., Tamirisa, S., Calvert, K., Salem, A., . . . Saraf, V. (2020). Data Driven Tools and Methods for Microtexture Classification and Dwell Fatigue Life Prediction in Dual Phase Titanium Alloys. *MATEC Web of Conferences: The 14th World Conference on Titanium*, *321, 11091*.

Venkatesh, V., Tamirisa, S., Sartkulvanich, J., Calvert, K., Dempster, I., Saraf, V., . . . Pilchak, A. (2016). ICME of Microtexture Evolution in Dual Phase Titanium Alloys. *Proceedings of the 13th World Conference on Titanium*, (pp. 1907–1912). doi:https://doi.org/10.1002/9781119296126.ch319

Waheed, S., S., Zheng, Z., Balint, D., & Dunne, F. (2019). Microstructural effects on strain rate and dwell sensitivity in dual-phase titanium alloys. *Acta Materialia, 162*, 136–148. doi:https://doi.org/10.1016/j.actamat.2018.09.035

Wang, F., & Cui, W. (2015). Experimental investigation on dwell-fatigue property of Ti–6Al–4V ELI used in deep-sea manned cabin. *Materials Science and Engineering: A, 642*, 136–141. doi:https://doi.org/10.1016/j.msea.2015.06.089

Wang, S., Aindow, M., & Starink, M. (2003). Effect of self-accommodation on α/α boundary populations in pure titanium. *Acta Materialia, 51*(9), 2485–2503. doi:https://doi.org/10.1016/S1359-6454(03)00035-1

Wanner, A., & Dunand, D. (2000). Synchrotron X-ray study of bulk lattice strains in externally loaded Cu-Mo composites. *Metallurgical and Materials Transactions A, 31*(11), 2949–2962. doi:https://doi.org/10.1007/BF02830344

Ward, C. (2015). Introducing the Data descriptor article. *Integrating Materials and Manufacturing Innovation, 4*(1), 190–191. doi:https://doi.org/10.1186/s40192-015-0041-0

Weaver, R. (1990). Diffusivity of ultrasound in polycrystals. *Journal of the Mechanics and Physics of Solids, 38*(1), 55–86. Retrieved from https://doi.org/10.1016/0022-5096(90)90021-U

Wegmann, G., Albrecht, J., Luetjering, G., Folkers, K.-D., & Liesner, C. (1997). Microstructure and mechanical properties of titanium castings. *Zeitschrift FFüuer Metallkunde, 88*(10), 764–773.

Weiss, I., & Semiatin, S. (1998). Thermomechanical processing of beta titanium alloys—an overview. *Materials Science and Engineering: A, 243*(1-2), 46–65. Retrieved from https://doi.org/10.1016/S0921-5093(97)00783-1

Weiss, I., Welsch, G., Froes, F., & Eylon, D. (1985). Mechanisms of Microstructure Refinement in Ti-6Al-4V Alloy. *Titanium: Science and Technology: Proceedings of the Fifth International Conference on Titanium*, (pp. 1503–1510). Retrieved from https://cdn.ymaws.com/titanium.org/resource/resmgr/ZZ-WCTP1984-VOL3/1984_Vol.3-1-J-Mechanisms_of.pdf

Wertz, J., Cherry, M., O'Rourke, S., Homa, L., Lorenzo, N., & Blasch, E. (2022). Multiscale Mixed Modality Microstructure Assessment for Titanium (M4AT) Data Set. *Materials Evaluation, 80*(8), 24–29. doi:https://doi.org/10.32548/2022.me-04274

White, J., Loretto, M., Smallman, R., & Winstone, M. (1984). The Effect of Dwell On Low Cycle Fatigue In IMI 829 (Ti 5331s), in Proc. *5th World Conference on Titanium*, (pp. 2297-2304).

Whittaker, M., & Evans, W. (2009). Effect of prestrain on the fatigue properties of Ti834. *International Journal of Fatigue, 31*(11-12), 1751–1757. doi:https://doi.org/10.1016/j.ijfatigue.2009.03.008

Wiedemann, M. (2023). Investigation on the Cold Dwell Fatigue Susceptibility of Ti-6Al-2Sn-4Zr-6Mo Billet and Forging for Aero-Engine Application. In M. Jackson (Ed.), *Proceedings of the 15th World Conference on Titanium.*

Williams, J., Baggerly, R., & Paton, N. (2002). Deformation behavior of HCP Ti-Al alloy single crystals. *Metallurgical and Materials Transactions A, 33*(3), 837–850. doi:https://doi.org/10.1007/s11661-002-0153-y

Williams, J., Sommer, A., & Tung, P. (1972). The influence of oxygen concentration on the internal stress and dislocation arrangements in α titanium. *Metallurgical and Materials Transactions B, 3*(11), 2979–2984. doi:https://doi.org/10.1007/BF02652870

Winstone, M., & Weaver, M. (1985). The strain controlled fatigue behaviour of a near-alpha titanium alloy. *Titanium: Science and Technology: Proceedings of the Fifth International Conference on Titanium*, (pp. 2275–2280).

Woodfield, A. et al. (1995). *Unpublished research.* GE Aviation, Evendale, OH.

Woodfield, A., & Lemaitre, G. (2020). Aerospace Titanium Alloy Melt Process Quality Improvements. *MATEC Web of Conferences: The 14th World Conference on Titanium, 321, 04008.*

Woodfield, A., & Shamblen, C. (2007). Titanium Alloy Melt Process Quality Improvements. *Ti-2007 Science and Technology: Proceedings of the 11th World Conference on Titanium*, (pp. 151–154).

Woodfield, A., Gorman, M., Corderman, R., Sutliff, J., & Yamrom, B. (1996). Effect of Microstructure on Dwell Fatigue Behavior of Ti-6242. *Ti'95: Science and Technology*.

Woodfield, A., Gorman, M., Sutliff, J., & Corderman, R. (1999). Effect of microstructure on dwell fatigue behavior of Ti-6242. *International Symposium on Fatigue Behavior of Titanium Alloys*, (pp. 111–118). Retrieved from https://www.osti.gov/biblio/20013312

Worsnop, F., Lim, R., Bernier, J., Pagan, D., Xu, Y., McAuliffe, T., . . . Dye, D. (2022). The influence of alloying on slip intermittency and the implications for dwell fatigue in titanium. Nature Communications. *Nature Communications, 13*(1), 5949. doi:https://doi.org/10.1038/s41467-022-33437-z

Wu, Z., Kou, H., Chen, N., Xi, Z., Fan, J., Tang, B., & Li, J. (2022). Recent developments in cold dwell fatigue of titanium alloys for aero-engine applications: a review. *Journal of Materials Research and Technology, 20*, 469–484. doi:https://doi.org/10.1016/j.jmrt.2022.07.094

Wynne, B., Davies, P., & Rainforth, W. (2008). Investigating Macrozones in Titanium Billet using Electron Backscattered Diffraction. *TMS: Supplemental Proceedings: Volume 1: Materials Processing and Properties*, (pp. 391–396).

Xi, G.; Lei, J.; Qiu, J.; Ma, Y.; Yang, R.;. (2020). A semi-quantitative explanation of the cold dwell effect in titanium alloys. *Materials & Design, 194, 108909*. doi:https://doi.org/10.1016/j.matdes.2020.108909

Xu, Y., Fox, K., Rugg, D., & Dunne, F. (2020). Cyclic plasticity and thermomechanical alleviation in titanium alloys. *International Journal of Plasticity, 134*. doi:https://doi.org/10.1016/j.ijplas.2020.102753

Yamrom, B., Sutliff, J., & Woodfield, A. (1994). Visualizing polycrystalline orientation microstructures with spherical color maps. *Proceedings Visualization '94*, 46-51. doi:https://doi.org/10.1109/VISUAL.1994.346338

Yang, L., & Rokhlin, S. (2013). Ultrasonic Backscattering in Cubic Polycrystals with Ellipsoidal Grains and Texture. *Journal of Nondestructive Evaluation, 32*(2), 142–155. doi:https://doi.org/10.1007/s10921-012-0167-3

Yang, L., Li, J., & Rokhlin, S. (2013). Ultrasonic scattering in polycrystals with orientation clusters of orthorhombic crystallites. *Wave Motion, 50*(8), 1283–1302. doi:https://doi.org/10.1016/j.wavemoti.2013.06.003

Yang, L., Li, J., Lobkis, O., & Rokhlin, S. (2012). Ultrasonic Propagation and Scattering in Duplex Microstructures with Application to Titanium Alloys. *Journal of Nondestructive Evaluation, 31*(3), 270–283. doi:https://doi.org/10.1007/s10921-012-0141-0

Yang, L., Lobkis, O., & Rokhlin, S. (2012). An integrated model for ultrasonic wave propagation and scattering in a polycrystalline medium with elongated hexagonal grains. *Wave Motion, 49*(5), 544–560. doi:https://doi.org/10.1016/j.wavemoti.2012.03.003

Yeh, M., & Huang, J. (1997). Internal hydrogen-induced subcritical crack growth in Ti6Al4V. *Scripta Materialia, 36*(12), 1415–1421. doi:https://doi.org/10.1016/S1359-6462(97)00046-8

Yeh, M.-S., & Huang, J.-H. (1998). Hydrogen-induced subcritical crack growth in Ti-6Al-4V alloy. *Materials Science and Engineering, 242*, 96–107.

You, R.; Zhang, M.; Qiu, J.; Fang, C.; Zhao, C.; Lu, B.; Ji, H.; Ma, Y.; Lei, J.; Yang, R.;. (2022). Influence of Hold Time on Dwell Fatigue Behavior in IMI834 Disc Forging. *JOM: Journal of Minerals, Metals, and Materials Society, 74*(10), 3733–3744. doi:https://doi.org/10.1007/s11837-022-05400-2

YouTube. (n.d.2019). Airbus A380 F-HPJ Greenland Fan Hub Recovery by GEUS / BEA (June 2019). Retrieved from https://Www.Youtube.Com/Watch?V=zPcSU0A1G9w

Zeng, L., & Bieler, T. (2005). Effects of working, heat treatment, and aging on microstructural evolution and crystallographic texture of α, α′, α″ and β phases in Ti–6Al–4V wire. *Materials Science and Engineering: A, 392*(1-2), 403–414. doi:https://doi.org/10.1016/j.msea.2004.09.072

Zhang, T., Wang, X., Ji, Y., Zhang, W., Hassan, T., & Gong, J. (2020). P92 steel creep-fatigue interaction responses under hybrid stress-strain controlled loading and a life prediction model. *International Journal of Fatigue, 140*, 105837. doi:https://doi.org/10.1016/j.ijfatigue.2020.105837

Zhang, Z., Cuddihy, M., & Dunne, F. (2015). On rate-dependent polycrystal deformation: the temperature sensitivity of cold dwell fatigue. *Proceedings of the Royal Society A: Mathematical, Physical and Engineering Sciences, 471*(2181). doi:https://doi.org/10.1098/rspa.2015.0214

Zheng, Z., Balint, D., & Dunne, F. (2016). Dwell fatigue in two Ti alloys: An integrated crystal plasticity and discrete dislocation study. *Journal of the Mechanics and Physics of Solids, 96*, 411–427. doi:https://doi.org/10.1016/j.jmps.2016.08.008

Zheng, Z., Balint, D., & Dunne, F. (2017). Mechanistic basis of temperature-dependent dwell fatigue in titanium alloys. *Journal of the Mechanics and Physics of Solids, 107*, 185–203. doi:https://doi.org/10.1016/j.jmps.2017.07.010

Zheng, Z., Stapleton, A., Fox, K., & Dunne, F. (2018). Understanding thermal alleviation in cold dwell fatigue in titanium alloys. *International Journal of Plasticity, 111*, 234–252. doi:https://doi.org/10.1016/j.ijplas.2018.07.018

Zheng, Z., Zhao, P., Zhan, M., Shen, S., Wang, Y., & Fu, M. (2022). The roles of rise and fall time in load shedding and strain partitioning under the dwell fatigue of titanium alloys

with different microstructures. *International Journal of Plasticity, 149, 103161*. doi:https://doi.org/10.1016/j.ijplas.2021.103161

Zherebtsov, S., Salishchev, G., Galeyev, R., Valiakhmetov, O., Mironov, S., & Semiatin, S. (2004). Production of submicrocrystalline structure in large-scale Ti–6Al–4V billet by warm severe deformation processing. *Scripta Materialia, 51*(12), 1147–1151. doi:https://doi.org/10.1016/j.scriptamat.2004.08.018

A   Summary of recent academic research of industrial activities

The body of this text introduced the background and current understanding of cold dwell fatigue failure. In this section, we briefly recall some of the major academic, industrial, and industry-sponsored research programs which provided significant advancement to the fundamental understanding of cold dwell fatigue. This is not meant to be an exhaustive literature survey, so each section will point to key outcomes from the programs while the references are cited throughout this document for the interested reader.

Academic research

Several major academic programs were supported around the world from government organizations, which are summarized below.

FAA Cold Dwell Program (1999-2009)

The FAA funded a multi-year program led by a team at The Ohio State University to investigate the fundamental mechanisms leading to cold dwell fatigue. The work was enhanced by an industrial advisory board consisting of representatives from an international team of major engine OEMs and JETQC members. The team consisted of experimentalists (Williams and Soboyejo groups), microscopists (Mills group), modelers (Ghosh group), and nondestructive evaluation (NDE) specialists (Rokhlin group). They were charged with understanding the fundamental factors contributing to early CDF failure, using this to build mechanism-based micromechanical models, and develop NDE methods to assess the degree of microtexture in forged titanium. Some key outcomes of this work were related to single crystal deformation behavior, slip transfer at alpha/beta interfaces, dislocation activity beneath dwell fatigue fracture surfaces, early crack propagation rates, a clearer understanding of critical microtextured regions at nucleation sites and fatigue facet planes, nondestructive detection of dwell fatigue cracks, and a model for volumetric sizing of microtexture from ultrasonic backscattering and attenuation. In addition, the team developed a crystal plasticity finite element model to predict crack nucleation under cold dwell fatigue conditions, which employed a wavelet-based time-scaling methodology permitting simulation to engine-relevant cycle counts. The major findings of this effort are summarized in two technical reports (Ghosh, et al., 2007; Mills, et al., 2018) and the associated literature cited throughout this document.

<u>EPSRC HexMat Program (2013-2018)</u>

HexMat was a five-year, Engineering and Physical Sciences Research Council (EPSRC) funded program coordinated by Imperial College London that used cutting edge experimental, characterization, and modeling techniques to explore five main themes:

- fundamental mechanisms,

- micromechanics,

- ultrasonics,

- aerospace performance, and

- nuclear performance of hexagonal materials (titanium and zirconium alloys).

A number of significant publications relating to cold dwell fatigue in titanium alloys resulted from this program (the full publications list for HexMat is available online (Imperial College London, 2023). Many HexMat publications are referenced elsewhere in this report.

<u>AFRL Structural Sciences Center Program (2013-2020)</u>

After the conclusion of the FAA-funded Cold Dwell Fatigue effort at The Ohio State University, various organizations within AFRL continued to fund work in this area including the Materials & Manufacturing Directorate (AFRL/RX) as well as the Aerospace Vehicles Directorate (AFRL/RQ). AFRL/RQ funded additional improvements to the Ghosh group code under the Structural Sciences Center. These included the incorporation of temperature-dependence, the development of a probabilistic version of the nonlocal crack nucleation criterion (Ozturk, Pilchak, & Ghosh, 2017), and a hierarchical length-scaling enabled by using the output of many CPFEM runs to train machine learning algorithms about the effect of microstructural parameters on response (Kotha, Ozturk, & Ghosh, 2020). These so-called parametrically homogenized constitutive models (PHCM's) or parametrically upscaled constitutive models (PUCM's) are a hugely important advancement toward the practical use of CPFEM in design and lifing tools. The latter modification, when coupled with the aforementioned WATMUS time-scaling methodology gives one the ability to perform micromechanical models at every integration point on a full-scale component finite element mesh on a desktop computer. This would represent a significant improvement over the linear elastic or non-linear elastic analyses often used today to design rotating components.

Industrial research

Due to the practical importance of dwell fatigue research, there have been many industrial research efforts. Many of these investigations remain company proprietary, but there are a few notable exceptions. In particular, Rolls Royce plc has worked closely with various UK universities and published many important papers related to dwell fatigue and Safran Aircraft Engines has also worked closely with French universities. In addition, several engine OEMs have worked collaboratively under the auspices of the Air Force Research Laboratory's MAI program focused on predicting microstructure and texture evolution during processing and its impact on tensile and fatigue behavior.

Metals affordability initiative (MAI) programs

For nearly 25 years, the US Air Force has led the MAI, which is an aerospace industry consortium made up of primary metal producers, forging suppliers and engine and airframe manufacturers. The goal of MAI is to reduce the time and cost to produce aerospace components which is achieved through the formation of activity integrated project teams (AIPT) who identify key technologies and work together in a precompetitive setting to develop and industrialize them for the benefit of the entire aerospace industry (Bayha, Evans, & Furrer, 2002; Martin & Evans, 2000). Significant effort has been made in the area of titanium alloys including the development of microstructure evolution models to predict the size and volume fraction of primary alpha during solution heat treatment which were embedded in the large-strain finite element package DEFORM™ (a product of Scientific Forming Technologies Corporation in Columbus, Ohio). Along with alloy composition, these models were used to predict location-specific tensile response through a neural network model. In a later program, texture evolution models were developed and implemented as a further refinement that considered the plastic anisotropy of the alpha phase.

Building on models developed under prior MAI programs, more recent effort has been focused on predicting fatigue behavior. With regard to CDF, Eureqa®, a commercially available software that automatically builds models using symbolic regression was used to calibrate and validate a model that explicitly captured the influence of MTR metrics on fatigue life. A total of 59 dwell fatigue tests were used to develop life models in Eureqa (Venkatesh, et al., 2020). Over 70 statistically based microstructure and microtexture parameters along with the maximum stress as a function of yield strength were used to identify the critical parameters that correlate with dwell fatigue life for these 59 datasets. Eureqa splits datasets into a training dataset and a validation dataset in order to perform cross validation and prevent overfitting. In this work, 80 percent of the data was used for model training and 20 percent for model validation Training data is used to

generate and optimize solutions, and the validation set is used to test how well those models generalize to new data.

A total of five Eureqa models that had similar model errors were chosen for predicting sample dwell life. The mathematical relationships in these models were automatically generated by Eureqa, each having slightly different formulations and generalization capability over the testing range. Eureqa successfully identified 3 MTR metrics, along with the percent yield strength of the dwell test, as critical model inputs for DLCF life prediction (Table A-1) . These results suggest that higher test stress levels and larger soft MTR sizes negatively impact DLCF life. In contrast, a larger fraction of soft MTRs and miscellaneous grains positively influence DLCF life. The significance of large soft MTRs is supported by many studies on dwell fatigue behavior in titanium alloys, which suggest that high stresses are developed at the interface between large soft MTRs that accommodate slip and hard MTRs that do not deform, leading to crack initiation and life shortfalls. On the other hand, having a large fraction of soft and randomly oriented grains will help to homogenize the strain distribution and improve life. All five Eureqa models were chosen for comparing sample dwell life prediction with measured failure life cycles. Figure A-1 shows that all the predictions, except one, were within a factor of two from the actual lifetime. This Ti-6-4 outlier had an extremely low life but contained average MTR metrics.

Table A-1. List of Eureqa™ model input parameters along with their sensitivity to dwell fatigue

Variable Name	% Impact on Model		Model Sensitivity to Variable
Misc. Alpha Grain Fraction		51%	
Mean Soft MTR Size	-100%		
Soft MTR Fraction		100%	
Fraction of Yield Strength	-100%		
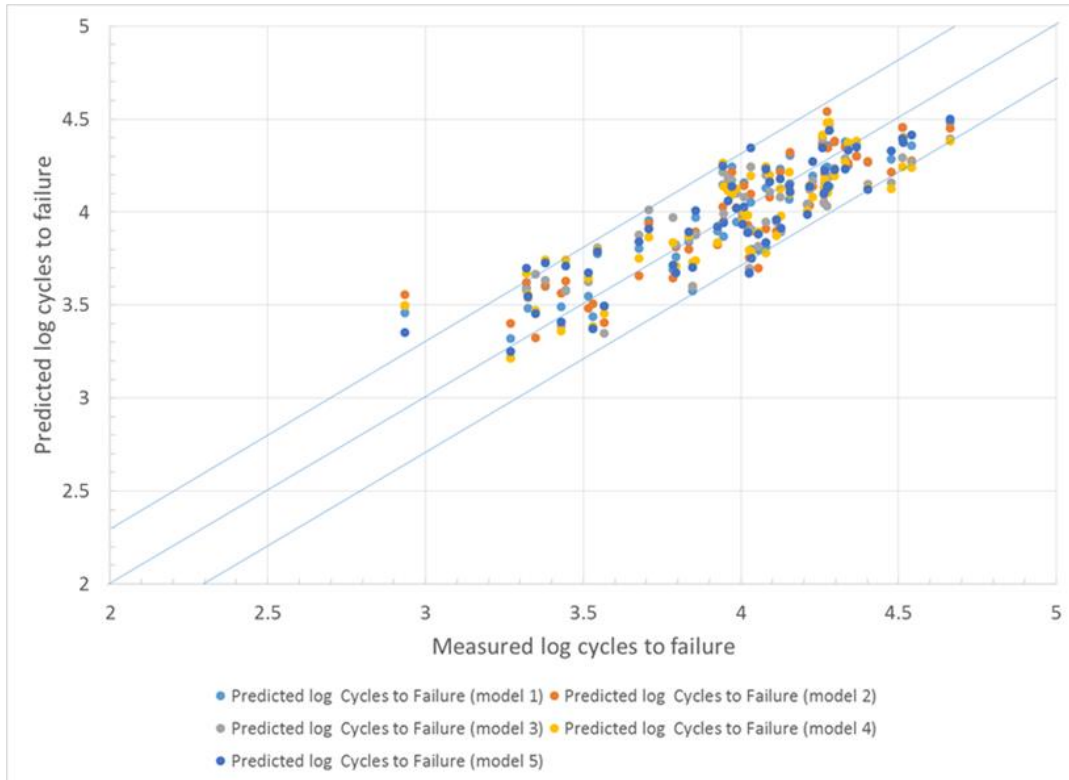
Figure A-1. Comparison of dwell fatigue lifetime predications using Eureqa™-based dwell life models for Ti-6242 and Ti-6-4

Rolls Royce plc/UK University Collaborations

In addition to the collaboration within the HexMat program discussed above, Rolls Royce plc has a long history of working with UK universities, most notably Swansea on mechanical testing including fractographic analysis, but also more recently with Imperial College (CPFE modeling as well as micro- and macro-mechanical testing and characterization), The University of Sheffield on microtexture quantification and the University of Manchester on techniques such as DIC in relation to deformation mechanisms in titanium alloys. Many of the papers resulting from these interactions are referenced throughout this report.

Safran Aircraft and Helicopter Engines/University Collaborations

The Aircraft and Helicopter Engine Divisions of the Safran Group have worked closely with several universities to understand scatter in LCF properties of titanium alloys. This included collaboration with ENSAM Paris, Centrale Paris, and ENSMA/PPrime which investigated the effects of crystallography through X-ray diffraction and EBSD measurements (Bridier, 2006; Delfosse, 2005; Gourbesville, 2000; Le Biavant-Guerrier, 2000). The viscosity and effect of dwell time on Ti6242 β forged LCF properties at room temperature were then explored at

mesoscale (Jousset, 2008; Lefranc, 2008). Microstructure formation in this alloy was analyzed with Nancy University (Appolaire, Aeby-Gautier, Da Costa-Teixeira, Hericher, & Denis, 2011; Gautier, et al., 2006) to understand the formation of 'featherlike' features and their crystallography associated (Germain, Samih, Delaleau, Gilgert, & Gey, 2020) which were observed to be the initiation site in Cold Dwell tests. Finer analysis, at microscale, on microtexture and its effect on plasticity and crack initiation were explored during cold dwell tests and modeled (Freiherr von Thungen, 2017; Kuzmenkov, 2012). More recently, a similar analysis was performed on Ti-6Al-4V (Lavogiez, 2020).

Synchrotron X-ray diffraction

Advances in synchrotron x-ray diffraction techniques have led to incredible new insights into the fundamental deformation behavior of titanium alloys. Early work in this realm were performed by Withers (Korsunsky, Wells, & Withers, 1998), Poulsen et al. (2001), Dunand (Wanner & Dunand, 2000), Suter et al. (2006), and Miller (Bernier, Park, Pilchak, Glavicic, & Miller, 2008; Miller, Bernier, Park, & Kazimirov, 2005). These techniques permit the nondestructive measurement of microstructure in 3D, including grain morphology, crystallographic orientation, and grain boundary character, as well as the ability to perform in-situ testing while monitoring lattice strain evolution and the development of internal orientation gradients. With a spatial resolution of ~1 µm, an orientation resolution of ~0.1°, and a strain resolution exceeding 10^{-4}, the technique has been applied to study fundamental deformation behavior in Ti-7Al (Chatterjee, et al., 2016; 2017; Maloth, et al., 2020; Mills, et al., 2018; Pagan, et al., 2017) (Turner, et al., 2016; 2017). Many of these studies also use the crystal plasticity finite element method to aid in the interpretation of the experiments and also as a way to further refine model parameters. This alloy was selected because it has similar composition to the alpha phase of industrially useful alloys like Ti-6-4 and Ti-6242 and, in part, because the larger grain size is more amenable to the near-field diffraction techniques, which allow for complete reconstruction of the microstructure at the stated resolutions. In contrast, far-field techniques allow the determination of grain centroids as well as average lattice strains along crystallographic fibers in orientation space (i.e., grains sharing a common diffraction vector).

Fewer authors have applied the far-field technique to two-phase alloys. Stapleton et al. (2008) have studied the evolution of lattice strain in the alpha and beta phases of Ti-6-4 under tensile loading and made predictions of the response using an elastic-plastic self-consistent model. Pilchak et al. (2020) have used a spatially resolved far-field techniques to map the strain fields ahead of fatigue cracks in Ti-6-4. Triantafyllou et al. (2022) have examined the evolution of lattice strains and stress redistribution during dwell fatigue of Ti-6-4 plate material. All of these

investigations utilized the far-field technique due to limitations associated with the fine grain size of conventionally processed Ti-6-4. Recently, however, Semiatin et al. (2022) have developed a heat treatment to coarsen the grain size of two-phase titanium alloys to provide more engineering-relevant material that is amenable to the near-field method. Further details on these and other techniques in high energy diffraction microscopy (HEDM) can be found in a review article by Bernier et al. (2020).

B Segmentation and quantification of microtextured regions

Several authors have undertaken the difficult task to quantify MTRs from EBSD data. The earliest attempts were by Yamrom et al. (1994) and Woodfield et al. (1996; 1999) from GE Aviation (now GE Aerospace). In the former publication, the authors developed spherical color maps based on the intersection of the c-axis with the facets of an icosahedron, which effectively combined pixels with similar crystallographic orientation into a common color. This allowed easy, direct visualization of the MTRs. Examples of these maps were shown previously in Figure 125, Figure 126, Figure 128, and Figure 132. Shortly thereafter, Woodfield et al. (1996) described a methodology to quantitatively measure MTR size. The authors scanned 5 mm x 5 mm regions of material at a step size of 1 μm and developed an automated computer code that would first identify primary alpha particles and then determine which alpha particles belonged to the same MTR. The primary alpha segmentation utilized a misorientation tolerance angle of 1.25° while the MTR segmentation relaxed this constraint to 20°. The results were used to develop a correlation between MTR parameters and dwell fatigue capability (Woodfield A. , Gorman, Corderman, Sutliff, & Yamrom, 1996; Woodfield A. , Gorman, Sutliff, & Corderman, 1999). With help from GE Aviation, Ari-Gur and Semiatin (1998) applied these techniques to study the development of microtexture during hot rolling of beta-annealed Ti-6Al-4V.

About a decade later, Wynne et al. (2008) analyzed the pole figures of a Ti-834 billet and identified the dominant c-axis orientations for each texture component. The authors then extracted subsets of the data for each dominant orientation and an angular spread around it. For the particular process path utilized, they found that there were two dominant classes of MTRs which accounted for 22% and 28% of the total scan area. The authors then manually placed ellipses over the identified MTRs Figure B-1 and observed that only about 50% by area of the region within the ellipses constituted the fraction of aligned grains with the remainder being comprised of either misaligned primary alpha or secondary alpha. They noted that the coarse step size of the scan precluded identifying the relative contribution of each constituent. It was further mentioned that a computer code was under development to automatically identify MTRs, which was later presented briefly during the UK plenary talk at the 2011 World Titanium Conference in Beijing. This set the foundation for the work of Fernandez-Silva et al. who presented the method in more detail at ICOTOM 2019 (Fernandez Silva, Wynne, Jackson, Bodie, & Fox, 2019).
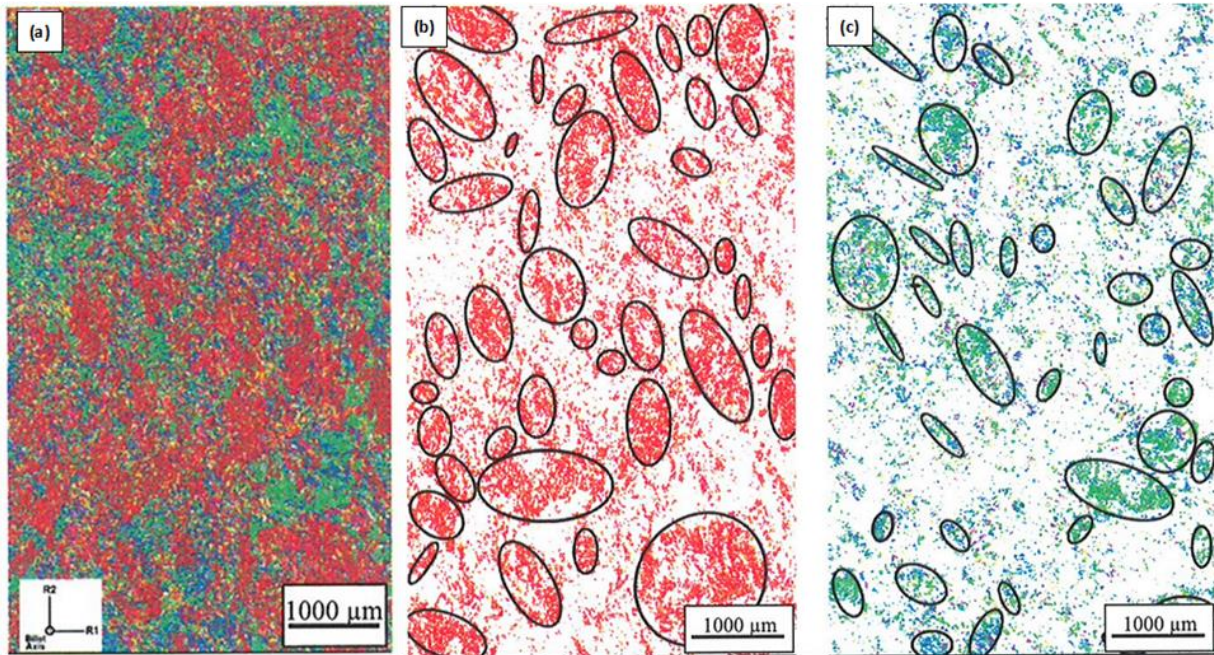
Figure B-1. (a) Inverse pole figure map collected from Ti-834 billet (b) and (c) show two classes of MTRs

The tool was further developed at The University of Sheffield by Fernandez Silva et al. (2023) during the study of macrozone evolution of Ti-834 forgings for compressor disk applications (Fernandez, 2021). This tool consists of an algorithm developed in MATLAB for automatic macrozone characterization from EBSD data sets. Contrary to other tools such as DREAM.3D, it uses a more restrictive approach based on the full misorientation of the crystals (i.e., both the tilting and rotation of the c-axis are considered). This methodology for macrozone identification requires the selection of three input parameters to define macrozone identification: (1) The grid size use to describe a kernel size the neighborhood of each pixel, (2) the Critical Disorientation is the minimum rotation angle between to pixels, and (3) the Critical Fraction can be considered a density criterion as it defined the number of pixels within the grid that must meet the critical disorientation condition for a pixel to be selected as part of a macrozone. There are two main steps in the algorithm. In the first step, a dimensionality reduction is carried out by filtering pixels that meet the disorientation and fraction criteria established with its neighboring pixels within a grid size followed by a second step where the remaining pixels that met the dimensionality reduction step are grouped into clusters that meet the criteria that will define the macrozone. The same disorientation angle is used in both steps.

Figure B-2 shows the outputs of the tool at several stages. Figure B-2 (a) shows the results following both clustering steps (black background are pixels that did not meet criteria). Figure B-2 (b,c) display macrozones containing more than 100 pixels. In Figure B-2 (d,e) perimeters and

ellipses are generated surrounding the macrozones to provide size measurements. Figure B-2 (f) shows the Euler map with overlapped calculated ellipses. These calculations are based on geometrical considerations alone and do not differentiate between 'good' or 'bad' macrozones and results may potentially suffer from dependence of subjective choice of the input parameters.
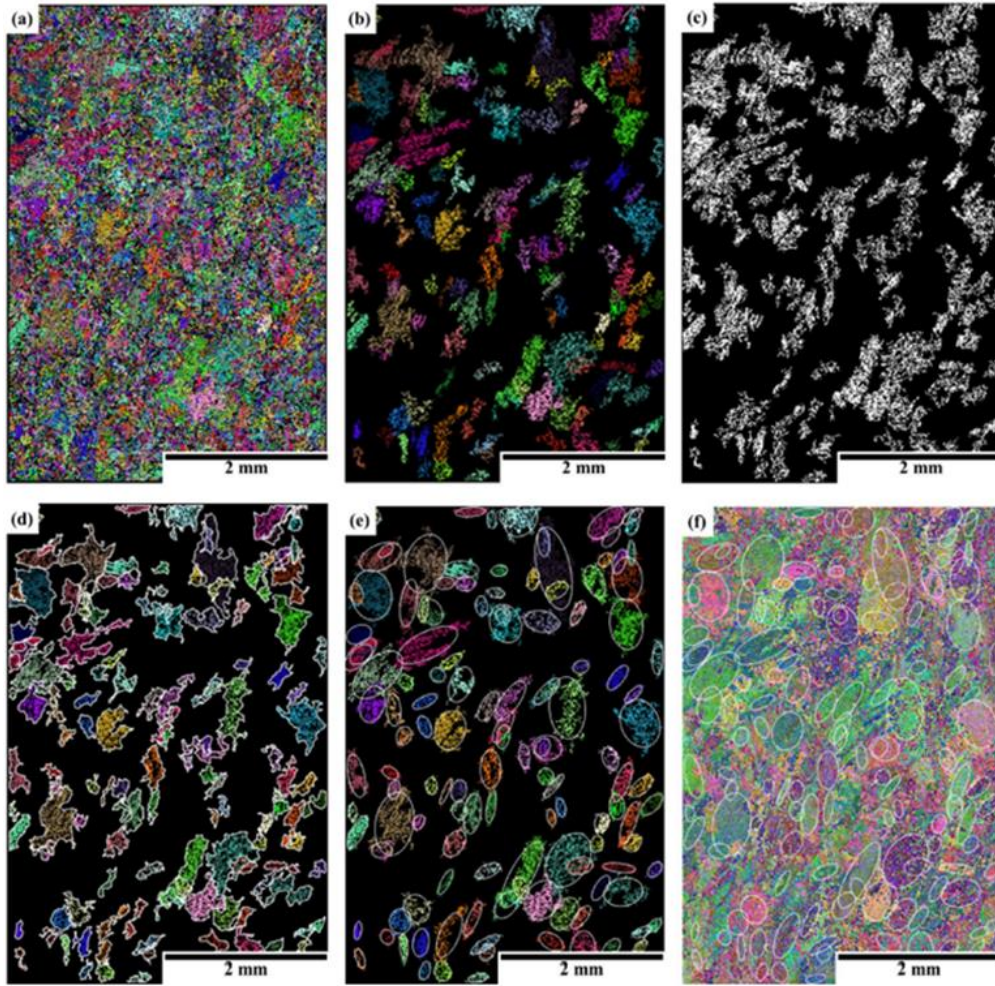
Figure B-2. Outputs of tool after macrozone identification in Ti64 Billet EBSD dataset covering area of 4x6mm with 10μm step size

(a) Clusters colored individually after inputs parameters are applied (b, c) Clusters with size threshold applied (d) Clusters with perimeters (e) Clusters with ellipses (f) Euler map with ellipses overlapped

Pilchak et al. (2016a) developed a filter for the DREAM.3D software package (Groeber & Jackson, 2014) to aid in the quantification of microtexture and published it in the NIST Materials Data Repository (Pilchak, et al., 2016b). The approach offered increased flexibility in clustering similarly oriented features into MTRs. For example, the conventional burn algorithm used in

EBSD data analysis checks the misorientation between a pixel and its first nearest neighbors. This may be problematic for materials with a high-volume fraction of transformed beta, scans with a coarse step size, or the presence of noise/misindexed pixels which may separate the similarly oriented grains. To overcome this, a two-step segmentation was utilized which first grouped pixels into grains using a small tolerance angle (e.g., 2º). In a second step, a noncontiguous grouping criterion was employed. The neighborhood around each grain was interrogated to look for other grains with the c-axis orientation within a given user-defined tolerance (e.g., 20º). It is important to note that using the c-axis misorientation was preferred to the classic misorientation for this step because the latter would identify two grains with identical c-axis orientation but rotated by an amount greater than the segmentation threshold as different grains. Alpha titanium is transversely isotropic, so the elastic response is dominated entirely by c-axis orientation. Moreover, the c-axis orientation is the dominant factor in determining which slip systems are active and the fracture mode of the MTR during dwell fatigue (e.g., faceted or striated growth). The search radius was chosen to be a function of the mean average diameter of the grains identified in the first step (typically taken to be 1.2~1.5, depending on the volume fraction of primary alpha). This noncontiguous grouping methodology was found to be ideal when trying to identify the size and shape of MTRs that ultimately form the faceted initiation sites on dwell fatigue fracture surfaces.

Spatial statistics is a branch of statistics that deals with the analysis of data that have spatial coordinates associated with them and thus lends itself well to the analysis of microtexture. Important concepts in spatial statistics include autocorrelation (spatial correlation among similar features) and cross-correlation (spatial correlation between two different features). These correlations are often referred to as two-point correlations or two-point statistics. A very comprehensive treatment can be found in Torquato's book on heterogeneous materials (Torquato, 2002) and in numerous papers by the same author. In brief, calculating the two-point statistics involves segmenting an image to identify the feature of interest and then placing vectors into that image in all possible locations, in all possible directions, and having all possible magnitudes and then determining if both the head and tail lie within the feature of interest. For each unique vector one can determine the probability that both the head and tail will fall in the same feature. Exemplar vectors are shown in a segmented image of MTRs in Figure B-3 (Images courtesy of Ayman Salem, Materials Resources LLC).

The associated two-point correlation is also shown. The latter plot is read by drawing an arrow from the center of the image to any other point and reading the probability at the head of the arrow. A vector of length zero returns the probability of finding a 'red' pixel in this case, which is equivalent to the volume fraction of the red phase. It is noteworthy that this analysis only

encompasses the material state at the tail and head of the vector and does not contain any information about the material between these positions. Thus, for small vector lengths one typically finds high correlations and there is generally an exponential decay in probability with increasing vector length. The utility of this analysis comes from the fact that it is a complete characterization of the microstructure which encompasses the size, morphology, and spatial arrangement of the microstructure into a compact form. From the two-point statistics in Figure B-3, one can see clearly that the MTRs are of high aspect ratio and that the elongation direction is slightly inclined to the vertical direction of the image. Furthermore, the fraction of the red phase is just greater than 0.24 by area. Following the arrow, one can see that the initially strong probabilities go through a minimum of ~0.05 before increasing again to ~0.10. This indicates that there are regions of similar orientation that are parallel but separate from one another.
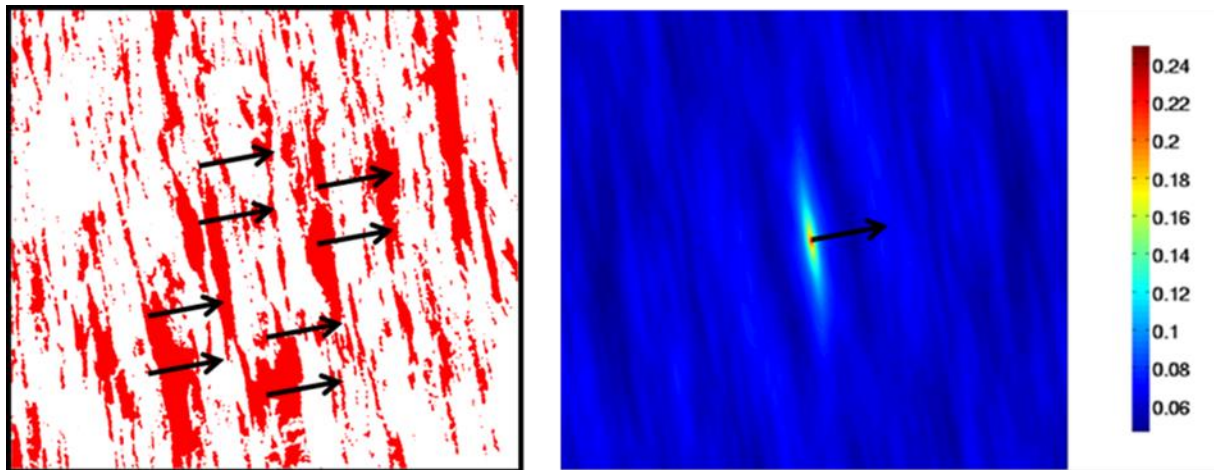
Figure B-3. Segmented MTRs (left) and associated two-point statistics (right)

The chord length distribution (CLD) is a complementary analysis often used along with the two-point statistics. In contrast to the two-point correlation, which analyzes the state at the head and tail of a vector, this metric is used to identify the size of continuous features in the image in one or more directions of interest. This is illustrated schematically in Figure B-4 where grey dashed lines represent chords and red lines represent lengths of particles of interest.
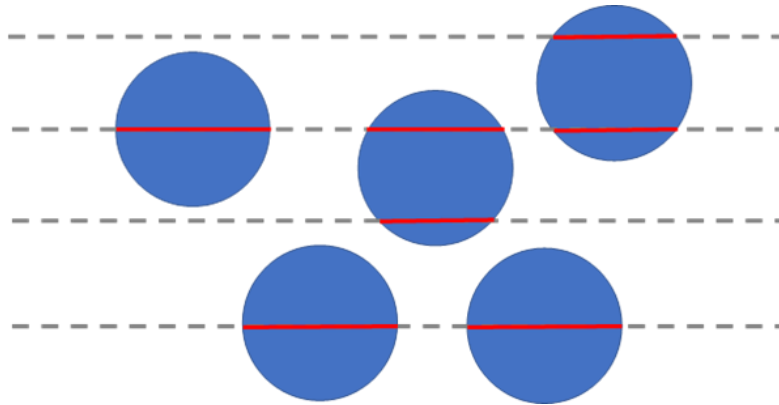
Figure B-4. Example of calculating the chord length distribution in a simple microstructure

The CLD provides the probability of observing a chord of a given length as a function of the line orientation and are often represented on polar plots (Figure B-5) through which line profiles can be taken and displayed as probability density functions (Figure B-6). The images and corresponding data analysis are courtesy of Ayman Salem, Materials Resources LLC.
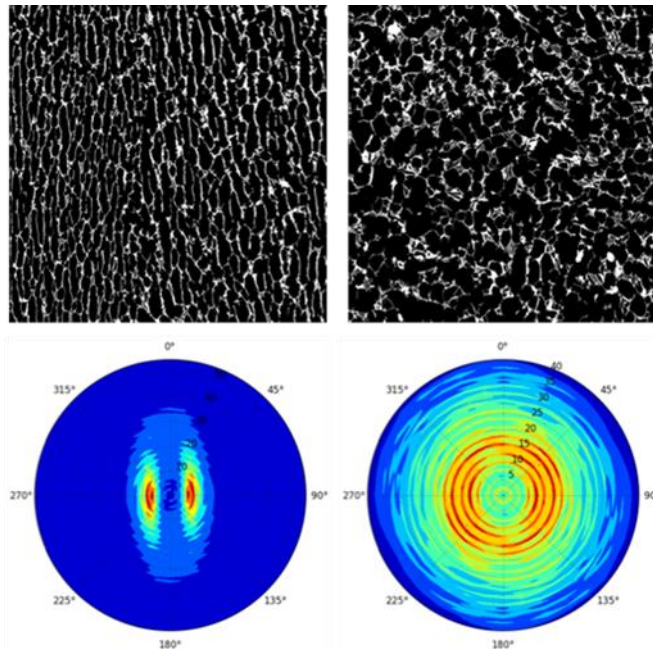
Figure B-5. Segmented backscattered electron images of Ti-6242 billet material and corresponding chord length distributions
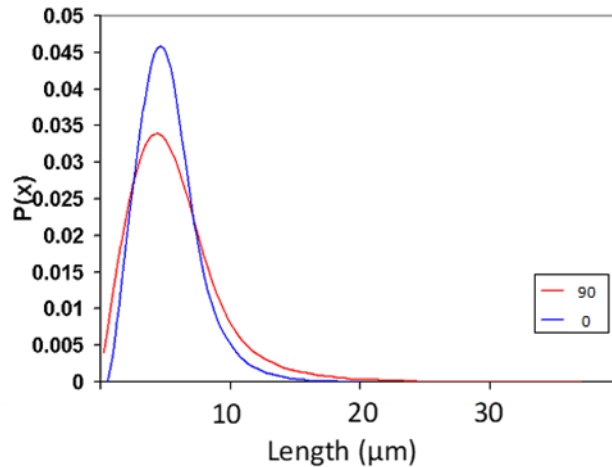
Figure B-6. Probability density functions along two-line profiles through a CLD

Salem et al. (2017) have made extensive use of two-point correlations and CLD's to characterize titanium microstructures. The authors developed the TiZone™ algorithm which uses machine learning tools to detect MTRs. The first step involves performing a clustering analysis (e.g., k-means clustering) and pattern recognition to identify different families of MTRs in orientation space. The second step involves mapping the identified families in real space to quantify the spatial statistics using the aforementioned tools. The process operates on individual tiles of EBSD data such that there is no need to stitch them ahead of time. The method was implemented on a cloud-based computing platform making it easily scalable and accessible from anywhere in the world, including smart phones. The software also focuses on interoperability and can handle data from any EBSD vendor. Standard analysis of MTRs includes determining the volume fraction of each class of MTRs present in the material and the range of c-axis orientations present each in the classes, calculation of the two-point statistics for each class and determining the CLD for each class. In addition, the orientation of the long axis of each class is found. The software also has an option to apply image processing algorithms to 'fill' the gaps in MTRs left by highly misoriented primary and secondary alpha. In this way, the CLD returns the MTR sizes that are more in line with the size of the faceted regions observed on dwell fatigue fracture surfaces. The TiZone™ algorithm has been used by the US Air Force for internal research activities (Pilchak, Szczepanski, Shaffer, Salem, & Semiatin, 2013).

While there are not yet any industry standards for MTR characterization, there has been progress toward this goal under the US Air Force MAI program. A major goal of the "ICME of Microtexture Evolution and its Effect on Cold Dwell/High/Low Cycle Fatigue Behavior of Dual Phase Titanium Alloys" program was to assess and further develop tools and methods for use by the industrial supply chain to identify and quantify MTRs. The activity integrated project team

(AIPT) applied Material Resources LLC's (MRL's) commercially available TiZone™ as well as the open-source DREAM.3D software. MRL's methods were described in detail at the 13th World Conference on Titanium in San Diego, California (Venkatesh, et al., 2016) while additional results were presented at the 14th World Conference in Nantes, France (Venkatesh, et al., 2020). The second approach utilized the open-source software, DREAM.3D. Building on the work of Pilchak et al. (2016a; 2016b) who created the c-axis misorientation segmentation filter, the AIPT developed pipelines to import and clean EBSD data, segment features based on pixel misorientation, and store the data in an efficient HDF5 file format. DREAM.3D outputs metrics like feature size, average misorientation, average MTR orientation, MTR density, etc. Post-processing scripts were developed in MATLAB to compute additional metrics including the angle between the average orientation and the stress axis, intensity, degree of spatial clustering, and hard/soft/initiator class labels, among others (Figure B-7, courtesy of Ryan Noraas, Pratt & Whitney). The standard MTR parameters and values used in the program (Venkatesh, et al., 2020) are shown in Table 4 (in Section 3.2.5.1.1), which highlights the minimum MTR area considered, as well as the c-axis-to-stress-axis misalignment values used for classification of hard, soft, and initiator MTRs. In addition, a single factor called MTR intensity, described in Equation (B-1), links several other parameters and was used to compare the severity of microtexture levels between datasets for various materials manufactured during this program:

$$MTR\ Intensity = \frac{\rho \cdot A \cdot \sigma_{mis}}{\Delta g_{avg}} \cdot \frac{1\ mm^2}{1E6\ \mu m^2} \cdot 100 \qquad\qquad \text{B-1}$$

where I_{MTR} is the MTR intensity, ρ is the MTR density, A is the MTR size and Δg_{avg} is the MTR average misorientation (defined as the average orientation of all pixels in the MTR relative to the MTR average orientation).
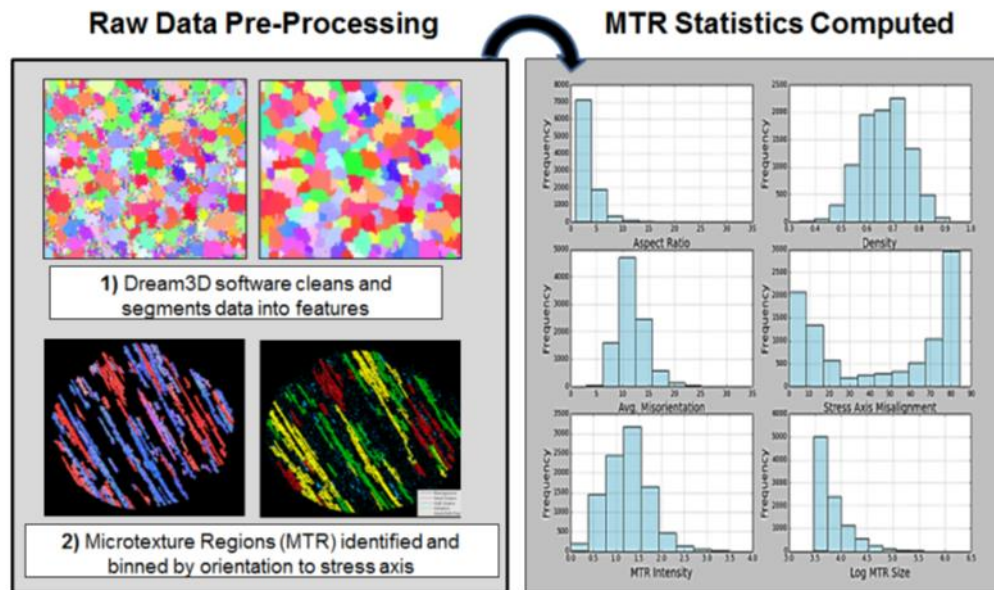
Figure B-7. Schematic illustration of the MAI MTR quantification framework

Pilchak et al. (2014b) also utilized two-point correlations to analyze microtexture in Ti-811 billet material and compared the results with ultrasonic characterization methods (the UT characterization is discussed in more detail in Appendix C). In this case, the authors mapped all c-axis orientations to patches of uniform area on the unit sphere, calculated the two-point correlation for each one, and then created a composite two-point correlation which can be interpreted as the probability of finding two correlated orientations regardless of the actual c-axis orientation. In hindsight, this analysis should have been performed by binning the orientations according to their local elastic stiffness tensor. Nevertheless, good agreement was obtained for average MTR sizes based on averaging the results obtained by segmenting the unit sphere into 10° and 15° bins.

MTU characterized Ti-64 and Ti-6246 billet material by means of polarized light microscopy and EBSD (Wiedemann, 2023). Based on the EBSD data the globular α grain size was evaluated. With $7 \pm 2\mu m$ Ti-6246 exhibits a three times smaller α grain size than Ti-64 with $23 \pm 14\mu m$. Figure B-8 shows the comparison the results of polarized light imaging and EBSD measurements of both alloys.

In addition to the finer microstructure, it is noticed that the Ti-6246 billet material does not show any larger contiguous areas as visible in the Ti-6Al-4V billet material. The MTRs were evaluated with a DREAM.3D pipeline published by (Venkatesh, et al., 2020). The results are shown in Figure B-9. The evaluated MTRs in Ti-6Al-4V were as large as 10^6 µm² whereas the evaluated MTRs in Ti-6246 do not exceed $1.5*10^3$ µm².
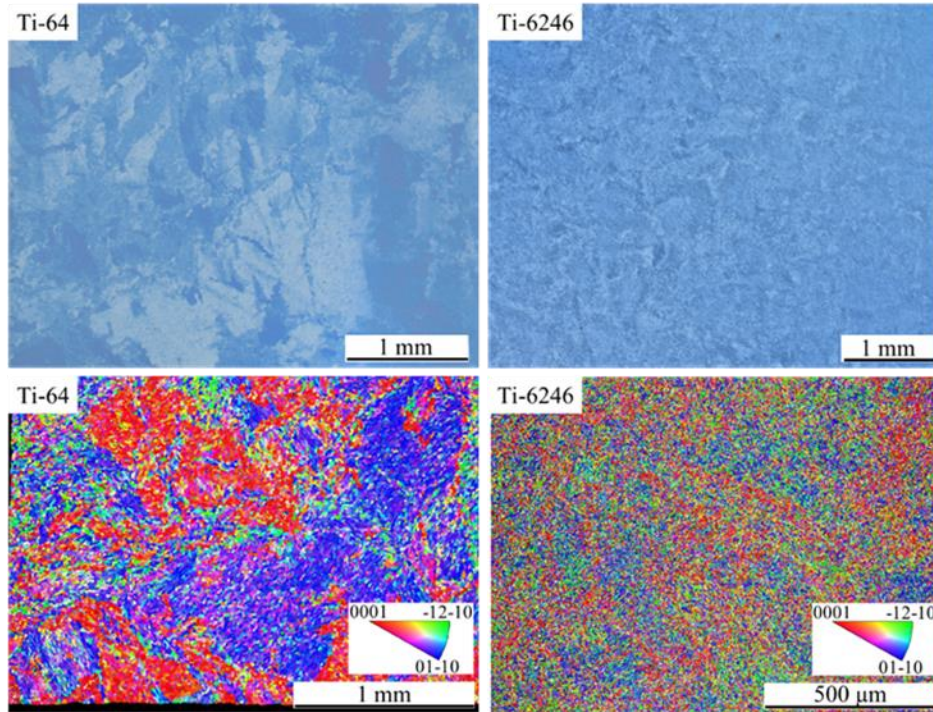
Figure B-8. Results of polarized light imaging and EBSD measurements for Ti-6Al-4V and Ti-6246 billet material
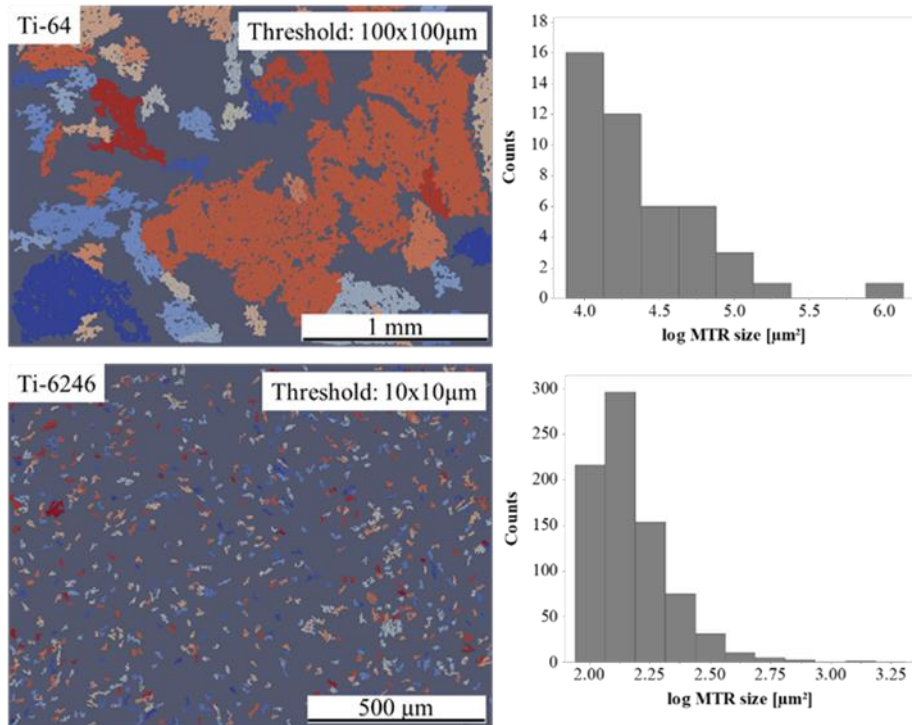
Figure B-9. Results of MTR evaluation of Ti-6Al-4V and Ti-6246 billet material with DREAM.3D

Optical and polarized light optical microscopy

Optical characterization methods have the potential to offer huge advantages in terms of cost and speed of data acquisition. Moreover, by taking advantage of the optical anisotropy of alpha phase titanium, it is possible to infer some information about crystallographic orientation. These techniques are limited somewhat in spatial resolution compared to EBSD; however, the increased data acquisition rates offer the potential for nearly an order of magnitude higher resolution than the EBSD step sizes currently being used to characterize MTRs. However, the size of the datasets introduce new challenges for data processing algorithms and the optical isotropy of the beta phase poses an additional challenge. In this section we describe several approaches currently being developed that leverage light optics.

Light optical microscopy

Macroetching of cross sections of billets and forgings has been widely used in the aerospace industry as a *qualitative* tool to assess the uniformity of the structure of the material at various stages of processing. These sections are compared to photographic standards within each organization based on their own internal requirements, but do not provide a quantitative characterization of microstructure. In an effort to improve on this, Toubal et al. developed an image processing method to analyze macroetched images and applied it to microtexture in an IMI-834 billet and forging (Toubal, Bocher, Moreau, & Lévesque, 2010). Images were collected using optical microscopy on macroslices taken from each product form. The authors noted that the contrast variations in optical images mirrored the elongated MTRs in the billet material and also along the flow lines expected based on the forging geometry. The digital greyscale images were analyzed using mean linear intercept and autocorrelation functions to estimate the MTR sizes. The autocorrelation of each image was taken to identify the long axis of the MTRs and then line profiles taken through the perpendicular direction were used to determine the correlation length. They compared this to the manually determined linear intercept results from five independent observers. High variability was found among the manual measurements, but the autocorrelation was not subject to this bias and was able to give the length, slope, and periodicity of MTRs present in the images.

Polarized light optical microscopy

Birefringence is the optical property of materials which gives rise to orientation-dependent refractive indexes. In this method, image contrast is formed as a result of the change in the polarization state of light after it interacts with the material. Methods were developed in the 1950's to use polarized light to determine the orientation of hexagonal crystals, however, the

methods were slow and cumbersome limiting their utility (Newton & Vacherm, 1954). In this section, we discuss several efforts underway to revitalize the technique in order to use polarization to deduce crystallographic orientation of optically anisotropic crystals. Due to the increased speed compared to EBSD, these techniques offer a potentially important tool for use in quality control strategies.

As early as 1980, Ginty et al. (1980) used polarized light to estimate the basal plane traces in a region of microstructure near a spurious ultrasound indication in a Ti-5Al-6V-2Sn forging (Figure B-10). They used a cross-polarized condition and rotated the sample through 360° and observed variations in the intensity of the light and also two extinctions (minima). By calibrating the polarizer/analyzer to a single crystal of known orientation, they could unambiguously identify the basal plane trace.
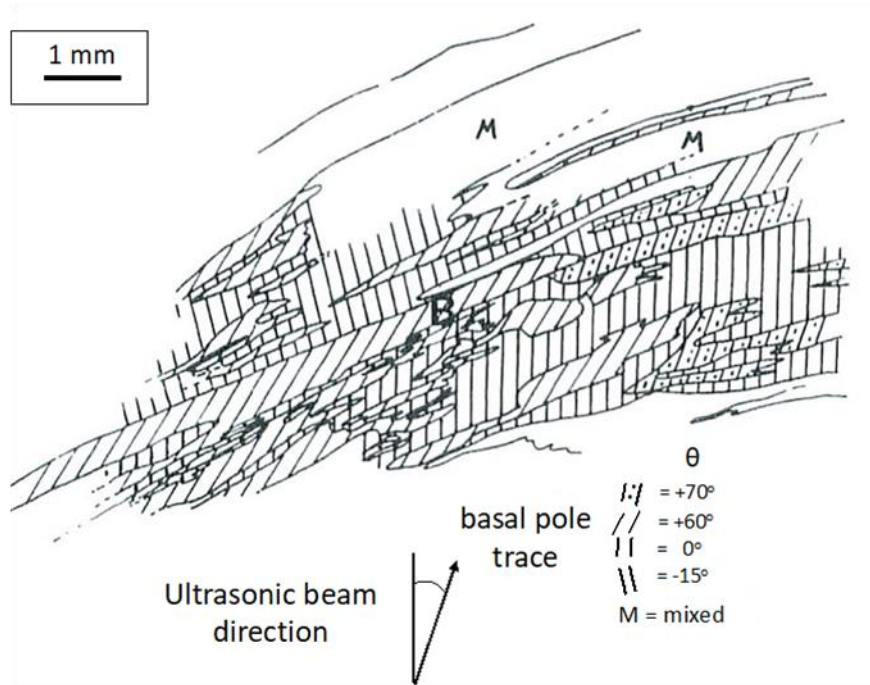
Figure B-10. Basal plane trace determination via polarized light

In the 2014-2015 timeframe, researchers at AFRL placed a high-precision rotating stage on top of an inverted brightfield polarizing metallograph (Uchic, Groeber, Woodward, Dimiduk, & Pilchak, 2015). The polarizer and analyzer were fixed in a cross-polarized condition and a series of images were collected at various intervals while rotating a single-phase Ti-7Al sample through a total angular range of 360°. The technique was termed Computational Polarized Microscopy (CPM). The images were flat-fielded and then rotated into the same orientation. Analysis of the aligned stack of images revealed some grains experienced no contrast variation while others oscillated from light to dark and back again. Other grains went through oscillations

as well, though with less variation in the maximum and minimum. Plots of reflected light intensity versus specimen rotation angle revealed a sinusoidal variation with varying mean, amplitude, and phase shift (Figure B-11) with a period of 180° being observed. This period implies that the c-axis can only be uniquely determined in one half of the pole figure (Figure B-12).
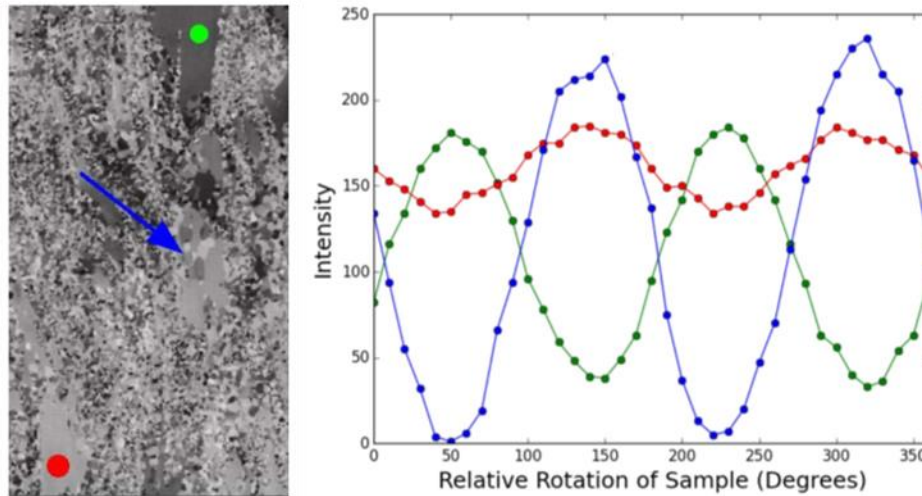
Figure B-11. Variation in reflected light intensity for three grains in a Ti-7Al sample
As a function of sample rotation relative to the incident polarization vector
Image courtesy of Michael Uchic, Air Force Research Laboratory
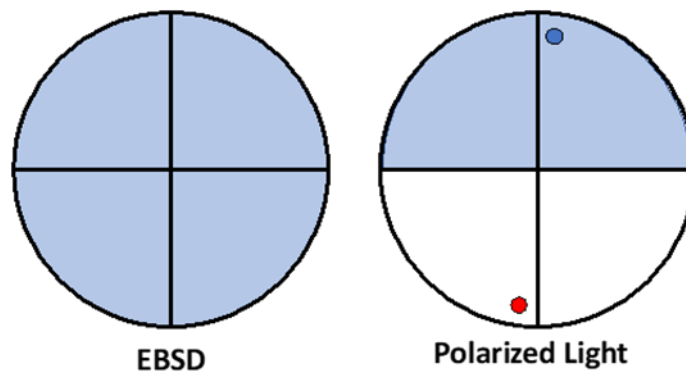
Figure B-12. Comparison of orientations accessible by EBSD vs. polarized light as represented by shaded regions on (0001) pole figures
According to theory the orientations represented by the blue and red dots are indistinguishable under polarized light

EBSD analysis of the same area provided the ground truth measurement. Grains which remained dark throughout the entire series were found to have the basal plane in the plane of polish while grains which oscillated from the lightest to darkest had the c-axis in the plane of polish. Grains with intermediate amplitudes had the c-axis at some angle inclined to the plane of polish. In all cases, the phase shift was correlated with the azimuthal orientation of the c-axis. The CPM data were fit to a sine wave, $I = A \sin(Bx+C) + D$, where A is the amplitude, B is the period, C is the phase shift, and D is the mean. The orientation-dependence of these parameters were plotted spatially (Figure B-13) and also as pole figures in Figure B-14 (these images are courtesy of Dr. Michael Uchic and Dr. Michael Groeber). The CPM and EBSD data were fused to create a correlation between grain orientation and sine-wave parameters. Using this correlation, the CPM data were assigned c-axis orientations and subsequently segmented using a 5° c-axis orientation tolerance. The results (Figure B-15) showed a reasonable correlation between the number and size of the large, unrecrystallized regions in the sample (which were intended to simulate MTRs in the single-phase Ti-7Al material), but the technique appeared to undersize the finer recrystallized regions. Nevertheless, the technique showed promise, but several important hurdles needed to be overcome. For example, it was impossible to uniquely determine an orientation from a single measurement and this preliminary work did not address the role of the beta phase (which is optically *isotropic*) and its impact on the deduced alpha-phase orientations.
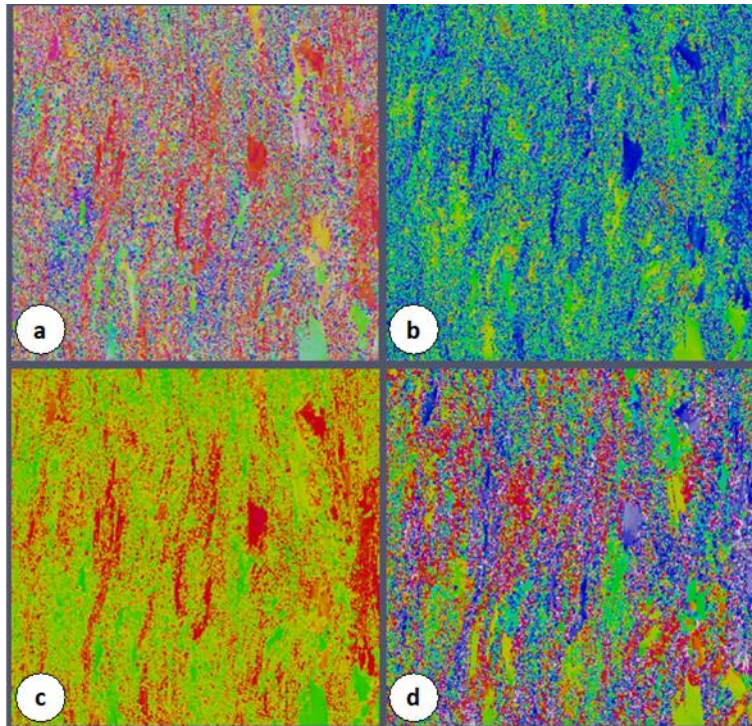
Figure B-13. (a) Normal direction inverse pole figure map, (b) amplitude, (c) mean, and (d)
phase shift for sine wave fits to the reflected polarized light intensity profiles
*Image courtesy of Michael Uchic, Air Force Research Laboratory and Michael Groeber now
with the Ohio State University*
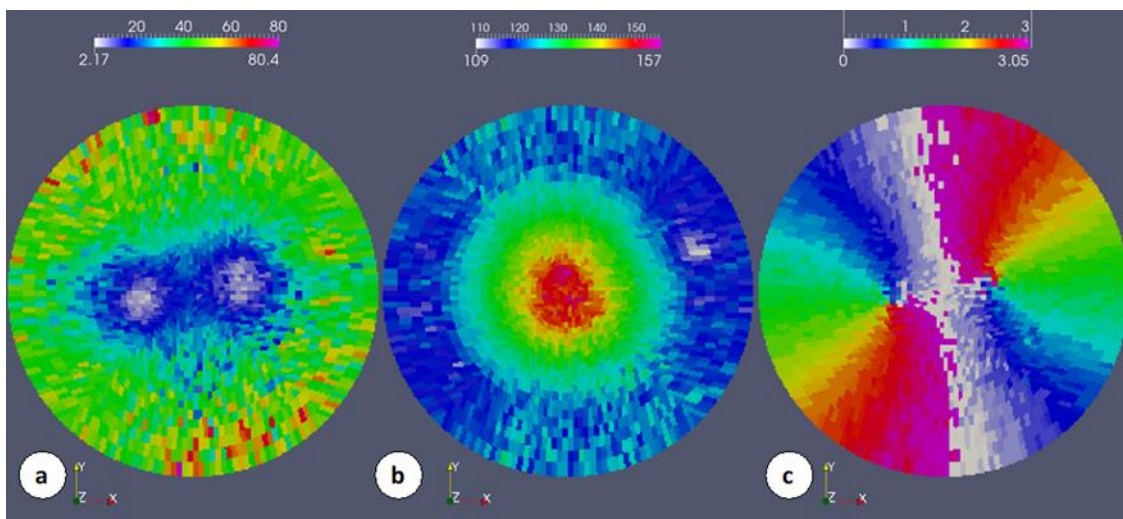
Figure B-14. Pole figures showing the orientation dependence of the (a) amplitude, (b) mean,
and (c) phase shift for the data in Figure B-13
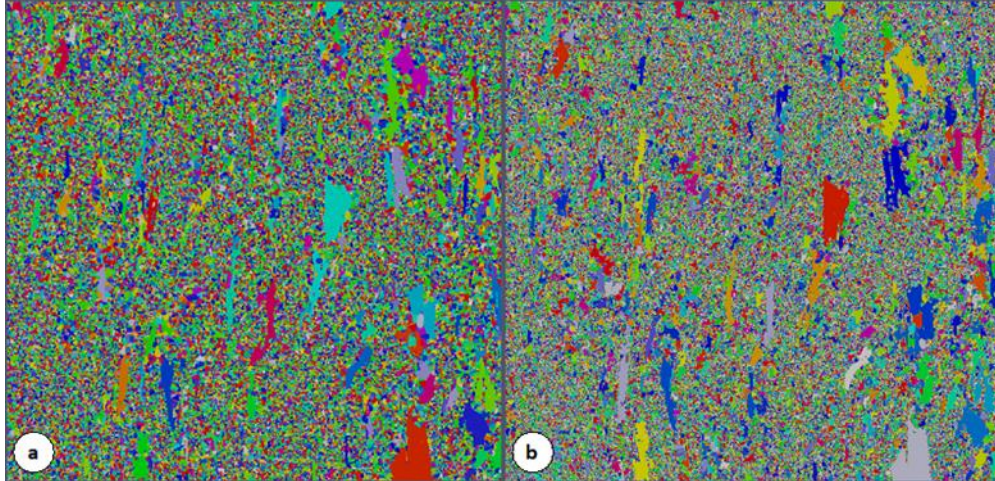
Figure B-15. Unique grain maps for data in Figure B-13 obtained from EBSD and computational polarized light microscopy techniques

Soon after this demonstration, AFRL leveraged this successful lab demo into a Small Business Innovative Research solicitation (Topic: AF171-098 (SBIR STTR America's Seed Fund powered by SBA, 2017b)). Two awards were made, one to MRL (SBIR STTR America's Seed Fund powered by SBA, 2017a) and another to Advanced Optical Technologies Inc. (AOT) (SBIR STTR America's Seed Fund powered by SBA., 2017c). The MRL team focused on linear polarized light while the AOT team developed the crystallographic polarization classification imaging (CPCI) method. Each company was later awarded a Phase II contract as well, AOT supported by AFRL (SBIR STTR America's Seed Fund powered by SBA, 2017d) and MRL supported by the Navy (SBIR STTR America's Seed Fund powered by SBA, 2021). Each company has produced a commercially viable product (Advanced Optical Technologies, 2022) and are actively supporting customers with analysis. These techniques are being evaluated against EBSD and other characterization modalities for potential application to industrial characterization of billet and finished forgings. MRL's TiPolar™ microscope is shown in Figure B-16. The unit is approximately 2.3 ft x 2.5 ft x 3.75 ft. All electronics are included within this form factor. It uses standard 110-volt wall plug and sits on casters to make it portable. The system has 2" x 3" of stage travel and it is capable of imaging at resolutions as fine as 0.4 µm with speeds up to ~1 million points per second. The data collected is processed locally using MRL's TiZone™ algorithm. A representative image from this microscope is compared with EBSD data in Figure B-17 (image courtesy of Matthew Cherry and John Wertz, AFRL).

Figure B-16. MRL's TiPolar microscope
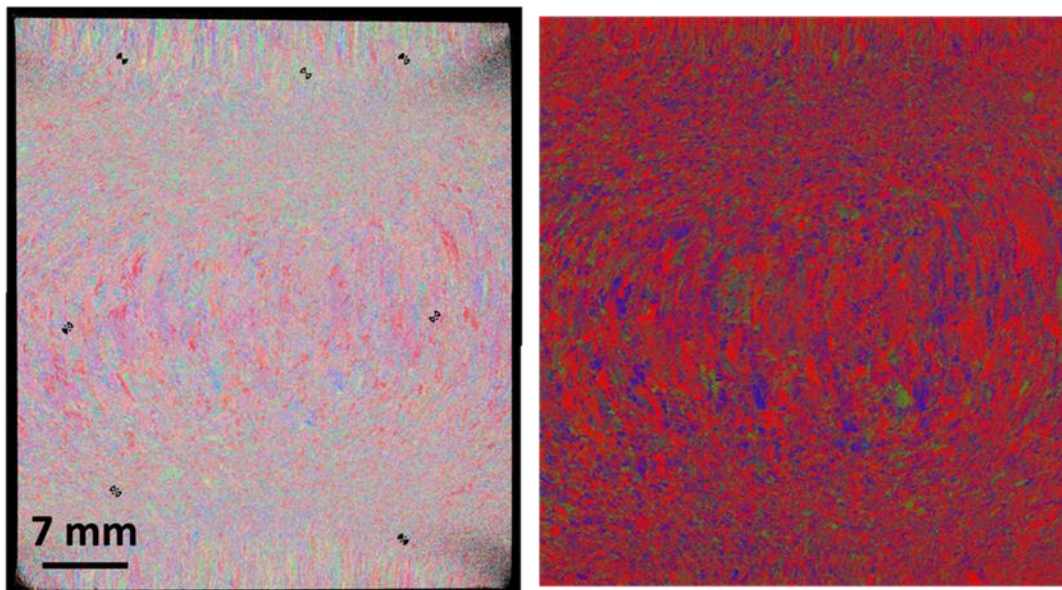
Figure B-17. Large area EBSD scan (left) and TiPolar C-map (right) of alpha+beta forged Ti-6242

During the AFRL SBIR programs, other researchers began exploring this field as well. Jin and De Graef at Carnegie Mellon University were supported by an ONR Vannevar Bush Faculty Fellowship Program under which they pursued the development of a forward model for polarized light microscopy. They reported early findings at the 2018 Microscopy and Microanalysis Conference. The findings included the imperfect correlation between the maximum intensity from a 360º series of polarized light images with EBSD c-axis inclination. The authors also

noted a correlation between the rotation index where the maximum intensity occurred (i.e., phase shift) and the azimuthal orientation of the c-axis as determined by EBSD. The authors reported that they developed a forward model for the polarized light experiment in order to create a dictionary-style indexing to correlate observed intensity profiles with crystallographic orientation. At the same conference, Safaie et al. (2018) published a short report on the preliminary application of this technique to the characterization of Ti-6Al-4V material. A detailed explanation of the technique was not provided, but the authors were able to produce basal pole figure maps for EBSD and polarized light and noticed a loose correlation between the two. The authors also noted the same 180º period of optical anisotropy mentioned above.

Böhme et al. (2018) compared c-axis orientations determined from polarized light with those obtained by EBSD on two lots of commercial purity titanium – one containing random orientations and the other exhibiting a basal texture. A series of images at different sample rotations relative to the polarizer and analyzer were obtained. The observed reflected light intensity was well described by a sine wave. The authors also observed the amplitude and phase shift to the c-axis inclination and azimuthal orientation, respectively. Their work overcame a potential issue with polarized-light-based methods in that the reflectivity changes from sample to sample. The authors used the randomly textured sample to develop a correlation between sine wave fit parameters and EBSD orientations. These fit parameters were found to be transferable and able to determine the orientations in the textured sample after normalizing each sine wave by its average intensity over a period of 180º. The same group (Morales-Rivas, Böhme, & Kerscher, 2020) reported similar observations at the World Titanium Conference in 2019 and noted that the technique may also have important implications on analyzing twins in deformed titanium.

Jin and De Graef (2020) published a more detailed report of their forward model and compared it to observed intensity profiles obtained by polarized light. The forward model represented the polarization state of the incident light as a four element Stokes vector. The polarization state is altered each time the light interacts with an element in the optical path of the microscope or the sample itself. Each element in the optical chain is represented by a 4x4 Mueller matrix which collectively modify the incident Stokes vector to model the experimentally observed intensity profiles. The authors used the model to interpret experimental observations on a single-phase Ti-7Al extrusion. This work highlighted several challenges that must be overcome for quantitative orientation determination via polarized light including orientation-dependent and non-uniform illumination, wavelength-dependence of the dielectric tensor, the role of oxide thickness on reflectivity, and the non-ideal behavior of various optical elements in the microscope (particularly the beam splitter). The CPM-determined c-axis orientations were compared with those obtained by EBSD. A good correlation with relatively low scatter was obtained for the

azimuthal orientation, but the c-axis inclination proved to be more challenging (Figure B-18). The authors also reported that the experimentally observed deviations decreased significantly when a non-linear scaling term was used to describe the amplitude of the reflected light (Figure B-19).
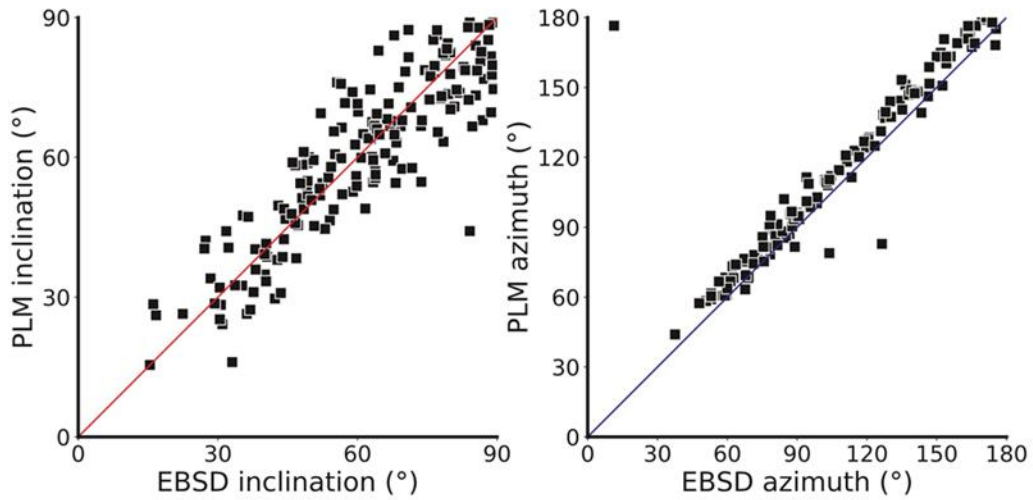

Figure B-18. Scatter plots comparing c-axis inclination and azimuthal orientation
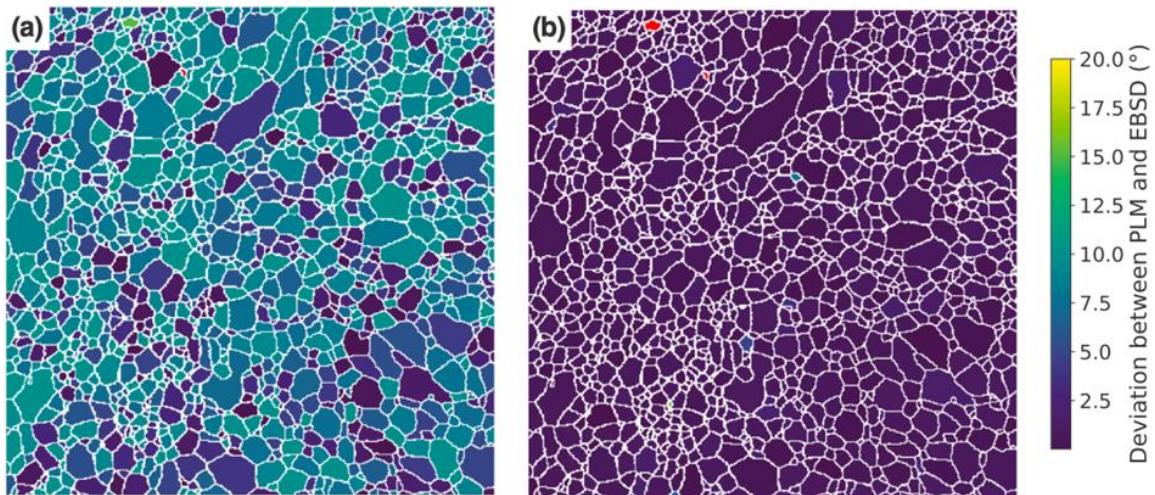*Obtained by polarized light microscopy (PLM) and EBSD*

Figure B-19. Deviation between PLM and EBSD assuming (a) linear scaling and (b) sin2 scaling

All of the papers reviewed to this point have been focused on single phase alpha alloys. Analysis of two-phase microstructures presents additional complexity. The beta phase is optically isotropic, so the techniques presented above are not able to determine local crystal orientations.

Further, the presence of beta phase will reduce the mean intensity of reflected light depending on the volume fraction present at the surface, which varies as a function of sectioning plane for lamellar and transformed beta regions of bimodal microstructures. In addition, differences in polishing rates for various microstructural constituents may produce surface relief that changes the local scattering response near grain and phase boundaries. Thus, care should be taken to produce a smooth, flat, and unetched surface for these techniques.

Despite these complexities, Hijazi et al. (2022) demonstrated the use of polarized light to analyze MTRs in rolled Ti-6Al-4V. The authors identified three classes and MTRs – basal ‖ ND, $\{10\bar{1}0\}$‖ ND and $\{11\bar{2}0\}$‖ND from polarized light microscopy. They reported that the fraction of MTRs identified by polarized light were in good agreement with those obtained by EBSD, though there was not an exhaustive discussion of the segmentation method for either modality. The authors were able to classify the three types of MTRs based on correlating the sample orientation, the polarizer/analyzer orientations, and the specimen rotation relative to the polarizer/analyzer when the reflected light intensity was brightest and hence the c-axis was known to be in-plane. This demonstrated the potential for application to two-phase materials. There were no discussions of identifying plunge angle of the c-axis for two-phase Ti alloys.

As mentioned earlier, a second type of polarimeter began development under AFRL SBIR funding at AOT. By They developed an orientation imaging technique based on polarized light microscopy that does not involve rotating the sample or the polarizer/analyzer. Recall that the Mueller matrix represents the complete linear response of a material to an electromagnetic wave. This response can be characterized according to the phenomenological descriptors shown in Figure B-20 (image courtesy Brian Hoover, AOT). Using a very sensitive non-imaging-laser-based-Mueller-matrix polarimetry, Hoover et al. (2018) demonstrated that there was sufficient response in the diattenuation, polarizance, and retardance (Figure B-21) to achieve quantitative orientation imaging via polarimetry.
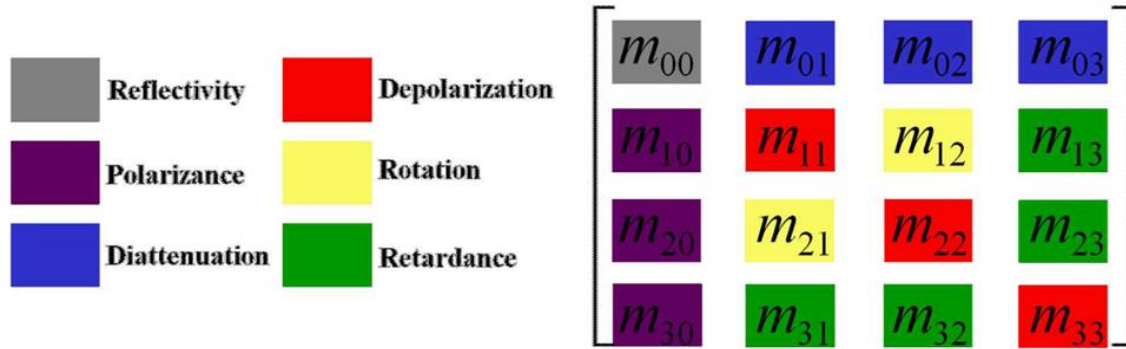
Figure B-20. Correlation between phenomenological mechanisms and Mueller matrix elements
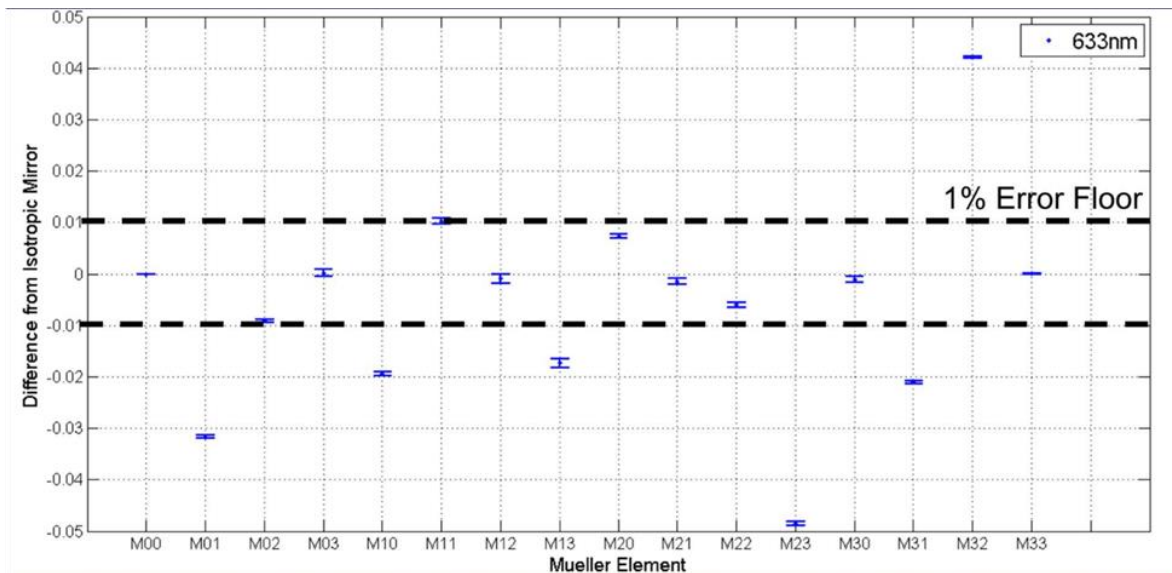
Figure B-21. Non-imaging normalized Mueller matrix polarimetry measurements for single crystal commercial purity titanium

To increase the measurement speed for use in imaging, Hoover et al. (2018; 2018b) developed a partial Mueller-matrix polarimeter. This device decreases data collection time by measuring only certain elements of the Mueller-matrix that show sensitivity to orientation. The specific functions are determined using machine learning algorithms. This enables rapid imaging over large fields of view. In an early design of the device, AOT reported that individual fields of view were of the order of 0.75" x 1.75" with a spatial resolution of 80-µm. The pixel resolution was further improved to be less than 3-µm for instantaneous fields of view of 1.33 cm^2 in a later iteration of the device (Figure B-22), and larger fields of view were made possible by stitching together multiple tiles. This modification was also accompanied by the development of a robust

electrodynamic model that enabled estimation of the azimuthal angle of the c-axis without the need to rotate the sample (Hoover, Turner, & Ornelas-Rascon, 2021). Calibration of the c-axis inclination is more challenging but is enabled by a small training procedure in which up to 10 grains are measured with EBSD and an optimizer seeks the optimal scaling factor.

C-axis maps collected with CPCI and EBSD on a Ti-7Al sample are shown in Figure B-23. Blind tests on single phase Ti-7Al and alpha+beta processed Ti-6Al-4V yielded a favorable comparison between EBSD and CPCI as shown in Figure B-24 and Figure B-25. The correlation is greatest for the single-phase Ti-7Al alloy with better than 7.5% agreement while the Ti-6Al-4V sample demonstrated ~11% agreement on average. The trend angle in Figure B-25 has a period of 180∘ such that Regions 1, 3, and 6 in the trend angle actually imply good agreement. The authors also performed EBSD scans of the same area on two different instruments and observed a ~3º RMS variation in the azimuthal orientation and a 2.5º RMS variation in the inclination.
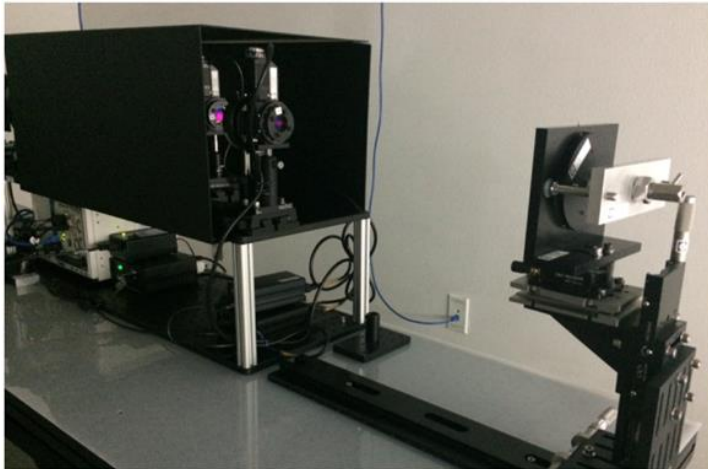
Parameter	Specification
Wavelength	632.8nm
Laser Power	0.5mW
Working Distance	40cm
Bistatic Angle	4°
Pixel Resolution	<3µm
Optical Resolution	12µm
iFOV Ø	13mm
Channels	6
Acq. Time	<30s

Figure B-22. Custom laser coherent PLM for wide-field orientation imaging and its preliminary specifications
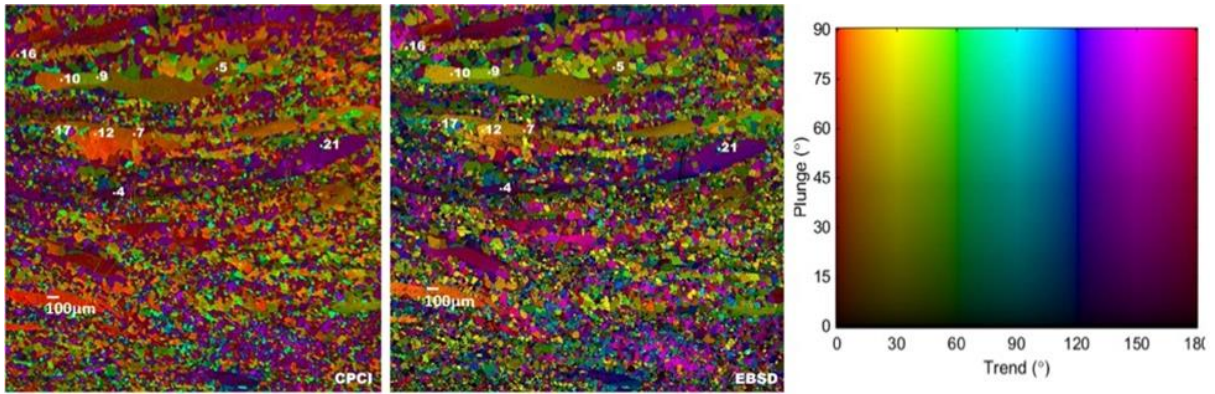
Figure B-23. Comparison of CPCI and EBSD with a custom color map
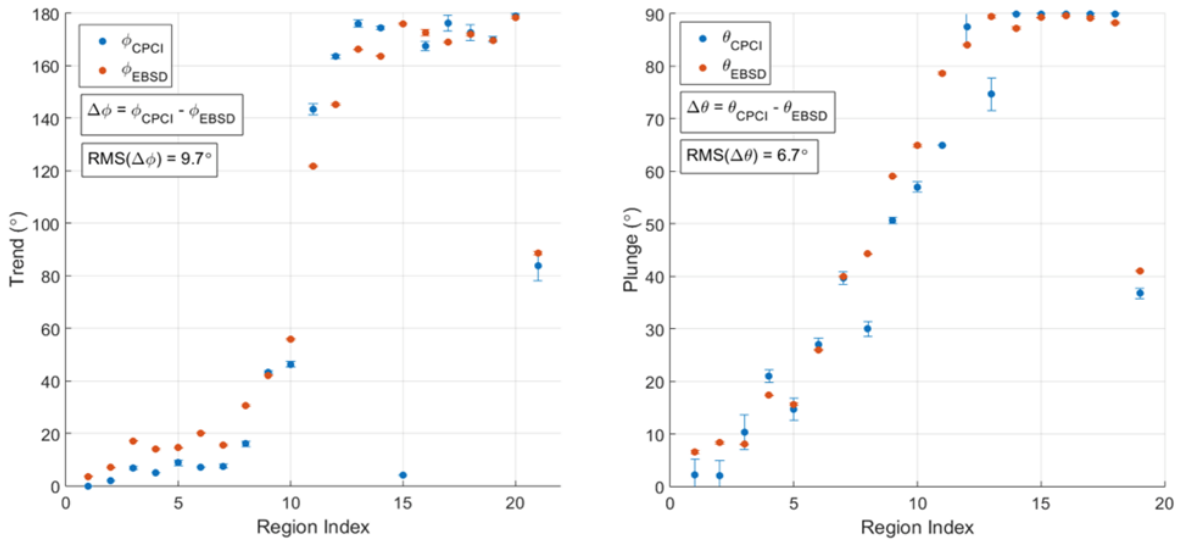
Figure B-24. Blind-test statistics comparing CPCI and EBSD measurements of c-axis orientation for a Ti-7Al sample
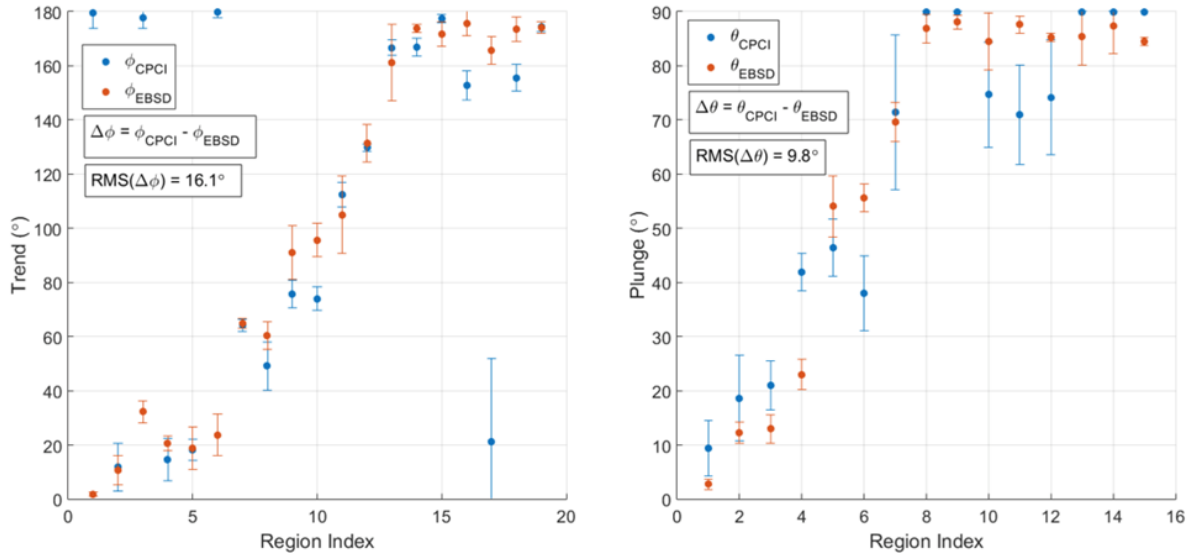
Figure B-25. Blind-test statistics comparing CPCI and EBSD measurements of c-axis orientation for a Ti-7Al sample

In summary, characterization techniques based on polarized light are very promising to enable large-area characterization of titanium alloys for use in process qualification and quality control. There are several key questions remaining that need to be overcome to fully reduce this technique to practice. These include achieving proper calibration of the inclination angle in the presence of confounding factors like alloy composition, phase fraction and morphology, texture, and variation in surface preparation.

C   Nondestructive characterization of microtexture

Ultrasound

Ultrasonic testing (UT) is a well-known nondestructive technique used to assess the quality of materials at the billet stage and again following forging and machining into the so-called sonic shape. Inspections for titanium alloys have been largely focused on identifying any melt-related anomalies (e.g., hard alpha) or conversion defects (e.g., cracking and voiding). There are many types of ultrasonic inspection and a full review is beyond the scope of this article. However, the interested reader can begin with online resources (for more information, see (Iowa State University, & Center for Nondestructive Evaluation, 2022)).

A basic ultrasonic setup is shown schematically in Figure C-1 (image courtesy of Stan Rokhlin). An unfocused single element transducer is used to introduce an ultrasonic wave (typically 5-10 MHz frequency) into the metal and the same transducer receives information coming back to it. This is known as pulse-echo mode. The transducer converts small displacements into electrical voltages that can be displayed on an oscilloscope or computer screen. The transducer can be coupled to the surface of the material, or the transducer and material can be placed in a water tank and an electric pulse is used to generate an elastic wave. Some of the incident wave will reflect off of the front surface of the material, but a fraction of the sound energy will be transmitted into the material. If there are no defects present the wave will reflect from the back wall and return to the transducer. However, if there are anomalies present in the material, the wave will also reflect from the defect and a second peak will be observed in the captured waveform.
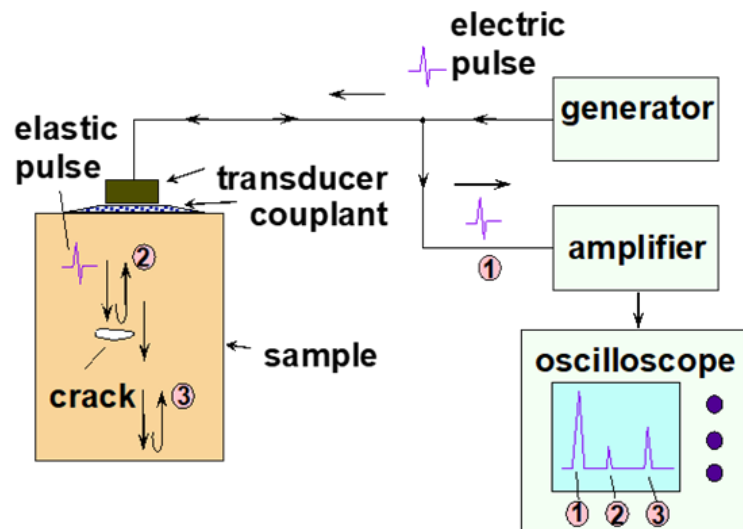

Figure C-1. Basic pulse-echo ultrasonic inspection method

Sensitivity to defects can be enhanced by using transducers with lenses to focus the beam at various depths. This is what is done for multizone inspection systems allowing for accurate determination through large section thicknesses. Phased array UT systems can also direct the beam and focus at various depths. If one focuses the transducer on the front of the sample, it is possible to generate a Rayleigh surface wave known more generally as a surface acoustic wave (SAW). These are a type of elastic wave which couple longitudinal and shear displacements resulting in elliptical particle motion in a plane that contains the wave propagation direction and the surface normal. The sound energy is concentrated near the surface and the resulting displacements can be detected using conventional transducers, laser vibrometers, or laser-based diffraction gratings. In contrast to the lower frequency bulk waves, SAWs are typically higher frequency and thus do not travel as far. This may include the use of frequencies between 50 MHz and 2 GHz, the former of which is useful on as-machined surfaces with a spatial resolution of 30~50 µm and the latter of which can provide higher spatial resolution but require metallographically prepared surfaces. They are useful, however, for detecting surface flaws and can also be used for microstructure characterization as discussed later.

Bulk waves also lose intensity to absorption and scattering as they propagate through the material. The combined effect of these two is known as attenuation (α). Absorption is the conversion of the elastic wave into other forms of energy, like heat, for example. Scattering is the change in direction of a wave from its original path. One source of scattering occurs when the wave interacts with microstructural features present in the material. Backscattering is a particular subset of scattering in which the sound energy is 'reflected' off of the grain boundaries and returns to the transducer. This is often referred to as grain scattering noise and is present between the front and backwall reflections. There are three basic scattering regimes which are categorized based on the grain size (d) relative to the wavelength (λ). These include:

1. The low frequency Rayleigh regime where $\lambda >> d$ where attenuation is proportional to d^3

2. The stochastic regime where λ is $\leq d$ and attenuation is proportional to d

3. The geometric regime where $\lambda << d$ and attenuation behaves as $1/d$

The primary alpha grain size and alpha lath thicknesses are much smaller than the 300~600 µm wavelengths used to inspect titanium alloys so they do not contribute significantly to scattering. However, these wavelengths are in line with typical MTR dimensions found in billet and forgings, and hence, these features contribute significantly to ultrasonic attenuation and scattering. This leads to two important points. First, the noise introduced into ultrasonic scans due to MTRs can mask and limit detection of actual flaws. Second, and more germane to the

present discussion, there is a plausible pathway to nondestructive characterization of MTRs using elastic waves. As discussed below, several academics have undertaken the inverse problem of estimating microstructure from both bulk waves and performing direct observation with surface waves.

<u>Bulk acoustic waves</u>

Volumetric ultrasonic scans are used to interrogate billets as well as forgings which have been machined into a sonic-friendly shape. Billet inspections are typically performed using phased array or multizone systems while forgings are generally inspected using one or more single element transducers. In the latter case, scan plans typically provide complete volumetric coverage with each location being interrogated from multiple surfaces. As this is already standard production practice for defect detection, there is a significant opportunity to use existing data streams and new analysis methods to characterize microtexture quantitatively and volumetrically in billets and forgings.

The interaction of bulk acoustic waves and MTRs has been the subject of reasonable attention over the past ~25 years beginning with the Engine Titanium Consortium's work sponsored by the FAA. The earliest works on industrially relevant two-phase Ti alloys were due to Ginty (1980), Han and Thompson (1997), Panetta et al. (1997b), and Blodgett and Eylon (2001). Later experimental and/or theoretical work by Margetan et al. (1994), Rohklin and co-workers (Bhattacharjee, et al., 2011; Ghosh, et al., 2007; Li, Yang, & Rokhlin, 2014; Li & Rokhlin, 2016; Lobkis, Yang, Li, & Rokhlin, 2012) (Lobkis & Rokhlin, 2010; Mills, et al., 2018; Pilchak, Li, & Rokhlin, 2014b; Venkatesh, et al., 2016; Yang, Li, & Rokhlin, 2013) (Yang, Li, Lobkis, & Rokhlin, 2012; Yang & Rokhlin, 2013), Humbert et al. (2009), Lan et al. (2014; 2015), and Blackshire et al. (2019) provided key insights into the interaction of ultrasound, texture, and microtexture. The following experimental conclusions can be reached:

- Ultrasonic attenuation and backscattering response are both affected by the presence, size, and aspect ratio of MTRs.

- The presence of MTRs reduces the ability to detect defects in wrought titanium where high noise may mask true defects (Gigliotti, Bewlay, Deaton, Gilmore, & Salishchev, 2000; Ginty, Hallam, Hammond, Jackson, & Robb, 1980).

- The mechanism of attenuation is due to orientation-dependent sound velocity in titanium which leads to beam distortion including beam steering, amplitude distortion, and phase distortion (Panetta, Margetan, Yalda, & Thompson, 1997b).

- For material with nominally equiaxed MTRs, ultrasonic attenuation increases linearly with MTR size in the range $0.1 < d_{MTR}/\lambda < 1.0$ where d_{MTR} is the width of the MTR in the direction of wave propagation and λ is the wavelength (Bhattacharjee, et al., 2011).

- For material with high aspect ratio MTRs, attenuation is greatest when the wave propagation direction is parallel to the elongation direction (Blodgett & Eylon, 2001).

- The reduction in attenuation is due to phase fluctuations/wavefront distortion caused by different sound velocities in adjacent MTRs with varying crystallographic orientation (Panetta, Margetan, Yalda, & Thompson, 1997b).

- For a signal from a defect with a diameter less than or approximately equivalent to the wavefront distortion, the received signal will be artificially increased resulting in an increased estimated flaw size; conversely, if the diameter of the defect is much less than the scale of the distortion, the received signal will be diminished compared to that of an MTR-free material (Panetta, Margetan, Yalda, & Thompson, 1997b).

- Ultrasonic backscattering noise is greatest when the size of the MTRs is of the order of the incident wavelength, which is common for radial inspection of billet material (Han & Thompson, 1997; Humbert, et al., 2009).

- For elongated (high aspect ratio) MTRs where the elongation direction is neither parallel nor perpendicular to the incident wave direction, such as those which may be found in forgings machined into a sonic shape, the effects on attenuation and backscattering discussed above are reduced (Blodgett & Eylon, 2001).

- The average backscattering response can be represented by a figure of merit (FOM) which is given by the expression FOM $= n^{1/2}A$ where n is the number of grains per unit volume and A is root mean square of the backscattering amplitude of a grain in an effective medium (Han & Thompson, 1997; Margetan, Thompson, & Yalda-Mooshabad, 1994).

- Large MTRs with planar boundaries may lead to discrete reflections above the reject threshold (Blackshire, Na, & Daugherty, 2019; Ginty, Hallam, Hammond, Jackson, & Robb, 1980).

- Mode-conversion or scattering from large, planar MTR boundaries can redirect sound energy to back or side walls resulting in unanticipated and potentially rejectable indications (Blackshire, Na, & Daugherty, 2019; Ginty, Hallam, Hammond, Jackson, & Robb, 1980).

- Diffuse MTRs with lower intensity and degree of crystallographic alignment are not effective scatterers (Ginty, Hallam, Hammond, Jackson, & Robb, 1980).

- Attenuation is negligible when the microstructural unit size is less than ~0.03 of the incident wavelength (Pan, Shong, & Li, 1990).

- Ultrasonic wave speed varies about 200 m/s with crystallographic orientation, which is sufficient to estimate variations in crystallographic texture (Lan, Lowe, & Dunne, 2014).

- It is possible to obtain (0001) pole figures direct from ultrasonic measurement in an immersion setup where the angle of incidence relative to the incident wave can be systematically adjusted (Lan, Lowe, & Dunne, 2015).

Based on the experimental work summarized above, it can be surmised that there is sufficient signal from the MTRs to enable quantitative characterization using ultrasonic methods. The pioneering work of Stanke and Kino (1984), Weaver (Weaver, 1990), and Rose (Rose, 1992) provides the theoretical basis for this activity. These authors provided the first unified theory that described scattering in Rayleigh, stochastic, and geometric scattering regimes as well as the transitions between them. The microstructure is represented by the spatial autocorrelation function of the elastic constants (i.e., two-point correlation and assumed it to be inverse exponential). These theories laid the foundation for models developed by Han and Thompson (Han & Thompson, 1997) to understand size and frequency effects on backscattering and for Rokhlin and coworkers (Li, Yang, & Rokhlin, 2014; Li & Rokhlin, 2016; Lobkis, Yang, Li, & Rokhlin, 2012; Lobkis & Rokhlin, 2010) (Yang, Li, & Rokhlin, 2013; Yang, Li, Lobkis, & Rokhlin, 2012; Yang, Li, Lobkis, & Rokhlin, 2012; Yang & Rokhlin, 2013) to solve the inverse problem to obtain microstructural parameters directly from ultrasonic measurements. These models treat the colonies or MTRs as polycrystalline ellipsoidal features and are represented by the two-point correlation function of the elastic constants.

Han and Thompson (Han & Thompson, 1997) developed a model to predict the ultrasonic backscattering coefficient for equiaxed and elongated colony alpha holding BOR with a parent prior beta grain. The Rokhlin group at The Ohio State University later built on this and developed several models to solve the inverse problem for MTRs which incorporated the effects of crystallite scattering for equiaxed and elongated MTRs. Lobkis and Rokhlin (2010) developed a simple analytical model for determining the characteristic microstructural length scales for bimodal microstructures and elongated MTRs based on the ratios of backscatter coefficients. Later, Yang et al. (2012), Yang and Rokhlin (2013) developed a model to relate attenuation and backscattering measurements in forged titanium alloys with nonequiaxed MTRs. The model

incorporated the effects of crystallite scattering, which becomes important for the higher frequency waves Figure C-2.
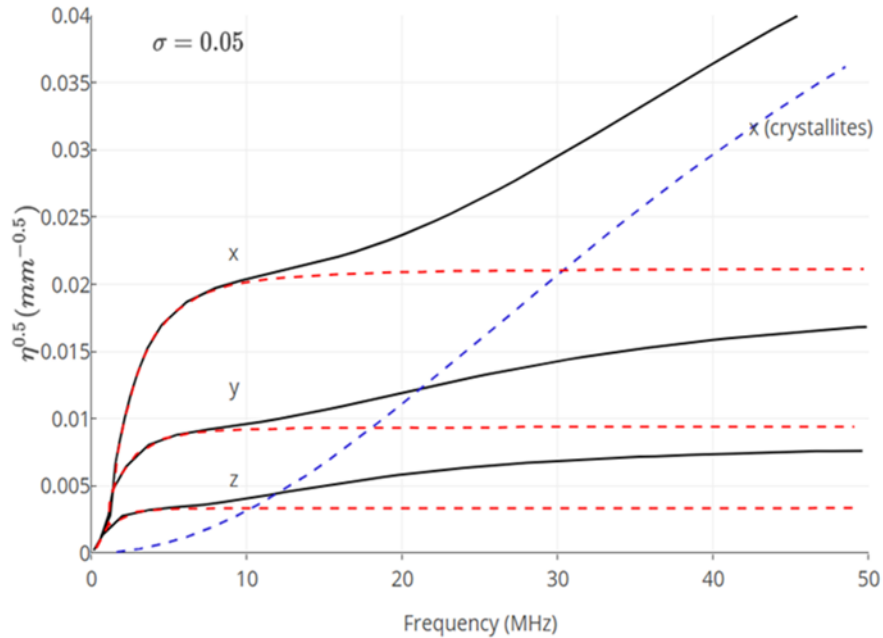

Figure C-2. Model results for contributions of crystallite (blue dotted line), MTR-induced (dashed red lines), and MTR + crystallite scattering (solid black lines)

These approaches had the drawback that they utilized the Born attenuation model that requires prior knowledge of elastic constants, which are difficult to measure and vary with heat treatment due to the elemental partitioning effect. Nevertheless, the results showed reasonable agreement with MTR sizes, particularly in the radial orientations typically varying by less than 25%. Model results in the MTR elongation directions in billets were more challenging and varied by a factor of up to 2.45x, which may be attributable to the limited sampling statistics from EBSD measurements as well as slight differences in the sample reference frames for EBSD and UT experiments (Pilchak, Li, & Rokhlin, 2014b). The analytical model developed by Rokhlin and colleagues (Li, Yang, & Rokhlin, 2014; Li & Rokhlin, 2016; Lobkis, Yang, Li, & Rokhlin, 2012; Lobkis & Rokhlin, 2010) (Yang, Li, & Rokhlin, 2013; Yang, Li, Lobkis, & Rokhlin, 2012; Yang, Lobkis, & Rokhlin, 2012; Yang & Rokhlin, 2013) has recently been assessed during an Air Force sponsored Metals Affordability Program and the results have been summarized in Venkatesh et al. (2016). The authors applied the techniques to subscale product forms at the intermediate beta-processed billet and alpha+beta-worked stages and found reasonable agreement between EBSD and UT-measured colony/MTR sizes (Figure C-3) with nominally equiaxed microstructure in the beta-annealed condition and high aspect ratio (2.75 and 6.5 for

two different billet processing routes). Discrepancies were attributed to volumetric sampling and highlighted the need for larger area characterization and also 3D characterization.
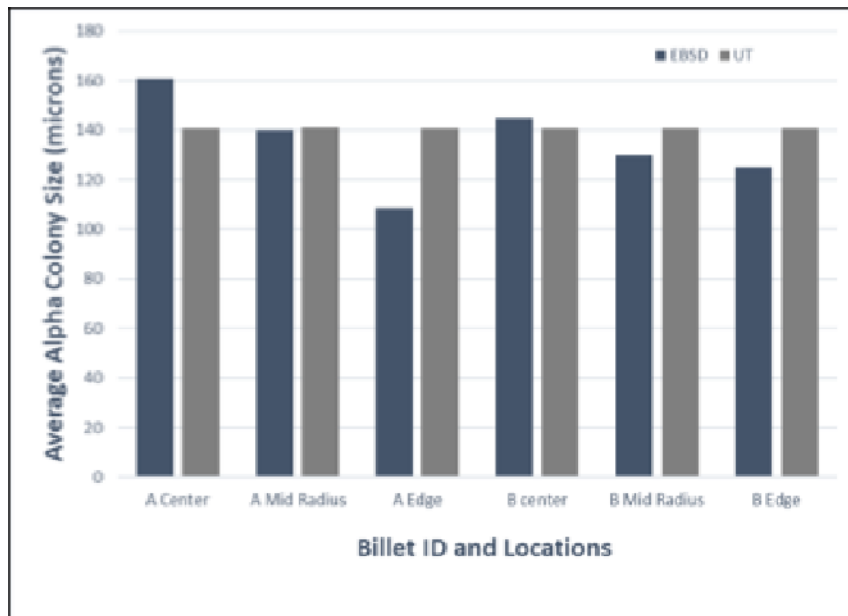

Figure C-3. MTR sizes obtained by EBSD two-point statistics and ultrasonic inversion at various locations in two different alpha+beta processed billets

Rokhlin et al. (2021) later developed the combined method that utilized directional backscatter ratios, attenuation-to-backscatter ratios, and longitudinal wave velocity measurements in three orthogonal directions. This approach is based on the far-field approximation model (Rokhlin, Li, & Sha, 2015) which reduces the number of elastic parameters to only two and does not require knowledge of the microstructure, texture, or elastic constants of individual phases. In this model, the macroscopic texture is assumed to be isotropic, which was found to be a reasonable assumption when averaging over large volumes and looking over many samples. For example, a typical maximum texture intensity is of the order of 2~3x random. Again, reasonable agreement was found between the ultrasonic inverse model and limited EBSD measurements.

We recommend the interested reader follow the references for model derivations and a more detailed discussion of the models, but we now briefly comment on the maturity and applicability of these models. First, these models show strong potential for reduction to practice in obtaining average characteristics of MTRs. Through additional EBSD work and development of stronger correlations, it is possible that these methods may find utility in qualifying and certifying low microtexture billet for demanding rotating applications. In this regard, the backscattering response holds the most promise. This technique could be applied during billet and forging

inspection directly. However, the most advanced inversion techniques require ratios of the backscattering coefficient in three orthogonal sample directions. While this may be applied to slices cut from billets or forgings for qualification or periodic validation that processes are staying within prescribed bounds, it is not possible to use for routine acceptance of every forging. However, Li et al. (2012) and Lobkis et al. (2012) have made progress on inspecting from multiple oblique incidence angles to obtain characteristic MTR dimensions as well as the orientation of the long axis of the MTR. With further development and maturation, this approach may prove valuable for inspecting and accepting forgings.

While mostly academic investigations were primarily described above, there has been considerable industrial effort as well. In fact, some of the work described above by Thompson, Margetan, Han, Panetta, and colleagues were performed as part of the FAA-funded Engine Titanium Consortium (ETC) activity. During this time, the Center for Nondestructive Evaluation (CNDE) at Iowa State worked closely with major engine OEMs with a primary focus on developing reliable inspection methods to detect hard alpha, but the work was also one of the first large, focused activities to relate ultrasonic scattering response to microstructural features. In addition to working titanium, this group also spent some time on nickel superalloys. In one report (Margetan, et al., 2005), they obtained ultrasonic backscattering data, calculated the FOM, and fitted it to a theoretical model to obtain the average grain size for polycrystalline nickel superalloys. The results (Figure C-4) show good agreement between the theoretical model and the FOM for small grain sizes up to about 35 µm after which there are discrepancies. This work was an important step toward more accurate and refined models for Ti alloys that were later developed.
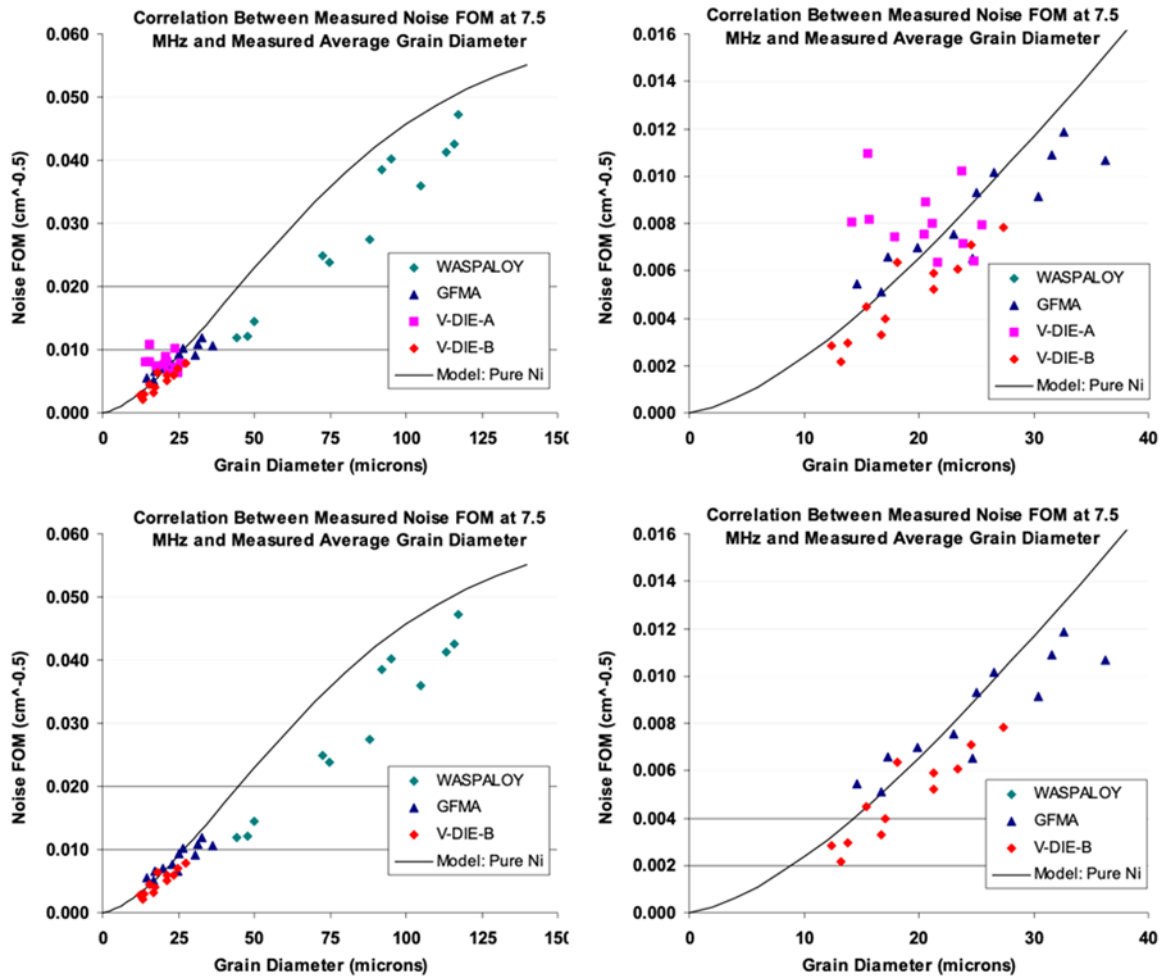
Figure C-4. Relationship between backscattering noise figure of merit (FOM) and grain size in various nickel superalloys

Plots on the right show the data at small grain diameters

The ETC/CNDE team also made important practical measurements on titanium alloy billets (Keller, et al., 2005). This included recommending best practices for phased array and multizone inspection methods as well as observations related to ultrasound/microtexture interactions in production-scale billets up to 14" in diameter. The following conclusions were reached:

- Scattering noise due to MTRs was greatest in 14" billet and decreased with billet diameter.

- The MTR-related noise resulted in a 2~4x variation in signal obtained from a flat bottom hole and the variability was large enough that it should be accounted for during inspection using a gain adjustment procedure.

- Flat bottom hole (FBH) and backwall amplitudes were generally well correlated. Locations with low (high) FBH amplitudes also had low (high) backwall amplitudes. There were exceptions, however, where local backwall amplitude was smaller than average and a nearby FBH was larger than average. Hence, they recommend using the backwall fluctuations as the general indicator of fluctuations for FBH signals.

- The variation in amplitude from the mean was higher for backwall signals compared to FBH signals indicating that using backwall reflections should provide a more conservative estimate of the latter.

- Though cylindrically shaped billets were inspected, there was a radial variation in high and low-noise response at a period of ~90°. This was related to prior conversion steps when the billet is in an intermediate square shape. This resulted in location-specific variations in ultrasonic velocity, attenuation, and backwall reflections and an expressed need to take these variations into consideration during inspection.

More recently, Bridier (2006) reported similar features in a Ti-6Al-4V billet inspected with a multizone system (Figure C-5). The billet was representative of one that would be used in compressor disk forgings.
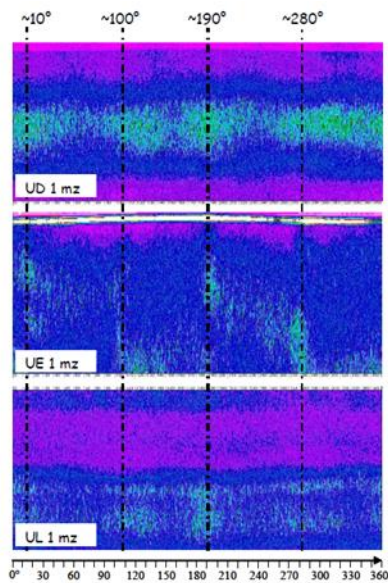
Figure C-5. Multizone C-scans of UD1, UE1, and UL1 phase
Angular locations of high noise regions indicated by black lines

This variation in response is due to underlying differences in crystallographic texture and MTR size and morphology distributions. This heterogeneity is carried through to the forging process and finished part. For example, while the forgings made from these billets are nominally

axisymmetric, the crystallographic texture in these regions may result in nonuniform plastic flow during forging (Semiatin & Bieler, 2001a). There are, of course, differences in location-specific strain and thermal histories throughout the forging which superimpose on top of the billet heterogeneity and lead to further variations in ultrasonic response as evident in the C-scans for various sectors of a Ti-6-4 compressor disk shown in Figure C-6 (Bridier, 2006) where the scale is relative to a 0.4 mm flat bottom hole. EBSD was used to analyze low and high noise regions of the disk, see Figure C-7, (Bridier, 2006). The analysis revealed similar crystallographic textures and MTR appearance in both regions, however, the high noise region was characterized by slightly more elongated regions with sharper, more aligned crystallographic orientations. This result is in line with prior understanding that impedance (i.e., elastic modulus) mismatches at MTR boundaries are responsible for generating backscatter. Diffuse/randomized MTR interfaces are ineffective scatterers and hence result in lower backscattering response.
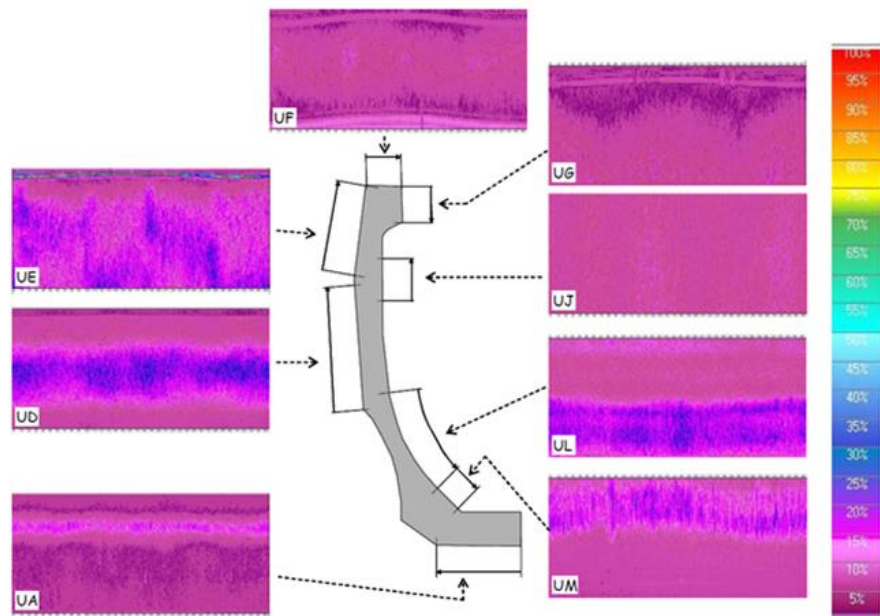
Figure C-6. Max UT noise level heterogeneities during 10 MHz multizone inspection
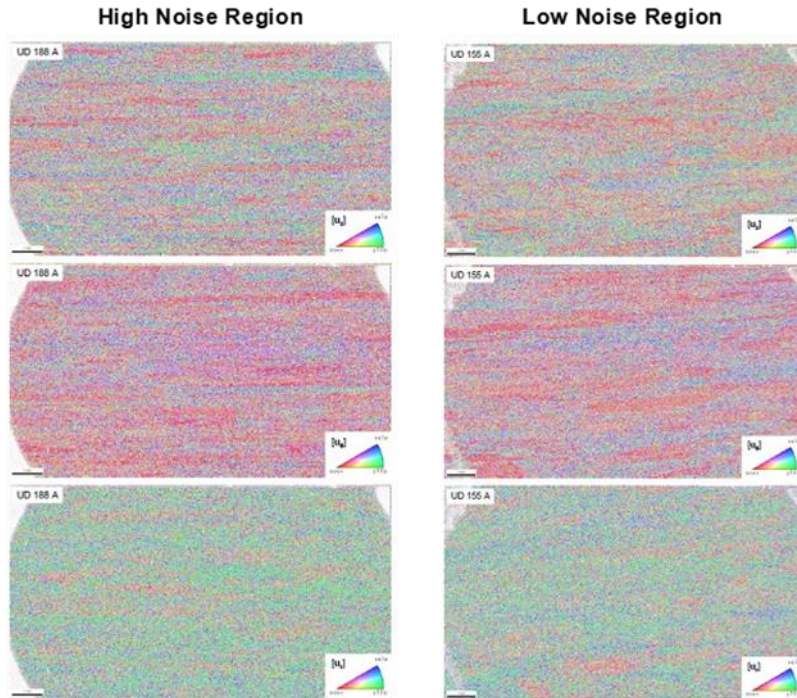
Figure C-7. Inverse pole figure maps covering 13 mm x 7 mm area projected in the axial, circumferential, and radial directions

Surface acoustic waves

As introduced briefly above, surface acoustic waves (SAWs) offer a unique method to potentially characterize MTRs. The technique relies on making spatially resolved measurements of local SAW velocity, which varies with crystallographic orientation as a result of the transverse elastic anisotropy of the alpha phase. This can be done using conventional transducers or lasers with the latter having better spatial resolution. If the region of measurement is smaller than the nominal MTR size, it is possible to capture multiple pixels. A complete history of these techniques is beyond the scope of this report, but the interested reader should begin by researching the phrase 'scanning acoustic microscope' and locating papers beginning with the early 1970's. In this article, we will discuss some of the more recent developments in this field and the application of these to titanium alloys.

Sathish and Martin (2002) used spherically focused transducers to perform scanning acoustic microscopy (SAM) on a titanium alloy sample. At a convenient defocus value (Z), the specularly reflected wave and the Rayleigh wave are observed to separate. The SAM methodology involves measuring the time delay between a reference position and the maxima of the specularly reflected signal (Δt_1) and the *minima* of the Rayleigh surface wave relative to the same reference

position (Δtr_1) at a defocus value Z_1. These measurements are then repeated at a second defocus value, Z_2, as shown schematically in Figure C-8.
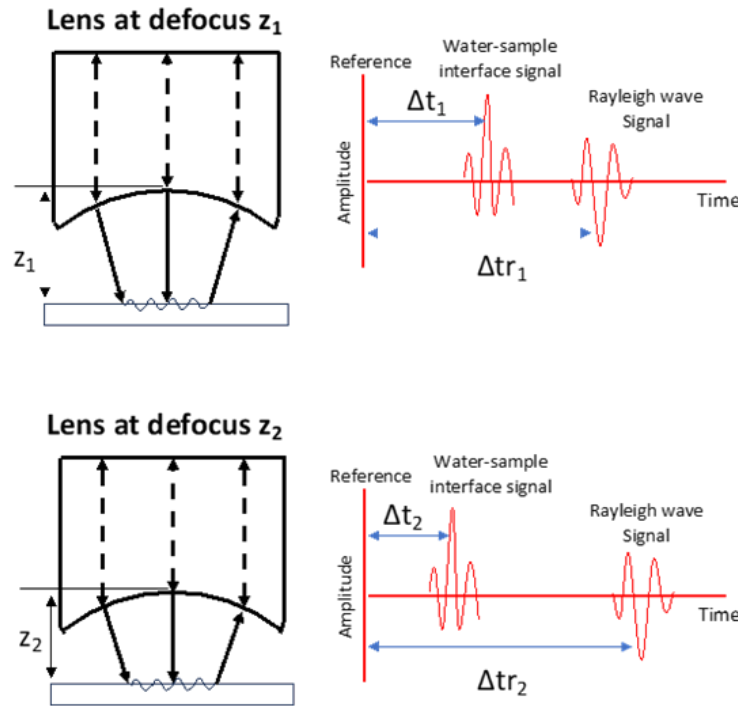

Figure C-8. Principles for measuring Rayleigh wave velocity

The Rayleigh wave velocity, V_R, is then obtained as follows:

$$V_R = \frac{2(Z_1 - Z_2)}{[(\Delta t_1 - \Delta t_2)^2 - (\Delta tr_1 - \Delta tr_2)^2]}$$
C-1

Using impulse excitation at a frequency of 200 MHz, the authors analyzed both fine- and coarse-grained titanium and created a Rayleigh wave velocity map at a spatial resolution of 200 µm, which was estimated to be less than one half the spot size of the incident beam. Despite the coarse resolution, the authors observed large regions of constant SAW velocity which were interpreted as MTRs (referred to as "colonies" in the paper) and verified by EBSD measurements through private communication with Gigliotti from GE's Global Research Center.

More recently, Wertz et al. (2022) have used scanning acoustic microscopy to analyze a large-forged Ti-6242 sample. The surface acoustic wave scan is compared with a large-area EBSD scan in Figure C-9. The forging direction is horizontal in these images and significant spatial variation in MTR size, shape, orientation, and intensity are evident. The small black spots are

fiducial marks used to align the two datasets (images courtesy of Matthew Cherry and John Wertz, AFRL). The top and bottom surfaces made contact with the forging dies which resulted in local cooling that raised the flow stress of the material resulting in very minimal deformation. The center of the forging contains deformed MTRs, but they are still relatively large in size. Between these two extremes is a region of relatively fine, random MTRs. The spherically focused SAM data can reliably identify these three characteristic regions.
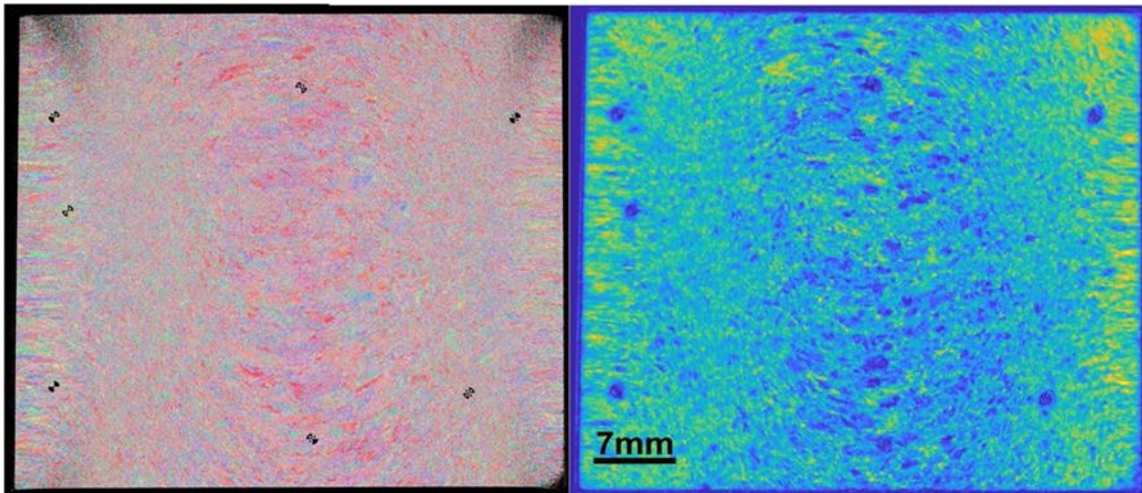
Figure C-9. Normal direction inverse pole figure map (Left); Corresponding Rayleigh SAW map on a forged Ti-6242 sample (Right)

The spatially resolved acoustic spectroscopy (SRAS) technique, developed at the University of Nottingham by Sharples and co-workers (Sharples, Clark, & Somekh, 2006), relies on the principles of SAM but utilizes lasers for the generation and detection of elastic waves. In contrast to most laser ultrasound techniques which focus on relative phase measurement or time of flight, the original SRAS measured the efficiency of SAW generation. The basic instrument is shown schematically in Figure C-10 (figure courtesy of Wenqi Li, Nottingham). The SAW is excited by a fixed frequency laser that is passed through a spatial light modulator which produces a grating on the surface of the sample. The SAWs are detected near, but not overlapping with, the "point" (area) of generation. By sweeping through a range of grating line spacings and measuring the SAW amplitude, the peak response can be found from which the SAW velocity can be calculated as the product of the frequency (f) and the wavelength (λ). The sample is rastered on a table beneath the laser and the measurement is repeated to create a map over the surface of the sample. Using this method, the velocity accuracy is of the order of 89 m/s. The spatial resolution of the technique is mostly limited by the size of the fringes created by the spatial light modulator. In an early version of the instrument, this was of the order of 0.8 mm, but the resolution was quickly

reduced to below 100 µm. In 2008, a resolution as low as ~25 µm was demonstrated (Sharples, Clark, & Somekh, 2006), but more recent reports are utilizing ~50 µm (Smith, et al., 2014). In principle, the technique could achieve ~5 µm spatial resolution if very high frequency (~3 GHz) surface waves are used, but this would require new detectors to be fabricated for this frequency range (Smith, et al., 2014). The optical power density is relatively small, ~12 W cm^{-2}, and hence is well below the limit to damage the sample (Sharples, Clark, & Somekh, 2006).
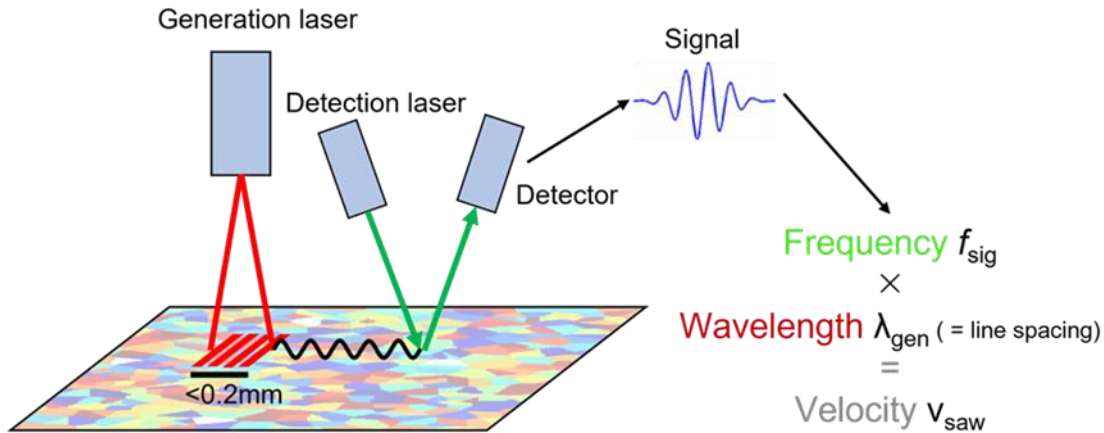
Figure C-10. Schematic of the spatially resolved acoustic spectroscopy system

This approach has the benefit of increased speed and spatial resolution compared to scanning acoustic microscopes that utilize conventional transducers. However, the method is still limited by the need to make multiple measurements using different grating spacings to find the optimum peak. For this reason, the Nottingham SRAS instrument was modified to analyze the frequencies generated by a broadband laser source through a fixed period grating (Smith, et al., 2014). The system as of 2014 is shown in Figure C-11 along with a schematic of the main features of the optical generation and detection systems and an example of the fringes created on the sample by the spatial light modulator with a line spacing of 19 µm.The Nottingham team and their collaborators have published several excellent examples demonstrating the use of SRAS on titanium alloys in the beta-annealed and alpha+beta processed conditions. Several examples are shown in Figure C-12, Figure C-13, Figure C-14 (Smith, et al., 2014), Figure C-15, Figure C-16 (Smith, et al., 2014), and Figure C-17. See the figure captions for additional details, but the examples include laboratory coupons, fatigue test specimens, and entire billet and forging cross sections. In Figure C-12 (Sharples, Clark, Li, & Somekh, 2008), one can see (a) an optical image, after chemical etching; (b) an EBSD orientation image; (c) a SRAS velocity map with waves propagating left-right; (d) a SRAS velocity map with waves propagating bottom-top; and (e) a SRAS velocity vector map, which combines the information from (c) and (d).

In Figure C-13 (Sharples, Clark, Li, & Somekh, 2008), the first four images are 700 x 700 μm, each pixel is 10μm square. They differ by the number of pixels used in the SLM image of the grating, which in turn determines the lateral resolution. The image on the right is 108 x 120 μm, and is a subset of the fourth image, acquired using a smaller step size (2 μm). The area of the scan is 154 x 106 mm, each pixel is 250 μm square. The lateral resolution is approximately 100 μm square. The image took around 6 hours to acquire, corresponding to a scan rate of approximately 12 points per second (Sharples, Clark, Li, & Somekh, 2008). In Figure C-15, the area of the scan is 154 x 106 mm, each pixel is 250 μm square. The lateral resolution is approximately 100 μm square. The image took around 6 hours to acquire, corresponding to a scan rate of approximately 12 points per second (Sharples, Clark, Li, & Somekh, 2008).
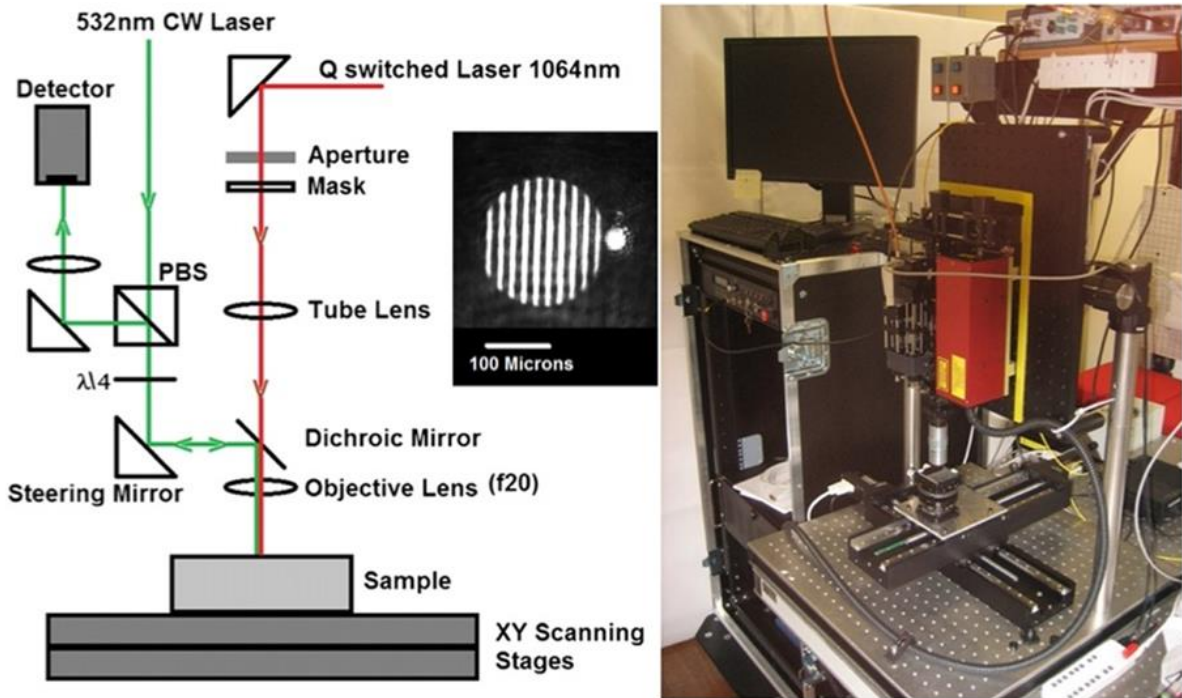
Figure C-11. Nottingham SRAS system, main features of generation and detection systems, example image
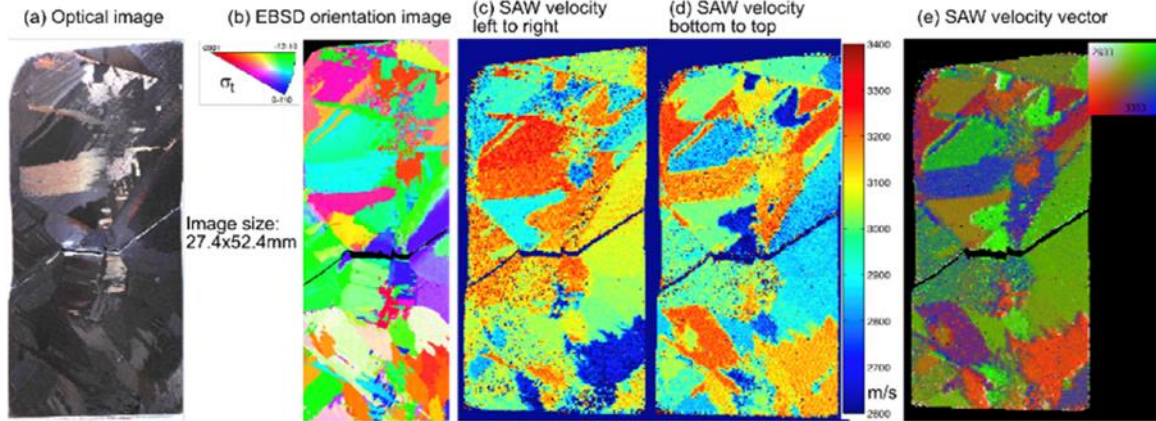
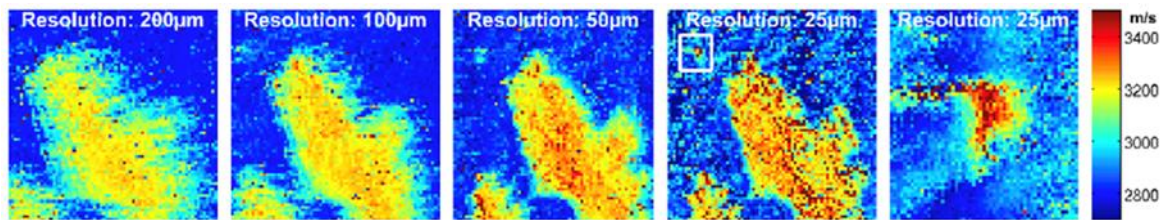Figure C-12. Images of a Ti-685 sample, 27.4x52.4mm in size

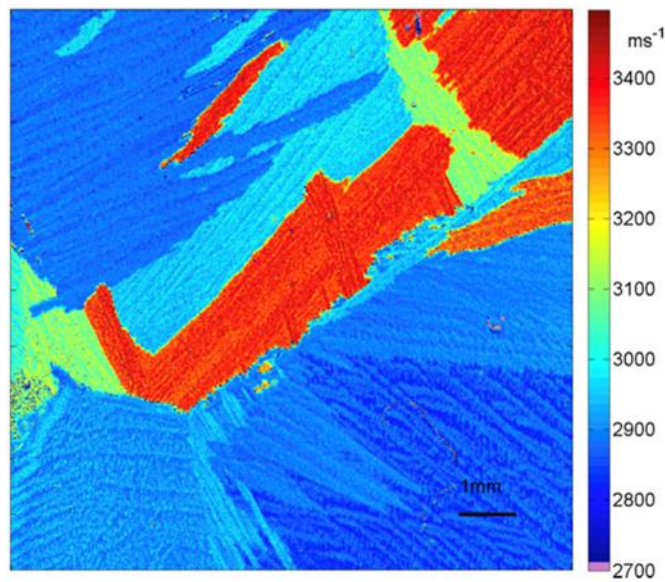Figure C-13. SRAS velocity maps of a Ti-685 sample, acquired using an excitation frequency of 328MHz

Figure C-14. SRAS velocity image of coarse-grained Ti-685 at spatial resolution of ~50 µm
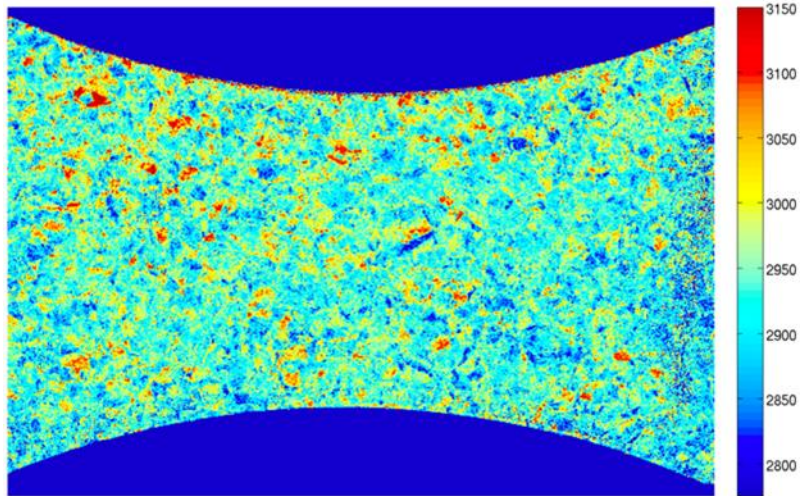
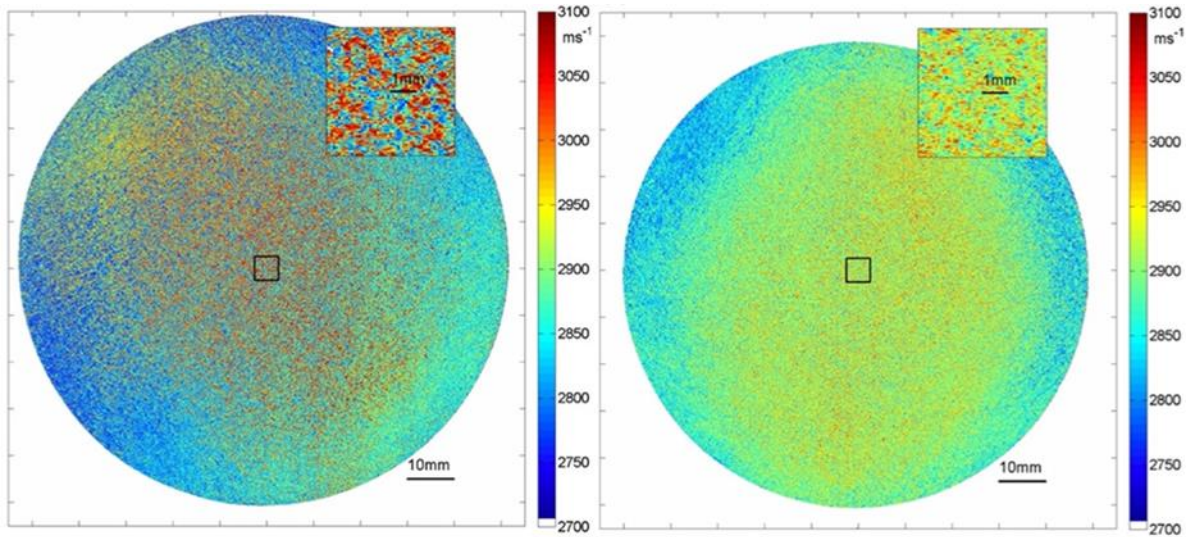Figure C-15. SRAS velocity map of Ti-6-4 sample using excitation frequency of 164 MHz

Figure C-16. SRAS velocity maps of Ti-6Al-4V billet cross sections from two different manufacturing routes
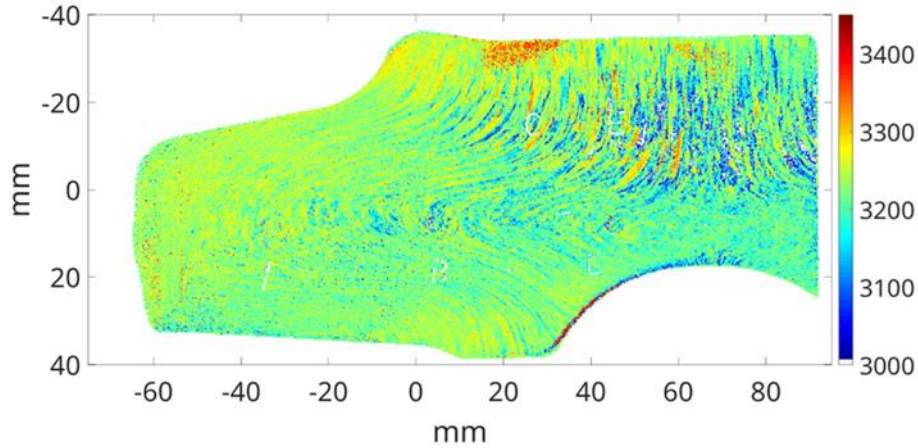
Figure C-17. SRAS velocity map of a titanium forging cross section
Grain/metal flow lines are evident; Figure courtesy of W. Li (Nottingham)

Having established a method to obtain reliable velocity measurements, the next challenge involves converting these measurements to crystallographic orientation which has been addressed by Dryburgh et al. (2020). The process involves collecting velocity maps with SAW propagation in several directions and then comparing the results to pre-calculated results from a velocity model that predicts orientation-dependent SAW velocity. The model relates crystallographic orientation and elastic constants to SAW velocity, but the inverse problem is ill-conditioned and does not lend itself well to analytical solutions. To circumvent this problem, the authors used cross-correlation to compare experimental to predicted SAW velocity surfaces, which was found to be robust to experimental noise. An example of this procedure is shown in Figure C-18. The location with the highest figure of merit is marked by the intersection of the dashed lines in (c). The orientation identified from the cross-correlation corresponds to (b) (Dryburgh, et al., 2020).
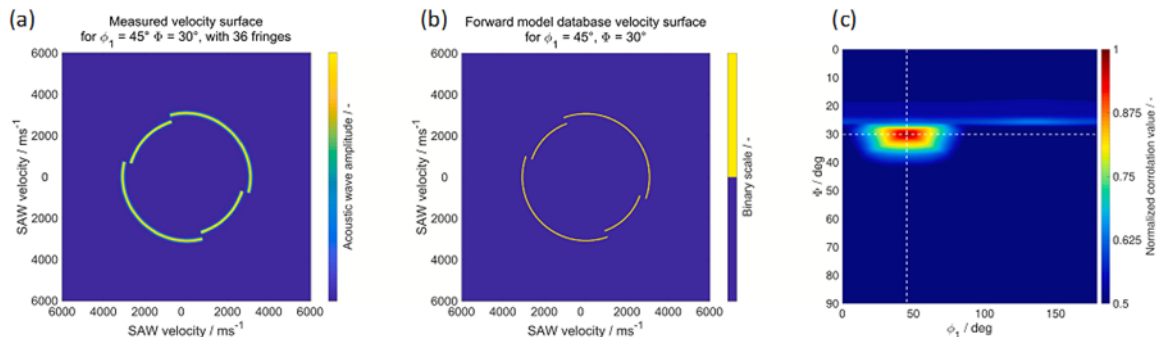

Figure C-18. (a) Measured SAW velocity surface (b) Model results (c) Results of cross-correlating (a) with entire SAW velocity surface database

C-21

The accuracy of the SAW model-based inversion methodology was established by comparing SRAS and EBSD data collected from the same region of a commercial purity titanium sample. The transverse isotropic linear elasticity of the hexagonal crystal means that the velocities are uniform in the basal plane. Hence, it is only possible to recover the c-axis orientation (which is described by the first two Euler angles). The second Euler angle, Φ, describes the inclination of the c-axis relative to the specimen surface while the first Euler angle, φ_1, describes azimuthal orientation of the c-axis. The accuracy of the determined orientation was found to be a function of the number of velocity measurements made in various directions, the velocity resolution (as defined by the full width at half max (FWHM) of the signal bandwidth), the signal to noise ratio, systematic measurement error, and the actual crystallographic orientation of the grain of interest (Dryburgh, et al., 2020).

It was found that measuring the velocity in at least 3 directions significantly reduced the error in the orientation determination for both Euler angles. Increasing the number of measurements to 90 reduced the error by ~0.5°. The orientation-dependence of the accuracy of the inversion was related to the orientation-dependence of the elastic constants, which changes slowly initially with increasing Φ and then increases especially in the range $40° \leq \Phi \leq 60°$. In addition, there is a mode hop that occurs at $\Phi = 28°$ below which a supersonic wave is observed and above which a conventional Rayleigh wave is observed when $60° \leq \varphi_1 \leq 120°$. This results in distinct errors for grains with Φ greater than or less than 28°. Determining the orientation for $\Phi \to 0°$ is particularly difficult as the velocity surface is quasi-isotropic and sub-m/s velocity resolution is required to distinguish the slight ellipticity of the surface making this a special case. The mean errors were found to be $\varphi_1 = 4.81°$ and $\Phi = 6.48°$ in the Rayleigh regime ($\Phi \geq 28°$) and these approximately doubled in the supersonic regime. Figure C-19 and Figure C-20 show maps of the SRAS-determined orientations compared to EBSD for be φ_1 and Φ. In general, there is very good agreement across the field and the largest errors are attributable to the special cases where the basal plane is in or near the plane of polish.
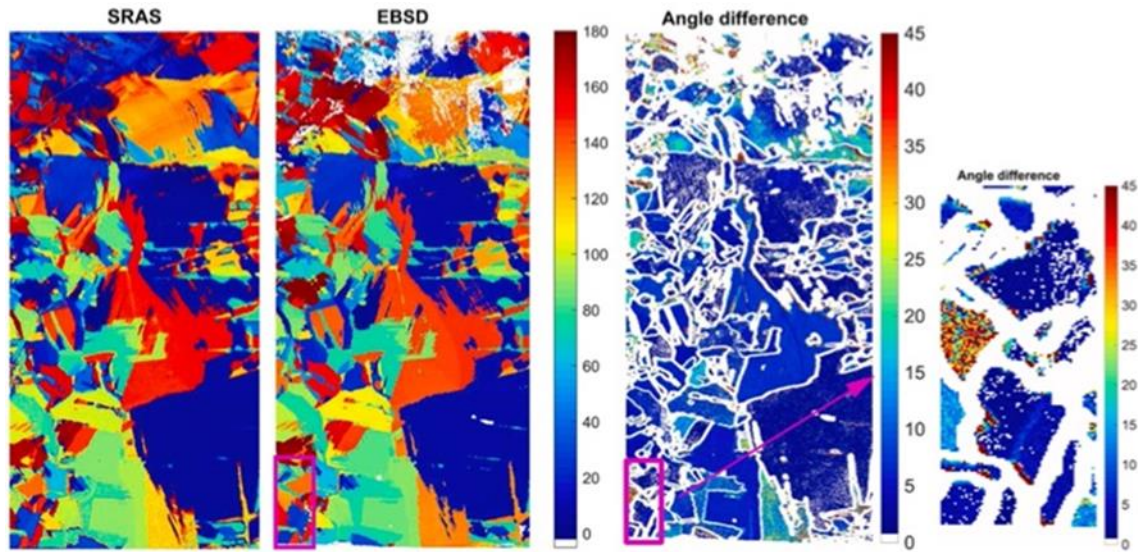
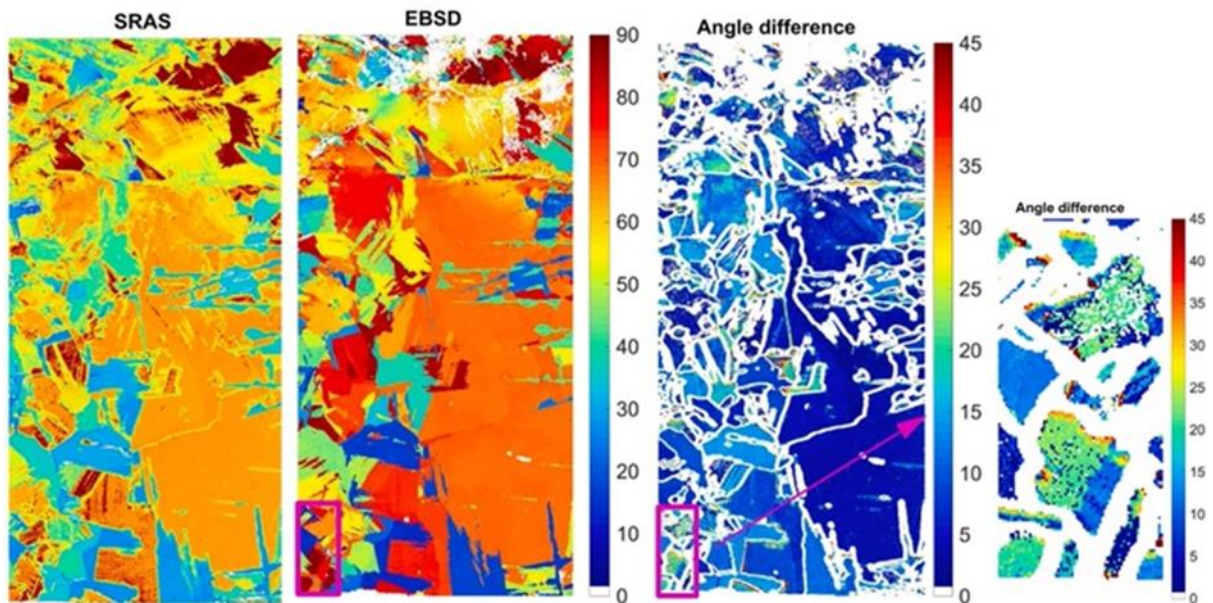Figure C-19. Comparison of SRAS and EBSD results for φ_1

Figure C-20. Comparison of SRAS and EBSD results for Φ

In summary, SRAS has many strengths, including that it can be performed in air using lasers with sufficiently low energy that they do not ablate and damage the sample. While most applications have been performed on materials with surface roughness $R_a \leq 100$ nm, the Nottingham team reports that using different detectors will make the method tolerate rougher surfaces with the ultimate goal of analyzing finish-machined components with curved surfaces

(Du & Zhao, 2017; Smith, et al., 2014) . The method can be applied to large samples and is limited only by the stage travel limits and, potentially, data analysis routines. It is relatively fast in its current state (up to ~2,000 points/second) with a path for further improvements (theoretically limited by the repetition rate of the laser). The method can make highly accurate velocity measurements and hence can be used to measure elastic constants in grains as small as ~30 µm in diameter (Du & Zhao, 2017) owing to its reasonably good spatial resolution (25~50 µm). While not discussed explicitly above, the technique can also be used for materials with cubic symmetry as well (Du & Zhao, 2017), which is an advantage over polarized light techniques that only work with optically anisotropic crystal symmetries (Clark, et al., 2019; Sharples, Clark, Li, & Somekh, 2008).

Despite these advantages, there are still a few weaknesses of the technique necessitating further development. First, it can only determine c-axis orientation and not the rotation about c-axis. This may be acceptable for some purposes (e.g., general characterization for relative comparisons of heats/processing routes, etc.), but may not be suitable for all (e.g., obtaining grain orientations for input into crystal plasticity finite element models, for example). Determining the crystallographic orientation from the SAW measurements requires accurate knowledge of elastic constants, which vary by alloy and even with in-spec variations in composition for a given alloy. While the technique itself can be used to measure the elastic constants, there is error associated with this measurement. Du and Zhao (2017) have used a very similar approach as SRAS to measure elastic constants in a range of materials with various crystal symmetries and observed up to a 6.8% variation in C_{44} while all other measurements were within 3%. While the spatial resolution is reasonable, it is not as good as other techniques like EBSD, which now has comparable speed to SRAS. The need to scan in multiple directions to obtain crystal orientation also adds time, but the aforementioned tolerance to surface roughness and the ability to scan curved surfaces will really set this technique apart from others.

At the time of writing, there are no commercially available SRAS systems available on the market. The system at Nottingham University was the only fully functional system for many years. Recently, Ales and Collins (2020; Collins & Ales, 2022) from Iowa State University have been working to integrate a SRAS system with the automated serial sectioning system, Robo-Met.3D (UES Inc., 2023) as a high-speed methodology to collect large volumetric EBSD-like datasets containing MTRs. The system is shown in Figure C-21 (images courtesy of T. Ales and P. Collins, Iowa State) in which (a) depicts the RoboMet with a laser safe enclosure and the inset shows the design of the inverted SRAS microscope. Figure C-21(b) shows tightly packed optics of system and beam paths while Figure C-21(c) shows multiple wave propagation angles for a single slice, rotated for subsequent alignment into a velocity file. There are plans to

commercialize these systems through the company Coherent Photon Imaging, LLC. IHI Corporation reported the first results from this system at the 2023 World Conference on Titanium. Specifically, Tsukada et al. (2024) have performed 3D analysis of three lots of material having MTRs of different sizes using this system and compared them with the sizes obtained by the ultrasonic scattering model of (Pilchak, Li, & Rokhlin, 2014b). Figure C-22 shows the basic experimental setup along with examples comparing EBSD to SRAS on the first slice and an example of the 3D reconstructed MTRs (Tsukada, et al., 2024). Meanwhile, Figure C-23 shows that there is reasonable agreement between the ultrasonic backscattering model, which requires measurements be made in three orthogonal directions, and the 3D measured MTR volumes.
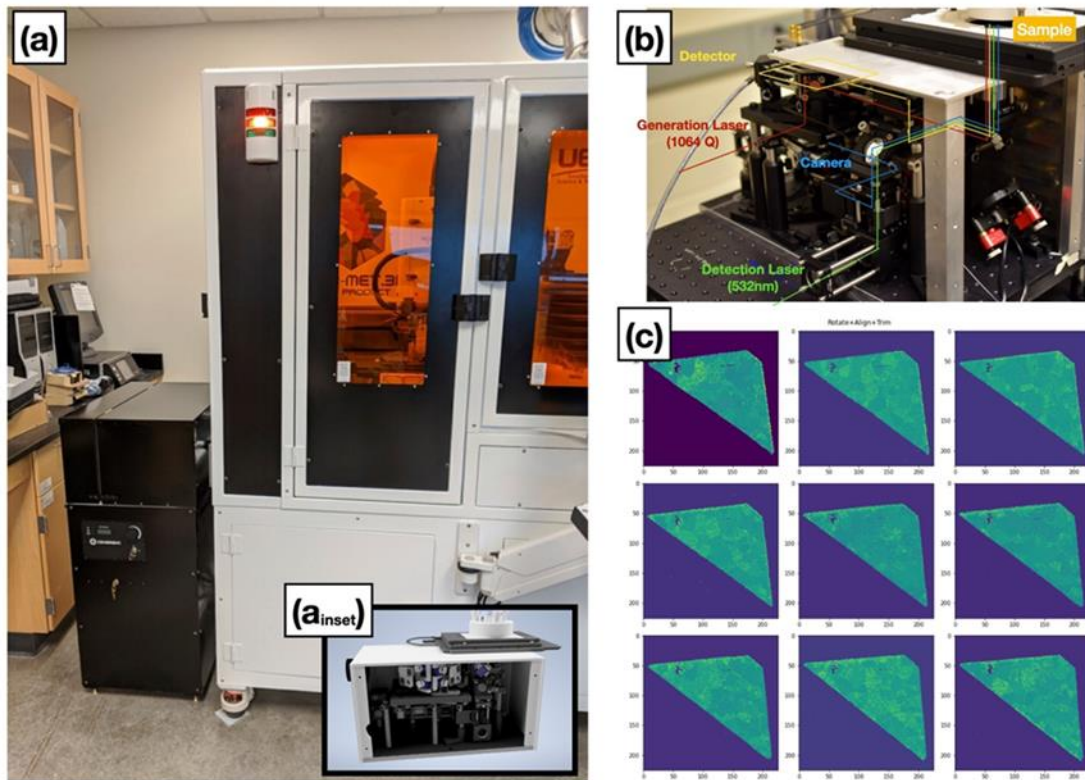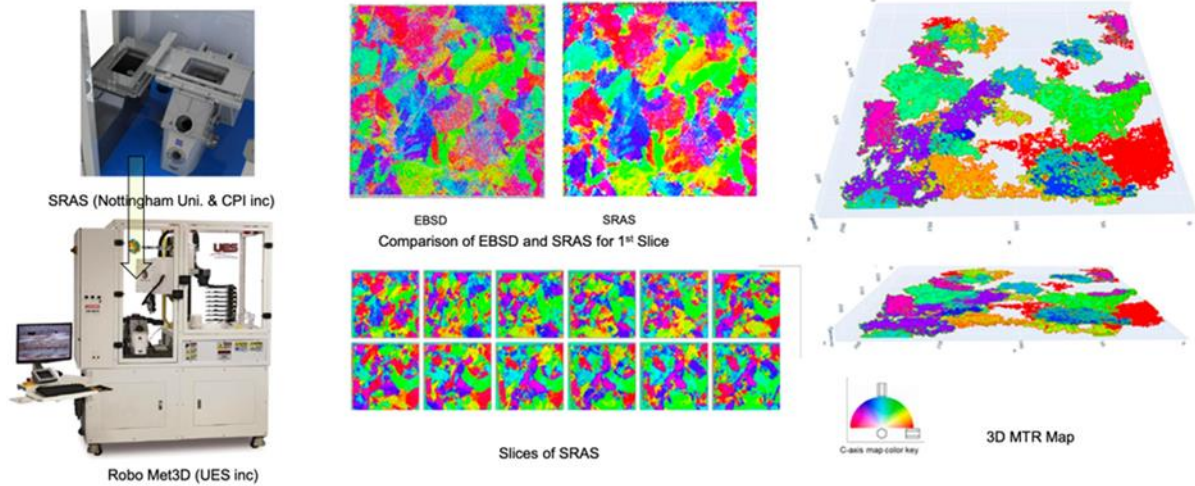

Figure C-21. 3D SRAS system

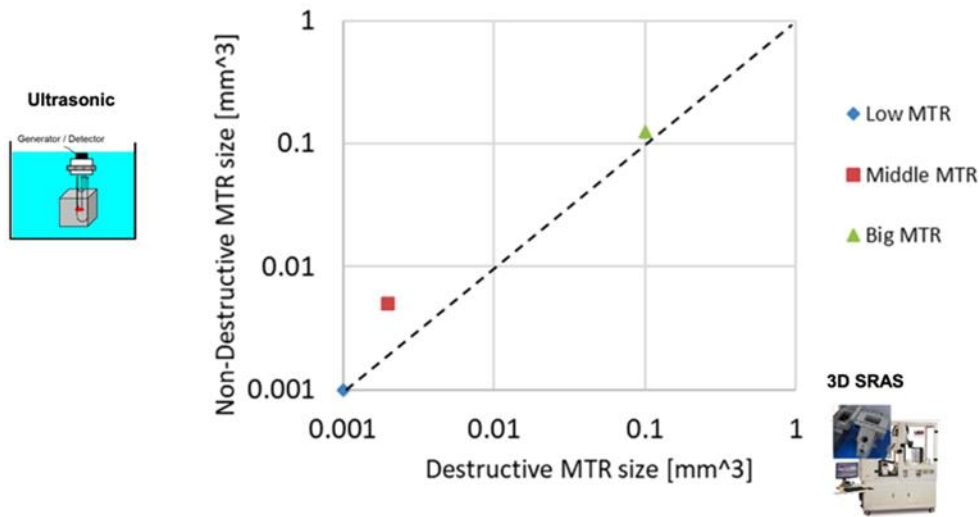Figure C-22. 3D analysis of MTRs using EBSD, SRAS, and RobotMet.3D by IHI Corporation

Figure C-23. Comparison of MTR sizes measured with destructively with SRAS and nondestructively with ultrasound

Eddy current testing

Eddy current testing (ECT) is a technique which relies on the process of electromagnetic induction. An alternating current is passed through a probe which creates a primary magnetic field. The probe is brought in close proximity to the part to be inspected and the expanding and contracting magnetic field induces a localized, secondary field (current) in the part (Figure C-24, reprinted with permission from, ©Iowa State University Center for Nondestructive Evaluation

(CNDE)). When the material is homogeneous and free from defects, the currents are well behaved and uniform. If a discontinuity like a crack is present, the secondary field will be disturbed as the current flows around the defect like an eddy in a stream of water – which is where the technique gets its name. This concentration of current can be detected and displayed to an operator to further interrogate that location and confirm the nature of the flaw.

ECT is sensitive to relatively small flaws. While it is routinely used to detect 750 µm x 375 µm cracks 90% of the time with 95% confidence, smaller cracks can be detected at a reduced probability of detection (POD). In fact, microstructural anomalies like surface-connected nonmetallic inclusions in nickel superalloys have been detected. The detection capability is limited by the size of the coil used for the inspection process. These coils are typically hand-wound under a microscope by skilled technicians and hence they are manufacturing-limited. If a smaller coil could be used, smaller flaws could be detected more reliably. Current commercially available coils are typically 0.5 to 1.0 mm in diameter.

Titanium exhibits a moderate anisotropic conductivity with a variation of ~6% between the c- and a-axes. Thus, when MTRs approach a sizable fraction of the coil diameter, there is substantial background noise in the response. This makes flaw detection difficult but does lead to the potential for nondestructively characterizing MTRs with ECT. This would be highly beneficial as ECT is used routinely to inspect new-make parts and also for routine inspection of in-service components both in hand-held and fully automated formats.
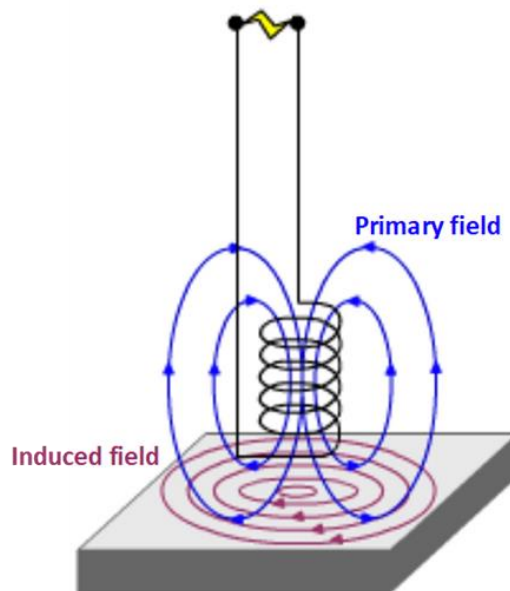

Figure C-24. Basic principles of eddy current testing

Cherry et al. (2016; 2014) have investigated the experimental feasibility using ECT to characterize microstructure of Ti alloys and also developed two different models to simulate eddy current response from a known orientation field. The authors prepared a coarse-grain, fully lamellar Ti-6Al-4V sample by heat treatment above the beta transus followed by slow cooling. The goal was to ensure that the alpha colony size was larger than the coil size so that the orientation-dependent conductivity of each grain could be isolated. The authors used a scanning ECT system to successfully map the microstructure (Figure C-25). Regions where the coil, which had inner and outer diameters of 1.0 and 1.5 mm, respectively, was contained within a single colony showed uniform conductivity with shapes that matched the underlying colony while regions with small colonies which had overlapping contributions to the conductivity did not directly match the microstructural morphology. The first synthetic aperture model, which essentially averaged material response beneath the coil, did a reasonable job at predicting the ECT response (Figure C-25 (c)). The second, and more rigorous model, improved on this approach by deriving the response from Maxwell's equations and ultimately calculating the impedance of the coil (Cherry M. , Sathish, Mooers, & Pilchak, 2016). An example image obtained from a scanning eddy current probe on an alpha+beta forged material is shown in Figure C-26. In this image, the forging direction is horizontal and the elongated streaks correspond to MTRs in the dead metals zone while the center of the forging contained nominally equiaxed or much lower aspect ratio MTRs (image courtesy of Matthew Cherry, AFRL).
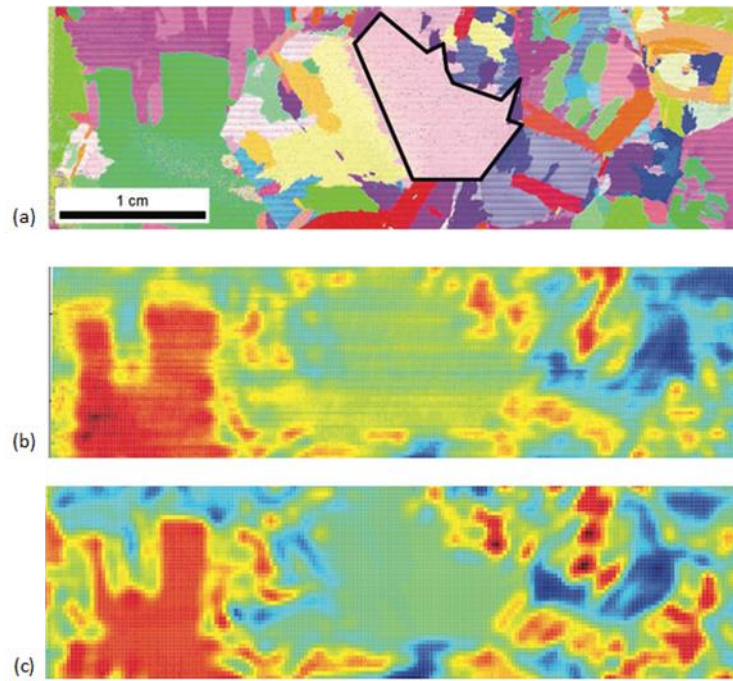
Figure C-25. (a) Inverse pole figure map of coarse-grain, fully lamellar Ti-6Al-4V sample
with (b) measured and (c) simulated eddy current response
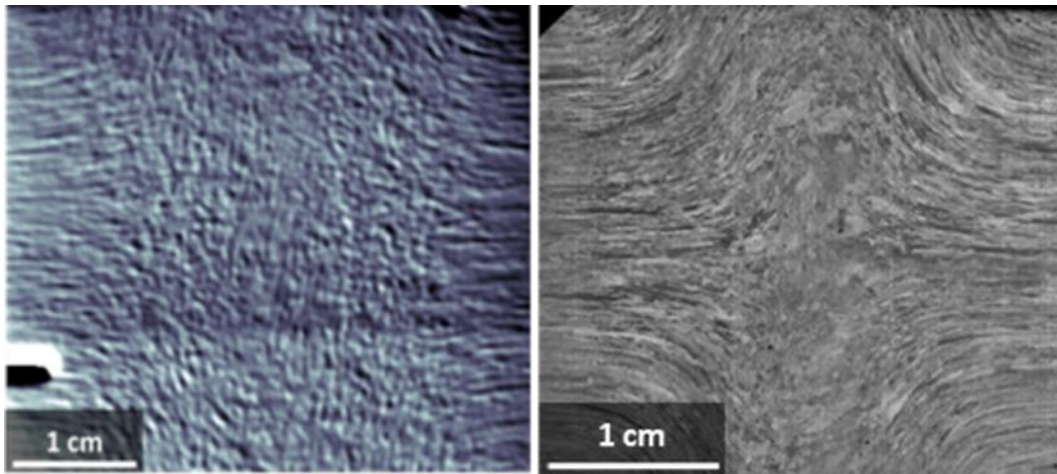

Figure C-26. (a) Eddy current response and (b) polarized light microscopy image of a forged
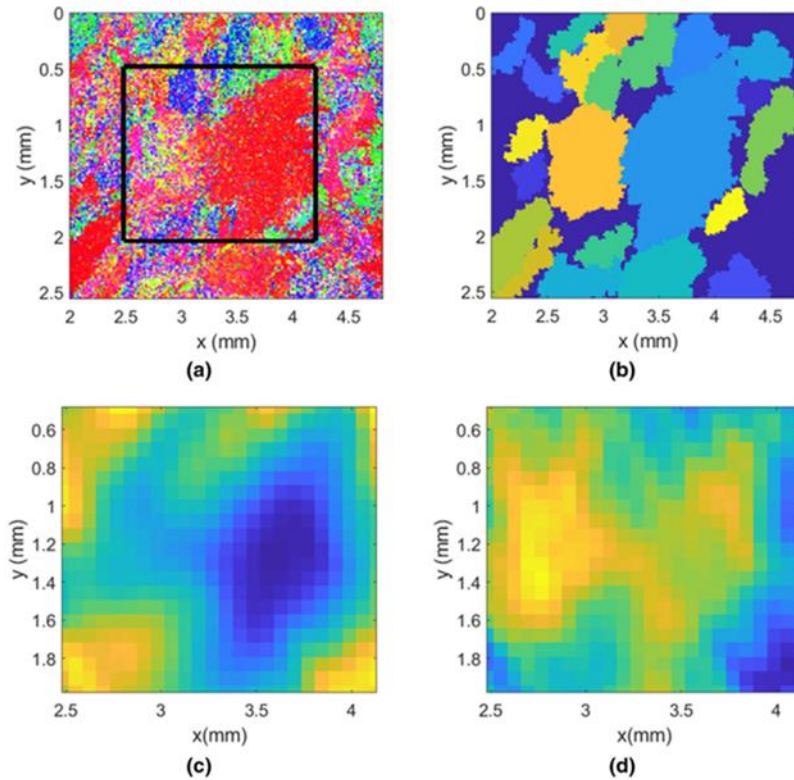Ti-6242 specimen

Figure C-27. (a) EBSD IPF map of a Ti-6Al-4V sample (b) DREAM.3D segmentation of EBSD data (c) Imaginary and (d) real portions of simulated Eddy current data

Homa et al. (2021; 2022) have made steps toward solving the inverse problem to obtain MTR orientation from eddy current response. Beginning with the forward model (Figure C-27) developed by Cherry et al. (2016), the authors modified the model to account for the fact that the grain (MTR) size is not known *a priori* and also to include MTR-specific ODFs (termed the crystallite ODF or cODF). The problem is challenging because there is not a unique eddy current response for a given set of fixed cODFs. This is due to the fact that the spatial distribution of the orientations will impact the signal. To get around this, the authors used an approximate Bayesian computation due to the inability to formulate a likelihood function. This method uses a modified posterior distribution obtained from a simulated dataset. Then, a Monte Carlo routine is used to identify the cODF that results in the best simulated eddy current response. Inversion results for four MTRs are shown in Figure C-28 with additional MTRs analyzed in the paper (Homa, Cherry, & Wertz, 2022). The method does a reasonable job capturing the general orientation of the c-axis both in terms of φ_1 (azimuthal) and Φ (inclination) and also predicts the distribution of crystallographic orientations as well. In some cases, the spread in orientations is also reasonably captured (e.g., 1 and 3). Because the MTR cODFs show essentially one c-axis orientation in the true experimental data, the alloy investigated presumably had a high-volume fraction of primary

C-30

alpha. Further work will be needed to address samples with a lower volume fraction where the transformation texture may lead to multiple peaks in the cODF corresponding to multiple c-axis orientations. This may prove challenging since ECT involves a volumetric sampling (though the skin depth is relatively shallow) and hence provides an average response. Thus, as a thought experiment, if there were an MTR comprised of 50% primary alpha c-axis texture perpendicular to the surface and 50% transformed beta with c-axes in the plane of polish, the impedance would be consistent with that of an MTR with all c-axes inclined 45° to the plane of polish.

While absolute cODF determination will prove challenging, it does not diminish the potential to use ECT to characterize general MTR characteristics for relative comparisons across a fleet of components, for example. Existing and new techniques to quantitatively analyze and compare the MTR-induced noise in eddy current scans can be used to discriminate between low, medium, and high degrees of microtexture. For this reason, for components scanned on automated ECT stations, it is recommended that raw data is stored for each spatial location on the component at new-make and at overhaul. Care should be taken to use a common reference frame for all scans. These data can be reanalyzed later if there are any situations that require understanding components with high degrees of microtexture, for example.
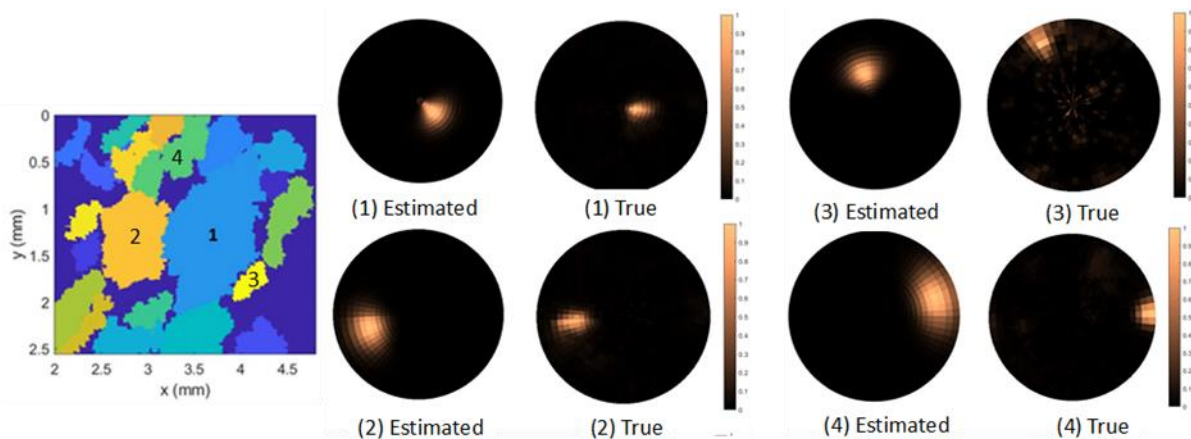

Figure C-28. Comparison of forward-model-estimated MTR cODF on (0001) pole figures

Resonant ultrasound spectroscopy

Livings et al. (2019) explored the use of resonance ultrasound spectroscopy (RUS) and, more specifically, process compensated resonance testing (PCRT) to detect MTRs in finish machined components. PCRT combines traditional resonance ultrasound spectra with advanced statistical analysis designed to sort parts in an automated fashion based on a pass/fail criteria. A major potential benefit of PCRT is that it is a fast, accurate, full-bodied technique capable of scanning

an entire part in ~30 seconds. Livings et al. (2019) performed a feasibility study using modeling and simulation to assess the sensitivity of the PCRT technique to MTRs in 100 simulated turbine engine disks. The authors presented a methodology to populate MTRs into the disks and then simulated the resonance modes to determine the robustness of the method to slight variations in geometry and material properties. The authors used pattern recognition and machine learning tools to determine the combination of resonance modes that were most influenced by MTRs. The authors concluded that PCRT is a viable approach to sorting finished components based on the presence of MTRs. The algorithm sorted 95% of the components correctly and of the missorted parts, 44% were found to have diffuse, low intensity MTRs.

Heat tint

Harper et al. (2007) demonstrated the power of heat tinting in the metallographic inspection of titanium alloys. In this process, a metallographically prepared sample is subjected to a brief heat treatment, which forms a thin oxide scale on the surface. Variations in the local composition, phase morphology, and crystallographic orientation affects the local oxidation rate. These regions appear distinct under light optical microscopy and hence reveal information about the state of microtexture in the material. While it was not possible to obtain specific crystallographic orientations, the technique provides a simple, large-area, cost-effective method to obtain qualitative and potentially semi-quantitative information about the size, shape, and frequency of MTRs in semi-finished and finished product forms. The authors optimized the heat treatment process and determined 566 $^{\circ}$C for 8~10 min was suitable to form a straw-colored oxide. Other time and temperature combinations either produced insufficient contrast or a blue, overoxidized condition, both of which resulted in poor contrast under optical metallography. An example of the heat tinting technique is shown in Figure C-29.
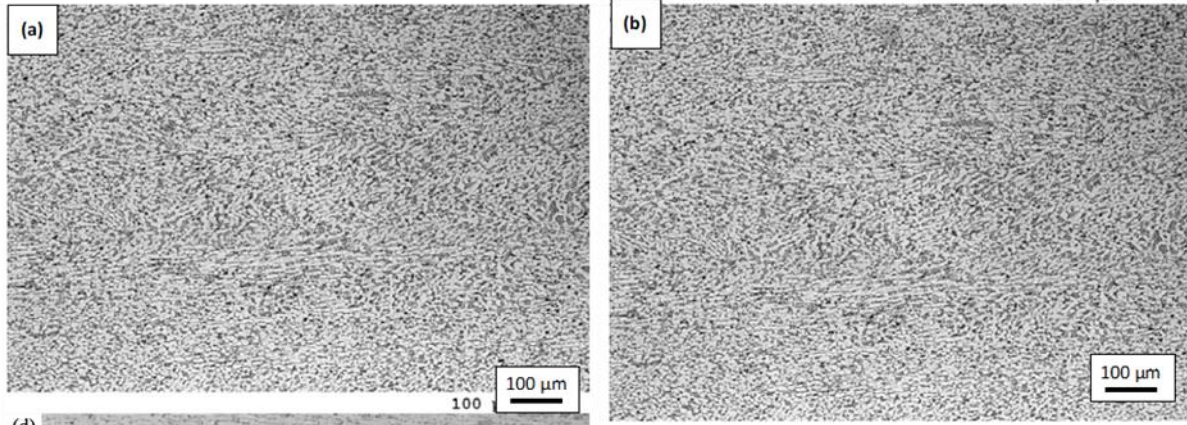
Figure C-29. (a) Conventional optical micrograph and (b) optical micrograph of heat tinted Ti-6Al-4V

Under an Air Force MAI Program (Cold Dwell Fatigue in Titanium Alloys Program), additional effort was performed relative to heat tinting. The AIPT collected large-area EBSD maps and then heat tinted the samples. Optical images were collected and then the images were segmented using the advanced image processing software MIPAR (Figure C-30). The segmented images were then analyzed using a specialized DREAM.3D pipeline to determine the size of the MTRs in each heat tinted sample.

The MTR sizes in terms of area quantified via heat tinting were compared with those obtained by segmentation of EBSD data (Figure C-31). Inspection of the cross-plotted data reveals there is some correlation up to MTR sizes of 3×10^4 μm^2 with a slight bias toward overestimating the MTR size. Beyond this size, large variations were observed between MTR and EBSD sizes. It is also noteworthy that an attempt was made to develop a correlation between the heat tint shade and local crystallographic orientation resulting in the inverse pole figure diagram in Figure C-30. While there is limited orientation resolution in this method, it has demonstrated to be a viable, fast, and low-cost method to assess large areas of material for screening purposes.
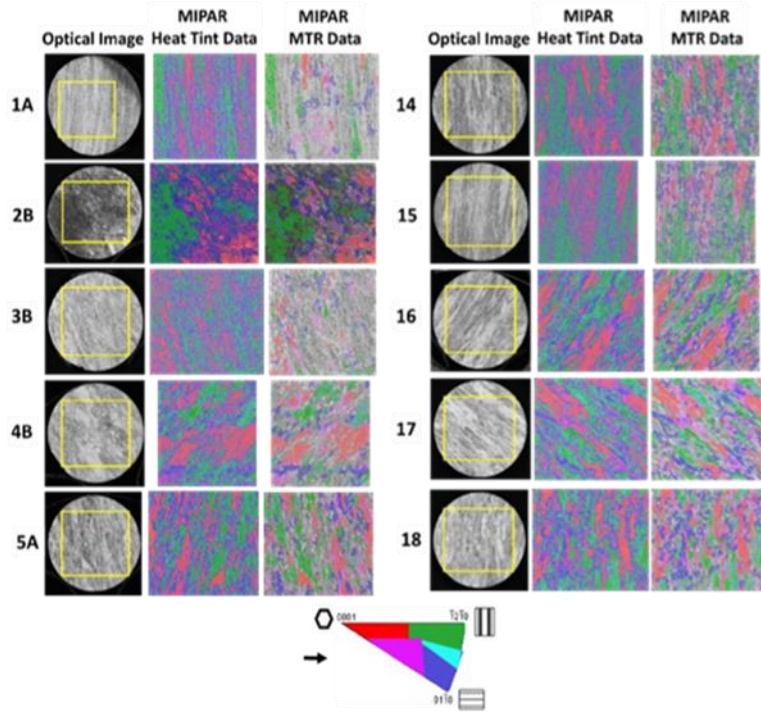
Figure C-30. Heat tinting results for samples containing various MTR sizes and morphologies
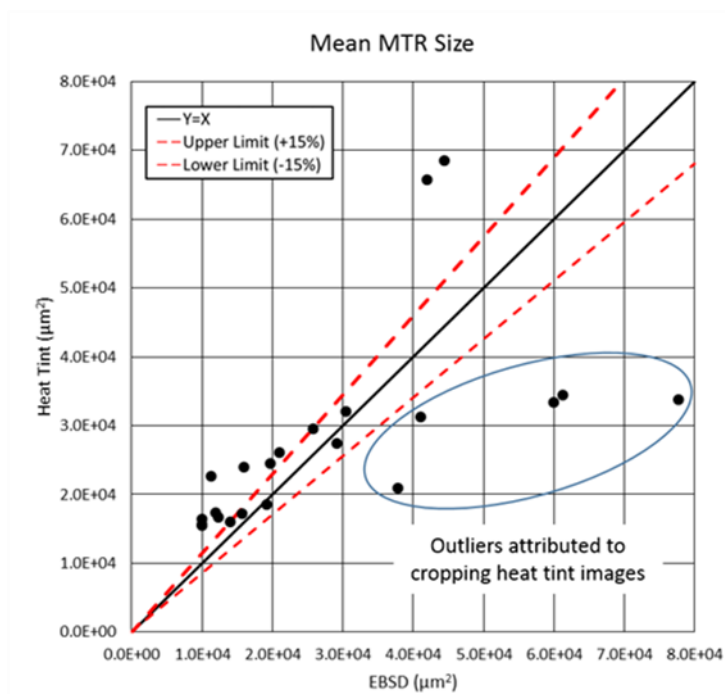

Figure C-31. Cross plot of MTR metrics derived from heat tinting and EBSD